Non-Polluting Composites Repair and Remanufacturing for Military Applications

PP1109

FINAL REPORT

1 Jan 1998 to 30 Sep 2002

A Final Report for
the SERDP office by

Army Research Laboratory

16 December 2002

Strategic Environmental Research and Development Program

Improving Mission Readiness Through Environmental Research

Table of Contents ……..i

List of Figures ……...xii

List of Tables ……...xxv

Executive Summary ……...xxviii

Synopsis of the Program …….xxix

1 ELECTRON-BEAM RESIN FORMULATION **1**

1.1 E-BEAM PREPREG 1

1.1.1 Selection Criteria *3*

1.1.2 Formulation Approach *4*

1.1.3 Resin Properties *6*

1.1.3.1 Density and Shrinkage 9

1.1.3.2 Thermal and Cure Characterizations 10

1.1.3.3 Fracture Toughness 10

1.1.3.4 Flexural Properties 12

1.1.4 Composite Properties *14*

1.1.4.1 General Resin/Composite Evaluations 14

1.1.4.2 AS4/CAT-M, an Optimized System 14

1.1.4.3 AS4/T-17 Prepreg, an Optimized System 17

1.2 E-BEAM VARTM RESINS 22

1.2.1 Selection Criteria *22*

1.2.2 Formulation Approach *23*

1.2.3 Resin Properties *25*

1.2.3.1 Design 25

1.2.3.2 Electron Beam Dose Effects 27

1.2.3.3 Viscosity Evaluation 27

1.2.3.4 Thermal and Cure Characterizations 28

1.2.3.5 Toughness and Strength Evaluations 32

1.2.4 Summary of Resin System Results *34*

1.2.4.1 CCM1 Resin Series 34

1.2.4.2 CCM2 Resin Series 37

1.2.4.3 CCM3 Resin Series 38

1.2.4.4 Cationic VARTM Resins 41

1.2.5 Process and Property Characterizations *45*

1.3 E-BEAM ADHESIVES 48

1.3.1 Selection Criteria *48*

1.3.2 Formulation Approach *49*

1.3.2.1 Epoxy Adhesive Toughening 50

1.3.2.2 Infinite Shelf Life Formulation Methods 51

1.3.2.3 Cationic Epoxy-Type Film Adhesives 51

1.3.2.4 IPN-Type Film Adhesives 55

1.3.3 Vacuum Bag Consolidation *56*

1.3.4 IPN Paste Adhesives *57*

1.4 BOND STRENGTH 58

1.5 E-BEAM REPAIR ADHESIVE FORMULATION 59

1.5.1 E-Beam Repair Adhesive Selection Criteria *59*

1.5.2 E-Beam Repair Adhesive Results *60*

2 ELECTRON BEAM RESIN AGING 63

2.1 APPROACH TO RESIN AGING STUDY 64

2.2 RESULTS OF RESIN AGING STUDY 65

2.3 CONCLUSIONS FOR RESIN AGING STUDY 71

3 REAL TIME *IN-SITU* SPECTROSCOPIC CHARACTERIZATIONS 71

3.1 EXPERIMENTAL 72

3.2 KINETIC MODEL DEVELOPMENT 74

3.3 UV AND EB KINETICS RESULTS 78

3.3.1 UV-Induced Cationic Polymerization *78*

3.3.2 EB-Induced Cationic Polymerization *81*

3.3.3 Influence of Water on Cure Behavior *84*

3.4 COMPREHENSIVE UNDERSTANDING OF EB KINETICS 85

4 E-BEAM REPAIR SPECIMEN ANALYSIS 86

4.1 TEST PANEL AND TEST RESULTS 86

4.2 ANALYTICAL MODEL DESCRIPTION 90

4.3 TEST RESULTS CORRELATION TO ANALYTICAL MODEL 91

4.4 SUMMARY 93

5 EB VARTM DEMONSTRATION ARTICLE 93

6 COST COMPARISONS OF OVEN AND ELECTRON-BEAM PROCESSING .. 98

6.1 PROGRAM DESCRIPTION 99

6.2 ASSUMPTIONS 104

6.3 COST OF CURING 106

6.4 SIMULATIONS RESULTS 107

6.4.1 Resin System 108

6.5 CONCLUSIONS 110

7 INDUCTION-BASED REPAIR AND REMANUFACTURING 112

7.1 BACKGROUND ON INDUCTION 113

7.1.1 Conventional Bonding Methods 113

7.1.2 Induction Heating. 114

7.1.2.1 Conductive Mesh Susceptors 114

7.1.2.2 Magnetic Particle Susceptors 115

7.1.2.3 Carbon-Fiber Composites 116

7.2 BENEFITS 117

8 MESH SUSCEPTORS –DEVELOPMENT 118

8.1 CHARACTERIZATION OF CURE KINETICS 118

8.2 FABRICATION OF SINGLE-LAP SHEAR SPECIMENS 121

8.3 PERFORMANCE COMPARISON OF ADHESIVE SYSTEM 124

8.4 PERFORMANCE OF BONDED REPAIR 125

8.4.1 Materials 126

8.4.2 Test Procedures 126

8.4.2.1 Single-Lap Shear Specimens 126

8.4.2.2 Double Cantilever Beam Specimens 127

8.4.3 Manufacturing Considerations *127*

8.4.4 Conventional Oven-Cure of Adhesives *127*

8.4.5 Induction Cure of Adhesives *128*

8.4.6 Materials Results *129*

8.4.6.1 Single-Lap Shear Specimens Tested in Tension 129

8.4.6.2 Double Cantilever Beam Specimens 131

8.4.7 Discussion *132*

8.4.7.1 Single Lap Shear Specimens Tested in Tension 132

8.4.7.2 Double Cantilever Beam Specimens 132

8.4.8 Bonded Repair Conclusions *133*

9 MESH SUSCEPTORS – APPLICATION TO REPAIR OF INTEGRAL ARMOR 133

9.1 INDUCTION BONDING EVALUATIONS 134

9.1.1 Thermal Criteria During Bonding and Repair *134*

9.1.2 Design for Uniform Heating *135*

9.2 SUSCEPTOR AND COIL DESIGN 138

9.3 COIL MOTION 139

9.4 COMPOSITE ARMOR SUBSYSTEM BONDING 141

9.5 ONE-STEP MULTI-LAYER COMPOSITE BONDING 143

9.6 CONCLUSIONS – MESH SUSCEPTOR REPAIR AND REMANUFACTURING 145

10 PARTICLE SUSCEPTORS - DEVELOPMENT 146

10.1 PARTICLE SUSCEPTORS IN ADHESIVES 146

10.2 EXPERIMENTAL MATERIALS AND EQUIPMENT 147

10.3 SAMPLE PREPARATION 150

10.3.1 Oven Cured Samples 151

10.3.2 Induction Cured Samples 151

10.3.3 Mechanical Testing Setup 152

10.4 ADHESIVE KINETIC CHARACTERIZATION 152

10.4.1 Particle Effect on Cure Kinetics 152

10.4.2 Degradation Limits 155

10.4.3 Mechanical Properties 156

10.5 PARTICLE EFFECTS 160

10.5.1 Particle Effect on Adhesive Cure Chemistry 160

10.5.2 Toughened Adhesives 160

10.5.3 Particle Effect on Bond Mechanical Performance 160

10.6 ANALYSIS OF STRENGTH TRENDS 161

11 PARTICLE SUSCEPTORS – APPLICATION TO REPAIR OF INTEGRAL ARMOR 162

11.1 BALLISTIC DAMAGE 162

11.2 RESULTS AND DISCUSSION 163

11.3 CIA REPAIR REQUIREMENTS 168

11.4 CONCLUSIONS 170

11.4.1 Magnetic Particle Susceptors for Induction Heating 170

11.4.2 Rapid Curing of Adhesive Systems. 170

12 CARBON-CARBON SUSCEPTORS – MODELS AND DEVELOPMENT 171

12.1 HEATING MECHANISMS FOR CARBON/THERMOPLASTICS 171

12.1.1 Theoretical Heating Model *172*

12.1.2 Joule Heating of Carbon Fibers *173*

12.1.3 Dielectric Hysteresis Heating at Fiber Junctions *173*

12.1.4 Heat Generated by Fiber Contact Resistance *174*

12.1.5 Material Properties *175*

12.1.6 Two-Ply Heating Model *175*

12.1.7 Two-Ply Model Results *177*

12.1.8 Through-Thickness Heating *178*

12.2 DEGRADATION STUDIES 179

12.2.1 Thermal Degradation Study *180*

12.2.2 Weight Loss Measurements *180*

12.2.3 Molecular Weight Characterization *182*

12.2.4 Electrical Degradation Study *183*

12.2.4.1 Mechanical Performance 184

13 CARBON-CARBON SUSCEPTORS – APPLICATION TO PROCESSING OF COMPOSITE SABOT 185

13.1 INDUCTION-BASED REMANUFACTURE OF THERMOPLASTIC COMPOSITE LAMINATES 185

13.2 PROCESS MODEL DEVELOPMENT FOR INDUCTION LAMINATOR 186

13.3 LAMINATOR PROCESS SPECIFICATION 186

13.4 MATERIAL DESCRIPTION 188

13.5 LAMINATOR PROCESS MODELS 188

13.5.1 Thermal Modeling *189*

13.5.2 Void Development *189*

13.5.3 Consolidation/Deconsolidation Model *189*

13.5.4 Coupled Bonding Model *190*

13.5.5 Intimate Contact Model *190*

13.5.6 Polymer Healing Model *191*

13.5.7 Coupled Bonding *192*

13.5.8 Viscosity Characterization of PEI *193*

13.6 SIMULATIONS TO ESTABLISH PROCESS SETPOINTS 193

13.7 INDUCTION COIL DESIGN 197

13.7.1 Laminator Coil Design *197*

13.8 FINAL LAMINATOR CONFIGURATION AND PROCESS SETPOINTS 198

13.9 EXPERIMENTAL LAMINATOR 200

13.10 PERFORMANCE AND QUALITY 201

13.11 CONCLUSIONS TO INDUCTION-BASED THERMOPLASTIC COMPOSITE LAMINATION 202

14 INDUCTION ELECTROMAGNETIC EFFECTS 203

14.1 INDUCTION PROCESSING 203

14.2 POSSIBLE DELETERIOUS EFFECTS OF INDUCTION FIELDS ON AIRCRAFT SYSTEMS. 203

14.3 HEATING EFFECTS 204

14.4 INTERFERENCE EFFECTS 205

14.5 MAGNETIC FIELD EMISSIONS 205

14.5.1 Electric Field Emissions *206*

14.5.2 Emission Standards for Antennas *207*

14.6 SUMMARY OF RECOMMENDATIONS 207

15 CO-INJECTION RESIN TRANSFER MOLDING FOR REPAIR AND REMANUFACTURING 208

15.1 SCALE-UP OF RESIN DOWN-SELECTION AND TESTING OF CIRTM COMPONENTS FOR NAVY MAST ENCLOSURE 211

15.2 PROCESSING & PROPERTIES OF CO-INJECTED RESIN TRANSFER MOLDED VINYL-ESTER/PHENOLIC COMPOSITES 212

15.2.1 Manufacturing Procedure 212

15.2.2 Materials 215

15.2.3 Short Beam Shear Testing 216

15.2.4 Double Cantilever Beam Testing 216

15.2.5 Durability Tests 219

15.3 FLAMMABILITY TESTING OF PHENOLIC/VINYL-ESTER CO-INJECTED COMPONENTS . 220

15.3.1 Processing 221

15.3.2 CIRTM Panel Testing 222

15.3.3 CIRTM Results 223

15.3.4 Conclusions 225

15.4 PROCESSING AND IMPACT TESTING OF MULTI-LAYER POLYURETHANE/EPOXY COMPOSITES 225

15.4.1 CIRTM Demo Processing 226

15.4.2 Impact Testing 228

15.4.3 Results and Discussion 228

16 ARMOR REPAIR 229

16.1 MECHANICAL PERFORMANCE OF UNDAMAGED AND REPAIRED ARMORS 229

16.2 MANUFACTURING PROCESS IMPACT 230

16.3 TEST COUPONS 231

16.3.1 Manufacturing Considerations 231

16.3.1.1 Backing Plate 231

16.3.1.2 Rubber Layer 232

16.3.1.3 Ceramic Strike Face 232

16.3.1.4 Cover Layer 232

16.3.1.5 Impregnation Resin 232

16.3.2 Manufacturing Processes 232

16.3.3 Single-Step Vacuum Assisted Resin Transfer Molding 232

16.3.4 Multi-Step Process 233

16.4 EXPERIMENTAL 233

16.4.1 Four-Point Bending 233

16.4.2 Test Matrix 234

16.5 FABRICATION OVERVIEW 234

16.5.1 Single-Step (VARTM) Manufactured CIA Beams 235

16.5.2 Multi-Step Manufactured Specimens 236

16.5.3 SC15 Multi-Step CIA Beam 236

16.5.4 SC11 Multi-Step CIA Beam 237

16.5.5 Effect of the Surface Mechanical Preparation on the Rubber Layer 238

16.5.6 Effect of the Surface Mechanical Preparation of the Rubber Layer 240

16.6 FABRICATION SUMMARY 241

16.7 STATIC AND BALLISTIC PERFORMANCE 241

16.7.1 Repair Designs 242

16.7.2 Initial Results 243

16.7.3 On-Going Research 244

17 COST ESTIMATES FROM CURRENT PRACTICE 244

17.1 ENVIRONMENTAL BASELINE 246

17.2 POTENTIAL ENVIRONMENTAL SAVINGS 251

17.2.1 Reduction in VOCs 251

17.2.2 Reduction in NO_x. 252

17.2.3 Reduction in Waste due to Shelf-Life Expiration. 252

17.2.4 Reduction in Production Debris Hazardous Waste. 252

17.3 COST SAVINGS. 253

17.4 EXPANDING COMPOSITES USAGE IN MILITARY ENVIRONMENTS 254

17.4.1 Joint Strike Fighter. 254

17.4.2 Advanced Enclosed Mast Sensor System. 255

17.4.3 Future Scout and Cavalry System. 255

17.5 SUMMARY OF COMPOSITE USE AND COST EVALUATION 256

APPENDIX A: STRAIN GAGE RESULTS FOR AIRCRAFT REPAIR 259

APPENDIX B: COST ANALYSES FOR EXAMPLE CASES 265

APPENDIX C: PUBLICATIONS FROM SERDP PP-1109 FUNDING 295

APPENDIX D: REFERENCES 307

LIST OF FIGURES

Figure 1. Example of cationic-based epoxy initiation reaction. 2

Figure 2. Example of cationic-based epoxy propagation reaction..... 3

Figure 3. Dynamic mechanical spectroscopy results for dry T-11 resin. 7

Figure 4. Dynamic mechanical spectroscopy results for wet T-11 resin. 7

Figure 5. Dynamic mechanical spectroscopy results for dry T-14 resin. 8

Figure 6. Dynamic mechanical spectroscopy results for wet T-14 resin. 8

Figure 7. Retention of dynamic storage modulus of neat T-11, T-14, and 3501-6 at various temperatures. 9

Figure 8. Schematic of compact tension test specimen (dimensions in inches). 10

Figure 9. Flexural strength of neat T-11 and T-14, dry and after saturation with moisture at 66°C/95% relative humidity. 13

Figure 10. Flexural modulus of neat T-11 and T-14, dry and after saturation with moisture at 66°C/95% relative humidity. 13

Figure 11. DSC of AS4/CAT-M Prepreg 14

Figure 12. 16-ply Vacuum-Bag-Cured AS4/CAT-M (100x). 15

Figure 13. 8-ply Vacuum-Bag-Cured AS4/CAT-M (100x). 15

Figure 14. 16-Ply Autoclave-Cured AS4/CAT-M (100x). 16

Figure 15. Photomicrograph of AS4/T-17 Laminate Showing Porosity. 19

Figure 16. Photomicrograph of AS4/T-17 Laminate with Improved Processing. 19

Figure 17. Mechanical Property Comparison of Porous and Nonporous Laminates. 20

Figure 18. Moisture Absorption of SBS Specimens. 21

Figure 19. SBS Strength of E-Beam-Cured Laminates. 21

Figure 20. Chemistry of an IPN-based VARTM resin. 24

Figure 21. Approach used to toughen the VARTM resin. 25

Figure 22. Percent Conversion of vinyl groups as a function of e-beam dose. 27

Figure 23. DMA plot for VCCM1.2 system 29

Figure 24. Storage and loss modulus as a function of temperature for post-cured VCCM1.1 and its derivative systems. 30

Figure 25. DMA results of post-cured VCCM1.2, VCCM4.2, and VCCMD.2 systems 30

Figure 26. DMA analysis for post-cured VCCMU3.1 and VCCMU31.1 resins 31

Figure 27. Wet DMA analysis of VCCM1.1 resin 32

Figure 28. SEMs of Fractured Surfaces of VCCM1.1 Resin and Derivatives: (a) VCCM1.1, (b) VCCM4.1, (c) VCCMD.1 33

Figure 29. SEMs of (a) VCCMU3.1 and (b) VCCMU3.1.1 34

Figure 30. Viscosity analysis of CCM1-based modified systems 35

Figure 31. DMA analysis of the CCM4 resin system. 36

Figure 32. Storage and loss moduli as a function of temperature for the CCM18 resin. 37

Figure 33. Viscosity analysis of CCM2-based modified systems. 38

Figure 34. Initial viscosity of the CCM3-based toughened systems. 39

Figure 35. Thermomechanical analysis of CCM26 (CCM3 with diluent D5 added). 40

Figure 36. C-stage curing viscosity of VEB-11 at 40°C. Working life = 90 minutes. 42

Figure 37. Photomicrograph of AS4/VEB-11 VARTM Laminate 43

Figure 38. Photomicrograph of E-Beam-Cured AS4/VEB-11 VARTM Laminate 44

Figure 39. Photomicrograph of Thermal-Cured AS4/VEB-11 VARTM Laminate 44

Figure 40. SBS Strength Comparison of Various AS4/VEB-11 Laminates 45

Figure 41. Flexural Strength Comparison of Various AS4/EB-11 Laminates 45

Figure 42. Property Map of VCCM1.1, VCCM4.1, and VCCMD.1 Systems 46

Figure 43. Slow-Dose Cure Profile for Adhesive Bond Curing. 54

Figure 44. Lap shear strengths of tested adhesive films. 55

Figure 45. Lap-Shear Results of Experimental E-Beam Adhesives 61

Figure 46. Adhesive Materials Submitted for CAI Investigation for Aerospace Applicability 62

Figure 47. FTIR Characterization for Cure of ADEP-01 at 30°C (□), 50°C catalyzed (o) and uncatalyzed (♦) 65°C (+), and 80°C (Δ). 62

Figure 48. Shelf life expires when material processing characteristics no longer meet specification limits. 63

Figure 49. Exploded view of sample between NaCl windows in sample holder. 65

Figure 50. MIR absorbance spectra for AF163-20ST adhesive film. Note the reduction in the 916 peak over a five-month period. 66

Figure 51. Performance of Thermal Versus E-beam Systems. 70

Figure 52. Schematics of the experimental setup used in the kinetic studies. 73

Figure 53. Plot showing reproducibility of experiments. Three runs were performed with DGEBA. UV light intensity = 45.8 mW/cm^2,T = 70C and initiator concentration = 0.68 wt.% 74

Figure 54. Glass transition temperature versus conversion of epoxy functional groups. 77

Figure 55. Comparison of data and model fit for PGE. UV light intensity = 40.5 mW/cm^2, T = 60 °C and initiator concentration = 0.44 wt% 79

Figure 56. Comparison of data and fit for PGE. UV light intensity = 12.05 mW/cm^2, T = 40°C and initiator concentration = 0.44 wt% 79

Figure 57. Comparison of data and model predictions based on PGE intrinsic rate values and no diffusion limitations for DGEBA. UV light intensity = 42 mW/cm^2, T = 60 °C and initiator concentration = 0.68wt% 79

Figure 58. Comparison of experimental data and diffusion limited reaction model predictions for DGEBA [UV intensity = 20 mW/cm^2, Temperature = 70°C and Initiator concentration = 0.185 wt% (k_{do}= 265043 and B=0.5911)]..... 80

Figure 59. Effect of initiator concentration and radiation intensity (left) and temperature (right) on the diffusion parameter k_{do} for DGEBA (UV experiments). For the temperature dependence plot, the intensity was 45 mW/cm^2 and the initiator concentration 0.68 wt%. 81

Figure 60. Typical experimental results and model predictions for PGE (EB experiments). Dose rate = 3750 rad/s, T=50°C and initiator concentration = 3 wt%..... 82

Figure 61. Relationship between initiation rate constant and EB dose rate obtained from experiments conducted using PGE (T=50°C and initiator concentration = 1 wt%)..... 82

Figure 62. Results for DGEBA (EB experiments) and comparison with model developed for PGE. Dose Rate = 7500 rad/s and initiator concentration = 1.06 wt%..... 83

Figure 63. Diffusion limited model predictions and experimental data for DGEBA. EB dose rate = 7500 rad/s, T = 50 °C and initiator concentration = 1.06 wt%. B=0.555 and k_{do} = 460817 liters/(mol·s) 84

Figure 64. Diffusion limited model predictions and experimental data for DGEBA. EB dose rate = 7500 rad/s, T = 60 °C and initiator concentration = 1.06 wt%. B=0.5568 and k_{do} = 993748 liters/(mol·s). 84

Figure 65. Plot showing the effect of water on the cure kinetics of DGEBA (T=60°C, Initiator concentration= 0.68wt% and UV Intensity = 42 mW/cm^2) 85

Figure 66. Drawing of Repair Coupon 87

Figure 67. Initial Nonlinear Behavior of Strain Gages with Specimen A-7. 89

Figure 68. Nonlinear Strain Behavior in Specimens A-8 and A-9. 90

Figure 69. Finite Element Model Used in Analysis 91

Figure 70. Strain Correlation of the Specimens 92

Figure 71. Stress Distribution in the E-Beam Adhesive 93

Figure 72. Tooling for aircraft access panel EB cure demonstration. 95

Figure 73. Carbon fabric preform lay-up of AS4 G-sized fibers on VARTM tool. 96

Figure 74. Viscosity profile of VCCM4 with PACM curing amine as a function of cure time at various isothermal temperatures. 96

Figure 75. Second Bag Lay-up Showing Porous Armalon 97

Figure 76. VARTM Access Panel after Thermal Staging Prior to E-Beam Curing. Note: A dry-spot resulted in the hexagonal region at the bottom of the photo. 97

Figure 77. Cost model flow diagram for processing of VARTM composites using "oven" or "e-beam" to cure the composite structure. 101

Figure 78. A typical EB facility layout including accelerator, processing, and shipping areas. Picture courtesy of Acsion Industries, (Pinawa, MB, Canada) 103

Figure 79. Typical arrangement for a vertical processing scan horn (a) and processing platform (b) for EB curing. Pictures courtesy of Acsion Industries, (Pinawa, MB, Canada). 103

Figure 80. EB penetration depth (in water) for selected commercial beam energies. 105

Figure 81. Production costs per square foot for EB ownership processing of flat panel composites (Model 3). 108

Figure 82. EB Processing of toll-based cure method for composite panels. 109

Figure 83. Production costs per square foot of composite panels for thermally cured systems in an oven. 110

Figure 84. Heating occurs when eddy currents are induced in a conductive material..... 114

Figure 85. Model of magnetic domains during hysteresis loss. Heat generation is caused by friction between magnetic domains. 115

Figure 86. The energy required to turn the internal magnet around once is proportional to the area enclosed by the hysteresis loop of the material. 116

Figure 87. Schematic outline of the heating mechanism in carbon-fiber-based composites where heating occurs primarily between conductive fibers of adjacent layers. 117

Figure 88. Comparison of kinetics model cure times to experimental cure times for varying degrees of cure. 121

Figure 89. Single-lap shear specimens were fabricated using this setup with copper wire mesh susceptors and Hysol EA9394 adhesive. <move to replace figure 77 above>.... 123

Figure 90. Temperature profile of lap-shear specimens demonstrating uniformity of heating in the process window offered by induction heating for repair. 123

Figure 91. Performance of the lap shear specimens. Induction-bonded specimens show better ±3σ performance than oven- or room-temperature-cured specimens..... 125

Figure 92. Induction-cured Hysol EA9359.3 single-lap specimens (Set-up and thermal field.) 129

Figure 93. Induction-cured DCB specimens (Set-up and thermal field.) 129

Figure 94. Single-lap shear specimens in tension..... 130

Figure 95. Thermal Gradient Effects During Induction Heating of Mesh Susceptors. 135

Figure 96. Temperature Profile for a Selected Solenoid Coil..... 136

Figure 97. Uniform and Non-Uniform In-Plane Thermal Gradients..... 136

Figure 98. Single-Step Processing of a Multi-Layered Composite. 137

Figure 99. Induction Heating Response of Mesh Materials for Similar Conditions. 137

Figure 100. Constant Temperature Achieved During Single-Step Processing of a Multi-Layered Composite. 138

Figure 101. Temperature profile of ceramic tile/steel mesh under vacuum with a conical coil. Difference between hot and cold spots is approximately 35°C 139

Figure 102. (a) and (b). Comparison of temperature profiles after 20 min. of heating (a) without and (b) with coil motion. The coil was moved rotationally about the center. 140

Figure 103. Temperatures of lines LI01 in Figures 95 (a) and (b). 140

Figure 104. (a) and (b). Surface temperature variation during bonding of ceramic tile to 7/16-in thick glass/epoxy composite, with coil motion. 142

Figure 105. Schematic of the lay-up sequence for one-step induction repair of a composite armor panel. 143

Figure 106. Surface temperature profile for single-step bonding with coil motion..... 144

Figure 107. Surface temperature variation at two different locations. 144

Figure 108. Spot locations for IR camera temperature measurement..... 145

Figure 109. Time/temperature response during one-step induction bonding as measured by the IR camera. 145

Figure 110. Single-step bonded multi-layer composite specimen. 145

Figure 111. Control of Heating Behavior by Magnetic Particle Composition. 147

Figure 112. Geometry of the induction coil. 148

Figure 113. Location and position of the lap shear specimens during processing. 149

Figure 114. Optimal measurement zone of the fiber optic temperature sensor. 150

Figure 115. Top and side views of the position of the fiber optic temperature sensor within the adherend. 150

Figure 116. Surface area bonded between two lap shear adherends..... 151

Figure 117. Geometry for the lab joint test including composite shims for nominal alignment..... 152

Figure 118. Conversion versus time for DICY cured epoxy adhesive using isothermal method in a DSC with and without the magnetic susceptor particles..... 153

Figure 119. Conversion versus time for DICY cured epoxy adhesive using isothermal method in a DSC with and without the magnetic susceptor particles..... 153

Figure 120. Graphic representation of cure time to 95% conversion as determined using isothermal DSC. 154

Figure 121. DSC experiment of DICY adhesive system determining the onset of thermal degradation..... 155

Figure 122. The heating rate of the DICY adhesive system, with 20% volume fraction magnetic susceptor particles, with a power setting of 1500W..... 156

Figure 123. Average lap shear strengths for all processing conditions. 159

Figure 124. Ballistic Test Fixture. 163

Figure 125. Residual Velocity After Penetration (Impact Velocity = 850 m/sec)..... 164

Figure 126. Dynamic Deflection and Static Bulge. 165

Figure 127. Cross-Section of Recovered Backing Plate Showing the Extent of Delamination. 165

Figure 128. Damage and Erosion of Cover Layer. 166

Figure 129. Damage in Ceramic Layer. 167

Figure 130. C-Scan Images of Virgin and Ballistic Damaged Backing Plates..... 168

Figure 131. Repair Hierarchy. 170

Figure 132. Schematic of the Induction Heating Process for Carbon/Thermoplastic Composites..... 171

Figure 133. Schematic of Induced Voltage Loops in the Composite. 172

Figure 134. Heating Mechanisms in Each Individual Conductive Loop. 173

Figure 135. Circuit Model for Dielectric Heating. 174

Figure 136. Circuit Model for Heating by Fiber Contact Resistance 175

Figure 137. Dielectric Properties of PEI (Ultem 1000, GE Plastics)..... 175

Figure 138. Schematic of 2-ply Heating Model..... 176

Figure 139. Comparison of Heating Patterns for [0/90] 2-ply Stack..... 177

Figure 140. Comparison of Heating Patterns for [0/45] 2-ply Stack..... 177

Figure 141. Model Through-Thickness Heat Generation of an 8-Ply Carbon-Fiber Laminate With Orientation $[0/90/0/-90]_s$ 178

Figure 142. Predicted Through-Thickness Temperature Profiles at Various Time Steps. ... 179

Figure 143. TGA Weight Loss Profile for PEI Resin and Prepreg (Heating Rate = 15 °C/Min) 181

Figure 144. Breakdown Voltage Measurements for Neat PEI Films 184

Figure 145. Schematic of Lamination Process. 187

Figure 146. Model Scheme used in Laminator Design..... 188

Figure 147. Strength Development of Neat PEI with Temperature..... 192

Figure 148. Viscosity-Temperature Relationship for PEI (Data Courtesy of GE Plastics). 193

Figure 149. Ply Interface Temperatures for Process Throughput of 10ft/min..... 194

Figure 150. Surface Layer Temperature, Void Fraction, and Bond Strength in Induction-Processed PEI (V = 10 ft/min, $T_{preheat}$= 800°F, Q_{in} = 8kW, T_{cooler} = 77°F). 195

Figure 151. Center Ply Temperature, Void Fraction, and Bond Strength in Induction-Processed PEI (V = 10 ft/min, $T_{preheat}$= 800°F, Q_{in} = 8 kW, T_{cooler} = 77°F). 196

Figure 152. Through-Thickness Bond Strength Variation (V = 10 ft/min, $T_{preheat}$= 800°F, Q_{in} = 8 kW, T_{cooler} = 77°F). 196

Figure 153. Schematic of Rectangular Coil for Lamination Stage..... 197

Figure 154. Temperature Profiles of 8-Ply Stack with Rectangular Coil..... 198

Figure 155. Induction-Based Lab-Scale Experimental Laminator. 201

Figure 156. Infrared Temperature Profile of Heating Zones. 201

Figure 157. Void Content Comparison Between Vacuum Debulk Baseline (l) and Induction-Processed Laminate (r). 202

Figure 158. Example of a co-injected dual-resin component with a structural vinyl-ester resin on one side and a fire-protective phenolic resin on the other. 209

Figure 159. Example of a co-injected angle section with balsa core demonstrating scaleup of the process to large, angular components. 210

Figure 160. Example of co-injected integral armor demonstrating the injection of three different resins (structural, fire-protective, and energy-dissipative) into a complex multifunctional component. This example also demonstrates the through-thickness reinforcement enabled by the CIRTM process. 210

Figure 161. An example of the improved ballistic protection offered by a co-injected, stitched integral armor panel. 211

Figure 162. Example of a VARTM repair of a honeycomb core structure. 211

Figure 163. Experimental setup used to manufacture the co-injected specimens. 214

Figure 164. Fracture toughness vs. crack length for co-injected specimens tested at different crosshead speeds. 219

Figure 165. Crack length vs. time for all materials tested. Two cracks developed in the 28-hour specimens; only the interface crack length was reported. 220

Figure 166. The CIRTM process for vinyl-ester/phenolic hybrid composites. 221

Figure 167. VARTM setup used for co-infusing epoxy and urethane resins simultaneously. 226

Figure 168. Processing temperatures for CIRTM processing of epoxy and urethane. 227

Figure 169. Normalized energy absorbed. 229

Figure 170. Example of Composite Integral Armor (CIA)..... 231

Figure 171. The arrangement of ceramic tiles. 231

Figure 172. A CIA panel in four-point bending 234

Figure 173. Load-deflection responses of single-step SC15 (VARTM) CIA beams 236

Figure 174. Load-deflection response of a multi-step SC15 CIA beam..... 237

Figure 175. Load-deflection response of a multi-step SC11 CIA beam..... 237

Figure 176. Evolution of the failure event on multi-step SC11 CIA beams..... 238

Figure 177. Load-deflection responses of single- and multi-step SC15 and SC11 CIA beams: Effect of the mechanical roughening of the rubber. 240

Figure 178. Failure at the interface of the backing and the rubber 241

Figure 179. Three potential repair designs (focus on the backing plate)..... 242

Figure 180. CIA panels repaired with a scarf patch repair 243

Figure 181. CIA beam ready to be repaired with a 1/1-scarf patch..... 243

Figure 182. Efficiency of induction-cured scarf repaired backing plates..... 244

LIST OF TABLES

Table 1. Model Cationic Resin Formulations 5

Table 2. DMA Data of Model Cation Prepreg Formulas 5

Table 3. Physical Properties of T-14 Resin 9

Table 4. Fracture Toughness of T-11 Resin 11

Table 5. Fracture Toughness of T-14 Resin 11

Table 6. Room-Temperature Flexural Properties of Neat T-11 Resin 12

Table 7. Short Beam Shear Strength of Cationic Composites with AS4 14

Table 8. Specimen Moisture Absorption 16

Table 9. Short Beam Shear Strength of AS4/CAT-M 17

Table 10. Flexural Properties of AS4/CAT-M 17

Table 11. Formulation of T-17 18

Table 12. Absorption of Moisture-Conditioned Specimens 20

Table 13. Flexural Properties of AS4/T-17 Cured at 25 kGy/pass 22

Table 14. Basic CCM Resin Properties 25

Table 15. Rubber Modifiers and Diluents for VARTM Toughening 26

Table 16. Generic Composition List of Additional Resins 26

Table 17. Viscosity Analysis of the Developed Resin Systems at Room Temperature 28

Table 18. DMA Analysis of IPN Based Formulations 29

Table 19. Wet DMA Analysis after 48-hour water boil in IPN Resin Formulations. 31

Table 20. Fracture Toughness Results 32

Table 21. Flexural Analysis of IPN Formulated Resins 33

Table 22. Properties of CCM1-Based Modified Resins 36

Table 23. Properties of CCM2-Based Modified Resins. 38

Table 24. Properties of CCM3-Based Modified Resins. 39

Table 25. Modifier and Toughening Additives Properties 40

Table 26. Composition of developed CCM Series Resins..... 41

Table 27. VEB-11 C-staging Cationic Resin Composition 42

Table 28. Properties of VARTM Resin Systems for E-Beam Processing..... 47

Table 29. Preliminary Composite Properties on AS4 5HS..... 47

Table 30. Adhesive Performance Targets based on Commercially Applied Technologies ... 48

Table 31. Modifiers and Diluents for Adhesives Formulation 49

Table 32. Cationic Curing Adhesive Formulations 53

Table 33: E-Beam-Curing Adhesive Properties 55

Table 34. Double Notch Lap Shear Results on Composites..... 58

Table 35. Overlap Shear Strength Results on Composites 58

Table 36. Joint Strengths of Al-Al Single-Lap Joints (D-1002)..... 59

Table 37. Adhesive Target Performance and State of the Art in E-Beam Systems..... 60

Table 38. Commercial Adhesive Al-Al Single-Lap Joint Strengths (D-1002)..... 61

Table 39. Aging Study Materials: Commercial and Formulated..... 68

Table 40. Aging of Thermal and E-Beam Systems 69

Table 41. Materials used in Experimental work 72

Table 42. Effect of temperature on the propagation rate constant for PGE (UV experiments) Photoinitiator concentration: 0.44 wt% 80

Table 43. Effect of light intensity on the propagation rate constant for PGE (UV experiments) Photoinitiator concentration: 0.44 wt% 80

Table 44. Effect of photoinitiator concentration on the propagation rate constant for PGE (UV experiments) (T=70°C and Light Intensity = 16.55 mW/cm^2 80

Table 45. Effect of temperature on intrinsic rate kinetic parameters (EB for DGEBA). Initiator concentration = 1.06 wt% 83

Table 46. Summary of Test Results 88

Table 47. Fixed cost data used to generate cost comparisons in EB vs. Oven cured VARTM Composite Panels. 107

Table 48. Model simulation systems and processing parameters. 108

Table 49. Cure Kinetics Model Parameters for Hysol EA9394 120

Table 50. Lap Shear Data for Hysol EA 9394 122

Table 51: Single-lap shear specimens tested in tension 130

Table 52: Double cantilever beam specimens 131

Table 53. Temperature Measurements at the Surface and Bond line 142

Table 54. Power and Process Times in Induction Field 152

Table 55. The amount of time to reach 95% cure for each temperature. 154

Table 56. Measured Lap Shear Strengths For Oven-Cured Samples. 157

Table 57. Measured Lap Shear Strengths For Induction-Cured Samples. 158

Table 58. Experimental Data of Neat Ultem 1000 Resin Under Various Heat Treatments. 182

Table 59. Degradation Study of PEI and AS4/PEI Prepreg Using GPC. 183

Table 60. Comparison of Mechanical Properties. 184

Table 61. Final Hardware Configuration and Setpoints for Experimental 8-Ply Laminator 199

Table 62. Mechanical Performance of Induction-Processed Laminates 202

Table 63. MIL-STD-461E RE101 limits on emitted magnetic field 206

Table 64. Electric field strength E as a function of frequency for magnetic fields of amplitudes 0.5 and 50 T acting over a 10 cm diameter area..... 207

Table 65. MIL-STD-461E RE102 limits on emitted electric field strength (E). Values in parentheses are extrapolated values. 207

Table 66. Co-injected Fiber Preforms and Resin Combinations 209

Table 67. Short Beam Shear Results..... 216

Table 68. Summary of DCB Results..... 218

Table 69. Test Matrix for Cone Calorimeter Testing. 223

Table 70. Summary of Cone Calorimetry Data at 50 kW/m^2 224

Table 71. Individual Processing Details for the Epoxy and Polyurethane Resins..... 227

Table 72. Specimen Identification and Construction Details. 228

Table 73. Aims of Mechanical Performance Evaluations for Repaired CIA. 230

Table 74: Test Matrix for the four-point bending testing of CIA beams..... 234

Table 75: Partial test results for the CIA beams tested in four-point bending..... 235

Table 76: Failure load and displacement results for the CIA beams tested in four-point bending..... 239

Executive Summary

This document reports on the results of a program funded by the DOD Strategic Environmental Research and Development Program (SERDP) to research, develop, and demonstrate affordable and environmentally friendly composite repair and remanufacturing technologies for stand-alone repair of DOD structures without creating new environmental problems.

The ultimate goal of the PP1109 program was to create momentum for out-of-autoclave processing technologies, such that electron beam and induction processing could be demonstrated as matured for specific military applications. Replacing current technical barriers in out-of-autoclave processing methods will substantially increase the rate at which new and environmentally favorable processing methods will become accepted in the composites industry. Critical to the implementation of these technologies is the ability to apply them in niche market areas, such as for repair of composite structures in various military environments. Continued successful use of these new composite materials in the field will result in increasing confidence in the maturity levels of the technologies. During the initial evaluation phases, electron beam technology appeared to have great potential for curing thick and multifunctional polymer matrix materials, such as composite integral armors (CIA). However, ceramic components of the CIA were evaluated demonstrating a significant limitation to e-beam curing for mixed thick section composite to metal and composite to ceramic applications. The limitation is the e-beam penetration depth, which even with high-energy electrons (1-10 MeV) is limited in very dense materials. Future developments might address the applicability of x-ray induced curing for such thick section structures. The program managers developed methods to investigate in real-time the kinetics of reactions for both a cationic initiator decomposition and initiation and epoxides consumption via cationic initiated polymerization. This technology will be essential during component design and selection of processing (dose and dose-rate requirements) to achieve uniformity in composite components manufactured or repaired using e-beam chemistry. Finally, the induction technology was fully developed for use in field repair of structural composite materials, especially non-carbon based composites, such as composite armors. The developed repair schemes and test panels provided sufficient evidence to justify technology transfer efforts in future CIA investigations and will provide an environmental advantage to the Future Combat Systems platforms being developed as part of the changing face of the Army.

Overall, the program has been successful at both identifying critical DOD environmental needs and finding practical solutions to these requirements for repair and remanufacturing of PMCs for military applications. The program focused on solutions to DOD repair and remanufacture, including demonstrating and marketing alternative raw materials for the E-beam and induction technology areas. Further, the program resulted in demonstrated reliability of these alternative systems. Demonstration of these new technologies has been completed. The predicted environmental benefit of newly formulated toughened resin systems and cure technologies have been proven out through rigorous material and process characterization and testing, and the cost drivers have been validated with a cost model evaluation. The most matured materials systems are being optimized for the selected DOD applications.

Synopsis of the Program

The technical objective of this program is to research, develop, and demonstrate a unique, affordable, environmentally friendly family of polymer matrix composite (PMC) manufacturing and repair technologies for stand-alone repair of current, soon-to-be-fielded, and future DOD structures. Repair concepts and technologies will be demonstrated on three DOD-specific problems, including the design and implementation of a repair procedure for the Army's combat vehicle composite integral armor; the development of several advanced concepts for non-autoclave manufacture and repair of thin composite skins for Air Force and Navy aircraft and Army rotorcraft; and the development of induction-based processing for 120-mm armor-piercing kinetic-energy tank round composite sabots used on the M-1A1 Abrams Main Battle Tank.

The program was divided into eight task areas represented by the flow diagram in Figure A. Tasks 1–3 occur generally sequentially and in parallel to Tasks 4 and 5. Tasks 7 and 8 occur intermittently throughout the program and Task 6 is the culmination of all work, demonstrating feasibility at the end-user level.

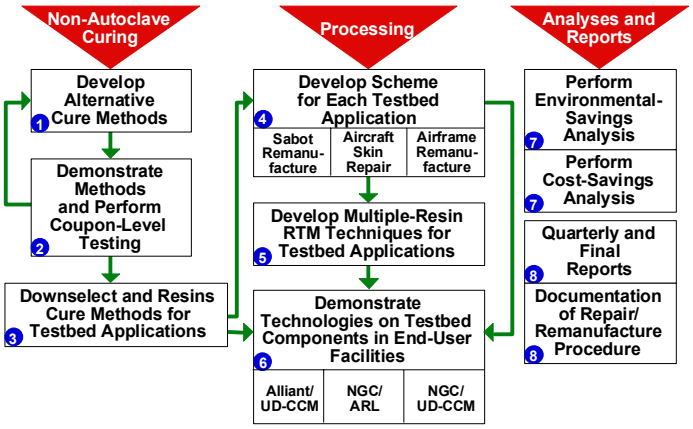

Figure A. Non-Autoclave Processed Composite Development.

The program was designed to take advantage of past and ongoing resourced programs within DOD and to capitalize on recent technological advances made in these leveraged programs. Several of these recent advances are in the development of resins and non-autoclave curing technologies that enable the proposed technologies to be inserted into DOD systems.

Historically, development of E-beam cured composite structures was limited by resin performance and processing methods. In our early developments, we formulated and characterized various resin systems using E-beam to achieve low VOC cured composites. However, the aerospace community is determined to achieve high-temperature resin properties using electron beam irradiation to cure epoxides-type resins. We controlled our processing condition around the experimental variable total dose because many of our formulations are free-radical cured materials, which are relatively insensitive to dose-rates. We subsequently processed all of our materials under controlled processing conditions to

produced highly cured composites and adhesives. During the Year Three effort, we extended our comprehension of resin performance to include processing variables (total dose, dose rate, beam energy). Consequently, we screened our toughening approach using both thermal and E-beam curing. This formulation approach facilitated greater understanding of the cure chemistry, and produced better networks on cure. During the Fourth Year, we established a method of monitoring cure progress and kinetics functions for electron beam cured epoxides in real-time, using a near-infrared spectrometer. Also, we investigated a new approach to e-beam resin formulating by exploring liquid crystal based adhesive formulations.

Induction processing has evolved from a simple model approach to a broad category of resin processing capabilities. We have shown in the past the ability to tailor the thermal field by selectively cutting screen meshes in a fixed induction field. In addition, we demonstrated uniform heating of an unmodified screen by rastering the induction coil (or field) across a large area. This second approach is the preferred method for processing of large area repairs in the field, but has the limitations of being sensitive to operator error. Since induction curing is not instantaneous, we propose using a robotic unit for controlling the induction heating. NAVAIR also produced a portable robotic unit that will suffice for field repair through an SBIR contract with Pushcorp, Incorporated of Dallas, Texas. Therefore, we continued to pursue the scientific value of induction cure limiting by incorporating Curie-limited induction particles into thermoset adhesives cured by both free radical and epoxy-amine reactions. We formulated a number of adhesive resins and demonstrated cure and adhesive strength in coupon level testing. Additionally, we addressed replacing thermoset composite materials with non-hazardous thermoplastic replacements for the Army munitions sabot program. The development of process control models and heating models for induction applications resulted in effective control of heating in carbon-fiber laminates, such that multi-ply carbon-fiber/thermoplastic laminates are compacted with low (<1%) void fraction. In addition to being non-hazardous, the thermoplastic materials have additional advantages in lower moisture uptake over current sabot systems. Lastly, we established through-thickness heating capabilities for thick-section composite repair in an inductive field. Thus, induction processing of composites is proving to be an effective means of obtaining performance composites and field level repair for DOD applications.

Our last year of effort addressed final documentation of the program accomplishments along with a final cost-savings analysis. This document is the complete summary of the work carried out in the development of non-autoclave processing methods for composite remanufacturing and repair applications for the military. Although the program has concluded, the success of this program has resulted in a number of secondary efforts with military contractors to implement both induction and e-beam processing strategies to reduce costs and weight, as well as achieve higher tolerance metrics for composite manufacturing.

A reduced environmental impact for DOD remanufacturing and repair using alternative cure technology is critical to the program success. However, the range of performance characteristics within DOD is extensive. Consequently, quantifying the impact that these new material and process technology developments will have on pollution mitigation occurs through a stair-step approach, where the total elimination of composite hazardous material and air pollutant production can be achieved only through a series of successful demonstrations and implementations of the proposed technologies. We show that the cost impact is not favorable financially with present regulations, but is favorable environmentally

for DOD. The demonstration articles were used as benchmark systems for demonstrating reduced impact of non-autoclave processed materials, although costs tended to be somewhat higher than with traditional processing methods. Our projections, based upon initial cost savings analyses show a potential net decrease in hazardous VOCs of 40%-60% and in hazardous wastes of 15-30% DoD wide by moving out-of-autoclave for repair and remanufacturing. As new materials are developed that meet performance requirements for other repair methods, including film adhesives, prepregs, and toughened high-temperature resins, the impact of implementation will be systematically increased.

The research team was made up of participants from government, industry, and academia with expertise in specialized resin formulation, alternative curing, and composite processing and repair. Table A shows the primary team members and author contributors to the current effort. Table B shows other contributors to research efforts and other management and editorial contributors, respectively.

Table A. PP1109 Team Member Summary

Organization	Team Members	Activities
U. S. Army Research Laboratory (ARL)	Mr. Bernard Hart Dr. Steven H. McKnight Dr. James M. Sands (PI) Dr. Eric Wetzel	program management; repair schema development; curing/bonding research (induction, resistance, UV, E-beam); co-injection studies, adhesion studies; process sensor integration, and repair performance testing; resin formulations, cost modeling
University of Delaware Center for Composite Materials (UD-CCM)	Dr. John W. Gillespie, Jr. Mr. Bazle Gama Dr. Crystal H. Newton Dr. Nicholas Shevchenko Dr. Shridhar Yarlagadda	curing/bonding research (induction, resistance, UV, E-beam); co-injection studies, coupon bond testing; transition to NSWC, induction model developments
Drexel University	Dr. Giuseppe R. Palmese Mr. Matteo Mascioni	curing/bonding research (E-beam); resin formulations, cure kinetics characterizations
Northrop Grumman Corp.	Dr. Anna Yen	E-beam (cationic resin formulation; E-beam airframe manufacture; aircraft skin repair
YLA, Inc.	Ms. Susan Robitaille	prepreg production
Applied Poleramic, Inc.	Mr. Richard Moulton	film adhesive and prepreg formulations
E-Beam Services, Inc.	Mr. Michael Stern	E-beam curing
Boeing Phatom Works, Seattle, WA	Dr. Mark Wilenski	E-beam curing, cure processes monitoring

Table B. Additional PP1109 Contributors to Success

Name	Affiliation
Dr. Lorence Augh	University of Delaware, Newark, DE
Mr. James Beymer	Boeing Phantom Works, Seattle, WA
Mr. Wai Chin	Army Research Laboratory, APG, MD
Mr. Urmish P. Dalal	University of Delaware, Newark, DE
Dr. Reza Debastani	Oak Ridge National Laboratory, Oak Ridge, TN
Dr. Narendra N. Ghosh	University of Delaware, Newark, DE
Mr. Bernard Hart	Army Research Laboratory, APG, MD
Dr. Dirk Heider	University of Delaware, Newark, DE
Dr. Ilia Ivanov	Oak Ridge National Laboratory, Oak Ridge, TN
Dr. Robert Jensen	Army Research Laboratory, APG, MD
Dr. Hee June Kim	University of Delaware, Newark, DE
Dr. Kevin Kit	Univ. of Tennessee at Knoxville, Knoxville, TN
Mrs. Melissa Klusewitz	Army Research Laboratory, APG, MD
Ms. Bina Modi	University of Delaware, Newark, DE
Mr. Steve Nguyen	Army Research Laboratory, APG, MD
Mr. Eric J. Robinette (Jason)	University of Delaware, Newark, DE
Mr. Nicholas Sisofo	University of Delaware, Newark, DE
Mr. Alan Teets	Army Research Laboratory, APG, MD
Mr. Mike Vick	Boeing Phantom Works, Seattle, WA
Dr. Shawn Walsh	Army Research Laboratory, APG, MD

Transition Plan and Successful Transitions

The success of PP1109 program can be measured in part by the great enthusiasm for the process technologies generated as a result of the focused research. Military equipment manufacturers enthusiastically supported and pursued technological developments of the out-of-autoclave processing alternatives for composite applications. The list of commercial and military interests continues to grow, even as this report is finalized. The following table (Table C) demonstrates the breadth of interaction established during this program. Despite the state of the technologies being relatively young, the investment of commercial entities in the future will result in fielding of a number of composite materials, both in the military and in the commercial markets. The program coordinators are greatly encouraged by the continued interest in these technologies.

Table C. Transition Efforts In EB and Induction Processing

Commercial/Miliatry Organization	Technological Developments
Boeing, Philadephia, PA	Structural spars and ribs for helicoptor airframe
Boeing Phantom Works, Seattle, WA	EB Processing of tail sections, rudders, and composite skins
Science Research Laboratory, Somerset, MA	EB cured adhesives for cryogenic applications
Air Force, Wright Patterson AFB, OH	Composites affordability initiative testing and processing
Sikorsky, Stratforc, CT	Comanche suprastructure components (EB processing, induction removal mechanisms)
Battelle, Columbus, OH	Induction limited processing for reformable adhesive application
Applied Poleramic, Incorporated, Benicia, CA	Resin and prepreg development for EB applications
YLA, Benicia, CA	Prepreg and fiber surface treatments for improved EB performance
National Research Council of Canada, Ottowa, ON	Kinetics of processing for EB resins
UCB Chemicals, Smyrna, GA	High strength adhesives through EB processing
Air Canada, Dorval, QU	EB adhesives for rapid repair of commerial airliners

1 Electron-Beam Resin Formulation

The electron beam (e-beam) accelerator is a source of ionizing radiation that can generate ionic species, free radicals, and molecules in excited states capable of initiating and sustaining polymerization. Depending on the chemistry of the resin system being irradiated, polymerization can occur by free radical, as well as ionic mechanisms. The polymerization of acrylic/methacrylic systems, maleic and fumaric polyester resins, and thiol-ene systems proceeds via free-radical mechanisms without initiators. These resin systems are ideal for formulating resins with long storage life and out-times. E-beam-induced polymerization of epoxies occurs cationically with the appropriate catalyst. Of these systems, free-radical-cured systems based on acrylate and methacrylate functionality and cationically cured epoxies catalyzed using diaryliodonium or triarylsulfonium salts like diphenyliodium hexalfluoroantimonate or triarylsulfonium hexalfluoroantimonate have shown the most promise for composites applications. Acrylate/methacrylate-based free-radical-cured systems have been studied extensively. These systems provide high reactivity, and they have good stiffness, good control over processing viscosity, and very long shelf life.

Among the shortcomings associated with acrylic systems are high cure shrinkage (8–20%), the potential for oxygen inhibition, and low T_g relative to high-temperature thermally cured epoxies. Cationically cured epoxies require a very expensive photoinitiator to enable polymerization. Cationically cured epoxies offer low shrinkage, exhibit high T_g, are not inhibited by oxygen, and do not require curing agents, as do their thermally cured counterparts. On the other hand, cationic systems tend to cure more slowly than acrylate/methacrylate systems, and the photoinitiators are easily poisoned by nucleophilic contaminants, such as nitrogen and alcohols, which can often be found on the surfaces of reinforcing materials or as part of epoxy resin compositions. Additionally, cationic epoxy systems suffer from a poor interfacial strength in carbon fiber laminates.

In this work, both free radically and cationically cured electron-beam resin systems are being formulated to address specific requirement limits and storage durability of the resin types. As such, the technical formulations are discussed in context of the end product developed.

1.1 E-Beam Prepreg

Cationic resin formulation efforts follow a basic building-block approach to develop new toughened e-beam-curable resins for composite matrix materials. Sufficient quantities of the new resin were produced to develop chemical and mechanical properties, evaluate repair on an aircraft structure, and demonstrate the manufacturing technique for a structural composite.

Over the past five years, hundreds of model formulations of e-beam-curable resins have been prepared. Using epoxy backbone and functionality, the structure/property relationships of e-beam-curing resins have been similar to those of thermal-curing resins. In addition, over 75 modifiers have been added to resins, increasing the resin performance by as much as 50% over baselines, however, little success has been achieved in improving the interfacial properties of the composites. With thermoplastic and elastomeric toughening, either single

or multiple phases, the modified resins still exhibit the high crosslink density characteristics of the epoxy continuous phase.

It is believed that chain extension of the epoxy continuous phase is critical to enable the modifiers to nucleate their energy dissipation. This has not yet been attempted with e-beam-curing resins. It is important that a ductile fracture pattern be achieved. It is also important to lower the crosslink density to allow for plastic flow and to raise the composite interlaminar shear strength by increasing shear bonding.

The primary function of modifiers is to toughen the resin. The addition of modifiers to the rigid extenders should not reduce the resin modulus at elevated temperature. For cationic curing epoxies, the modifier requirements are as follows:

- epoxy-compatible low-molecular-weight oligomer or monomer
- a non-nucleophilic, aromatic, or heterocyclic ring in the backbone
- stable at ambient temperature

The modifier can be either a difunctional co-reactant with a very high percent of reactivity or a multifunctional modifier.

The objective of this task was to reformulate the e-beam-curing cationic resin, CAT-M, and associated adhesives to extend the toughness, durability, and thermal performance to meet 250°F/wet service for aircraft repair and remanufacturing. To date, cationic resins for prepreg applications meet T_g and modulus goals but provide very poor interlaminar strength and toughness.

All matrix resins and adhesives are modified epoxies (a blend of four epoxies—Dow 742, 556, 332, and 439) cured using diphenyliodonium hexaflouroantimonate cationic catalyst. The first stable species, a Bronsted acid of $H^+SbF_6^-$ along with H^+F^-, is believed to be responsible for breaking the epoxy ring, ionizing the hydroxyl, and propagating via homopolymerization, which is the same as thermal cure (Figure 1).

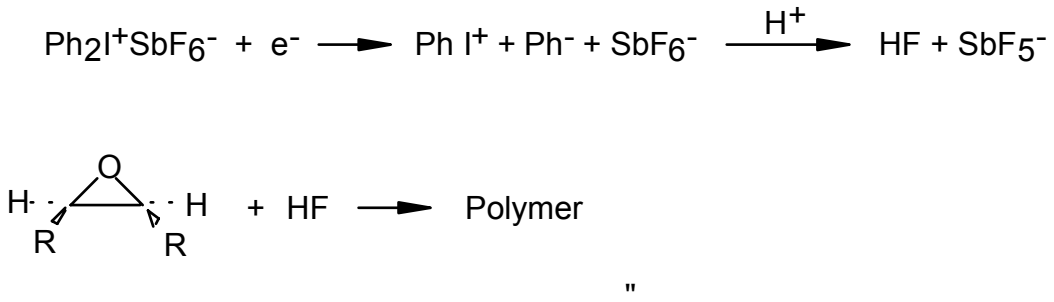

Figure 1. Example of cationic-based epoxy initiation reaction.

Although the propagation steps (Figure 2) and the chemistry are the same as in thermal cure, the mechanism to cure to a high level of completion in a solid state with electronically excited molecular species is unknown.

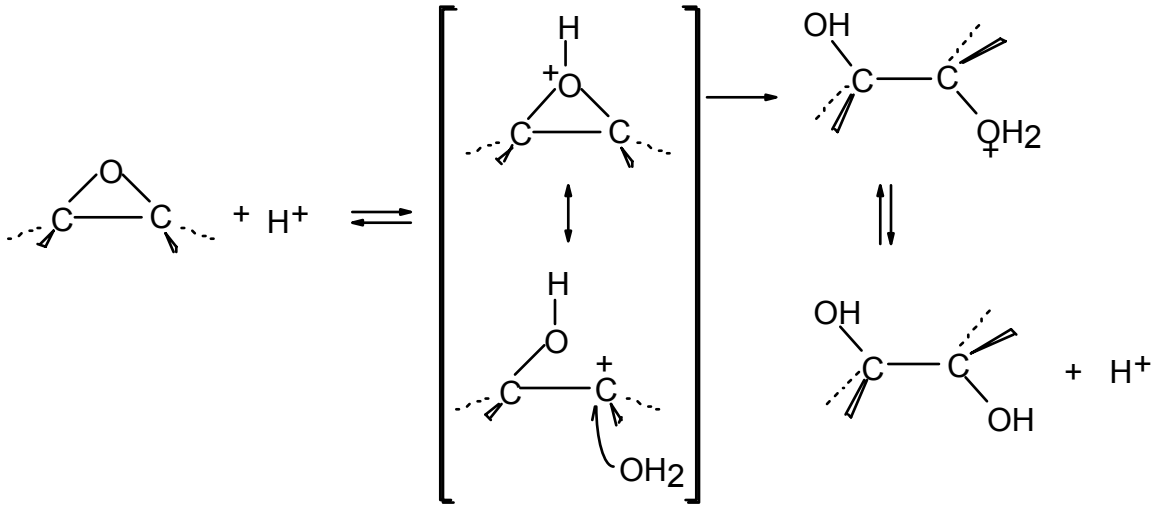

Figure 2. Example of cationic-based epoxy propagation reaction.

Trace water in the raw material can result in a 1,2 diol or glycol, which can react with groups to form a highly crosslinked brittle matrix. Cationic resins need to be toughened before they are of practical value, especially for aircraft applications. The most common way to achieve toughening is to co-react alcoholic hydroxyls in-situ during curing. However, the usual reduction of modulus and T_g will occur. As with thermal curing, a balance between toughness and T_g or modulus is needed. Although the propagation mechanism is the same as in thermal cure, radiation-induced excited molecular intermediates drive the reaction to completion in the solid state. Thermal homopolymerization cures follow classic time, temperature, transformation (TTT) diagrams, where T_g is no more than 20°C higher than T_{cure}. However, the e-beam community is still in debate over whether or not e-beam reactions violate classic TTT or merely provide stable reactive species that provide a long-time for the high degree of cure to be achieved under irradiation. Additionally, probes used to evaluate the cured resins, provide necessary thermal energy to allow the cure to advance during the evaluation, which could provide false evidence of TTT violations. While the debate continues, the ultimate result of the technology developments proves that e-beam curing is still very immature compared with the thermal baseline technologies being targeted for replacement.

1.1.1 SELECTION CRITERIA

The following are the criteria used for prepreg resin downselection. In our studies, each resin formulation had to pass all the tests indicated. If one test failed, no further testing was conducted for that particular formulation.

1. **Radiation cure properties** (determined from gamma calorimetry):

- Gelation < 40 kGy. All of the cationic-initiated epoxies that were studied evidence gelation at doses less than 15 kGy.
- Curing dose < 120 kGy. Curing dose depends on the type of the initiator used.

2. **Dynamic Mechanical Analysis (DMA):**

- DMA modulus > 350 ksi (2.4 GPa). The modulus of most epoxy resins is about 450 ksi (3.1 GPa). However, the modulus slowly drops off as temperatures approach the glass transition (T_g).
- T_g > service temperature + 30°C.

3. **DMA after 2 hours @ 177°C postcure:**

- Postcure DMA modulus < 10% different from DMA modulus prior to postcure. This test is to gage the degree of cure from the initial e-beam curing. A difference between the two values of greater than 10% indicates that significant residual uncrosslinked species remained after the initial cure.

4. **DMA after 24-hr water boil:**

- Weight gain < 3%
- DMA modulus after water boil < 10% different from DMA modulus prior to conditioning.
- Wet T_g > service temperature + 20°C.

1.1.2 FORMULATION APPROACH

The goal of this formulation effort was to improve the toughness of baseline resins. Two types of toughening agents were added to the epoxy formulations: (1) polyethersulfone (PES) and (2) thermoplastic acrylic. The best formulations (T-11 and T-14, and T-17) were selected for further evaluation based on the gamma calorimetry and DMA data. Gamma calorimetry was used to determine the gel point. The e-beam dose at which the temperature begins to rise is defined as the gel point. DMA was used to determine the T_g.

A series of nine model formulations was investigated (Table 1), including a dendrimer (Boltorn EZ, obtained from YLA, Inc., Benicia, CA, USA) that is an epoxy-terminated polyol with a viscosity of about 25,000 cps at ambient temperature. Reactive liquid rubbers such as Hycar rubber and related tougheners provide a neat balance of properties if precipitated during cure into a second phase with particle size in the 1–5 micron range. In e-beam curing, the precipitation of the rubbery phase was not achievable due to instant gelation. Therefore, the second-phase emulsion must be accomplished in the liquid state prior to cure. Several epoxies with varying polarities, with and without modifiers, were formulated with the dendrimer and screened via ultraviolet cure. All formulations cured to clear single-phase castings. The model expected to have the best chance of second phase formation, M-25, was e-beam-cured along with M-24 as a control. Hydrogenated Bis-A (1510), which results in cycloaliphatic structures, accelerates reactions compared to its non-hydrogenated counterpart (332). However, all of the experiments performed to date indicated that there was no phase separation in these samples.

Table 1. Model Cationic Resin Formulations

M Series	11	13	16	21	22	23	24	25
332	100	94	100	60	70	80		
556							70	70
1510							30	30
chain extender-1 (GP)				15				
chain extender-2 (GP)					30	20		
dendrimer Boltorn-EZ								8
TBBPA	5							
542		6						
DPI-1	2.8	2.8	2.8	2.5	2.5	2.5	3	3

The cured Model M series resins were tested by DMA, as shown in Table 2. M-22 was left in the oven overnight and gelled; no DMA data was obtained. Comparing M-21 and M-23 with controls (M-11, M-13, M-16), the multifunctional chain extender used in M-21 looks very encouraging. Past models with difunctional reactants indicated incomplete reaction. Although the initial modulus and T_g are lower for M-21 than for the controls, a 50% retention of modulus at higher temperature, 150°C, was observed for M-21. The modifier used in M-21 warrants further investigation. This modifier can be added to prepreg and adhesive resins but will not be used for the VARTM resins because of its excessively high viscosity.

Table 2. DMA Data of Model Cation Prepreg Formulas

M Series	11	13	16	21	23	24	25
T_g (°C)	170	170	175	140	150	150	125
Temperature @ 50% of modulus	143	118	96	152	107	142	125
Flexural modulus, ksi (GPa)	261 (1.8)	305 (2.1)	345 (2.4)	256 (1.77)	147 (1.0)	207 (1.4)	262 (1.8)

The difunctional chain extender used in M-23 reduces the initial modulus by 50%. This model will be eliminated unless significant toughening is observed in the resins. M-24 and M-25 with 8% dendrimer incorporation were poorer in elevated- temperature properties. The results showed the expected plasticization from the modifier. The dendrimer did not precipitate as a second phase. The latest data indicates that the key to obtaining a successful precipitation of dendrimer lies in the blending of the single-phase epoxies used, including not only the types of epoxies but also the proportion of each epoxy in the blend. Two blends of single-phase epoxy with the modifier precipitated out as a second phase after curing are

currently being investigated and show promise. These resins will be e-beam cured and evaluated.

As expected, both types of thermoplastic modifier reduce the rate of curing, although thermoplastic acrylic appears to affect it less. TP acrylic is a micropulverized powder and is a dispersed second phase with a partially solublized and bonded particle interface. It did not chemically inhibit curing. Because e-beam cure rates can be achieved rapidly with high electron dosing, particle toughening seemed to provide the most stable mechanics in the formulations. T-11, T-14, and T-17 resins contain TP acrylic as a toughening agent. The DMA spectroscopy results for the T-11 and T-14 resins cured at 200 kGy are shown in Figure 3 through Figure 6 for dry and wet (48-hr water boil) T-11 and dry and wet T-14. Dry T_g from E* for both systems is around 200°C; wet T_g, is about 170°C. However, the DMA curves for T-14 are much better than for T-11, especially the much smaller β peak from the tan δ curve of T-14. The β peak in the DMA is likely the low-molecular-weight components produced from the low-dose (<10 kGy) e-beam, which was used to prevent cracking of the sample during cure. Such short segmental chains created during the low-dose pass affect the final mechanical properties. However, in the case of composite curing, the exotherm during curing will likely dissipate through the carbon fibers, which should prevent the low-molecular-weight components, such as the β peak, from forming.

1.1.3 RESIN PROPERTIES

The resins that met the downselection criteria were further evaluated for initial mechanical properties. The dynamic moduli of the neat resins were also measured in a Rheometrics RDS-II dynamic mechanical spectrometer from the torsion of rectangular coupons. One set of coupons of each resin type was conditioned in a humidity cabinet set at 66°C/95% relative humidity until saturated with moisture. Another coupon set of each resin type was desiccated prior to testing. The tests on dry and wet specimens were run at a scan rate of 5°C/min. From plots of the data, it is apparent that the only unambiguous measure of glass transition temperature can be obtained from the tan δ curves. The T_gs from the tan δ curves for dry and wet specimens of T-11 are 230°C and 218°C, respectively. The corresponding dry and wet T_gs for T-14 are 220°C and 205°C, respectively; they are very similar to the aforementioned DMA data. The wet T_g is therefore only slightly lower than the corresponding dry T_g for each material, although the shoulder in the tan δ curves becomes more pronounced in the wet specimens. A better predictor of hot/wet performance than T_g is the drop in storage modulus with temperature. The reduction in G' with temperature for these e-beam-cured resins is compared with that of thermally cured 3501-6 in Figure 7. At 150°C (300°F), for example, 3501-6 retains approximately 75% of its room-temperature storage modulus, while the corresponding moduli retention for dry and wet e-beam-cured resins is 50% and 42%, respectively. The poor retention of properties for the e-beam-cured resins can be attributed again to the low-molecular-weight components formed during cure. As can be seen from the RDS curves, the β peaks are similar to those from DMA. This experiment correlating the storage modulus with temperature will be repeated for composite specimens.

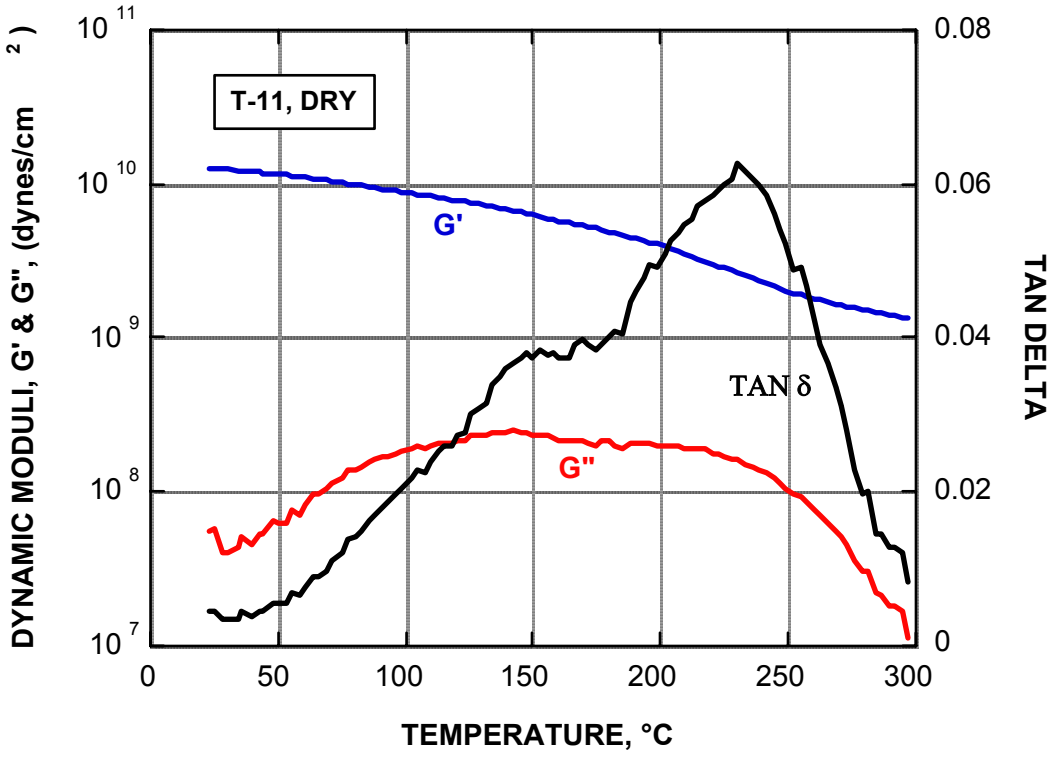

Figure 3. Dynamic mechanical spectroscopy results for dry T-11 resin.

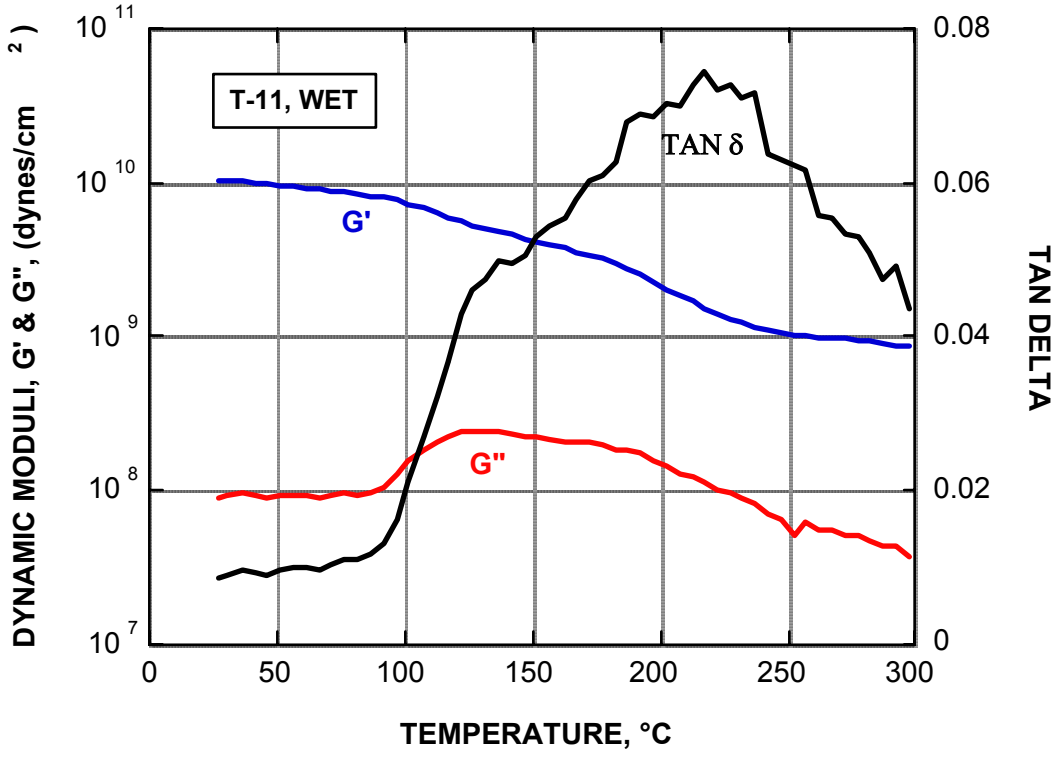

Figure 4. Dynamic mechanical spectroscopy results for wet T-11 resin.

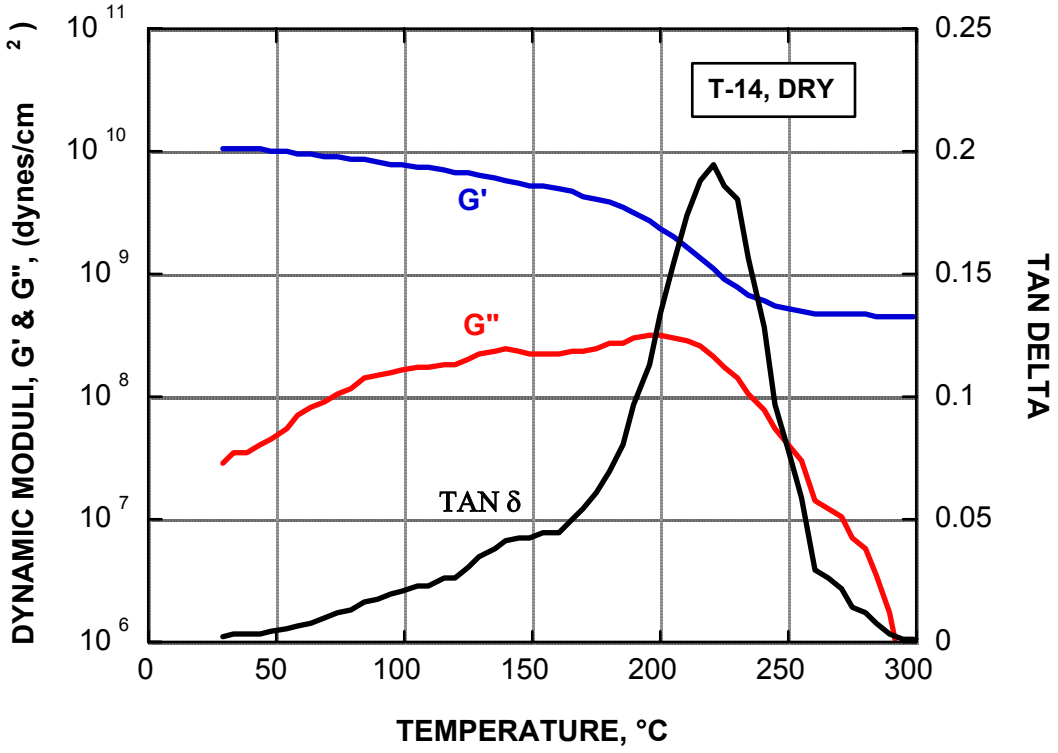

Figure 5. Dynamic mechanical spectroscopy results for dry T-14 resin.

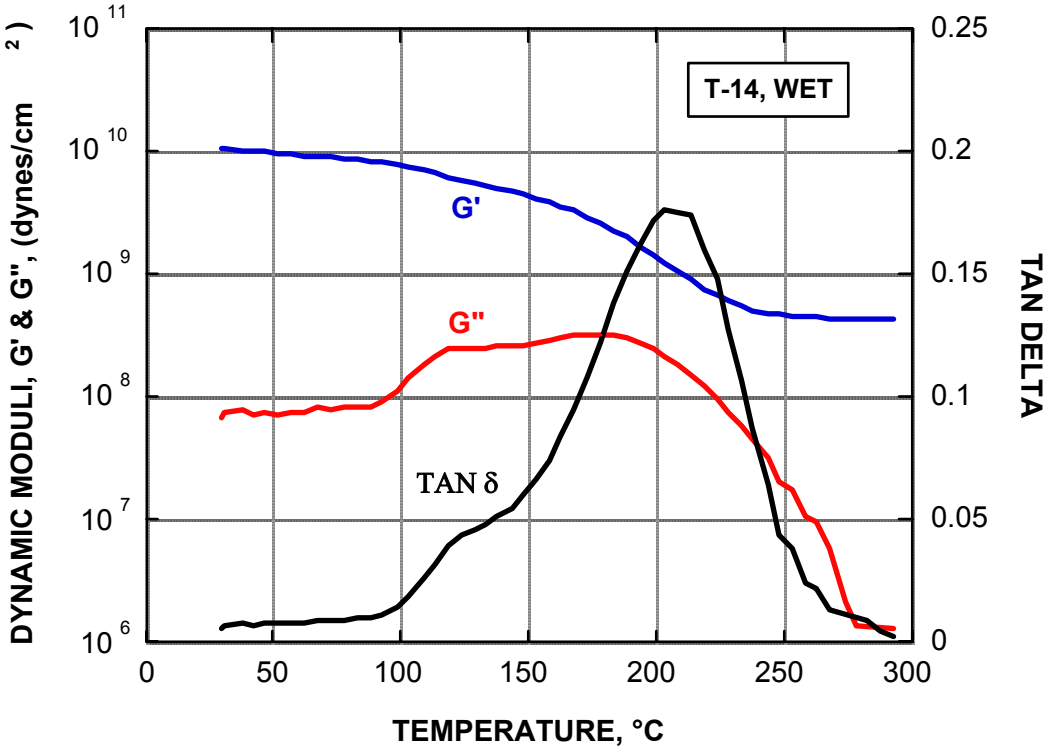

Figure 6. Dynamic mechanical spectroscopy results for wet T-14 resin.

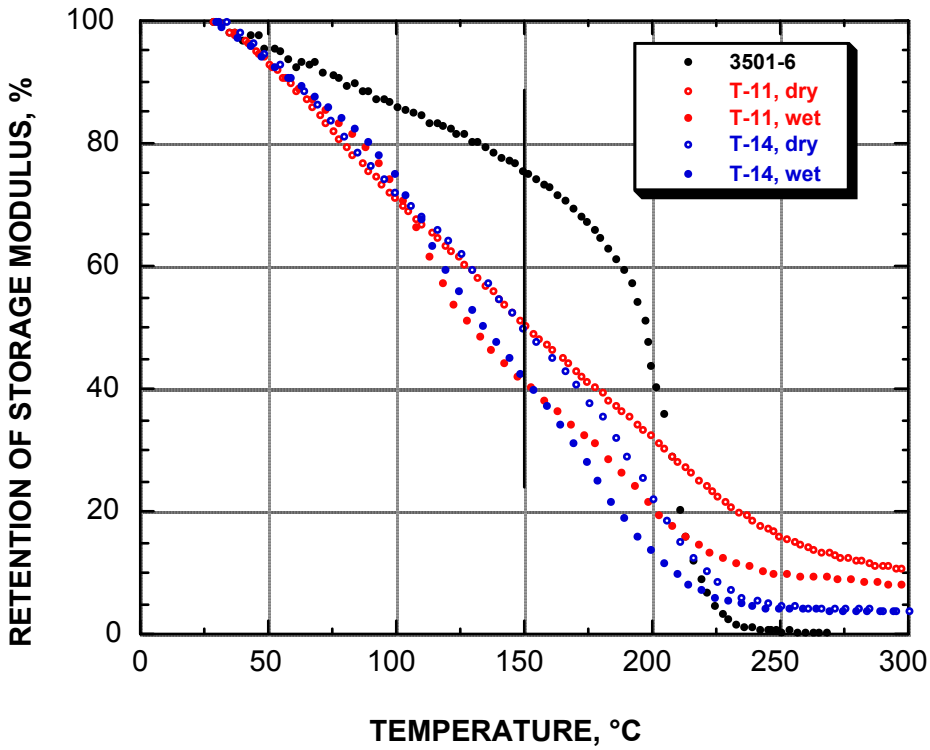

Figure 7. Retention of dynamic storage modulus of neat T-11, T-14, and 3501-6 at various temperatures.

1.1.3.1 Density and Shrinkage

The resin density and shrinkage of T-14 are shown in Table 3. The difference in the cured and uncured resin density is negligible. The T-14 resin did not shrink but expanded slightly after curing at an e-beam dose of 200 kGy. Similar behavior was observed for the resin postcured at 200°C for 2 hours after e-beam curing. The postcure was conducted to relieve residual stresses caused by the high-energy e-beam curing.

Table 3. Physical Properties of T-14 Resin

Density (g/ml)	Condition	Volumetric Shrinkage	Linear Shrinkage
1.2124	uncured	—	—
1.2121	e-beam: 200 kGy	-0.025 %	-0.008 %
1.2123	e-beam: 200 kGy thermal: 2 hrs @200°C	-0.008 %	-0.003 %

1.1.3.2 Thermal and Cure Characterizations

A cross-section of the resin plaques, T-11 and T-14, revealed a variation in color from the surface (reddish-brown) to the midplane (yellowish-brown). Samples from both of these areas were analyzed by differential scanning calorimetry (DSC). The sample from the T-11 interior of the plaque did not display any exotherm on heating in nitrogen up to 300°C; however, the sample from the surface of the plaque displayed an exotherm (approx. 3.3 mcal/mg) beginning at about 100°C, indicating an advancement of cure with the thermal energy supplied. Similar results were observed for the T-14 sample. The center of the T-14 appeared to be fully cured when analyzed by DSC; however the surface of the T-14 panel underwent additional cure in the DSC, exhibiting an exotherm of approximately 9.5 cal/g and peaking at about 135°C. The color of the surface specimen also changed from reddish-brown to yellow at the end of the run. These results indicate a nonuniform cure through the thickness of the as-received plaque, with the degree of cure higher in the interior than at the surface.

1.1.3.3 Fracture Toughness

The fracture toughness of the neat resin was determined from compact tension tests in accordance with ASTM E399-83. Test specimens with dimensions shown in Figure 8 were sectioned from the resin plaque, and notches were machined as indicated. One batch of specimens was then dried for a minimum of 48 hrs in a vacuum oven at 40°C and tested under ambient conditions. Two more batches of specimens were isothermally aged at 121°C—the T-11 for 54 hrs, the T-14 for 102 hrs, and both for 168 hrs—and tested at room temperature. At least five specimens were tested for the unaged baseline and each aging condition, and data was collected for four crack extensions in each specimen to give a minimum of 20 measurements of fracture toughness for each specimen batch. The test results are shown in Table 4 and Table 5 for T-11 and T-14, respectively. The data is fairly consistent and indicates a slight increase in fracture toughness with aging, possibly due to the additional thermal cure that occurs under these conditions. The fracture toughness of the unaged T-14 material is approximately 40% higher than that of unaged T-11.

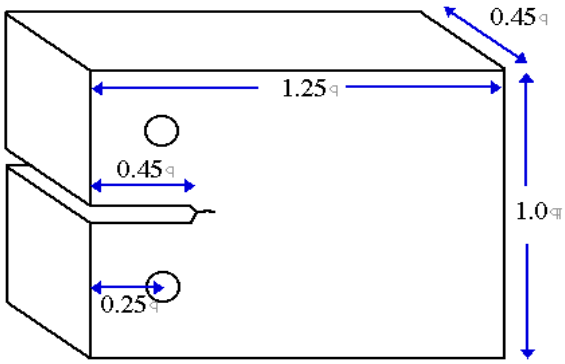

Figure 8. Schematic of compact tension test specimen (dimensions in inches).

Table 4. Fracture Toughness of T-11 Resin

Specimen No.	Conditioning	Fracture Toughness (psi.in$^{0.5}$)				Average (±s.dev.)
		KQ_1	KQ_2	KQ_3	KQ_4	
T-11-15	Dried 48h @ 40°C in vac. oven	265	271	282	255	245 ± 30
T-11-17		285	240	277	257	
T-11-20		215	229	301	279	
T-11-12		221	232	228	224	
T-11-14		215	211	207	204	
T-11-02	Aged 54h @ 121°C in air	271	285	291	281	278 ± 12
T-11-08		284	287	287	270	
T-11-19		254	273	278	269	
T-11-01		274	278	276	258	
T-11-04		262	289	302	291	
T-11-03	Aged 168 h @ 121°C in air	292	297	299	301	293 ± 15
T-11-10		273	286	290	284	
T-11-11		281	294	294	288	
T-11-13		302	307	323	295	
T-11-16		246	290	297	298	
T-11-18		309	309	301	285	

Table 5. Fracture Toughness of T-14 Resin

Specimen No.	Conditioning	Fracture Toughness (psi.in$^{0.5}$)				Average (±s.dev.)
		KQ_1	KQ_2	KQ_3	KQ_4	
T-14-05	Dried 48h @ 40°C in vac. oven	326	340	365	398	342 ± 19
T-14-11		330	340	347	327	
T-14-14		331	349	359	368	
T-14-17		328	340	350	361	
T-14-18		334	337	337	354	
T-14-19		330	304	334	313	
T-14-02	Aged 102h @ 121°C in air	425	373	384	378	378 ± 20
T-14-03		360	396	391	394	
T-14-04			316	355	384	
T-14-09		397	401	367	374	
T-14-13		359	365	377	385	
T-14-21		377	378	381	382	
T-14-01	Aged 168 h @ 121°C in air	328	375	377	371	370 ± 15
T-14-06		351	360	353	381	
T-14-07		379	371	388	403	
T-14-08		363	366	368	377	
T-14-12			355	371	374	
T-14-15		367	366	386	388	

1.1.3.4 Flexural Properties

Flexural test specimens were sectioned from the T-11 plaque with faces perpendicular to the x- and z-directions. The latter specimens bowed after being sectioned, suggesting that cure shrinkage at the midplane of the plaque is greater than that at the surface (also observed in DSC studies). The results of flexural tests on as-fabricated (and vacuum-dried) specimens, performed under ambient conditions, are summarized in Table 6. Although the mid-plane of the plaque appears to have a higher degree of cure than the surface, the results indicate no significant differences in the flexural properties of the two regions. However, the properties appear to be lower than the corresponding flexural stiffness and strength of neat thermally cured 3501-6 epoxy.

Table 6. Room-Temperature Flexural Properties of Neat T-11 Resin

Specimen Category*	Specimen No.	Flexural Strength (ksi)	Average (s.dev.) (ksi)	Flexural Modulus (Msi)	Average (s.dev.) (Msi)
A	T-11-X01	7360		0.445	
	T-11-X05	7005	6625	0.437	0.433
	T-11-X06	6650	(635)	0.425	(0.008)
	T-11-X09	6435		0.427	
	T-11-X10	5680		0.431	
B	T-11-Z10	6985		0.422	
	T-11-Z01	6540	6810	0.383	0.389
	T-11-Z03	6885	(355)	0.384	(0.019)
	T-11-Z07	7270		0.379	
	T-11-Z02	6380		0.375	
C	T-11-Z06	7890		0.405	
	T-11-Z09	7020	7640	0.402	0.397
	T-11-Z05	9510	(1435)	0.408	(0.016)
	T-11-Z08	6150		0.374	

* A: specimens cut perpendicular to x-axis
B: specimens cut perpendicular to z-axis and tested with surface from the plaque midplane in tension
C: specimens cut perpendicular to the z-axis and tested with the original plaque surface in tension

One batch of T-14 flexural test specimens was conditioned at 66°C/95% RH until saturated with moisture, while a second set was desiccated prior to testing. Three-point flexural tests were conducted at ambient temperature and 82°C for both wet and dry T-14 specimens, with a minimum of six specimens for each material/test condition. The results are summarized in Figure 9 and Figure 10. The flexural strengths are not as high as expected (or observed for thermally cured epoxies such as 3501-6), which may be due to the significant void content of the neat resin plaques. The flexural stiffness of the neat resin shows a significant decline with temperature at relatively low temperatures. For example, the flexural stiffness of dry T-14 is 410 ksi at room temperature; this modulus drops to 79 percent and 57 percent of the room temperature values, respectively, at temperatures of 82°C (180°F) and 104°C (220°F).

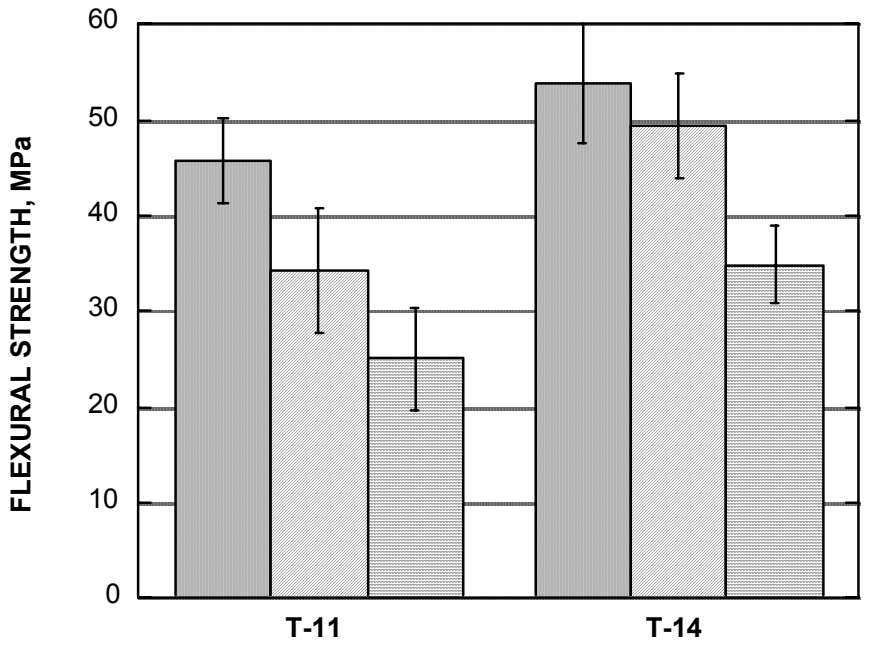

Figure 9. Flexural strength of neat T-11 and T-14, dry and after saturation with moisture at 66°C/95% relative humidity.

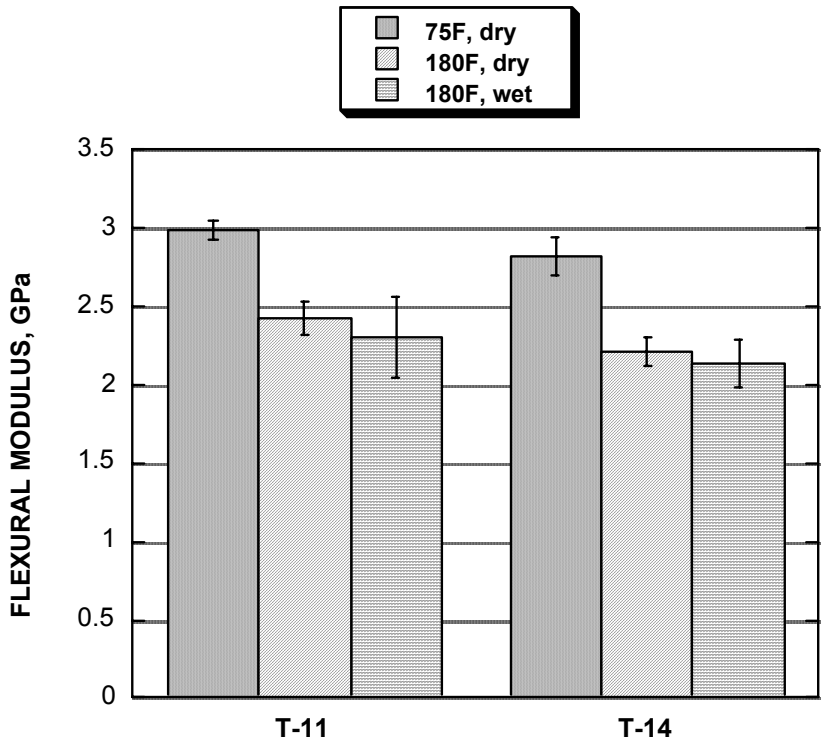

Figure 10. Flexural modulus of neat T-11 and T-14, dry and after saturation with moisture at 66°C/95% relative humidity.

1.1.4 COMPOSITE PROPERTIES

1.1.4.1 General Resin/Composite Evaluations

Four different resin formulations (M30, M31, M32, and M33) were prepared for improving resin toughness. M30 is a cationic epoxy with poly(ether sulfone) (PES) and a co-reacting oligomer. M32 and M33 are multifunctional cationic epoxies with Perstorp's dendrimer. M31 is a nanocomposite. The M31 resin did not cure with E-beam, even at a dose as high as 150 kGy. The three curable resin systems were prepregged with AS4 fibers and subjected to two different E-beam doses, 80 kGy and 150 kGy. The cured unidirectional laminates were then tested for short beam shear (SBS) strength (Table 7). The SBS strength of these resin systems did not show improvement over the work with earlier E-beam curing epoxies. SBS values are still around 10 ksi and below the 13 to 15 ksi targets of thermally cured epoxies.

Table 7. Short Beam Shear Strength of Cationic Composites with AS4

	M30 (80 kGy)	M30 (150 kGy)	M32 (80 kGy)	M32 (150 kGy)	M33 (80 kGy)	M33 (150 kGy)
Strength (ksi) st. dev.	**8.6** **0.4**	**9.4** **0.3**	**9.5** **0.2**	**10.3** **0.1**	**9.3** **0.2**	**9.3** **0.4**

1.1.4.2 AS4/CAT-M, an Optimized System

The first batch of prepreg, AS4/CAT-M unidirectional prepreg, was evaluated. Manufactured by YLA, Inc., the prepreg has a net resin content of 36.8% by weight. The evaluation included prepreg differential scanning calorimetry (DSC) analysis, thermal processing with and without applied pressure, and composite mechanical properties.

DSC analysis was carried out at a heating rate of 10°C/minute from ambient temperature to 300°C. The exotherm peak, (shown in Figure 11) is narrow and sharp, with a peak temperature of 186°C. These data indicate that the debulking is relatively stable to temperatures around 130°C (266°F).

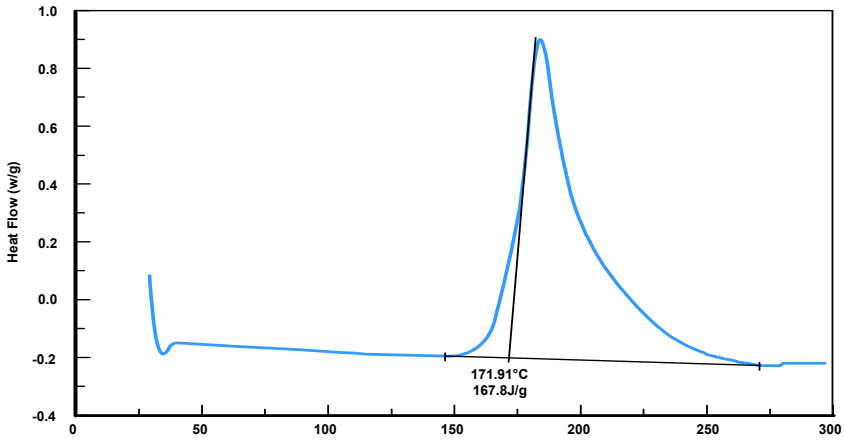

Figure 11. DSC of AS4/CAT-M Prepreg

Three composite panels were fabricated using thermal cure to determine the baseline properties of the AS4/CAT-M composite laminate. One 8-ply 7" x 8" panel and one 16-ply 7" x 8" panel were debulked ply-per-ply at room temperature. The panels were cured under vacuum-bag at 160°F for one hour and 350°F for two hours. No external pressure was applied to the panels. For the third panel (16-ply), the cure was completed in the autoclave using a typical epoxy two-hour cure cycle with an autoclave pressure of 85 psi and a cure temperature of 350°F.

The three laminates were examined ultrasonically (C-scan) and by optical microscopy. Both test methods indicate significant porosity in vacuum-bag-cured laminates. The autoclave-cured laminate exhibited no porosity. Figure 12 is a photomicrograph of the 16-ply vacuum-bagged laminate, Figure 13 is of the 8-ply vacuum-bagged laminate, and Figure 14 shows the 16-ply autoclave-processed laminate. The 16-ply vacuum-bagged laminate has slightly higher porosity than the 8-ply vacuum-bagged laminate. The autoclaved laminate shows some resin-rich areas, which is indicative of the very low viscosity of the resin at 350°F, resulting in fabric settling during cure.

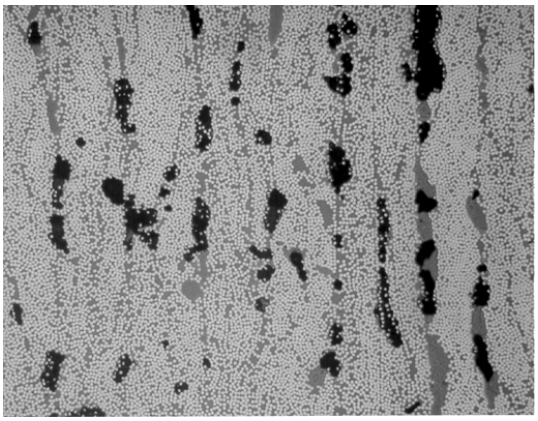

Figure 12. 16-ply Vacuum-Bag-Cured AS4/CAT-M (100x).

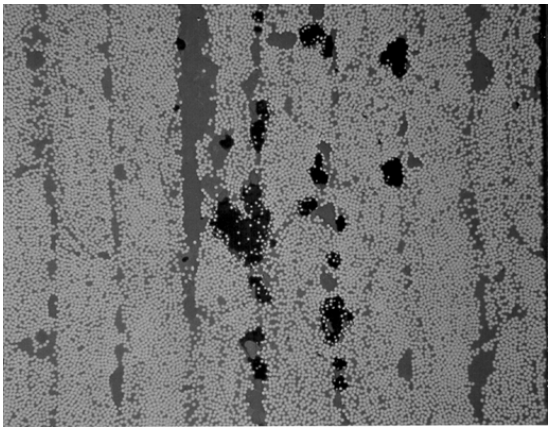

Figure 13. 8-ply Vacuum-Bag-Cured AS4/CAT-M (100x).

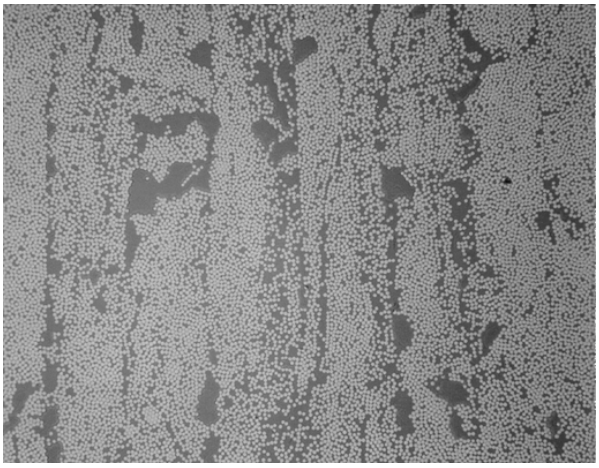

Figure 14. 16-Ply Autoclave-Cured AS4/CAT-M (100x).

Flexural (0°) and SBS properties of AS4/CAT-M were evaluated under ambient, 180°F dry and wet, and 250°F dry and wet conditions. Three-point flexural testing was conducted per ASTM D790 [1], and the SBS strength was determined per ASTM D2344 [2]. Specimens for wet testing were moisture conditioned using a 3-day water boil. The percent average moisture absorption for all specimens is shown in Table 8. Vacuum-bag-cured specimens have 10–20% higher moisture absorption because of the porosity of the laminate.

Table 8. Specimen Moisture Absorption

	Vacuum-Bag-Cured Average Moisture Absorption (%)	Autoclave-Cured Average Moisture Absorption (%)
SBS Specimens	0.97	0.80
Flexural Specimens	0.68	0.57

Table 9 shows the SBS strength of AS4/CAT-M at various testing conditions. As expected, vacuum-bag-cured specimens exhibit much lower SBS strength, which is again attributed to laminate porosity. Although the quality of autoclave cured laminate was excellent, the SBS strength is still lower than an amine-cured epoxy resin systems such as 3501-6 (16 ksi at ambient).

Table 9. Short Beam Shear Strength of AS4/CAT-M

	RTA strength (ksi)	180° F/dry strength (ksi)	180°F/wet strength (ksi)	250°F/dry strength (ksi)	250°F/wet strength (ksi)
vacuum only	8.2	6.8	7.3	5.1	5.4
	8.6	7.1	7.1	5.5	4.9
	8.2	7.3	7.1	5.4	5.3
average	**8.3**	**7.1**	**7.2**	**5.3**	**5.2**
std. dev.	0.2	0.3	0.1	0.2	0.3
85 psi	11.2	9.5	8.5	7.3	6.8
autoclave	11.5	9.5	9.0	7.7	6.8
pressure	11.6	9.3	9.0	8.0	7.0
average	**11.4**	**9.4**	**8.8**	**7.7**	**6.9**
std. dev.	0.2	0.1	0.3	0.4	0.1

Table 10 shows the flexural properties of AS4/CAT-M. The vacuum-bag-cured specimens exhibit much lower strength and modulus values compared to the autoclave-cured specimens. Additionally, there is a much more drastic knockdown in properties after 180°F wet. For instance, at 180°F/wet, there is 63% strength retention for the autoclave-cured laminate and only 55% for the vacuum-bag-cured laminate. At 250°F/wet, retention of properties was only 49% and 43% for the autoclave-cured and vacuum-bag-cured laminates, respectively. This suggests that the service temperature of this resin system is only 180°F/wet maximum, not suitable for 250°F/wet service.

Table 10. Flexural Properties of AS4/CAT-M

	RTA strength (ksi)	RTA modulus (Msi)	180°F dry/wet strength (ksi)	180°F dry/wet modulus (Msi)	250°F dry/wet strength (ksi)	250°F dry/wet modulus (Msi)
vacuum only	248.7	18.0	196.5/143.4	16.8/16.8	**124.1**/107.2	**17.2**/15.7
	243.1	16.9	168.1/137.5	16.5/17.5	—/108.4	—/15.6
	252.8	17.1	—/129.2	—/16.4	—/104.2	—/15.7
Average	**248.2**	**17.3**	**182.3/136.7**	**16.7/16.9**	**—/106.6**	**—/15.7**
st.dev.	4.9	0.6	20.1/7.1	0.2/0.6	—/2.2	—/0.1
85 psi autoclave pressure	253.8	18.0	197.3/166.8	18.2/19.0	**171.4**/131.7	**18.3**/17.2
	260.1	17.9	189.6/150.1	18.2/18.0	—/122.8	—/17.4
	256.7	17.7	—/166.8	—/18.0	—/126.5	—/17.4
Average	**256.9**	**17.9**	**193.5/161.2**	**18.2/18.3**	**—/127.0**	**—17.3**
st.dev.	3.2	0.2	5.4/9.6	0/0.6	—/4.5	—/0.1

1.1.4.3 AS4/T-17 Prepreg, an Optimized System

Laminate processing of the E-beam-cured prepreg material lay-up started with hot debulking at 160°F for 1–2 hours under vacuum. The best and most efficient way of achieving the final cure is to immediately expose the assembly after the hot debulking stage to E-beam energy

for the final cure. However, in most cases the E-beam capability is not readily available; hence, shipping the assembly to an E-beam facility is a common practice. Very often in such cases, the hot debulked panels are shipped on the project plate under vacuum to prevent air from infiltrating the lay-up. In addition to the added shipping cost of this approach, losing vacuum during shipping is common. This result is panels having to be rebagged and hot debulked for an additional hour prior to curing at the E-beam service facility.

To eliminate the requirement for shipping on a project plate and, more importantly, to eliminate the need for additional hot debulking at the E-beam facility, an alternate prepreg material was developed during this reporting period. The prepreg lay-up needs to be fully consolidated after the initial hot debulking process, so the lay-up can be shipped freestanding. The matrix resin needs to contain enough thermoplastic (or oligomer), so that the T_g of the prepreg is above ambient. On heating, the resin will flow in the usual manner for prepreg. The increased resin flow also reduces the bulk factor (per-ply thickness of the prepreg) after debulking. The T-17 matrix resin was developed by Applied Poleramic Incorporated (API, Benicia, CA) to add more "memory" to minimize rebound after lay-up. The viscoelasticity was changed from a previous formulation by increasing the fraction of PES oligomer to 14%. The PES is Radel A-100 pre-dissolved in Epon 332. Table 11 shows the formulation of the T-17 matrix resin.

Ten pounds of T-17 resin were sent to YLA for prepregging with AS4 fibers. The unidirectional carbon-fiber prepreg received from YLA is 12 in wide with per-ply thickness of 6.5 mil. The prepreg quality was excellent and had good tack. A room-temperature debulking study was conducted by debulking individual prepreg ply under vacuum.

Table 11. Formulation of T-17

Component	Parts Per Hundred
Epon 332	70
Epon 742	22
Zeon 351	3
Coupler (Bis-A epoxy)	2.5
DPI-1 (catalyst)	2.5
Additive	1.5
439 (multifunctional epoxy)	44

For a 16-ply lay-up, per-ply thickness of 6.15 mil was achieved after room-temperature debulking. The lay-up was bagged using the double-bag technique. To establish the baseline properties, the 16-ply lay-up was thermally cured by heating the lay-up to 170°F under vacuum. After the temperature reached 170°F, the inner bag vacuum was turned off, and the vacuum on the second bag was applied and maintained while heating the laminate to 350°F. Final cure was at 350°F for 2 hours. Per-ply thickness of the cured laminate measured 6.06 mil; the photomicrograph in Figure 26 indicates porosity in the center section of the laminate. This panel was sent to the University of Dayton Research Institute (UDRI, Dayton, OH) for

flexural and SBS testing at ambient conditions. The SBS strength was 10.4 ksi, the flexural strength 177.0 ksi, and the modulus 19.6 Msi. The SBS strength is comparable to AS4/CAT-M data; however, there is a reduction of approximately 30% in flexural strength due to the addition of thermoplastic component in the matrix resin.

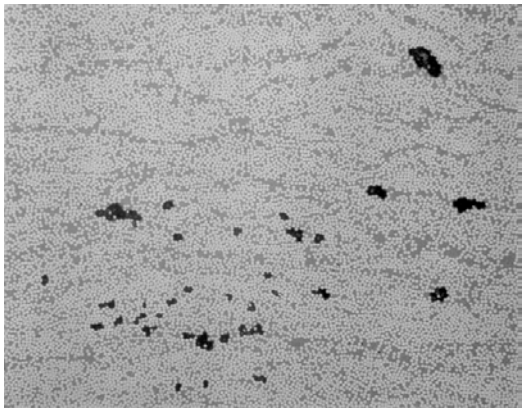

Figure 15. Photomicrograph of AS4/T-17 Laminate Showing Porosity.

Figure 16. Photomicrograph of AS4/T-17 Laminate with Improved Processing.

A second 16-ply laminate was processed using a slightly modified processing cycle to prevent porosity from developing during cure. Using the same double vacuum-bagging technique, the lay-up was heated to 170°F and allowed to dwell at that temperature for one hour under vacuum. After one hour, vacuum on the first bag was turned off, vacuum on the second bag was turned on, and heating was continued to 350°F for 2 hours. The cured laminate looked excellent (Figure 15), and per-ply thickness was reduced to 5.88 mil, which is comparable to autoclave-cured laminate per- ply thickness. Resin content by weight of 30.9% and fiber volume of 59.1% were determined from acid digestion. There is no detectable porosity in the photomicrograph of the second laminate (Figure 16). The mechanical performance of this panel was also evaluated. SBS strength of 12.19 ksi, flexural strength of 189.46 ksi, and flexural modulus of 17.21 Msi were obtained for the non-porous laminate. The per-ply thickness of this non-porous laminate was 5.8 mil per ply, while the porous laminate had a per-ply thickness of 6.0 mil. A comparison of the SBS and flexural properties of the porous and non-porous laminates is shown in Figure 17. A 7% improvement can be seen for the flexural strength values, but a much greater improvement, 17%, is realized for the SBS strength numbers. This is not surprising; because of the small SBS specimen size, any defects such as porosity in the specimen will result in a drastic decrease in the tested values.

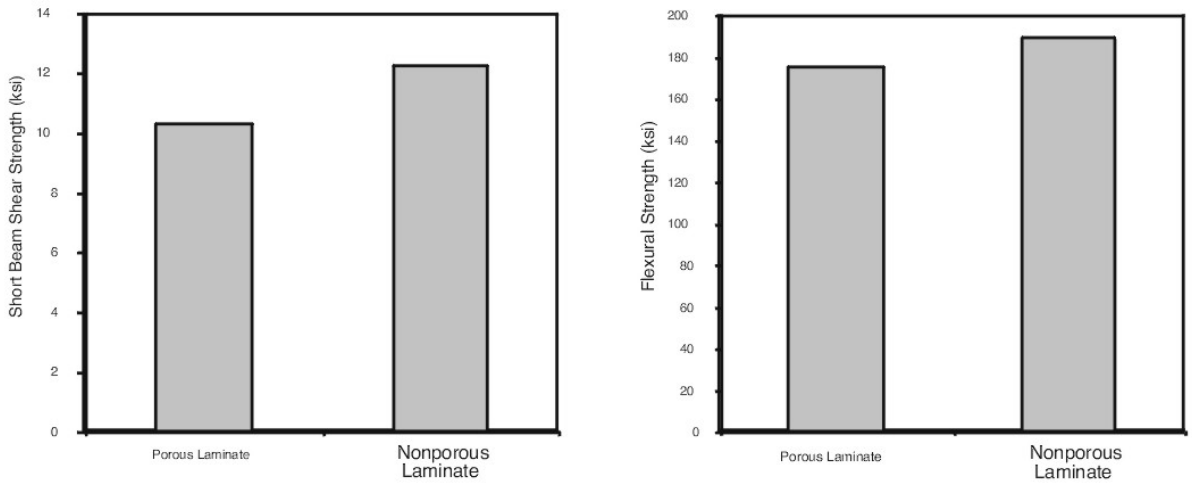

Figure 17. Mechanical Property Comparison of Porous and Nonporous Laminates.

Thirty specimens from each panel were machined to 1" x 0.25" for SBS testing. Prior to testing, two-thirds of the specimens were conditioned using a 3-day water-boil for hot/wet testing. Moisture absorption of the conditioned specimens is listed in Table 12. Figure 18 shows a bar chart of the moisture pick for each set of specimens. Percent moisture absorption for specimens C-1 and C-2 is much lower than that for specimens A-1, A-2, B-1, and B-2. It appears that the high dose rate of E-beam produces more highly crosslinked networks in C-1 and C-2. It is important to point out that the high dose rate (75 kGy/pass) also creates a large amount of exotherm during cure. The curing process from the high dose rate is from not only the E-beam energy but also the heat generated during exotherm. This suggests a degree of cure of close to 100 percent for laminates C-1 and C-2, and was validated by the DSC data, which showed no residual exotherm for C-1 and C-2. The combination of the high dose rate and the exotherm produces a molecular network that is much more efficient, containing a much smaller amount of free volume. Since the moisture uptake of a composite laminate is closely related to the free volume in the molecular network, it is not surprising to see a smaller weight gain for laminates C-1 and C-2.

Table 12. Absorption of Moisture-Conditioned Specimens

	Day 1 (% Gain)	Day 2 (% Gain)	Day 3 (% Gain)
A-1	0.46	0.51	0.59
A-2	0.52	0.54	0.65
B-1	0.35	0.45	0.55
B-2	0.40	0.54	0.63
C-1	0.27	0.33	0.35
C-2	0.20	0.25	0.33

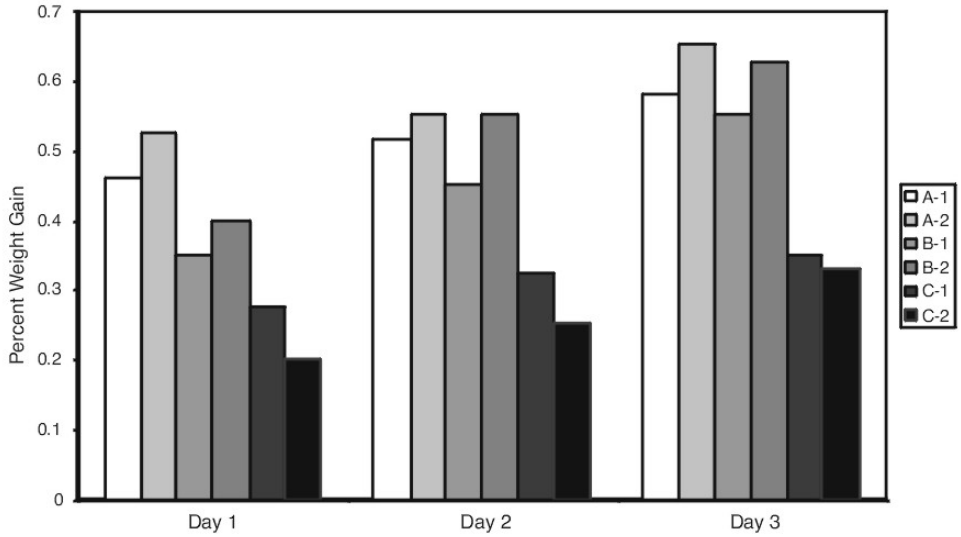

Figure 18. Moisture Absorption of SBS Specimens.

SBS testing was conducted using ASTM D2344 at room-temperature/dry, 180°F/wet, and 220°F/wet conditions. The data are shown in Figure 19. A minimum of five specimens was tested for each condition. In addition to the three aforementioned laminates, an AS4/T17 laminate was E-beam cured at Acsion Industries using their 10 MeV machine at a curing dose of 25 kGy/pass for a total dose of 150 kGy. The SBS data for this laminate were also shown in the figure. In almost every condition, SBS strength increases with dose rate. Although the increase is not huge (about 7.5% from 5 kGy to 75 kGy for 220°F/w), the trend is consistent.

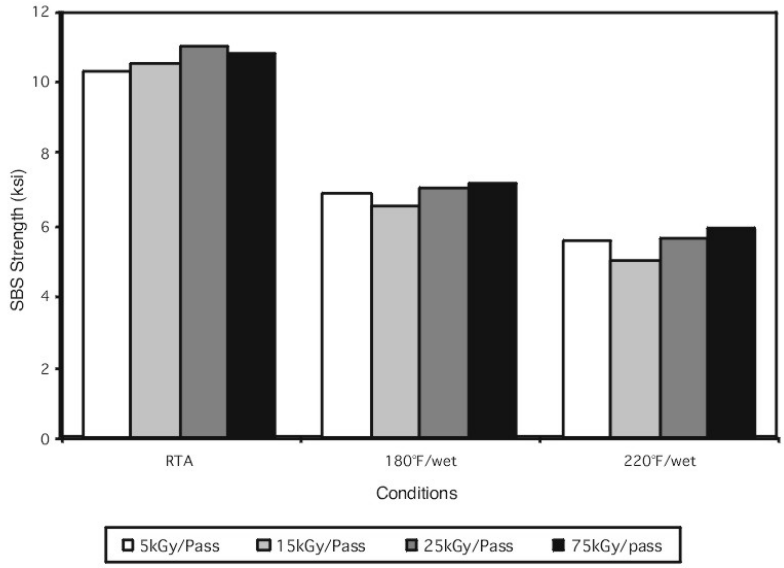

Figure 19. SBS Strength of E-Beam-Cured Laminates.

For the AS4/T-17 laminate cured at 25 kGy/pass, flexural properties were also determined at RTA, 180°F/wet, and 220°F/wet as shown in Table 13. The wet specimens were conditioned in 3-day water boil. The 3-point flexural testing was conducted according to ASTM D790. The average data were based on three specimens, and the modulus was taken between 10 and 40% of the ultimate load. Hot/wet specimens exhibited good retention of properties compared to the room-temperature specimens.

Table 13. Flexural Properties of AS4/T-17 Cured at 25 kGy/pass

	RTA	180°F/wet	220°F/wet
Strength (ksi)	183	167	157
Modulus (Msi)	18.4	17.8	18.1

1.2 E-Beam VARTM Resins

Vacuum assisted resin transfer molding (VARTM) has become an important composites processing technique. In the VARTM process, the liquid resin converts into a non-tacky solid during cure. Curing is accomplished via chemical reactions between monomers, which leads to the formation of a three-dimensional network. Energy for this process can be supplied in various forms, such as heat or radiation. There are various sources for radiation, including microwave, infrared, ultraviolet (UV) light, and electron beam. Thermal curing has traditionally been preferred over radiation curing for fabricating thick polymer-matrix composites because of the limited penetration depth of radiation and the high cost of radiation equipment. However, recent developments and better electron-beam equipment has revived interest in radiation curing. In addition to reduced processing time, e-beam curing offers many advantages over traditional thermal curing, including the following:

- Unlimited material shelf life
- Reduced energy consumption
- Curing at selectable temperatures
- Curing of complex-shaped parts with inexpensive tooling
- Line-of-sight cure
- Shorter curing time
- Lower health risk
- Low volatile organic content (100% solids resins)
- Reduced cure shrinkage

In order to take advantage of e-beam curing, the developed resin should form a partially cured structure that can be easily transported for complete curing by electron beam. In addition, resins that can be processed using non-autoclave techniques such as VARTM and RTM should be developed to realize the significant cost savings associated with this technique.

1.2.1 SELECTION CRITERIA

The most important requirement for VARTM resins is a viscosity of less than 500 cps at processing temperature. Presently available and commercially used VARTM resins are based on epoxy or vinyl ester. The presence of unsaturated bonds in vinyl-ester resin allows

curing by several different methods. Vinyl-ester resins have T_gs around 250°F, but they exhibit very low toughness compared to commercially available epoxy resins. On the other hand, thermally cured epoxy resins designed for VARTM often have a low T_g. The primary objective of this research is to develop a new generation of toughened VARTM resins with the following properties:

- Viscosity less than 500 cps at processing temperature
- T_g between 250°F and 350°F
- Fracture toughness above that of presently available resins
- Ability to be cured thermally as well as by radiation
- Unlimited shelf life
- Environmentally friendly
- Commercially available or easily scaleable monomers

1.2.2 FORMULATION APPROACH

Radiation can initiate free radical or ionic polymerization. In this program, a new generation of radiation-cured systems based on free radical curing is examined. This novel system uses interpenetrating polymer network (IPN) synthesis. Figure 20 shows the chemistry of the developed resin forming the IPN. In addition, work has been performed to develop cationic systems for VARTM application.

The curing process of an epoxy-vinyl-based IPN system involves step-growth as well as free-radical polymerization. The step-growth reaction takes place between epoxy and amine, while free radical curing brings about polymerization in the vinyl group. The resin is a mixture of difunctional epoxy, tetra-functional amine, a unique monomer with epoxy and vinyl functionality, and di-vinyl monomers. The resin mixture is cured initially at low temperature, where the epoxy-amine forms a polymer network, while the vinyl monomer remains un-reacted inside the network. The epoxy end of the unique monomer used in the resin becomes a part of the epoxy-amine network upon initial thermal curing, while the vinyl end remains pendant on the network. This constitutes a C-stage structure. The C-stage material is then cured completely by e-beam to form a second network of vinyl monomers or diluents. The polymerization of pendant vinyl groups along with the diluents provides co-continuity between the two networks. The combination of two networks forms an IPN. Since the two polymer networks were formed sequentially, it can be called a *sequential IPN*.

The advanced feature of this formulation approach is that the resin can be tailored in various ways to meet any specific property requirement. By varying the functionality of the epoxy monomer, the crosslinking density of the C-stage system—and hence the T_g of the cured system—can be varied. The number of pendant double bonds on the epoxy-amine network can also be varied, which affects the crosslinking density of the vinyl network with the epoxy-amine network. The effect on the property of the cured system when the diluent is changed is also measurable. The resin system shown in Figure 21 meets the viscosity requirement of the VARTM process and also provides a glass transition temperature in the range of 250°F. To approach a T_g of 350°F, the crosslinking density of the C-stage network and the number of pendant double bonds were varied. The composition of formulated high T_g resin was varied to form a high T_g resin with moderate viscosity and a high T_g resin with low viscosity. The toughness of these materials does not meet the standard set by epoxy-

based VARTM resins. To improve the toughness of developed IPN-based VARTM resins, two approaches were taken:

1) Synthesis of a new homo- or copolymer by varying the reactive diluent.
2) Modification of the existing polymer through the addition of a second polymeric component.

The first approach involved the use of diluents with different functionalities as well as different backbone structures. The second approach is also called *blending*. Rubber is the most commonly employed blending agent for the toughening of polymers. Rubber provides a disperse phase into a rigid plastic matrix and also provokes yielding of the matrix material. As a result, the blend shows considerably higher fracture toughness than the parent polymer. However, in order to achieve satisfactory performance, a certain degree of chemical interaction between the resin and the modifier is required to improve the interfacial adhesion. To overcome this limitation, a compatible rubber agent whose functionality is adjusted according to the chemical nature of the matrix was added. In addition to the use of a rubber modifier, the second approach also involved the use of dendritic polymers. These polymers have a functional compatibility with the matrix that makes them soluble in uncured resin. However, during curing, they precipitate from the solution and phase separate. The second phase results in overall toughening of the two-phase blend.

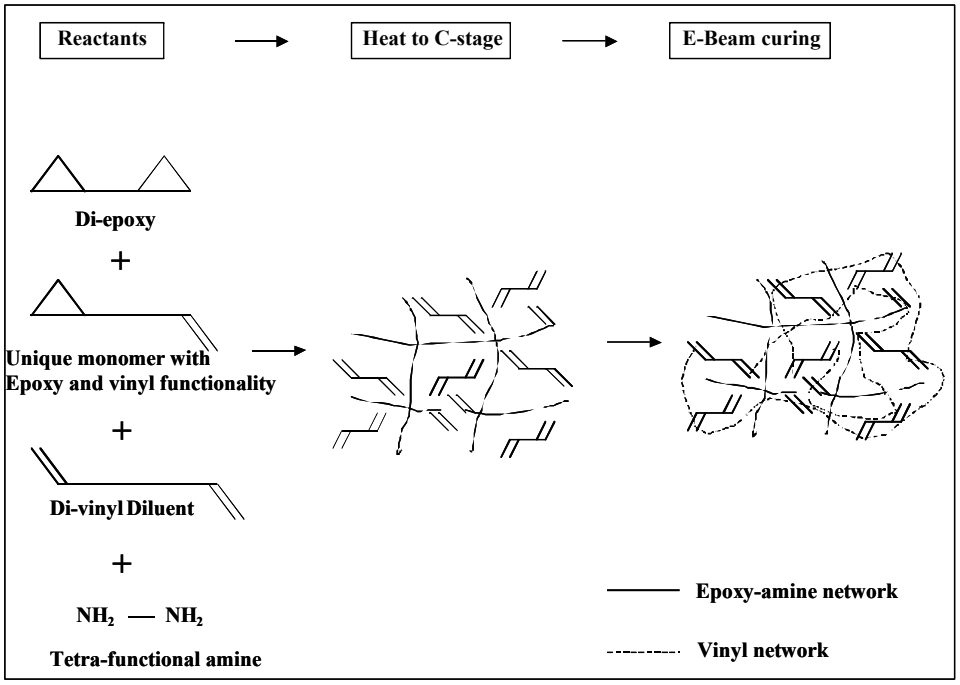

Figure 20. Chemistry of an IPN-based VARTM resin.

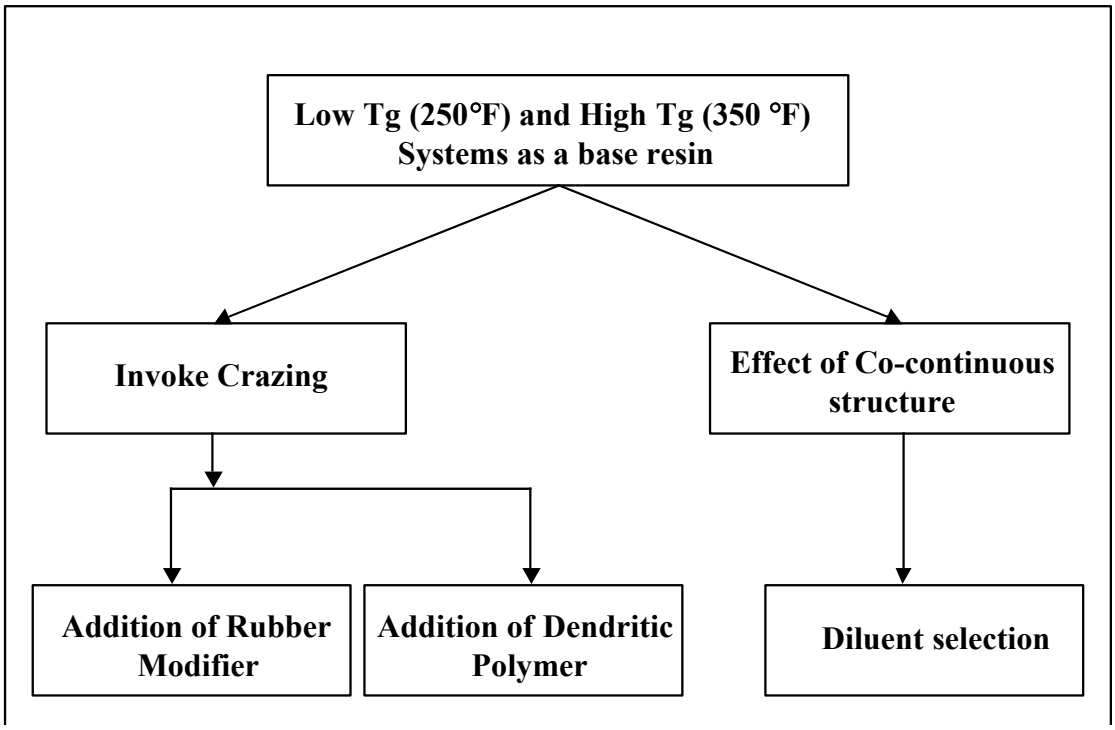

Figure 21. Approach used to toughen the VARTM resin.

1.2.3 RESIN PROPERTIES

1.2.3.1 Design

As mentioned earlier, the developed resin based on an IPN system is made up of two parts: the step-growth epoxy-amine part and the free-radical-curable vinyl part. The base resins used in the study are CCM1, CCM2, and CCM3 (Table 14). They all contain diluents but no rubber modifier. CCM1 is a low T_g resin with low viscosity. CCM2 and CCM3 are the base resins with high T_g. The viscosity of CCM2 is lower than that of CCM3.

Table 14. Basic CCM Resin Properties

Resin	T_g	Viscosity (cp)		
		30°C	40°C	50°C
CCM1	Low (250°F)	200	170	95
CCM2	High (350°F)	340	135	125
CCM3	High (350°F)	1050	550	200

The replacement of diluents or addition of modifier to these developed resins to increase the toughness created a series of resins. The features and properties of diluents and rubber modifiers investigated are shown in Table 15.

Table 15. Rubber Modifiers and Diluents for VARTM Toughening

	Features	Viscosity - 25°C	Functionality
D1	Hard and high T_g	8 cps	Di-
D2	Aromatic backbone	—	Di-
D3	Flexible	—	Mono-
D4	Flexible and high impact strength	25 cps	Di-
D5	Cyclic group with high T_g	11 cps	Mono-
D6	Low shrinkage	67 cps	Di-
R1	High elastomer content and high viscosity	1500-2500 poise	Di-
R2	High elastomer content and moderate viscosity	40-80 poise	Di-
R3	High elastomer content and moderate viscosity	20 poise	Di-

The series of resins formulated using these constituents and base resin is tabulated with their composition in Table 16. Each number in parenthesis suggests the overall weight percentage of that component in a resin mixture.

Table 16. Generic Composition List of Additional Resins

Set	Base resin	Diluents (Overall percentage)		Modifier (Overall Percentage)
CCM4	CCM1	D1 (30)	D2 (20)	R1 (5)
CCM5	CCM1	D1 (30)	D2 (20)	R1 (10)
CCM6	CCM2	D1 (30)	D2 (20)	R1 (5)
CCM7	CCM2	D1 (30)	D2 (20)	R1 (10)
CCM8	CCM3	D1 (25)	D2 (25)	R1 (5)
CCM9	CCM3	D1 (25)	D2 (25)	R1 (10)
CCM10	CCM1	D1 (30)	D2 (20)	R2 (10)
CCM11	CCM1	D1 (30)	D2 (20)	R3 (10)
CCM12	CCM2	D1 (30)	D2 (20)	R2 (10)
CCM13	CCM2	D1 (30)	D2 (20)	R3 (10)
CCM14	CCM3	D1 (25)	D2 (25)	R2 (10)
CCM15	CCM3	D1 (25)	D2 (25)	R3 (10)
CCM16	CCM1	D3 (30)	D2 (20)	—
CCM17	CCM1	D4 (30)	D2 (20)	—
CCM18	CCM1	D5 (30)	D2 (20)	—
CCM19	CCM1	D6 (30)	D2 (20)	—
CCM20	CCM2	D3 (30)	D2 (20)	—
CCM21	CCM2	D4 (30)	D2 (20)	—
CCM22	CCM2	D5 (30)	D2 (20)	—
CCM23	CCM2	D6 (30)	D2 (20)	—
CCM24	CCM3	D3 (25)	D2 (25)	—
CCM25	CCM3	D4 (25)	D2 (25)	—
CCM26	CCM3	D5 (25)	D2 (25)	—
CCM27	CCM3	D6 (25)	D2 (25)	—

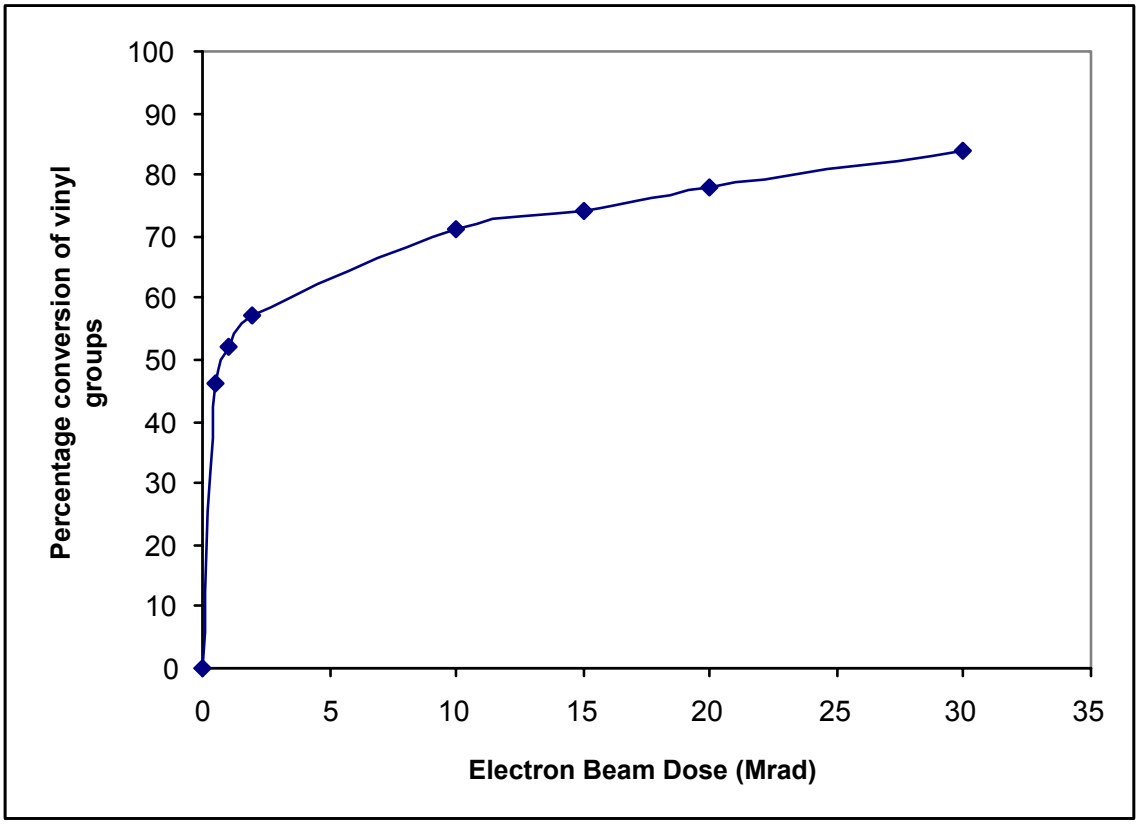

Figure 22. Percent Conversion of vinyl groups as a function of e-beam dose.

Each of these sets was mixed thoroughly and degassed before being cured at low temperature to form a C-stage structure. The C-stage material was then exposed to e-beam for complete curing.

1.2.3.2 Electron Beam Dose Effects

To determine the optimum e-beam dose required for cure, Fourier transform infrared (FTIR) spectroscopy was used. Several samples of one formulation were C-staged and then exposed to varying levels of e-beam dose. The conversion obtained as a result of e-beam exposure was then measured and compared. The range of e-beam dose selected was from 0.5 Mrad to 30.0 Mrad because most of the radiation-cured systems evaluated thus far cure between 7.0 and 25.0 Mrad. The plot of e-beam dose versus percentage conversion of vinyl group is shown in Figure 22. The conversion increases rapidly with an increase in e-beam dose for low doses. Once the e-beam dose increases beyond 2.0 Mrad, the increase in conversion slows down. Since the increase in dose also increases process cost, a tradeoff exists between conversion and process economy. Based on that, for the present work a dose of 20.0 Mrad was selected as optimum.

1.2.3.3 Viscosity Evaluation

Resin viscosity is an important factor in VARTM processing. The viscosity of the developed resin was measured at the beginning of the curing process at three temperatures. Viscosity

experiments were carried out on a Brookfield Model LVDV II+ digital viscometer. Sample temperature was controlled with the Brookfield small sample adapter and Brookfield bath/circulator model TC-200. The viscometer consists of a fixed outer cylinder and a spindle that rotates at a constant angular velocity. The spindle is connected to a torque spring, which measures the frictional resistance offered by the sample. The viscometer converts the resistance into viscosity.

All components of the synthesized resin except the curing agent were mixed and heated to the desired temperature. The curing agent amine was added after the equilibrium temperature was reached. Approximately 10 ml of sample was measured and used for viscosity analysis. After the addition of amine, initial viscosity was measured. Viscosity data was collected at various temperatures.

Viscosity is one of the selection criteria for VARTM resins. The viscosity of the developed resins was measured without curing agent at room temperature using a rotational viscometer (Table 17). The viscosity of F1-modifier-based resin is much lower than that of the A1-modifier-based low T_g systems. The increase in viscosity with the addition of dendrimer to VCCM1.1 and VCCCM1.2 is less than that resulting from addition of the same amount of reactive elastomer to those systems, which is both the expected and desired result. VCCMU3.1 uses more low-viscosity (hyperbranched dendritic) diluent than CCM3, which helps to lower the viscosity of the formulation. The addition of dendrimer U1 to VCCMU3.1, as well as the addition of reactive elastomer to VCCM1.1, increases the viscosity beyond the VARTM maximum of 500 cps. However, these measurements were carried out without the curing agent, which has a viscosity of 180 cps, thus making the set part A and B mixtures near or below 500 cps.

Table 17. Viscosity Analysis of the Developed Resin Systems at Room Temperature

Set	Viscosity without curing agent (cps)
VCCM1.1	290
VCCM4.1	470
VCCMD.1	370
VCCM1.2	390
VCCM4.2	550
VCCMD.2	430
VCCMU3.1	395
VCCMU3.1.1	535

1.2.3.4 Thermal and Cure Characterizations

The glass transition of the cured resin was measured using a DuPont 983 Dynamic Mechanical Analyzer (DMA) interfaced with a DuPont 9900 thermal analyzer. A sample with dimensions of approximately 30 mm x 10 mm x 2.5 mm was prepared from the cured resin matrix. The specimens were placed in the test grips, and the arm displacement was zeroed. The heater assembly surrounding the sample provided a uniform temperature

environment. The DMA was run in fixed-frequency mode at 1.0 Hz. The peak-to-peak amplitude was kept between 0.1 and 0.3 mm. The sample was heated at 5°C per minute to the final temperature of 200°C or 250°C for low and high T_g systems respectively. The shear storage (E') and loss (E") moduli obtained were stored as a function of temperature.

Table 18 shows the value of T_g and storage modulus after E-beam irradiation and post-curing. T_g values were obtained from the loss modulus versus temperature plot as the temperature associated with the loss maximum. Figure 23 shows plots of storage and loss moduli as a function of temperature for VCCM1.2 resin systems at two stages. It is apparent from the plot that the storage modulus decreases after post-curing, while T_g increases. This trend was observed for all systems, as shown in Table 18. Post-curing increases molecular motion, which releases trapped radicals to continue the reaction, increasing final group conversion and T_g.

Table 18. DMA Analysis of IPN Based Formulations

Set	After E-beam curing		After post-curing	
System	T_g (°C)	Storage Modulus (GPa)	T_g (°C)	Storage Modulus (GPa)
VCCM1.1	107	3.5	132	3.0
VCCM4.1	122	2.8	129	2.5
VCCMD.1	97	2.5	119	2.3
VCCM1.2	110	2.8	125	2.6
VCCM4.2	112	3.2	125	3.1
VCCMD.2	95	2.6	110	2.3
VCCMU3.1	140	2.6	172	2.6
VCCMU3.1.1	127	3.1	165	3.0

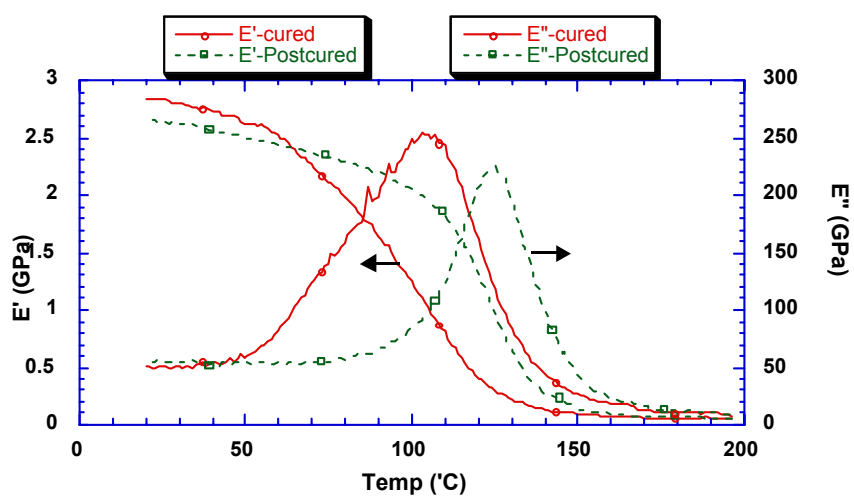

Figure 23. DMA plot for VCCM1.2 system

DMA plots of post-cured VCCM1.1, VCCM4.1, and VCCMD.1 are shown in Figure 24. It is evident from the plot of VCCM4.1 and VCCM1.1 that the addition of reactive elastomers

does induce a slight decrease in T_g and storage modulus. This effect is consistent with rubber toughened epoxy materials that cure by thermal means as well [3]. However, greater deterioration of these same properties (T_g and E') was observed for the dendrimer-modified systems. The T_g of the base system VCCM1.1 dropped by 15°C upon addition of dendrimer E1, as shown by the DMA plot of system VCCMD.1. Unfortunately, retention of storage modulus is an additional requirement for resin selections in this program. The decrease in storage modulus for VCCM1.1, VCCM4.1, and VCCMD.1 at 120°C was 50%, 53%, and 65%, respectively. For VCCM1.2, VCCM4.2, and VCCMD.2 at 120°C, the decreases were equivalently poor at 53%, 60%, and 80%, respectively.

Storage and loss moduli plots for post-cured VCCM1.2, VCCM4.2, and VCCMD.2 are shown in Figure 25; the trend for reactive elastomer and dendrimer was similar to that observed for VCCM1.1 and its derivative systems.

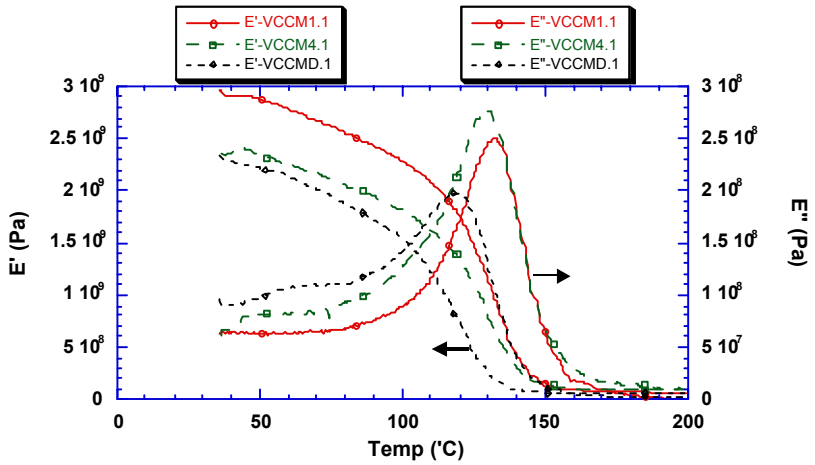

Figure 24. Storage and loss modulus as a function of temperature for post-cured VCCM1.1 and its derivative systems.

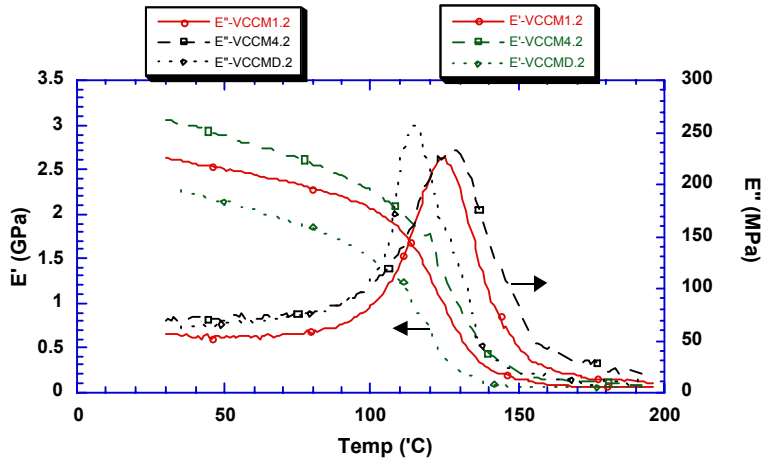

Figure 25. DMA results of post-cured VCCM1.2, VCCM4.2, and VCCMD.2 systems

Figure 26 displays DMA results of post-cured VCCMU3.1 system along with the VCCMU3.1.1. Inclusion of dendrimer U1 in the second network of the IPN decreased the T_g by 7°C, as shown by VCCMU3.1.1. Systems VCCMU3.1 and VCCMU3.1.1 retained 50% of storage modulus at 150°C.

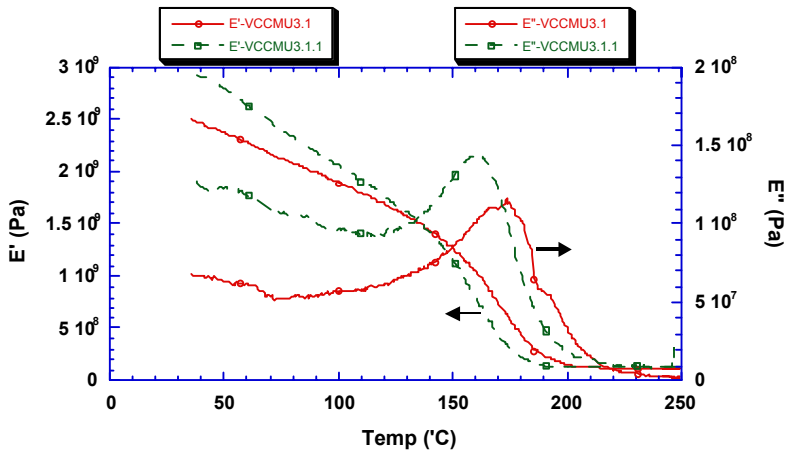

Figure 26. DMA analysis for post-cured VCCMU3.1 and VCCMU31.1 resins

Two sets of cured and post-cured samples of the systems discussed thus far were conditioned by boiling for 48 hours in deionized water. Multiple DMA runs were conducted per sample, and the weight gain of water was recorded for the boiled samples.

Table 19 shows wet T_g and weight gain results. The weight gain was less than 2% for all systems. However, as with most epoxy-based systems [4], substantial drops in T_g were observed for both low and high T_g systems. The T_g reductions typically range from 15–20°C and were found to be reversible. In addition, 48-hour water-boil conditioning also resulted in a 10–20% decrease in storage modulus, a result consistent with water plasticization in polymers.

Table 19. Wet DMA Analysis after 48-hour water boil in IPN Resin Formulations.

	After E-beam curing			After post-curing		
System	T_g (°C)	Storage Modulus (GPa)	Weight gain (%)	T_g (°C)	Storage Modulus (GPa)	Weight gain (%)
VCCM1.1	113	2.8	<2	113	2.5	<2
VCCM4.1	110	2.2	<2	110	2.8	<2
VCCMD.1	92	2.3	<2	102	2.5	<2
VCCM1.2	110	2.7	<2	115	2.6	<2
VCCM4.2	105	2.7	<2	110	2.2	<2
VCCMD.2	95	2.2	<2	108	2.0	<2
VCCMU3.1			<2	153	2.4	<2
VCCMU3.1.1	127	2.7	<2	142	2.1	<2

Figure 27 shows the plot comparing conditioned and dry VCCM1.1 resin. It also shows plots of E' and E" from DMA runs of the wet sample after drying at 200°C, which shows 90% recovery in T_g.

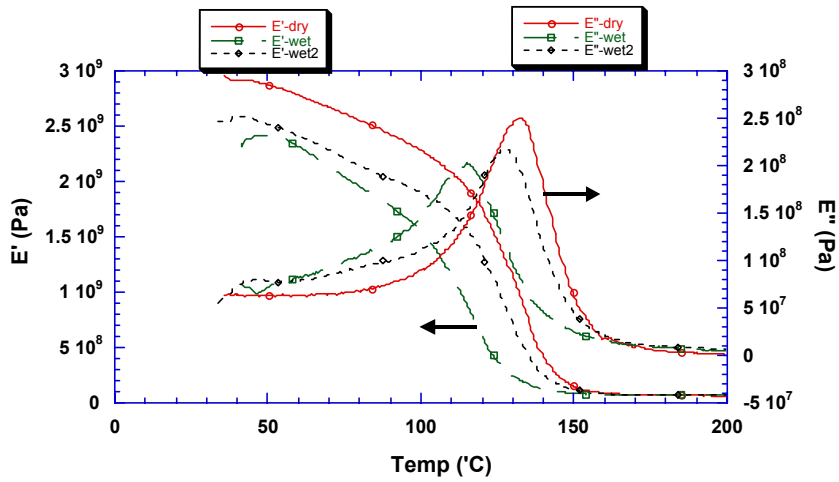

Figure 27. Wet DMA analysis of VCCM1.1 resin

1.2.3.5 Toughness and Strength Evaluations

Fracture toughness measurements were conducted using single-edge-notch bending specimens in according with ASTM D 5045 [5]. The critical stress intensity factor (K_{Ic}) and the strain energy release rate (G_{1c}) are summarized in Table 20 for the set of 8 resin systems under investigation.

The VCCM4.1 resin modified with reactive elastomer showed an increase in toughness of 50%. The addition of dendrimer E1 to VCCMD.1 resulted in only a 25% improvement in toughness but a substantial deterioration in T_g and E' performance in the VCCM1.2-derived resins.

The high-temperature resin VCCMU3.1 was modified using dendrimer U1, which unlike E1 dendrimer reacts with constituents of the second network of an IPN. This resin, VCCMU3.1.1, exhibited 100% improvement in toughness over the base VCCMU3.1 system.

Table 20. Fracture Toughness Results

Set	Critical stress intensity factor (K_{1c}) MPa $m^{0.5}$	Strain energy release rate (G_{1c}) J / m^2
VCCM1.1	1.20 ± 0.05	300 ± 40
VCCM4.1	1.40 ± 0.05	500 ± 60
VCCMD.1	1.18 ± 0.05	376 ± 40
VCCM1.2	1.27 ± 0.05	346 ± 40
VCCM4.2	1.19 ± 0.05	352 ± 40
VCCMD.2	0.96 ± 0.05	252 ± 30
VCCMU3.1	0.80 ± 0.05	180 ± 30
VCCMU3.1.1	1.16 ± 0.05	360 ± 40

Flexural properties of the material were measured in three-point bending in accordance with ASTM D 790-96a [1]. The flexural properties of E-beam-cured and post-cured samples are shown in Table 21. The flexural strength of VCCM1.1-based resin was higher than that of VCCM1.2-based resins. The systems modified using reactive elastomers—VCCM4.1 and VCCM4.2—performed satisfactorily. However, VCCMD.1 and VCCMD.2 exhibited 30% *lower* flexural strength and modulus than their counterparts VCCM1.1 and VCCM1.2, respectively. On the other hand, dendrimer modification of the high T_g systems showed promise.

Table 21. Flexural Analysis of IPN Formulated Resins

Set	After E-beam curing		After post-curing	
System	Flexural strength (psi)	Flexural Modulus (ksi)	Flexural strength (psi)	Flexural Modulus (ksi)
VCCM1.1	19500 ± 1000	635 ± 35	18403 ± 1000	530 ± 25
VCCM4.1	18410 ± 1000	550 ± 25	18672 ± 1000	560 ± 35
VCCMD.1	13855 ± 1000	470 ± 35	10819 ± 1000	450 ± 35
VCCM1.2	16999 ± 1000	600 ± 75	14139 ± 1000	550 ± 45
VCCM4.2	16170 ± 1000	520 ± 25	16712 ± 1000	550 ± 35
VCCMD.2	11472 ± 1000	470 ± 25	10000 ± 1000	450 ± 35
VCCMU3.1	16000 ± 1000	600 ± 75		
VCCMU3.1.1	16010 ± 1000	500 ± 25	15000± 1000	550 ± 25

The fracture surfaces of the base and modified resins were examined using scanning electron microscopy (SEM). The purpose of this study was to observe the distinct dispersed phase rubber or dendrimer. The degree of phase separation and the size of the particles were of particular interest in this part of the investigation. Figure 28 shows SEM of the fractured surface of the VCCM1.1 resin and its derivatives, VCCM4.1 and VCCMD.1.

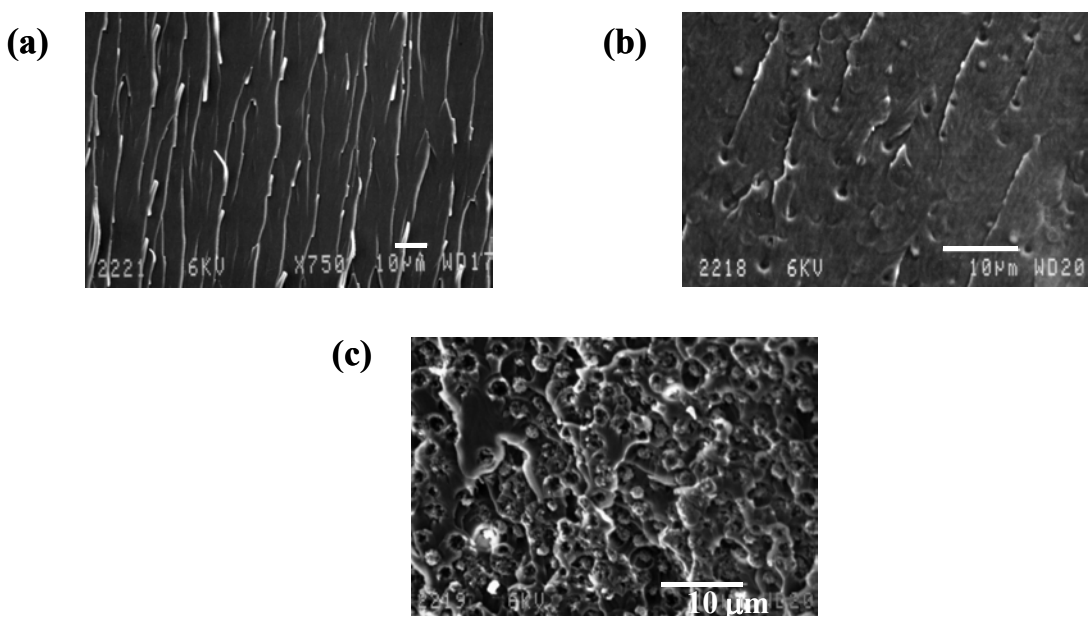

Figure 28. SEMs of Fractured Surfaces of VCCM1.1 Resin and Derivatives: (a) VCCM1.1, (b) VCCM4.1, (c) VCCMD.1

It is clear from the SEMs that the addition of rubber and dendrimer to the base resin creates a dispersed phase. The particle size formed by the addition of rubber is approximately 1μm, whereas particle sizes of approximately 2–3 μm were observed with the addition of dendrimer. The volume fraction of particles formed by the toughening agent was found to correlate with the amount of toughening agent added to the system. The amount of dendrimer used in VCCMD.1 was that of the reactive elastomer used in VCCM4; this is clearly visible in the micrograph comparison. VCCMD.1 shows that the particles have cavitated and fractured; yet the toughness has not improved. The voids formed by the rubber particles are more elliptical than those formed by the dendrimer. This elliptical shape of the voids is a result of shear deformation. Cavitation and shear deformation at the fractured surface correlates with the toughness results for VCCM4.1.

Figure 29 shows SEMs of VCCMU3.1 and VCCMU3.1.1 systems. Voids at the fractured surface of VCCMU3.1.1 systems are clear indication of the dispersed phase formed by the dendrimer U1.

(a) **(b)**

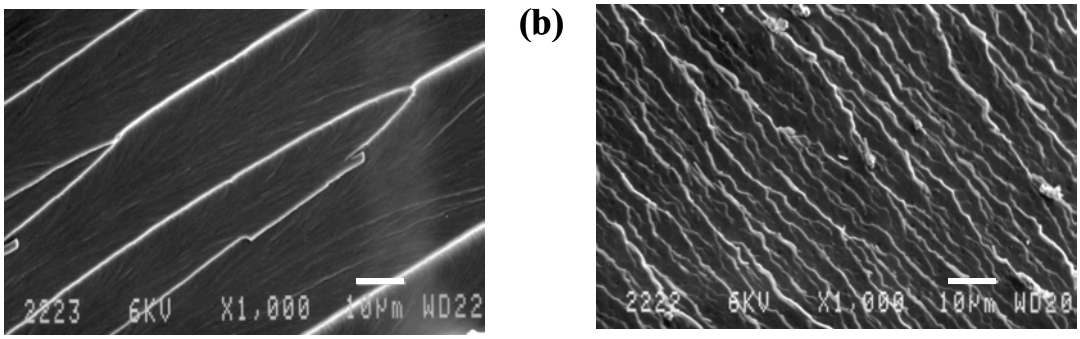

Figure 29. SEMs of (a) VCCMU3.1 and (b) VCCMU3.1.1

1.2.4 SUMMARY OF RESIN SYSTEM RESULTS

1.2.4.1 CCM1 Resin Series

Figure 30 shows the initial viscosity of all the systems based on CCM1 resin at various temperatures. The initial viscosity of all sets decreases with an increase in temperature. They all exhibit viscosity significantly below the criteria required for VARTM processing.

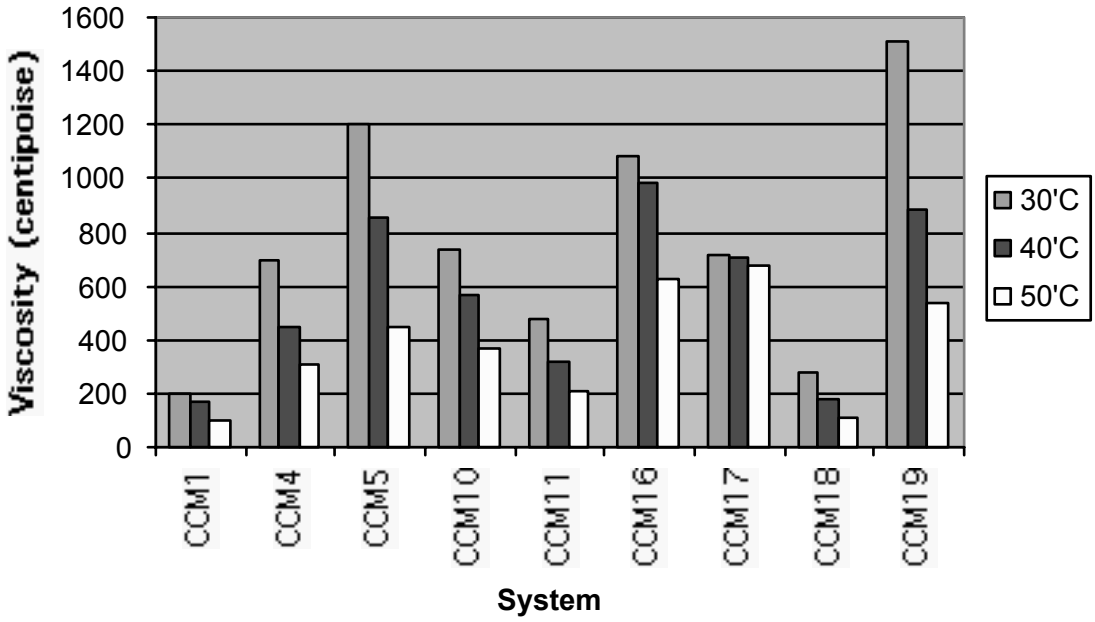

Figure 30. Viscosity analysis of CCM1-based modified systems

The viscosity, T_g, storage modulus E', G_Q, and K_Q data for CCM1-based resins are shown in Table 22. Empty entries in the table indicate that the analysis was underway at the time of this report. The combined analysis gives a broader view on the performance of the resin. CCM4 and CCM5, the systems with a rubber modifier added, show no change from the base resin in terms of T_g. The plot of storage modulus and loss modulus as a function of temperature for the CCM4 system is shown in Figure 31. At T_g, the material becomes rubber-like. Hence, the loss modulus shows a peak at glass transition temperature. For the CCM4 system, T_g is well exhibited by a distinct peak of loss modulus at 120°C. Although the viscosity of the CCM5 resin is higher than that of the base resin CCM1, it is significantly lower than required by VARTM processing. The addition of 10 wt% R1 rubber to the system increases the fracture toughness of the base resin by approximately 134%. The addition of low-viscosity rubber R3 to the base resin, CCM1, also results in a T_g of about 120°C. However, the critical strain energy release rate at the fracture initiation is less than that of the base resin.

Table 22. Properties of CCM1-Based Modified Resins

	Viscosity (cps)			Tg (°C)	E' at room temperature	G_Q (J/m^2)	K_Q ($Mpa.m^{0.5}$)
	30°C	40°C	50°C				
CCM4	693	450	307	117	3.25 GPa		
CCM5	1200	850	450	120	2.15 GPa	883.86	2.034
CCM10	735	565	363	95			
CCM11	475	315	210	120	2.5 GPa	464.82	1.452
CCM16	1080	985	625	85	2.25 GPa	2458.84	
CCM17	720	710	680	70	3.0 GPa	3959.72	
CCM18	275	175	112	116	2.8 GPa		
CCM19	1512	885	540	72	2.5 GPa	4330.16	3.532

The effect of replacing the diluent of the CCM1 resin resulted in a low T_g of the modified system. The diluents D3, D4, and D6—corresponding to resin systems CCM16, CCM17, and CCM19, respectively—resulted in T_g below 100°C. These diluents were used because of their flexible backbones. The resin systems with these flexible diluents failed at high fracture energy. They exhibited fracture toughness values 4 to 6 times higher than those of the base resin, but at the expense of the T_g. The resin system CCM18 exhibited a T_g value similar to that of the base resin. The plot of storage and loss modulus as a function of temperature for the CCM18 system is shown in Figure 32. The storage modulus shows the elastic energy stored by the system. Generally, the storage modulus of the system decreases with the increase in temperature. As seen in Figure 32, for the CCM18 system, the storage modulus remains unchanged up to 100°C. This characteristic of the system indicates higher fracture toughness. Most of the developed systems showed acceptable storage modulus at room temperature.

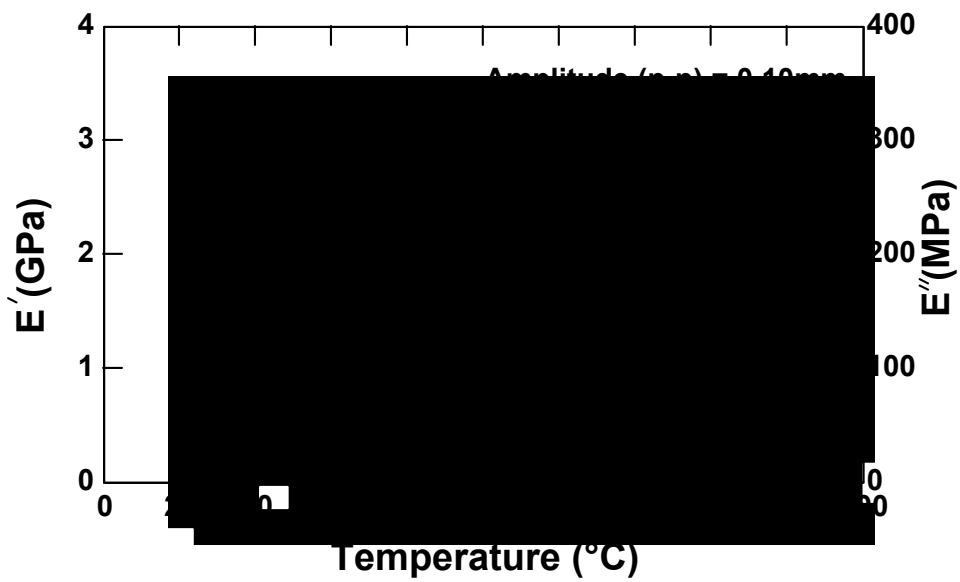

Figure 31. DMA analysis of the CCM4 resin system.

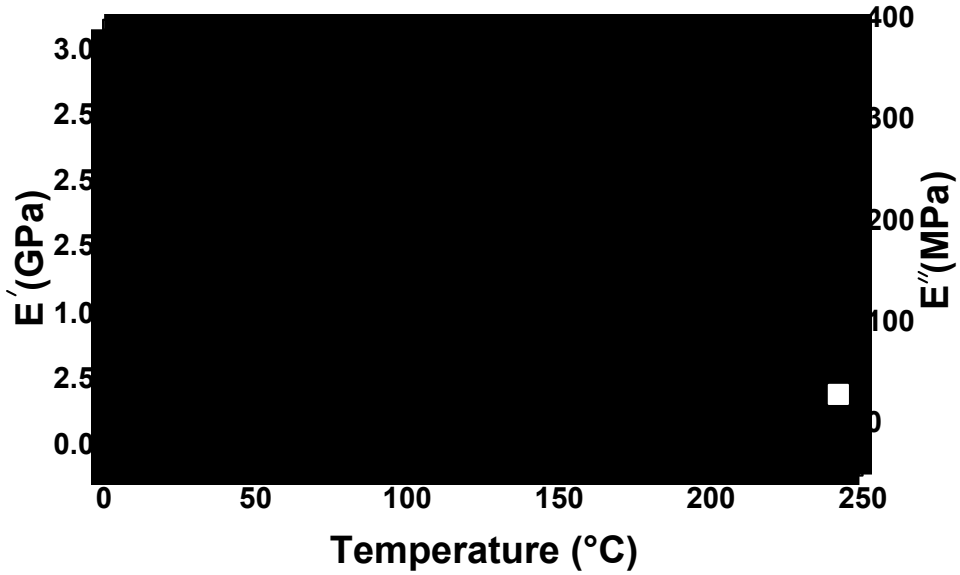

Figure 32. Storage and loss moduli as a function of temperature for the CCM18 resin.

1.2.4.2 CCM2 Resin Series

The CCM2 resin is a high T_g low-viscosity resin. The modifications used for the CCM1 system were also applied to the CCM2 system. The viscosity analysis of the modified CCM2 system is shown in Figure 33.

The results of fracture toughness and viscosity analysis along with T_g analysis are shown in Table 23. The cured CCM2 resin has higher crosslinking then the CCM1 resin, which gives a higher Tg for the CCM2 resin. However, the increase in crosslinking density reduces the toughness of the system. It has been shown that the addition of rubber to a highly crosslinked system does not provide significant improvements in toughness. However, the system under investigation, CCM2, does not fall in that highly crosslinked category. Hence, little attempt was made to increase the toughness via the addition of rubber modifiers. The addition of 5 weight percent of rubber (CCM6) to the CCM2-based resin yields a fracture toughness of 487.22 J/m^2. Further addition of rubber modifier results in deterioration of toughness and thermal stability.

Table 23. Properties of CCM2-Based Modified Resins.

	Viscosity (cps - 50°C)	T_g (°C)	E' at room temperature	G_{1C} (J/m^2)	K_{1C} ($Mpa.m^{0.5}$)
CCM6	267	148	2.15 GPa	487.22	1.625
CCM7	392	150	2.5 GPa	289.35	1.079
CCM12	309	142	1.75 GPa		
CCM13	264	152		367.93	
CCM20	465	99	3.0 GPa	315.45	
CCM22	375	155	1.55 GPa	379.11	1.268
CCM23	467	75	2.0 GPa		

Another commonly used approach to increase the toughness of the highly crosslinked materials is to blend them with the ductile, tough materials. In the present study, a similar concept was adopted in the form of diluent replacement. The CCM20 to CCM24 resins show the effect of diluent on T_g. Since, the CCM21 resin could not be cured, it is not included. As mentioned earlier, the use of diluent with flexible backbone such as D4 and D6, reduced the T_g of the base resin dramatically. The addition of D5 diluent with cyclic backbone to the base resin (CCM22) imparts toughness similar to CCM13 system with rubber modifier R3.

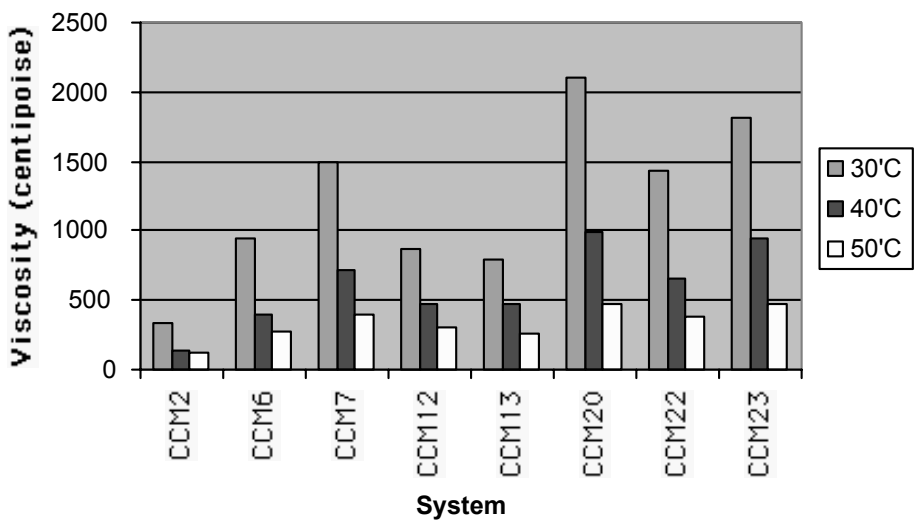

Figure 33. Viscosity analysis of CCM2-based modified systems.

1.2.4.3 CCM3 Resin Series

The CCM3 system is similar in C-stage structure to the CCM2 system. However, the diluent content makes this system viscous compared to CCM2. The initial viscosity of the CCM3-based modified resin at various temperatures is shown in Figure 34. The VARTM process allows the use of temperatures higher than room temperature. At 50°C, the viscosities of the modified resins fall close to the limit for VARTM processing.

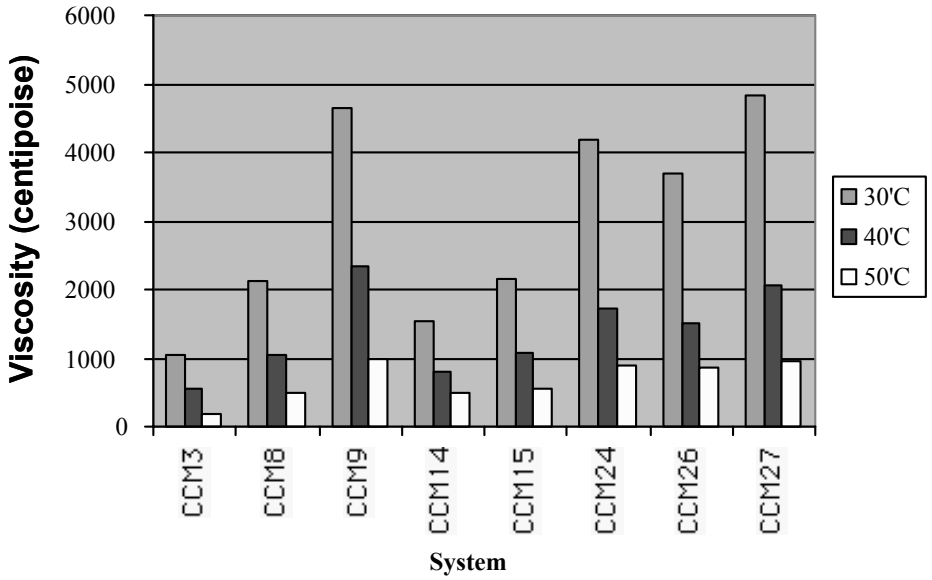

Figure 34. Initial viscosity of the CCM3-based toughened systems.

Table 24 shows the rheological, thermomechanical, and mechanical properties of CCM3-based modified systems. CCM15 resin is the base resin CCM3 with the addition of rubber modifier R3. This system exhibited high toughness but low T_g. CCM26, the system containing the D5 diluent, demonstrated an excellent T_g. The toughness of the CCM26 system is also comparable to that of the rubber-modified CCM14 resin. The DMA analysis of cured the CCM26 system is shown in Figure 35. The CCM3-based systems all show exceptionally high values of storage modulus at room temperature.

Table 24. Properties of CCM3-Based Modified Resins.

	Viscosity (cp at 50°C)	Tg (°C)	E' at room temperature	G_{1C} in (J/m^2)	K_{1C} ($Mpa.m^{0.5}$)
CCM8	505	160	3.15 GPa		
CCM9	1000	156	2.6 GPa		
CCM14	495	144	2.65 GPa	472.49	
CCM15	565	139	2.75 GPa	647.42	
CCM24	900			233.46	1.0227
CCM26	860	165	2.15 GPa	472.22	1.492
CCM27	950	120	2.85 GPa		

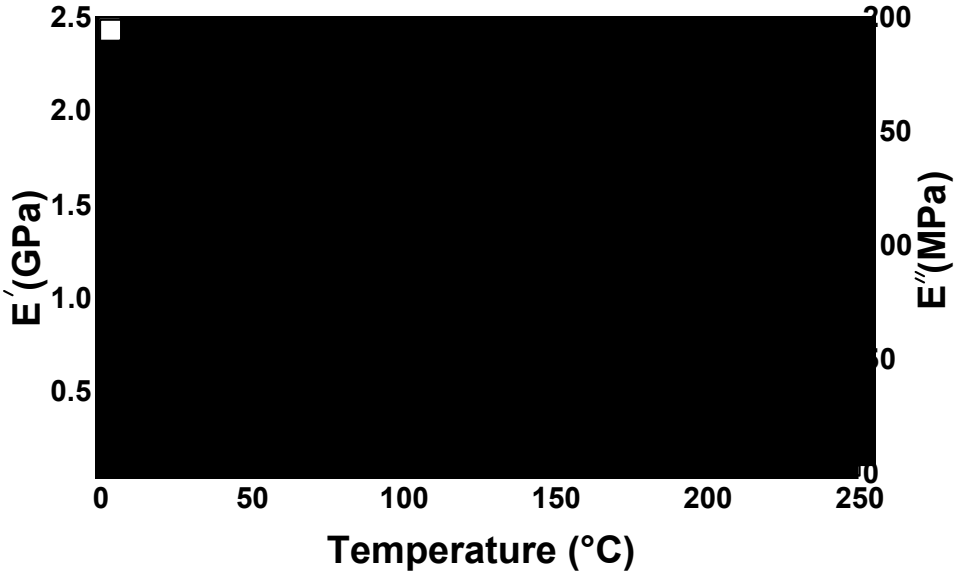

Figure 35. Thermomechanical analysis of CCM26 (CCM3 with diluent D5 added).

A number of monomer materials were explored before establishing the two resin series based on CCM 1 and CCM3. The matrix of materials is too extensive to include. Once downselection was made, however the general classes and features of the materials that were tested in conjunction with CCM1 and CCM3 are described in Table 25. F1 and A1 modifiers, which are partially methacrylated epoxy monomers, were used to replace the bifunctional monomer—monomer containing epoxy and vinyl functionalities—of the IPN. R1 is a CTBN type elastomer, while modifiers E1 and U1 are low-viscosity dendritic polymers with epoxy and vinyl functionalities, respectively.

Table 25. Modifier and Toughening Additives Properties

	Features	Viscosity (cps)	Functionality
F1	Flexible, epoxy and methacrylate group	~9,000	Di-
A1	Hard, epoxy and methacrylate group	~6,000	Di-
R1	High elastomer content and high viscosity	150,000–250,000	Di-
E1	Epoxy dendrimer and low viscosity	10,000–20,000	10-12
U1	Vinyl dendrimer and low viscosity	15,000	~14
D1	Hard and high T_g	8	Di-

The series of resins formulated using the constituents in Table 25 and CCM1 and CCM3 is reported in Table 26. Resin VCCM1.1 is based on CCM1 but uses the F1 modifier, which has a flexible backbone with methacrylate, and epoxy functional groups. VCCM4.1 resin is a rubber-toughened version of the VCCM1.1. The use of dendrimer E1 with VCCM1.1 resin

yields VCCMD.1 resin. A similar methodology was used to formulate VCCM1.2 resin and its derivatives. Resins based on VCCM1.1 and VCCM1.2 are low T_g systems.

VCCMU3.1 and VCCMU3.1.1 are high T_g resins. VCCMU3.1 resin is based on CCM3 resin but contains more diluent D1. Modified VCCMU3.1.1 resin is a mixture of dendrimer U1 and VCCMU3.1 resin.

Table 26. Composition of developed CCM Series Resins

Set	Base resin	Modifier	Toughener
VCCM1.1	CCM1	F1	
VCCM4.1	VCCM1.1		R1 (5%)
VCCMD.1	VCCM1.1		E1 (10%)
VCCM1.2	CCM1	A1	
VCCM4.2	VCCM1.2		R1 (5%)
VCCMD.2	VCCM1.2		E1 (10%)
VCCMU3.1	CCM3	Higher D1 content	
VCCMU3.1.1	VCCMU3.1		U1 (10%)

Each of these sets was mixed thoroughly and degassed before curing at 50°C to form a C-stage structure. Mixing of monomers with reactive elastomers (R1) and dendritic polymers (E1 and U1) produced homogeneous and clear mixtures. Upon curing at 50°C for three hours, the blends became opaque, a result of formation of secondary phases within the matrix. These secondary phases are attributed to the rubber and dendrimer in the systems. The C-staged materials were subsequently exposed to E-beam irradiation to complete the cure of the second matrix. All samples were irradiated to a 20 Mrad total dose using a cure schedule at E-Beam Services that included 2 passes at 0.5Mrads, 4 passes at 1.0 Mrad and 3 passes at 5.0Mrad. The samples had darkened substantially after the first 6 passes (5.0 Mrad) indicating high conversion of monomers. Some of the E-beam processed samples were then subjected to a thermal post-cure of 180°C for 1 hour, to allow residual stresses from E-beaming to relax from the matrix.

1.2.4.4 Cationic VARTM Resins

VARTM processing of VEB resin was initiated. To have ambient gelation with E-beam cure/post cure, two basic technologies have dominated. One type is a Lewis acid-type ambient cure with a cationic E-beam postcure. The other is an amine/epoxy cure with an E-beam free-radical postcure. A two-part resin system, called VEB-11 whose formulation is shown in Table 27 was developed by Applied Poleramic Inc. (Benicia, CA, USA) to take advantage of the C-stage development using acid C-stage with cationic E-beam curing.

Table 27. VEB-11 C-staging Cationic Resin Composition

Part A		Part B	
Component	**Parts Per Hundred**	**Component**	**Parts Per Hundred**
Epon 332	63	Benzyl alcohol	36
Epon 742	19	BL	33
Coupler	5	Lewis Acid	10
SR-203	5	DPI-1	21
SR-350	8		
955	1		
Dicup	0.1		

The coupler in part A is a bis-A epoxy with double bond on one end, similar to those materials used in IPN based resins to achieve network coupling; SR-203, SR-350, and 955 are acrylics; and Dicup is an acid cure catalyst. Both benzyl alcohol and BL are reactive diluents; DPI-1 is an E-beam activated initiator, iodonium salt described previously and commercially produced by Sartomer (Smyrna, GA, USA) under the trade name CD-1012.

The viscosity profile of VEB-11 at 40°C is shown in Figure 36. The viscosity increases drastically after 90 minutes at 40°C and reaches 1300 cps after 2 hours. At 30°C, the VEB-11 mixture does not gel for at least two days; at 80°C the mixture gels in 4 hours. The resin is mixed at a 10:1 ratio by weight of parts A and B at room temperature. The viscosity of the mixture at ambient is about 2000 cps. For the first panel processing, the mixture was not degassed. To extend the working time of the resin, injection was carried out at room temperature. However, the tool was heated to 80°F (27°C) during the injection.

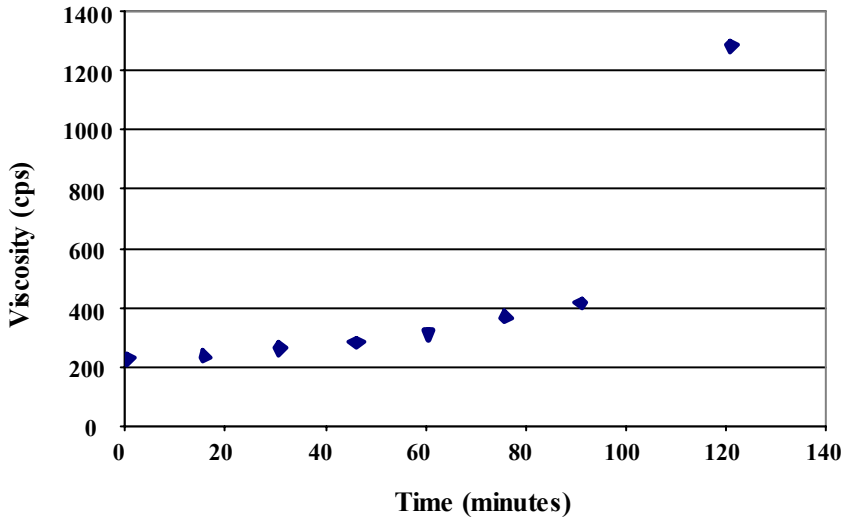

Figure 36. C-stage curing viscosity of VEB-11 at 40°C. Working life = 90 minutes.

The VEB-11 VARTM panel was fabricated using a double-bag VARTM technique. The preform is a 6-ply AS4 carbon fabric with conventional G sizing on the fiber surface. After

the injection was complete, the vacuum source on the first bag was shut down and the second vacuum left on. This panel was a control and was cured thermally at 175°C (350°F) for 2 hours under full vacuum using the outer bag. The cured laminate was examined using ultrasonic scan and laminate physical analysis was also conducted to determine the resin content and fiber volume of the panel. The fiber volume was only about 48%, resin content by weight 42%, and a void content 1.6%. The fact that the fiber volume was lower than expected was attributed to the low temperature of the tool (80°F) during injection. The resin flow at that temperature was very slow due to its high viscosity. Consequently, more resin was injected, resulting in a resin-rich laminate. A second panel was prepared, and the tool was heated to 110°F (75°). The resin injection was completed in 10 minutes, in contrast to 40 minutes for the first panel.

The AS4 fabric preform was laid up on a 1-in.-thick plate using the double vacuum bagging technique. This thinner tool was used for better heat conduction to the preform. The two-part VEB-11 resin was degassed after mixing to allow the small bubbles to escape to the top. The room temperature resin mixture was injected into the preform, which had been heated to 135°F. Total injection time to fill the part was 10 minutes. The panel was heated to 350°F under the second bag vacuum for 2 hours. The laminate was examined under the microscope; the photomicrograph showed excellent quality with no indication of porosity as shown in Figure 37. Acid digestion was conducted to determine the physical properties of the laminate. The resin content by weight was 29%, the fiber volume 62%. The laminate was tested for flexural and interlaminar shear properties at room temperature. The average SBS strength value for this laminate was 5.4 ksi; the average flexural strength and modulus were 100.3 ksi and 10.3 Msi, respectively. The flexural data is better than previous VEB-6 data (strength = 88 ksi; modulus = 8.0 Msi). The SBS strength of AS4/VEB-11 (5.43 ksi) is similar to that of AS4/VEB-6 (5.98 ksi).

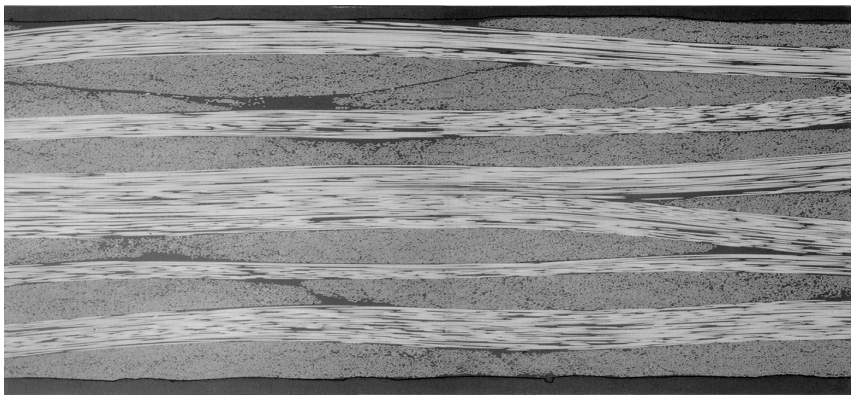

Figure 37. Photomicrograph of AS4/VEB-11 VARTM Laminate

A third VARTM panel was also processed. The panel was cooled after resin injection and removed from the project plate. The panel was machined in half; one half was cured freestanding in an oven at 350°F for 2 hours, and the other half was cured using E-beam. The excellent laminate quality obtained can be seen in the photomicrographs in Figure 38 for the E-beam cured portion and Figure 39 for the thermally cured portion of the laminates. Both panels were tested for flexural and interlaminar shear properties at room temperature. Additionally, acid digestion for fiber volume determination and DSC were conducted. The

fiber volume was found to be 55.9%, the resin content by weight 33.3%. The total E-beam dose for the laminate was 150 kGy from a 10 MeV machine. From the DSC trace shown in Figure 14, there is a small exotherm at about 100°C with ΔH of 3.42 J/g. The thermally cured portion of the laminate did not show any exotherm.

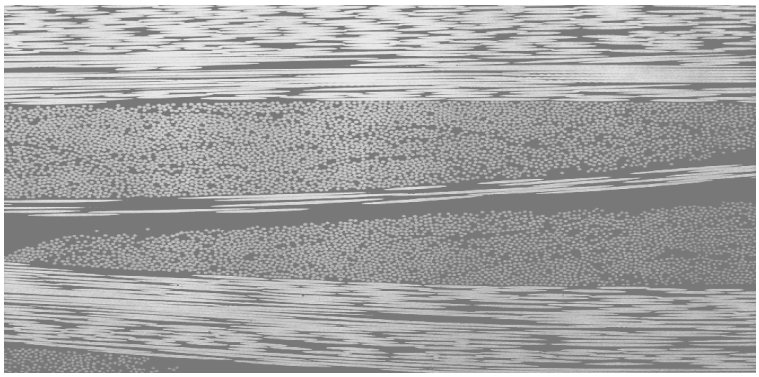

Figure 38. Photomicrograph of E-Beam-Cured AS4/VEB-11 VARTM Laminate

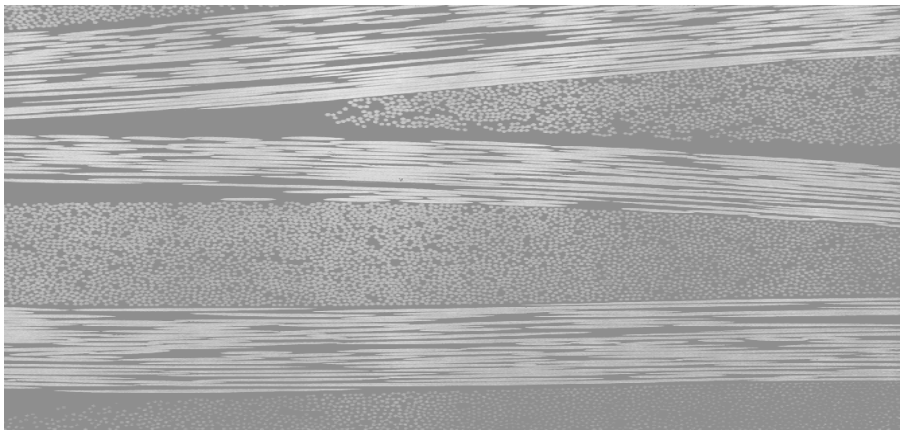

Figure 39. Photomicrograph of Thermal-Cured AS4/VEB-11 VARTM Laminate

The mechanical properties, SBS strength and flexural strength, tested at ambient indicated that the E-beam cured laminate has higher values (approximately 17%) than the thermal cured laminate. The comparison of the data is shown in Figure 40 and Figure 41 for SBS and flexural strength, respectively. Although exotherm was detected from DSC even after the laminate was E-beam cured, it apparently did not affect the properties at room temperature. It seems that the small amount of unreacted component makes the resin more ductile, which improves the room temperature properties. However, the unreacted component reduces the hot/wet properties.

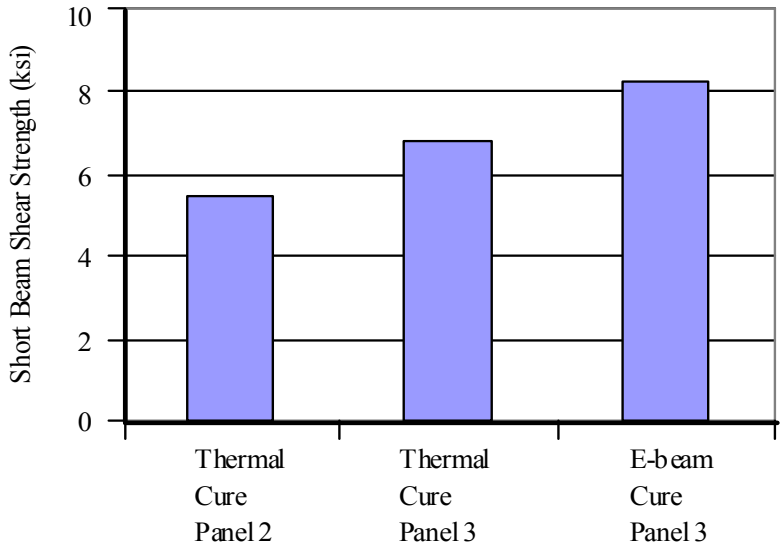

Figure 40. SBS Strength Comparison of Various AS4/VEB-11 Laminates

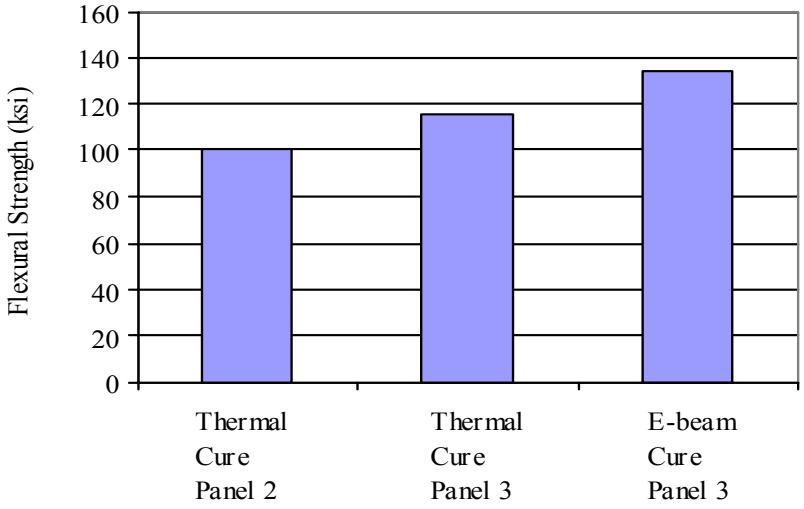

Figure 41. Flexural Strength Comparison of Various AS4/EB-11 Laminates

1.2.5 PROCESS AND PROPERTY CHARACTERIZATIONS

In order to represent the importance of developing materials that achieve both process and performance specifications, we developed a performance map that includes five critical physical properties that influence performance and processing in these VARTM resins. The schematic property maps shown in Figure 42 can be used to compare the performance of resin systems at a glance, where the best blend of performance and processing will result in a large area being mapped out by the resin when plotted. The three systems based on VCCM1.1 resins are represented in this figure. VCCM4.1 and VCCMD.1 are materials

toughened with reactive liquid elastomers and dendritic polymers, respectively. Although all systems need viscosity requirements, as expected, the dendrimer-modified system shows a significant viscosity advantage. However, the mechanical properties are inferior to those of the base and reactive-elastomer-modified systems, as shown by the significantly reduced area enclosed by the dashed line perimeter. Thus, VCCM1.1 and VCCM4.1 have been down selected as 250°F resin systems for benchmarking repairs based upon E-beam curable VARTM technology.

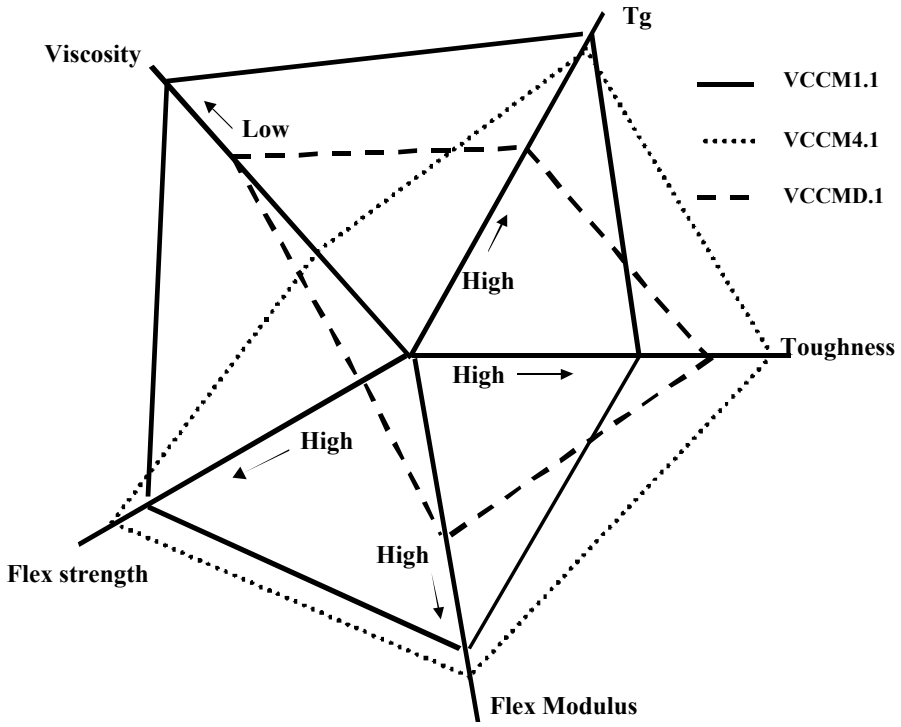

Figure 42. Property Map of VCCM1.1, VCCM4.1, and VCCMD.1 Systems

The high T_g systems developed thus far show significant improvement over the base resin reported. In fact, processing and mechanical properties approach those of the downselected low T_g systems.

Table 28 summarizes post-cure properties of the most promising resin systems developed thus far and include data for untoughened and toughened 250°F and 350°F systems. These materials are being used to fabricate and characterize carbon-fiber composite systems and will be used in repair studies in the coming year. Preliminary properties for composites fabricated using early versions of the VARTM resins are given in Table 29.

Table 28. Properties of VARTM Resin Systems for E-Beam Processing

Resin Description	VCCM1.1 250°F VARTM Resin	VCCM4.1 Toughened 250°F VARTM Resin	VCCMU3.1 350°F VARTM Resin	VCCMU3.1.1 Toughened 3
[1]T_g (°C)	132	129	172	165
[1,2]wet T_g (°C)	113	110	153	142
Viscosity (cps) RT	290	470	395	535
Viscosity w/curing agent (cps) RT	~240	~320	~280	~350
Flexural Modulus (ksi) [1]	530	560	550	550
Flexural Strength (ksi) [1]	18.4	18.6	16.0	15.0
K_{IC} ($MPam^{0.5}$) [5]	1.2	1.4	0.8	1.2
G_{IC} (J/m^2) [5]	300	500	180	360

1. T_g from DMA (5°C/min) E" peak
2. 48 hr. water boil

Table 29. Preliminary Composite Properties on AS4 5HS

Property	VCCM1.2	VCCM4.2
Volume fraction (%)	55	55
Void content (%)	<1	<1
Tensile strength (ksi)[6]	95±6	99±3
Tensile modulus [6]	10.2±0.8	10.0±0.6
Compressive strength (ksi) [7]	59±7	71±5
Compressive modulus (Msi)[7]	8.2±0.3	8.7±0.3
Iosipescu shear strength (ksi)[8]	12±0.7	11.6±0.4
Iosipescu shear modulus (Msi)[8]	0.65±0.03	0.64±0.04
Flexural strength (ksi)[1]	92±4	100±4
Flexural modulus (Msi)[1]	6.5±1.8	7.7±0.6
Short beam shear strength (ksi)	7.1±0.4	7.9±0.3

For high T_g resin systems, VCCMU3.1 and VCCMI3.1.1 performances are satisfactory. With viscosity below 500 cps, these resins showed high flexural strength, and T_g. Overall, VCCM1.1 and VCCMU3.1 are better base systems, while VCCM4.1, and VCCMU3.1.1 are improved toughness systems. The impact of toughness of the resin on composite performance will be demonstrated later in this report.

1.3 E-Beam Adhesives

The ability to perform effective repairs of composite structures on military structures will be governed to a large extent by the properties of the repair adhesives. Previous research has shown that there are no e-beam adhesives that match the performance standards of thermally cured epoxies. This may be attributed to a number of factors. Notably, the inability to effectively toughen the e-beam resins results in adhesives with poor resistance to peel and delamination. Hence, the development of adhesives in this program mirrors the other e-beam resin development efforts in that a major goal is to toughen the existing e-beam systems so that they can be used as structural adhesives. Furthermore, adhesive materials must be available in a variety of product forms to provide flexibility in repair and remanufacturing operations. These product forms include two-part pastes, one-part pastes, supported and unsupported films, and low-viscosity liquids. Our initial efforts have focused on development of toughened two-part pastes and infinite-shelf-life one-part pastes and films. To date, our greatest success has been in formulating two-part adhesives based on the CCM series of IPN-based e-beam resins.

1.3.1 SELECTION CRITERIA

The adhesives currently being used for thin-walled structural repair will be evaluated to provide baseline property values. Most repairs of these types employ either 250°F or 350°F curable epoxy film adhesives or two-part pastes. These materials have been well characterized; Table 30 gives some typical target values for adhesive formulations based on the properties of thermally cured adhesive baselines. Our goal will be to approach these performance target values for each relevant product form.

Table 30. Adhesive Performance Targets based on Commercially Applied Technologies

Property	Target Value
Glass transition temperature	95-105°C
Service temperature	82-95°C
Tensile modulus (RT)	3.0 GPa
METAL-METAL BONDS	
Lap shear strength RT (Al-Al)	35–43 MPa
Lap shear strength service temperature	16–28 MPa
Floating roller peel	8–11 KN/m
Sandwich peel	75–100 Nm/m

Critical properties to be measured and tabulated will include characterization of the adhesive T_g (dry and wet), elastic constants, strength, and toughness, as well as adhesive bond properties for metal-metal, composite-composite, and composite-metal joints. The properties of the new resins will be compared to those of the baseline thermally cured adhesives to assess relative performance. The results of the mechanical testing will be augmented by corresponding chemical and physical characterization of the resins.

Lap-shear strength for both aluminum-aluminum and composite-composite joints was the primary screening evaluation. Adhesives that matched or approached the performance of

their thermally cured counterparts were selected for further evaluation. This screening procedure also permitted rapid feedback on performance deficiencies in certain instances. For down-selected candidates, the bonded adhesive joints will be evaluated using climbing drum peel [9], lap-shear [10], wedge-crack extension [11], and other testing as deemed necessary to gain confidence in the properties of newly developed materials.

1.3.2 FORMULATION APPROACH

As discussed earlier, two major classes of radiation-curable systems will be used in this program. These include the low-shrinkage C-stage free-radical CCM systems based on epoxy and urethane chemistries, as well as the cationic cured CAT-M systems. During this task, activities will focus on modifying these systems to improve fracture toughness. The team developed these systems by formulating toughening agents into the base resins, as is typical of a second-phase toughener, or via novel approaches to toughening based on resin chemistry whereby flexible linkages are incorporated into the radiation-curable resin backbone.

The untoughened s-IPNs have good strength properties but are quite brittle. However, these systems may be toughened through a number of methods. In thermally cured epoxies, toughness is improved by the addition of rubber, which is chemically bonded into the network through reactive end-groups [12]. The rubber components that were studied for adhesives evaluation included various butadiene-nitrile liquid rubbers, dendritic polymers, and preformed particles. Also, suitable diluents were used to modify base formulations to control the viscosity of formulated adhesives. Table 31 lists the modifiers and diluents that were used in this work.

Table 31. Modifiers and Diluents for Adhesives Formulation

ID	Description	Functionality
M1	CTBN – Epoxy Adduct	Epoxy
M2	CTBN – Epoxy Adduct	Epoxy
M3	CTBN – Epoxy Adduct	Epoxy
M4	CTBN – Adduct (Low Viscosity)	Epoxy
M5	CTBN – Adduct (Low Viscosity)	Epoxy
M6	CTBN	Carboxy
M7	ATBN	Amine
M8	ATBN	Amine
M9	ETBN – Styrene Blend	Epoxy - Vinyl
M10	ETBN	
M11	Polester Polyol - epoxy	Epoxy
M12	Polester Polyol - epoxy	Epoxy
M13	CORE-Shell Acrylic	—
D1	Low Viscosity Methacrylate	Methacrylate
D2	Viscosity D1-Methacrylate	Methacrylate
D3	Low Viscosity Mono Methacrylate	Methacrylate
CE1	Epoxy Chain Extender	—
CE2	Epoxy Chain Extender	—

Base resin formulations for the IPN-based adhesives were similar to those described earlier. However, diluent and modifier selection were used to control processing and cure properties. The diepoxide that was selected is the bis-phenol A based epoxy, EPON 828, provided by Shell Chemical, Inc. Along with the selected bis (*p*-aminocyclohexyl) methane, PACM, the epoxy demonstrates a T_g of approximately 175°C. This temperature is suitable for adhesive repair of Army materials; however, the T_g of the epoxy network can be increased through the addition of a high-function (tetrafunctional) amine or aromatic amines. PACM, an aliphatic amine provided by Air Products, Inc., is selected because of the importance of the environmental impact of the resin formulations. PACM is less caustic and hazardous than alternative aromatic amines.

1.3.2.1 Epoxy Adhesive Toughening

As with most pure epoxy networks, the e-beam-cured EPON 828/PACM/methacrylate network is very brittle. Consequently, the material is inadequate for most adhesive applications. Improving the toughness of these s-IPN blends is key to creating an alternative cure adhesive by this approach. Other research efforts have demonstrated the challenges associated with toughening epoxy resins, especially cationic epoxy resins that are cured through e-beam methods [13, 14]. However, toughening of brittle epoxy networks has been accomplished by Kinloch, Riew, and others over the past decade [15]. The body of work in toughening of epoxy networks has demonstrated that brittle thermosets can be toughened without a significant sacrifice in T_g through two approaches: the addition of rubber and the addition of chain extenders.

The first method of toughening involves the addition of a second phase, commonly a rubber or thermoplastic, to the thermoset. A functionalized rubber is added to the uncured epoxide/amine mixture and co-cured with the epoxy network. During cure, the rubber becomes insoluble in the growing epoxy network and separates into rubber domains. The small rubber concentration [16] in the network causes discrete rubber particles (0.2-5μm) to form inside the network [17,18,19]. These rubber particles improve toughness by changing the energy absorption of the matrix and inhibiting premature failure of the thermoset, which often results from small defects. Alternatively, the second phase is added as rubber or thermoplastic particles. The size, surface binding, and concentration of the particles greatly influence the toughness of the thermoset [18,19]. Often, the surface of the particles is coated with an adhesion promoter to enhance the interaction between the thermoset and the filler. Generally, the addition of discrete particles for toughening is less effective than the addition of reactive rubbers [20].

The second method of toughening thermosets is to add chain-extenders to the network [19]. The average distance between crosslinks is a key parameter governing the toughness of the network. Through insertion of a fraction of oligomers into the network, the average number of crosslinks per unit volume is reduced, providing greater flexibility to the network although usually at the expense of the T_g.

Toughening of s-IPNs has been evaluated using a reactive rubber and a reactive dendrimer. Upon curing, both the rubber and the dendrimers phase-separate into discrete rubber domains. Although cure conditions reportedly affect the formation of the rubber domain size

and consequently the overall matrix toughness, we have not evaluated the impact of cure conditions in this study. A maximum toughness enhancement in a pure-epoxy matrix is obtained with rubber loading between 8% and 12% by weight. Dendrimer suppliers report that optimum toughness of epoxy formulas of these materials is also 10% by weight. For the purposes of this report, a number of reactive rubber and dendrimer-like polymers were explored; the tested materials are listed with their characteristics in Table 31.

1.3.2.2 Infinite Shelf Life Formulation Methods

Base formulation of experimental one-part adhesive resins is designed by controlling the extent of reaction of the epoxy matrix. The issue of gelation in condensation-type reactions where monomer A-A reacts with monomer B-B and B_3N can be predicted and controlled. Gelation is the point when an infinite network exists. The gel point can be predicted from the number and functionality of the monomers present in the condensation reaction. The following is an example of a condensation reaction:

$$A+A + B_3N \rightarrow A\text{-}A\text{-}BNBB\text{-}AA\text{-}BBNB\text{-}$$

where B_3N is tri-functional (f=3). The critical point for gelation (α_c), defined as the point extent of conversion of "B" required to form an infinite network, is defined as follows:

$$\alpha_c=1/(f-1).$$

Thus, controlling the extent of reaction conversion is achieved by controlling either the amine functionality or the epoxy functionality of the system. A blend of mono- and multi-functional amines generates a high-molecular-weight, soluble, hyperbranched polymer. The stability of such a molecule is dependent upon the reaction completion of the epoxide/amine. Alternatively, monofunctional epoxides can be added to the mixture to decrease the probability of infinite network formation.

Our initial experiments demonstrated that limiting the epoxy network formation in EPON 828/PACM/dimethacrylate adhesives does produce a process-friendly material with high stability. The epoxy network was thermally cured in the presence of the free-radical monomers to create a paste-like substance. The amine was suitably end-capped to prevent premature gelation but permit network formation during E-beam radiation. These materials were then evaluated for shelf-life stability using FTIR. The results are reported in subsequent sections.

1.3.2.3 Cationic Epoxy-Type Film Adhesives

This task involves evaluation of E-beam-curing adhesive films suitable for composite repair. During this reporting period, eight E-beam cationic adhesive films were developed and tested for single lap-shear strength. In addition, various surface treatments for aluminum substrates were investigated because E-beam has been shown to adversely affect the performance of the bonding layer in treated aluminum.

Aluminum substrates used for testing cationic adhesive require different surface preparation from thermal-curing epoxy adhesives. Most primers used for aluminum surface preparation of thermally cured systems are epoxies containing amine-curing agents. Since E-beam curing cationic systems are not compatible with amine curing agents, conventional primers,

such as BR127, cannot be used to prime aluminum surfaces for E-beam bond characterization. Other primers, such as METLBOND 6726, are epoxy wash and do not contain amines, rendering them highly compatible with E-beam processing. However, some of these epoxy-wash systems degrade under E-beam irradiation and frequently exhibit lower protection limits against harsh environments. For the current cationic adhesive screening, we elected to bond onto bare aluminum or silane-treated aluminum surfaces. A combination of two surface treatments, Forest Product Lab (FPL) and phosphoric acid anodized (PAA), was applied on the aluminum prior to bonding [21]. FPL is a sulfuric acid sodium dichromate etch and is stable without primer. PAA is applied on top of FPL treated aluminum surfaces. PAA is reported to produce a stable oxide surface for up to 72 hours prior to bonding. Fortunately, the screening for cationic adhesives does not involve corrosive conditions, but rather room-temperature characterization. The second treatment explored is the SERDP sponsored Sol-gel treatment. Sol-gel is a more expensive surface treatment and is stable for only 24 hours prior to bonding. However, previous explorations in the CAI (Composites Affordability Initiative, a large Air Force program exploring new composite technologies, including E-beam) have qualified this approach to characterizing E-beam-processed adhesives. Therefore, our data will be easy to compare with results obtained by the CAI.

All of the cationic cured E-beam film adhesives were developed by Applied Poleramic, a subcontractor to Northrop Grumman Corporation. Each adhesive film was approximately 10 mils thick without scrim support. The formulation specifications are shown in Table 32. These cationic films are composed primarily of cycloaliphatic epoxide—a highly reactive monomer—and the chain-extending diol bisphenol-A. Formulation EBA-8 is similar to EBA-3 with a slightly larger concentration of anhydride. These formulations explore the impact of anhydride in the cure process under E-beam irradiation, a phenomenon that has not been characterized experimentally. EBA-6 and EBA-7 contain GP-2 and GP-1, respectively. These two monomers were synthetically prepared by G. R. Palmese under the University of Delaware SERDP contract and were discussed for resin developments earlier in this report. Recall that GP-1 and GP-2 are both di-hydroxy terminated oligomers designed to increase the flexibility of the E-beam-processed matrix by decreasing the crosslink density in the network. The remaining compounds in these adhesive films are viscosity modifiers and tackifiers that allow the formation of room-temperature stable films. Additional small quantities of activation materials, such as phenol, are included to increase reactivity during the early stages of E-beam processing.

Table 32. Cationic Curing Adhesive Formulations

	EBA-1	EBA-2	EBA-3	EBA-4	EBA-5	EBA-6	EBA-7	EBA-8
Cycloaliphatic Epoxy	25	20	30	10		10	10	30
Solid Bisphenol-A Epoxy	61	72	65	65	60	65	50	60
B-OH		5	5					5
Phenol		2.8	1.5					1.5
MTHPA			3					5
605				15	30			
TEP	12.5			10	10	10	10	
DPI	1.4	2.8	2.8	2	2	2	2	2.8
GP-1							30	
GP-2						15		
6040/430	1/0.5	0.3/0.1	1/0.5	1/0.5	1/0.5	1/0.5	1/0.5	1/0.5

Because these film adhesives are in development, very little effort was invested in obtaining adhesives that "wet" the aluminum at low temperatures. Rather, these films were subjected to light heating and pressure (180°F for 30 minutes) in a press during lap-shear assembly. The pressure was applied to reduce the film thickness to 50% of the initial thickness. Heating these films increased both the flow viscosity and the wetting capability of the films and allowed uniform bond line control to be achieved in all of the sample materials. The final bond line thickness is 5.0 mil. After cooling, the lap-shear panels that are E-beam processed (namely EBA-1, EBA-2, and EBA-3) were taped tightly to minimize contact stresses resulting from handling, and the lap-shear samples were shipped to Steris Corporation in Libertyville, Illinois, for E-beam curing.

Because these adhesives are consolidated in the laminates, no additional pressure is applied during the E-beam curing step. Consequently, if the films are rapidly processed and the aluminum panels heat prior to C-stage or gelation of the film adhesives, then debonding of the aluminum plates would be expected. Therefore, we elected a slow-dose curing profile that minimizes the heating in the bond line. The cure dose applied is shown in Figure 43. The delay between passes was included to prevent overheating of the specimens and to allow processing to occur using the normal throughput manner of the E-beam source. The large surface area produced adequate ambient temperature cooling between passes during the staging of the adhesives in Steps 1 and 2. Based upon earlier experiences, the adhesives will have achieved sufficient cure after two passes to cause gelation, which will result in strong bonds during the remaining cure steps. The cure rate is increased for steps 3–5 to ensure complete conversion and moderate heating in the adhesives. The total energy dose was 150 kGy.

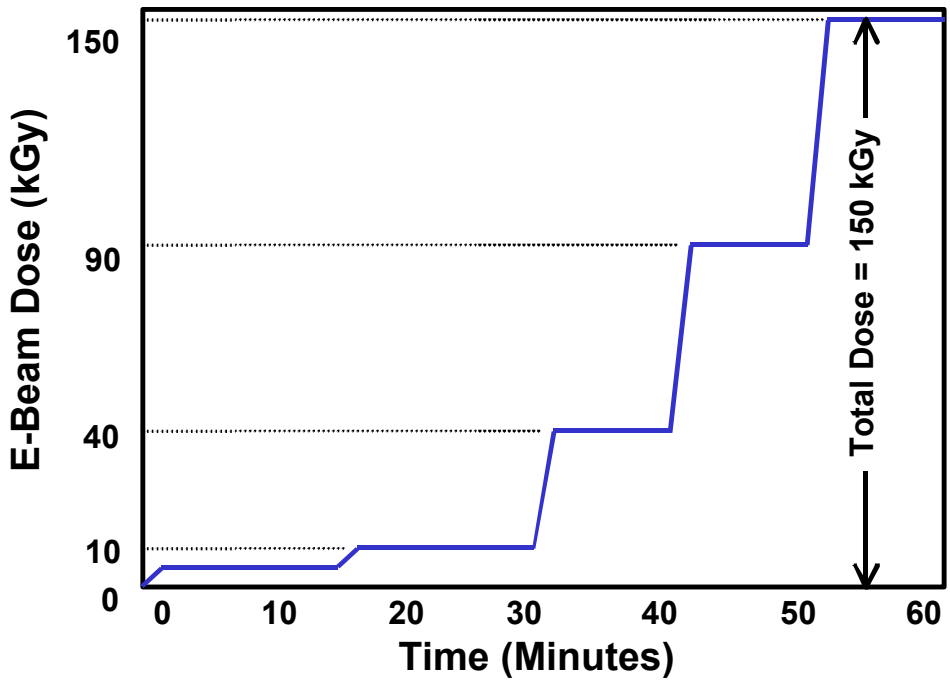

Figure 43. Slow-Dose Cure Profile for Adhesive Bond Curing.

The remaining adhesive formulations (EBA-4, EBA-5, EBA-6, EBA-7, and EBA-8) were received too late for inclusion in the E-beam run. We therefore evaluated these materials by thermal screening. These adhesives were thermally cured at 250°F and 40 psi for 2 hours. If the lap-shear strength of the thermal system is promising, it will be selected for further curing using E-beam. In addition to the E-beam-curing adhesives, control lap-shear specimens using FM73 were fabricated to validate the aluminum surface treatments. FM73 were cured in a press at 250°F and 40 psi for 2 hours.

Results of the room-temperature lap-shear strength of the E-beam curing adhesive and FM73 control are shown in Table 33. The lap-shear strength of FM73 treated with FPL/PAA is acceptable, and the failure mode is 100% cohesive. This result suggests that the surface treatment is adequate for the aluminum adhesive testing. EBA-3 showed much lower lap-shear strength for the Sol-gel treated aluminum surface preparation. Thermally cured EBA-3 is slightly higher (7%) than the thermal/E-beam-cured specimens. The 2% increase in the anhydride concentration of EBA-8 leads to a dramatic 22% increase in lap-shear strength. Figure 44 is a bar chart of lap-shear strengths for the tested adhesive films. Both EBA-4 and EBA-8 lap-shear values are about 96% of those of FM73. The failure modes for most of the E-beam-curing adhesives are adhesive, not the desirable cohesive failure. The only cohesive failure mode observed for the E-beam-curing adhesive film is EBA-7, which contains GP-1 oligomer. The room-temperature lap-shear values are low for EBA-6 and EBA-7, which is considered to be due partly to the brittle nature of the film. According to Applied Poleramic, the film viscosity for EBA-6 and EBA-7 was not optimized. During the lap-shear panel preparation, small pieces of the films broke off, hindering the fabrication of EBA-6 and EBA-7.

Table 33: E-Beam-Curing Adhesive Properties

		EBA-1	EBA-2	EBA-3	EBA-3	EBA-3	EBA-4	EBA-4	EBA-5	EBA-6	EBA-7	EBA-8
ST		*	*	*	*	Sol-Gel	*	*	*	*	*	*
Cure		Ther/EB			Thermal			Ther/EB	Thermal			
Individual Measurements	A						4420		3259			
	B		2508		3234	1910	4434		3501	1036	2145	4211
	C	1546	2372	3094	3184	1992	4262	4054	3461	1097	2513	4494
	D	1808	2223	3308	3680	2834	4081	4338	3386	1356	2640	4211
	E	1976	2597	3344	3751	2380	4737	3964	3449	1725	2498	4215
	F	2138	2883	3516	3964	2788	4401	3815	3449	1842	2607	4632
Average		**1867**	**2516.6**	**3316**	**3563**	**2381**	**4389**	**4043**	**3418**	**1411**	**2481**	**4353**
Std. Dev.		253	249	173	340	431	217	220	86	363	197	198
Failure Mode		adhesive	adhesive	adhesive	adhesive	adhesive	adhesive	adhesive	adhesive	adhesive	cohesive	adhesive

* indicating FPL/PAA surface treatment

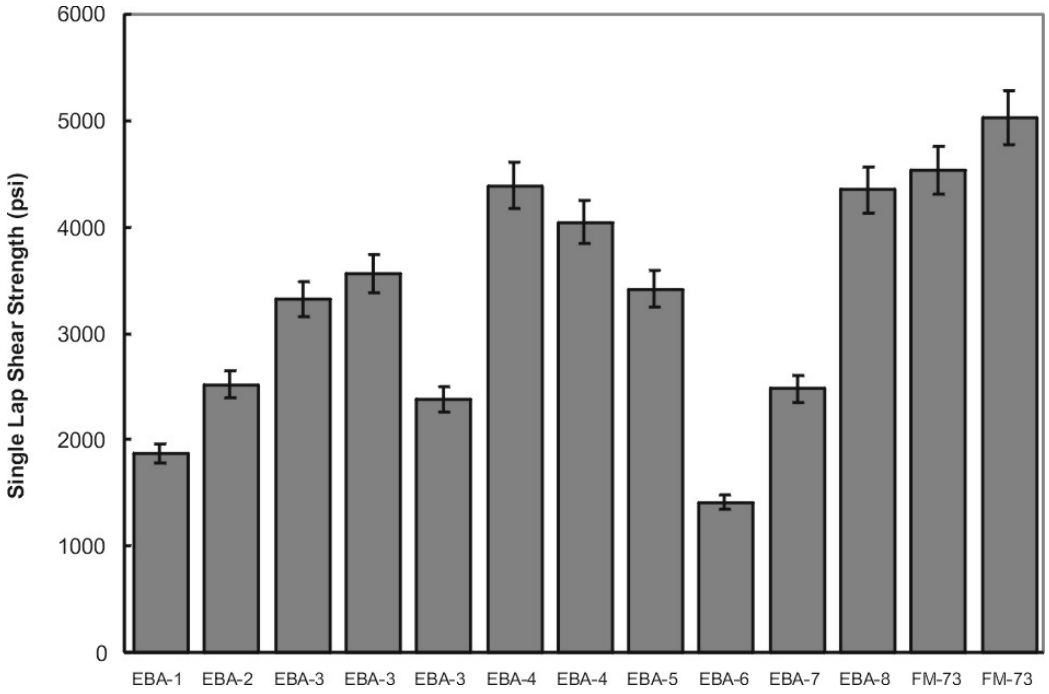

Figure 44. Lap shear strengths of tested adhesive films.

1.3.2.4 IPN-Type Film Adhesives

In addition to evaluating true homopolymer-cationic-cured epoxy E-beam adhesives, we also explored E-beam processing of hybrid designs based on simultaneous cure of the IPN structural adhesives. This novel approach uses the DPI initiator to cure the epoxy matrix while E-beam simultaneously excites free-radical propagation in the methacrylate matrix.

This approach was discussed previously (Figure 20) and results in one-step-processed IPNs. The monomer blend consists of two independent networks that cure simultaneously by E-beam processing.

To improve performance, we screened adhesive composition by curing a series of FR/Cat-Epoxy blends with E-beam. We attempted to screen these hybrid materials using thermal curing but recognized early in our efforts that the cure rate variation between the two network types produced inconsistent extent of cure in the two networks. We believe that the differences between network cure conversion could be optimized for thermal cure by selection of the free-radical initiator. However, both concentration and initiation temperature are variables, making this determination a non-trivial effort. Therefore, we cured the materials directly with E-beam and evaluated the extent of network conversion based upon diamond-tip ATR-FTIR and DMA. The results from this study are still undergoing evaluation; however, it is significant to note that one composition of these hybrid IPN structures resulted in a high-T_g and micromechanically linked network, while all other compositions produced independent networks with cure-dependent T_g performance. The unusual characteristic of single-network relaxation occurred for a 50/50 weight blend of monomers, which is 40/60 mole fraction (FR/Epoxy) of difunctional monomers. We previously attempted an adhesive film experiment (JCAT1) that demonstrated excellent lap-shear performance [22]. By coincidence, the formulation of JCAT1 is very close to the optimized concentrations determined in the recent screening.

1.3.3 VACUUM BAG CONSOLIDATION

Most of our developments for screening of E-beam adhesives have progressed using a hot-press and light positive pressure (5–15 psi) to obtain consolidation and achieve uniform bond line thickness. Recently, however, we learned of unusual processing conditions being applied under the CAI. The CAI group implemented a cure schedule that included lay-up of the adhesive panels followed by vacuum-bag consolidation and oven staging. We had not previously considered the impact of negative pressure on adhesive performance and therefore were surprised by the results presented on ADEP01 evaluated under the CAI. Consequently, we undertook a simple analysis of the performance of adhesives cured under both positive and negative consolidation pressure.

Initial screening of vacuum-bag consolidation involved characterization of performance knockdown of a commercial paste adhesive (Hysol EA9394) when processed under vacuum. We prepared a group of lap-shear panels under both light positive pressure (15 psi) and full vacuum pressure (14 psi or 30mmHg). The results of this test demonstrated at least a 20% knockdown in the performance of the commercial system when processed using vacuum consolidation.

Following the commercial paste demonstration, we evaluated green strengths in ADEP01 cured under the same two consolidation conditions. Previously, we showed that ADEP01 possessed a good green strength at 1000–1200 psi using positive pressure. Upon curing in vacuum, we observed a substantial loss in performance to 400–600 psi. These reductions in performance are consistent with CAI results, where final strengths of ADEP01 achieved only 1200–1600 psi. We also experienced knockdown in performance on a series of modified ADEP01 adhesives that achieved low lap-shear strengths with E-beam cure.

Fortunately, the loss in performance resulting from vacuum processing is a common difficulty with adhesives. We therefore determined the primary sources for these performance losses in ADEP01 and prepared materials to compensate for the vacuum impact. The most common method of improving performance is to decrease the volatile concentration in the adhesives. Unfortunately for our situation, ADEP01 is formulated to be a non-VOC-emitting resin and therefore does not possess highly volatile monomers. The second approach is to change the viscosity of the adhesive components. This second approach is achieved by forming an adduct phase of the amine-component with much higher molecular weight epoxides. Epoxy adducts possess partially reacted amines that are much less likely to bloom to the interface of the aluminum when negative pressure is applied. We optimized the adduct formation by formulating to an amine-rich resin with good spreading viscosity.

Last, we recognized that most of the trouble with vacuum consolidation results from expanding air bubbles in the adhesive pastes. These air bubbles are incorporated into the resin phase during the blending of Part A and Part B in the two-part systems. Since the IPNs are developed using two-part epoxy-amine chemistry, we are unable to eliminate this mixing step. However, the art of adhesive application has been greatly advanced in the last ten years by the introduction of meter-mixing tools such as those available through MixPac. These mixing units enable measuring and mixing of adhesive pastes in a high-shear low-air environment. The adhesive components are injected from a two-channel syringe into a mixing-tube. With continued application of pressure on the syringe, the resin components are pressed down the mixing tube and are shear-blended until the two components exit the nozzle end of the mixing chamber as a single blended resin. These tubes provide unique ability to blend moderate viscosity two-part paste adhesives with very little incorporation of air on blending. The elimination of air from the adhesives results in greater retention of performance during vacuum-bag processing.

From these negative pressure consolidation studies, we have determined a number of methods for reducing air entrapment in our adhesive pastes. We therefore can proceed with our development of paste adhesives for E-beam cure with confidence that vacuum processing of these materials will be an option once formulations are optimized.

1.3.4 IPN PASTE ADHESIVES

The toughness of model adhesive formulation was evaluated using single-edge notch flexure specimens. The tests were performed in accordance with ASTM D 5045 [5]. The effect of 5% rubber addition to base IPN resins was in some instances dramatic. The toughness was increased substantially for many of the modifiers that were examined. In two cases, toughness increased by nearly a factor of two. Further research is needed to optimize the toughness improvements in these resin systems and this work is presently ongoing. However, the ability to toughen these e-beam resins is significant and is a major accomplishment to date. The improved toughness should have a direct impact on the performance of joints produced using these modified resins. The mechanical properties of the adhesives have been tested on composite lap-shear specimens. Prepared samples were tested as both green and fully cured adhesive specimens. The results are shown in Table 34 and Table 35.

Table 34. Double Notch Lap Shear Results on Composites

Sample ID	Bond Strength	T_g (^oC)
CA5	2000±100 PSI	120
CA6	2300±100 PSI	121
CA1	1550±100 PSI *	90†
CA2	2000±100 PSI	88†
Loctite Hysol EA9394	3200±100 PSI	78
* Sample failed in the bond-line † Epoxy network not fully cured (FTIR)		

Table 35. Overlap Shear Strength Results on Composites

Sample ID	1.4 Bond Strength	T_g (^oC)
CA1 (2-pt)	2900±100 PSI	120
CA2 (2-pt)	2750±100 PSI	121
CA3 (2-pt)	3100±100 PSI	120
CA4 (2-pt)	3400±100 PSI	121
Loctite Hysol EA9394	3700±100 PSI	78

From the mechanical data, it is evident that the bond strengths of the e-beam adhesives are adequate. We observed composite failure in all samples except for CA1, which is a one-part adhesive formulation. The toughened one-part adhesive, CA2, demonstrated both better adhesive strength and better toughness than the untoughened case. We have not determined the source of this improvement.

The T_g of each of these adhesive samples was also measured using DMA and results are shown. The target T_g of a 250°F adhesive is well within the scope of this effort. We are currently working to further increase the T_g of the network by modifying the acrylate network content and the ratio of epoxy to acrylate in the mixture.

Since these adhesives produced joints that exceeded the strengths of the composite adherends, further tests were performed on aluminum-aluminum lap joints to determine the ultimate properties of the adhesive. Aluminum (7075-T6 and 2024-T3) coupons were surface-treated prior to bonding. The surface treatments employed were all chromate-free to maintain the goal of environmentally friendly bonding and repair methods. In this case, the aluminum was etched using the P-2 process. For comparison, joints were also bonded using commercially available adhesives. FM73 and EA9628 were selected as film adhesives, and E9394 was used as a two-part paste formulation.

The results of the aluminum-aluminum lap-shear testing (Table 36) are very encouraging. The strengths are higher than what has been reported for previously developed e-beam adhesives. They also approach the film adhesive baselines. The large degree of scatter must be addressed during production of our best candidate materials. Failure analysis of the joints revealed less than consistent degrees of cure, indicating uneven e-beam irradiation. However, on closer inspection, the degree of cure was consistent throughout the sample, and the discoloration appears to result from varying degrees of “trapped” electrons in the matrix.

A thermal post-bake equilibrates the samples and demonstrates uniformity in the color and cure profiles.

Table 36. Joint Strengths of Al-Al Single-Lap Joints (D-1002)

Sample ID	Lap Shear Strength	T_g
MA3	3000	127
MA4	3130	120
MA5	3700	115
MA6	**5627**	**118**
MA23	2793	100
MA24	1829	106
MA43	1183	87
MA73	2503	99
Hysol EA9394	3000	78
Cytec FM73	5875	116
Hysol EA9628	5670	122

1.5 E-Beam Repair Adhesive Formulation

At present, composite repair is accomplished to a large degree through autoclave processing of repair adhesives. Non-autoclave repair mechanisms are typically insufficient to restore performance levels for structural damage. Thus, structural damage usually requires replacement of the composite component or autoclave repair. The repair of large composite matrix military structures out of autoclave is governed to a large extent by the availability of E-beam and induction repair adhesives. However, previous research has shown that E-beam processed adhesives do not achieve the performance standards of autoclave processed epoxies. This may be attributed to a number of factors. Notably, the inability to effectively toughen the E-beam resins results in adhesives with poor resistance to peel and delamination. Hence, the development of adhesives in this program mirrors the other E-beam resin development efforts in that a major goal is to toughen existing E-beam systems so that they can be used as structural adhesives. Furthermore, adhesive materials must be available in a variety of product forms to provide flexibility in repair and remanufacturing operations. These product forms include two-part pastes, one-part pastes, supported and unsupported films, and low-viscosity liquids. Our initial efforts have focused on development of toughened two-part pastes and infinite-shelf-life one-part pastes and films. To date, our greatest success has been in formulating two-part adhesives based on the CCM series of IPN-based E-beam resins.

1.5.1 E-Beam Repair Adhesive Selection Criteria

The adhesives currently being used for thin-walled structural repair will be evaluated to provide baseline property values. Most repairs of these types employ either 250°F or 350°F curable epoxy film adhesives or two-part pastes. These materials have been well characterized; Table 37 gives some typical target values for adhesive formulations based on the properties of thermally cured adhesive baselines. In adhesive paste development, we

have achieved many of the critical performance goals, and the paste adhesive performance is designated in the state-of-the-art (SOTA) column in Table 37.

Table 37. Adhesive Target Performance and State of the Art in E-Beam Systems

Property	Target Value	SOTA
Glass transition temperature	> 95-105°C	100-130°C
Service temperature	82-95°C	~90-110°C
Tensile modulus (RT)	3.0 GPa	2.97 GPa
METAL-METAL BONDS		
Lap shear strength RT (Al-Al)	35–43 MPa	25-42 MPa
Lap shear strength service temperature	16–28 MPa	17-29 MPa
Floating roller peel	8–11 KN/m	6-13 KN/m
Sandwich peel	75–100 Nm/m	

Lap-shear strength for both aluminum-aluminum and composite-composite joints was the primary screening evaluation. Adhesives that matched or approached the performance of their thermally cured counterparts were selected for further evaluation. This screening procedure also permitted rapid feedback on performance deficiencies in certain instances. For down-selected candidates, the bonded adhesive joints will be evaluated using climbing drum peel (ASTM D 1781) [9], lap-shear (ASTM D 1002) [10], wedge-crack extension (ASTM D 3762) [11], and other testing as deemed necessary to gain confidence in the properties of newly developed materials.

1.5.2 E-BEAM REPAIR ADHESIVE RESULTS

The toughness of model adhesive formulations was evaluated using single-edge notch flexure specimens. The tests were performed in accordance with ASTM D 5045 [5]. The effect of 5% rubber addition to base IPN resins was in some instances dramatic. The toughness was increased substantially for many of the modifiers that were examined. In two cases, toughness increased by nearly a factor of two. Further research is needed to optimize the toughness improvements in these resin systems; this work is underway. However, the ability to toughen these E-beam resins is significant and is a major accomplishment to date. The improved toughness should have a direct impact on the performance of joints produced using these modified resins.

Since these adhesives produced joints that exceeded the strengths of the composite adherends, further tests were performed on aluminum-aluminum lap joints to determine the ultimate properties of the adhesive. Aluminum (7075-T6 and 2024-T3) coupons were surface-treated prior to bonding. The surface treatments employed were all chromate-free to maintain the goal of environmentally friendly bonding and repair methods. In this case, the aluminum was etched using the environmentally preferred P-2 process. For comparison, joints were also bonded using commercially available adhesives. FM73 and EA9628 were selected as film adhesives, and EA9394 was used as a two-part paste formulation. Table 38 shows characteristic performance for the baseline systems.

Table 38. Commercial Adhesive Al-Al Single-Lap Joint Strengths (D-1002)

Sample ID	Lap Shear Strength	T_g
Hysol EA9394	3000	78
Cytec FM73	5875	116
Hysol EA9628	5670	122

The results of 1998 produced a two-part adhesive paste with exceptional aluminum-aluminum lap-shear performance on E-beam cure. The adhesive formulation was down selected for further modification and for testing with various filler packages. The resulting adhesive performance is shown in Figure 45. The impacts of filler (calcium carbonate, CaCO3) on the adhesive strength were evident in lap shear testing. The unfilled material was also evaluated for high-temperature performance. Those results are also shown in Figure 45. These strengths are higher than any reported performances for previously developed E-beam adhesives. They also approach film adhesive baselines reported earlier.

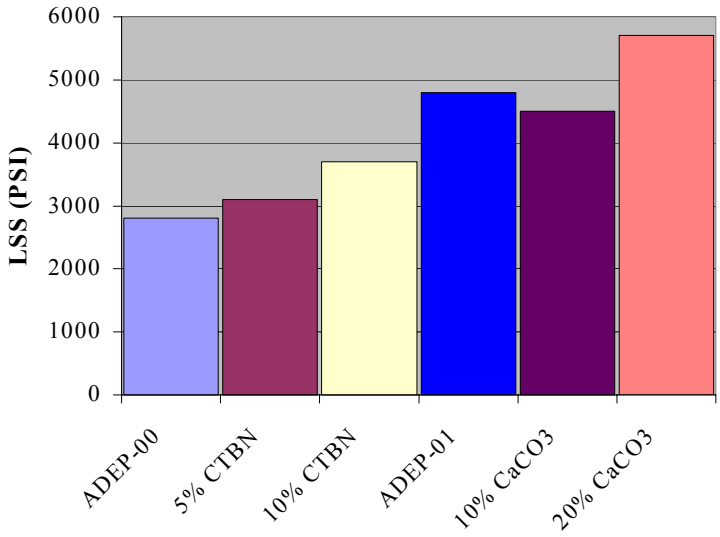

Figure 45. Lap-Shear Results of Experimental E-Beam Adhesives

As a result of the success of paste adhesives, further recognition and characterization of this formulation has been sought through the Composites Affordability Initiative (CAI), which is an Air Force Program for developing new aerospace grade materials. The submitted formulation is designated ADEP-01 and was submitted on August 3, 1999. The results of this submission are expected by the end of December 1999. ADEP-01 is the tradename selected for these E-beam cured pastes. A sample label for marketing this material is presented in Figure 46.

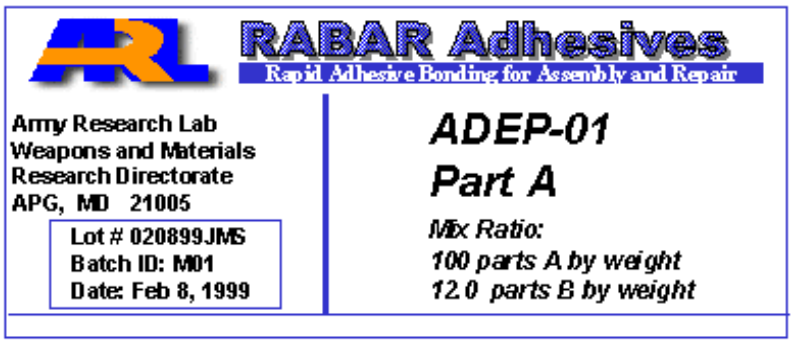

Figure 46. Adhesive Materials Submitted for CAI Investigation for Aerospace Applicability

The ADEP-01 E-beam cure adhesive system is not optimized for repair applications because of lengthy cure cycles for C-stage IPN formation. A study has been initiated to enhance cure performance and C-stage formation of ADEP-01 to facilitate an improved repair scheme. This evaluation involved characterization of C-stage formation over a range of temperatures and with the addition of a catalyst. The target preparation cycle was a one-day cure at room temperature or a one-hour cure at 50°C. In addition to cycle time, performance must also be maintained.

The result of the cure-formation analysis is to determine effective cure cycles and optimal cure conditions for C-stage generation. The target cycle times imply the need for catalytic cure of the epoxy-template to form the C-stage resin. We evaluated the influence of cure temperature and catalyst on the cure rate to demonstrate rapid-cure feasibility with these adhesives. Cure conversion of ADEP 01 as a function of cure time at various temperatures is presented in Figure 47.

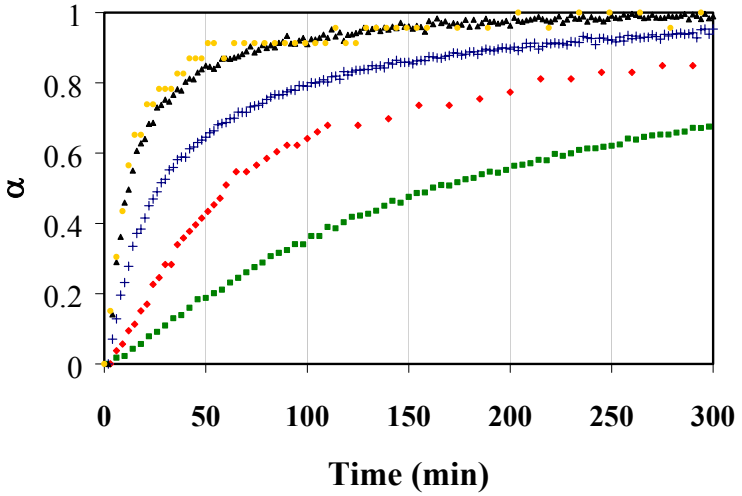

Figure 47. FTIR Characterization for Cure of ADEP-01 at 30°C (□), 50°C catalyzed (o) and uncatalyzed (♦) 65°C (+), and 80°C (Δ).

The one-day cure at room temperature seems to be achievable with the appropriate catalysts and reaction blends. However, the impact of the modified cure cycle on resin performance has not been tested. Further, catalyzed reactions are often accomplished by lowering the activation energy of the reaction pathway. The initial concern arose with this design that an accelerated aging phenomenon may result. However, as is demonstrated in the aging study, which follows, the resins are quite stable over long periods.

Finally, the ADEP-01 resins have found a niche application in cryogenic applications. Through a cooperative arrangement with Science Research Laboratory (Somerset, MA, USA), the Army Research Laboratory (ARL) has been providing ADEP-01 resin for testing for cryogenic bonding applications. The unfilled resin has been modified by SRL to meet processing requirements for cyro-based adhesive applications through a commercial filler package addition including calcium carbonates and other powders. The SRL modified ADEP-01 adhesive has subsequently exceeded all other resin options being explored by SRL under a phase II SBIR funding for NASA. Consequently, additional resin is required to expand the test matrix for ADEP-01 cryo-based testing to validate the technology and demonstrate reproducibility in batch manufacturing of the resin. The program constitutes one of the successful technology transitions achieved for materials developed under the SERDP funding.

2 Electron Beam Resin Aging

Many adhesive and composite material systems cure slowly during storage prior to use. For these systems, processing and performance requirements can be met only within the designated storage period or shelf life (Figure 48). Shelf life is generally documented under a required level of reduced-temperature storage. Shelf-life restrictions are determined for each resin system by evaluating changes in the characteristics of the resins or components of two-part resin systems under various storage conditions. The limitations are based on maintaining characteristics that allow suitable process ability and quality of the cured materials. Resins or components of resin systems that have exceeded shelf life are partially cured, can no longer be used, and are considered hazardous waste.

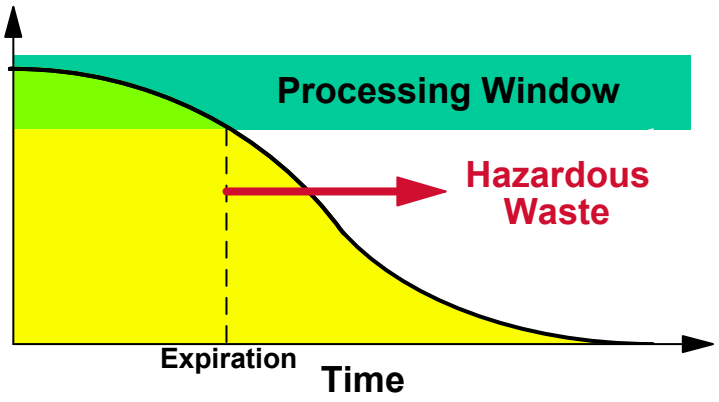

Figure 48. Shelf life expires when material processing characteristics no longer meet specification limits.

Common materials used for composite repair in DOD applications are one- and two-part epoxy adhesives and resins, epoxy film adhesives, and glass- or carbon-fiber/epoxy prepregs. The one-part systems have all the materials needed to achieve full cure and must be stored under controlled-temperature conditions to slow the curing process. The two-part systems must be mixed to cure at expected rates; however, the epoxy part (Part A) can cure by itself, although at a slower rate. Shelf-life limits for these materials are typically six to twelve months. The new formulations are designed for cure by e-beam or induction processing and should have an extended shelf life. In particular, the formulations for e-beam cure are expected to have an infinite shelf life. An aging study is being performed to verify these expectations.

2.1 Approach to Resin Aging Study

The purpose of this program is to develop resins that cure by alternative technology such as induction and E-beam. One advantage of alternative-cure materials is the ability to develop resin systems with near-infinite shelf life. To verify the proposed shelf-life dependency of alternative-cure resins, an aging study is being performed.

The extent of conversion or reaction propagation of a resin is evaluated at room temperature. Although many commercial adhesives define a finite shelf life of these systems at sub-ambient conditions, DOD repair strategies must include technology that is sustainable under ambient conditions. Therefore, we evaluate the aging performance for a subset of commercial materials—including adhesives, films, and prepregs—that are used in the repair of composite and aluminum structures. The aging behavior for alternative-cure resins developed through this program is also characterized. The test matrix for the aging study increases as additional materials are developed.

The approach used in this study is to monitor the concentration dependence of a molecular moiety as a function of time. As a material degrades, the concentration of various reactive groups is depleted through interaction with the environment, including water, carbon monoxide, and UV light. Thus, we evaluate the concentration of reactive groups, critical to the cure behavior of the resins, and associate loss of concentration with environmental degradation. To monitor this degradation, Fourier transform infrared (FTIR) spectroscopy—a technique that is sensitive to molecular structure—is applied. Either mid-infrared (MIR) [4000 to 400 cm^{-1}], or near-IR (NIR) [7000 to 4000 cm^{-1}] was used to monitor the samples, where the selection of technique is dependent upon sample preparation and resin functionality.

The sample preparation could differ slightly depending on the initial state of each material (prepreg, adhesive film, liquid resin, solid resin) and the range of wavenumbers used. As shown in Figure 49, all the samples are compressed between two 25-mm-diameter NaCl transparent crystal windows. For liquid resin systems, except for SBIR-ARL1, no additional preparation was needed before placing the sample on the crystal. In the MIR range, the adhesive film samples and the prepreg sample were diluted in acetone. The resin/acetone solution was then added to the crystal, and the acetone was allowed to evaporate off the crystal, leaving only the resin. The SBIR-ARL1 resin system was also diluted in acetone before being placed onto the crystal because the sample is not a liquid but a solid. A spacer was used between the crystals to regulate the thickness of each sample and to reduce

evaporation losses. For the MIR range, a Teflon spacer was used for all materials. For the NIR range, a lead spacer was used for resin systems, and no spacer was needed for adhesive films. After the sample was compressed between the NaCl crystals, it was placed in a cell holder for the duration of the study. At appropriate intervals, spectra were obtained to evaluate extent of cure. Between measurements, the samples were stored in a desiccator at room temperature.

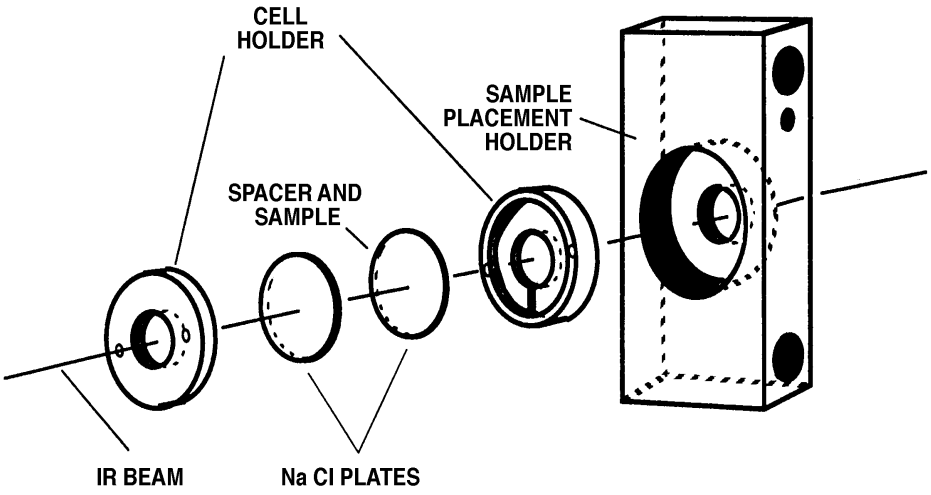

Figure 49. Exploded view of sample between NaCl windows in sample holder.

2.2 Results of Resin Aging Study

The effects of aging are evaluated using the fraction converted or extent of cure based on heights of significant peaks in the absorbance spectra. Figure 50 serves as an example for AF163-20ST adhesive file. The peak at 916 cm^{-1} is monitored as a function of time with a notable reduction in height.

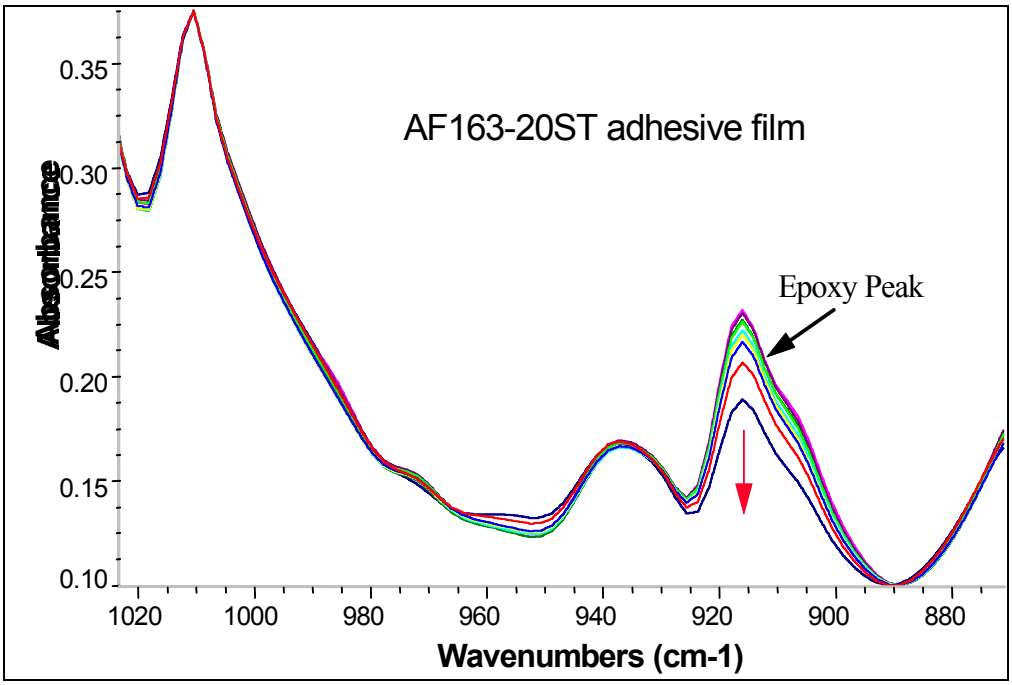

Figure 50. MIR absorbance spectra for AF163-20ST adhesive film. Note the reduction in the 916 peak over a five-month period.

The materials evaluated in this study include both commercial and laboratory prepared resins. The commercial systems include resins, adhesives and prepregs that cure by thermal methods that are currently on the market. The laboratory resins are part of the E-beam resin development effort under the current program. These initial resin systems are sample systems with chemistries akin to expected final adhesive formulations, but without having the known materials mechanical performances. The E-beam developed resins for practical applications will not be available in time to incorporate in detail in this analysis. The materials included in the program are described in some detail below. The results observed for these materials are expected based on knowledge of the chemistry and supplier storage recommendations in comparison to experimental conditions for the aging study.

Hysol 9390 is a commercial two-part epoxy system. The two parts, Part A containing epoxy and Part B containing amine, are both liquids that are mixed prior to use. Part A can begin to cure without the addition of Part B, causing the primary limitation on shelf life for this system. Part B is expected to have less effect on aging. Part A was evaluated using both MIR and NIR. In both cases, significant changes in the spectra are observed, although at different times. The NIR results lag behind the MIR results, and differences in the sources of variability may have an effect on the cure timeline. Hysol 9390 Part B was evaluated using the reaction of an amine functional group. Due to the spectral overlap that occurs in the MIR region for the amine peak, only the NIR spectrum was used. Only small changes are noted in the NIR results for Part B. More rapid changes would be expected following mixing of the two parts for Hysol 9390.

AF163-20ST is a commercial adhesive film. For MIR, the film was dissolved in acetone, and the solution put on the NaCl window and allowed to dry. For NIR, a piece of the film

was placed directly on the NaCl window. Results from both MIR and NIR show significant effects of aging on the extent of cure.

Hysol 9628.045 PSFK is a commercial adhesive film. Hysol 9628.045 PSFK has not aged significantly, and the results fluctuate. The aging of this sample is somewhat surprising. The sample contains both epoxy and amine; therefore, aging should occur at a more rapid rate. One explanation for the fluctuation in the results for this sample and others is that the baselines for the peaks under study change over time, causing errors in quantifying the results. In the MIR spectra for Hysol 9628.045, there is a clear indication that the baselines have changed. Effects of the acetone solvent drying may be important. Future work includes the same specimen preparation for MIR with a thorough drying procedure in a vacuum oven.

R6376 prepreg is a reformulation of an epoxy prepreg. Significant effects of aging on extent of cure are observed in both MIR and NIR. Greater variability in the NIR results may be due to a thinner specimen than is desirable. For both wavenumber ranges, the specimen is prepared by dissolving the resin from the prepreg and then drying the solution on the crystal window. This produces a specimen of appropriate thickness for MIR but a rather thin specimen for NIR.

CAO1 is a one-part epoxy/methacrylate system formulated at ARL. No changes were observed in the MIR range. Variability was high in the NIR range, most likely an effect of significant effects in the baseline. There was some concern regarding the peak selected for measurement. Based on results by Horaleck [23], a double-bond methacrylate peak is being evaluated, but more study is needed to confirm this selection. However, the epoxy peak (916 cm^{-1}) was also evaluated to demonstrate stability. Again, changes were minimal for the materials stored under ambient conditions.

CAO2 is also a two-part epoxy/methacrylate system formulated at ARL. Only the Part A component is evaluated here, as Part A contains the reactive epoxy and acrylate functionality. No changes were observed in the MIR range. NIR evaluation of this material was begun at the same time as the CAO1 material, and the effects of baseline variability were so pronounced that no measurements were recorded. CAO2 is the chemical equivalent of the ADEP-01 resin designed to meet structural requirements with an additional handling capability. The resin can be mixed in two parts allowing a C-stage formation, which bonds parts together under ambient conditions and causes tool-free processing via E-beam to be achieved. Additionally, this approach improved ability to keep alignments and consolidation pressures during the processing phase of the C-stage, which improved overall bonding strengths in the adhesives, and reduced adhesive bonding scatter. ADEP-01 shows excellent stability, owing to the two-part formulation. Out-times at room temperature have exceeded one year in cryogenic evaluations.

SBIR-ARL1 is a one-part epoxy formulated by Merlin Technologies, Incorporated as part of an SBIR program with ARL. Initial results may indicate no changes in extent of cure with time based on MIR observations. However, the initial degree of unreacted monomer is significantly lower than for commercial prepregs with shorter shelf life. Consequently, the resin mixture is well advanced in curing, and may not meet performance needs for aerospace level applications. No NIR measurements are available for this material.

The materials in the aging study are listed in Table 39. The table is divided into two sections, thermal and E-beam, where the physical form, reactive functional group, and approximate

excitation wavenumber are presented. The reactive groups for the resins in this study are amines, epoxies, acrylates, and methacrylates. New systems added since the 1998 report are E-beam-curable T-11 and T-14 prepregs, E-beam-curable CCM1 VARTM resin, EB3605 model system, and E-beam-curable Epreg1 prepreg. A detailed description of the other samples was provided in the last report.

The sample preparation could differ slightly depending on the initial state of each material (prepreg, adhesive film, liquid resin, and solid resin) and the IR range used for characterization. All the samples are compressed between two 25 mm diameter NaCl transparent crystal windows. The adhesive films and prepregs were cast onto the NaCl crystals from acetone solution. A spacer was used between the crystals to regulate the thickness of each sample and to reduce evaporation at the sample edges. For the MIR range, a Teflon spacer was used for all materials. For the NIR range, a lead spacer was used for resin and paste systems, while no spacer was required for the cast films. At appropriate intervals, spectra were obtained to evaluate extent of cure. Between measurements, the samples were stored in a desiccator at room temperature in a cabinet.

Table 39. Aging Study Materials: Commercial and Formulated

Thermal-curable systems				
Sample	**Source**	**Application of Material**	**Functional group**	**Wavenumber (cm^{-1})**
9390 part A	Hysol	Two-part paste	Epoxy	916
9390 part B	Hysol	Two-part paste	Primary amine	6510
AF163-2OST	Cytec Fiberite	Adhesive film	Epoxy	4530
9628.045 PSFK	Hysol	Adhesive film	Epoxy	4530
SBIR-ARL1	Merlin Technologies	Prepreg resin	Epoxy	916
R6376	Northrop	Prepreg	Epoxy	916
E-beam-curable systems				
Sample	**Source**	**Application of Material**	**Functional group**	**Wavenumber (cm^{-1})**
CAO1	Army Research Lab	One-part paste	Methacrylate	945
CAO2	Army Research Lab	One-part paste	Methacrylate	945
T-11	Applied Poleramic	Prepreg resin	Epoxy, methacrylate	4530
T-14	Applied Poleramic	Prepreg resin	Epoxy	4530
CCM1	UD-CCM	VARTM resin	Epoxy, methacrylate	916, 945
Epreg1	UD-CCM	Prepreg resin	Methacrylate	945
EB3605	UCB Radcure	Model system	Epoxy, acrylate	916, 982

In the MIR, evaporation and dimensional fluctuations have a profound effect on the measured intensity because the sample volume is small; therefore, a reference peak is used. The reference peak is selected from the non-reactive sample regions, including methyl

hydrogen and benzyl C-C stretches. In the NIR region, sample volumes are hundreds of times larger than for MIR, so a reference peak is not required. Variation in concentration with time is addressed using a two-point baseline method.

Results to date for the aging study are shown in Table 40. The relative error for FTIR analysis is ±5%. Thermal-curable Hysol 9390 part A, which contains epoxy functional groups, did not show any aging over 15 months. Similarly, part B of the same system did not age during the same period. Both systems were studied using NIR spectroscopy. Similar performance was observed for the epoxy-formulated SBIR-ARL1 prepreg resin, which did not age over 6 months. Note that SBIR-ARL1 is a vitrified system at room temperature. The commercial thermally curable adhesive film AF163-20ST showed relatively rapid aging at room temperature. Its epoxy group conversion was observed at 65±5% over a period of 18 months. Another commercial adhesive film, 9628.04 PSFK, also exhibited gradual decay of epoxy group by 50%. R6376 prepreg, which is a reformulation of epoxy prepreg, aged approximately 65% in 3 months. These last three samples are among those materials that require cold storage to achieve a shelf life of 6–9 months.

Table 40. Aging of Thermal and E-Beam Systems

Thermal-curable Systems						
Products	**Months**					
	3	**6**	**9**	**12**	**15**	**18**
9390 part A	2.0%	4.0%	3.0%	5.0%	5.0%	
9390 part B	4.0%	6.0%	8.0%	10.0%		
AF163-2OST	38.0%	57.0%	65.0%	66.0%	69.0%	65.0%
9628.045 PSFK	0.0%	10.0%	31.0%	44.0%	50.0%	
R6376	65.0%	67.0%	68.0%			
E-beam-curable Systems						
Products	**Months**					
	3	**6**	**9**	**12**	**15**	**18**
CAO1	0.0%	0.0%	0.0%	0.0%	0.0%	0.2%
CAO2	3.0%	3.0%	0.0%	0.0%	0.0%	0.0%
SBIR-ARL1	0.0%	0.0%	NR	NR	NR	0.0%
T-11	12.0%	11.0%	NR	NR	NR	< 10.0%
T-14	9.0%	8.7%	9.2%	9.5%	9.5%	< 10.0%
CCM1	5.0%	4.9%	5.5%	5.4%	6.1%	< 10.0%
Epreg1	0.0%	< 10.0%	NR	NR	NR	< 10.0%
EB3605	Not measured until the 18th month					< 10.0%
NR = Not recorded						

E-beam-curable systems included in this study are VARTM resins, prepreg, and one-part paste adhesives. One-part epoxy/methacrylate based formulations, CAO1 and CAO2, were characterized using the methacrylate group. They did not show any aging after 21 months. During evaluations, it was noted that some discrepancy was observed between the salt-plate-aged resins and bulk samples. For example in one system, the salt plate-based IR data showed approximately 60% aging, while for the same material sampled from the bulk, less than 10% aging was observed during the same time interval. This difference was attributed to the moisture-absorbing nature of salt plates. Water accelerates the epoxide ring opening, which contributes to the rapid aging observed for epoxy-based studies. This effect was more pronounced for thin samples in the MIR experiments. Thus for the epoxy based e-beam systems testing was performed on fresh samples taken from sealed containers of aging resins. This introduces an error of roughly 10% because of variations in thickness and sample alignment. The low-viscosity VARTM based resins showed epoxy conversions less than 10% for 18 months. The model system EB3605 a model system representative of our IPN materials aged less than 10% over two years. Cationic E-beam-curable epoxy-based prepreg resin systems T-11 and T-14 also demonstrated aging less than 10%. The E-beam-curable prepreg, Epreg1, which contains only methacrylate groups, showed only 10% aging over 18 months. Overall, compared to thermal-curable systems, E-beam curable systems showed greater stability for room-temperature storage as shown in Figure 51.

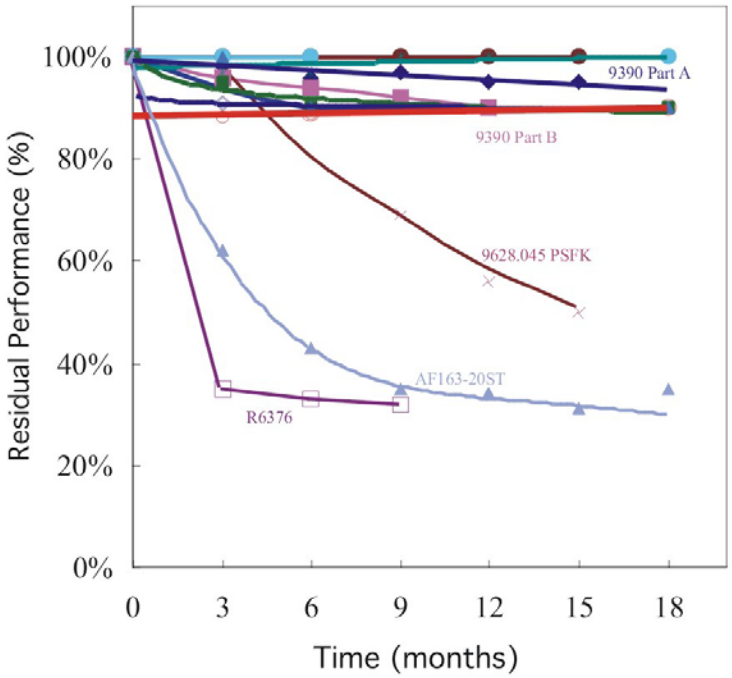

Figure 51. Performance of Thermal Versus E-beam Systems.

(a) Full graph

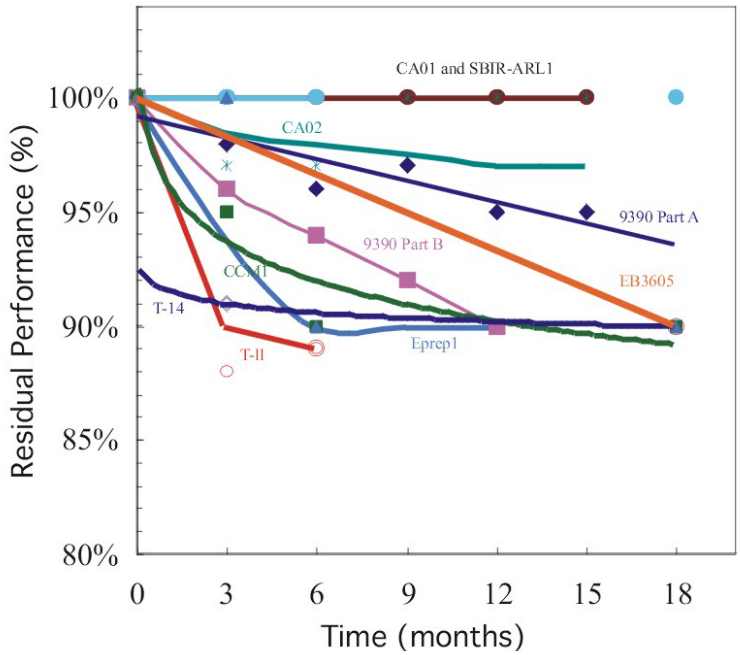

(b) Enlargement of high-residual-strength zone.

2.3 Conclusions for Resin Aging Study

The results indicate that new formulations based on E-beam irradiation show promise to provide extended shelf life and to provide increased out-time for resins, owing to room temperature storage capability of E-beam systems.

3 Real Time *In-Situ* Spectroscopic Characterizations

There has been a growing interest in radiation (ultraviolet or electron-beam [e-beam]) curing of resins and composites [24 - 31]. Such materials have a broad range of applications and present significant advantages over traditional thermally cured thermosets. Typical applications of polymeric materials cured by ultraviolet (UV) and electron beam (EB) radiation include coatings, inks, adhesives, and composite materials for applications such as aircraft components. Among the advantages of this class of materials, the most relevant are shorter curing times, lower energy consumption, and reduced overall manufacturing costs as compared to typical thermally cured systems. Despite good thermal properties and significant processing advantages, epoxy-based composites manufactured using EB systems suffer from low compressive strength, poor interlaminar shear strength, and low fracture toughness. Furthermore, many aspects of the cure processes such as chemical kinetics and the influence of processing conditions on the final material properties are not yet fully understood.

Although some work has been performed in recent years in the assessment of the kinetics of relevant photo-induced polymerizations [32], to our knowledge the scientific community has never carried out real-time *in-situ* kinetic measurements for polymerizations induced by EB irradiation. In the present work, we developed a technique to perform such measurements based on near infrared spectroscopy (NIR). The details of the technique and the results

obtained for UV and EB induced cationic polymerization of monofunctional and difunctional epoxy systems will be presented. A kinetic model has also been developed to predict conversion versus time as a function of relevant kinetic parameters and processing conditions.

3.1 Experimental

Table 41 shows the materials used in this work and their chemical structures. Two epoxy systems were considered in this work. Phenyl Glycidyl Ether (PGE) was used as a model compound to assess the intrinsic kinetics for the cationic polymerization reactions. Diffusion limited kinetic studies of Diglycidyl ether of bisphenol A (DGEBA) were used to develop diffusion limited kinetic models. Notice that the structures of the two monomers are similar in the fact that PGE closely approximates the phenyl glycidyl portions of a DGEBA. This suggests that in the absence of diffusion limitations, the kinetic parameters for the two systems should be the same for a given set of experimental conditions. All reactants were dried using 4Å molecular sieves (Aldrich Chemical Company, Inc). The sieves were conditioned at 175°C for 12 hours prior to use. Such drying limits water concentration to below 0.1% in the reactants.

Table 41. Materials used in Experimental work

Material	Chemical Structure
1. Phenyl glycidyl ether (PGE) from Aldrich Chemical Company, Inc. USA.	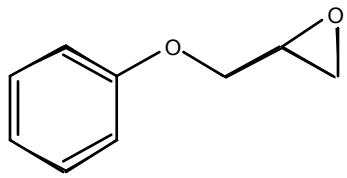
2. Diglycidyl ether of bisphenol A (DGEBA). EPON 828 from Shell Chemicals USA. (n=0.127)	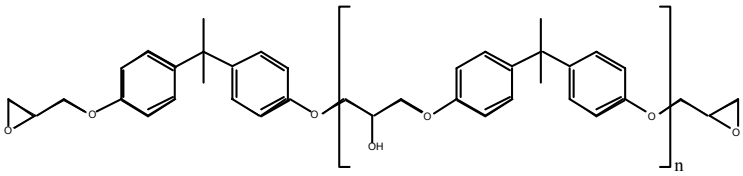
3. Diphenyl iodonium hexafluoroantimonate CD1012	$\{C_6H_5I^+C_6H_4OCH_2CHOHC_{12}H_{25}\}\{SbF_6^-\}$

Fiber Optic Near IR Spectroscopy - The kinetic analysis performed in this work is based on a near infrared (NIR) spectroscopy technique. The experimental apparatus consists of a NIR spectrometer, a temperature controller, a radiation source (UV or EB), and a specially designed sample holder. The overall setup is shown in Figure 52.

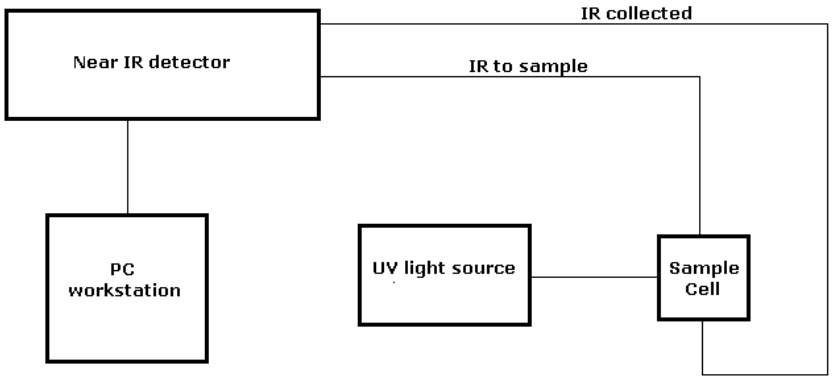

Figure 52. Schematics of the experimental setup used in the kinetic studies.

The NIR measurements were performed using a spectrometer possessing spectral range from 1160 to 2250 nm with a resolution of 4 nm. The infrared light is produced by a white light source that is connected to the sample holder via a low-hydroxyl silica fiber with SMA type connectors at both ends. Light travels from the end of the fiber optic cable to the sample through an optical link that collimates the light into a more focused beam. The focused beam passes through the sample and is subsequently collected by another focusing device that passes the light to a fiber optic cable connected to the spectrometer. A computer processes the data and provides NIR spectra in real time. The spectrometer was adjusted to allow the collection of NIR spectra at time intervals as low as 0.166 s. The samples in the present kinetic studies were placed in a specifically designed sample holder designed to maintain the IR path length through the sample constant. The sample holder was fashioned from an aluminum block and was designed to align input and output radiation sources (UV, EB, IR), and to accommodate heating elements for temperature control. Upon irradiation, the disappearance of epoxy groups was monitored versus time by measuring and following the changes in the characteristic epoxy peak height. The characteristic epoxy peak in these experiments corresponds to a wavelength of 2209 nm. For PGE experiments a steady a stable reference peak at 2163 nm was also found. Calibration curves were constructed that indicate a linear relationship between the characteristic peak height and the concentration of epoxy functional groups. Thus, the spectra were analyzed by calculating the ratio between the characteristic epoxy peak height at a given time and the peak height at time t = 0, the instant when the UV light was turned on. Representative relative concentration plots for the UV induced cure of DGEBA are given in Figure 53. The plot contains data from three experiments conducted using the same reaction parameters (temperature, photoinitiator concentration, light intensity) and show the good reproducibility of the experimental setup.

Sample Preparation and Irradiation: - PGE and DGEBA systems with varying photoinitiator concentration were prepared. For UV samples the maximum photoinitiator concentration was about 1 wt.% to insure an even dose through the thickness of the specimen. EB cure experiments were carried out with photoinitiator concentrations up to 3 wt.%. The thickness of the reacting samples varied from 0.5-0.65 mm for UV experiments (in order to ensure optimal UV light penetration) and about 3 mm for the EB experiments. Temperatures ranging from 40 to 90°C were investigated. After placing the samples of

interest in the holder assembly, the system was maintained at the desired temperature for several minutes prior to initiating the reaction. This allowed the surface of the monomer film to equilibrate and maintain a constant profile during reaction. Subsequently, radiation at a given UV intensity or EB dose rate was applied and kept on for a specified period of time or until the reaction was complete (i.e., until the characteristic epoxy peak height totally disappeared or stopped changing).

The experimental setup described previously was coupled to a radiation source (UV or EB) in order to perform the kinetic studies. A Novacure™ light source equipped with appropriate bandpass filters (365 nm) was used for UV cure experiments. This apparatus also allows an accurate control over UV light intensity delivered to the sample. EB cure experiments were carried out at the Boeing Radiation Effects Laboratory. The Boeing EB accelerator operates at 10 MeV beam energy. A constant pulse rate of 15 pulses/s was used for our experiments and dose rate was adjusted up to 26000 rad/s by controlling the pulse width. For the majority of experiments a dose of 5 Mrad applied continuously was delivered prior to terminating spectroscopic measurements.

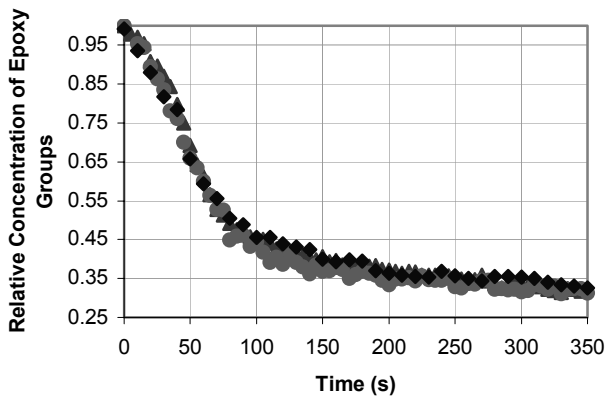

Figure 53. Plot showing reproducibility of experiments. Three runs were performed with DGEBA. UV light intensity = 45.8 mW/cm^2,T = 70C and initiator concentration = 0.68 wt.%

3.2 Kinetic Model Development

The kinetic model for DGEBA radiation induced cure is based on an intrinsic kinetic model based on PGE cationic polymerization experiments that will be extended to take into account severe diffusion limitations encountered with crosslinked DGEBA resins by mathematical accounting for the diffusion limitations using free volume theory. Without delving into mechanistic details, one way that the initiation reaction for radiation induced cationic epoxy polymerization using a photoinitiator can be represented is as follows,

$$C + h\nu \rightarrow H^+ + X \qquad (1)$$

$$H^+ + M \rightarrow H\text{-}M^+ \qquad (2)$$

where C is photoinitiator present in the system, hν is the radiation energy, M the epoxy monomer, and X is a mixture of initiation products that is assumed not to participate directly in the polymerization reactions that follow. The first equation summarizes a series of

reactions, by which one diaryliodonium salt molecule reacts due to the UV or EB radiation to produce the hydronium ion. The second equation represents the formation of an active epoxide molecule or active center capable of initiating polymerization ($H\text{-}M^+$).

The decomposition of the photoinitiator upon irradiation can be modeled based on the assumptions that the generation of active centers is first order and that the life of the cationic active centers is very long (and therefore such active centers are not deactivated during the polymerization). This allows expressing the concentration of the photoinitiator

By equation 3:

$$C(t) = C(t = 0) - I \qquad 3$$

where I is the concentration of cationic active centers. The rate of formation of active centers is then given by the following expression.

$$\frac{dI}{dt} = k_i \cdot C(t) = k_i \cdot [C_o - I] \qquad 4$$

$$I(t = 0) = 0$$

$$C(t = 0) = C_o$$

Integrating equation 4 with respect of time for the given initial conditions yields equation 5.

$$I(t) = C_o \cdot [1 - \exp(-k_i \cdot t)] \qquad 5$$

We assume that the rate of polymerization is dependent on monomer concentration and active center concentration, thus the rate of monomer depletion is given by the following second order expression.

$$\frac{dM}{dt} = -k_p \cdot M \cdot I \qquad 6$$

Combining equations 5 and 6 and integrating with respect of time yields the following equation relating dimensionless monomer concentration (i.e., monomer concentration divided by initial monomer concentration M_0) to time, initial photoinitiator concentration and the rate parameters k_i and k_p .

$$\frac{M}{M_o} = \exp\{-k_p \cdot C_o \cdot t + \frac{k_p \cdot C_o}{k_i} \cdot [1 - \exp(-k_i \cdot t)]\} \qquad 7$$

Based on the assumption (also confirmed by a calibration) of a linear relationship between peak height and epoxy monomer concentration, the relative concentration of epoxy groups measured by analyzing NIR spectra can be assumed equal to the expression in equation 7.

Since C_o (the initial concentration of initiator in gmol/liter) can be easily calculated based on monomer and initiator known densities and molecular weights, this model has two unknown

parameters k_i and k_p. An iterative fitting program was created to obtain numerical values for the model parameters k_p and k_i. The program was used to fit relative epoxy group concentration versus time data to values predicted using equation 7. The fit was performed with a least-squares analysis; in other words, the computer routine calculated the sum of the squared errors between each data point and the value predicted by equation 7 and found the values of the model parameter that minimized this sum.

This model is appropriate if diffusion limitations in the system are negligible (and this can be considered to be the case for PGE above 40°C). If diffusion limitations are important in the system, as in the case of DGEBA resins where gelation and vitrification phenomena occur, the model needs to be modified. In particular, in the case of DGEBA resins, the value of the polymerization constant k_p cannot be considered constant with respect of time. As it is will become clear from the experimental data shown in later sections, the apparent reaction rate constant decreases with respect of time, and becomes very small as vitrification phenomena and other diffusion limitations occur in the system. We will handle this mathematically by calculating an apparent propagation rate constant k:

$$\frac{dM}{dt} = -k \cdot M \cdot I \qquad 8$$

$$k = k_p \cdot \eta$$

The efficiency factor η depends on the diffusion and reaction parameters in the system, based on the following equations [33].

$$\eta = \frac{1}{1 + Da} \qquad 9$$

$$Da = k_p \frac{1}{4 \cdot \pi \cdot d \cdot D \cdot L}$$

where L is Avogadro's number, D is the diffusivity, and d is the collision diameter in the specific system. The diffusivity in the system can then be expressed as a function of the free volume as follows:

$$D = D_o \cdot \exp[B \cdot (1-1/f)] \qquad 10$$

where B is a fitting parameter and D_o is the temperature-dependent Arrhenius diffusivity. By lumping some parameters together, the Damkoehler number Da can be expressed as:

$$k_{do} = 4 \cdot \pi \cdot L \cdot d \cdot D_o \qquad 11$$

$$Da = k_p / \{k_{do} \cdot \exp[B \cdot (1-1/f)]\}$$

The free volume f available for the reaction is a linear function of the departure of the system temperature from the conversion-dependent glass transition temperature.

$$f = f_o + \alpha \cdot (T - T_g) \qquad 12$$

Where f_o is the fractional free volume at the glass transition state and has been estimated for epoxy systems as 0.025 [34]; α is the thermal expansion coefficient, which for DGEBA-type resins is found to be equal to $4.84 \cdot 10^{-4}$ K^{-1}. As far as the glass transition temperature, samples of DGEBA cured up to a known conversion (i.e. reacted until the final limiting conversion is achieved) were tested with a differential scanning calorimeter in order to assess their glass transition temperature, and the relationship between T_g and conversion of epoxy groups was modeled using the Di Benedetto equation [35], one of the most widely used correlations to relate glass transitions and extent of cure in thermoset systems:

$$\frac{(T_g - T_{go})}{T_{go}} = \frac{(E - F) \cdot \alpha}{1 - (1 - F) \cdot \alpha} \qquad 13$$

where E and F are two fitting parameters, α is the conversion of epoxy groups (or in general the extent of cure) and T_{go} is the glass transition temperature of the unreacted resin (measured to be equal to 263 K). The values of E and F were calculated fitting experimental data to the equation, and the values for E and F of 0.58 and 0.32 respectively were calculated. The resulting plot of experimental data points (obtained through DSC measurements of the glass transition temperature and NIR measurements of chemical conversion) is shown in Figure 54.

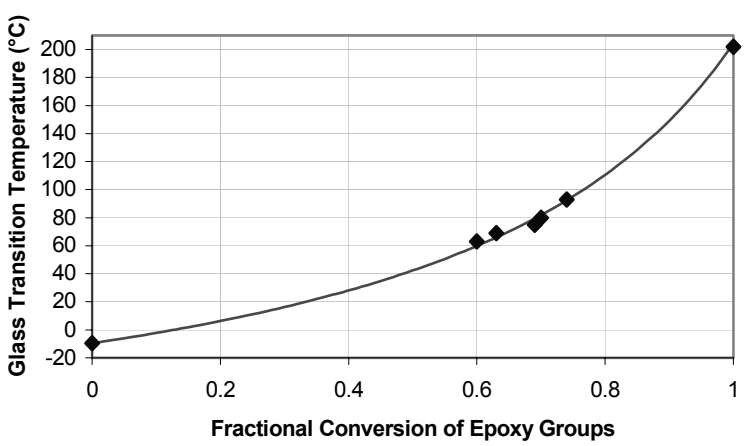

Figure 54. Glass transition temperature versus conversion of epoxy functional groups.

Once the relationship between T_g and conversion is mathematically assessed and the intrinsic parameters k_i and k_p are known from the PGE studies, the expressions above can be used to model the system behavior as a function of two fitting parameters k_{do} and B. By carrying out experiments at different conditions, the dependence of reaction and diffusion parameters on temperature, concentration of initiator and radiation intensity can be assessed.

3.3 UV and EB Kinetics Results

3.3.1 UV-INDUCED CATIONIC POLYMERIZATION

Representative results of PGE reaction studies are given in Figure 55 and Figure 56. These show relative epoxy concentration as a function of time as full conversion is approached. At longer times the relative concentration for PGE reaches 0 for the temperature range investigated. It must be noted that these samples were dried using molecular sieves. However, PGE rapidly absorbs moisture from the environment even during the short time periods necessary for sample preparation. Even low concentration of water in the system can result in inhibition periods lasting up to 60 seconds for the range of light intensity and photoinitiator concentrations evaluated in this investigation. The lag period can be eliminated by carefully drying the samples by purging using dry gases in the sample holder. For low water content << 1 wt.% the rate of epoxy conversion following the lag period was found not to depend on water content. Analysis of the data using the model developed above does not take into account the inhibition period. Treatment of the influence of water on cure behavior will be the subject of future communications. Figure 55and Figure 56 also show the fits of the two-parameter model for the reaction of PGE. These are representative of typical results and demonstrate the model can accurately represent the experimental behavior.

Table 42 contains the parameters obtained from fits of PGE isothermal reaction data collected for temperature ranging between 40 and 90 °C while keeping light intensity and photoinitiator concentration constant. The data show that the within the limits of experimental error the initiation rate constant (k_i) is independent of temperature and the propagation rate constant (k_p) increases with temperature. In fact the propagation rate constant behaves in an Arrhenius fashion. The influence of light intensity on k_i and k_p is shown in Table 43. The initiation rate constant was found to be linearly dependent on light intensity while, as expected, the propagation rate is practically invariant with light intensity. The data reported in Table 44 show that both k_i and k_p are not affected by the initial concentration of photoinitiator used. These data suggest that we have a robust model to describe the cure behavior of PGE and that this system does not exhibit significant diffusion limitations in the temperature range investigated.

The experimental reaction behavior of DGEBA in comparison to the two-parameter model predictions based on PGE derived rate constants is shown in Figure 57. This plot is representative of all other conditions investigated. The model fits the initial portion of the DGEBA reaction curve very well and begins to deviate at around 50 % conversion where vitrification of the reacting mixture due to crosslinking results in severe diffusion limitations that limit conversion. Thus a model that also takes diffusion limitations into account is needed. Such a model was presented previously, as a modification to the dilute region kinetics. In addition to the intrinsic rate parameters k_i and k_p this model requires values of k_{do} and B for each set of temperature, initial photoinitiator concentration, and light intensity conditions. A representative fit of the model to the data is given in Figure 58. The model captures the reaction behavior well and is in very good agreement with experimental results. Some observations have been made when fitting our model to the data. For all experimental conditions investigated, the value of B has been found to be very close to 0.55 (+/- 0.05). Additionally, a linear relationship exists relating the product of light intensity and photoinitiator concentration to the effective diffusion rate constant k_{do} as shown in Figure 59.

Also shown in Figure 59 is the apparent Arrhenius behavior of k_{do}. These observations allow the model to be viable as the kinetic component of a process since a limited number of parameters are required to implement the model over a wide range of processing conditions.

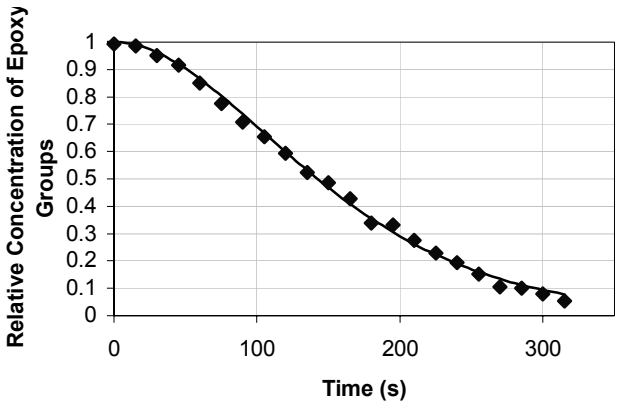

Figure 55. Comparison of data and model fit for PGE. UV light intensity = 40.5 mW/cm^2, T = 60 °C and initiator concentration = 0.44 wt%

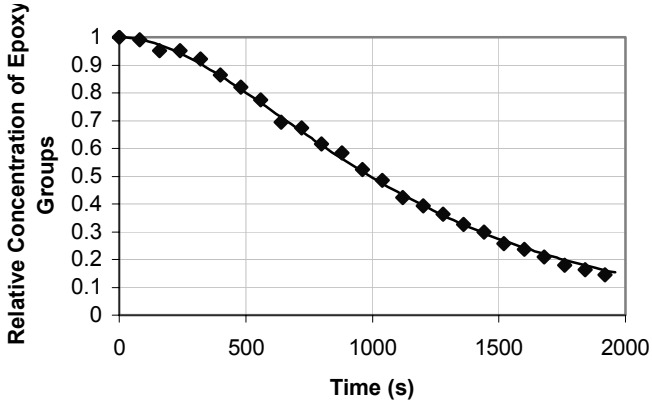

Figure 56. Comparison of data and fit for PGE. UV light intensity = 12.05 mW/cm^2, T = 40°C and initiator concentration = 0.44 wt%

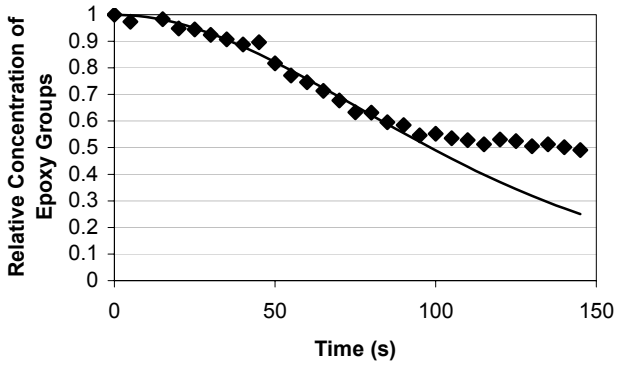

Figure 57. Comparison of data and model predictions based on PGE intrinsic rate values and no diffusion limitations for DGEBA. UV light intensity = 42 mW/cm^2, T = 60 °C and initiator concentration = 0.68wt%

Table 42. Effect of temperature on the propagation rate constant for PGE (UV experiments) Photoinitiator concentration: 0.44 wt%

Temperature °C	Intensity mW/cm^2	k_i s^{-1}	k_p liter/(mol·s)
40	16.55	0.00174	0.22
50	16.55	0.00159	0.80
60	16.55	0.00165	2.11
70	16.55	0.00182	4.11
80	16.55	0.0018	8.14
90	16.55	0.00179	12.50

Table 43. Effect of light intensity on the propagation rate constant for PGE (UV experiments) Photoinitiator concentration: 0.44 wt%

Temperature °C	Intensity mW/cm^2	k_i s^{-1}	k_p liter/(mol·s)
60	7.54	0.00041	2.14
60	16.55	0.0017	2.31
60	25.02	0.0034	2.37
60	40.47	0.0063	2.25
60	45.09	0.0069	2.40

Table 44. Effect of photoinitiator concentration on the propagation rate constant for PGE (UV experiments) (T=70°C and Light Intensity = 16.55 mW/cm^2

Initiator conc. % w/w	k_i s^{-1}	k_p liter/(mol·s)
0.5	0.00182	4.11
0.75	0.00205	4.20
1	0.0019	4.35

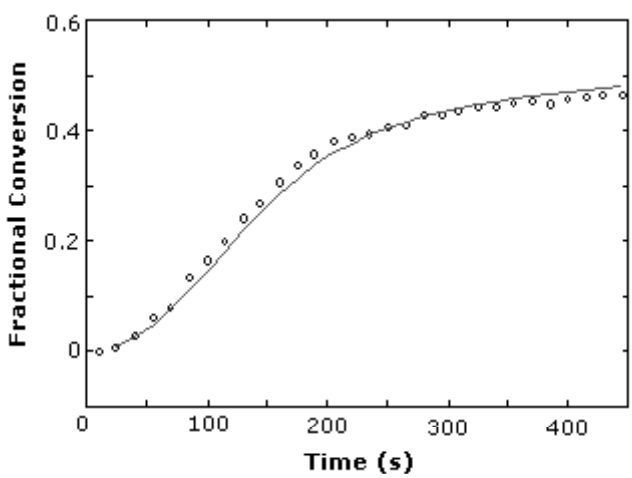

Figure 58. Comparison of experimental data and diffusion limited reaction model predictions for DGEBA [UV intensity = 20 mW/cm^2, Temperature = 70°C and Initiator concentration = 0.185 wt% (k_{do}= 265043 and B=0.5911)].

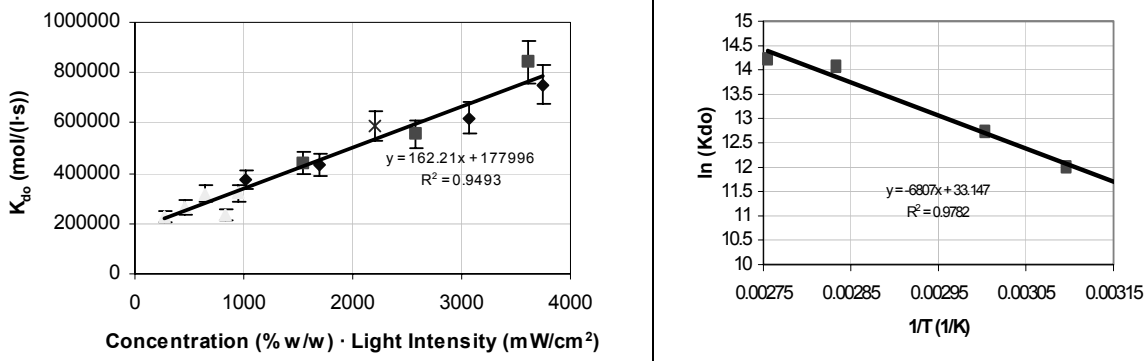

Figure 59. Effect of initiator concentration and radiation intensity (left) and temperature (right) on the diffusion parameter k_{do} for DGEBA (UV experiments). For the temperature dependence plot, the intensity was 45 mW/cm^2 and the initiator concentration 0.68 wt%.

3.3.2 EB-INDUCED CATIONIC POLYMERIZATION

EB cure experiments conducted with PGE were used to evaluate the influence of EB dose rate on the rate constant for initiation. This rate constant was obtained by fitting the two parameter rate model described earlier to data obtained by reacting PGE for a total of 5 Mrad for a number of dose rates keeping temperature and initiator concentration constant. Figure 60 is representative of one such experiment and Figure 61 plots the values obtained for k_i as a function of dose rate. As with the UV induced polymerization the two parameter intrinsic reactivity model faithfully reproduces the EB cure data for PGE. Moreover, the initiation rate constant was found to be linearly proportional to the EB dose rate.

The influence of temperature on the rate parameters k_i and k_p was investigated by analyzing the initial portion (non-diffusion limited) of DGEBA reacted under EB for isothermal cure temperature ranging between 40 and 90°C. The results of these experiments are given in Figure 62. The relative epoxy conversion curves show that increasing temperature increases reaction rate as well as final conversion as was the case for the UV cured samples. Also shown in Figure 62 are the two parameter model fits to the initial portion of the conversion curves. The k_i and k_p parameters associated with these fits are given in Table 45. The results indicate that as was the case for UV cure, the temperature in the range investigated does not affect k_i but does influence k_p in an Arrhenius fashion. Moreover the values of the propagation rate constants and the final conversions (for DGEBA) obtained from the EB experiments closely match those obtained from the UV cure work. Other experiments also indicate that k_i and k_p are independent of catalyst concentration.

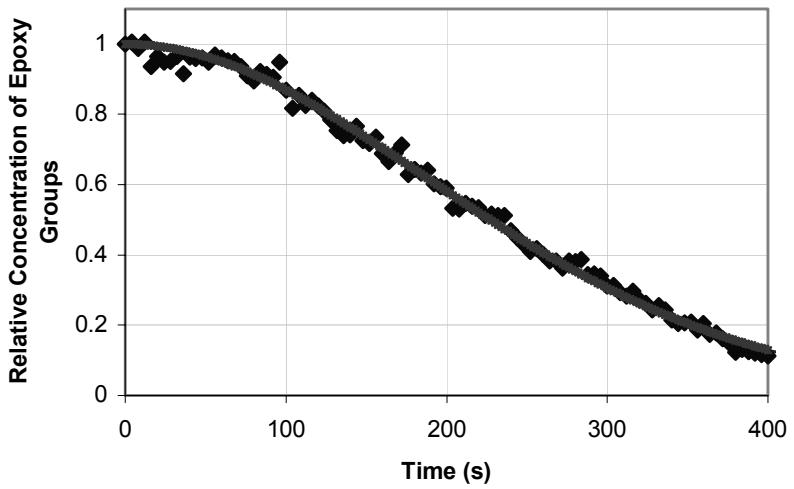

Figure 60. Typical experimental results and model predictions for PGE (EB experiments). Dose rate = 3750 rad/s, T=50°C and initiator concentration = 3 wt%

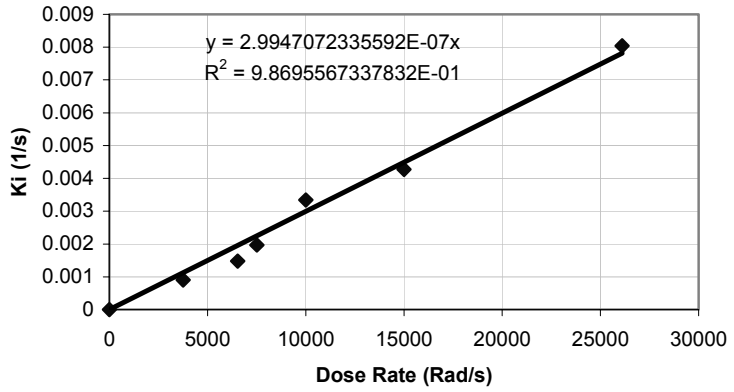

Figure 61. Relationship between initiation rate constant and EB dose rate obtained from experiments conducted using PGE (T=50°C and initiator concentration = 1 wt%)

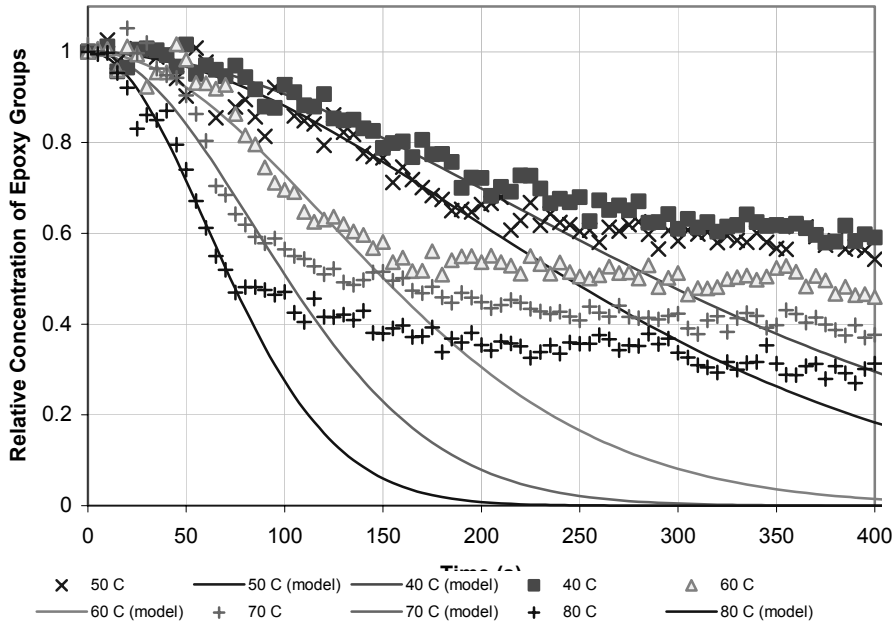

Figure 62. Results for DGEBA (EB experiments) and comparison with model developed for PGE. Dose Rate = 7500 rad/s and initiator concentration = 1.06 wt%

Table 45. Effect of temperature on intrinsic rate kinetic parameters (EB for DGEBA). Initiator concentration = 1.06 wt%

Temperature °C	Dose rate rad/s	k_i s^{-1}	k_p liters/(mol·s)
40	7500	0.00279	0.385
50	7500	0.00210	0.802
60	7500	0.00205	2.025
70	7500	0.00201	4.078
80	7500	0.00195	8.497

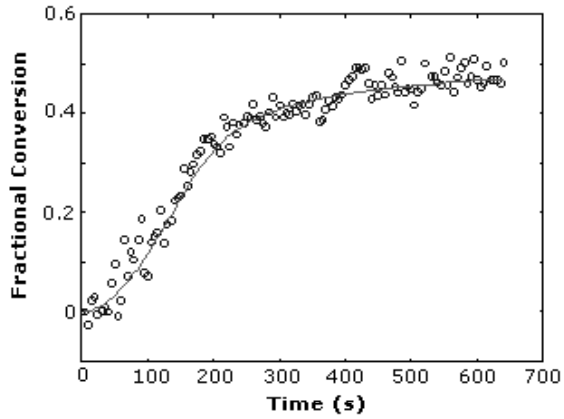

Figure 63. Diffusion limited model predictions and experimental data for DGEBA. EB dose rate = 7500 rad/s, T = 50 °C and initiator concentration = 1.06 wt%. B=0.555 and k_{do} = 460817 liters/(mol·s)

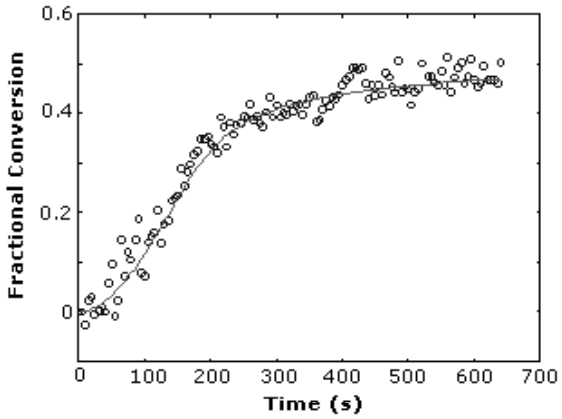

Figure 64. Diffusion limited model predictions and experimental data for DGEBA. EB dose rate = 7500 rad/s, T = 60 °C and initiator concentration = 1.06 wt%. B=0.5568 and k_{do} = 993748 liters/(mol·s).

3.3.3 INFLUENCE OF WATER ON CURE BEHAVIOR

The experiments discussed thus far and the accompanying modeling efforts were all based on dry epoxy systems. It is well known that water and other hydroxyl containing materials influence the cationic reaction of epoxies [36]. Following is a brief discussion concerning preliminary NIR experimental data for radiation induced epoxy polymerization in the presence of water. Figure 65 shows the reaction behavior of DGEBA at 60°C under UV radiation in its dry state and containing 0.80 wt.% water. The conversion profile for the two experiments is very different. In the presence of water a significant lag period is observed. The length of the lag period was observed to depend on water concentration. Once the reaction begins, the rate of conversion is greatly increased compared to the dry system. Thus water has two effects on the radiation induced cationic reaction of epoxies: it delays its onset, and accelerates it once the reaction starts. Similar results have been obtained under EB irradiation.

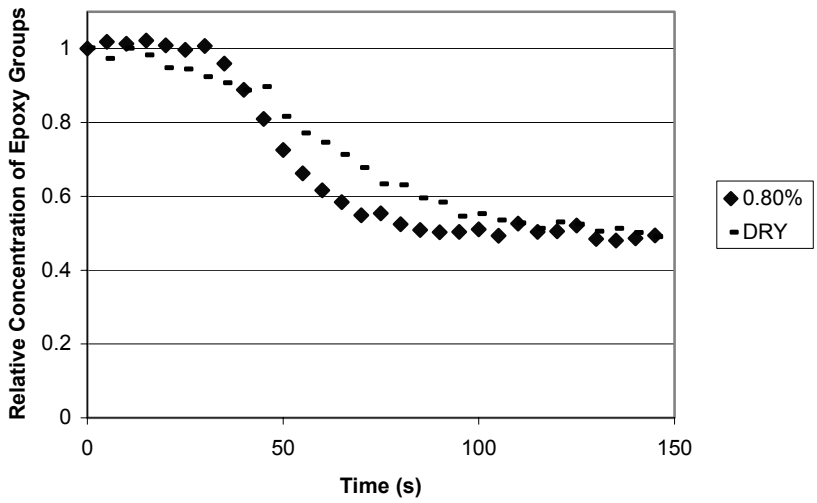

Figure 65. Plot showing the effect of water on the cure kinetics of DGEBA (T=60°C, Initiator concentration= 0.68wt% and UV Intensity = 42 mW/cm^2)

3.4 Comprehensive Understanding of EB Kinetics

A new experimental approach has been developed in this study to characterize the cationic cure kinetics of dry epoxy systems induced by UV or EB irradiations. To our knowledge this is the first time that real-time *in-situ* studies of high-energy EB induced polymerization have been investigated via spectroscopic methods that provide direct composition measurements. In addition, a kinetic model was developed to describe the behavior of typical epoxy systems in terms of chemical kinetics coupled with diffusion limitations. The experimental data obtained are in very good agreement with the proposed model. This allowed the characterization of the relationship between kinetic and diffusion parameters in the system and key processing variables, such as temperature, radiation intensity and photo-initiator concentration.

Some general conclusions can be reported. First, as anticipated, due to the structural similarities between PGE and EPON 828 molecules, it was found that for a given set of experimental conditions the kinetic parameters calculated for PGE accurately describe the system behavior for DGEBA at low conversions, i.e., when diffusion limitations in the system can be considered to be negligible. A second important result is that the very good agreement between the developed model of the data strongly suggests that in fact the cationic active centers are long lived and do not deactivate at appreciable rates. Moreover, for the radiation intensities and dose rates considered in this study, the initiation characteristic time scale is much longer than the time required for complete monomer conversion. This suggests that in the case of polyfunctional epoxy resins the properties of the final polymer network could be influenced by the manipulating initiation versus vitrification time scales. With the exception of initiation rate constant (k_i) values, UV and EB induced epoxy polymerizations can be described by the same model. Finally, water content was found to influence

polymerization behavior. Ongoing work focuses on extending the kinetic model to address the influence of water.

4 E-Beam Repair Specimen Analysis

This test program was to compare an E-beam repair to the baseline thermal cured repair on a bonded composite patch. Initial failure, ultimate failure, and the scatter of the limited specimens were compared to each other and the baseline prediction. With only the manufactured technique changed, only material properties of the adhesive were altered in the analytical comparison. The initial failure of the specimens is usually the design parameter used in a strength prediction for an adhesive since the ultimate failure could be 2-3 times larger then the initial failure. Since the load factor of a structure is that ultimate is only 1.5 times that of limit, then, in an adhesive bonded structure, it is the initial failure load of the patch that drives the limit load more then the ultimate load.

4.1 Test Panel and Test Results

A quasi-isotropic 24-ply laminate coupon with a center repair was manufactured, tested, and analyzed to compare several techniques in manufacturing repairs. The AS4-fiber coupons were compared to the baseline, standard repair to identify any reduction or similarity in strength and failure mode. Figure 66 shows a drawing of the specimen that was tested. Strain gages on the panel insured that the loading was uniform along the length and no bending was imposed during loading. The specimens, with a 15:1 scarf ratio, are typical in analyzing repairs under tension and failure is typically at the center of the panel or around the bonded repair patch.

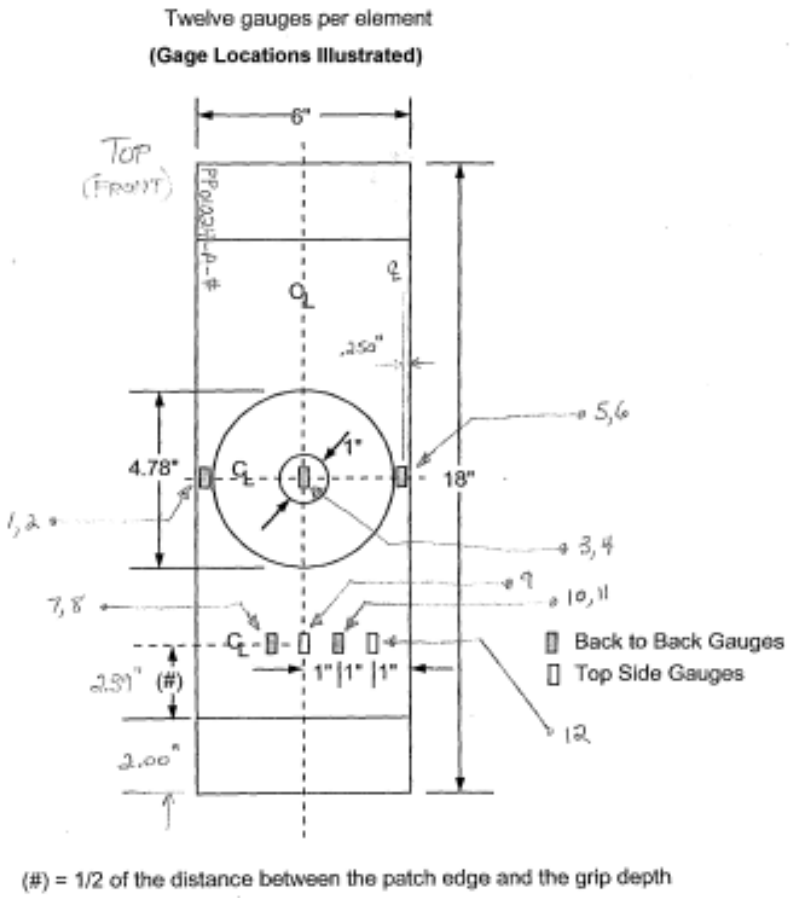

Figure 66. Drawing of Repair Coupon

The tests were conducted using a 50,000 lb test fixture in the mechanical testing facilities at Northrop Grumman. The specimens were coded with number so that there was no knowledge of which manufacturing technique was used on each specimen until after they were tested. Table 46 shows a summary of the failure loads for all the specimens with comments from the test engineer taken during the test and from observations in the strain gage readings. The type of patch construction used groups the results.

Table 46. Summary of Test Results

Specimen ID	Max Load (Lbs)	Test Engineer Comments	Comments of Strain Gage Readings	Patch Type
PP01024-A-4	49,930	Load cell range exceeded - Test aborted	Center (4) nonlinear @ 30-34,000 lbs	Baseline: FM73 pre-cured patch
PP01024-A-4a	48,790	Specimen re-loaded to failure	Initial failure at 34-36,000 lbs	Baseline: FM73 pre-cured patch
PP01024-A-5	47,680		Initial nonlinearity at ~36,000 lbs	Baseline: FM73 pre-cured patch
PP01024-A-7	47,900		Nonlinear @ 30,000 lb	Baseline: FM73 pre-cured patch
PP01024-A-1	31,030		No pre-failures captured in strain gages	pre-cured patch, E-beam cured
PP01024-A-2	18,440	Patch failure with some backside delamination	No pre-failure captured in strain gages	pre-cured patch, E-beam cured
PP01024-A-3	20,700		Some nonlinearity at 14-16,000 lbs @ gage 2 & 4	pre-cured patch, E-beam cured
PP01024-A-6	30,930	Damage indicated at 27,800 lbs (Audible at 27,200 lbs)	Nonlinear at 12-14,000 lbs.	EBA4 staged patch, E-beam cured
PP01024-A-8	37,560		Nonlinear @ 12-14,000 lbs	EBA4 staged patch, E-beam cured
PP01024-A-9	39,710		Nonlinear @ ~15,000 lb	EBA4 staged patch, E-beam cured

From the data summary one can see a difference in the ultimate failure loads between the groups of specimen. The baseline repair thermally cured FM73, resulted in an average failure of 48,575 lbs (8,095 lbs/in). The thermally staged composite patch with EBA4 at 160°F for one hour then E-beamed cured is 36,067 lbs (6,011 lbs/in) while the pre-cured patch thermally consolidated at 160°F for one hour then E-beam cured demonstrated ultimate failure at 23,390 lbs (3,898 lbs/in). Considering the same prepreg lay-up and the use of adhesives for the specimens were equal, the processing of the batch was the major variable amongst these specimens. Thus, the use of E-beam precured patch on a bonded repair patch has shown up to 51% reduction in strength. There was also significant more scatter in the ultimate load for the E-beam repairs over that of the baseline. However, in the initial load or

the on-set of nonlinearity in the adhesive, the results were mixed with little scatter in the initial nonlinearity of the staged patch but significant initial damage in the pre-cured patch.

With fiber modulus contributing most to the stiffness of the panel, both the baseline and E-beam coupons followed a similar stress-strain loading. The strain gages on all specimens appeared to behave in a linear manner until a load of approximately 15,000 lbs (2,500 lbs/in) on the E-beam specimens and 30,000 (5,000 lbs/in) on the baseline specimens. The only strain gages that showed significant nonlinearity were those (Gage 3 and 4) in the middle of the patch. All others were linear until failure. Figure 67 and Figure 68 show the critical strain gages plotted for specimens 7-9. All other strain gages for the specimens are provided in an appendix of this report.

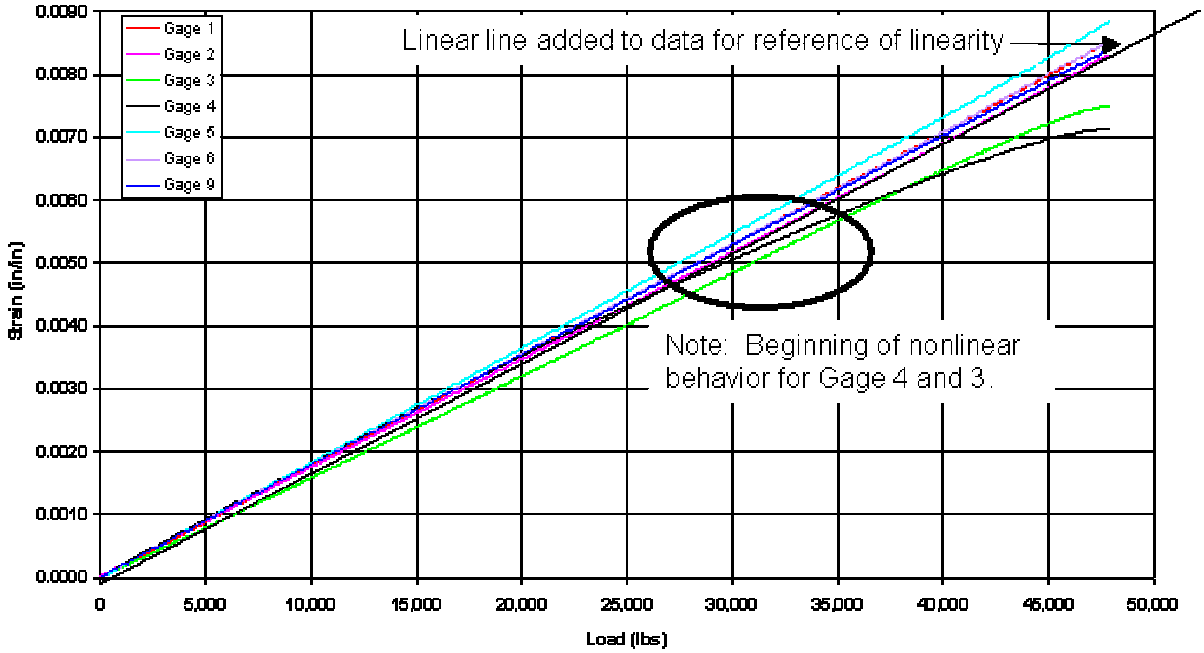

Figure 67. Initial Nonlinear Behavior of Strain Gages with Specimen A-7.

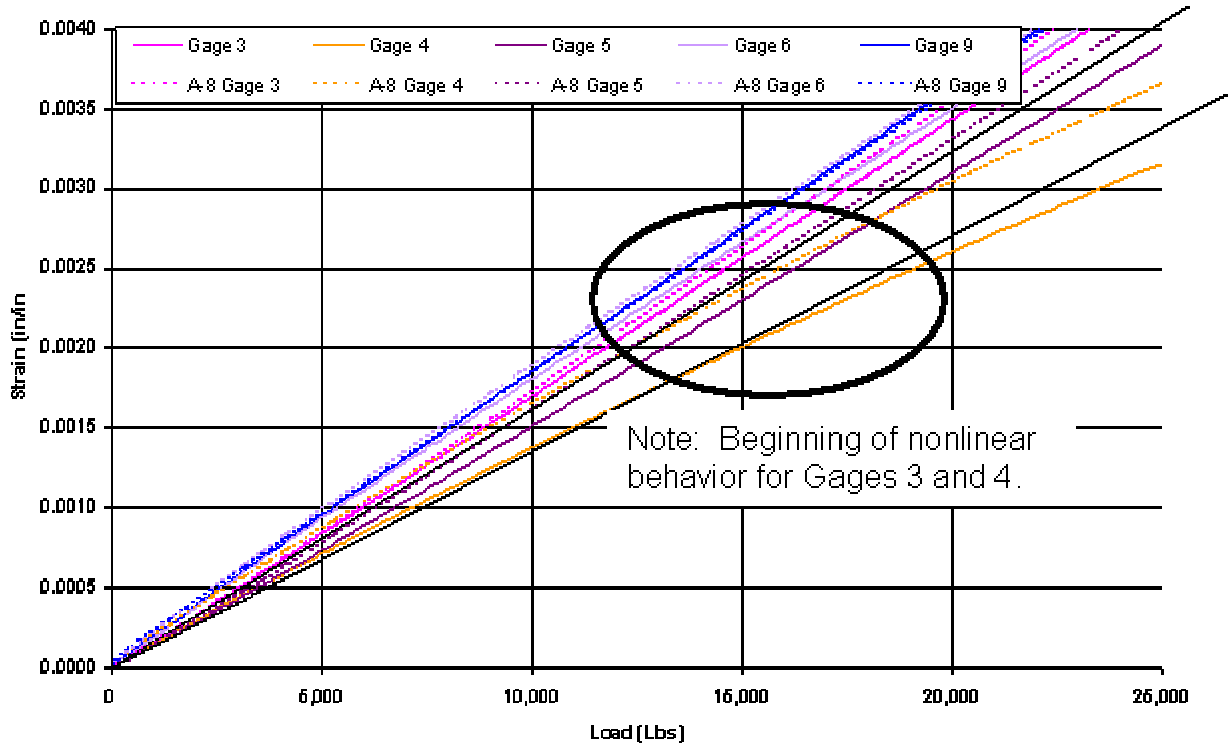

Figure 68. Nonlinear Strain Behavior in Specimens A-8 and A-9.

Nonlinearity of a strain gage is not trivial to detect. It can be challenged amongst those who are viewing the data when there are inconsistencies in the trend. However, with the coupons that are shown here, the nonlinearity is strongest in the center of the repair patch. This is similar to the analytical predictions as well as intuition. As the adhesive in the repair starts to load in a nonlinear fashion, the strain in the center of the patch lags behind the strains in other gages. The trend of nonlinear behavior is slight be distinct when compared to a linear line as shown in the figure.

The nonlinearity detected in the strain gages on the patch is due to the adhesive bond line, the adhesive is more ductile then the composite fiber and resin. The adhesive once stretched to nonlinear measures will seldom return to its original shape and retain its original stiffness. Not all of the adhesive needs to be nonlinear to induce a nonlinear behavior on the surface strain gage. In most cases, there are distinct areas in the bond line that will undergo nonlinear behavior, only when a large percentage of the bond line is behaving nonlinear is final bond line failure likely. Most of the time, the strain in the remaining parent laminate exceeds its ultimate value and a brittle failure occurs there. These are the two primary competing failures mode in bonded composite repair panels. With no strain gages in the bond line exactly, this nonlinearity can only be demonstrated by analysis.

4.2 Analytical Model Description

To analyze the stress and strain distribution in the E-beam repair specimens, a 3-D solid finite element model was built to represent the baseline and E-beam specimen. Note, due to

the geometry being the same, only one model was constructed and properties were modified to represent the different materials. The finite element model represented one-quarter of the specimen and symmetry was imposed at two of the centerline edges. There were 2,312 elements used in the model and 2,466 nodes, each with 3 DOF. The parent and patch laminates were modeled with 6 sub-laminate plies, each representing a 0/90/-45/+45 ply. Figure 5 shows the model and how it was loaded and constrained. The model is configured to illustrate the comparison of the predicted strains to the strain gages as well as to show the impact of the ductile adhesive on the over-all nonlinear behavior of the specimen.

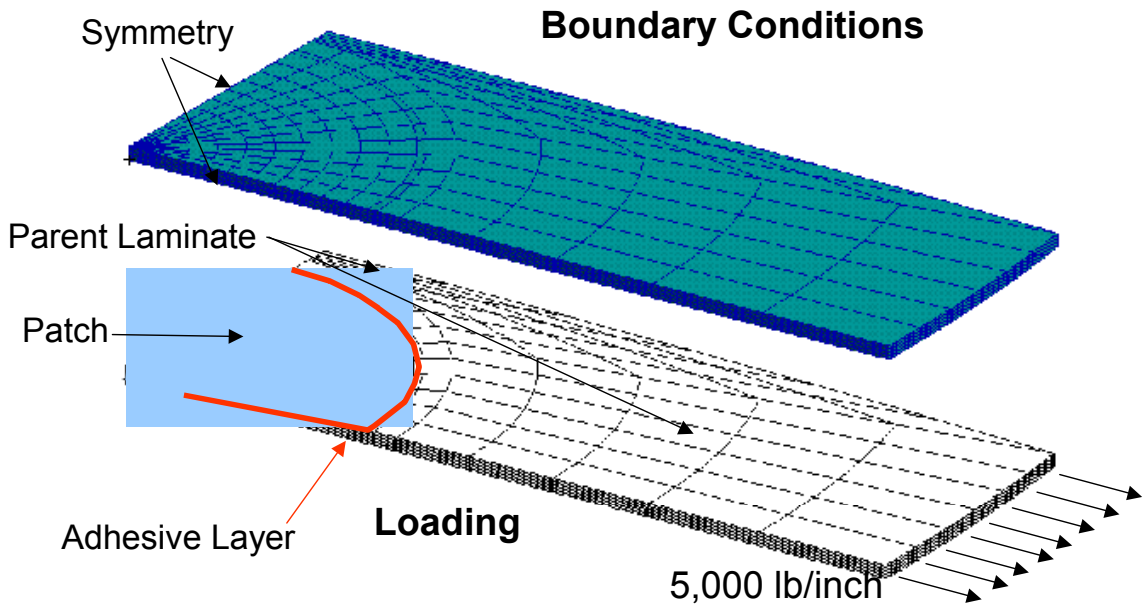

Figure 69. Finite Element Model Used in Analysis

4.3 Test Results Correlation to Analytical Model

The strain prediction for this model is shown in Figure 70 for a 4,000-lb/inch load with correlation to average strain readings for those in the center of the panel. All other strain gages were within 10% of the predicted strains. The load level is kept well within the linear range for correlation. This assumes that the low strength of the adhesive used and manufacturing techniques that were demonstrated did not impact the stiffness of the bond line adhesive. With the fiber stiffness being the same in all specimens and also the driving force, there was little influence of bond line stiffness on the strain gages.

When comparing the adhesives between the baseline and E-beam specimens, the primary difference was the point of nonlinearity observed and the average shear strength. Both adhesives exhibited similar average shear stiffness. However, the data for the E-beam adhesive showed an average strength of 3,880 psi while the FM73, used in the baseline, is significantly higher (~9 ksi). The adhesive in the staged patch specimens started nonlinear behavior around 13,000 lbs of loading and continued to carry load for almost 2.5 times that load to over 30,000 lbs. This would imply that a significant portion of the adhesive is failed and the load was redistributed to other parts of the adhesive and finally remained in the

parent laminate and did not go into the patch. This caused the nonlinearity of the E-beam specimens to be exhibited as early as 2,500 lbs/in of load. The adhesive was unloading the patch along the centerline of the specimen thus causing the most noticeable effect on Gage 4 that was on top of the larger area of patch. The patch never failed, thus showing the load remained in the parent (i.e. loaded) portion of the specimen.

The baseline adhesive FM73 was stronger and could transfer more of the load to the patch. However, like the E-beam adhesive patch, there were some signs of nonlinearity in its behavior after 30,000 lbs or 5,000 lbs/in of loading. This was a lot higher then that exhibited in the staged patch where nonlinear behavior initiated at less then 2,500 lbs/in. The stress distribution in the ramped adhesive bond line is shown from the analytical model in Figure 71. The stresses peak along the centerline that runs parallel to the applied load and reduces as one follows the circle to lines that are perpendicular with the applied load. The characteristics of the adhesive bond line are typical in all bonded joints. If the bond line strength is strong enough to not yield or go into nonlinear behavior, then the load and strain distribution between the patch and the parent laminate of the specimen remains roughly equal. Once the adhesive starts to loose stiffness in the nonlinear regime, the load and strain in the patch reduces quickly.

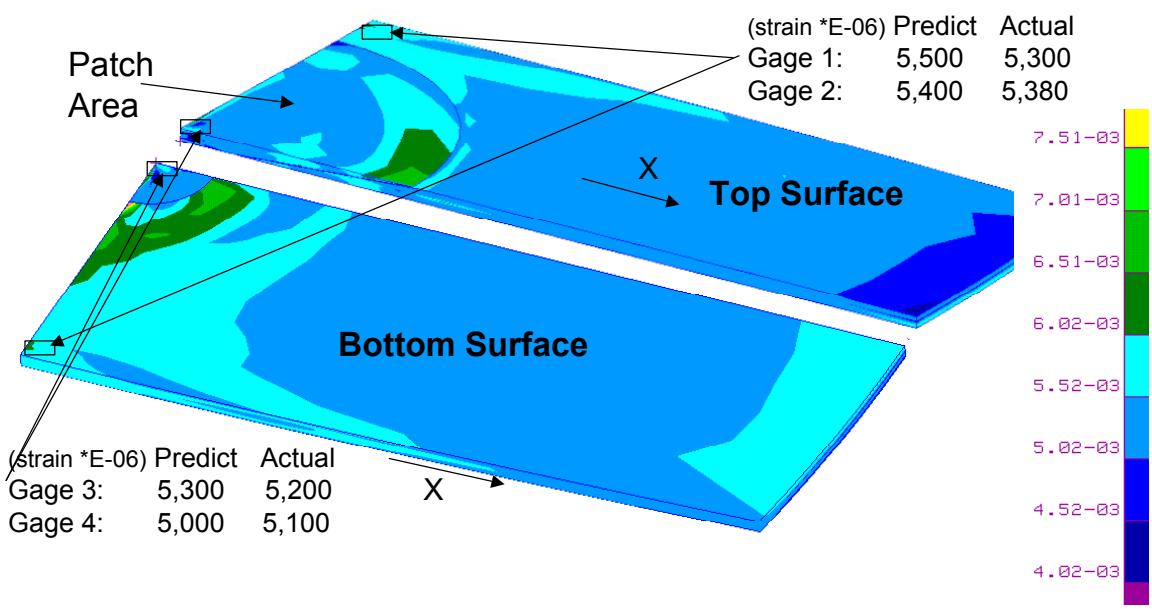

Figure 70. Strain Correlation of the Specimens

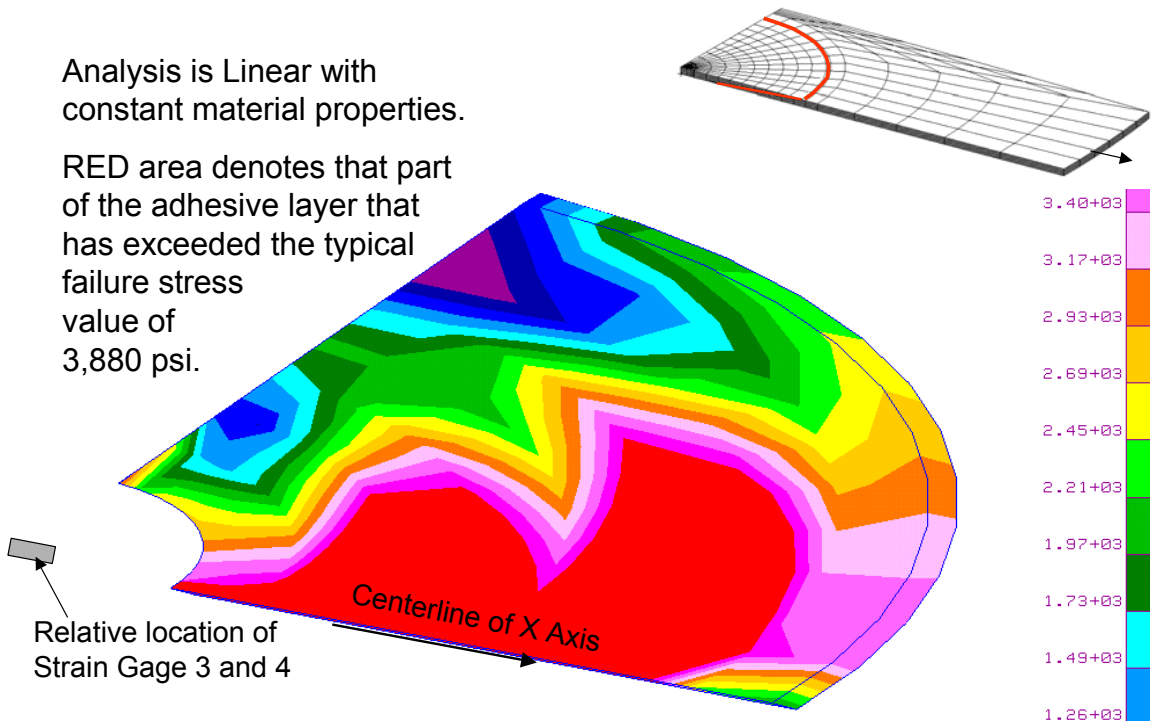

Figure 71. Stress Distribution in the E-Beam Adhesive

4.4 Summary

The test results pointed out several characteristics that were unique to the E-beam cure specimens. The most obvious from the test results were that the baseline specimens performed consistently better then the E-beam specimen, by at least 50% in most cases. As far as structural performance, this shows that some improvement is needed to replace the baseline procedure.

When the E-beam patch was staged prior to the final curing, there was less scatter in the results then when the patch was pre-cured. If one were to calculate a design allowable from the two sets of E-beam repairs, although the initial failures of the staged patch were lower, the allowable would be approximately the same as the higher failure of the pre-cured patch since those specimens exhibited higher scatter in the initial failure. There was also more ductility and nonlinear behavior in the staged patch, where the ratio of final (ultimate) failure to initial nonlinear behavior load was 2.77:1 as compared to the pre-cured patch were this ratio was 1:1 in two of the three specimens. The ductility of failure is better then a brittle failure where there is no early indication of the failure progressing.

5 EB VARTM Demonstration Article

An airframe access panel was fabricated using VARTM VCCM4 resin supplied by Drexel University. The aluminum tooling used for the part is shown in Figure 72. The access panel

included two integrally bonded hat stiffeners. The preform was a six-ply lay-up of AS4 5HS carbon fabric as shown in Figure 73. Prior to the preform lay-up, the tool surface was cleaned and waxed for ease of release. A ½" metal coil used as the resin runner for flow distribution was placed around the part. Full vacuum was achieved for the first bag as well as the second bag. The two-part resin system, VCCM4 and the amine-curing agent was mixed and injected at room temperature. Viscosity of the mixed resin at room temperature was less than 400 cps as shown in Figure 74, and would not gel for at least 5 hours at 30°C (86°F). The amount of time at the temperature was sufficient enough to allow for injection to complete with reasonable resin viscosity. The resin was injected from the top of the tool and flowed downward at all directions. Glass breather was used in between the first and second bag to allow for vacuum, however, because of the breather it was difficult to see the resin flow during the injection. Even after one hour of resin injection into the part, there was no resin witness from the vacuum outflow line. Second bag was removed to have a better view of the resin flow. It turned out that the resin had completely filled the part. The part was then allowed to sit at room temperature overnight without vacuum. Then it was cured at 50°C (122°F) for 5 hours without vacuum. After debagging the part, it was discovered that there was excessive resin flowed downward and leaving the part with resin-starved areas on the back of the part. Although the part was left at room temperature for more than 5 hours for the resin to gel prior to thermal curing, however, the resin was apparently able to flow downward without the vacuum pressure from a second bag. The part was unfortunately not salvageable.

Lessons learned from the first part fabrication:

1. It is not necessary to wax the tool. A thin Frekote coating should be enough to release the processed part. Additionally, wax may contaminate the VARTM resin system.
2. ½" diameter metal coil used as resin runner is too large. The coil collected too much resin, and prevented resin witness on the outflow line.
3. The space between the resin runner and the carbon preform should be less than 1". If the gap is too large, the areas tend to collect too much resin and preventing efficient resin flow.
4. Resin injection should start from the bottom to the top of the tool for a better control of the resin flow.
5. Breather used for the second bag should be some type of see-through material for a better viewing of the resin front movement during injection.
6. Second vacuum bag is necessary to keep the additional pressure on during resin gelling at room temperature and during heat-up in the oven. It seems that the viscosity of VCCM4 will decrease slightly when heated initially at 50°C (122°F).

A decision was made to do a second part fabrication using the same resin system. This time a ¼" metal coil was used as resin runner. The gap between the resin runner and the preform was only about ½" wide. Porous Armalon was used as a breather for the second bag. Although the color of porous Armalon was light brown as shown in Figure 75, resin front was not difficult to detect during the injection. Three injection ports were created at the three lower sides of the tool. The resin was injected from the lower edge of the tool to the top as indicated in Figure 76 showing the resin outflow vacuum line at the top of the tool. The resin mixture was injected at room temperature, which was only about 16°C (60°F). The total injection time was about 1 hour and 15 minutes. The injection time was much longer than expected and was likely caused by the low viscosity at low room temperature during the

injection. Full vacuum of the second bag on the part was maintained during the injection and also during the two days at room temperature prior to thermal curing. The part was then thermally staged at 122°F (50°C) for 5 hours and during that time full vacuum on the part was also maintained. Figure 6 shows the part after debagging and visual inspection indicated good consolidation. The VARTM processing of the access panel was fairly successful, except for a very small dry area on the top edge at the cut-off area. No resin runner was placed near the cut-off. The cut-off area was also the resin outflow line, if the resin runner was placed too close to the resin outflow line, it might flow out of the vacuum line prematurely and preventing the resin from filling out the entire preform.

The thermally staged access panel was shipped free standing to E-Beam Services Inc., Cranbury, New Jersey, for e-beam curing. The part was e-beam cured using the 10 MeV machine in the following steps of curing starting with 1, 2, 2, 5, and finally 10 MR/pass for a total e-beam dose of 20 megarad. Temperature stripes were placed on the part during each pass, a temperature reading of 110°C (230°F) was detected after the last pass of 10 MR/pass. The cured access panel looked good. It was trimmed and ready for display. This second demo part was successfully fabricated using much improved VARTM processing and subsequently shipped without vacuum bag for the final free standing e-beam curing.

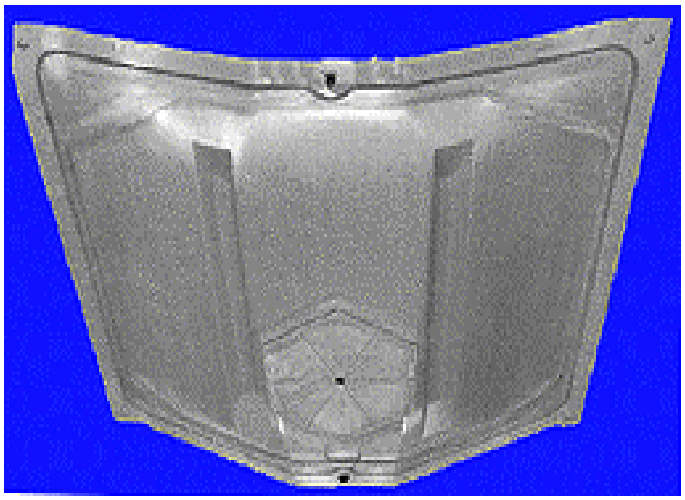

Figure 72. Tooling for aircraft access panel EB cure demonstration.

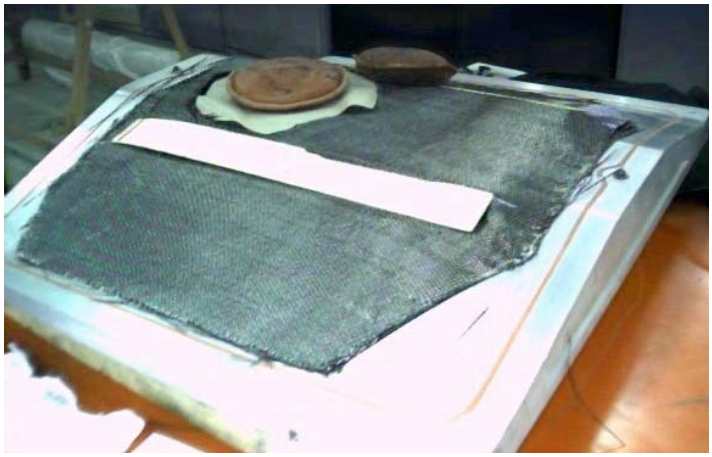

Figure 73. Carbon fabric preform lay-up of AS4 G-sized fibers on VARTM tool.

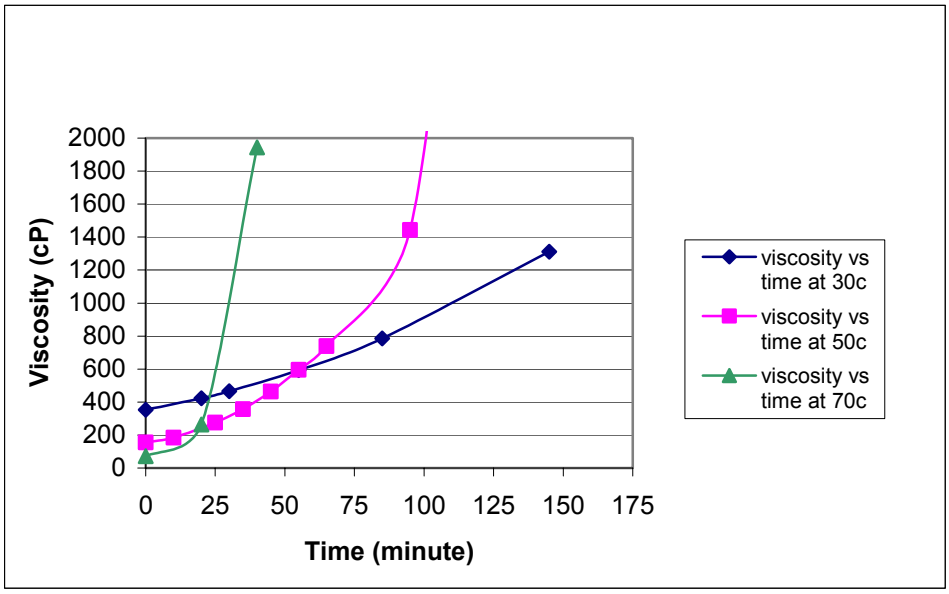

Figure 74. Viscosity profile of VCCM4 with PACM curing amine as a function of cure time at various isothermal temperatures.

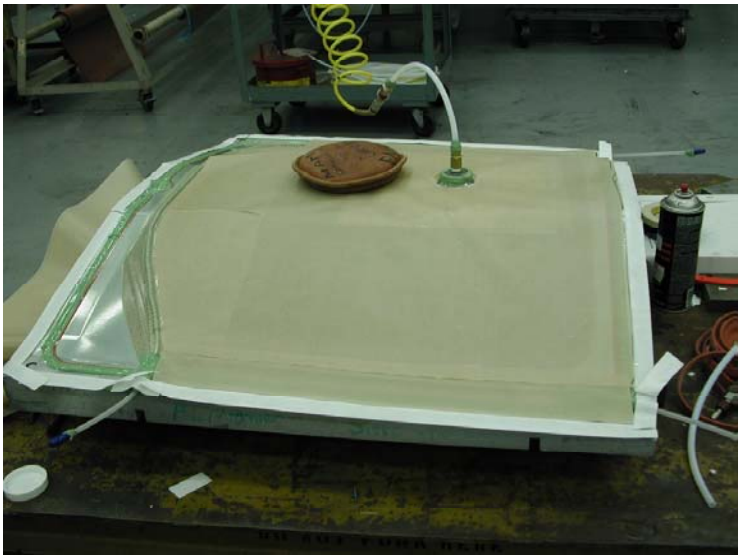

Figure 75. Second Bag Lay-up Showing Porous Armalon

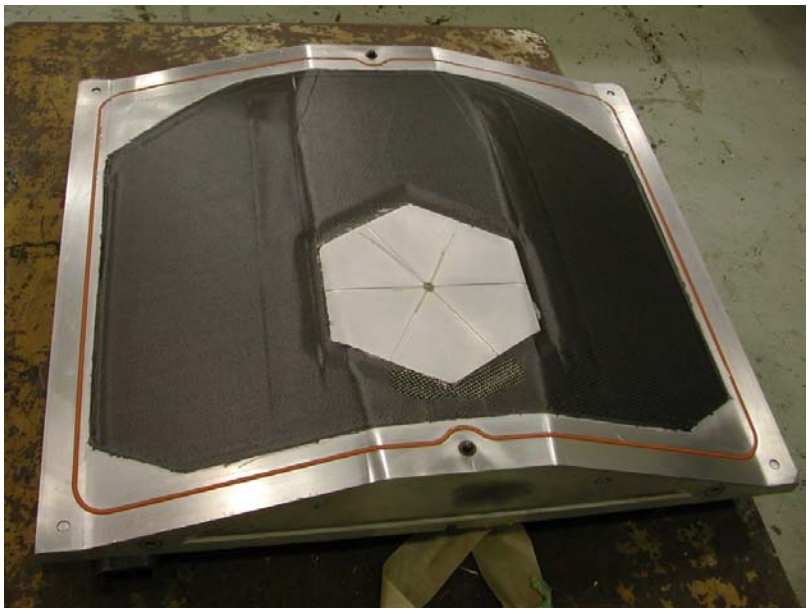

Figure 76. VARTM Access Panel after Thermal Staging Prior to E-Beam Curing. Note: A dry-spot resulted in the hexagonal region at the bottom of the photo.

6 Cost Comparisons of Oven and Electron-Beam Processing

In this section, a model compares the manufacturing costs associated with fabrication of a flat-panel glass composite plate using vacuum assisted resin transfer molding (VARTM) in combination with thermal oven curing or electron beam irradiation curing to process composite thermosets. By integrating process mapping, hierarchical event-driven simulation, and activity-based costing the model determines the optimum conditions and the benefit or cost trade-offs associated with manufacturing performance composites using alternative curing technologies, such as electron beam curing. In the conclusion of the model evaluation, a determination is made that demonstrates the impact of resin cost on total manufacturing costs for the various components, and demonstrating how various scenarios from ownership to toll processing can be implemented by a manufacturer to keep total processing costs from electron beam curing relatively competitive with oven curing processes.

The basic model implemented for the following analysis is based on Scott Jones CIRTM model in SIMPROCESS (CACI International, Inc., Arlington, VA, USA) [37]. SIMPROCESS integrates process mapping, hierarchical event-driven simulation, and activity-based costing into a single tool and allows accurate computation of industrial costs to be determined under various imposed constraints and economic conditions. Activity based costing embodies the concept that a business is a series of inter-related processes, and that these processes consist of activities that convert inputs to outputs. The cost modeling approach manifests this concept, and builds on it by organizing and analyzing cost information on an activity basis. Although maintaining accurate accounting of every possible scenario of processing for the manufacturing demonstration is not feasible, the cost model implemented is relatively comprehensive. Local cost data was collected for labor, equipment, electric, fabric, resin, freight, toll charges, and the Maximum Achievable Control Technology (MACT) compliance cost [38].

Dynamic computer models were designed for VARTM composite processing of S2 glass fabric using a vinyl ester and an E-beam resin with the option of oven or E-beam curing. Note, that despite the understanding that autoclave processing is the worst-case pollution scenario, the model does not address this curing technology. The current emphasis on low-cost processing methods to develop thick section composites compels a comparative study for traditional liquid molding rather than autoclave prepreg comparisons [39]. The vacuum bagging employed by this process simulation was effective in minimizing hazardous air pollutant (HAP) levels to remain under the new MACT legislation of emitting no more than 10 tons per year of any single listed HAP at any single site, where a site is defined as a collection of related processing buildings [38]. The NESHAP legislation was implemented for United States industry in August 2001 and will begin to effect financial viability of commercial industries as early as 2005.

In SIMPROCESS, a computer generated manufacturing facility simulates the flow of raw materials and worker resources to create finished products using a three-shift working cycle that operates the plant 24 hours per day for one calendar year.

Among the key advantages to electron beam processing is the high cost of tooling associated with traditional thermal processing methods. Because the cost of tooling varies significantly with part size, part complexity, and dimensional complexity, the model does not attempt to add this complexity. Therefore, costs are developed for fixed costs associated with thermal versus EB processing for flat panel composites. Since net cost per part will be the most significant change associated with changing fiber types, the cost model is developed with only S2 glass fabric as the cost baseline. The finished parts from the model include various surface area panels ranging from 10 to 100 ft^2 (9290 to 92903 cm^2), but keeping the thickness of all parts at a constant 0.75 inch (1.9 cm). The impact of increasing surface area results in cost variations that are coupled with batch processing limitations for the thermal and EB cure techniques.

6.1 Program description

SIMPROCESS employs processes, resources, and entities to construct a business model. A production plan was setup in the model to include laborers, equipment, and materials with a best practices approach to manufacturing that avoids over constraining the resources or entities, e.g., having a resource either too busy or idle. People, materials, and equipment are examples of resources, while orders, fabric, completed parts, and work-in-process are examples of entities.

The basic flow diagram of the model is demonstrated in Figure 77. The model consists of three essential processing stages, which include preparation for manufacture and lay-up, curing, and finishing. Each of these segments contributes to the costs of manufacturing. However, due to the selected composite configuration, the greatest impact variables in the model include initial materials costs and equipment and curing costs. The steps occurring in each process phase of the model are described below.

The first step in the model involves setting up the production run. At the outset of production, a work-order generated, work scheduled, and materials procured to achieve optimum processing flow. A 24-hour seven day per week manufacturing schedule was utilized in the model, so all capital resources are used to the optimum limits. Next, the manufacturing work area was setup, including the cutting station and lay-up areas. Although this condition does not contribute to materials costs in the modeling, the activity (time) is a cost item for the laborers employed to perform the activity, adding to the total cost of manufacturing.

Once the initial conditions for manufacturing are completed, the actual processing of materials components begins. Initially, the configurations of the manufactured part are determined, including number of layers of fabric required to make a part 0.75 inches thick. With our selected part thickness, 29 layers of glass fabric where used. These parameters are passed along to the manufacturing cycle. The fabric layers required for assembling a part of a defined size are cut to size from the bolts and evaluated for quality assurance. The approved dry fabric pieces are stacked in the prescribed sequence and fiber alignment at the lay-up station and placed into the part mold. The layer placement was also inspected for quality; the dry-fabric lay-up is completed. It should be noted that in addition to quality inspection, the model tracks scrap and poor quality materials that fail the inspection and is able to report waste materials amounts throughout the processing phase. As no resin materials are utilized to this point, waste fabric is considered an industrial waste, which is defined as non-

hazardous materials waste from manufacturing production. Costs for disposal of the industrial wastes can therefore also be included in any detailed analyses.

Once a dry preform is established, the infusion process begins. The distribution medium and peel ply layers are cut and added to the mold configuration. As the process is modeling vacuum assisted resin transfer molding, the top-layer of the mold is a vacuum layer, which for this study will be a disposable vacuum media. The vacuum bag was cut and installed around the part. The gates, vents, infusion and vacuum lines were setup and installed. Once the configuration is completed, the dry preform is evacuated and the vacuum bag seal inspected for leakage.

After lay-up and mold preparations are complete, the resin mixture is prepared. Typical resin systems involve a two-component resin that is blended just prior to infusion. A limitation of the two-part resin is the limited processing window in which to infuse the part. The parameters associated with infusion time include the resin viscosity and the rate of change of viscosity, as well as any exothermic heat generated in the bulk resin. The model encompasses basic parameters for gelation time and initial resin viscosity to compute approximate infusion times for large parts. While the computation is not precise, a conservative estimate of total infusion time is achieved, which can be used to establish baseline production costs. During infusion, resin is supplied at atmospheric pressure. The pressure differential arising from the resin source at atmospheric pressure, along with the evacuated preform, stimulates resin impregnation of the fibrous preform. The infusion line was closed when the resin mixture started to gel. The parts were inspected after infusion. An additional feature of the production business model is included to track hazardous wastes and production wastes associated with the infusion process. As the raw materials in the resin are classified as hazardous materials, the wastes encountered with non-reacted resin are also considered hazardous wastes. Once the resin is cured into a solid waste, however, it is no longer considered hazardous material but is tracked as part of the industrial waste contribution to manufacturing. Such items as vacuum bags, distribution media, infusion lines, and in-complete parts are hazardous wastes. However, manufacturing practice generally involves carrying infusion lines and infusion media into the curing phase with the composite part. As a result, the final status of most of these media is as industrial wastes.

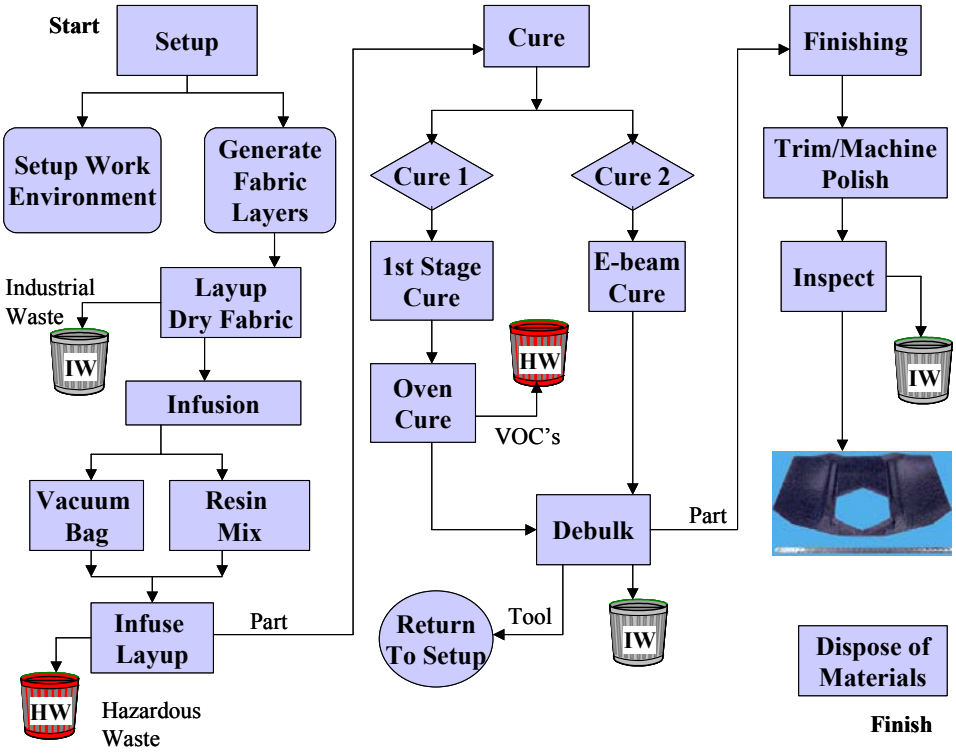

Figure 77. Cost model flow diagram for processing of VARTM composites using "oven" or "e-beam" to cure the composite structure.

It is worth noting that even during infusion the EB and thermal systems behave somewhat differently, and therefore, each system is treated to a different curing schedule. The vinyl ester resin used in creating baseline data for the composite manufacturing is a two-part resin that has a limited out-time once mixed. By contrast, the EB resin selected for this study can be either a one-part resin with a low viscosity and no gelation without EB treatment, or a two-part resin that is handled similar to vinyl esters with a limited processing time, but which fully gels at room temperature. In the case of the EB resins, the assumption is employed that the resin does gel before EB is applied, and therefore, the assembled part and all infusion and lay-up components need not be shipped to the EB facility for toll-based curing, nor transported to the EB curing stage for ownership based curing. In all cases, the EB lay-ups are not heated, and therefore, no oven is used for EB manufacturing. In recent experimental developments, however, it has been demonstrated that oven post-curing of EB cured resins produces improved materials performance in the final composites, without sacrificing dimensional tolerance advantages associated with EB curing [40-41].

After infusion, thermal cured assemblies were cured for 2 hours at 140 °F (First Stage Cure). The purpose of this curing stage is to stage the resin into a lightly linked gel state. The lower processing temperature prevents rapid acceleration of the thermal curing, which can result in exothermic conditions and run away reactions that cause explosive or combustive conditions. Once the materials are staged through vitrification, the energy associated with crosslink formation in the resins is released at a much slower rate, allowing for higher post-cure temperatures. A similar limit exists for EB cured resins, however, in the case of EB cure,

changing the applied dose-rate controls the exothermic heating. Dose rates from 0.5 to 10 Mrad per pass are common processing ranges for composites, with thicker parts requiring lower dose/pass equivalents. Also, for two-part EB resins, the room temperature staged resin is sufficient to prevent substantial exothermic conditions from developing, allowing higher dose/pass for initial treatments. The electron beam cure cycle assumes a total applied dose of 20 Mrad, a number demonstrated to fully convert accessible functional groups in all the resins developed for EB processing. As a cost factor, the total number of passes required to reach an applied dose of 20 Mrad increases the processing time for EB curing, and contributes to higher costs and greater user burden on the EB resource. The minimum number of passes is used in the model, so a best-costs scenario is created for EB.

The infusion media and infusion lines were discarded after this first cure operation for the vinyl ester parts, while these material were maintained throughout the processing phase for EB components. The thermally staged vinyl ester composites were separated from the mold after vitrification as vacuum pressure could be released without spring-back or deformations occurring to the structures. The mold was subsequently prepared and returned to the beginning of the manufacturing cycle. The EB system was fully cured under EB prior to returning the molds for reuse. It is relevant to note in this analysis, that because VARTM molding is used, no effort was undertaken to reduce mold costs for EB processing, despite the understanding that high-cost molding is among the cost savings for EB versus conventional resin transfer molding. The VARTM aspect eliminates this advantage between the two test conditions selected. The next step in the thermal cure is a post-cure of the vitrified parts. Parts were held for 3 hours at 250 °F in the oven.

Another aspect of the processing that impacts the costs of manufacturing dramatically is the effect of batching in the curing phase. For the oven cured vinyl esters, the batch size was dependent on both the oven size and the part size. The number of parts that were committed to the oven is based on the available volume and the oven-to-part dimension analysis. For the electron beam cure, the batch size was dependent on the vault configurations, the cart size, and the part size. Recognize also that VOC's may be emitted during oven curing due to the open cure environment and the commercial formulations of the vinyl ester resins. The EB cured part, however, does not have VOC's as the resins are designed with 100% non-volatile elements, providing for improved environmental control. The cycle time for the EB curing depends on the applied dose, the part size, and the size of the track for the EB vault (e.g., number of carts in the processing train). A typical EB processing warehouse is shown in Figure 78, where the EB source is shielded to prevent radiation exposure to the users. The processing zone is reached through a conveyor system that translates the parts into a vault for curing. A vertically mounted electron beam horn inside of a vault area is shown in Figure 79. The conveyor is also shown with a sample panel mounted in the beam path. The conveyor system can be either a pass through or directional type, as shown. The advantages of vertically mounted processing are increased processing size capability and potential for rotational design implementations for curing of asymmetric structures. The advantages of directional conveyor include the ability to shuttle a part quickly across the beam multiple times to apply doses rapidly in incremental amounts. The model for EB curing assumes a pass-through processing conveyor, where the component receives a given dose for each pass around the conveyor track (non-shuttling). This method means that a single part will require nearly identical processing times to multiple parts, where a train of components can be sent

continuously through the beam. Therefore, in the models, costs for processing using EB are approximately constant up to the number of cars that reside in the processing conveyor.

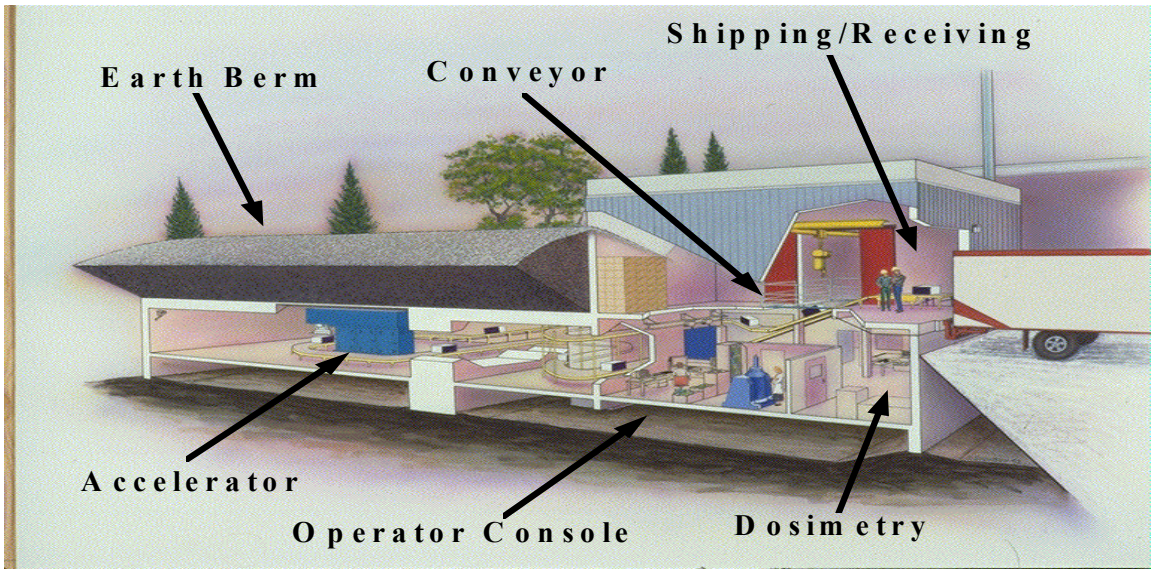

Figure 78. A typical EB facility layout including accelerator, processing, and shipping areas. Picture courtesy of Acsion Industries, (Pinawa, MB, Canada).

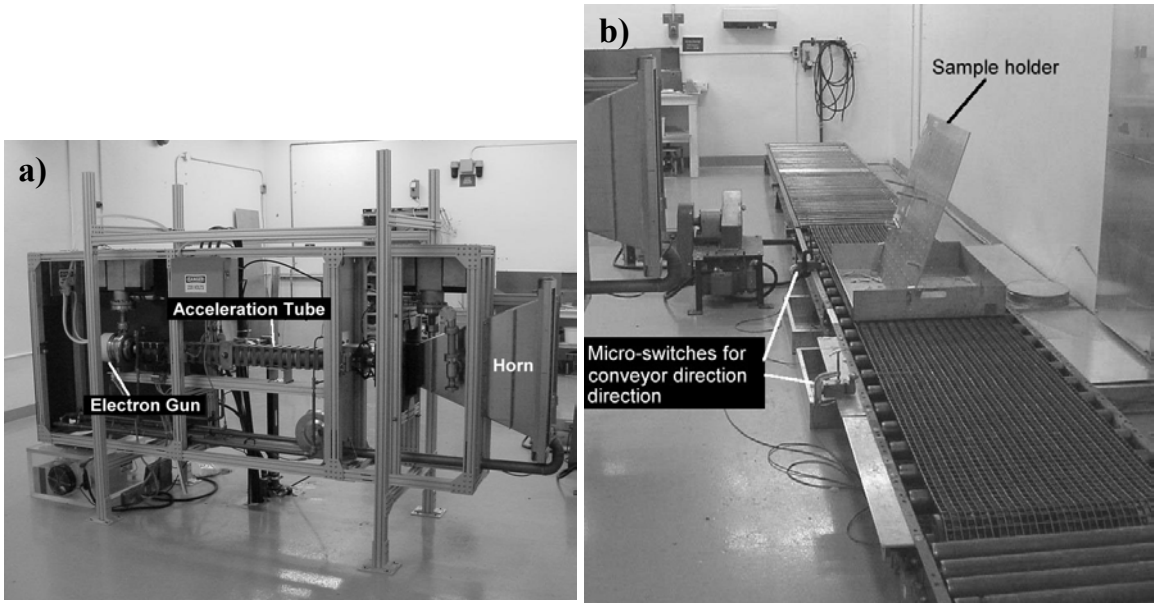

Figure 79. Typical arrangement for a vertical processing scan horn (a) and processing platform (b) for EB curing. Pictures courtesy of Acsion Industries, (Pinawa, MB, Canada).

Once the EB and oven materials are cured, the composites are debulked from the curing tools and sent to a finishing stage. During finishing, excess material resulting from the vacuum infusion method is trimmed away from around the perimeter of the part. This trim is considered an industrial waste for both techniques as the resin is fully cured. The trimmed part is inspected, repaired (if necessary), and submitted to further cost-equivalent processing stages. For example, for a composite panel that will be joined with other manufactured specimens, holes are machined through the part at the finishing stage. The machined part is inspected and repaired as needed. Once inspected and approved, the part is considered a finished component and goes into the manufactured count. The time to perform trimming and machining was not a consideration for the model comparison as both materials were treated similarly; therefore, not impacting cost variation to the processing.

6.2 Assumptions

The basic calculation for manufacturing cost involves a summation of all capital costs. The capital costs include labor, equipment and materials costs. Once a net cost is established for a given manufacturing cycle (number or parts), the cost per unit is calculated to normalize all processing costs. A comparative plot of cost per unit as a function of manufactured units is a part of the cost analysis.

A number of computational assumptions were required for each of the processing methods selected. Since the initial cost conditions will be carried into final product cost through a depreciation and maintenance contribution, the initial costs datum play a significant role in the cost per unit. For this study an oven of reasonable size to cure the largest manufactured part is selected and cost averaged for the model. Blue M Company (Williamsport, PA, USA) provided the oven costs [42]. The oven specifications include a 60 kW oven with a chamber dimension of 12 x 12 x 6 ft with 10 removable shelves. The addition of removable shelves allowed for increased batch sizes for smaller parts. It is demonstrated that batching of components can substantially lower net costs of manufacturing for oven-processed components. The effect of processing delays on performance of the composites is not considered a factor in the modeling developments. Oven batch sizes of 1 (60 and 100 ft^2), 20 (24 ft^2) and 80 (10 ft^2) parts were used in the models.

The EB processing is significantly more complex than the oven method. A consequence of the complexity of EB processing is worker safety, which requires substantial shielding of the processing zones in order to protect from stray radiation. Therefore, the work environment used to calculate costs includes both a processing unit and the required shielding. Additionally, a transport mechanism is required to move the fabricated parts through the EB process chamber. Each of these features contributes significantly to the final installed cost of an EB facility. Two cost functions are included for this analysis. One approach assumes an initial capital outlay to purchase an EB processing unit for the manufacturing facility. This approach gives direct manufacturing cost comparison to the oven processing approach described. A second approach is based on the recognition that resource time for an EB unit in this facility is severely underutilized. Consequently, a calculation is made assuming that existing EB facilities are used to cure the composite structures. This second case then incorporates expected additional costs associated with transport of the resin impregnated and cured composites to and from the manufacturing floor from the EB contract facility. Costs for transport are acquired from CF Motor Freight (Baltimore, MD) [43].

The purchased EB gun and electronics is a 150 kW by 10 MeV unit. The high-energy electrons allow a uniform dose to be applied from one side of the 0.75-inch thick composites as shown in Figure 80. The penetration is dependent upon structural density. The case for 1 g/cm^3 is shown in the figure. The cost of such a high energy unit is not substantially greater than for a 5 MeV system, as the total costs of acquisition include shielding and vault design, which are 50% of the total purchase cost. The vault is typically constructed either using an earthen berm, or more commonly, lead impregnated concrete walls. The particular configuration must be capable of housing a composite structure of 100 ft^2 on a continuous cycle. The costs of construction for an EB facility were provided from average facility costs calculated by IBA (Swedensborough, NJ, USA) [44].

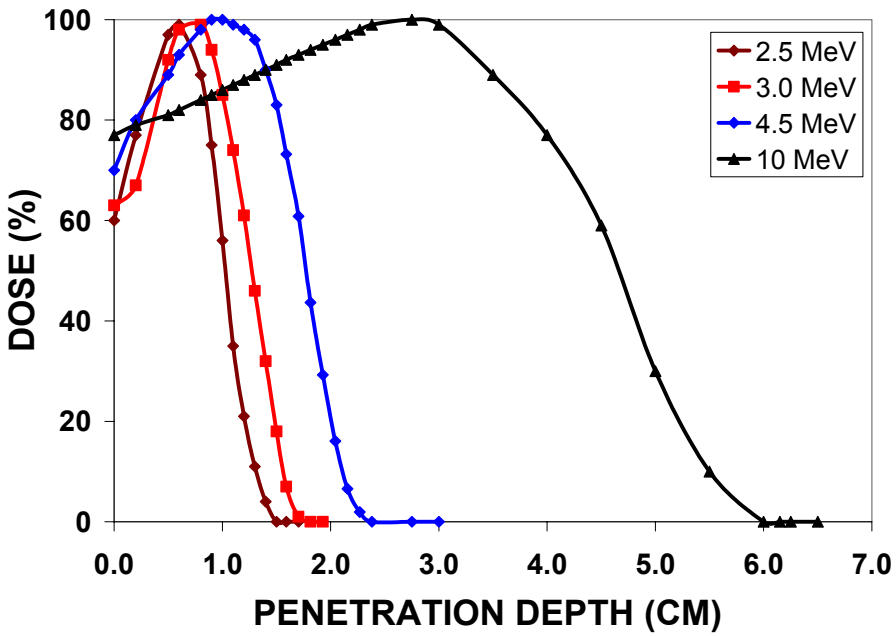

Figure 80. EB penetration depth (in water) for selected commercial beam energies.

In order to keep costs comparative, a similar EB configuration was used to generate toll-based costs for EB processing. A 150 kW and 10 MeV electron beam was assumed and the costs of transport were included assuming a contract with the toll facility of E-Beam Services (Cranbury, NJ, USA). The vault developed for the EB Services facility is the largest available in the industry in the USA. The facility permits a 10 x 10 ft part continuous entrance and exit with good production efficiency. The transport carts are 52 x 100 inch, which provides about 60 % to 70% utilization of the beam spread depending on part size. EB parts were also batched in the processing model to obtain maximum efficiency when the beam is on. Batch sizes of 40 (10 ft^2), 20 (24 ft^2), and 10 (60 and 100 ft^2) were used.

6.3 Cost of Curing

With the selected equipment, the total costs for ownership-based operation of the equipment are figured based on two calculations. The first calculation is the real-time use fact, which is based on the average electric consumption for the operations. To establish baseline costs for electric use, a cost figure of $0.064/kWhr was assumed, based on electric costs from the University of Delaware (Newark, DE, USA). This number is approximately equivalent to the national average for electric costs per kWhr. A computation of costs of operation per cure cycle could then be determined from the power rating of the equipment and the time required to achieve full cure. The second calculation used in the model is a depreciation and maintenance factor. These numbers are acquired from the commercial entities supplying the equipments and include average useful life of the equipment and annual maintenance issues associated with the equipment.

For toll-based processing using EB, the facilities owners assume costs for electricity and maintenance. Therefore, a toll-based charge is assumed based on time required for curing of the composite parts. However, with toll-based processing, the additional costs of transportation are added to the formula. Freight charges are calculated based on class of material being shipped, weight of products shipped and locations of the shipping and receiving facilities. A significant cost break is achieved with loads exceeding 100,000 lbs. The charges used in the model are for shipping from the Army Research Laboratory (Aberdeen PG, MD, USA) to the EB Services facilities in Cranbury, New Jersey, USA. A toll charge to apply a 20 Mrad dose requires approximately 50 minutes to achieve at a nominal rate of $750 for 10 and 24 ft^2 parts. The time to cure increases with part size and complexity, as the beam spread is adjusted to meet the width requirements. Widening the beam has an effect of decreasing dose rate, causing longer cure cycles. Therefore, for each beam parameter change, EB Services provided approximate cure times and costs. Therefore processing costs were $825 (61 minute) for 60 ft^2 and $1650 (122 minute) for 100 ft^2. It should be mentioned that the ability to cure 100 ft^2 parts is limited for a single horn configuration. Therefore, in the model, we assume the ability to cure one half of the part and rotate the position under the scan horn and cure the additional half of the part. The need for the additional passes greatly increases the time required to cure the large parts.

The final calculation included in the model is relevant only to the thermal cured system. Due to the nature of VARTM resins in general, a compliance cost was assumed to address emissions costs from liquid molding in the composite panels. Should a vinyl ester-type resin be selected for the thermal processing, emissions of styrene will potentially add to the total costs of production. Therefore, a compliance cost is calculated based on output volume and using the MACT 2004 tax base of $0.24/lb of composites [45]. The results show that this effect would be minimal for processing under VARTM conditions.

Table 47 summarizes the fixed cost figures used in the models to generate comparative data between EB-ownership, EB-toll, and oven processing of flat plate composites of various sizes.

Table 47. Fixed cost data used to generate cost comparisons in EB vs. Oven cured VARTM Composite Panels.

	EB Toll	EB Ownership	Oven Ownership
Electric Costs	None	$0.064 /kWhr	$0.064 /kWhr
Resin Costs	$10 / lb	$10 / lb	$1.60 /lb bulk $3.10/lb catalyst $3.71/lb accelerator $3.95/lb inhibitor
Fabric Costs	$6.30/lb	$6.30/lb	$6.30/lb
Labor Costs – skilled	$70/hr	$70/hr	$70/hr
Labor Costs – unskilled	$60/hr	$60/hr	$60/hr
Labor Costs – supervisor	$70/hr	$70/hr	$70/hr
MACT	None	None	$0.24 / lb composite
Depreciation/Maintenance	None	10 years at $300 K/yr	10 years at $57K/yr
Purchasing Costs	None	$3 M	$57 K
Toll Charges	~$800 /hr	None	None
Process Shipping Charges < 100 k lb > 100 k lb	 $0.16-2.08 / lb $0.14 – $0.16 /lb	None	None

6.4 Simulations Results

The variations of model systems that were investigated are described in Table 50. The basic context of the models was discussed previously. The results of various parameter variations from the proposed experiments will be discussed here. The model studies will be referred to frequently by either the process method or by the model number identification shown in the table as part of the discussion.

Table 48. Model simulation systems and processing parameters.

Model Number	6.4.1 RESIN SYSTEM	Curing Method
1	Vinyl ester or epoxy	Oven cured, 2-hour staging at 140°F followed by 3-hour cure at 250°F.
2	Cationic cured epoxy or methacrylate	E-beam cured, toll-based processing adding 20 Mrad over entire surface area. Includes shipping costs.
3	Cationic cured epoxy or methacrylate	E-beam cured, ownership-based processing adding 20 Mrad over entire surface area.

Figure 81 shows the processing costs per square foot of 0.75 inch composites manufactured for E-Beam processing for ownership of the E-Beam facility as a function of total production volume. A few key items are easily discerned. First, initial costs in manufacturing the first part cause higher per unit for the first ten parts. However, after 10 parts are processed, production costs level off to a constant per unit cost. Second, the cost per square foot is lower for larger composite panels, but average costs level off toward larger parts (> 60 sq ft). The leveling point is related to the balance between batch size and resource availability for processing of parts of this size. Lastly, the time variation between the cost of the first unit produced and the second unit produced is smaller for increased part dimensions.

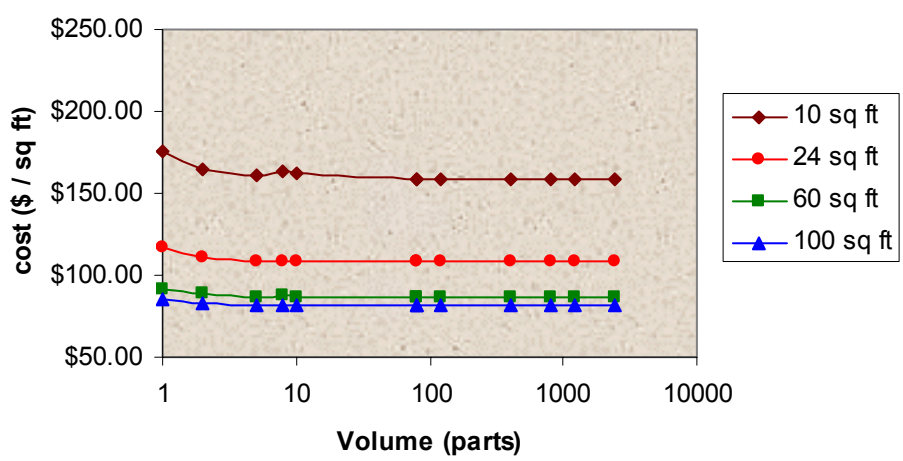

Figure 81. Production costs per square foot for EB ownership processing of flat panel composites (Model 3).

Toll-based EB processing has long been believed to be an excellent entry level processing approach for composite structures. In order to validate the processing value of EB toll versus

ownership, the net cost of producing the same composite parts is determined for a non-ownership case. Figure 89 shows the cost per square foot for the same composite structures processed using a facility toll EB source. One clear trend is the high cost of processing for just a single unit. Although performing one and two part lay-ups is not a manufacturing cycle, these costs accurately reflect the cost of performing repair of composite panel as well. Consequently, the evidence for using toll-based processing for repair is also demonstrated in the present model. Again, costs level out for larger production runs. For this special case, however, the costs level out at higher production numbers for the smaller parts, reflecting the advantage of fee-based processing. Since the cost per hour is constant, cycling multiple parts under the EB scan-horn to apply doses continuously across many parts reduces the net cost per part until the beam usage is maximized.

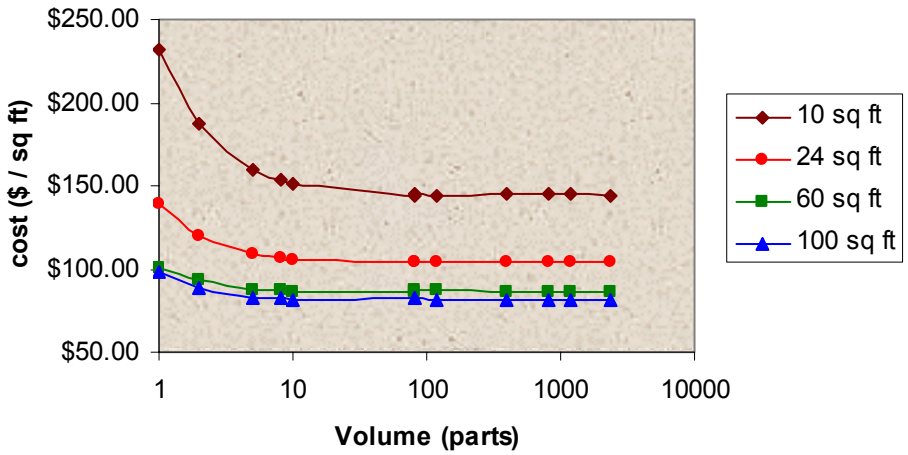

Figure 82. EB Processing of toll-based cure method for composite panels.

The final comparative case is for oven-based processing. Due to the low-cost nature of the oven, only an ownership case is considered. The processing cost per square foot using an oven for the same panels is demonstrated in Figure 90. Immediately evident is the lower cost associated with low-volume production. Additionally, the advantages of batch curing are evident for process runs including more than ten production units. A key technical barrier that is not captured by this study, however, is the effect of generating parts larger than the oven capacity. Unlike EB, which can be varied to achieve cure in large structures, the oven dimensions are fixed. Once the scale of parts exceeds the oven dimension, additional capital costs will be required. Consequently, the decreasing cost per square foot with size has reached a minimum in the case of 100 square foot parts for our selected oven. To prepare a 1000 square foot part, the model will require adjustments and additional capital depreciation and maintenance costs that will increase the average costs substantially. Again, however, it is apparent that increasing the volume beyond 1000 parts will not decrease costs per unit significantly unless additional resources are added.

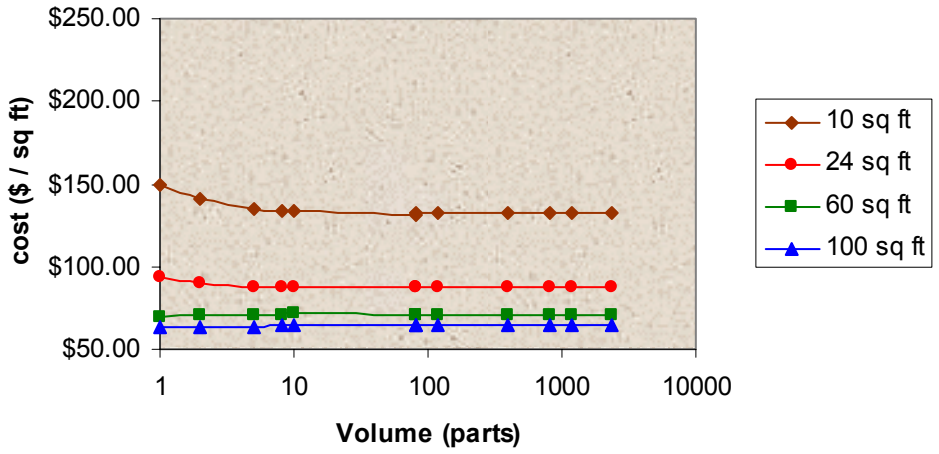

Figure 83. Production costs per square foot of composite panels for thermally cured systems in an oven.

The current cost model does not consider costs of tooling variations between EB cured and thermal cured composite structures. Due to tolerance issues in the manufacturing process, tooling costs can reach millions of dollars per unit for thermal cured composites as metallic tools are often created with defined coefficients of thermal expansion (CTE) that closely mimic composite cure shrinkages. The advantage of these high-cost tools is in generating extremely tight tolerances in the fabrication of composite structures. However, for VARTM processing, this level of tooling cost is eliminated, as the VARTM processing is inherently less precise. The cost of autoclave curing could also be investigated, but without introducing additional tooling costs, or impacts of size limitations on the autoclave purchasing costs, the results would show a similar trend.

6.5 Conclusions

Some key conclusions that result from this modeling evaluation are the impact of capital costs on net processing costs and the minimal impact that compliance charges would have on final product cost, given the current regulations and tax rates. The impact of MACT on the small manufacturer is likely to be more substantial than on military providers, due in part to volume differences. However, as the military adds additional low-cost composite materials to the fielded platform portfolio, additional production suppliers will be essential to meet the increased demand (volume), and commodity composite fabricators will be strongly impacted in supplying military equipment. Additionally, the Army currently is developing a composite replacement parts program entitled "Composite Body Parts," where sheet metal components with high corrosion replacement rates will be re-engineered using low-cost composite alternatives. Currently the program is in developmental funding. The components developed in the program will provide extensive insertion of composite media to the Army legacy infrastructure.

Although, EB processing has the potential to produce a higher number of total parts, the lack of high volume applications for large composite products in the military will cause the need for instantaneous throughput to be a minimal cost benefit for the producer. The EB processing unit is utilized at only about 5% of capacity in the model demonstrated, while other composite fabrication items are used to their full potential. Therefore, the processing bottleneck occurs in lay-up rather than cure process resources. Coupled with the shorter curing times and decreased energy consumption, the impact of a high-volume EB processing unit is a greater turn-over rate, and faster time to market for a given structure. However, the cost benefit of rapid production rates is not realized in full due to limited production volumes outlined in the process model. Additionally, the stability of EB resins and long shelf life provide a substantial reduction potential for hazardous wastes. The oven-processed resin is extremely time-sensitive once the raw materials are blended, causing a high potential for excess wastes in the infusion process. The value of stability to achieving optimum fill volumes and highly reproducible components is also not captured in the process models as described. Consequently, the worst-case scenario for EB processing has been explored, and under a worst-case comparison, EB processing will be significantly more costly due to high initial capital and high resin costs, compared to current thermal processing methods. Environmental controls and regulations alone are not significant enough to convince commercial industry to re-capitalize equipment and change processes for current process methods.

Again, a key advantage to new EB processing technology is a reduction in compliance restraints on a commercial enterprise. The EB resins are among the few viable resin formulations that effectively meet highly restrictive California emissions requirements [46]. There are no volatile organic compounds (VOCs) emitted due to the 100% solids content of resins used for EB cure applications. The environmental value of non-emitting resin systems will continue to be a value added benefit for future composite developers, even though current technical performance metrics do not warrant changing current processing methods. Commercial industry should keep pursuing new cure technologies for composite applications in new product venues, in order to maximize environmental responsibility and provide optimum value for the composites customer.

Two bases effectively drive the higher costs of EB processing: 1) resin cost and 2) equipment cost. In the case of ownership for EB vs. oven, the EB equipment costs 50 times more than a typical oven. However, the oven resource is utilized at approximately 60% of availability, while the EB unit operates at only 5% of capacity. Although the usage rates vary significantly, the model did not account for the increased service life of the EB unit. Effectively, the processing costs for EB could be reduced by a factor of twelve for a direct comparison with oven. However, the authors believed that extending EB service life into 100 years was unrealistic and would not effectively capture cost trends. Therefore, the highest reasonable capital cost depreciation and maintenance was applied, which elevated the EB processing costs. Second, the resins available for EB are not in high demand. The lack of commercial competition for manufacturing of EB resins additionally caused resin costs to be high. Without the implementation of commercial enterprise to drive costs down, EB resins are assumed to remain at a premium price rate for some duration. A reasonable assessment of the resin costs should allow for reducing costs with increasing volumes of commercial product produced. This aspect of the market effect on material costs could also not be reliably implemented in the model system. A key finding from the model however,

demonstrated that even using a relatively high cost thermal system, the average resin cost per square foot is 4 times as high for EB systems, due to the volume discounts available on thermal resins. Upon analysis of a one year processing cycle for EB or oven ownership, the total costs for materials are 72% of net operating cost for EB versus only 61% for the thermal cured case. This difference is difficult to overcome when total compliance costs account for only about 1.25% to 1.5% of final part costs. The initial resin costs cannot be recovered without the incorporation of tooling based costs in the models. Unfortunately, EB and oven comparisons for VARTM processing will inevitably demonstrate lower production costs for the oven processed case as a result.

In summary, the model analysis shows clearly that under current developmental status of EB for composite applications, the effective cost of production for composite structures will be somewhat higher using EB.

EB processing is still a very cost effective processing technology for certain niche market applications. For instance, composite designs where net shape parts are essential would benefit greatly from the advanced resin designs afforded through EB processing. Additionally, composite structures composed of dissimilar materials or asymmetric interfaces could be created and cured using EB, producing novel structures that are not achievable using thermal methods. The analysis above also demonstrates a cost comparison with the lowest cost basis of processing currently available, i.e., low-cost resins with low-cost VARTM infusion. To apply EB technology to more advanced processing techniques such as prepreg or RTM lay-up methods would further improve the cost factors in favor of EB methods. However, for the current analysis, thermal processing methods still appear to be a preferred method of achieving low-cost processing of thick section composite structures through VARTM of flat panel materials. Additional developments in the niche market environment for EB processing are currently underway, where an emphasis on environmental stability and low-shrinkage with low-temperature processing can be essential to achieving complex geometries with exceptional tolerances. The future of EB is indeed bright, despite cost challenges uncovered under this model evaluation.

7 Induction-Based Repair and Remanufacturing

The increasingly widespread use of composite materials in defense and aerospace applications has resulted in an urgent need for fast and efficient field and depot-level repair techniques for these components. The search for cost-effective environmentally friendly manufacturing methods has led to the study of induction heating for bonding and processing of composites. Within a composite part, heat is generated at a high rate by a susceptor upon application of an intense, oscillating magnetic field. Supplying the energy needed for curing thermoset resins and adhesives or for thermoplastic bonding is a critical concern in field repair applications, and induction heating is an ideal choice. Research to date [47-52] has demonstrated that this method shows great promise for rapid repair and processing of composite parts.

The search for cost-effective environmentally friendly manufacturing methods has led to the study of induction heating for bonding and processing of composites. Electromagnetic cure

methods involve using induction or electrical resistance heating focused directly at the material to be cured. Induction heating occurs when a current-carrying body, or coil, is placed near another conductor, the susceptor material. The magnetic field caused by the current in the coil induces a current in the susceptor. This induced current causes the susceptor to heat due to Joule heating or, in the case of a ferromagnetic material, to hysteresis losses. Carbon-fiber reinforcement in composite materials can function as the susceptor. For other material systems, the susceptor is a metallic mesh or magnetic particles. Energy can be introduced into the precise region to be cured both in the plane of the structure and at the specific depth required.

7.1 Background on Induction

Induction heating occurs when materials are subjected to a high-frequency magnetic field. There are two primary heating mechanisms: eddy-current-based heating and magnetic hysteresis-based heating. For composites, both mechanisms are embodied in three classes of susceptors or heating elements: (1) conductive mesh/adhesive or resin systems, (2) magnetic-particle-based resin or adhesive systems, and (3) carbon-fiber-reinforced composites. Carbon-fiber-based composites are treated as a separate class because the heating mechanism is somewhat different since it is the conductivity of the fibers that causes heating. Each class is discussed in the following sections.

7.1.1 CONVENTIONAL BONDING METHODS.

There are two conventional approaches for joining polymer matrix composites: mechanical fasteners and surface bonding techniques.

Mechanical fasteners are the most basic joining method. However their integration into the structure often creates a weak point in the material. This weakness provides an incentive to surface bond the materials [53].

Surface bonding techniques are preferred to mechanical fasteners due to their superior load transfer characteristics. Of these surface-bonding techniques, the most common are elevated temperature-cure, thermosetting adhesives. These thermosetting adhesives usually require temperatures of 120 – 200°C for 5 to 120 minutes to complete the bond [54].

The most common ways of heating the bond lines are convection ovens, thermal blankets, and radiant heaters. Convection ovens work by heating the surrounding air, which then transfer heat to the adherend. Thermal blankets heat the adherend by direct contact. Radiant heaters transfer their energy to the adherend via infrared radiation. All of these processes heat the outer surface of the adherend, and the heat is then conducted to the bond line. This requires the exposure time to be extended in order to adequately heat the entire adhesive to the appropriate temperature, reducing overall process efficiency. The cure temperatures of certain adhesive systems might be high enough to exceed the temperatures at which the adherends begin to degrade. Additionally, for composite materials, the cure temperature of certain adhesive systems may be near the degradation limits of the adherends. In these cases, longer adhesive cure cycles increase the likelihood of adherend thermal degradation.

7.1.2 INDUCTION HEATING.

Induction heating works by exposing a conductive or magnetic material to a high frequency electromagnetic field, usually between 50 kHz and 100 MHz. Any material that heats up when exposed to an electromagnetic field is called a "susceptor" material. The electromagnetic field can induce heating through two mechanisms. If the susceptor material is conductive, then eddy currents are induced in the conductor, and the conductor will then heat due to resistive effects. If the material is magnetic, hysteresis losses from the magnetization-demagnetization cycles causes additional heating. This mechanism of heating is called hysteresis heating.

The primary advantage of using induction heating is that direct contact with the bond line is not necessary. The electromagnetic field is able to penetrate through materials, to a certain depth, and induce heating. This allows the possibility of localized heating of only the bond line and not the surrounding adherends. A vehicular component would be assembled through application of a susceptor-doped adhesive at the bond line. Exposing the bond line to an electromagnetic field would then heat and cure the adhesive, completing the bond. The versatility of the geometry and the ease of repair make induction heating ideal for fieldwork or for non-contact heating. Additionally, direct bond line heating greatly reduces process times compared with conventional heating methods. Conventional methods rely on conducting heat to the bond line through the adherend, which is an inefficient process. Induction processing eliminates this step by heating the bond line directly.

7.1.2.1 Conductive Mesh Susceptors

The change of magnetic flux induces eddy currents in the conductive mesh, and heating occurs primarily by Joule heating (Figure 84). Eddy currents are magnetically induced body currents in the material that flow primarily in peripheral loops perpendicular to the field so as to create flux fields, which oppose the magnetic field. As the frequency of the applied magnetic field increases, eddy currents are increasingly generated in the outer layers of the conductor (skin effect).

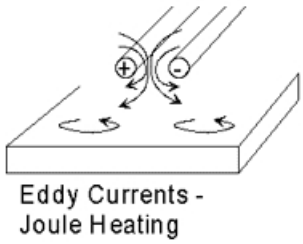

Figure 84. Heating occurs when eddy currents are induced in a conductive material.

In our research for SERDP, metal wire meshes, typically made from copper, aluminum, or stainless steel, are impregnated with an appropriate adhesive or resin and placed at the bond line. The magnetic field is applied to generate heat and cure the adhesive or resin system.

The mesh wires may also be surface treated to improve adhesion between the mesh wires and the resin or adhesive system.

This program is taking advantage of enabling technologies co-developed by ARL and UD-CCM in which the metal mesh susceptors are specially designed for optimized in-plane heating [47].

Two general types of adhesive susceptors have been previously investigated. The first is the use of metal screens located within the bond line [55]. Once exposed to the electromagnetic field, the screen begins to heat resistively. The limitation of this approach is that the heating is unbounded and usually non-uniform. From this lack of homogeneity, certain regions may be under-cured or thermally degraded. Although, these problems can possibly be avoided through the use of temperature sensors and varied power programs, this complexity allows a great deal of room for error leading to lower mechanical strengths.

7.1.2.2 Magnetic Particle Susceptors

Induction heating can also occur due to hysteresis losses. Hysteresis losses occur in ferromagnetic materials such as iron and nickel. Heat generation is caused by friction between magnetic domains when the material is magnetized first in one direction and then in the other. The domains may be regarded as small magnets that turn around with each reversal of direction of the magnetic field (Figure 85). Work (energy) is required to turn them around. The rate of expenditure of energy (power) increases with an increased rate of reversal (frequency). The energy required to turn the internal magnet around once is proportional to the area enclosed by the hysteresis loop (Figure 86) of the material. The hysteresis loop relates induced magnetic flux density to the applied magnetizing force. Hysteresis heating may or may not be the main heating effect, depending on the part geometry.

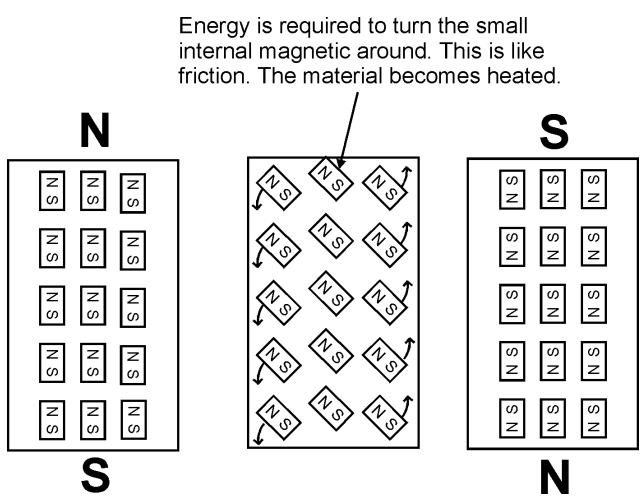

Figure 85. Model of magnetic domains during hysteresis loss. Heat generation is caused by friction between magnetic domains.

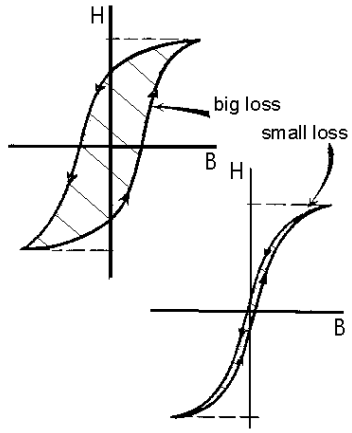

Figure 86. The energy required to turn the internal magnet around once is proportional to the area enclosed by the hysteresis loop of the material.

In our research for SERDP, magnetic fields are applied to magnetic-particle-loaded resin systems. Specialized adhesive systems are being formulated with magnetic particle content of up to 20–30% by volume (application had 50% loading). These adhesives are placed in the bond line, and upon application of a suitable field, the particles cause the adhesive to cure and create a weld. Higher frequencies (~MHz) are required to heat the small magnetic particles that are mixed into our induction welding implants.

The second type of adhesive susceptor is the magnetic powder with Curie temperature-limited heating [56, 57, 58]. These materials use hysteresis heating and, if all other heating effects are dominated by the hysteresis heating, will not heat beyond their Curie temperature. The benefit of this approach is that magnetic powders can be chosen whose Curie temperature can be matched to the adhesive system [59, 60, 61]. If the electromagnetic field is powerful enough to maintain this hysteresis heating, then the adhesive will dwell at this temperature for as long as it is exposed to the field [62]. This feature allows the user to eliminate any temperature sensing devices or power regulation; the temperature at which it dwells is self-regulating. This feature greatly improves the simplicity of the system and uniformity.

In this paper, we demonstrate the use of induction heating of magnetic powder susceptors for thermal curing of adhesive systems and investigate whether induction heating can reduce process times compared with traditional heating methods.

7.1.2.3 Carbon-Fiber Composites

Due to the electrically conductive nature of carbon fibers, carbon-fiber composites can be induction heated by themselves. Our previous research has shown that the primary heating mechanism is the dielectric loss at junctions of fiber overlap between layers of the composite [63 - 65]. This also implies that unidirectional carbon-fiber composites will show minimal heating. A schematic of the heating mechanism is shown in Figure 87.

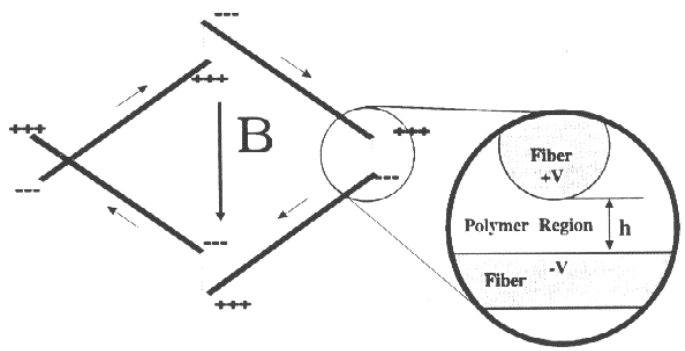

Figure 87. Schematic outline of the heating mechanism in carbon-fiber-based composites where heating occurs primarily between conductive fibers of adjacent layers.

The carbon-fiber heating phenomenon can be used for a variety of applications, such as non-autoclave cure of carbon-fiber thermosets, rapid processing of carbon-fiber thermoplastics, repair using carbon-fiber prepreg systems, etc. The SERDP Program is taking advantage of our unique knowledge of these mechanisms to demonstrate the applicability of induction heating to near elimination of hazardous waste in the production of the Army's M829E3 composite sabot (See Section 13).

7.2 Benefits

Induction heating has many advantages over competing techniques, such as radiant or convection heating and laser technologies. Some of the main advantages are summarized below:

- **Environmentally sound**—This clean non-polluting process exhibits reduced VOC emissions.
- **Accurate temperature control**—Direct control of temperature is possible through continuous power control.
- **Localized volumetric heating**—Uniform heating through the thickness of the bond line reduces warpage and residual stresses.
- **Improved quality**—Heat is induced in the product without contact, thus reducing the rate of rejected parts.
- **Minimized distortion**—Site-specific process delivers heat exactly where it is needed and as rapidly as needed, so other locations on the part are not exposed to heat flux.
- **Energy-efficient process**—Up to 80% of the expended energy is converted into useful heat to save costs.
- **Maximized productivity**—Instantaneous heat allows for increased production rates.

Other advantages of induction include reduction of volatile organic compound and nitrogen oxide emissions by processing out of the autoclave, processing a much smaller volume, and eliminating processing steps. In addition, induction offers internal non-contact heating; the possibility of a moving heat source (the coil) to heat large areas; high efficiency; control of the heat generation by coil design or by susceptor design; and powerful, portable, and easy-to-operate units. The current effort seeks to exploit these advantages and develop induction-based processing and repair technologies for composites used in DoD applications.

8 Mesh Susceptors –Development

Repairs of composite parts commonly use an adhesively bonded patch over the damaged area. Proper curing of the adhesive used in the repair is crucial to the integrity and strength of the repaired component. Although room-temperature-curing adhesives have been extensively used in many repair applications, they have the disadvantage that complete curing often requires many hours or days. The time to complete cure can be reduced by application of heat to the patch, usually by the use of heat blankets or heat lamps. However, these methods are inefficient and, in some cases, insufficient, since substantial heat is inevitably lost to the surrounding material and environment. Induction heating, on the other hand, enables local and rapid heating of the area close to the adhesive bond line.

As described previously in this report, not only are there significant environmental advantages related to the development of infinite-storage induction-curable repair adhesives, but another significant advantage is the ability of induction-based curing to rapidly heat and cure the adhesive under vacuum conditions, significantly reducing VOC emissions. Additionally, induction-based heating eliminates the need for NO_x-generating autoclaves for thermally cured repairs.

8.1 Characterization of Cure Kinetics

To ensure proper curing of adhesives using induction heating, it is necessary to establish appropriate process windows. The process window is then used to optimize the bonding process with respect to temperature and time. Factors that dictate the process window include cure kinetics, evolution of exotherms, flow and wetting, and thermally induced residual stresses. Adhesive cure kinetics is the most dominant factor and must be addressed to determine cure time as a function of temperature as well as ultimate degree of cure. A typical room-temperature-curing epoxy system (Hysol EA9394) was chosen for evaluation of accelerated cure properties. This system is a two-part epoxy room-temperature-curing paste adhesive with a suggested cure time of 3 to 5 days at room temperature, making it an ideal candidate for accelerated cure studies.

Differential scanning calorimetry (DSC) was used to characterize the cure kinetics of the thermosetting polymer [47, 66]. Since the heat evolution dQ/dt measured by the DSC results from the chemical crosslinking reaction, it is possible to relate the heat evolution dQ/dt to the rate of reaction $d\alpha/dt$ and the conversion α. This can be accomplished by using the following relationships:

$$\frac{d\alpha}{dt} = \frac{1}{\Delta H_{tot}} \left(\frac{dQ}{dt} \right)_t \tag{1}$$

$$\alpha = \frac{1}{\Delta H_{tot}} \int_{t_o}^{t} \left(\frac{dQ}{dt} \right)_t dt \tag{2}$$

where ΔH_{tot} is the total heat of reaction, generally determined by averaging the reaction exotherms measured from several dynamic temperature DSC runs. Various chemical kinetic models can then be fit using data obtained from isothermal DSC experiments.

The mechanistic models of thermoset cure that usually provide a more accurate representation of crosslinking reactions are not generally applicable to complex systems such as formulated adhesives. Since the goal is to provide a process window for accelerated cure, the specific cure mechanisms need not be critically assessed. Alternatively, several empirical models have been successfully used to predict curing of thermosetting polymers. One popular model was proposed by Kamal and Sourer [67] (Equation 3) and has found widespread acceptance for a number of crosslinking reactions (including epoxies) and is used to fit the adhesive studied here.

$$\frac{d\alpha}{dt} = \left(k_1 + k_2 \alpha^m\right)\left(\alpha_u - \alpha\right)^n \tag{3}$$

In the expression, α is the degree of conversion, α_u is the temperature-dependent maximum conversion, k_1 and k_2 are Arrhenius-type rate constants, and m and n are constants usually assumed to sum to 2 but are often allowed to vary freely. The α_u term arises from the fact that the entire heat of reaction is not released during isothermal cure due to the decreased mobility of the polymer chains as crosslinking occurs. Performing a series of isothermal cures enables values for the model parameters to be determined and used to predict the cure kinetics of the adhesive.

Fifteen dynamic differential scanning calorimetry (DSC) runs were performed to evaluate ΔH_{tot} of the adhesive. The epoxy (part A) and hardener (part B) were mixed in the recommended ratios by weight before being immediately inserted into the DSC (TA Instruments 2908), where they were heated at 10°C/min from 0°C to 200°C. The resulting cure exotherm was integrated to evaluate the heat of reaction. The average and standard deviation of ΔH_{tot} was 354.8 ± 14.7 J/g. This average value is used in Equations 1 and 2 to relate the isothermal heat data to α and $d\alpha/dt$.

Isothermal DSC runs were also performed at temperatures ranging from 80°C to 160°C. Samples of adhesive and hardener were mixed and placed in the pre-heated DSC cell. Data was collected until the heat flow returned to the baseline value. The isothermal heat flow was related to α and $d\alpha/dt$ using Equations 1 and 2. Equation 3 was then used to fit the $d\alpha/dt$ versus α curves for each isotherm. Each isothermal DSC run was followed by a residual DSC run at 10°C/min from 0°C to 200°C. A value of α_u was determined from

$$\alpha_u = 1 - \frac{\Delta H_{res}}{\Delta H_{tot}} \tag{4}$$

where ΔH_{res} is the residual heat of reaction. The parameters m and n were permitted to vary freely. Analysis of each experiment produces values for all of the kinetic parameters at that specific temperature. In general, it was found that Equation 3 enabled reasonably good fit of the data, the fit being better at higher temperatures. Analysis of the data indicated that k_1 is nearly constant regardless of temperature. All of the parameters are summarized in Table 49.

Table 49. Cure Kinetics Model Parameters for Hysol EA9394

Parameter	Value
k_1	0.120 ± 0.107
k_2	4.098×10^6 exp(-5533.9/T(K)) (1/min)
m	0.593 ± 0.070
n	1.407 ± 0.073
α_u	$0.712 + 1.8\times10^{-3}$ T (°C)

The model enables prediction of the entire curing process over a wide range of processing temperatures. The prediction of cure time at a specific temperature is of greatest interest to the application of induction techniques to accelerate adhesive cure. Figure 88 shows model predictions for cure time compared to the experimentally observed cure times. A family of curves is generated for the range of values of α from 0.7 to 0.99. Here, cure time is defined as the amount of time necessary to reach the specified value of α for each temperature. It is seen that at the lower temperatures, it is not possible to attain high values of α. For example, at 100°C it is not possible to obtain a value of α greater than 0.9. If a greater degree of cure is desired, it is necessary to increase the cure temperature to about 140°C. The curves also show that the times to cure are generally very short, particularly at the higher temperatures. Above 140°C, a value of α of 0.95 could be achieved within 2 min. At the relatively low temperature of 80°C, it took less than 12 min. to achieve a value of α of 0.8. This is comparable to the value of α_u of 0.79 for the adhesive when cured at room temperature for 120 hrs. The results were used to determine process windows for the induction-assisted accelerated cure of this adhesive.

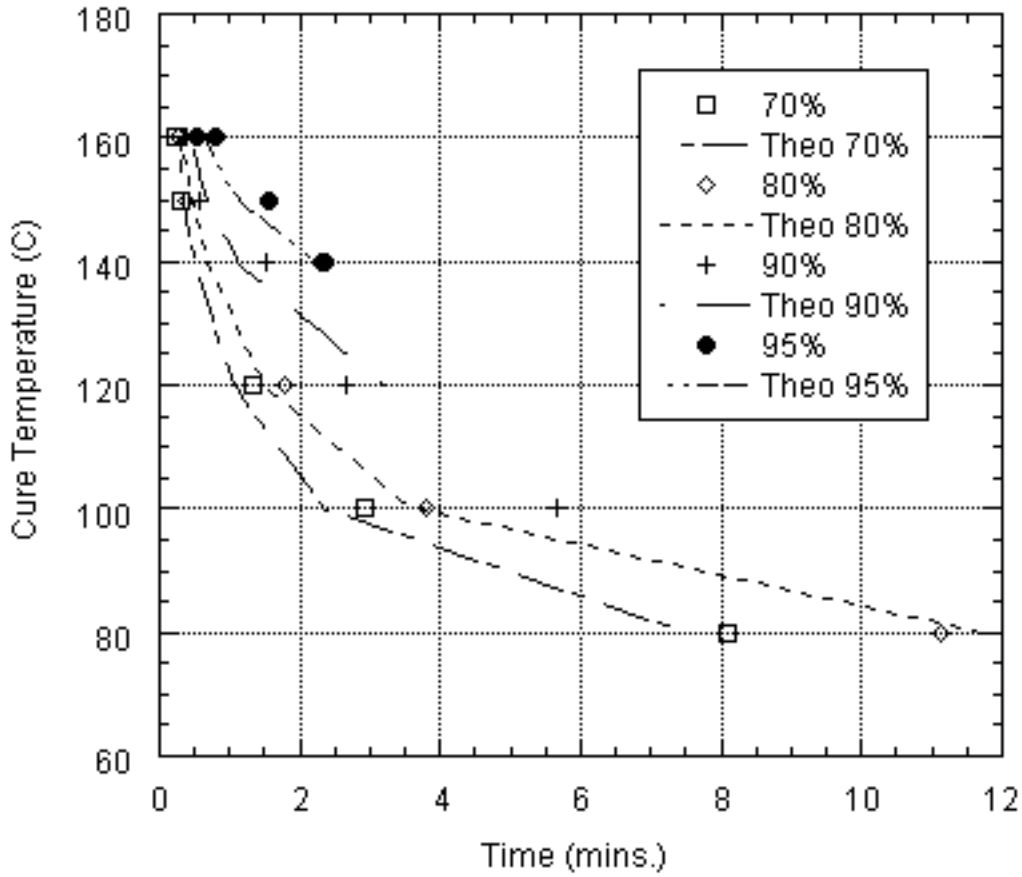

Figure 88. Comparison of kinetics model cure times to experimental cure times for varying degrees of cure.

8.2 Fabrication of Single-Lap Shear Specimens

To compare nominal strengths and study the effect of a susceptor material in the bond line, several types of single-lap shear (SLS) specimens were fabricated according to ASTM D1002 [68]. The adherends were satin-weave glass/epoxy. A panel consisting of 34 plies of prepreg was prepared in an autoclave and cured according to the manufacturer's recommendations. The 3.0-mm-thick cured panel was cut into pieces of adherends, each measuring 102 mm x 25 mm (4 in. x 1 in.). Eight cases of SLS specimens under various curing conditions were fabricated (Table 50). Case A represents the condition for use of the adhesive as recommended by the manufacturer. In each of Cases C to H, the susceptor embedded in the adhesive layer was a copper mesh with a wire density of 30 x 30 per in^2 and wire diameter of 0.15 mm (0.006 in). This mesh was chosen from preliminary tests of SLS specimens using this mesh, which showed reasonable shear strengths compared to similar tests using various other mesh densities and metal types.

Table 50. Lap Shear Data for Hysol EA 9394

Case	Adhesive Curing Process	No. of Specimens Tested	Mean Nominal Shear Strength and Standard Deviation (MPa)	Coefficient of Variation (%)
A	Room-temperature cured for 120 hrs. without susceptor	7	14.8±1.0	6.76
B	Oven cured at 160°C for 1 hr. without susceptor	4	18.1±2.1	11.60
C	Room-temperature cured for 120 hrs. with copper susceptor	5	12.3±0.9	7.32
D	Oven cured at 100°C for 1hr. with copper susceptor	4	14.7±0.6	4.08
E	Oven cured at 160°C for 1 hr. with copper susceptor	4	13.2±0.6	4.54
F	Induction cured at 100°C for 15 mins. with copper susceptor	6	15.2±0.7	4.60
G	Induction cured at 160°C for 10 mins. with copper susceptor	6	14.3±0.8	5.59
H	Induction cured at 100°C for 15 min. with copper susceptors (DNS specimens).	6	16.9±0.7	4.14

The copper mesh was cut into rectangular strips of 25.4 mm x 12.7 mm (1 in. x 0.5 in) and wetted with the mixed adhesive on both sides before being placed in the bond area. The corresponding mating surfaces of the adherends were also applied with the adhesive by means of a wooden applicator. In each case, vacuum consolidation was used to ensure uniformity of applied pressure and adhesive bond line thickness between specimens. The SLS specimen was secured onto a base plate with Kapton™ tape. A support plate of thickness equal to that of the adherend was used to support the top adherend as it was bonded to the bottom adherend. A piece of bagging film was placed onto the arrangement and sealed on all four edges of the base plate with tacky sealing tape. Vacuum was drawn from the interior via a plastic hose. When the vacuum pressure was applied, excess adhesive was immediately squeezed out from the sides of the SLS specimen. After the adhesive had cured or hardened, the excess adhesive was removed by filing off the edges of the SLS specimen.

Different curing conditions are identified as separate cases in Table 50. Cases A–E are baseline cases. In Cases B, D, and E, where the adhesive in the specimens was cured at elevated temperatures while still under vacuum consolidation, the entire setup was placed in a conventional oven, which was preheated to the desired temperature (either 100°C or 160°C), for at least 1 hour. The oven has an outlet that enables the plastic hose to be drawn out of the chamber and connected to the vacuum pump.

In Cases F, G, and H, where the adhesive was cured by induction heating, the entire setup was held vertical by a vise grip attached to one end of the base plate, and placed in between an induction coil shaped like an earmuff, as shown in Figure 89. The induction unit was capable of generating a peak-to-peak current of between 0 and 55 amps at a frequency of 284 kHz. A thermal camera was positioned in front of the setup to capture the full-field surface

temperature of the bonded area as the induction heating proceeded. The data was fed to a computer and displayed in real-time on a color monitor. The temperature tended to be a little higher at the edges and corners of the bond area initially, but after about 20 s, the temperature distribution became very uniform throughout the bond area. A typical temperature profile with time at the center of the bond area is shown in Figure 90. In Table 50, the selected process windows of 10 and 15 minutes for Cases F and G respectively were guided by the cure kinetics study described earlier.

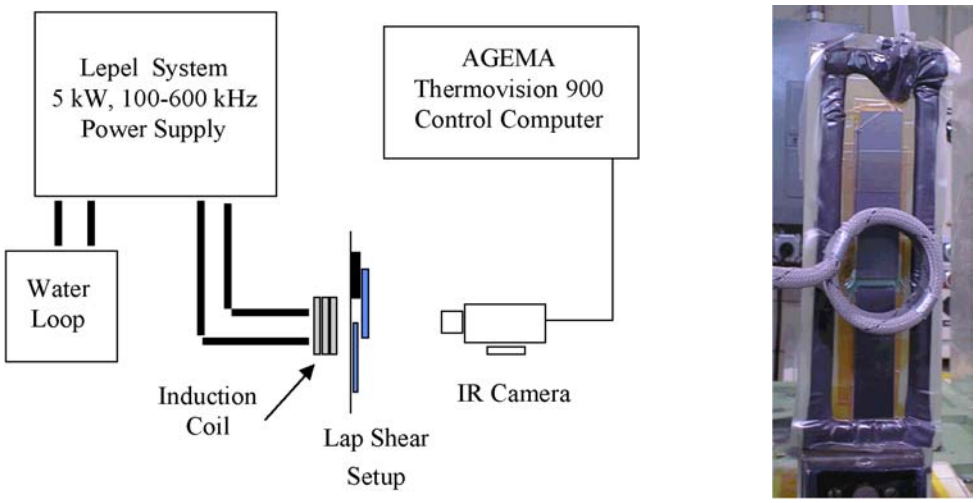

Figure 89. Single-lap shear specimens were fabricated using this setup with copper wire mesh susceptors and Hysol EA9394 adhesive.

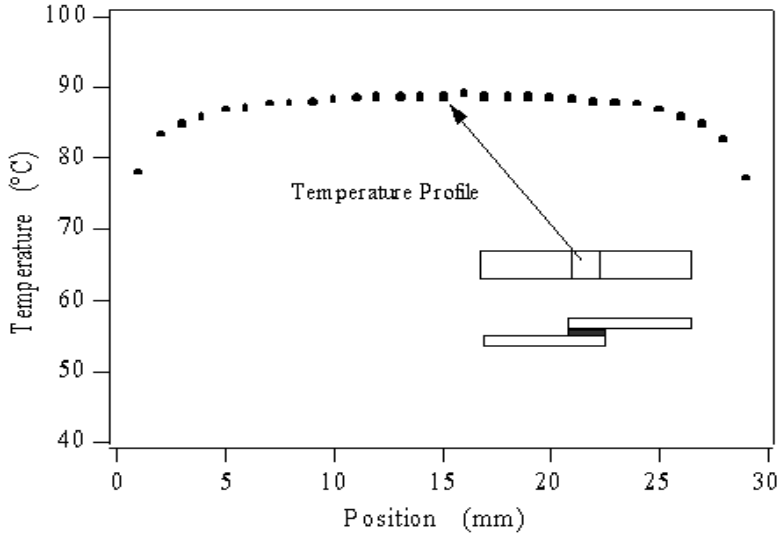

Figure 90. Temperature profile of lap-shear specimens demonstrating uniformity of heating in the process window offered by induction heating for repair.

8.3 Performance Comparison of Adhesive System

All SLS and DNS specimens were tested to failure in an Instron universal testing machine. The mean nominal shear strengths and associated standard deviations are given in Table 50. The results are plotted in Figure 91, where values of the mean ±3 standard deviations are used. Interestingly, the presence of the copper susceptor seems to reduce the scatter of the data, as shown by comparing the standard deviation values of Cases A and B with those of Cases C and E. Indeed, all the cases of SLS specimens with susceptors (C, D, E, F, G and H) have lower coefficients of variation. In a typical failed SLS specimen that has been cured by induction, although the adhesive layer had failed, the mesh susceptor was still partially attached to both adherends. The maximum load was reached just prior to sudden cohesive failure of the adhesive layer. This value of load is used to compute the nominal shear strength of the specimen in Table II-22. After fracture of the adhesive layer, the specimen was still able to support a small load due to the copper susceptor. On subsequent application of load, the copper wires eventually fractured, but approximately half of the mesh remained attached on each adherend. The presence of the susceptor provided alternative crack paths through the adhesive layer and in between the spaces within the mesh. The overall effect may be a decrease in sensitivity to microvoids or defects in the adhesive layer, leading to less scatter in the strength data.

Elevated-temperature cure at 160°C for specimens without susceptors (Cases A and B) increases the shear strength but also significantly increases the amount of scatter in the data. For room-temperature-cured adhesives, inclusion of a susceptor decreases the average nominal shear strength (Cases A and C). This is probably due to the increase in bond line thickness, although a stress analysis of an SLS joint containing a susceptor layer has not yet been carried out. Elevated-temperature cures at 100°C and 160°C for specimens with susceptors show improvement in nominal shear strengths, regardless of whether the heat was supplied in a conventional oven (Cases D and E) or through induction heating (Cases F and G). Significantly, in both methods of heating, the average strength of specimens cured at 100°C is higher than that of specimens cured at 160°C. It appears that there is an optimal elevated curing temperature above which the strength will begin to decrease. An increase in α_u with temperature would result in an increase in resin strength but also a reduction in fracture toughness. Consequently, the stress state in the specimen due to the mechanical loads is unchanged. Specimens cured at 100°C may be less notch sensitive due to the higher toughness than specimens cured at 160°C.

It is concluded that induction heating can be successfully used to accelerate the curing of room temperature cure adhesives at elevated temperatures, since the results did not show substantial reduction in the joint strength of induction cured specimens. For the adhesive used in this study, curing time was reduced from 120 hours to 15 minutes.

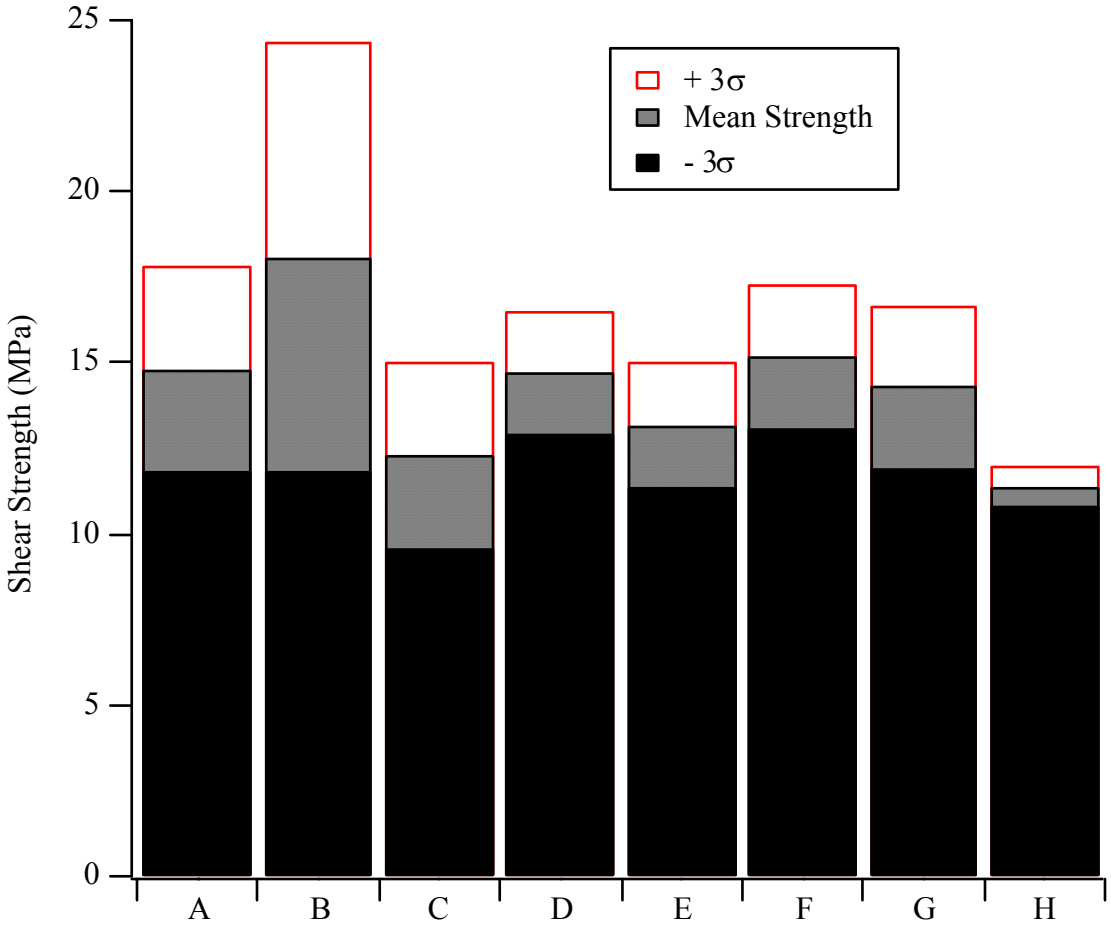

Figure 91. Performance of the lap shear specimens. Induction-bonded specimens show better ±3σ performance than oven- or room-temperature-cured specimens.

8.4 Performance of Bonded Repair

A bonded repair is performed by application of an adhesively bonded patch to a damaged area. Traditionally, the hardening of the adhesive has been performed by placing the joint, and hence the structure to be bonded, in an oven or autoclave until the adhesive is fully cured. An inherent drawback to such techniques is the very long cure times required for complete cure. The technique of electromagnetic induction, on the other hand, is able to locally and rapidly heat the area close to the adhesive bond line. This is especially important in the case of composite integral armor repair due to the thick sections of the various layers that compose the structure. The feasibly of using induction heating for the hardening of adhesives in composites bonded joints is investigated in the present work.

In this work, adhesively bonded single-lap shear (SLS) specimens and double cantilever (DCB) beam specimens were fabricated using two epoxy paste adhesives that cure at a relatively low-temperature. Dexter Hysol EA9359.3NA and EA9394 adhesives were

selected. The adhesives were either oven-cured or induction-cured. The materials used and the specimen preparations are presented next. The test procedures are then described. Finally, the procedure used for the oven-cure and induction-cure of the adhesives is described.

8.4.1 MATERIALS

The adherend used was a 6mm thick woven-fabric composite plate. It consisted of 10 layers of Vetrotex S2-Glass plain weave fabric, with a [0/90] orientation (where the fabric warp direction is at 0° and the weft direction is at 90°), impregnated with a toughened low-viscosity Applied Poleramic SC15 epoxy resin system. The adherends were fabricated, at the University of Delaware Center for Composite Materials (UD-CCM), by the vacuum assisted resin transfer molding process (VARTM). Prior to any bonding operation, the adherend surfaces were grit-blasted and subsequently thoroughly cleaned with acetone.

In this study, two commercially available epoxy paste adhesives are compared. The adhesives were selected for their ability to cure at a relatively low-temperature for a short period of time. Furthermore, the two adhesives offer different mechanical properties; one adhesive is ductile (i.e., has a relatively low modulus and a relatively high elongation to failure), whereas the other adhesive presents higher relative structural characteristics (i.e., a relatively high tensile modulus for a relatively shorter elongation to failure). Both adhesives are toughened epoxy adhesives manufactured by Loctite Aerospace (USA). The former adhesive system is a two-part Hysol EA9359.3NA paste adhesive system that cures at 82°C for 1 hour. According to the manufacturer's datasheet, it has a bulk tensile modulus of 2.2GPa for an elongation at failure of 10%, and a tensile strength of 31MPa. The latter adhesive system is a two-part Hysol EA9394 adhesive system that cures at 66°C for 1 hour. According to the manufacturer's datasheet, it has a bulk tensile modulus of 4.2GPa for an elongation at failure of 1.7%, and a tensile strength of 46MPa.

8.4.2 TEST PROCEDURES

The specimens were tested in a universal INSTRON 4484 testing machine. The specimens were tested following three test procedures, in order to allow for comparisons to be made. The single-lap shear (SLS) specimens were tested in tension. The DCB specimens provided a mean to compare the fracture toughness of oven-cured specimens with that of induction-cured specimens.

8.4.2.1 Single-Lap Shear Specimens

Single-lap shear (SLS) specimens were fabricated according to ASTM D1002. The adhesive was either oven-cured or induction-cured as described in the following section. The adherends were obtained from 300mm long, 150mm wide, and 6mm thick adherend plates manufactured by the vacuum assisted resin transfer process (VARTM) at UD-CCM. The totality of the specimens, for each adhesive system and each curing process, were manufactured in one operation. The panels were then cut into test specimens, each measuring 275mm long by 25mm wide. The SLS specimens were tested in tension according to ASTM D1002.

8.4.2.2 Double Cantilever Beam Specimens

In addition to the SLS specimens, double-cantilever beam (DCB) specimens were also fabricated using either conventional oven-cure or induction-cure techniques (described below). The adherend material was identical to that of the SLS specimens. In a DCB specimen a layer of adhesive is sandwiched between two adherend arms. The initial delamination was made by inserting a layer of Kapton film, 50μm in thickness, in between the two adherends. The tests specimens were cut from the cured sandwich plates and were 25mm wide. One inch by one inch aluminum cubes were then bonded to each side of the specimen where the initial delamination was made. An overnight room-temperature cure adhesive was selected for this operation. The edge of the specimens was then painted white with a brittle Enamel paint and marked at 5mm intervals to enable crack length to be monitored during the test.

The Double Cantilever Beam (DCB) specimen is well suited for testing thin adhesively bonded joints consisting of sheets of composite materials. The specimens were mounted in a fixture to load the end blocks and the end of the specimens was supported in order to keep the beam orthogonal to the direction of the applied load. The load and the ram displacement were recorded on a computer throughout the test, including the unloading cycle. Crosshead speeds of 0.01mm/min and 0.05mm/min were used during the loading and the unloading cycles, respectively. The load and displacement data were noted for crack growth measured every 1 mm from the tip of the insert, for the first 40mm, then every 5mm for a total length of about 60mm. The crack length was measured along the edge of the specimen with a traveling microscope. The specimens were not pre-cracked, and the initiation and propagation values were determined in one loading-unloading cycle, using a simple beam theory data reduction technique.

8.4.3 MANUFACTURING CONSIDERATIONS

The oven-cure and induction-cure procedures, used to harden the adhesive, are presented in this section. It is noted that in each case vacuum consolidation was used to ensure uniformity of the applied pressure and hence ensure a constant adhesive bond line thickness. First, a steel tool plate was cleaned with acetone and a Freekote™ release agent was applied. The bottom adherend was then placed directly on the tool plate. The adhesive was next applied on one side of each adherend, and the adherends were then put into contact. Pieces of peel ply, breather cloth, and vacuum bagging materials were then placed onto the stack, which was sealed on all four edges of the base plate with tacky sealing tape. Vacuum was drawn for the interior via a plastic hose. The stack is now ready for the hardening of the adhesive.

8.4.4 CONVENTIONAL OVEN-CURE OF ADHESIVES

In the conventional oven-curing technique, the stacks of SLS and DCB specimens, prepared following the procedure shown above were cured in a convection oven, under vacuum, for at least 1 hour. Based on the manufacturers' recommendations, the EA9359.3NA and EA9394 adhesives were cured at temperatures of 82°C and 66°C for one hour, respectively. The panels were subsequently cut into test specimens with a diamond-coated rotating saw.

The adhesive thickness of the oven-cured SLS specimens was measured with an optical microscope and was found to be 0.18mm. Similarly the adhesive thickness of the induction-

cured specimens was 0.45mm, due to the presence of the stainless steel mesh at the bond line. In order to allow for comparisons to be made, thin strips of metal mesh susceptors were inserted along the width of the outer edges of the oven-cured DCB panels, and hence achieve a comparable constant adhesive thickness. The adhesive thickness of the oven-cured DCB specimens was subsequently measured to be similar to their corresponding induction-cured specimens, i.e. about 0.45mm.

8.4.5 INDUCTION CURE OF ADHESIVES

The induction-cured specimens were also prepared following the procedure described above. However, a metal susceptor is sandwiched between two layers of adhesive to allow for the induction heating mechanism to take place. A stainless-steel mesh, with a wire density of 5 by 5 per square cm and a wire diameter of 0.165mm, was embedded in the adhesive layer. The stack was then placed, horizontally, in front of the induction coil. It is noted that the distance between the induction coil and the susceptor mesh is important as it allows controlling the maximum heating temperature.

In the present study, the susceptor temperature was controlled by preparing a stack, but without adhesive layers. A Kapton film was wrapped around the surfaces in contact with the susceptor mesh, to avoid damage and overheating. The stack was then set underneath the induction coil, at a selected distance, and the power was increased from 50% to 100%, in 10% increment. The susceptor material temperature was recorded in two ways. An AGEMA Thermo-vision 900 thermal camera was positioned in front of the set-up to capture the full field surface temperature of the bond area. Also, placing E-type thermocouples at the susceptor/adherend interface allowed to monitor the temperature generated at the bond line. The steady state temperature was noted from each increment in power. Once a susceptor steady state temperature of about 82°C and 66°C was found to be possible within the range of the power potentiometer, the set distance was kept constant for the experiment. For instance, distances of 19mm and 11mm were selected for the SLS and DCB specimens, respectively.

It may be noted that owing to the different areas to be bonded, a different coil shape has to be used for the SLS and DCB specimens. A ‘radiator’ shape coil was used for the fabrication of the SLS specimens, as shown in Figure 92. Whereas a 2-turn rectangular coil, as shown in Figure 93, was used for the fabrication of the DCB specimens. The steady state surface temperatures, recorded from the thermal camera may also be seen in Figure 92 and in Figure 93 (in °F) for the SLS and DCB specimens, respectively. After manufacture, the specimens were cut on a diamond-coated dry saw. An adhesive bond line thickness of 0.45mm was measured for all induction-cured specimens.

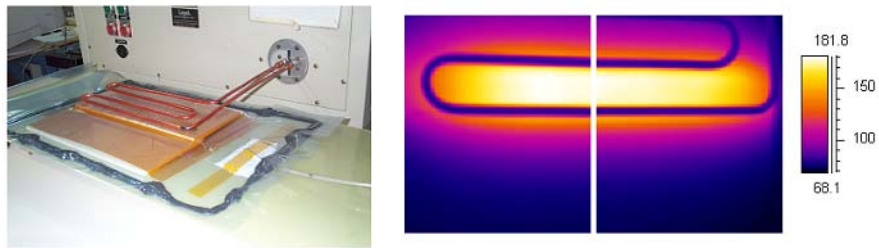

Figure 92. Induction-cured Hysol EA9359.3 single-lap specimens (Set-up and thermal field.)

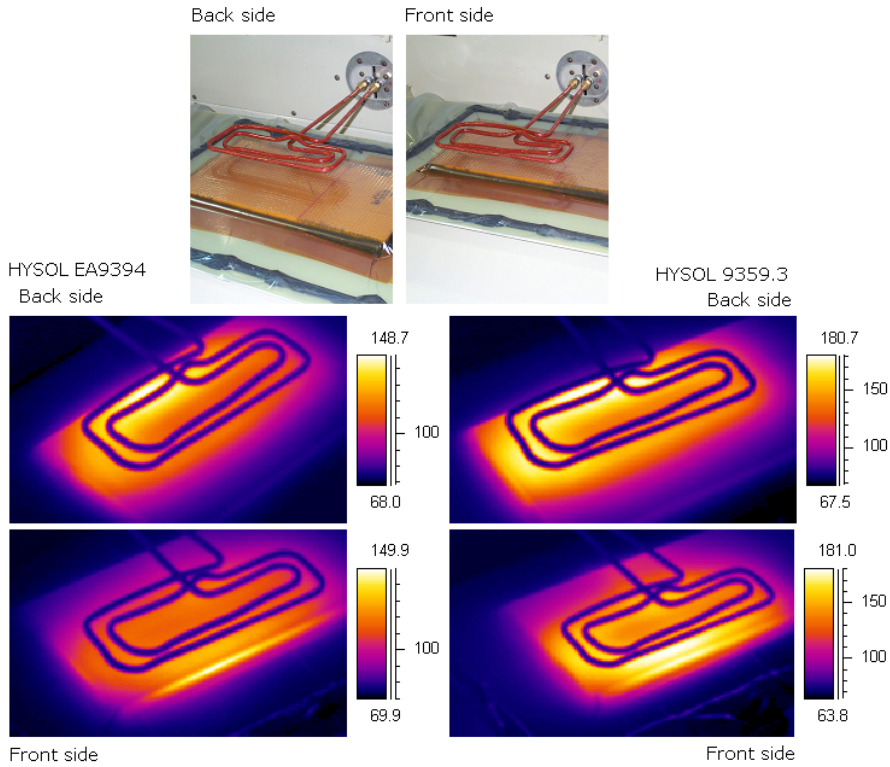

Figure 93. Induction-cured DCB specimens (Set-up and thermal field.)

8.4.6 MATERIALS RESULTS

8.4.6.1 Single-Lap Shear Specimens Tested in Tension

The results for the oven- and induction-cured SLS specimens tested in tension are shown in Table 51 below. Apparent shear stress and standard deviation values are also shown in Figure 94. To allow for comparison, the dashed line in this figure represents the values of the maximum and minimum apparent average shear stress of the oven-cured specimens. In Table 51, it may be seen that the scatter in results was relatively low for all the SLS specimens

tested in tension. Indeed, the maximum coefficient of variation is only of 4.8% for the oven-cured EA9359.3 specimens.

Table 51: Single-lap shear specimens tested in tension

	Adhesive	Apparent shear stress (MPa) [Standard Dev.]	CV %
Oven-cured specimens	EA 9359.3	15.6 [0.75]	4.8
	EA 9394	14.9 [0.5]	3.3
Induction-cured specimens	EA 9359.3	13.9 [0.45]	3.2
	EA 9394	13.9 [0.57]	4.1

In Figure 94, it may be seen that the oven-cured specimens were relatively stronger than the induction-cured specimens, for both adhesive systems. In Table 51, the average apparent shear stress at failure of the induction-cured EA9359.3 and EA9394 specimens may be seen to be 11% and 6% lower than their corresponding oven-cured specimens. Also in Figure 94, it may be seen that the adhesive type has a relatively small effect on the strength of the oven-cured specimens. The SLS specimens made with EA9359.3 adhesive were slightly stronger than those made with EA9394 adhesive. However, this was not the case for the induction-cured specimens, as the apparent shear strength may be seen statistically identical for both adhesive systems.

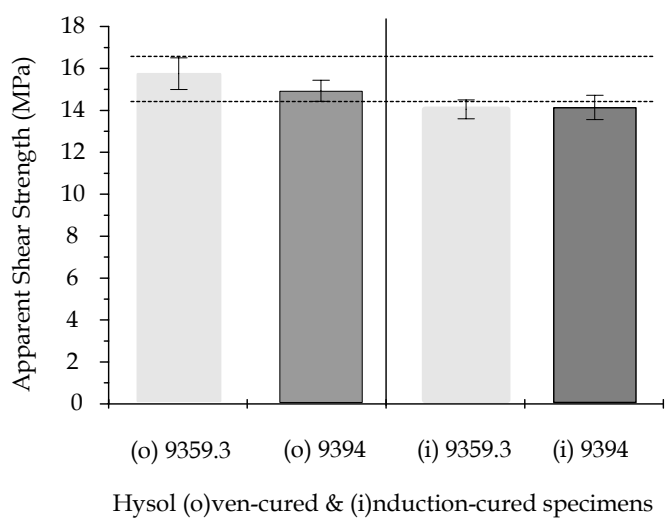

Figure 94. Single-lap shear specimens in tension

The loci of joint failure for the oven-cured and induction-cured specimens were found to be slightly different, but independent of the adhesive system. The locus of failure of the oven-cured specimens was interfacial between the adherend and the adhesive, although some cohesive fracture within the adhesive was also seen by visual observation. It may be noted that the amount of cohesive fracture within the adhesive was a little higher for the EA9359.3

specimens and this correlates well with their higher nominal strength. On the other hand, the crack path on the induction-cured specimens has been constrained to a small area between the metal mesh and one of the adherend. The loci of joint failure were by interfacial failure and cohesive fracture within the adherends. The metal mesh may be seen to be responsible for the small decrease in strength of the induction-cured specimens.

8.4.6.2 Double Cantilever Beam Specimens

The test results for the oven-cured and induction-cured DCB specimens are shown in Table 52 below. The scatter in results is significant and characteristic of this type of test. The maximum coefficient of variation was found to be about 19% for the induction-cured EA9394 specimens. It may be noted that the high values of coefficient of variation reported are partly due to the rising R-curves (i.e., the resistance to crack propagation increases with crack length).

Table 52: Double cantilever beam specimens

	Hysol	G_{Ic} (J/m^2) [Standard Dev.]	CV (%)
Oven-cured specimens	EA 9359.3	1693 [198]	12
	EA 9394	1218 [127]	10
Induction-cured specimens	EA 9359.3	1455 [132]	9
	EA 9394	1206 [226]	19

In Table 52, the value of average critical fracture energy may be seen to be dependent on the adhesive type. The average critical fracture energy of EA9359.3 specimens was 1693J/m^2 and 1455J/m^2 for the oven-cured and induction-cured specimens, respectively. These values may be seen statistically identical, about 1600J/m^2. For the specimens fabricated with the EA9394 adhesive, the values of the average critical fracture energy were lower, and at about 1200J/m^2, and this irrespectively of the method of hardening of the adhesive. This represents a 25% decrease in critical fracture energy.

The loci of failure were seen to be dependent on the method of hardening. The loci of failure of oven-cured specimens may be seen to be along the adhesive/adherend interface, with islands of adhesive being left on each side of the adherend. The loci of failure of the induction-cured specimens may also be seen to be interfacial, although the crack was constrained to move along one interface only and was not allowed to jump through the stainless steel susceptor mesh. These loci of failure are not significantly different and may be seen consistent with the above results, i.e. the critical fracture energy is only dependent on the adhesive type, and not on the mode of hardening of the adhesive. It may be noted that the purely interfacial loci of failure of the induction-cured specimens may have resulted in the slightly lower values of average critical fracture energy, when compared with the corresponding values for the oven-cured specimens.

8.4.7 DISCUSSION

It is apparent from the results shown in the present work that bonded joints for which the adhesive was induction-cured were as strong as their corresponding oven-cured joints. Induction heating may therefore be seen as a technique that can be safely used to harden adhesives. The results were however seen slightly different according to the method of testing.

8.4.7.1 Single Lap Shear Specimens Tested in Tension

For the SLS joints tested in tension, the oven-cured specimens were always found stronger than their corresponding induction-cured specimens. The average apparent shear strength of the joints was seen to be a function of the adhesive type and the method of hardening. Induction heating was shown to lead to a reduction in the apparent shear strength of the joints of about 6% and 10% for the specimens fabricated with EA 9359.3 and EA 9394 adhesives, respectively. Also the strength of the induction-cured specimens was observed to be statistically equal, and therefore independent of the adhesive system used.

The mechanics of deformation and failure of single-lap shear joint may be seen to be complicated. The geometry of the single-lap shear specimen results in stress concentrations and the failure of such joints arises due to a combination of tensile, shear and peel deformation within the adhesive layer. One of the general conclusions made on the testing of single-lap joints in tension is that joints made with flexible adhesives are more likely to be able to tolerate these stress concentrations, and hence give higher joint strength. Indeed, inhibiting a failure by peel stresses allows the joint to develop its shear capability. From the present results, it may be seen that the oven-cured adhesives with the higher elongation to failure (EA 9359.3) resulted in the higher joint strength, and this is hence in agreement with the above statement.

However, the apparent shear strength of the induction-cured specimens was observed to be slightly lower than that of the oven-cured specimens and also independent of the adhesive system used. The constraint of the crack path to the mesh/adhesive interface may have resulted in the lower strength of the induction-cured specimens. The loss in strength was however marginal. It may be concluded that although the induction-cured specimens were at the most 10% weaker than corresponding oven-cured specimens, the induction heating technique led to strong, sound, adhesively bonded joints.

8.4.7.2 Double Cantilever Beam Specimens

The average values of the critical fracture energy, G_{IC}, of the DCB specimens were seen to be independent of the method of hardening, i.e., only dependent on the adhesive type. Induction heating of the adhesive was found to have no influence on the toughness of the joints. The Hysol EA 9359.3 adhesive specimens were found to have a G_{IC} value of about 1600 J/m^2, whether oven- or induction-cured. On the other hand, the specimens fabricated with EA 9394 adhesive were found to have a G_{IC} of about 1200J/m^2. The EA9359.3 adhesive may be seen to be relatively tougher than the EA9394 adhesive. This 25% increase in fracture toughness value resulted in the generally higher values of joint strength of specimens made with EA 9359.3 adhesive system. Tougher adhesive are more likely to tolerate the various stress

concentrations present in an overlap joint, allowing the adhesive to develop its shear capability, and resulting in higher joint strength.

8.4.8 BONDED REPAIR CONCLUSIONS

A study of the feasibility of using induction heating as a mean of hardening adhesives in composite bonded joints has been performed. From the present work, induction-cured specimens were seen to be as strong as corresponding oven-cured specimens. The strength of the joints was however seen to be dependent on the loading mode.

Induction-cured single-lap shear specimens tested in tension were found to be only marginally weaker than their corresponding oven-cured specimens. The inclusion of a stainless steel mesh in the induction-cured joints resulted in only a small decrease in the apparent shear strength of the joints. The strength of the joints was also found to be slightly dependent on the adhesive system used. The adhesive with the highest elongation to failure produced the strongest joints.

The Mode I critical fracture energy of induction and oven-cured specimens was measured. The results corresponded well with the results from the single-lap shear specimens tested in bending. The critical fracture energy of the specimens was affected only by the adhesive system. The method of curing had no influence on the value of critical fracture energy. The adhesive system with the highest elongation to failure (EA 9359.3) was also seen to have the highest value of G_{IC}.

The conclusion from this work is that induction heating may be regarded as a sound and efficient method for the bonding and repair of composite structures.

9 Mesh Susceptors – Application to Repair of Integral Armor

Initial studies were performed to assess the applicability of induction-based repair of the Army's composite integral armor using metal mesh susceptors. Desirable repair features for composite armor can be summarized as follows:

- One-step process for multi-layer repair
- Heated from outer surface (one-sided access)
- Vacuum consolidation
- Gap filling
- Variable damage area (multi-hit)
- Rapid portable process
- Renew structural, ballistic and signature performance

The induction-based repair system can address all of these requirements, in addition to using adhesive systems that have no shelf-life requirements.

9.1 Induction Bonding Evaluations

Most military applications require high-performance adhesives, which typically are high-temperature-curing systems (250° and 350°F). To enable the specific application of induction bonding to integral armor, a carbon/epoxy substrate system was used to study susceptorless induction bonding and also to assess the effect of the mesh or eddy-current susceptor on bond strengths. In addition, a glass/vinyl ester substrate was also used for bond strength tests, due to the increasing use of such systems in military vehicles. The glass/vinyl ester composite was fabricated by VARTM, which utilizes fiber preforms and resin systems and has no shelf-life requirements. Similar performance was achieved comparing induction bonding with the baseline autoclave bonding process.

While performance evaluation of induction bonding has proven successful, a key issue that has not been addressed so far is thermal uniformity during bonding. Bonding tests to date have been performed on lap-shear-type specimens, which are not representative of typical repair or bonding scenarios, where the bonding/repair surface can be large, curved, etc. This issue has been addressed in the present work, with a focus on achieving in-plane and through-thickness thermal uniformity during induction bonding.

9.1.1 Thermal Criteria During Bonding and Repair

In a typical induction bonding process, the mesh susceptor is placed between two composite adherents to generate heat at the bond line. For adequate resin flow and consolidation, the susceptor typically contains some resin or adhesive, such as in resin-impregnated metal meshes. Consolidation pressure is generally applied by vacuum bagging, though non-metallic rollers may be used for additional pressure. The induction coil used is designed to "fit" the part, including complex shapes and geometries, which is one of the major advantages of induction heating. For large parts, the coil can be moved at a specified velocity to provide necessary heating.

Several researchers [69 - 77] have conducted tests on the use of metal mesh susceptors and resistive heating for bonding of composites. A common problem with metal mesh susceptors subjected to a magnetic field is the resulting non-uniform temperature distribution. Induction coils typically generate non-uniform magnetic fields, although uniform fields can be generated for a few specific coil designs with limited work areas (center of a circular coil). Bonding tests to date have used these types of coils to generate uniform temperatures at the bond line; however, the test configurations are not representative of typical bonding or repair geometries.

The two key requirements of the mesh susceptor are uniform temperature distribution in the plane of the mesh and minimal thermal gradients through the thickness direction of the composite. Figure 32 shows a typical in-plane thermal response of a metal mesh under vacuum using a conical induction coil. The temperature difference between the center and the outside of the mesh (approximately 40°C) is higher than desired (±10 °C).

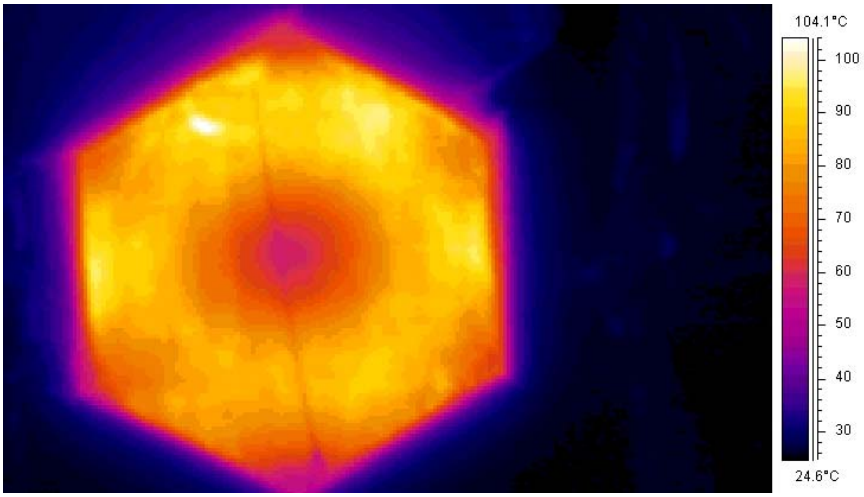

Figure 95. Thermal Gradient Effects During Induction Heating of Mesh Susceptors.

In cases where there is only one bond line, through-thickness gradient is not an issue. However, in thick-section or multi-layered composites, where multiple bond lines are present, it is critical to achieve through-thickness uniformity for optimal performance. This research has demonstrated the ability to bond multiple layers of a composite system in a single step using induction to preferentially heat the bond lines.

During induction processing of a multi-layered composite, mesh susceptors at different depths or thickness locations heat differently due to the changing magnetic field. Typically, the field decays exponentially with distance from the coil, and the meshes closer to the coil heat more than the meshes further away from the coil. The present effort examines techniques to achieve uniform temperatures at the various bond lines.

9.1.2 DESIGN FOR UNIFORM HEATING

There are several approaches to achieve in-plane thermal uniformity during induction heating of mesh susceptors. The simplest approach is to develop a coil design that can generate a uniform field resulting in uniform heating in the mesh. An example of this is the solenoid coil setup that was used in induction bonding evaluations of mesh and adhesives during the first two years of this program. In this coil design, a uniform field is developed within the coil, and the lap-shear specimen is placed inside the coil. The resulting thermal profile is uniform (Figure 96); however, this coil configuration is not suitable for repair, as the mesh, or bond line, has to be inside the coil.

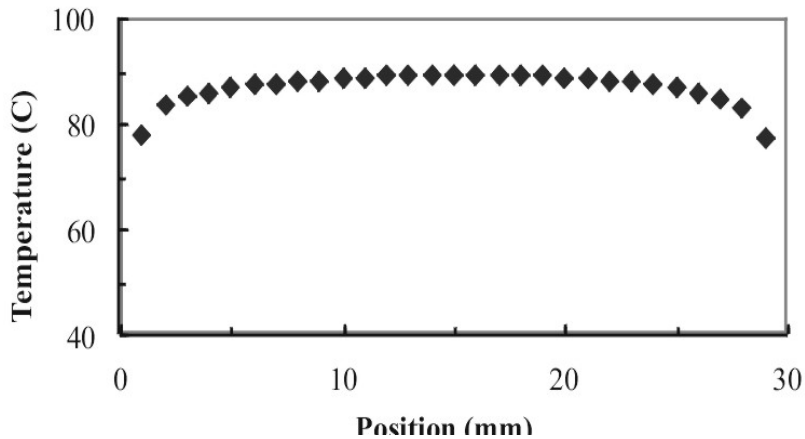

Figure 96. Temperature Profile for a Selected Solenoid Coil.

Thermal uniformity can also be achieved through relative motion between the mesh and the induction coil. The key parameters are the motion pattern and the rate of motion. An example of the effect of coil motion is shown in Figure 97. The uniformity was achieved after several trials using different motion patterns and rates. For repair scenarios, this is probably the best solution, as motion of the heat source (induction coil) is necessary especially for large damage areas or multiple damage zones. It is also within the capabilities of a depot level repair.

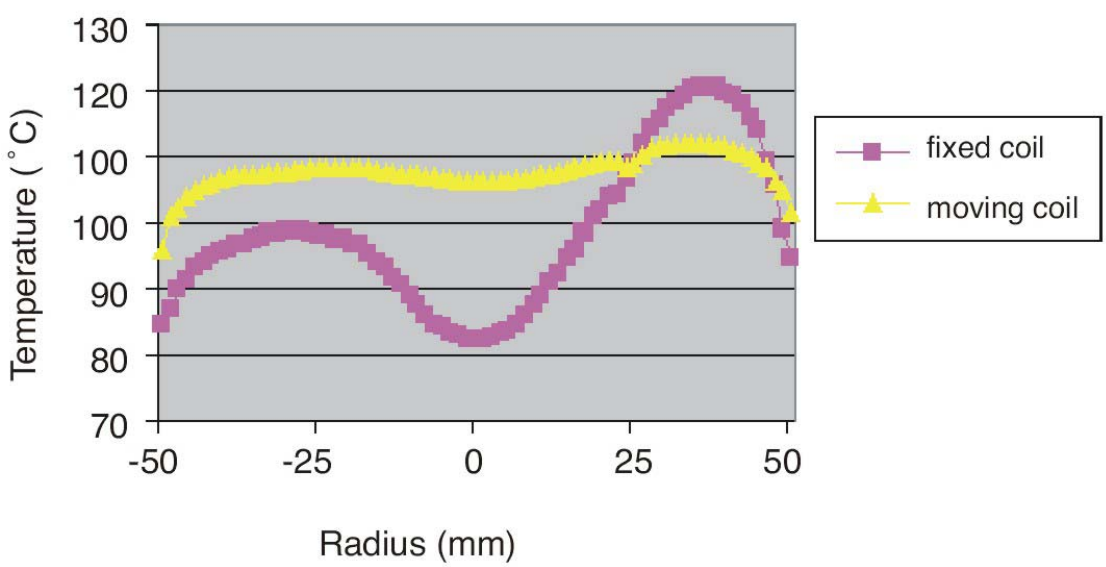

Figure 97. Uniform and Non-Uniform In-Plane Thermal Gradients.

Through-thickness thermal gradients pose a significant challenge. The magnetic field decays exponentially with distance or depth into the part and limits the maximum thickness of the

part that can be bonded or repaired. Early demonstrations were successfully conducted with part thickness of up to 1.5 inches, and larger thicknesses are possible with an increase in power. During initial bonding tests of multi-layered composites (CIA in this case), gradients of up to 30 to 40°C were measured between different bond lines, as shown in Figure 98. The meshes used in all the bond lines were identical in material (steel) and geometry.

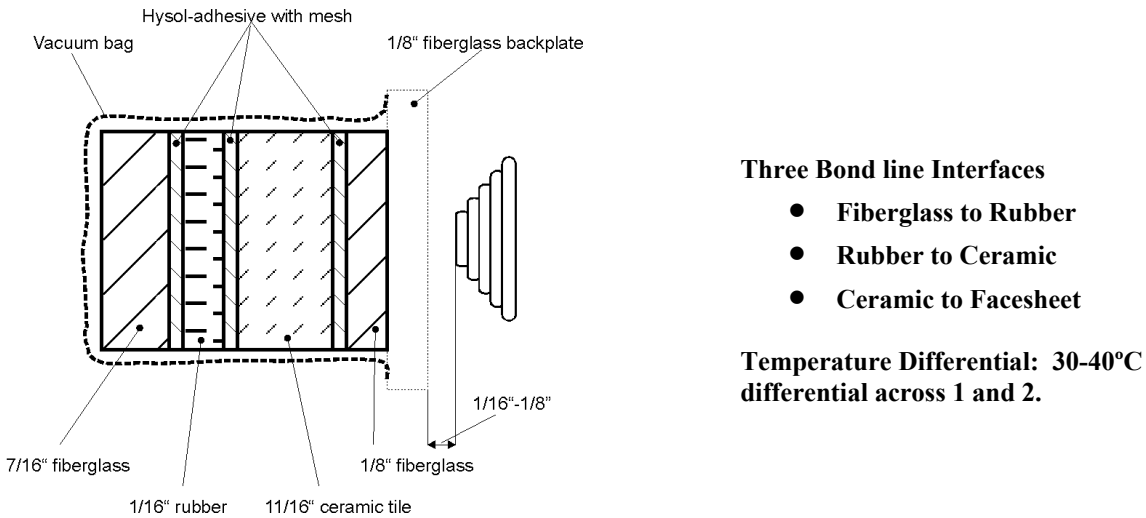

Figure 98. Single-Step Processing of a Multi-Layered Composite.

Thermal uniformity in the thickness direction was achieved by proper selection of mesh material for each interface or bond line. Since the mesh heating rate is dependent on the mesh material (copper, steel, etc.), one can select low-heating materials for bond lines close to the coil (high field) and high-heating materials for bond lines further away from the coil (low field). A study was undertaken for four types of mesh materials—steel, copper, brass, and aluminum—to estimate the heating rates of these materials. For a constant power level, the maximum steady-state temperature was measured for each mesh material, keeping all other parameters fixed. Figure 99 shows measured temperatures at a constant induction power, with steel heating the most and brass the least. Based on these results, one can use steel meshes at the farthest interface or bond line and brass or aluminum at the closest interface.

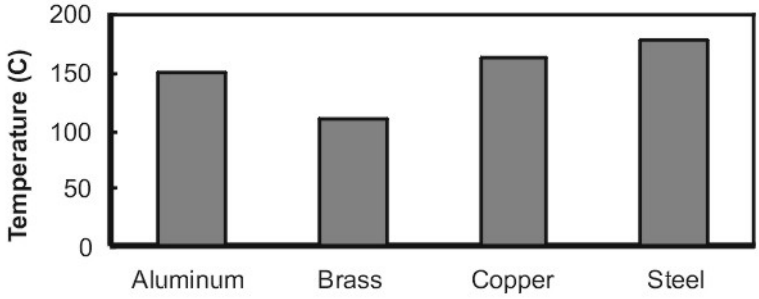

Figure 99. Induction Heating Response of Mesh Materials for Similar Conditions.

To test the concept of using selective mesh materials to reduce thermal gradients in the thickness direction, the multi-layered composite stack in Figure 100 was bonded together. The closest bond line to the coil was bonded using aluminum meshes, and the two bond lines above and below the rubber layer used steel meshes. Thermocouples were placed at the bond lines (2 per bond line) to measure temperature during induction heating and cure. The measured temperatures (insert Figure 100) indicate through-thickness thermal uniformity (within 10°C) demonstrating that designed selection of mesh materials for each bond line can solve the problem.

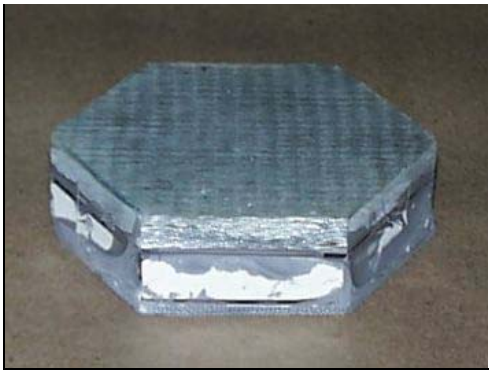

Interface	Facesheet/ Tile	Tile/ Rubber	Rubber/ Backing
Mesh	Aluminum	Steel	Steel
Measured* Temperature at Equilibrium	164°C	172°C	175°C

* Average of two thermocouples

Figure 100. Constant Temperature Achieved During Single-Step Processing of a Multi-Layered Composite.

9.2 Susceptor and Coil Design

For bonding integral armor components, two mesh types studied were used:

Copper mesh: 30x30 mesh
0.006-in. diameter
crosswire cloth

Steel mesh: 30x30 mesh
0.0065-in. diameter
crosswire cloth

Initial experiments focused on heating a ceramic tile, with different coils positioned on one side and the mesh fixed on the other side with Kapton tape, under vacuum pressure. These experiments determined that the steel mesh was heating up faster than the copper mesh and required a lower power setting to reach adequate temperatures for adhesive cure. Greater heating for the same power translates to higher depth of penetration, which means that thick composite parts can be heated through. This is required for armor repair, where the adhesive to be heated is generally more than an inch from the outer surface.

Figure 101 shows the temperature profile of a ceramic tile/mesh under vacuum pressure for a conical coil. The temperature differential between the center and the outside of the tile (approximately 35°C) is greater than allowable for adhesive repair.

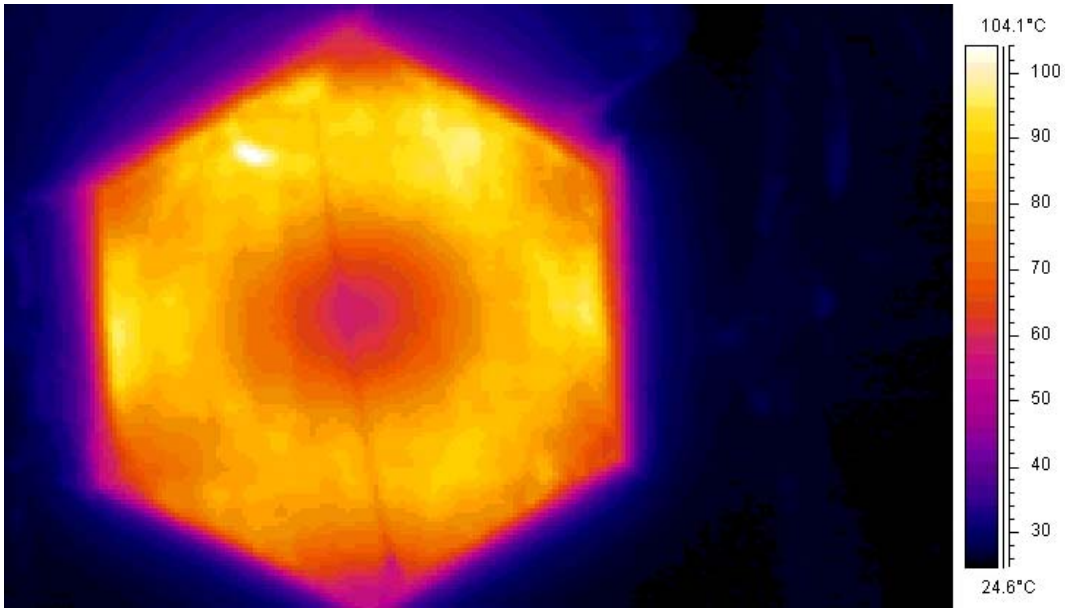

Figure 101. Temperature profile of ceramic tile/steel mesh under vacuum with a conical coil. Difference between hot and cold spots is approximately 35°C

Temperature differentials can be reduced by coil design, coil motion, or mesh susceptor design. Coil and mesh designs are in progress to reduce this differential as much as possible.

9.3 Coil Motion

One technique to achieve more uniform temperatures is to use a moving coil. An ABB robot system with six degrees of freedom was used for this purpose. The coil was mounted on the robot head using a plexiglass attachment. Several different motion patterns were examined to determine the optimal coil motion for uniform temperatures in the ceramic tile system. Figure 102 show comparisons of heating profiles without and with motion respectively and demonstrate the ability of coil motion in improving the uniformity of temperatures in the mesh. Figure 103 shows the actual temperature along the lines marked in Figure 102. The temperature differential is reduced from 40°C to 10°C in the plane of the mesh susceptor.

(a)

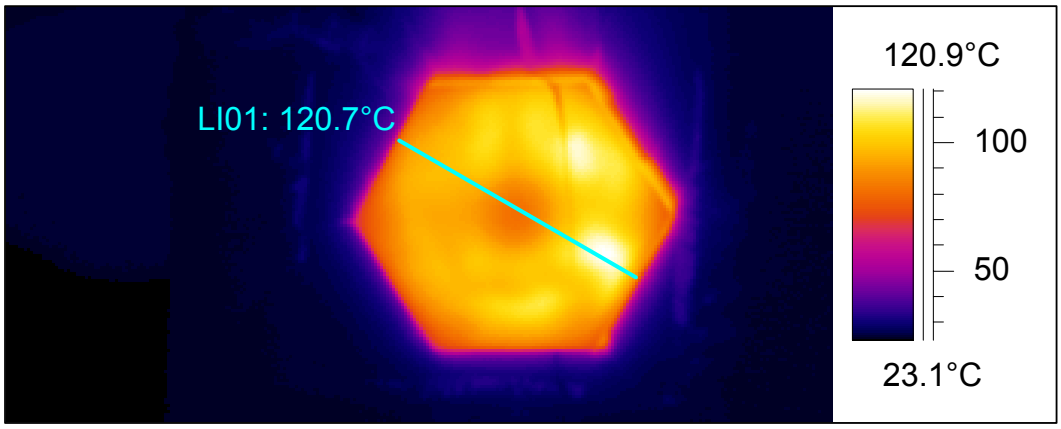

(b)

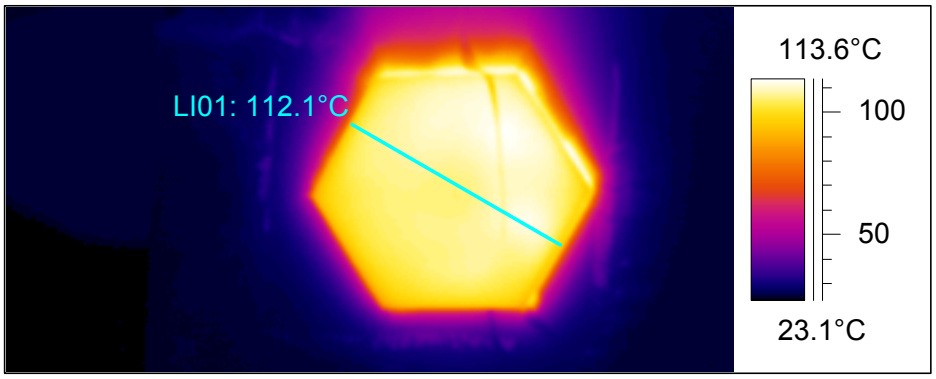

Figure 102. (a) and (b). Comparison of temperature profiles after 20 min. of heating (a) without and (b) with coil motion. The coil was moved rotationally about the center.

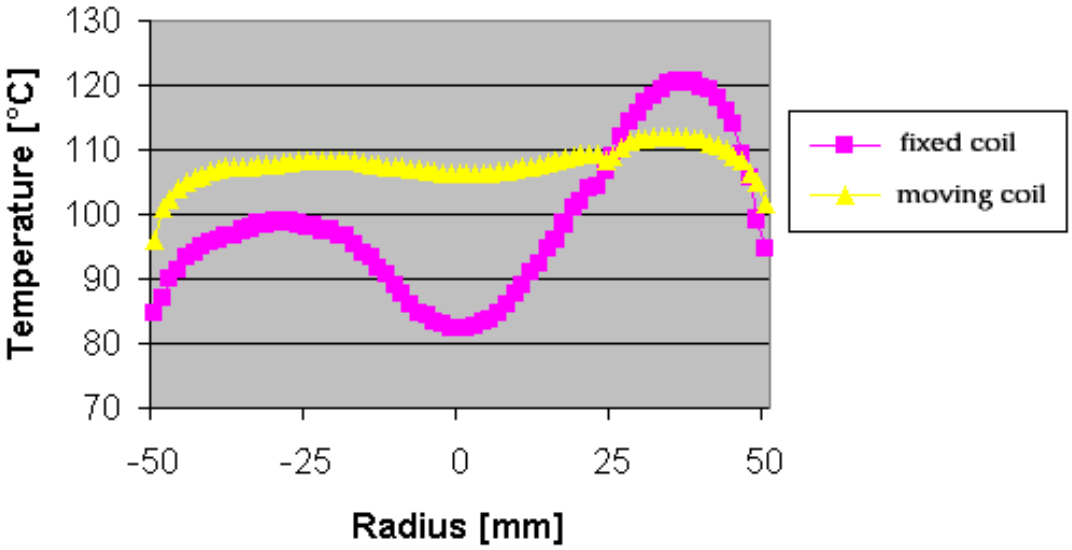

Figure 103. Temperatures of lines LI01 in Figures 95 (a) and (b).

The motion pattern used to obtain the temperature profiles was selected after several different patterns, such as circles of various diameters, were tested. It is a polygon-shaped movement, where, in one full turn, the coil passes over the center of the tile four times and helps achieve a satisfactory uniform temperature profile. Further work is in progress to determine optimal movement patterns for various repair sizes and shapes. Additionally, algorithmic codes could be designed to predict optimum heating geometries for known field patterns or coil designs.

9.4 Composite Armor Subsystem Bonding

Viewed simplistically, composite armor consists of four basic subsystems including a thin facesheet (graphite/epoxy or glass/epoxy), ceramic tile for ballistics, rubber layer to absorb tile fragments, and a thick composite layer for structure and ballistics.

Repair of armor after ballistic impact typically involves replacing the first three layers or subsystems. For demonstration purposes, the current effort focused on single-step and multi-step bonding of all subsystems using steel mesh susceptors with the Hysol EA 9394 adhesive system and the coil configuration described in the above sections. The following materials were chosen as representative of the four subsystems:

- **Thin facesheet**—1/8-in. fiberglass/epoxy
- **Ceramic tile**—11/16-in. ceramic
- **Rubber layer**—1/16-in. rubber
- **Thick composite layer**—7/16-in. fiberglass/epoxy

Initially, the influence and behavior of each subsystem or each part to its neighboring part during induction heating was examined. The following sequence of bonding tests was carried out:

- Bonding a 1/8-in. fiberglass and a 1/16-in. rubber sample
- Bonding a 1/16-in. rubber layer and 11/16-in. ceramic tile
- Bonding a 11/16-in. ceramic tile and 7/16-in. fiberglass
- Bonding thin fiberglass/rubber/ceramic/thick fiberglass in one step

The first three experiments produced the necessary data about power requirements for heating each subsystem/neighbor up to the curing temperature of the adhesive. In addition, the temperature difference between the adhesive layer and the top surface was determined by placing thermocouples at the adhesive layer and monitoring the top surface with an IR camera. It is necessary to control temperature differentials between the surface and the bond line when two or more subsystems are bonded, so that the adhesive at the bond line does not overheat and degrade.

In all the bonding tests, the coil was moved along the pattern developed during coil motion studies, and the adhesive was heated to a temperature of 100 ± 10 °C at the bond line. Table 53 and Figure 104 show the results of bonding an 11/16-in-thick ceramic tile to a 7/16-in composite panel. A frequency of 351 kHz was applied for 20 minutes. The coil was moved about the test specimen in a circular motion around the center of the tile.

Table 53. Temperature Measurements at the Surface and Bond line

	Temperature Reading of IR Camera			
Thermocouple position	Spot 1	Spot 2	Hotspot	Thermocouple
Backside of fiberglass	—	—	143	—
Mesh	77.8	84	117.2	117.1

(a)

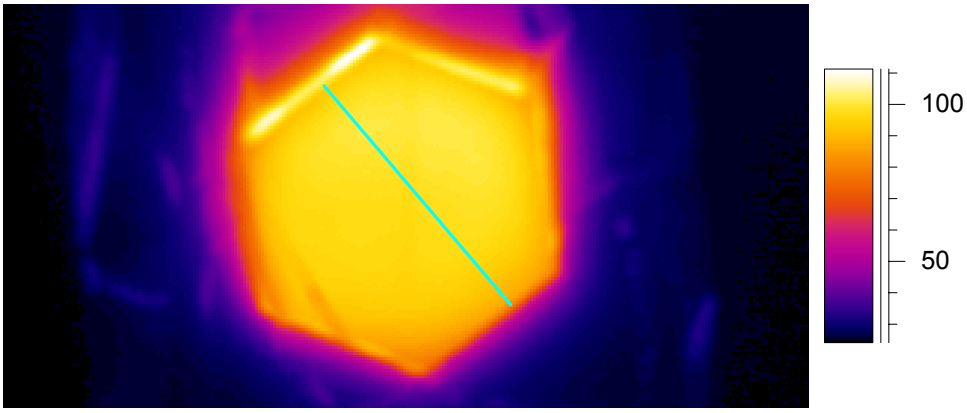

(b)

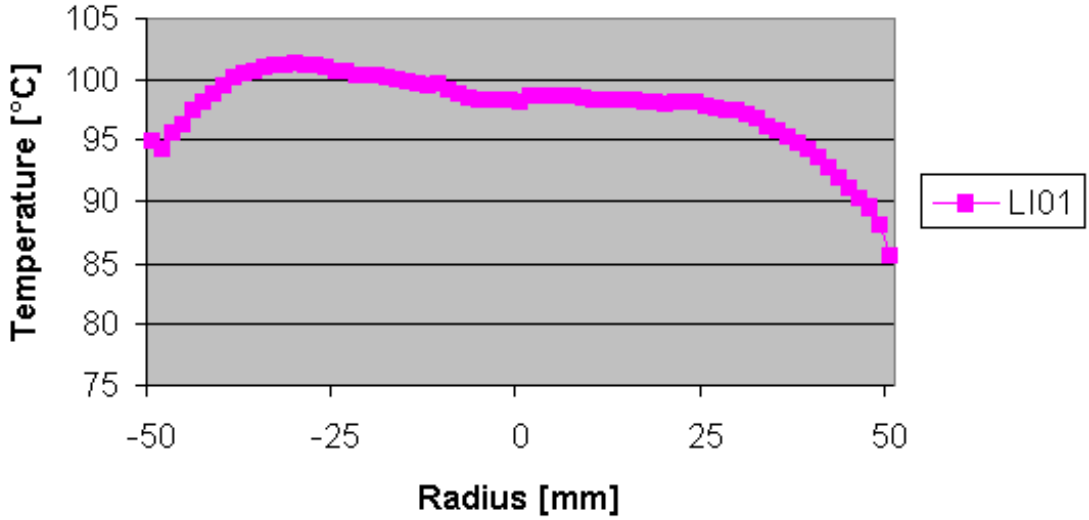

Figure 104. (a) and (b). Surface temperature variation during bonding of ceramic tile to 7/16-in thick glass/epoxy composite, with coil motion.

9.5 One-Step Multi-Layer Composite Bonding

The final experiment was to bond all four subsystems together in a single step. This would simulate an actual repair procedure of a multi-layered multifunctional composite armor panel. The four subsystems bonded together were

- **Thin facesheet**—1/8-in. fiberglass/epoxy
- **Ceramic tile**—11/16-in. ceramic
- **Rubber layer**—1/16-in. rubber
- **Thick composite layer**—7/16-in. thick fiberglass/epoxy

Figure 105 shows a schematic of the lay-up for this process. A layer of mesh/adhesive was placed between each subsystem, resulting in three adhesive layers or bond lines as shown in Figure 105. The layers were placed on a backing sheet and vacuum-bagged for consolidation pressure. The same coil and motion pattern was used as before. The coil is a one-sided conical coil, which permits curing from one side of the lay-up. Access to both sides of the part is often not possible for field repair applications. A coil frequency of 351 kHz was applied for 20 minutes.

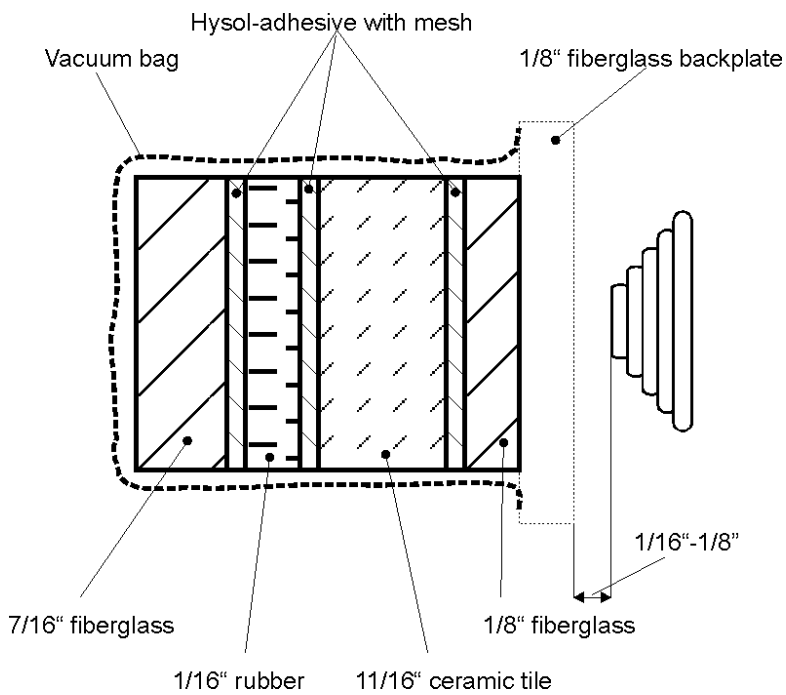

Figure 105. Schematic of the lay-up sequence for one-step induction repair of a composite armor panel.

Temperature profiles of the surface during the heating process are shown in Figure 106 and Figure 107. Surface temperatures are fairly uniform except at the edges of the part. However, this is not a major issue because in a realistic repair scenario, there will be no edges as seen in this case, since the repair fills in a damaged area. One of the primary challenges was to ensure similar temperatures in all three bond lines, despite the different distances from the coil. The thermal properties of each subsystem were important for this,

and the high thermal conductivity of the ceramic tile played a significant role in maintaining similar temperatures across the bond lines.

With IR spot locations provided in Figure 108, the time-temperature response during the heating process is shown in Figure 109. The entire process took approximately 30 minutes, which demonstrates the rapidity of the process. During this process, a heating depth of up to 1.25 in. was demonstrated. Greater depths are possible and are the subject of future investigations. Figure 110 shows a photograph of the final bonded sample with the multiple layers. Good-quality bond lines were obtained at all three interfaces.

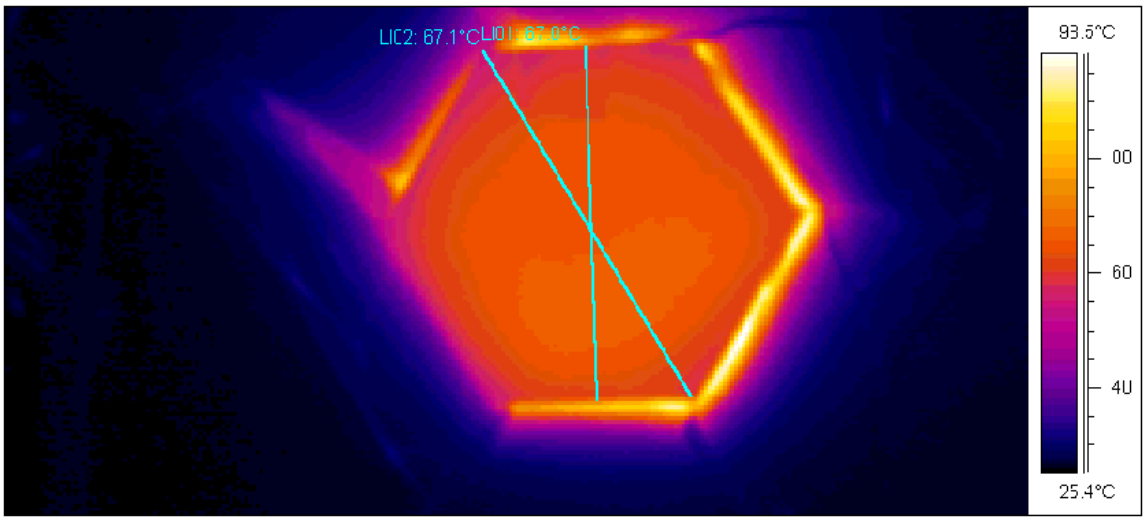

Figure 106. Surface temperature profile for single-step bonding with coil motion

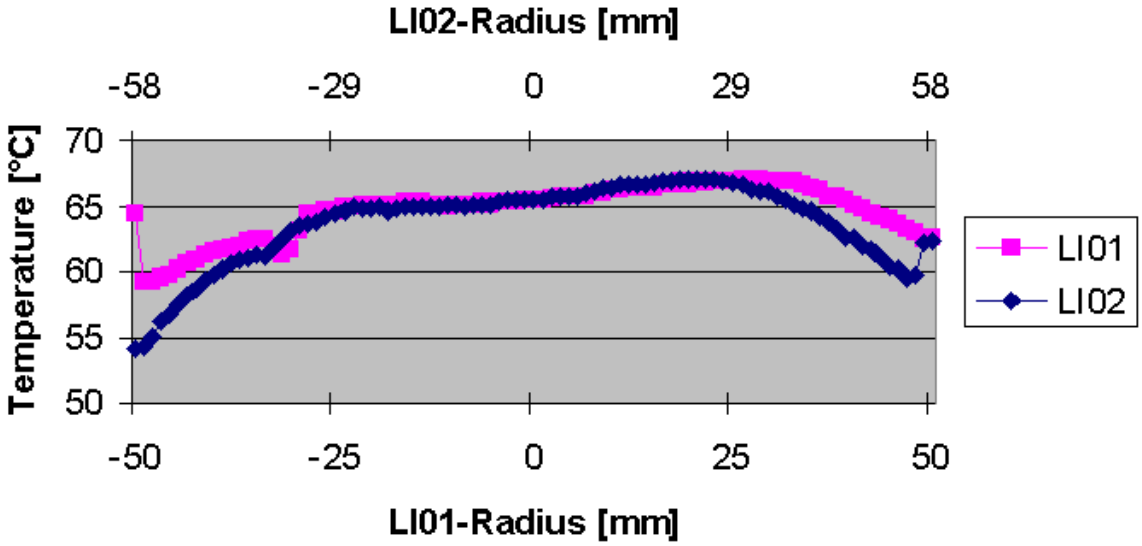

Figure 107. Surface temperature variation at two different locations.

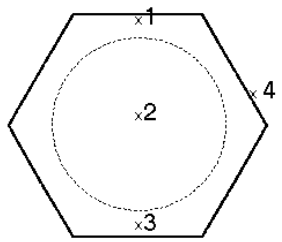

Figure 108. Spot locations for IR camera temperature measurement.

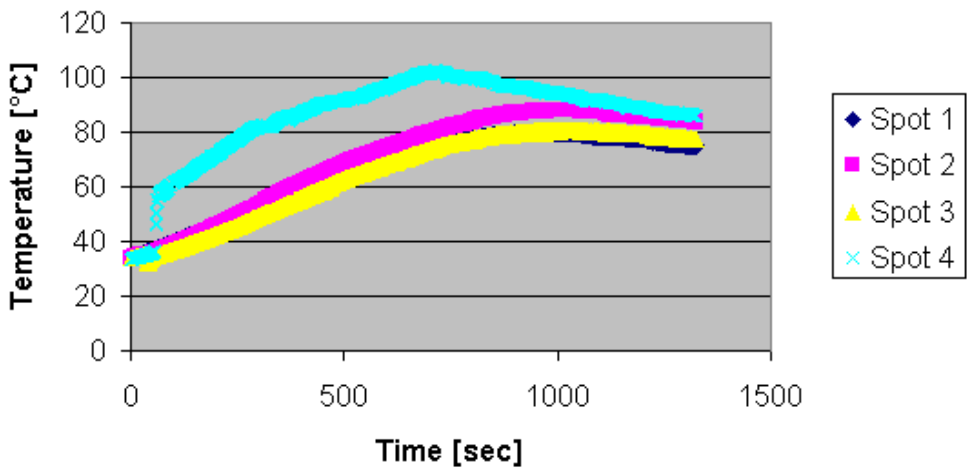

Figure 109. Time/temperature response during one-step induction bonding as measured by the IR camera.

Figure 110. Single-step bonded multi-layer composite specimen.

9.6 Conclusions – Mesh Susceptor Repair and Remanufacturing

The current work has established that induction heating using conductive mesh susceptors can be used to rapidly cure thermosetting adhesives under a VOC-reducing vacuum condition. We also established that the presence of these susceptor materials, although not

optimized, does not adversely affect the mechanical performance of the bond line when considering the low scatter in lap shear strength. Additional work is needed to optimize both the susceptors and the resin systems. Optimization of the process will be paralleled with more aggressive strength and durability testing.

10 Particle Susceptors - Development

10.1 Particle Susceptors in Adhesives

One disadvantage of metal screen susceptor materials is that there is no inherent upper limit to the temperature that the metal screen will achieve during processing. To prevent bond line or adherend damage due to overheating, temperature sensing and power regulation are necessary, or the process must be repeatable enough to allow for *a priori* determination of input power requirements.

An alternate approach is to use magnetic particles as the susceptor material. Magnetic materials heat inductively due to magnetic hysteresis mechanisms. The magnetic energy density of these materials drops drastically near their Curie temperature. If a susceptor is designed so that it heats only due to magnetic mechanisms, it cannot be inductively heated beyond its Curie temperature. This behavior imposes an inherent temperature limit on the induction heating process.

To capitalize on this effect, materials were synthesized with high magnetic energy densities and controllable Curie temperatures. The heating behaviors of these materials are shown in Figure 111. Note the rapid heating and steady dwell temperatures of these materials. Matching the dwell temperatures with a desired processing temperature enables the process temperature to be maintained without temperature sensing or power regulation. For example, these magnetic powders can be mixed into elevated-temperature adhesives. Matching the Curie temperature of the powders with the cure temperature of the adhesive enables the adhesive to be cured in an induction field.

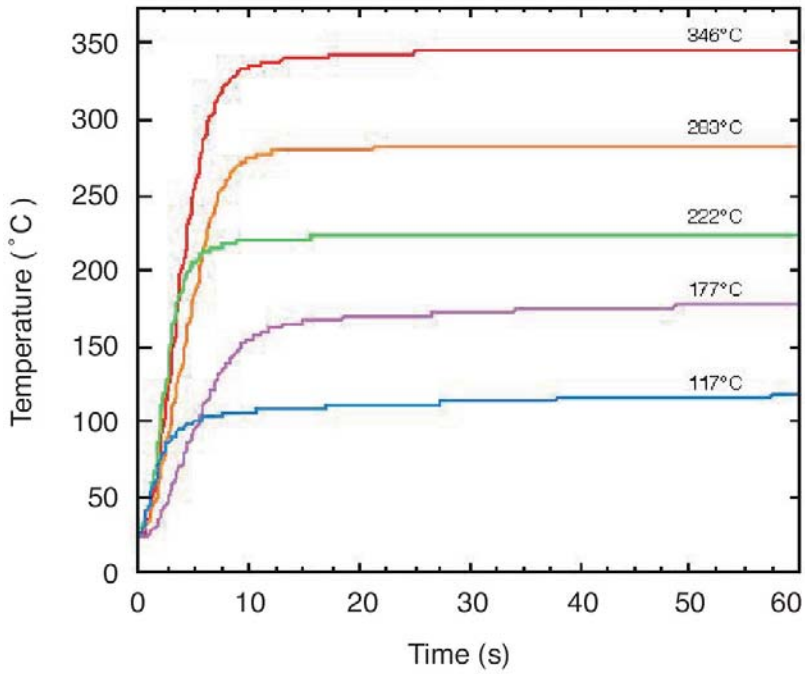

Figure 111. Control of Heating Behavior by Magnetic Particle Composition.

10.2 Experimental Materials and Equipment

The adhesive system chosen was a dicyandiamide (DICY) cured epoxy that is ETBN toughened. This adhesive was chosen for its excellent mechanical properties, phase separation characteristics, and cure temperature, which is similar to the dwell temperatures of the magnetic particles. The adhesive's mechanical strength comes from two contributions, networking of the monomers and toughening from the rubber particles.

The adhesive's formulation is environmentally stable for room temperature storage providing a working life of at least one year. The cured adhesive possesses the generally desired characteristics of high thermal stability (250°F), good solvent resistance, and low moisture uptake.

The magnetic susceptor particles chosen were FP160 nickel zinc ferrite (PowderTech Corp., Valparaiso, IN). The nickel zinc ferrite is a soft ferrite. Although the particles do not have a clear Curie temperature, the magnetization does diminish gradually with temperature. The saturation magnetization of the particles is approximately zero (non-magnetic) by 250°C, producing a limiting condition on heating.

As-received magnetic particles were ball milled for 3 hours prior to the addition of the DICY adhesive. This step reduces the particle size to approximately 10 to 100μm in diameter.

In order to minimize the impact of particle settling in the adhesive matrix during processing and storage, the milled FP160 was coated with a reactive surface modifier. The modifier selected was (3-glycidoxypropyl)trimethoxysilane (GPS), which was added to the dry FP160

through 1% water solvent casting. The treated particles were filtered and heat-treated at 93°C for one hour prior to mixing with the resin. The silane monomer adds reactive functionality that chemically binds the particles to the matrix during the cure process.

The adherends were constructed of forty plies of unidirectional glass fiber/8551 epoxy prepreg. After fabrication they were cut into 1.0 x 4.0 x 0.2 inch pieces.

An induction unit operates by sending an AC current through a conductive coil, which then generates an AC magnetic field. This study uses an Ameritherm (Scottsville, NY) induction unit, which operates at frequencies between 10-15 MHz. The magnitude of the AC magnetic field is adjusted by the "load power" setting. The "load power" or LP increases the amount of current that enters the coil and thus increases the magnetic field. The LP ranges from 0 to 1500W, although this value does not correspond to the amount of power being dissipated within the coil. The magnetic field strength is also not necessarily linearly proportional to the load power. Although, the magnetic field produced is not linearly proportional with the load power.

The coil used on the induction unit has a unique geometry, a solenoid designed specifically to process five lap shear specimens simultaneously (Figure 112). The coil is a three turn copper solenoid with the copper tube having a diameter of 0.125 inches. The solenoid's dimensions are approximately 6.5 inches in width, 2 inches in height and 1.5 inches in length with more rounded corners.

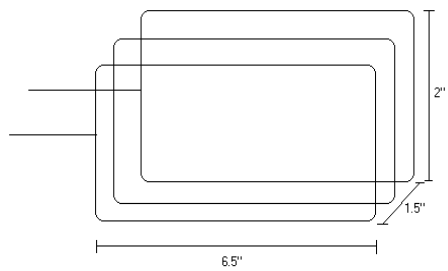

Figure 112. Geometry of the induction coil.

With this geometry, it was possible to process all five of the specimens simultaneously thereby decreasing processing inconsistencies. The 0.5-inch overlap of the lap shear specimens were placed next to one another as shown by Figure 113.

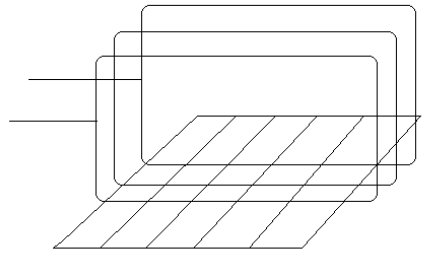

Figure 113. Location and position of the lap shear specimens during processing.

The frequency is dependent upon the inductance of the coil and the capacitance within the circuit. The frequency is given by,

$$f = \frac{1}{2\pi\sqrt{(LC)}}, \tag{1}$$

where L is the inductance of the coil and C is the capacitance within the circuit. Thus a particular combination of capacitance and inductance must be chosen for the frequency to fall between the induction unit's specifications.

We measured the coil's inductance with an LCR meter, to be 1.042μH. Configuring the Ameritherm unit to an internal capacitance of 100pF, the theoretical frequency should be 15.57MHz. This is within 8% error from the actual frequency reported by the Ameritherm unit of 14.38MHz.

A thermocouple was not chosen as a temperature sensor because of two reasons. Most thermocouples are composed of metal, which then can heat inductively. Also, thermocouples use a voltage difference to measurer the temperature and an AC magnetic field can produce noise to alter the voltage signal. In order to obtain accurate temperature data, we used a fiber optic temperature sensor, manufactured by FISO (Quebec, Canada), embedded in the bond line of the lap shear specimens. This experiment was performed once to obtain the correct temperature measurements and was not conducted for all of the specimens. The measurement zone of the fiber optic temperature sensor is approximately 10 millimeters in length, and located at the end of the sensor (Figure 114).

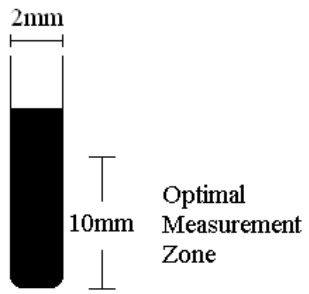

Figure 114. Optimal measurement zone of the fiber optic temperature sensor.

Figure 115 displays the fiber optic sensor geometry in the lap shear bond line. The fiber optic sensor's entire measurement zone is embedded at the center of the bond line. A groove was made in one of the lap shear surfaces, so that the fiber optic sensor was in direct contact with bonding surface. A piece of Kapton film was placed over the fiber optic sensor so that it could be removed from the bond line once the experiment was complete.

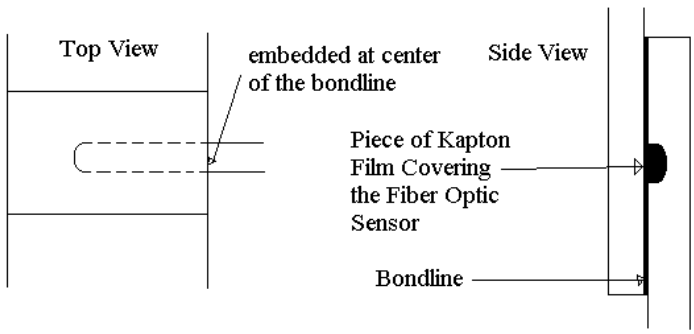

Figure 115. Top and side views of the position of the fiber optic temperature sensor within the adherend.

A differential scanning calorimeter (DSC) was used to analyze the cure characteristics of the epoxy. An isothermal method was used for the analysis. First, the sample chamber with the reference is heated to 180°C. The sample is then placed into the sample chamber at temperature. The crossover point ($\Delta H=0$) was used as the initial cure time ($t=0$) in the conversion analysis.

10.3 Sample Preparation

Preparing the surface of the lap shear specimenss consisted of surface abrasion and then cleaning the remaining surface. The surface abrasion was accomplished by grit blasting with 50 μm aluminum oxide grit at 80 psi. The bonding area was the only surface treated by abrasion. Once this was completed, the specimens were cleaned with deionized water and allowed to dry. When the lap shear specimens were dry, acetone was applied to remove any residual contaminants off the surface.

The epoxy adhesive was blended with the magnetic particles at 50% by weight (20% by volume). The mixing was done by hand, until particle wet-out was achieved, followed by dispersion in a high-speed mixer (7000 rev/s) for approximately twenty minutes. Care was taken to keep temperatures below 70°C during blending. After high-speed mixing, the mixture was placed in a vacuum chamber at full vacuum (25 – 28 mmHg) and 50°C to degas for sixteen hours.

The adhesive was applied to the pretreated area of the lap shear, 2.54 cm wide x 1.27 cm overlap (Figure 116). It was spread on both lap shear adherends on the area as an even coat approximately ten mils thick. Finger pressure was used to insure intimate contact between the adherends. Kapton® tape was then wrapped around the bond area to ensure that contact was maintained during the cure. A small amount of flash remained on both sides of the specimen.

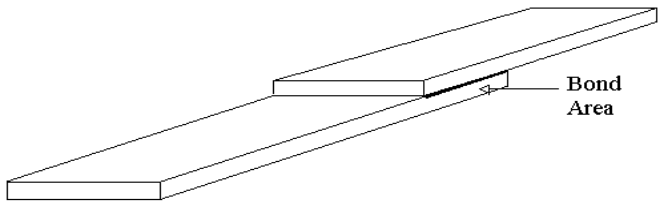

Figure 116. Surface area bonded between two lap shear adherends.

10.3.1 OVEN CURED SAMPLES

To characterize baseline adhesive performance, two sets of five lap shear specimens were oven cured at 175°C for one hour. The first set did not contain any magnetic particles, only the adhesive formulation. The second set contained the particle-doped adhesive described previously.

10.3.2 INDUCTION CURED SAMPLES

The lap shear specimens were placed within the coil, on top of four sheets of Kapton film to prevent electrical arcing from the coil. All five of the lap shear specimens were processed simultaneously for each set of experimental conditions. They were located in the center of the coil (but resting on the lower coil windings), directly adjacent to one another as previously described. Table 54 displays the powers and times for each set of samples cured in the induction field.

Table 54. Power and Process Times in Induction Field

Power Level	Processing Times		
500 W	15 Min	30 Min	60 Min
1000 W	15 Min	30 Min	60 Min
1500 W	13 Min	30 Min	

10.3.3 MECHANICAL TESTING SETUP

All of the mechanical testing was done with an Instron 4505, with a 10kN load cell. There was a consistent length of 11.43cm between the pull grips preceding each pull test. To minimize the preload due to bending, shimming tabs were placed on either side of the lap joint. Figure 117 illustrates the Instron geometry.

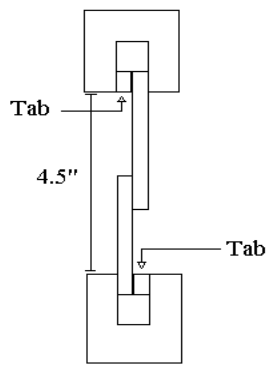

Figure 117. Geometry for the lab joint test including composite shims for nominal alignment.

10.4 Adhesive Kinetic Characterization

10.4.1 PARTICLE EFFECT ON CURE KINETICS

To determine whether the magnetic particles influenced the cure chemistry of the adhesive system, a cure kinetics comparison was made. 180°C isothermal DSC runs were performed on the uncured adhesive, both with and without magnetic particles. Figure 118 shows conversion as a function of time for two experimental runs.

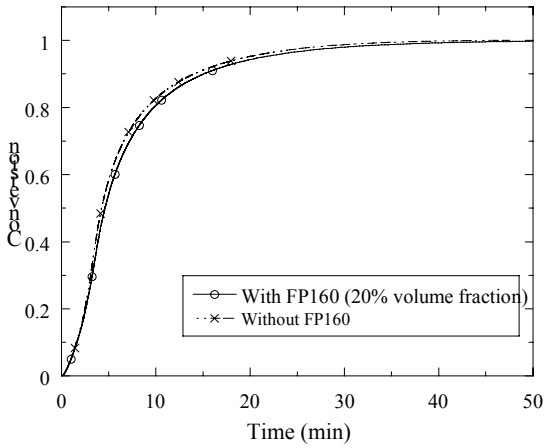

Figure 118. Conversion versus time for DICY cured epoxy adhesive using isothermal method in a DSC with and without the magnetic susceptor particles

The conversion rates for both the adhesive with the magnetic particles and the adhesive without the magnetic particles are approximately identical. They both react initially at the same rate and both reach full conversion ($\alpha = 1$) at the end of the cure cycle (50 minutes). Therefore, as expected, the addition of the magnetic particles does not appear to impact the cure chemistry for the adhesive.

To quantify the complete cure kinetics for the DICY adhesive system, isothermal runs on the DSC were performed at varying temperatures. The runs were performed using unfilled adhesive, since the results of section 3.1.1 showed that the magnetic particles do not affect adhesive cure chemistry. Figure 119 shows conversion histories for each temperature.

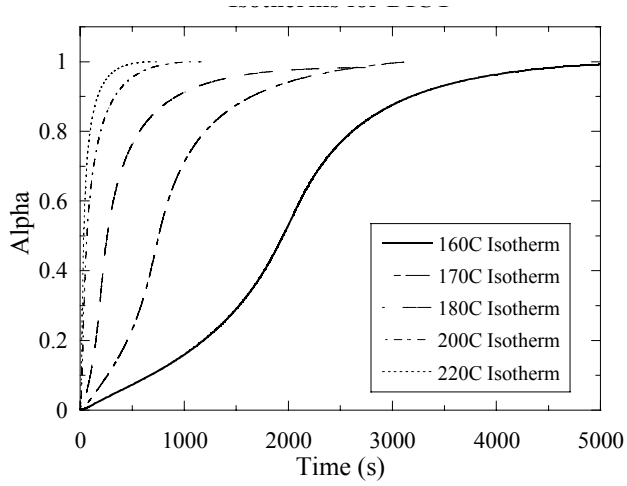

Figure 119. Conversion versus time for DICY cured epoxy adhesive using isothermal method in a DSC with and without the magnetic susceptor particles.

From the graph, it can be seen that fastest cure occurs in the 220°C isotherm, achieving almost full conversion within six minutes. The 160°C isotherm has the slowest cure, achieving almost full conversion within 80 minutes. The rest of the isotherms cure accordingly, an increase in temperature resulting in a quicker cure. Table 55 lists time to reach 95% cure for each of the isothermal runs.

Table 55. The amount of time to reach 95% cure for each temperature.

Temperature (°C)	Time to reach 95% Cure (min)
160	57.138
170	36.367
180	23.080
*190	14.647
200	9.296
*210	5.899
220	3.744
*Note: The 190°C and 210°C isothermal cure times have been interpolated using Equation 2.	

Figure 120 shows time to achieve 95% cure as a function of temperature. This data is well modeled by an Arrhenius equation:

$$F(T) = 0.2359e^{\frac{-12876.7}{RT}}, \qquad (2)$$

where R is the universal gas constant, T in degrees Celsius, and the equation fits the data with 99.921% accuracy. This graph and curve fit are useful for estimating necessary cure times as a function of temperature.

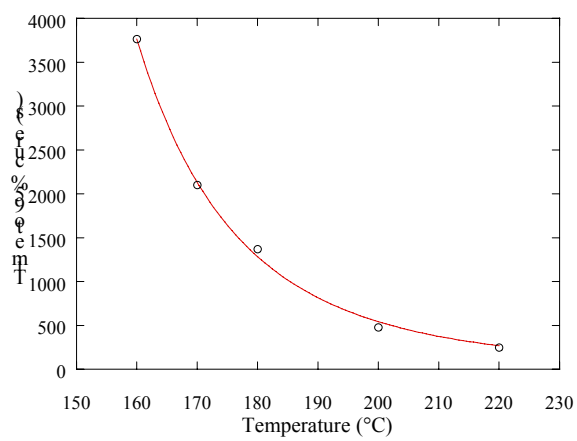

Figure 120. Graphic representation of cure time to 95% conversion as determined using isothermal DSC.

10.4.2 DEGRADATION LIMITS

In order to determine the thermal degradation limits of the adhesive system, a DSC run was performed on the unfilled adhesive. A heating rate of 10°C per minute was used up to 375°C. Figure 121 demonstrates a typical heat flow condition showing both cure (100-200°C) and degradation >250°C for the adhesive system in a nitrogen environment.

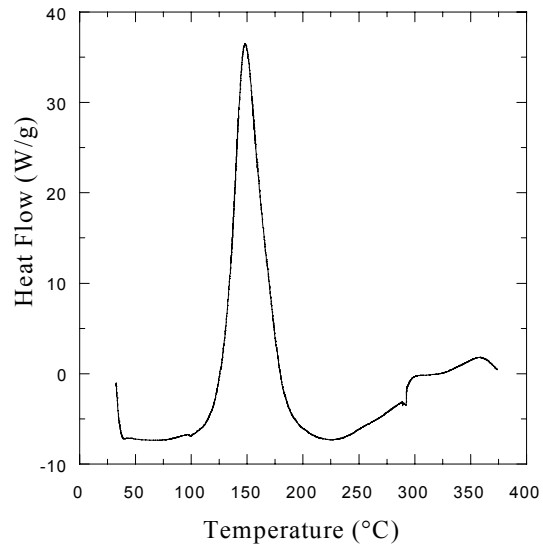

Figure 121. DSC experiment of DICY adhesive system determining the onset of thermal degradation.

Complete cure for the adhesives was evaluated based on the peak area between 100 and 220°C. However, above 250°C, some heat is observed and is consistent with continued cure of the adhesive at elevated temperatures. However, above 280°C, the adhesive seems to show evidence of degradation. This is consistent with reports that DICY/cured epoxies are thermally stable to 250°C. In this effort, our regulated temperatures should not exceed this temperature thresh-hold in order to keep away from degradation impacts in the material performance evaluations.

A measurement of the temperatures reached within the adhesive was done with a fiber optic sensor embedded within the bond line of the two adherends. Figure 122 depicts the temperature reached within the bond line at 1500W, with 50% weight fraction of magnetic particles.

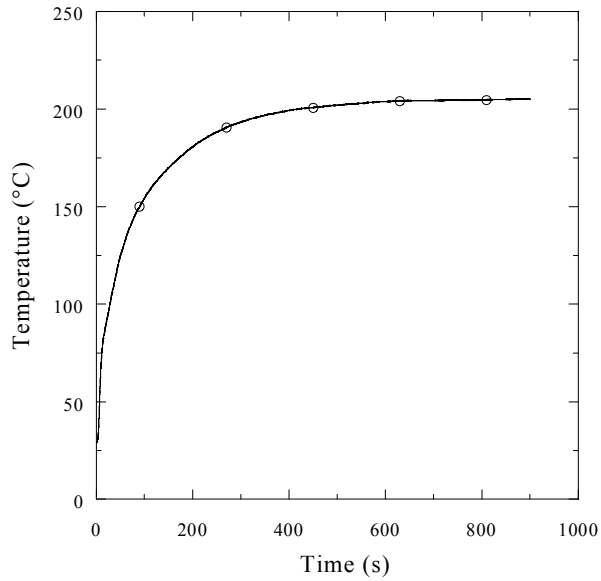

Figure 122. The heating rate of the DICY adhesive system, with 20% volume fraction magnetic susceptor particles, with a power setting of 1500W.

It can be seen that the temperature of the adhesive reaches equilibrium in approximately five minutes. In this particular experiment, the load power was set to 1500W and asymptotically approaches a value of approximately 210°C. Once it has reached this temperature, the adhesive dwells at this temperature regardless of time exposed to the induction field. The maximum temperature reached in the experiment, is well blow any degradation temperature so we can confidently process using this method.

We were unable to directly measure temperature histories at power levels of 500W and 1000W because of equipment failure. However, previous experiments with a similar adhesive system achieved temperatures of 220°C, 180°C, and 165°C at 1500W, 1000W, and 500W, respectively. The heating rate changed only slightly for various power levels, with the time to reach the dwell temperature ranging from five to seven minutes. We expect similar general heating behavior for the adhesive system used in this study.

10.4.3 MECHANICAL PROPERTIES

Table 56 shows the lap shear strength for the oven-cured samples.

Table 56. Measured Lap Shear Strengths For Oven-Cured Samples.

Thermal Cure	Displacement At Failure (cm)	Length (cm)	Width (cm)	Load At Failure (N)	Lap Shear Strength (MPa)	Average (MPa)	STD (MPa)
Without FP160	0.371	1.232	2.629	603.018	38.9043	30.2832	5.415614
175°C for 1 Hour	0.296	1.42	2.649	378.384	24.4118		
(No bond line controls)	0.327	1.377	2.637	424.312	27.3749		
	0.356	1.443	2.55	473.015	30.5170		
	0.306	1.356	2.619	468.221	30.2078		
With FP160	0.317	1.367	2.601	419.327	27.0533	28.2551	1.384195
175°C for 1 Hour	0.368	1.367	2.662	440.679	28.4309		
	0.382	1.384	2.573	468.607	30.2327		
	0.259	1.379	2.616	445.388	28.7346		
	0.312	1.344	2.662	415.773	26.8240		

The average mechanical strength of the oven-cured adhesive without the addition of the magnetic particles was 30.3 MPa. The average mechanical strength with the addition of the magnetic particles was 28.3 MPa, or a 6.5% decrease in mechanical strength. Therefore, the addition of the magnetic particles slightly diminishes the mechanical strength of the adhesive system. We can attribute part of this loss in strength to the increased stiffness at the bond line due to the high filler volume. The increased stiffness in the bond line incurs an increased stress load in less resin, resulting in higher overall strains.

Table 57 depicts the lap shear strengths for the induction-cured samples. All of the lap shear specimens displayed a cohesive failure. There was no correlation between location in the induction coil and the mechanical strength of the individual lap joints.

Table 57. Measured Lap Shear Strengths For Induction-Cured Samples.

Processing Power (Watts)	Processing Duration (min)	Displacement at Failure (cm)	Length (cm)	Width (cm)	Load At Failure (N)	Lap Shear Strength (MPa)	Average (MPa)	STD (MPa)
500	15	0.066	1.394	2.591	123.005	7.93	4.9	2.8
		0.034	1.326	2.642	48.038	3.09		
		0.061	1.369	2.642	100.658	6.49		
		0.027	1.367	2.596	31.240	2.01		
500	30	0.332	1.237	2.626	316.891	20.44	18.8	2.3
		0.434	1.410	2.609	320.098	20.65		
		0.302	1.384	2.639	315.281	20.34		
		0.234	1.476	2.710	264.782	17.08		
		0.258	1.410	2.573	243.652	15.71		
500	60	0.329	1.349	2.637	383.439	24.73	23.7	1.0
		0.300	1.367	2.606	368.106	23.74		
		0.330	1.247	2.601	364.823	23.53		
		0.288	1.364	2.621	379.177	24.46		
		0.318	1.384	2.586	343.017	22.13		
1000	15	0.244	1.374	2.642	301.466	19.44	18.7	1.9
		0.316	1.316	2.644	321.132	20.71		
		0.229	1.387	2.581	276.742	17.85		
		0.346	1.488	2.642	244.932	15.80		
		0.275	1.318	2.621	301.806	19.47		
1000	30	0.240	1.341	2.672	258.878	16.70	19.5	1.7
		0.350	1.298	2.629	304.734	19.66		
		0.269	1.359	2.588	302.799	19.53		
		0.362	1.359	2.667	326.253	21.04		
		0.439	1.273	2.629	321.667	20.75		
1000	60	0.333	1.496	2.654	341.904	22.05	19.4	2.1
		0.307	1.377	2.596	256.807	16.56		
		0.290	1.359	2.609	295.898	19.09		
		0.271	1.270	2.591	323.252	20.85		
		0.368	1.349	2.619	287.231	18.53		
1500	13	0.331	1.303	2.731	268.768	17.33	17.7	1.6
		0.244	1.260	2.621	309.230	19.95		
		0.245	1.349	2.619	250.507	16.16		
		0.220	1.344	2.639	269.168	17.36		
1500	30	0.244	1.372	2.611	312.782	20.17	17.7	2.5
		0.202	1.379	2.621	289.767	18.69		
		0.154	1.410	2.625	212.961	13.73		
		0.189	1.326	2.583	266.299	17.18		
		0.207	1.351	2.626	289.804	18.69		

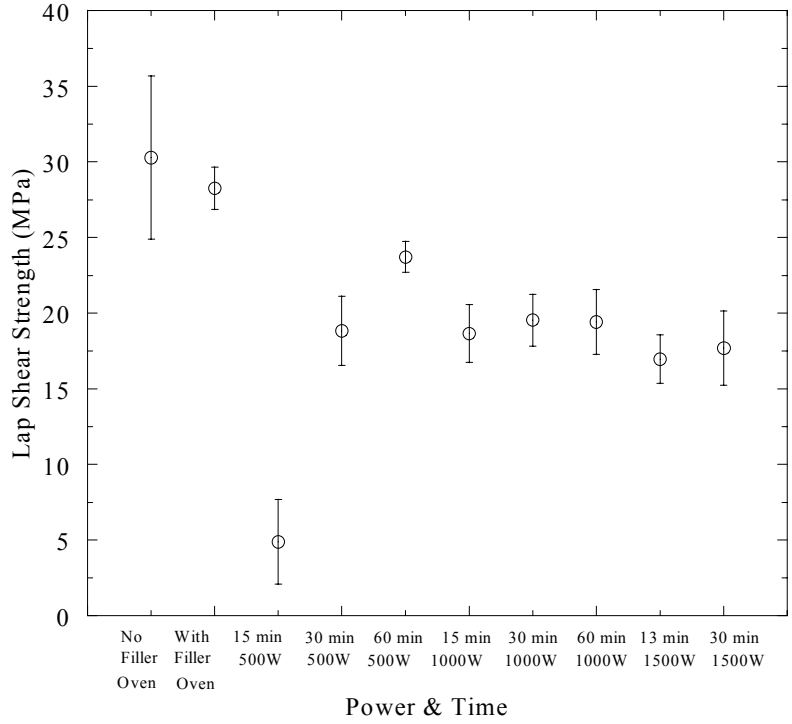

Figure 123. Average lap shear strengths for all processing conditions.

Figure 123 shows the average lap shear strength and standard deviation for each of the processing conditions. The maximum strength achieved by induction processing occurs at 500W for sixty minutes. At 500W for fifteen minutes, the adhesive still possessed liquid-like properties (the flash was wet to the touch), and did not provide significant mechanical strength. At 1000W, there was not a significant improvement in mechanical strength between processing for fifteen minutes and sixty minutes. The same trend occurs for processing at 1500W where strength only increased marginally with increased processing time. This shows that at high power levels further exposure to the induction field will not greatly enhance mechanical strength. All of the induction-cured samples exhibit lower strength than the oven-cured sample, with the 500W for 60-minute case reaching 84% of the oven-cured filled sample.

10.5 Particle Effects

10.5.1 Particle Effect on Adhesive Cure Chemistry

The DSC measurements demonstrated that the magnetic particles do not interact chemically with the DICY adhesive. This result is not surprising since they are stable oxide particles that do not give off any gases or interact with the organic chemistry is the adhesive.

10.5.2 Toughened Adhesives

The strength of a thermosetting adhesive is determined by two different mechanisms: network formation and toughening effects. Network formation refers to the degree of completion of cure, with strength increasing continuously as the degree of cure approaches 100% conversion of reactive groups. In general, unmodified thermoset epoxies and acrylic type adhesives are relatively brittle and fail under relatively low stress conditions. Therefore various toughening modifications are commonly designed into thermosetting adhesives.

A phase-toughened adhesive contains rubber particles, which improve the adhesive's fracture toughness. Adhesive failure typically occurs due to crack formation and propagation. If a crack reaches a rubber particle, the low modulus of the rubber phase reduces the local stress concentration at the crack tip, slowing the growth rate. As particle size decreases, the dispersion of particles throughout the adhesive matrix is improved, increasing their toughening effect. However, if the rubber particles are too small, their toughening effect is negligible. Therefore, there is an optimal particle size for achieving maximum adhesive toughness [78].

There are two traditional approaches to incorporating secondary particles in an adhesive. The first method is adding the preformed particles to the adhesive *a priori*. In this approach, the optimal size of the particles is selected prior to curing and is well controlled. The most significant drawback is that the adhesive viscosity dramatically increases, making handling difficult and often requiring a change in formulation to improve substrate wetting and bonding. Additionally, the preformed particles perform less efficiently than particles formed *in situ* [79]. The second approach is to formulate the adhesive to develop particles during the cure process through phase separation. Typically, the secondary phase is a modified rubber or thermoplastic that has a high compatibility with the uncured monomer of the adhesive. However, on heating, the adhesive network begins to crosslink and the particles begin to coalesce and drop out from the forming network due to decreases in favorable mixing [80]. The particle size continuously grows during cure until molecular motion is limited by vitrification. Since the processes of monomer aggregation and network formation have independent kinetic characteristics, different processing histories result in different sizes and numbers of equilibrium particle domains. Additionally, very rapid processing can result in trapping of the secondary tougheners in the matrix and create decreased matrix performance characteristics both thermally and mechanically.

10.5.3 Particle Effect on Bond Mechanical Performance

The presence of the magnetic particles, at 50% wt., within the adhesive did appear to significantly affect the average lap shear strength. Among the variables that should be

addressed in future efforts is constant bond line and adherend thickness, which will reflect in more uniform performance in adhesive testing. If the specimen with the highest lap shear strength in the oven cured unfilled sample is discounted, the average load at failure between the filled and unfilled DICY adhesive is equivalent within statistical error.

10.6 Analysis of Strength Trends

Obviously, thermal histories play a crucial role in the curing of the adhesive. In general, induction heats the adhesive rapidly and then dwells at some relatively stable temperature. Therefore, the only effect of time at a constant power, after the initial five-minute ramping period, is further time spent at the dwell temperature. The heating ramp rate only alters slightly between various power settings, but in all cases approaches its dwell temperature within five to seven minutes. Therefore, the major effect of the power is the determination of the final dwell temperature, with higher power levels producing higher dwell temperatures. We know this effect to be a result of the impurities associated with the FP160 selected for the experiments.

Based on the DSC runs and temperature histories, we can assume that thermal degradation is probably not occurring within the adhesive. According to the DSC run, the onset of degradation begins around 280°C, while the FISO data indicates a maximum temperature of 210°C in the adhesive during induction processing. Also, the 1000W and the 1500W cases show no decrease in mechanical strength with longer exposure to the induction field. These two observations imply that thermal degradation of the adhesive is not occurring.

In the 1000W and the 1500W case, after 15 minutes of exposure to the field, there was negligible increase in mechanical strength. Therefore is likely that the samples were fully cured after the initial 15 minutes.

In the case of 500W, more time in the induction field caused an increase in mechanical strength. Therefore, the degree of cure must be increasing with time.

We know that the maximum mechanical strengths of the 500W case are larger than that of the 1000W, which is larger than that of the 1500W case. It was concluded earlier that the 1000W and the 1500W cases were fully cured after 15 minutes. Since, all of the cases are probably fully cured, the most likely difference is the toughening phase size. The 500W case is better toughened than the 1000W case, which is better toughened than that of the 1500W case. So the better mechanical strengths of 500W case to the 1000W, and the 1500W case, is probably due to the toughening effect.

Most likely this is due to the fact that the rubber particles were able to attain larger sizes. Since the rubber particles aggregate to larger sizes over time, the cure at higher powers, and higher temperatures, must be curing too fast for the optimal particle size to form. Therefore, the 500W case probably allowed for the curing to occur slowly enough that rubber particles could attain larger diameters than the 1000W case or the 1500W case.

The fact that the 500W case has mechanical strengths weaker than that of the oven cured base samples could be two possible reasons. There is the possibility that the 500W for 60 minutes was not fully cured. To test this possibility, another experiment would have to be performed for 500W for 120 minutes. If the lap shear strength of the new experiment would yield higher results then we could conclude that the 500W for 60 minutes was not fully

cured. But, if the data yielded equal strengths than we could conclude that the 500W for 60 minutes was fully cured. The other possibility is that the 500W case for 60 minutes was fully cured but the toughened phase particles are too small.

In the three load powers performed, it seems as though the 500W produces the optimal time-temperature profile for the ETBN toughened DICY cured epoxy adhesives. It comes closest to approximating the loads yielded by the oven-cured samples.

11 Particle Susceptors – Application to Repair of Integral Armor

While the induction-based repair procedure has the potential to reduce hazardous waste, it is essential that the repaired part meet the performance requirements dictated by the application. Hence, the initial work done under the program focuses on evaluating the performance of induction-based repair procedures. The goal is to obtain performance similar to that achieved with conventional repair procedures. The testbed chosen was repair of damage in Composite Integral Armor (CIA), which is the next-generation armor solution for the U.S. Army.

11.1 Ballistic Damage

Composite Integral Armor (CIA) panels were impact tested with machine gun projectiles at a nominal impact velocity of 850 m/sec. The armor panels were clamped on a steel fixture at four corners with C-clamps. Figure 39 shows a schematic of the test fixture. Two pieces of wood (38-mm × 19-mm × 305-mm) were placed between the armor target and the steel fixture. A 2024 aluminum witness plate (0.51-mm thick) was placed behind the armor target. The impact velocity and residual velocity of the projectile was measured by taking X-ray radiographs at controlled time intervals. The pitch and yaw angles were also measured from radiographs and were found to be minimal and in the range from –2º to 2º. The maximum back face dynamic deflection of the armor was measured from the deformation of the witness plate, and the maximum permanent deflection (residual deflection) after springback was measured directly from the back face of the armor after the projectile impact. The contour of dynamic deflection along a chord of the witness plate was also measured.

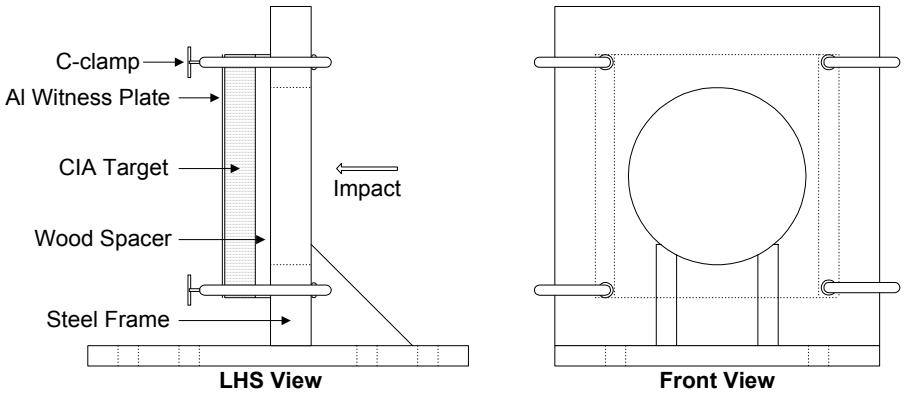

Figure 124. Ballistic Test Fixture.

The CIA panels after ballistic impact and penetration have been systematically investigated to identify the damages and associated mechanisms in individual layers. The panels are mechanically dissected layer-by-layer, and digital pictures are taken at every step. This dissection process also helped identify the required steps for repair of these impact damaged armor panels. Following removal of the cover, ceramic, and rubber layers, the damaged backing plates are nondestructively tested using ultrasonic C-scan. A one-inch-diameter piezo-electric transducer has been used (1.0 MHz frequency). These scans are compared to the scans of undamaged panels to identify macro-damage such as delaminations.

11.2 Results and Discussion

The CIA targets without delaminations (designated "B" or "Baseline") and with implanted delaminations (designated "D" or "Delam") are identified with numbers from B0 to B5 and D1 to D5, respectively. Figure 40 shows the residual penetration velocities of all targets. Zero residual penetration velocity represents incomplete penetration. Out of six baseline armor targets, complete penetration is observed in three targets (B0, B1, and B5) at the nominal impact velocity (850 m/sec.). Three Delam targets (D2, D3, and D5) were complete at the nominal impact velocity. While these test results are inconclusive (approximately half of the targets of each type is penetrated by the projectile), the ballistic performance of the Baseline and Delam armor targets appears similar. These results suggest that the critical delamination size that would significantly reduce ballistic performance would be larger than the 100-mm studied here.

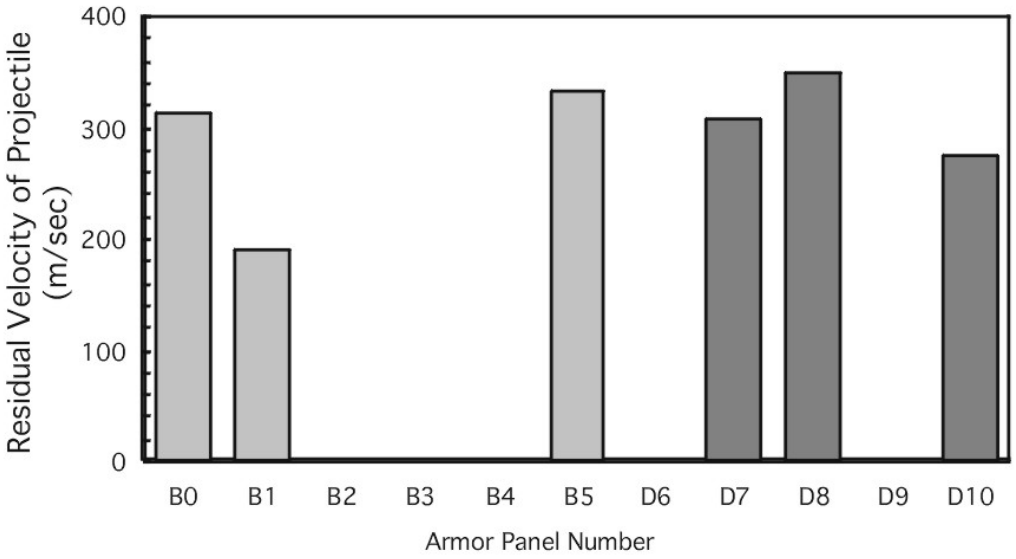

Figure 125. Residual Velocity After Penetration (Impact Velocity = 850 m/sec).

The average dynamic deflection contour along the armor diagonal and the maximum residual deflection are presented in Figure 126. The dynamic deflection represents the maximum deformation that occurred during the impact event. If the penetration is complete, the dynamic deflection of the central region is obtained through extrapolation. The maximum average dynamic deflection of Baseline and Delam armor targets is found to be 40 mm (Figure 126a). However, the scatter in the Delam targets is more than that of the Baseline targets. The average maximum residual deflection (Figure 126b) of Baseline targets is 6.3-mm and that for Delam targets is 9.2-mm. The higher residual deflection of Delam targets suggests higher permanent macro- and micro-damages induced in the backing plate, which is not evident from the average dynamic deflection.

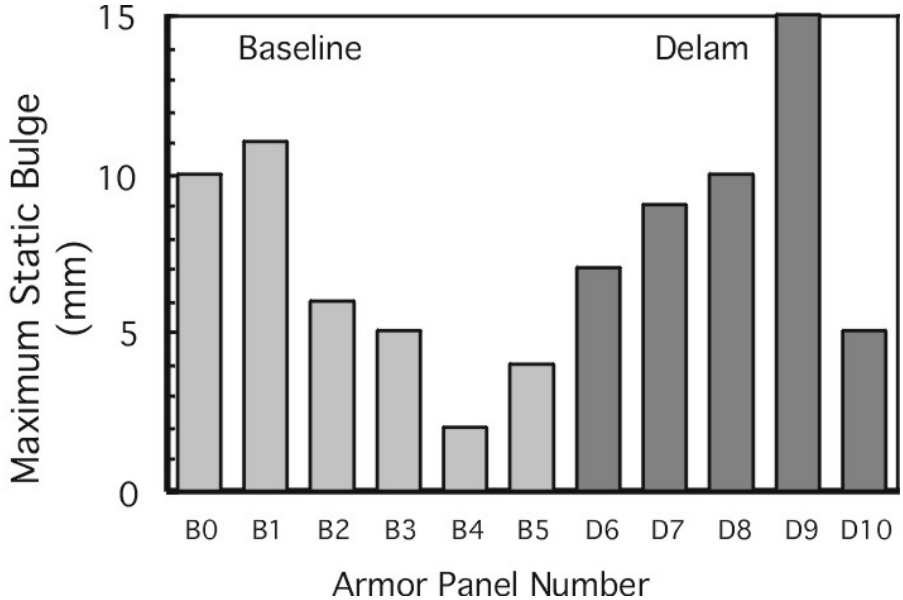

(a) Maximum Static Bulge

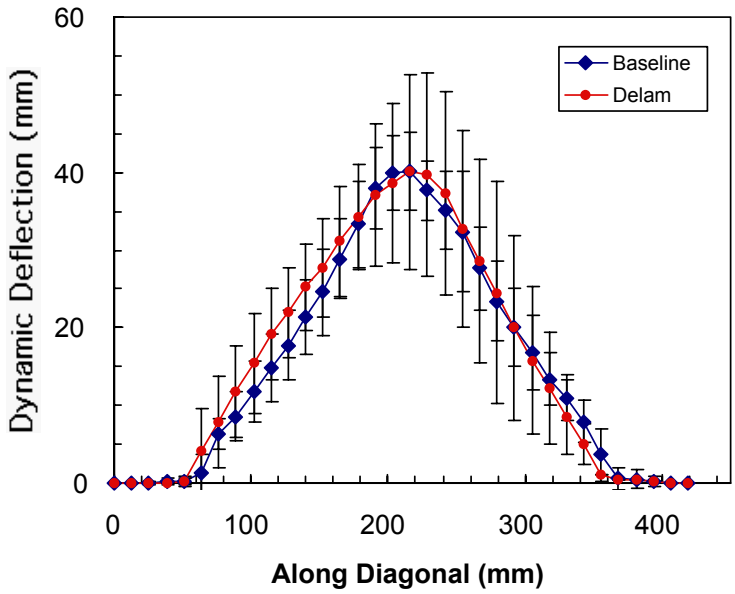

(b) Dynamic Deflection Along Armor Diagonal

Figure 126. Dynamic Deflection and Static Bulge.

Two representative recovered backing plates (as described later) are sectioned at the impact centerline to examine the extent of delamination (Figure 127). Wire spacers are used to make all the delaminations visible. Both the Baseline and Delam panels show delaminations extended up to the edge of the panels. However, the delamination of the Baseline panel is distributed close to the impact side, while the Delam panel shows delamination growth only in the plane of pre-implanted delaminations. The uniform distribution of delaminations through the thickness in the Delam back plate represents lower bending stiffness than the baseline and explains why the maximum residual deflection is higher.

(a) Baseline – Complete

(b) Delam – Incomplete

Figure 127. Cross-Section of Recovered Backing Plate Showing the Extent of Delamination.

(a) Baseline B1 – Complete

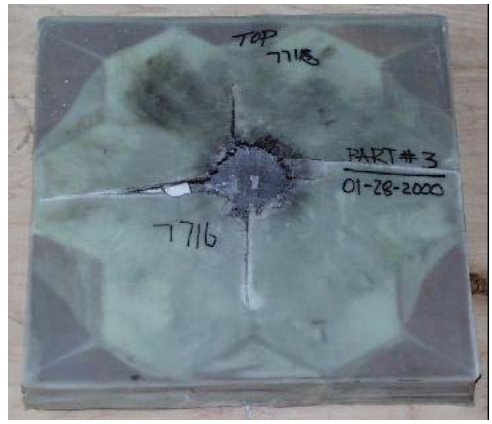

(b) Baseline B3 – Incomplete

(c) Delam D1 – Incomplete

(d) Delam D3 – Complete

Figure 128. Damage and Erosion of Cover Layer.

The extent of damage in the cover layer is shown in Figure 128. The cover layers show damage/erosion of about 50-mm diameter and tearing along the in-plane 0º and 90º directions. The diameter of the projectile is much smaller, which indicates that ejected ceramic particles eroded the cover. Extensive damage of the cover is found when the ceramic fracture is severe, and most of the surrounding tiles are also damaged extensively, as shown in Figure 44. The normal force created by the fractured ceramic confined by the cover and backing plate is sufficient to rupture the cover. The cover layer is carefully removed from the ceramic tiles to match the hexagonal geometry (Figure 129). The damage in the central tile is severe and has been transformed into a fine ceramic powder. However, the surrounding tiles are also badly damaged in some cases. The extent of damage in the surrounding tiles (sympathetic damage) is comparable for both baseline and Delam configurations. Significant difference in the level of sympathetic damage exists between complete and incomplete penetration. The broken ceramic tiles and corresponding rubber layers are then removed. The surrounding wooden pieces are also removed to recover the backing plate.

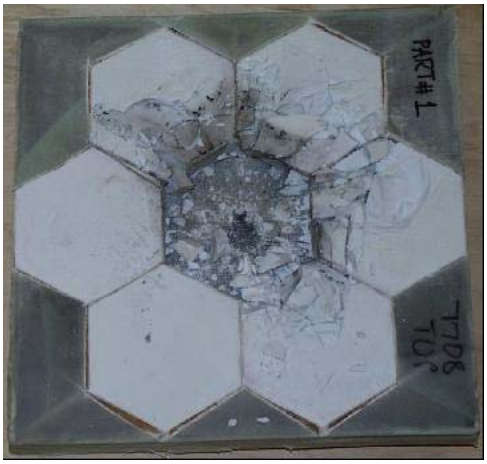

(a) Baseline B1 – Complete

(b) Baseline B3 – Incomplete

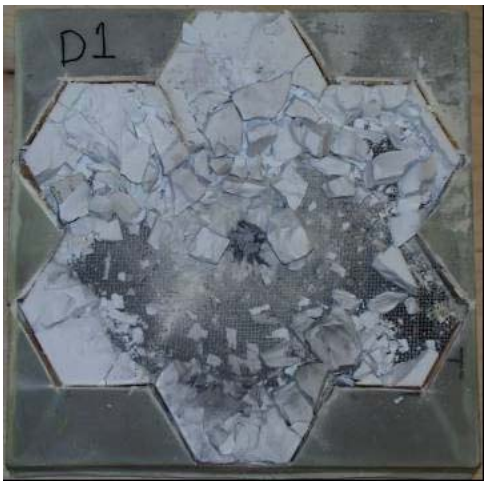

(c) Delam D1 – Incomplete

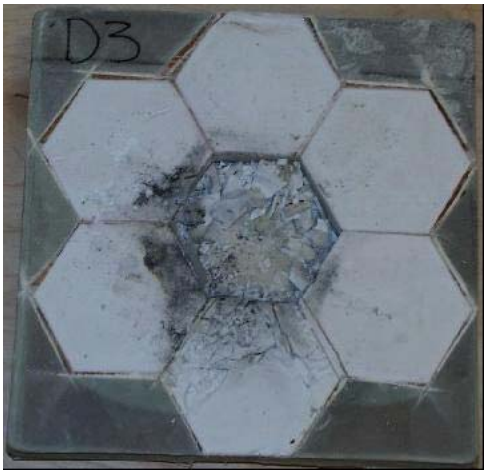

(d) Delam D3 – Complete

Figure 129. Damage in Ceramic Layer.

The recovered backing plates are C-scanned and compared with similar backing plates without any damage, as shown in Figure 130. The C-scan of the ballistically tested backing plates shows widespread delamination damage, which was also reported earlier (Figure 127). The extent of impact-induced delamination in the Delam panels is similar to that of the Baseline, which tells us that only a small area of pre-implanted delamination does not change the overall delamination generated through ballistic impact. Similar dynamic deflection and delamination observed in both the Baseline and Delam CIA panels suggests that the stress wave transmitted to the backing plate ahead of the projectile might cause equivalent delamination and micro-damages in both targets.

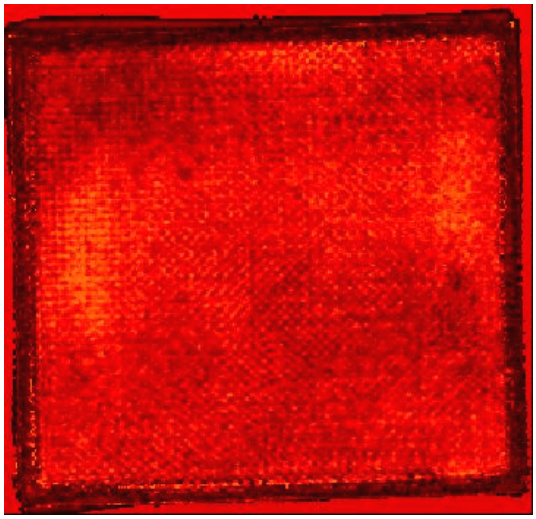

(a) Baseline – Virgin

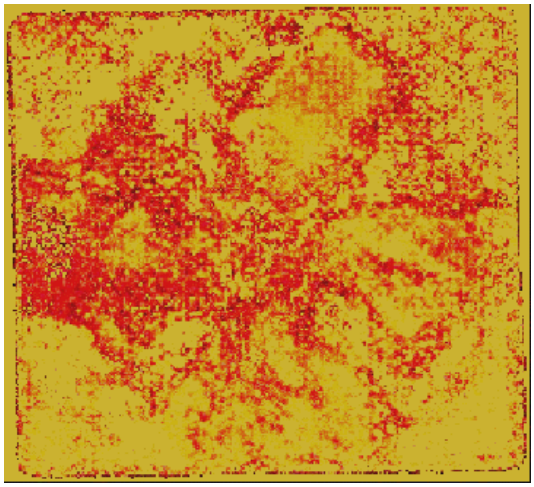

(b) Baseline B1 – Complete

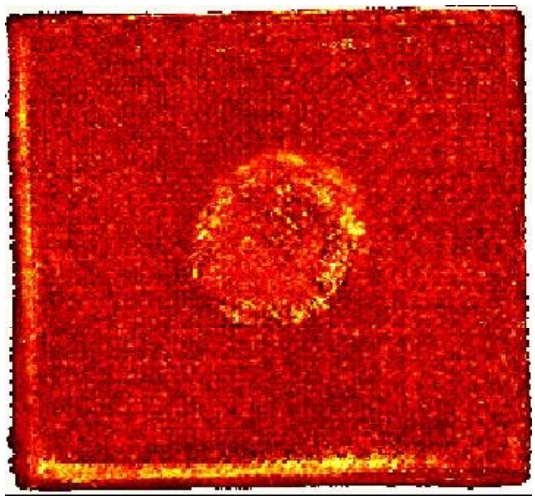

(c) Delam – Virgin

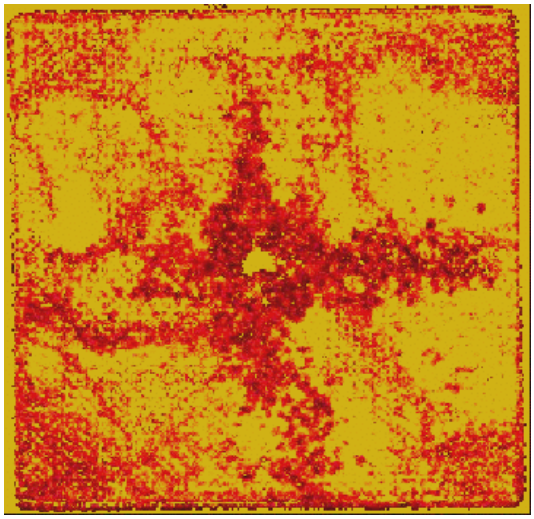

(d) Delam D1 – Incomplete

Figure 130. C-Scan Images of Virgin and Ballistic Damaged Backing Plates.

11.3 CIA Repair Requirements

An assessment of damage in CIA panels subject to ballistic impact has been performed. In all cases, repair of the backing plate, ceramic layer, and cover layer may be necessary to restore armor performance. The key question is whether repair of the backing plate is necessary to restore performance to acceptable levels and is being addressed in the current effort. Repair of composites is technologically and logistically practical and can be performed in the field. However, for composite armor to be considered a viable alternative to metal armor in ground vehicles, repair of CIA must meet the following criteria [81].

- The structural, ballistic, and signature performance must be renewed. To meet these performance levels, parts must be consolidated under vacuum.
- The repair procedure must be successful when access to the external side of the armor is restricted.
- The repair procedure must be able to be carried out in a variety of environmental conditions.
- The repair must be carried out reasonable quickly. In general, unit level field maintenance cannot exceed four hours, tools must be easily transportable and durable, and procedures must be simple and use a minimum number of tools.
- A repair procedure involving as few steps as possible is desired. In this case, a method of processing multiple interfaces in one step is desirable.
- In-plane and through-thickness temperature gradients in the system during heating/cure must be minimal (typically ±10ºC).
- Gaps must be minimized.
- The repair procedure must address variable damage (multi-hit) areas.

The repair procedures of thin composite aerospace structures are well developed [82 - 86]. A general repair guideline for aerospace structures was proposed by the Navy for repair of aircraft [87]. However, repair of thick-section composite and integral armor is relatively new. Monib et al. [88] used resin infusion to repair thick-section composites following the methods described by previous authors [89]. Contractors for DoD established a hierarchical repair strategy including a three-level design for multi-layer thick-section composites, which served as a baseline for this effort. Gama and others [90] proposed implementing this strategy for multi-layer composites, as per Figure 46. The three repair levels are distinguished according to the extent of through-thickness damage in the panel. Level I corresponds to damage in the outer layer only (e.g., low-velocity impact). Level II includes damage in layers 1 and 2 (e.g., delaminations, small projectiles). Level III is represented by extensive damage in all layers including the composite backing plate (e.g., ballistic).

For the CIA testbed, the repair methodology shown above was adopted. Induction-based adhesive cure will be used to bond multiple layers and complete the repair in a single step. The testbed will demonstrate Level III repairs (ballistic impact) and quantify post-repair ballistic performance.

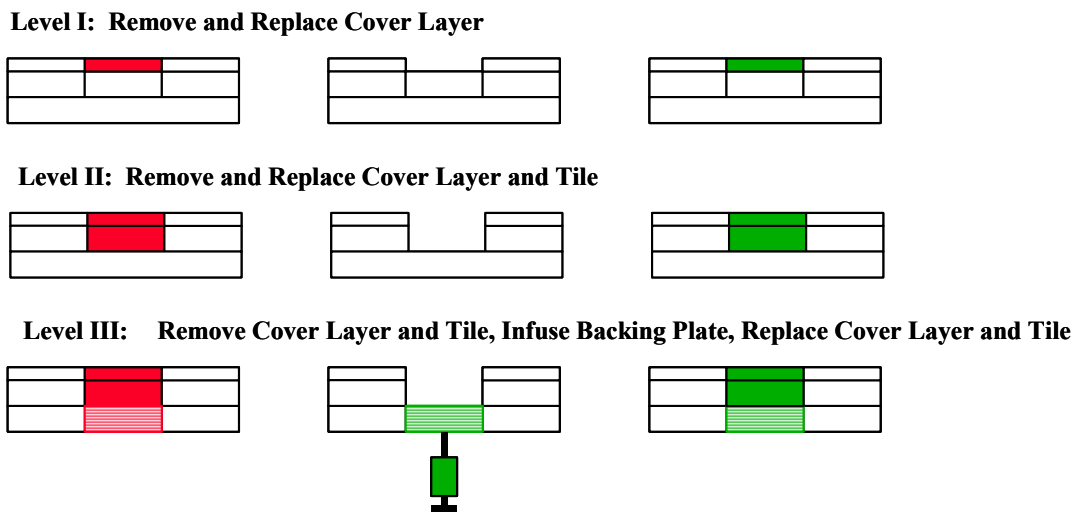

Figure 131. Repair Hierarchy.

11.4 Conclusions

11.4.1 Magnetic Particle Susceptors for Induction Heating

We have shown that induction heating can achieve thermal powers necessary for thermal curing, enabling both rapid heating and high dwell temperatures. This achievement is not trivial, and has been made possible only through recent advancements in induction processing equipment. Specifically, the commercial availability of high frequency (greater than 10 MHz) self-tuning induction power supplies has allowed for efficient energy transfer to magnetic susceptor particles.

The main advantage of induction heating is the Curie temperature of the magnetic susceptor particles. With a well-defined Curie temperature, the system is thermally self-regulating. Curie limiting was only partially utilized in our study. The magnetic particles in our study did not possess a well-defined Curie temperature. The temperatures at which the adhesive dwelled continued to rise slowly, never approaching a final temperature asymptotically. There are much better magnetic materials for Curie temperature control and if they were used, they would display better heating performance.

11.4.2 Rapid Curing of Adhesive Systems.

The choice of an adhesive system is critical for effective utilization of induction heating. The epoxy adhesive system is based on a commercial formulation that was designed to cure thermally in approximately one hour. Thus, it is sensitive to time-temperature profiles, which affect the size of the rubber particles. The adhesive system evaluated is not designed to cure inside of fifteen or thirty minutes. Induction heating would serve as an optimum type of curing for an adhesive system without a dependency on the heating rate (e.g., free radical initiated). These types of adhesive systems would best utilize the advantages of induction heating over other types of thermal curing.

To fully demonstrate induction heating as method for rapid adhesive processing, a comprehensive analysis must be undertaken of a heating rate insensitive adhesive system. We are preparing to do this with additional formulations adhesive system, which have the pre-formed rubber particles added *a priori*. Eliminating the phase separation issue from the performance will allow us to address issues associated with rapidly formed thermoset network structures independently.

12 Carbon-Carbon Susceptors – Models and Development

12.1 Heating Mechanisms for Carbon/Thermoplastics

Induction heating for carbon fiber reinforced thermoplastic composites is based on the fact that eddy current flows along conductive paths within the composite subjected to an alternating magnetic field generated by the induction coil (Figure 132). The frequency and the intensity of the magnetic field penetrating the composite as well as the loop area of the conductive path determine the electromotive force (emf) or induced voltages, which in turn govern the heating of the composite (Figure 133).

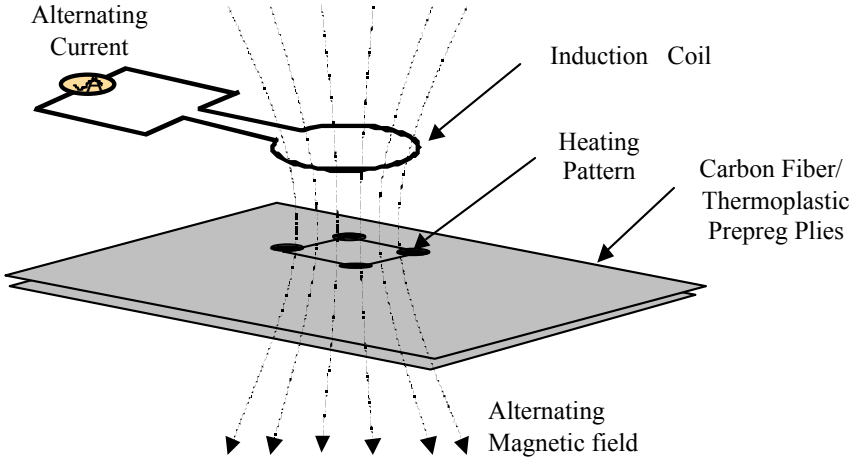

Figure 132. Schematic of the Induction Heating Process for Carbon/Thermoplastic Composites

The primary objective of this study is to investigate the heating mechanisms of carbon/thermoplastics and then determine the relationship between the induction coil and material parameters and heating. Once this relationship is determined, it will be possible to perform parametric studies using the major process variables in order to optimize and meet the thermal requirements for the potential production of thermoplastic-based composite structures.

12.1.1 THEORETICAL HEATING MODEL

Alternating magnetic field lines intersecting the laminate induce emf's within each conductive loop and are governed by Faraday's Law of Induction [47]. Loops are formed between adjacent plies through the junctions, where fibers overlap each other. As a result, the induced current flows along the carbon fibers and either through the polymeric region or by direct contact of fibers, into its adjacent ply, as shown in Equation 1. Generally the emf induced in a circuit is directly proportional to the time rate of change of magnetic flux through the circuit and is calculated from

$$emf = \omega A B_0 = 2\pi f A B_0 \tag{1}$$

where B_0 is the maximum value of the magnetic field normal to the area of the conductive loop, A is the area of the conductive loop, and f is the time rate of change of magnetic flux.

Once the emf values for all conductive loops in the calculation domain are obtained, Kirchoff's voltage and current conservation laws are applied to the network of conductive loops. Kirchoff's voltage law (KVL) [48] requires that the algebraic sum of all voltages around the loop should be zero while Kirchoff's current law (KCL) means that current is conserved at each node. In mathematical terms, they can be expressed as follows:

$$\begin{aligned} &\sum \text{Voltage Drop} = \text{Induced emf} && ;\ \text{Kirchoff's Voltage Law} \\ &\sum \left(\text{Incoming Current} - \text{Outgoing Current}\right) = 0 && ;\ \text{Kirchoff's Current Law} \end{aligned} \tag{2}$$

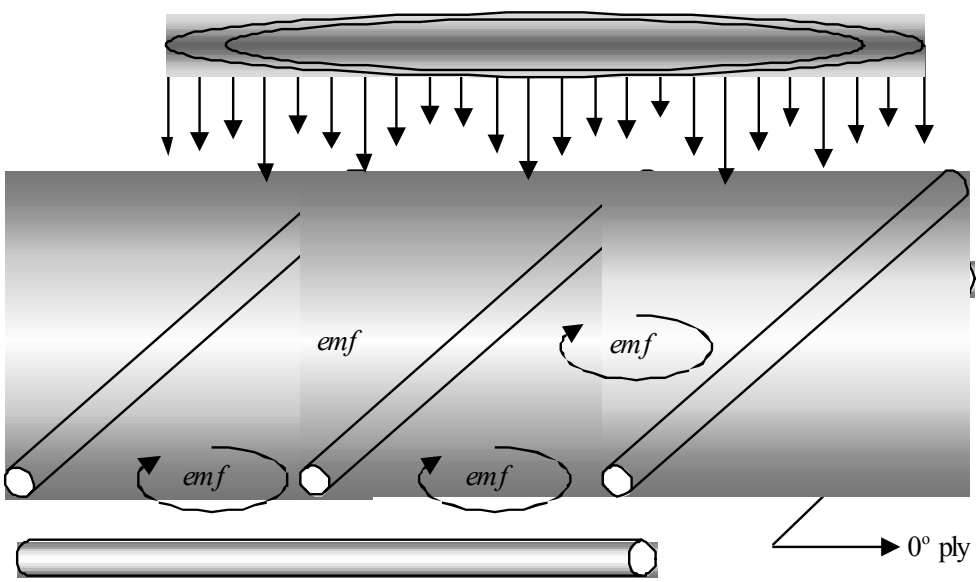

Figure 133. Schematic of Induced Voltage Loops in the Composite.

Three heating mechanisms are possible within the composite:

- Joule heating due to the inherent electrical resistivity of the carbon fibers.
- Dielectric heating of the polymer at the fiber junctions.
- Contact resistance at the fiber junctions.

In general, prepregs have nonuniform surface roughnesses, which makes it difficult to determine which mechanism is dominant at a certain region in the interface between plies. In addition, it is not easy to estimate the electrical contact resistance between carbon fibers of adjacent plies. The heating mechanisms are shown schematically in Figure 134 and described in detail in the following sections.

Previous authors [47-51] have compared joule heating in the fiber and dielectric heating in the matrix and shown that dielectric heating is the dominant mechanism. The current effort includes the contact resistance mechanism and performs a parametric study of all three mechanisms for the process variables defined for thermoplastic laminates. Successful modeling will identify the key heating mechanism and optimize induction-based processing parameters to meet quality and performance requirements. This will enable transition from thermosets to thermoplastics, thus eliminating potentially large hazardous waste stream due to shelf-life expiration.

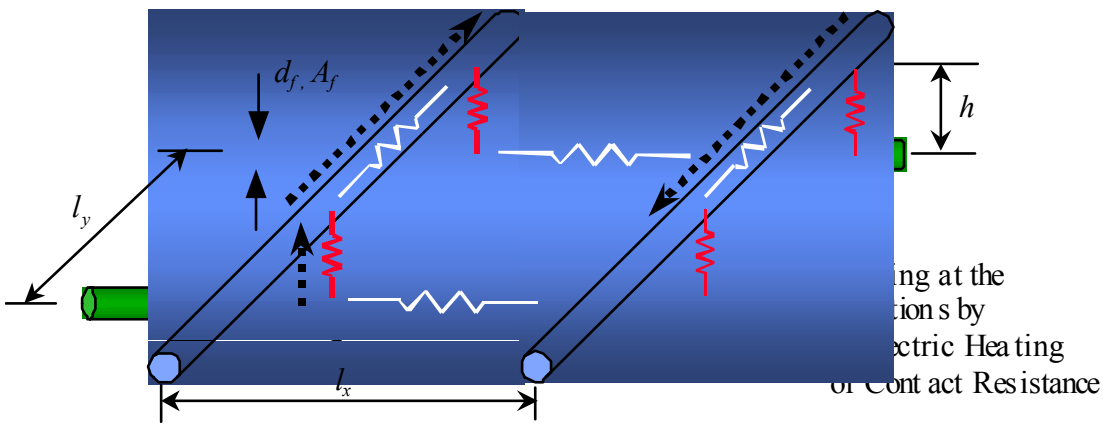

Figure 134. Heating Mechanisms in Each Individual Conductive Loop.

12.1.2 JOULE HEATING OF CARBON FIBERS

Each carbon fiber is treated as a resistor and the heat generated is calculated from

$$P_{fiber} = I_{fiber}^2 R_{fiber} \tag{3}$$

where I_{fiber} is the induced current flowing in the fiber and R_{fiber} is the resistance of the fiber [49,50]. R_{fiber} can be expressed as

$$R_{fiber} = \rho_{fiber} \frac{l_x}{A_{fiber}} \quad \text{or} \quad \rho_{fiber} \frac{l_y}{A_{fiber}} \tag{4}$$

where l_{fiber} and A_{fiber} are the length and cross-sectional area of the fiber, respectively. Note that l_{fiber} varies according to the mesh size.

12.1.3 DIELECTRIC HYSTERESIS HEATING AT FIBER JUNCTIONS

If the distance between the fibers at the junction is enough to form a capacitor, dielectric heating takes place, since the molecular dipoles in the matrix cannot rotate with the same

frequency of the induced voltages in the fibers [52]. The dissipation factor (tan δ), which is one of the electrical properties of the matrix, determines how much heat will be dissipated. The impedance of the capacitor is 1/(ωC tan δ), where ω is the angular frequency of the alternating current and C is the capacitance of the material. Considering the configuration of the fiber junction shown in Figure 135, the capacitance of the dielectric material can be expressed as follows:

$$C = \kappa\varepsilon_0 \frac{A_P}{h} \tag{6}$$

where κ is the relative dielectric constant of the material and ε_0 is the permittivity of vacuum (8.85×10^{-12} f/m). A_p and h are the projection area and distance between the fibers at the junction, respectively. Therefore, the impedance of the capacitor (Z_C) can be written as

$$Z_C = \frac{h}{\omega\kappa\varepsilon_0(\tan\delta)A_P}. \tag{7}$$

The heating generated by the capacitor is as follows:

$$P_{junction} = \frac{(V_{junction})^2}{Z_C} = \frac{\omega\kappa\varepsilon_0(\tan\delta)A_P(V_{junction})^2}{h} \tag{8}$$

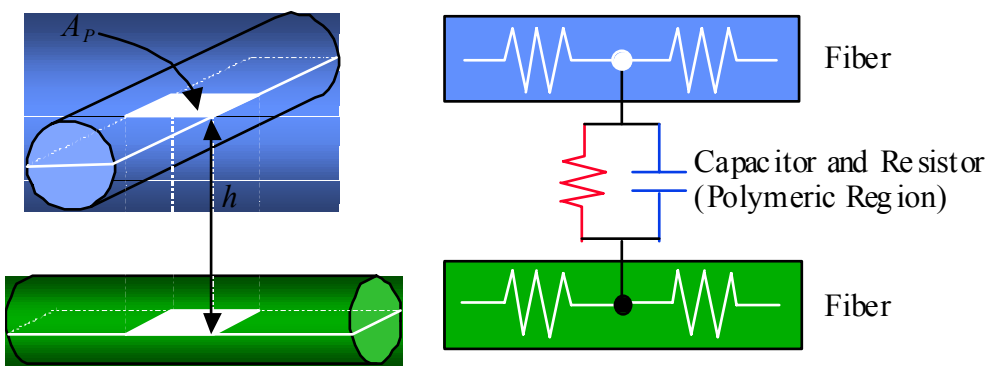

Figure 135. Circuit Model for Dielectric Heating.

12.1.4 Heat Generated by Fiber Contact Resistance

If the fibers at the junction are in contact or the distance between fibers is very short, heating can occur at the contact region due to contact resistance between the fibers. However, as mentioned previously, it is hard to quantify the contact resistance, as it is a function of surface roughness of prepreg and the laminate processing parameters. A simple resistor can model the fiber contact and the heating mechanism (Figure 136), and through parametric studies and experiments, the contact resistance is estimated.

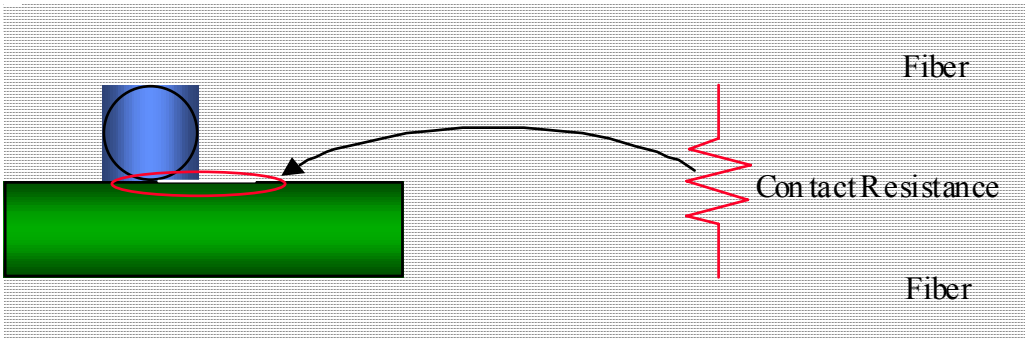

Figure 136. Circuit Model for Heating by Fiber Contact Resistance

12.1.5 Material Properties

In this study, AS4 carbon fiber and polyetherimide (PEI) thermoplastic prepreg was selected as the test matrix because it serves as a model system for proposed military munitions manufacture and provides high-process temperature limits. The diameter of the carbon fiber was 8 μm, and the electrical resistivity was 15.3 μΩm. The dielectric constant (κ) and dissipation factor (tan δ) for the PEI were measured by experimental studies. The experimental results show that the dielectric constant and dissipation factor can be assumed to be constant for frequencies up to 4 MHz as shown in Figure 137.

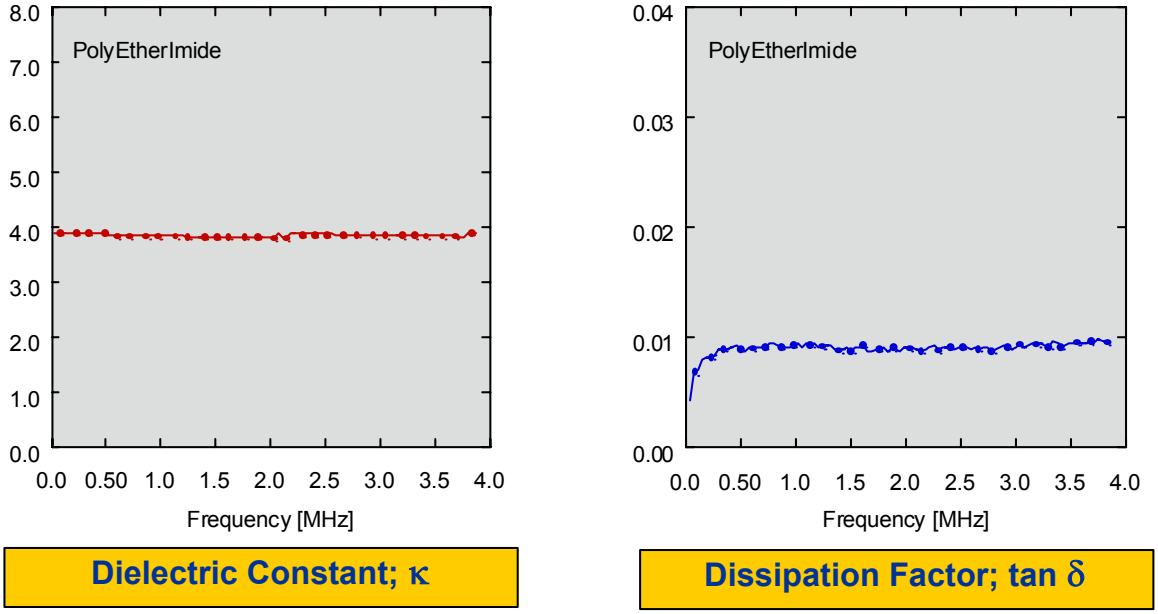

Figure 137. Dielectric Properties of PEI (Ultem 1000, GE Plastics)

12.1.6 Two-Ply Heating Model

Initial models focused on addressing the heating behavior of 2-ply prepreg stacks. This enables us to perform a detailed parametric study, followed by experimental verification to

assess the model's capabilities. A schematic describing the model procedure is shown in Figure 138.

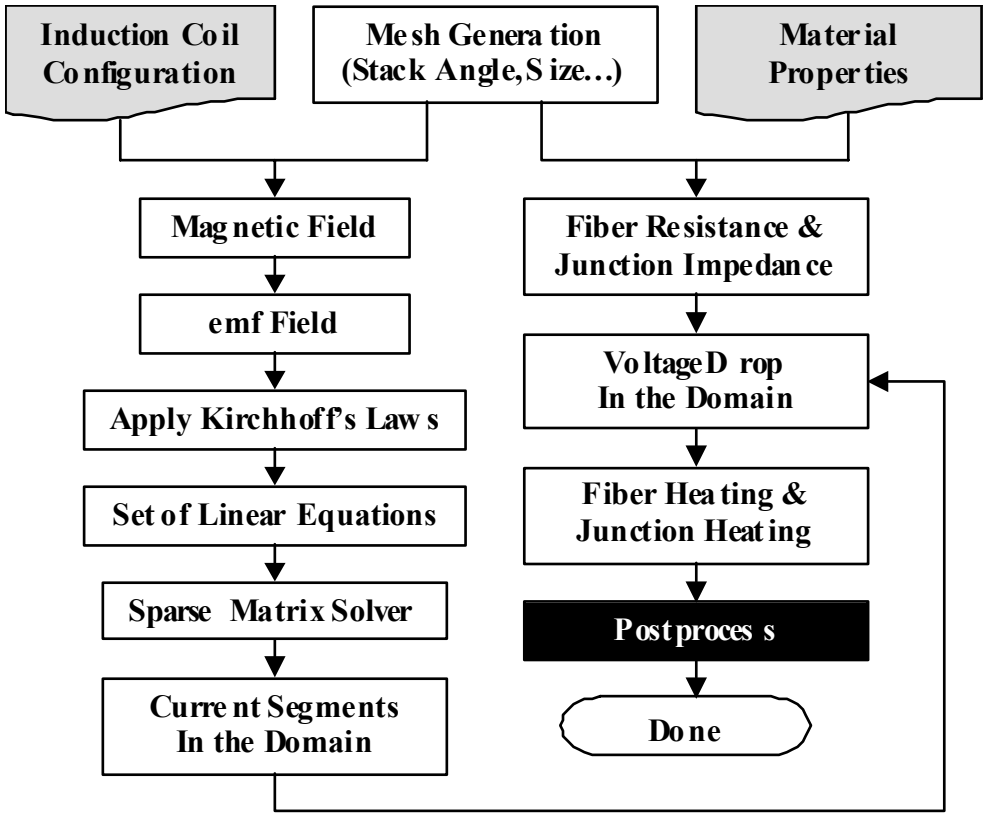

Figure 138. Schematic of 2-ply Heating Model

Since carbon/thermoplastic prepregs, such as AS4/PEI or AS4/polyetheretherketone (PEEK), have approximately 20 fibers per 5-mil (127-µm) width, we can estimate that about 790,000 fibers exist in a one-meter-wide prepreg. Therefore, cross-ply or angle-ply prepregs are simplified by a conductive loop network using a finite number of fiber grids with an assumption that fibers and junctions within each conductive loop have the same resistance and current values. It is expected that this type of meshing will generate good qualitative results, and if the mesh becomes denser, we can expect more precise results in the quantitative sense.

The process variables used in the model are coil type (pancake, conical, paper clip, and solenoid), coil size (outer dimension, inner dimension, number of turns, spacing between turns), distance between induction coil and composite, the frequency of the current in the induction coil, and the size and geometry of the composite.

Variables in the numerical model for parametric studies are mesh size and density, fiber-fiber distance at the interface of two plies, and fiber-fiber contact resistance or equivalent impedance for fiber junction.

12.1.7 Two-Ply Model Results

Initial experiments focused on evaluating numerical predictions qualitatively. This was done by heating 2-ply stacks at various angles—[0/90], [0/θ]—under a known magnetic field and comparing measured heating patterns, obtained using a calibrated thermal infrared camera, with the 2-ply model predictions. Results are shown (Figure 139 and Figure 140) for two select cases: a cross-ply stack [0/90] and an angle-ply stack [0/45]. Qualitatively, there is excellent correlation between the predicted pattern and the actual measured heating profile.

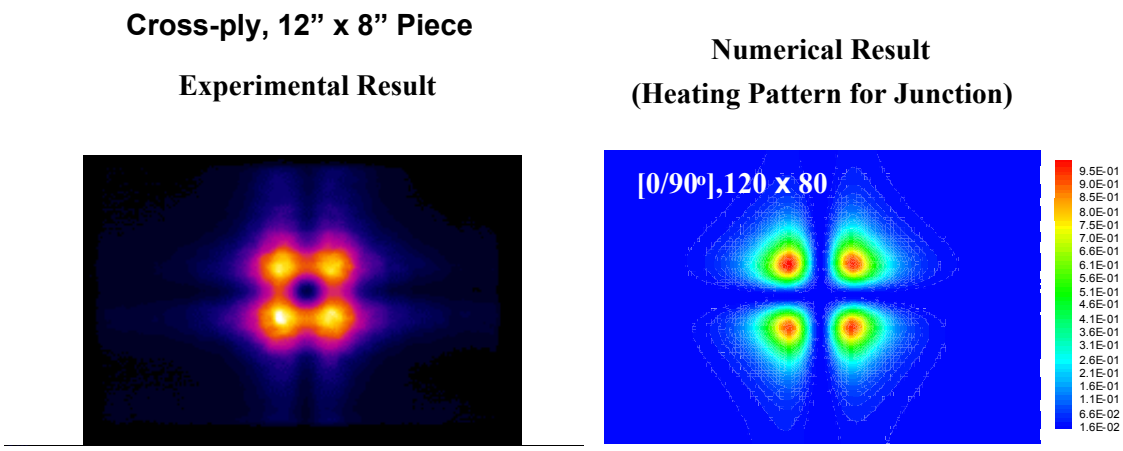

Figure 139. Comparison of Heating Patterns for [0/90] 2-ply Stack

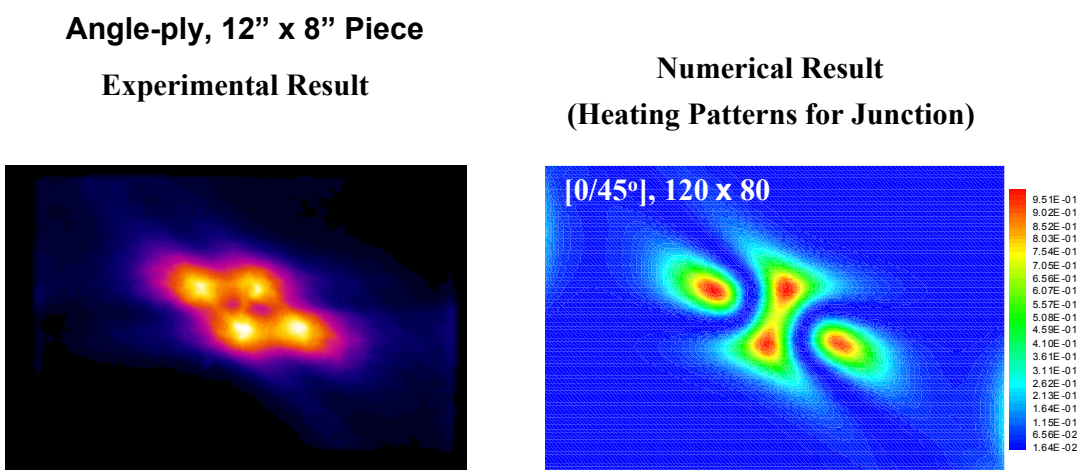

Figure 140. Comparison of Heating Patterns for [0/45] 2-ply Stack

Predictions in these figures were obtained by parametric studies with the three heating mechanisms (fiber heating, dielectric, and contact resistance) in the 2-ply stack. These studies show that the junction heating effects are greater than fiber heating by an order of magnitude. In other words, the primary heating in carbon/thermoplastics occurs at the junction and can be dielectric or contact resistance based, depending on the process variables.

Quantitative predictions are not as accurate and difficult to compare, because the model predicts heat generation rather than temperature. Work is continuing to optimize process variables and to extend the 2-ply model to multi-ply cases.

12.1.8 THROUGH-THICKNESS HEATING

The 2-ply model has shown that during induction processing, heating occurs predominantly at the junctions between fibers of adjacent plies or along the ply-ply interface. This raises the question of the uniformity of the temperature profile through the thickness of the composite. Figure 141 shows a typical heat-generation profile that can be expected for an 8-ply stack. As seen in the figure, heat generation occurs at the interface between any two plies that do not have the same fiber orientation.

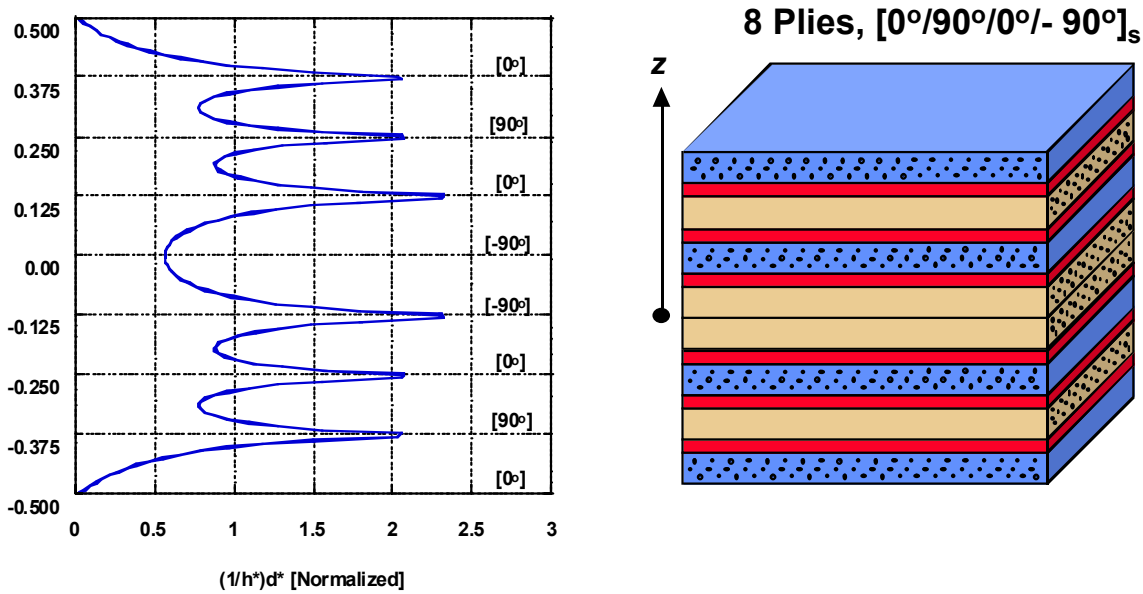

Figure 141. Model Through-Thickness Heat Generation of an 8-Ply Carbon-Fiber Laminate With Orientation $[0/90/0/-90]_s$

Since many structural laminates of interest to DOD are fabricated from 8-ply stacks similar to those shown in the above figure (or quasi-isotropic laminates built from such 8-ply stacks), it is necessary to identify not only surface heating profiles but also through-thickness heating profiles for quality and performance. It is essential that the temperature gradient across and through the thickness of the 8-ply stack is small during induction heating or significant performance degradation can result.

A one-dimensional transient heat transfer model was formulated using a finite difference scheme to predict temperature profiles through the thickness, based on heat generation shown in the above figure. Predicted temperature profiles are shown in Figure 142, showing transient, as well as steady-state results. Results show that temperature variations across the thickness of the 8-ply stack are insignificant after one second, which is within the range of the process cycle time. This is expected due to the small thickness of each ply and has been borne out by experimental measurements.

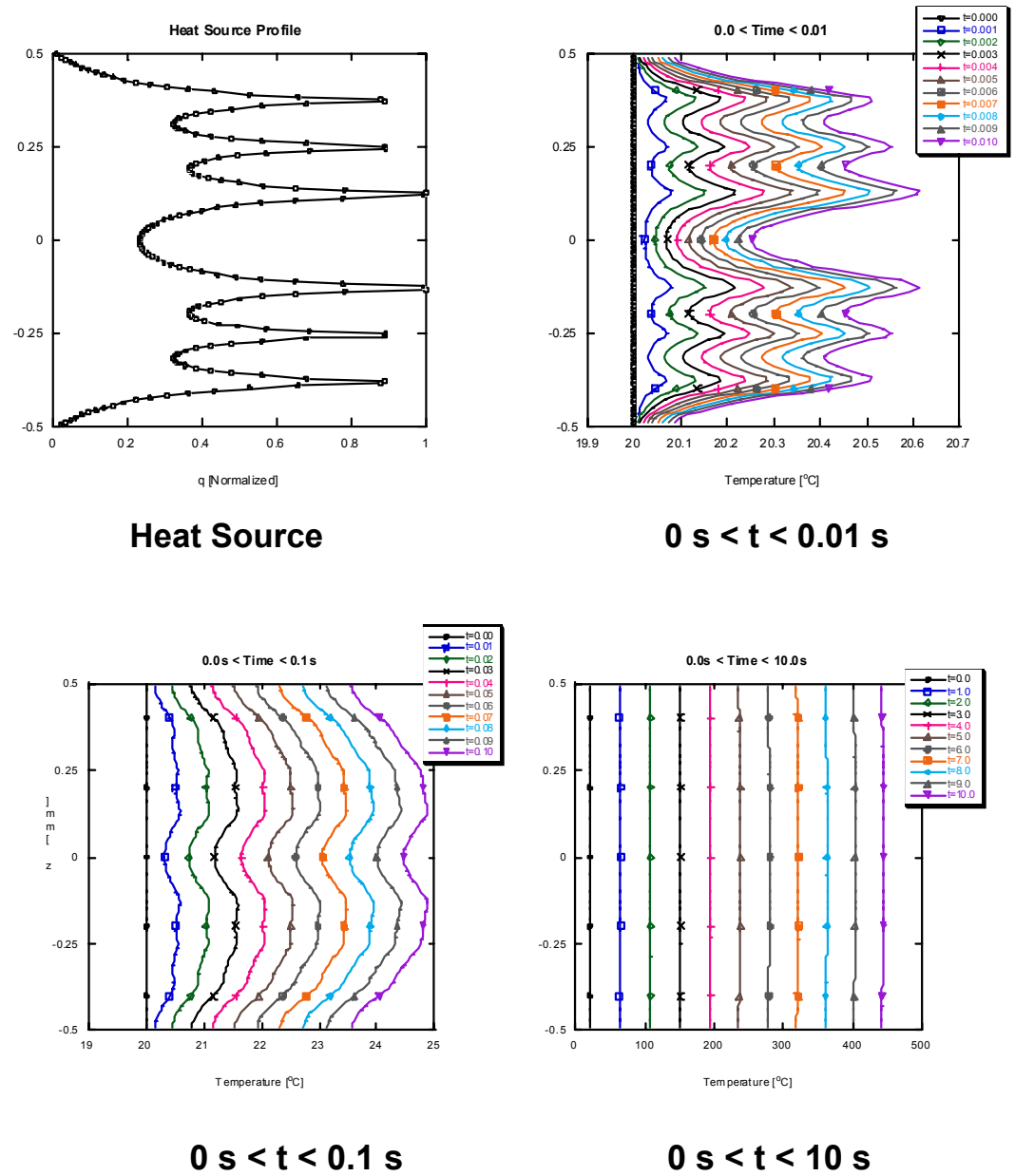

Figure 142. Predicted Through-Thickness Temperature Profiles at Various Time Steps.

12.2 Degradation Studies

Electromagnetic induction processing of thermoplastic-based laminates is currently being evaluated and perfected to produce a 10-fold decrease in cycle times for production and a resultant decrease in production costs. This process requires that carbon-fiber-based composites be subjected to large alternating electromagnetic fields. In addition to the issues

of degradation of the matrix in induction-based processing, in the EM gun program glass- and carbon-based polymer composite compulsator components experience very large fluctuations in electromagnetic energy during charging and discharging. These systems are subject to potentially critical polymer degradation as a result of a little-studied phenomenon known as thermoelectric degradation. When polymers degrade through any mechanism, they suffer significant losses in strength, stiffness, and durability.

The focus of this effort is on identifying degradation mechanisms during electromagnetic induction processing and quantifying their effects on performance. There are two possible degradation scenarios associated with induction-based processing of carbon/thermoplastics: thermal degradation and electrical degradation due to dielectric breakdown in the matrix.

12.2.1 THERMAL DEGRADATION STUDY

Weight loss and molecular weight (MW) measurements were used to characterize thermal degradation of both neat resin and prepreg. Thermogravimetric analysis (TGA) was used for weight loss measurements in both air and inert (nitrogen) atmospheres. Gel permeation chromatography (GPC) was used to obtain molecular weight measurements. In addition, dissolution times for resins in a good solvent (methylene chloride) were also measured.

12.2.2 WEIGHT LOSS MEASUREMENTS

TGA for both neat PEI and AS4/PEI prepreg indicates no measurable weight loss of the bulk material up to 500 °C, as shown in Figure 143. Isothermal TGA data also shows that no weight loss was observed at 350 °C, for up to 1 hr. Approximately 2% weight loss was observed at 450 °C after 30 min, which indicates significant degradation. Since the normal processing temperature is 330 °C, thermal degradation of the bulk material is expected to be minimal as long as the electromagnetic induction processed material does not exceed the processing window.

Neat PEI samples were exposed to various thermal histories using a TGA chamber, and the glass transition temperature was measured using DMA. Changes in resin color and dissolving time in a good solvent (methylene chloride) were also noted. As shown in Table 58, no significant changes in glass transition temperature were observed. However, the color of the resin changed from yellow to black, and the dissolving time increased significantly when temperature and time increased. Oxygen in the atmosphere also affects the color change and dissolving time in the solvent. In several cases (G~K), there was some gel left over in the solution, which obviously indicates that crosslinking reactions occurred in the polymer.

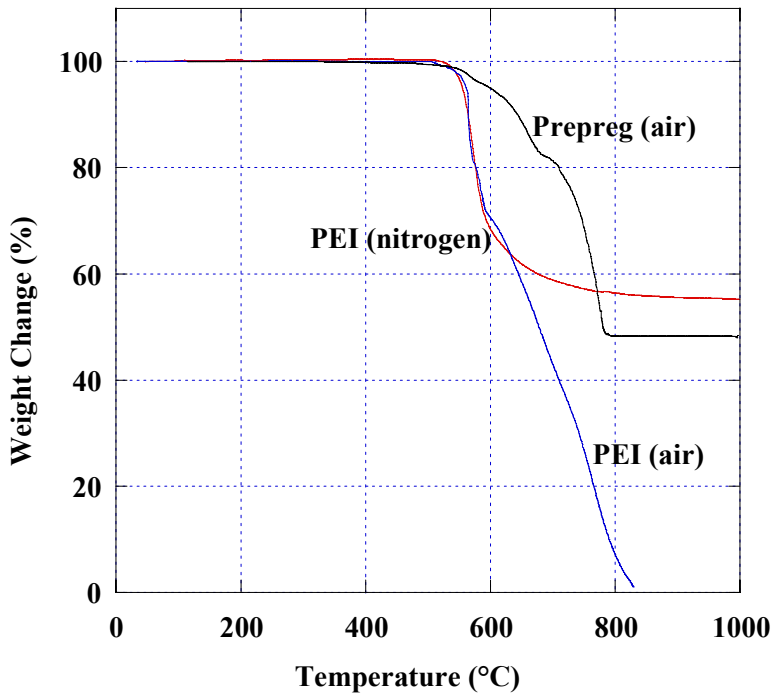

Figure 143. TGA Weight Loss Profile for PEI Resin and Prepreg (Heating Rate = 15 °C/Min)

The TGA study shows that weight loss alone is not sufficient to identify the degree of degradation of the polymer. The initiation of crosslinking in the polymer is a better measure of the onset of degradation. Crosslinking on a composite surface hinders diffusion of polymer chains during processing of complex parts and may result in poor bonding and performance.

Table 58. Experimental Data of Neat Ultem 1000 Resin Under Various Heat Treatments.

Sample	Condition of Heat Treatment	Atmosphere	T_g from DMA (°C)	Color Change	Dissolving Time in Solvent (Methylene Chloride)
A	No treatment		210	None	Less than 2 hr
B	330°C, 30 min	Nitrogen	210	None	Less than 2 hr
C	330°C, 30 min	Air	210	Mild	3 hr
D	350°C, 30 min	Nitrogen	210	None	4hr
E	350°C, 60 min	Nitrogen	210	Mild	5 hr
F	350°C, 30 min	Air	210	Moderate	6 hr
G	350°C, 60 min	Air	210	Moderate	Some left over as a gel
H	400°C, 30 min	Nitrogen	210	Moderate	Some left over as a gel
I	400°C, 60 min	Nitrogen	210	Moderate	Some left over as a gel
J	400°C, 30 min	Air	210	Severe	Some left over as a gel
K	400°C, 60 min	Air	210	Severe	Some left over as a gel

12.2.3 MOLECULAR WEIGHT CHARACTERIZATION

Gel permeation chromatography (GPC) was used to assess the extent of crosslinking. According to the literature and preliminary experimental observations, crosslinking reaction tends to be dominant over chain scission (breakup of chains) in the early stages of degradation of thermoplastic polymers (PEEK and PEI). Crosslinking reactions typically occur at lower temperatures (~350 °C) than the onset of weight loss observed by TGA (~450 °C). GPC is one of the most frequently used techniques to measure the polymer molecular weight (MW) and its distribution (MWD). The MWD curves show the changes caused by crosslinking or chain scission. For example, if crosslinking is dominant over chain scission, there are higher MW chains; as a result, a broader curve will be obtained that has a peak intensity shifted to the left (shorter elution times) compared to a baseline polymer elution. If chain scission is dominant, the curve will be broadened to the right or longer elution times.

Most of the samples evaluated exhibited peak intensity shifts to shorter elution times, which indicates that crosslinking is dominant. All the curves were recalculated after the intensity values were divided by the peak intensity. The normalized area under the curve can be used as a qualitative measure of the extent of crosslinking. The intensity normalized area increases with crosslinking.

Results from GPC analysis are shown in Table 59. Neat resin and prepreg specimens were tested under various thermal histories in air, nitrogen, and vacuum atmospheres. All the GPC curve areas were intensity normalized with the neat resin case (Sample A). In the neat resin study, no change is observed up to 350 °C for 30 min in nitrogen (A~D). However, in the presence of air (atmospheric oxygen), significant increases in the GPC curve areas are observed, indicating the presence of crosslinked polymer chains. Samples D and F show the effect of atmosphere, F and J the effect of temperature, and J and K the effect of time in a reactive atmosphere (air). The GPC area indicates the onset of crosslinking (and degradation) at lower temperatures than weight loss tests and hence is a better tool to quantify degradation and establish process limits. For prepreg processed under vacuum conditions, some crosslinking occurs at 350 °C (1.13 compared to 1.08 baseline) while

significant crosslinking degradation occurs at 400 °C. In comparison, specimens processed in air exhibit higher levels of degradation at both test temperatures, as expected.

The induction-processed samples were subjected to high frequency magnetic fields for approximately 1 min, which was chosen based on design cycle times in electromagnetic induction based process for manufacture of laminates. Magnetic field parameters were selected to mimic process conditions in the manufacturing process. Preliminary tests performed under vacuum atmosphere indicate no measurable polymer degradations under these conditions, even though the composite laminate does reach the degradation temperatures of 380 °C and 400 °C (samples X and Y, respectively).

Table 59. Degradation Study of PEI and AS4/PEI Prepreg Using GPC.

Sample	Process	Temperature (°C)	Time (min)	Atmosphere	Area Ratio Under the GPC Curve
A	Resin	No treatment	—	—	1.00
D	Resin	350	30	Nitrogen	1.00
F	Resin	350	30	Air	1.10
J	Resin	400	30	Air	1.13
K	Resin	400	60	Air	1.28
L	Prepreg	No treatment	—	—	1.07
M	Autoclave	330	20	Vacuum	1.08
N	Autoclave	350	60	Vacuum	1.13
O	Autoclave	400	60	Vacuum	1.60
P	Oven	330	20	Air	1.21
Q	Oven	350	30	Air	1.31
R	Oven	350	60	Air	1.39
S	Oven	400	30	Air	1.37
T	Oven	400	60	Air	1.48
U	Induction	309	1	Vacuum	1.07
V	Induction	319	1	Vacuum	1.07
W	Induction	330	1	Vacuum	1.08
X	Induction	387	1	Vacuum	1.05
Y	Induction	405	1	Vacuum	1.06

12.2.4 ELECTRICAL DEGRADATION STUDY

Dielectric breakdown of polymers results in localized damage, which leads to deterioration of the mechanical properties of the composite. Several mechanisms can occur and lead to breakdown, such as, discharge breakdown and intrinsic breakdown. In this effort, the purpose is to identifying electromagnetic parameters that produce breakdown and not to elucidate the mechanisms for this breakdown. Thus, we show that dielectric breakdown is not likely to occur during electromagnetic processing of AS4/PEI.

Breakdown measurements were performed on neat PEI films of various thicknesses. The junction of fiber overlap is the region of expected breakdown and the thickness of PEI in these regions is small (sub-micron). Thin films, as small as 100 nm, were fabricated using a solvent-based spin-coating technique.

The dielectric breakdown voltages for neat PEI films of varying thickness are presented in Figure 144. The breakdown voltage increases as the sample thickness increases. The voltage required for breakdown in a 100-nm film of PEI is ~350 V. The voltage-drop in the induced current loops during electromagnetic processing is an order of magnitude smaller. For example, the induced voltage due to a three-turn coil with 10 A current at a frequency of 10 MHz and affecting a 0.1 m square loop in the composite is only 40 V. It may be concluded that dielectric breakdown of the matrix is unlikely during electromagnetic processing of AS4/PEI composites.

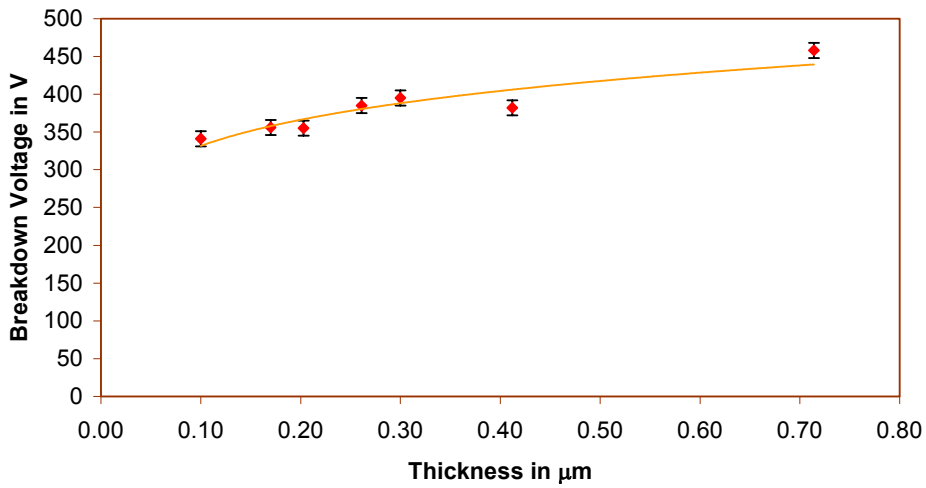

Figure 144. Breakdown Voltage Measurements for Neat PEI Films

12.2.4.1 Mechanical Performance

Short beam shear (ASTM D 2344) [66] and compression (ASTM 695) [67] tests were performed with autoclaved and electromagnetic induction processed AS4/PEI specimens. These two properties are directly related to the matrix properties in the composite and are sensitive to matrix degradation. High pressure (75 psi) was used in order to eliminate the void content effect on properties. Measured void contents were less than one percent for both samples. The mechanical test results are shown in Figure 61 and indicate no loss in performance due to electromagnetic induction-based processing of AS4/PEI.

Table 60. Comparison of Mechanical Properties.

	Apparent Shear Strength [psi]	Compressive Strength [ksi]
Electromagnetic Induction Processing (A)*	11300 ± 500	120.1 ± 1.2
Autoclave (B)**	11500 ± 500	118.3 ± 1.8
Process A: **Autoclaved at vacuum** **Induction heated**	****Process B :** **Autoclaved at vacuum** **Autoclaved at 75 psi** **Autoclaved at 75 psi**	

13 Carbon-Carbon Susceptors – Application to Processing of Composite Sabot

The ability to induction process carbon-fiber-reinforced composites is being used in the design and fabrication of composite sabots. Initial sabot design and fabrication used carbon-fiber-reinforced thermoset prepregs, resulting in a potentially large hazardous waste problem due to shelf-life requirements and VOC emissions during processing. It is estimated that the raw material requirements (prepreg) will exceed 1 million pounds annually, and the potential waste during thermoset processing is significant. This problem can be avoided by the use of carbon-fiber-reinforced thermoplastic prepregs, due to their infinite shelf-life. In addition, VOC emissions during thermoplastic processing are insignificant compared to thermosets.

However, the barrier to the use of thermoplastics is their ability to meet performance and throughput requirements. Induction processing of carbon-fiber thermoplastics offers a potential solution to this problem and provides volumetric heating of the thermoplastic prior to consolidation. UD-CCM has used induction to successfully heat and consolidate multi-layer laminates from 2 to 80 layers. This work has shown that induction offers the potential for an order-of-magnitude reduction in cycle times (volumetric heating rates in excess of 400F/sec were achieved) and full consolidation under vacuum pressure compared to traditional compression and autoclave processes.

Work to date has established in-plane and through-thickness heating models for carbon-fiber-based composites and the relationship between material parameters and heating. The present work uses these models and develops a process simulation for an induction-based manufacturing process that can fabricate carbon/thermoplastic laminates at high throughputs.

13.1 Induction-Based Remanufacture of Thermoplastic Composite Laminates

DOD has increasing use of carbon-fiber-reinforced thermoset prepregs, resulting in a potentially significant hazardous waste stream due to shelf-life expiration and VOC emissions during processing. It is estimated that the raw material (prepreg) requirements for one particular application will exceed 1 million pounds annually when that weapon system goes into full-scale production, and the potential waste is estimated at 20% of the total [91]. This problem can be avoided by the replacement of thermoset-based carbon-fiber composite laminates with carbon-fiber-reinforced thermoplastic prepregs, due to their infinite shelf-life. In addition, VOC emissions during thermoplastic processing are insignificant compared to thermosets.

However, a major barrier to the use of thermoplastics is their ability to meet both performance and throughput requirements (100+/day). Induction processing of carbon-fiber thermoplastics offers a potential solution to this problem by enabling rapid volumetric heating of the thermoplastic prior to consolidation as described earlier. This technology will enable reduction in cycle times, while maintaining quality, compared to conventional compression molding processes.

The key thermal requirement of induction processing for lamination applications is rapid, uniform heating of the composite for maximum throughput and quality. This requires an

understanding of the heating mechanisms during induction processing, followed by optimization of the critical process parameters. It is also essential to determine possible degradation mechanisms and process windows due to the rapid heating requirement.

13.2 Process Model Development for Induction Laminator

Induction heating of carbon composite laminates offers the potential for rapid processing, as high internal heat input can be applied over a short distance to quickly heat the material to temperatures exceeding the melt temperature of the resin. In addition, as the heating is volumetric, full consolidation can be achieved across the entire cross-section with the application of high pressure. As the heating is localized and concentrated, a modest power supply is sufficient to heat the laminate, and the induction coil can be tailored for both optimum power input and throughput. With the use of pressure from controlled temperature rollers, full consolidation can be achieved throughout the material. This study is aimed at applying the knowledge already gained in rapid thermoplastic processing methods towards designing an induction-based lamination process.

UD-CCM has already developed models capturing the important physical phenomena governing material property development in the automated tape placement process for carbon-fiber thermoplastics. These models examined the heat transfer, consolidation, intralaminar and interlaminar void formation, degree of bonding between plies, and effect of processing defects such as void content and ply waviness on laminate strength. These models have the capability of operating in the critical, highly transient regions caused by process start-up or geometrically imposed velocity changes, where process quality must be maintained. These models can be extended to multi-layer processes to determine optimal equipment and process conditions for manufacturing high quality parts. By using a model-based predictive approach, these models can be integrated and used to train a neural-network-based simulator enabling real-time feedback for process control.

The major advantage of induction heating technology is that it enables rapid volumetric heating resulting in multi-layer consolidation at high throughputs. The size and shape of the induction coil can also be tailored to provide an optimum induction field to heat the composite rapidly. Models of induction heating in carbon fiber composites have been developed in the previous year effort. These models will be applied to this work to determine internal heat generation patterns as a function of coil geometry, shape, and coil position with respect to the composite. From these studies, a laminator design will be developed which provides for maximum production rates with uniform internal temperatures within the laminate.

13.3 Laminator Process Specification

Performance and process specifications of the laminator were developed through discussions with Alliant TechSystems (contractor for sabot production). The major specifications are outlined below:

1. 8-ply laminates $[0/30/0/-30]_s$
2. Nominal Part Dimensions: 12"x36" ± 0.025"
3. Machine to be fed with stacks of [0/30] or [0/-30] sub-laminates
4. Throughput:
Requirement: Better than 12 fpm (15 sec for 36" component)
Design Goal: Better than 15 fpm
5. Machine must accommodate graphite/thermoplastic systems with nominal processing Temperatures of 625 + 20°F
6. Following heating above melt temperature, part must be consolidated under pressure. Pressure must be applied until part centerline is cooled below de-mold temperature to avoid deconsolidation.
7. Uniform cooling from both sides of part to ensure flatness (<1.5%).
8. Void content of consolidated laminate must be sufficiently low to enable die cutting operation without material damage and to allow good part production within the 10-degree wedge former.
9. Laminate design should maintain alignment of 0° layers.

Figure 145 is a schematic of the finalized design for the experimental laminator. Note that this process is symmetric about the mid-plane of the laminate and is composed of four fundamental thermal stages: a preheat stage, an induction heating stage, a consolidation stage (roller), and a cooling stage. The processing parameters at each location are critical in determining the final quality of the consolidated sheets and as such are modeled separately to determine optimal conditions. In this process, a preheater source is used to generate contact between the individual plies (to facilitate induction heating) and a cooling shoe is used to prevent deconsolidation or void growth within the layer after consolidation.

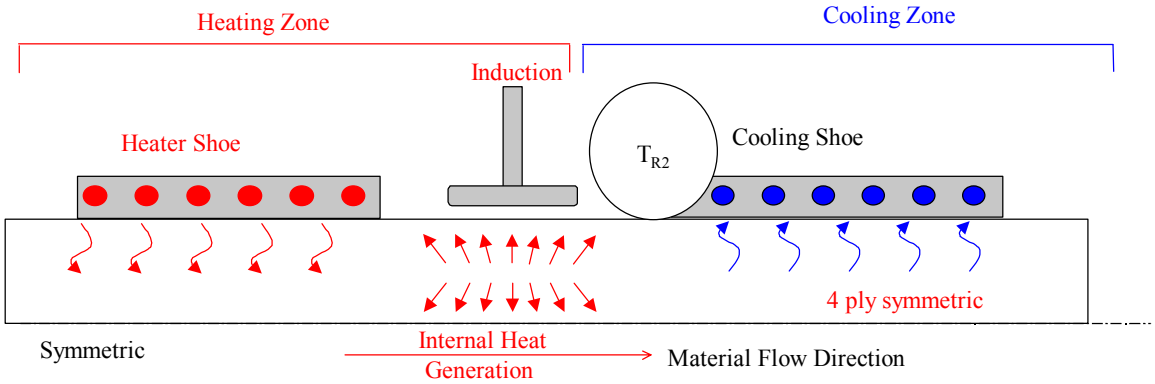

Figure 145. Schematic of Lamination Process.

Induction heating is used as the primary heat source, as a large amount of energy can be transferred to the laminate in a short period of time and the energy can be transferred to all layers within the laminate. Induction provides significant flexibility in varying throughput rates without requiring hardware changes by simply increasing power levels. In contrast, surface-heating technologies (e.g., oven, IR) would require increased heating zone lengths to allow for sufficient energy and time for heat to diffuse into the interior. This would require a unique hardware design for each velocity of interest. The large energy transfer applied by induction through the entire thickness of the laminate thus allows for rapid throughput of the

feed material. The material is fed through the laminator using a series of feed rollers (not shown). These rollers control the velocity and direction of the composite sheets and provide tension to the 0° layer to maintain alignment. A consolidation roller shown in the figure is used to consolidate the sheets using localized pressure, which is applied to the melted material. A cooling shoe located downstream is used to rapidly quench the laminate and is required to prevent the hot internal voids within the material from growing to unacceptable levels after consolidation.

13.4 Material Description

The principal material used in this study is an AS4/PEI carbon fiber prepreg with a nominal thickness of 0.007in (0.1778mm). PEI is an amorphous high-performance thermoplastic introduced in 1982 by GE Plastics under the Ultem trademark. High strength and rigidity at elevated temperatures, long-term heat resistance, highly stable dimensional and electrical properties and broad chemical resistance characterizes the material. Key material parameters are T_g = 400°F, $T_{process}$ = 625°F and $T_{degradation}$ > 700°F. The laminate to be fabricated is composed of 8 plies with a stacking sequence of $[0°/+30°/-30°/0]_s$.

The selected material replaces a carbon fiber based epoxy system that was initially used for sabot production, thus eliminating shelf-life and hazardous waste disposal issues.

13.5 Laminator Process Models

A set of process models that capture the important process phenomena, such as heat transfer, consolidation and coupled bonding, are shown in Figure 146. These models have the capability of operating in the critical, highly transient regions caused by process start-up of geometrically imposed velocity changes, where process quality must be maintained. These models are used as a simulation tool to define hardware parameters that satisfy the process specifications and material quality requirements. The following sections provide brief descriptions of the models used.

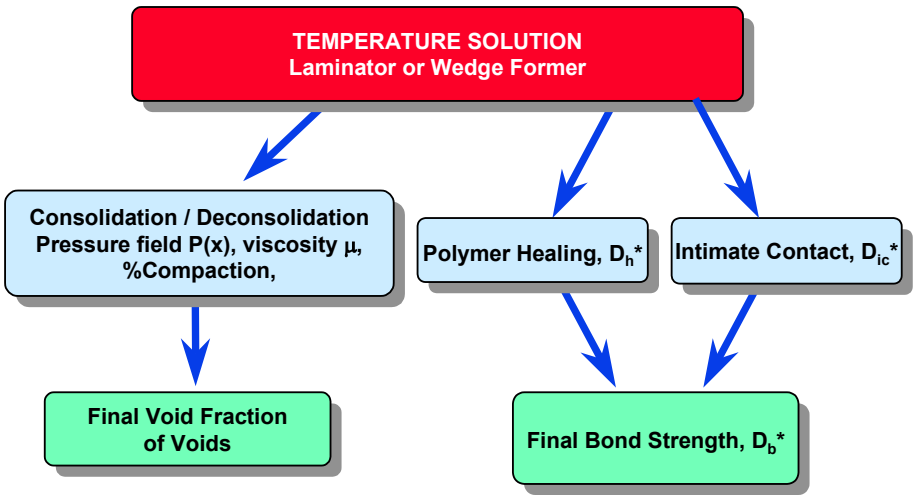

Figure 146. Model Scheme used in Laminator Design.

13.5.1 THERMAL MODELING

Thermal modeling enables the setpoints for preheat, induction power, and cooling to be established for a given throughput. Thermal modeling is also essential to size process elements such as shoe length and roller diameter. A two-dimensional transient thermal transport model, called T2D, has been developed for this process. It has the ability to model mass transport, moving boundary solutions, and internal heat generation. The model can simulate various boundary conditions, which include forced and free convection, full or partial insulation, radiation losses (Infrared heat), forced contact, and gas impingement from single high flow nozzles. This model can also model multiple materials with anisotropic properties. The heat diffusion equation used in this model is as follows:

$$\frac{\partial T}{\partial t} = \frac{k_x}{\rho c_p}\left(\frac{\partial^2 T}{\partial x^2}\right) + \frac{k_y}{\rho c_p}\left(\frac{\partial^2 T}{\partial y^2}\right) + V\frac{\partial T}{\partial x} + \frac{1}{\rho c_p}\dot{q} \qquad (3)$$

The heat generated by the induction source $\dot{q}$ and the thermal transport term that includes the process velocity V in the x direction are included in this equation. ρ is the density of the PEI/carbon fiber laminate, c_p is the specific heat, and k_x and k_y are the conductivities of the laminate in the x and y (through-thickness) directions, respectively.

T2D uses an Alternating Direction Implicit (ADI) finite difference scheme to solve for temperatures within the process domain. This solution technique is unconditionally stable such that the solution remains stable for all space and time intervals. Hence, there are no restrictions on Δx and Δt. The thermal model provides the temperature history at the critical locations within the process and the process models use this thermal data to determine the quality (void content and degree of bonding) within the laminate.

13.5.2 VOID DEVELOPMENT

A high-quality laminate fabricated by this process must have an average void content of less than 1.5% within the deposited layers as well as complete intimate contact at the interface between the layers. This low void content can only be achieved if the pressures and temperatures applied to the laminate are such that the voids are locked in under pressure until temperatures fall below T_g. For this reason, a pressurized cooling shoe is used such that void growth (deconsolidation) can be minimized. The shoe is also placed as close as possible to the consolidation roller to reduce the time at which the melt is exposed to normal atmospheric pressure. The following is a brief description of the consolidation model used in this study. These models, coupled with the thermal history, enable force/pressure requirements to be established that in turn enable heating/cooling shoes and roller sizes to be calculated. The consolidation model also predicts width changes, which can be coupled with process requirements.

13.5.3 CONSOLIDATION/DECONSOLIDATION MODEL

The dominant void dynamics mechanism pertaining to this process is void compression within layers due to the effects of cooling and compaction under the rollers and shoes. A compressible squeeze flow model of a Newtonian fluid in a two-dimensional geometry, developed by Ranganathan et al. [92, 93] is used to develop the pressure field under the

rollers. Consolidation under the rollers is modeled as a squeeze flow continuum in which the rheological properties are dependent on the temperature, fiber volume fraction, and void content. The consolidation model also defines the roller/substrate contact area required for the heat transfer analysis. A macroscopic flow model was developed to account for void transport, while a microscopic void dynamics model was used to account for void compression due to the predicted pressure distribution. The pressure distribution generated is also used to determine the degree of intimate contact at the interface between layers.

Away from the rollers, deconsolidation is the dominant mechanism. At high temperatures, the material viscosity is low, and therefore, voids can grow if insufficient pressure is applied. The internal void pressure acts as a driving mechanism for this growth, with atmospheric pressure acting as an equilibrium pressure boundary condition measured experimentally. A uniform pressure distribution is applied at the sliding shoes, which is representative of the case where the shoe is free to rotate and conform to any flow behavior of the resin. A more detailed study of the void dynamics model pertaining to this process has been published in the literature [92, 93].

13.5.4 COUPLED BONDING MODEL

The coupled bonding model is comprised of two sub models which both concurrently describe the development of bond strength within the laminate. This model is important, as it will enable us to select setpoints for the laminator such that the laminates will survive the die cutting operation, in the next stage of the M829E3 sabot production line, without delamination of any layers. The first model describes the degree of interfacial contact that develops between two rough surfaces. The second sub-model describes the development of bond strength across this new interfacial area.

13.5.5 INTIMATE CONTACT MODEL

The degree of intimate contact is defined as the ratio of the instantaneous base width of an idealized rectangular asperity on the tow surface to the wavelength of an assumed periodic arrangement of the asperities. The mechanism of intimate contact is dependent upon the relative surface roughness, the interface temperature profile, and the pressure field at the tow interface. The intimate contact model employed in this study follows that presented by Mantell and Springer [94]. The solution to the pressure field developed in the squeeze flow model is applied to a semi-empirical model as follows:

$$D_{ic}(\tau_{ic}) = R_c \left[\int_0^{\tau_{ic}} \frac{P}{\mu} \, d\tau \right]^{\frac{1}{5}} \qquad (4)$$

where D_{ic} represents the fraction of interfacial area in intimate contact at any Lagrangian instant τ, during the process, μ is the temperature-dependent fiber-matrix viscosity, and P represents pressure. R_c is the roughness constant, and represents a "lumped" coefficient based on experimentally determined information of the surface asperities. A typical value for a fairly smooth surface for AS4/PEI based on experiments for AS4/PEEK is 0.29 and is used in this study.

13.5.6 POLYMER HEALING MODEL

Polymer healing is a temperature dependent phenomenon that is governed by the migration of polymer chains across the interfacial area in contact. The degree of healing is a function of both temperature and residence time at temperatures exceeding the glass transition temperature. The polymer chains are more mobile at these elevated temperatures, thus allowing for healing across the interface. Full healing across a fully developed interface is essential if the material is to have maximum strength and toughness. The healing model employed in this study was developed by Bastien and Gillespie [95] and was applied to PEEK-based thermoplastic systems by Agarwal [96]. Chao extended this work for PEI-based composites and it is this model that is used in this study [97].

Bastien and Gillespie [98] developed a non-isothermal model that describes the healing phenomena for PEI based composites. They extended the work of Wool [99], which considers the strength development to be dependent on the interdiffusion of polymer chains (reptation theory) that progressively heals the interface. This model proposes that the strength of two polymer interfaces is proportional to the contact time, $t^{1/4}$ for isothermal processes and increases to a plateau level at the reptation time [100]. This leads to a model of the strength of a healed region during isothermal bonding as follows:

$$\frac{\sigma}{\sigma_\infty} = \left(\frac{t}{t_r}\right)^{1/4} \tag{5}$$

where σ is the healing strength, t is the contact time, t_r is the reptation time (time required to completely heal the interface), and σ_∞ is the asymptotic strength corresponding to a fully healed interface. The temperature dependent reptation time is represented by and Arrhenius equation as follows:

$$t_r = B_r \exp\left(\frac{A_r}{T}\right) \tag{6}$$

The coefficients A_r and B_r were determined experimentally by Bastien and Gillespie from compression molding lap shear data to be 59728 K^{-1} for Ar and ln B_r = -105.6. They extended the model for non-isothermal conditions by summing the incremental strength increase for small isothermal time steps Δt. Thus the final strength is calculated as a sum of the strength contributions for the (n) time steps. This is defined as

$$\frac{\sigma(t)}{\sigma_\infty} = \sum_{n=0}^{t_p/\Delta t} \frac{t_{n+1}^{1/4} - t_n^{1/4}}{t_r^{1/4}} \tag{7}$$

where t_p is the total process time. This equation converges for sufficiently small time steps. An analogous relationship exists for toughness and is given by the square of Equation 7.

Figure 147 is a plot of the times required to achieve full strength and toughness with variation in constant temperature. It is seen that once the temperature increases above 540°F (280°C) the time required to achieve full bond strength (assuming 100% intimate contact) is small. Thus, from this result it appears as though the strength development in PEI based composites is attributed to the development of interfacial area rather than polymer migration.

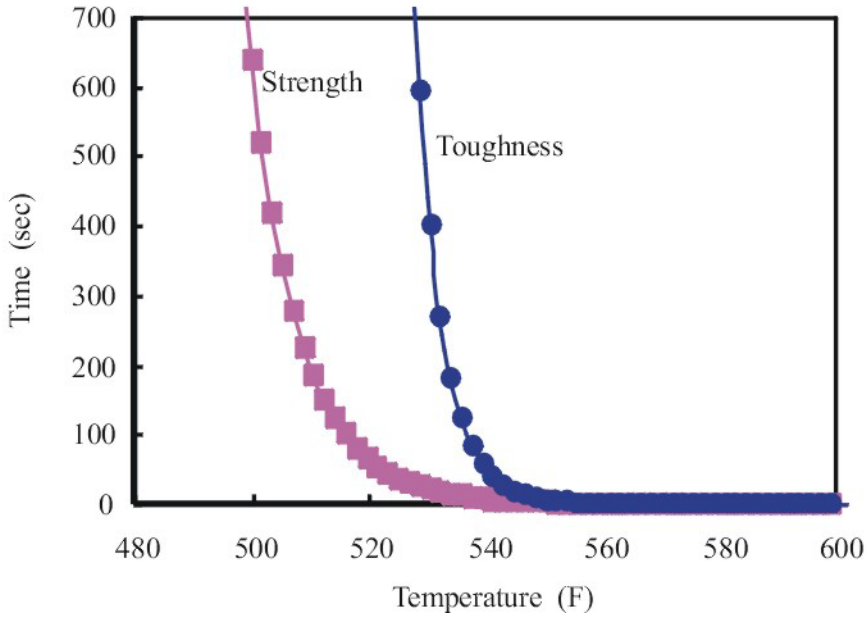

Figure 147. Strength Development of Neat PEI with Temperature.

13.5.7 COUPLED BONDING

Intimate contact is necessary to initiate healing across the interface. Therefore, a coupled bonding model was developed which takes into account the mechanisms of polymer healing and intimate contact simultaneously is used as a model prediction for through-thickness strength development. In this model, the degree of healing for each spatial increase in intimate contact is integrated throughout the process history to give the final degree of bonding. Thus by using a convolution integral, the resulting bond strength developed at the interface in dimensionless form can then be found as follows

$$D_b(\tau_h) = D_{ic}(0)D_h(\tau_h) + \int_0^{\tau_p} D_h(\tau - \tau')\left(\frac{dD_{ic}}{d\tau}\right)_{\tau'} d\tau \qquad (8)$$

where, $(\tau-\tau')$ is the time duration available for the incremental area to heal, and $D_{ic}(0)$ is the initial degree of intimate contact at $\tau = 0$. In the tow-placement process, the residence time of the tows under the consolidation roller, τ_{ic}, which also represents the available time for intimate contact to develop, is small relative to the time available for healing to occur, τ_h. Thus the development of intimate contact under the roller is considered to develop instantaneously, and is modeled using a Heaviside step function. In equation form, the coupled degree of bonding becomes:

$$D_b(\tau_h) = D_{ic}(0)D_h(\tau_h) + \int_0^{\tau_p} D_h(\tau - \tau')H(\tau - \tau')\Delta D_{ic}(\tau)d\tau \qquad (9)$$

The subsequent development of healing is tracked for each stepwise increase in intimate contact to give the final bond strength. This equation is a simplified yet accurate evaluation of the degree of interfacial bonding for this process. The accuracy of Equation 8 was

examined in a separate study, where the bond strength predictions were found to be in good agreement with experimental data obtained from short beam shear testing of in-situ consolidated panels with variation in torch gas temperatures [101,102].

13.5.8 VISCOSITY CHARACTERIZATION OF PEI

The temperature dependent viscosity behavior of PEI is modeled by a modified Arrhenius equation as shown below:

$$\eta(T) = A \exp\left(\frac{B}{T - T_g}\right) \qquad (10)$$

The above equation was fitted to experimental data for PEI to obtain the constants A = 107.4 Pa-s and B=630.0. The temperature dependent viscosity based in this model is shown in Figure 148. Also plotted on this chart is experimental data (GE Plastics) in the higher temperature ranges. These data were extrapolated to the glass transition temperature of 410°F (210°C) to determine the constants in Equation 9.

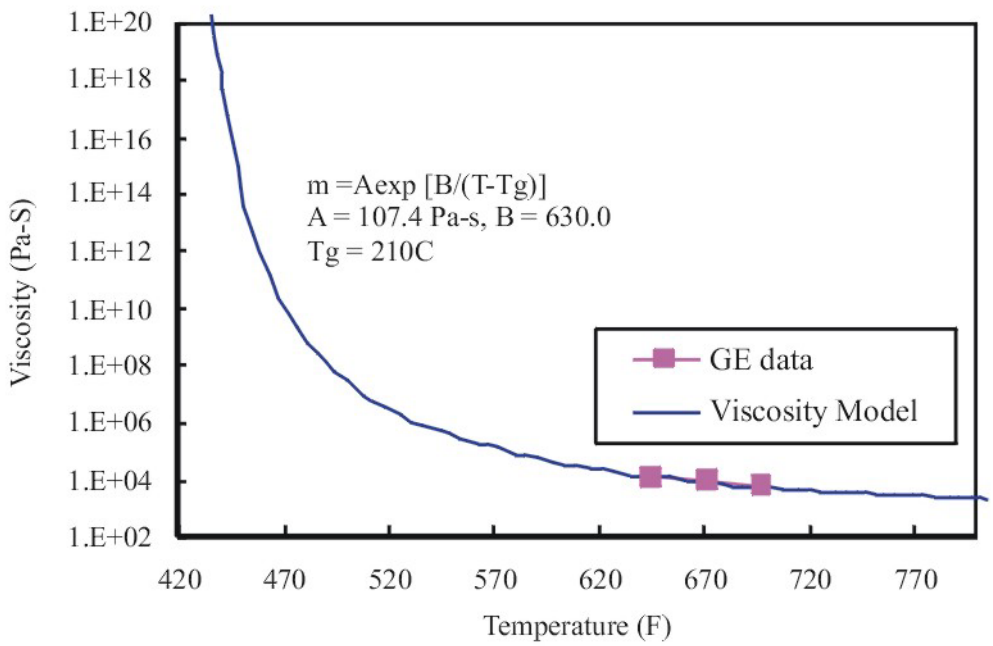

Figure 148. Viscosity-Temperature Relationship for PEI (Data Courtesy of GE Plastics).

13.6 Simulations to Establish Process Setpoints

The process models described above were incorporated into a FORTRAN simulation to determine the optimal hardware specifications of the laminator. Each element in the process is optimized separately with the goal of achieving the desired thermal and/or material quality (void content and degree of bonding) upon exiting the process element. The optimal process specification for each hardware element is then combined into an overall process simulation to determine any interaction between the constitutive parts of the process. A number of

difference case studies were carried out to determine the through thickness properties as a function of the thermal signature of the overall process.

Figure 149 is a plot of the ply temperatures with a process throughput of 10 fpm (50mm/s) and induction power maintained at 8 kW. The 8 kW heat input was chosen such that maximum material temperature does not exceed the degradation temperature of PEI (750°F). The heater and cooler shoe lengths are both set at 6 inches, and the consolidation roller is 4 inches in diameter and maintained at room temperature. The induction field is applied to a volumetric region with dimensions of 1" x 12" x 0.04". The induction source is spaced 3 inches from the heater and cooler shoes to avoid heating due to the induction field. The heater shoe is set to 800°F (430°C) such that the material exit temperature is 480°F (250°C). The hardware specifications presented are optimal specifications based on an extensive parametric study where induction power, heater shoe temperature, shoe lengths, and relative element locations were examined.

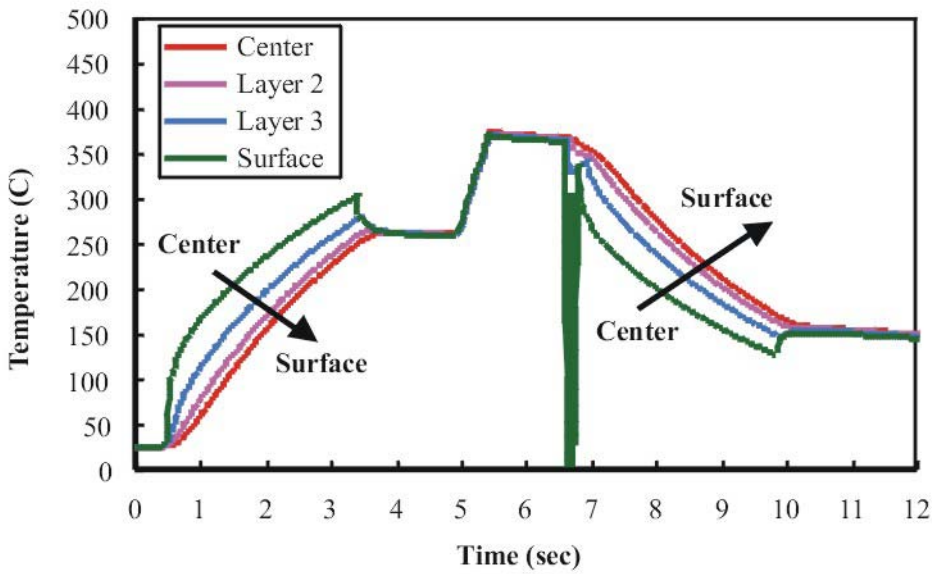

Figure 149. Ply Interface Temperatures for Process Throughput of 10ft/min.

In this study, the consolidation roller and the incoming material are both set at room temperature (77°F). The external loading to each element is variable up to a maximum of 3500 lbs. The initial thickness of the laminate is 8 plies x 0.127 mm (0.005 inches). Since the process is symmetric about the laminate mid-plane, only one half of the process domain need be examined.

From Figure 148, one can see that the heater and cooling shoe regions behave as expected and a sharp increase in temperatures is observed at the 1-in induction coil region. The sudden temperature drop of the surface ply is due to the consolidation roller, which is modeled as a forced contact boundary condition. The predicted temperature profiles are then applied to the consolidation and bonding models to determine the through thickness bond strength and void fraction.

Figure 150 is a snapshot of the surface ply process temperatures, void growth/compaction, and bond strength development for the lamination process with the thermal data from Figure

149. The void fraction and bond strength development, are shown with bond strength varying between 0 and 1, where 1 represents maximum strength. From this plot, one can see that bond strength develops primarily at the cooling shoe due to the favorable temperature and pressure conditions. Little bond strength is obtained at the roller as the cool roller increases viscosity such that polymer flow is prevented. This represents the worst-case scenario as the surface is modeled as a forced contact problem with the roller at room temperature, and a linear approximation is assumed across the surface ply. In actual conditions however, the temperatures at the interface will be hotter as a non-linear temperature profile exists across the surface ply and as such will allow for more favorable conditions towards improving bond strength. In summary, the roller force and temperature represents the critical mechanism for material quality development based on intimate contact and void compression at the surface of the laminate. The effect of this roller will not be as evident within the laminate as the thermal profile of the remaining interfaces does not vary significantly in this critical region.

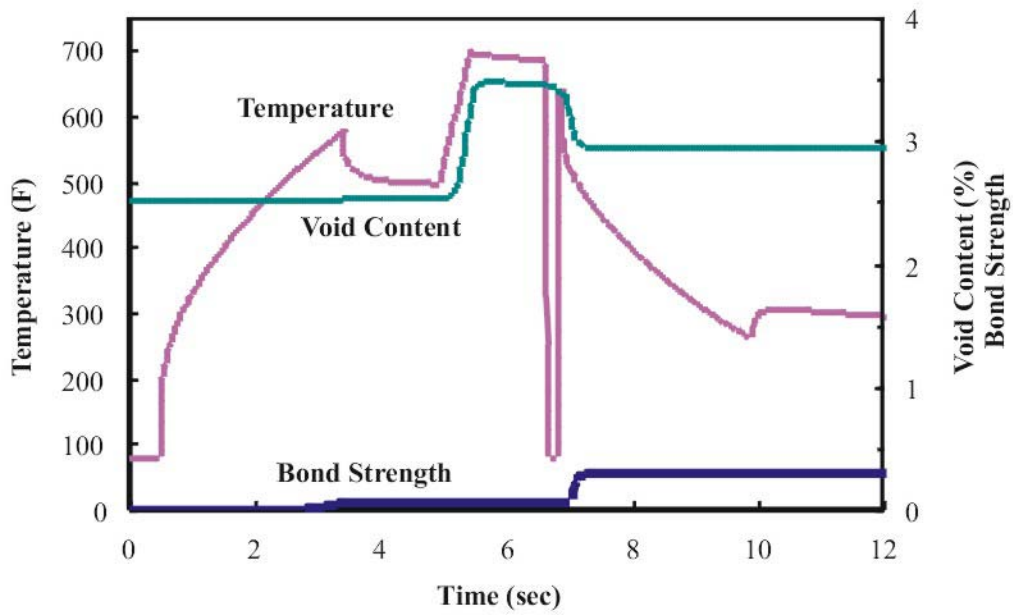

Figure 150. Surface Layer Temperature, Void Fraction, and Bond Strength in Induction-Processed PEI (V = 10 ft/min, $T_{preheat}$= 800°F, Q_{in} = 8kW, T_{cooler} = 77°F).

In addition, the final void fraction in the surface ply is high (3%), as the material is quenched at the surface and prevented from consolidating under the cool roller. Successful void compaction can be achieved on the surface if the cooling shoe temperature is increased such that the viscosity remains low when entering the cooling shoe.

Figure 151 is a plot of the material property development of the center ply under the same process conditions. Note that the bond strength is considerably higher in the interior of the laminate, as the material is not exposed to the cool consolidation roller. Also note that the final void fraction is lower at the center of the laminate as the material is considerably warmer (≈ 480°F) when entering the cooler shoe such that void compaction occurs under pressure from the cooling shoe.

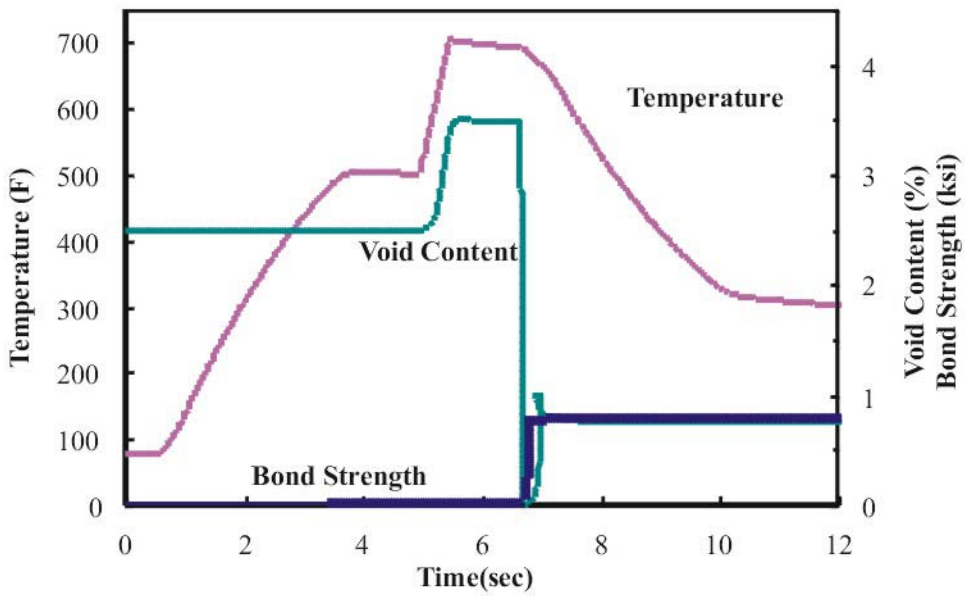

Figure 151. Center Ply Temperature, Void Fraction, and Bond Strength in Induction-Processed PEI (V = 10 ft/min, $T_{preheat}$= 800°F, Q_{in} = 8 kW, T_{cooler} = 77°F).

When each ply is examined separately, the through thickness profile of both bond strength and void fraction can be generated at various stages in the lamination process. Figure 152 is a plot of the through-thickness bond strength after two critical regions: the heater shoe and consolidation roller. The bond strength is high for the internal plies and drops off at the surface due to cooling from the roller in the compaction region. The process simulation can be used to optimize set points to achieve the required level of bonding in the laminate.

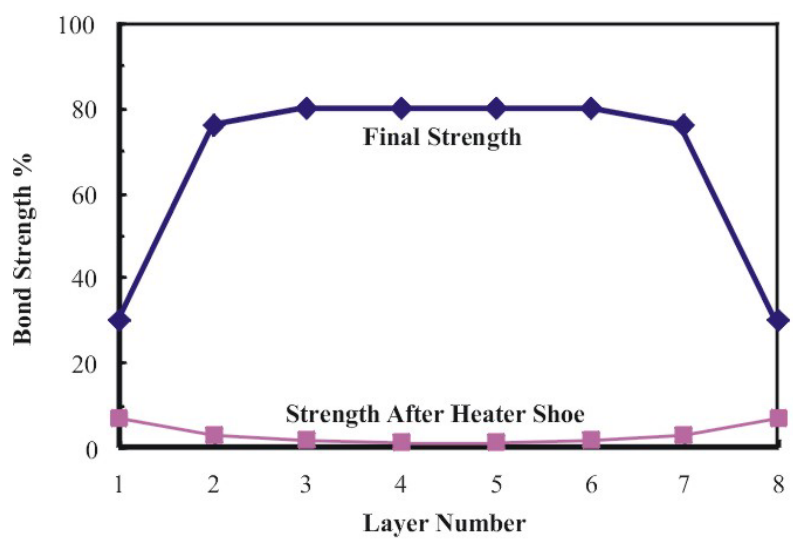

Figure 152. Through-Thickness Bond Strength Variation (V = 10 ft/min, $T_{preheat}$= 800°F, Q_{in} = 8 kW, T_{cooler} = 77°F).

13.7 Induction Coil Design

A major advantage of induction heating technology is coil design flexibility. The size and shape of an induction coil can be "fit," or matched, to the composite part that is to be heated, even for geometrically complex shapes. It is also possible to use a simple coil design and heat complex geometric shapes using programmed motion with a robot. Based on induction coil models, coil designs were developed for a 12-in wide laminate process. This involves lamination or consolidation of an 8-ply prepreg in the desired orientation into a consolidated laminate with specified quality. This is achieved by induction heating the prepreg stack up to process temperature, followed by consolidation under pressure.

13.7.1 LAMINATOR COIL DESIGN

The function of the laminator or the lamination stage is to fabricate 8-ply thermoplastic laminates at high throughputs (~20 ft/min.) and desired quality. Thus, the induction heating stage of this process step has to uniformly and rapidly heat the incoming material (8-ply prepreg stack) up to the process temperature while allowing continuous material flow. The challenge is to handle incoming prepreg stacks of various orientations and still meet the rapid and uniform heating requirements.

Several different coil configurations were modeled and tested resulting in the selection of a rectangular (or paperclip shaped) coil for the laminator. The coil geometry and resultant temperature profiles are shown in Figure 153 and Figure 154, respectively.

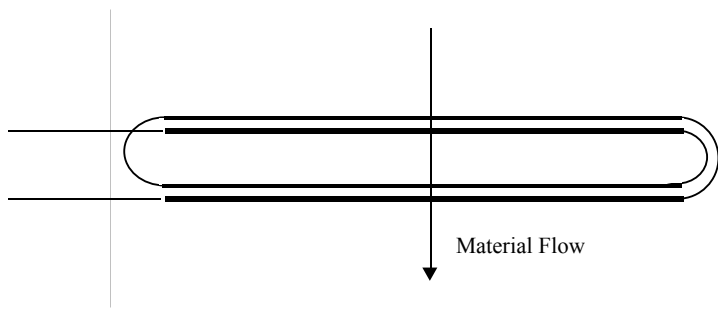

Figure 153. Schematic of Rectangular Coil for Lamination Stage

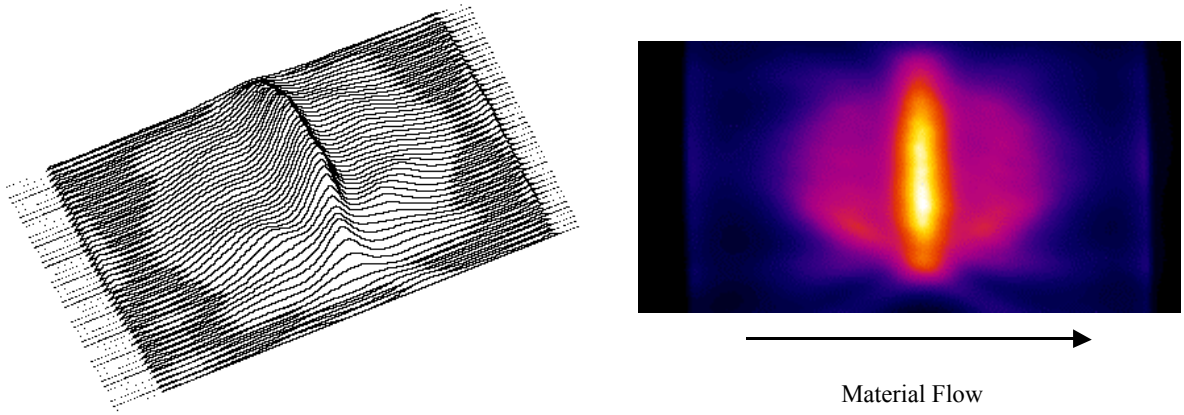

Figure 154. Temperature Profiles of 8-Ply Stack with Rectangular Coil

The rectangular coil geometry has been optimized to production level design criteria as a result of work under this program. The final design specifications are proprietary for the full scale induction processing unit..

13.8 Final Laminator Configuration and Process Setpoints

Table 61 shows a summary of the final process and hardware parameters for the lamination process based on an extensive model-based parametric study with variation in process velocity. The required induction power to the AS4/PEI composite is based on, achieving the target centerline temperature of 625°F, with a maximum allowable temperature of 715°F (380°C) in the induction zone.

From this table, one can see that the power and heat input requirements increase rapidly with increase in velocity, especially in the heater shoe section. The high temperatures required in the heat shoe at high velocity correlates directly with the small residence time that the heat can flow to the center of the laminate. Due to these high temperature requirements, the surface of the laminate at the exit of the heater shoe can be close to the melt temperature. As stated previously, it is important to limit the amount of surface area of the shoe under pressure that is in contact with the melted material.

Table 61. Final Hardware Configuration and Setpoints for Experimental 8-Ply Laminator

HARDWARE STATION	Hardware Specification	3ft/min	6ft/min	12ft/min	20ft/min
Heater Shoe T_1=482°F T_1=625°F	**6-in. length Resistance Heaters**	**505°F 482°F**	**610°F 792°F**	**939°F 1180°F**	**1454°F 1788°F**
Induction Power T_{max} = 716 °F	**1-in wide**	**3.2KW**	**5.7KW**	**9.1KW**	**12.3KW**
Cooling Shoe	**6-in length water cooled**	**257°F**	**140°F**	**77°F**	**77°F**
Consolidation Roller Force F_{roller} = 3200lbs	D_b (F_{shoe}=3200lbs) D_b (F_{shoe}=1600lbs) D_b (F_{shoe}=800lbs)	81.08% 80.01% 79.74%	89.91% 89.02% 88.61%	82.71% 80.40% 79.24%	81.60% 77.52% 75.30%
	V_f (F_{shoe}=3200lbs) V_f (F_{shoe}=1600lbs) V_f (F_{shoe}=800lbs)	0.74% 0.79% 0.80%	0.76% 1.24% 1.77%	1.91% 2.21% 2.47%	3.13% 3.13% 3.14%
Consolidation Roller Force F_{roller} = 3200lbs	D_b (F_{shoe}=3200lbs) D_b (F_{shoe}=1600lbs) D_b (F_{shoe}=800lbs)	70.55% 70.54% 70.53%	79.61% 78.14% 77.43%	75.53% 72.08% 70.26%	72.88% 71.12% 67.87%
	V_f (F_{shoe}=3200lbs) V_f (F_{shoe}=1600lbs) V_f (F_{shoe}=800lbs)	0.82% 0.86% 0.88%	0.76% 1.24% 1.77%	1.91% 2.20% 2.47%	3.13% 3.13% 3.14%
Consolidation Roller Force F_{roller} = 3200lbs	D_b (F_{shoe}=3200lbs) D_b (F_{shoe}=1600lbs) D_b (F_{shoe}=800lbs)	61.20% 61.18% 61.17%	71.63% 69.34% 68.18%	70.31% 65.51% 62.74%	68.52% 66.42% 61.96%
	V_f (F_{shoe}=3200lbs) V_f (F_{shoe}=1600lbs) V_f (F_{shoe}=800lbs)	0.93% 0.98% 1.01%	0.76% 1.24% 1.77%	1.91% 2.21% 2.47%	3.13% 3.13% 3.14%

The power requirement seems to vary linearly with velocity, although this linearity is also related to the heat input from the heater shoe and the residence time in the free air region between the heater shoe and induction zone. The optimal cooling shoe temperature also varies with process velocity. The reason for varying the cooling shoe temperature is to allow sufficient time for the voids to be compressed at the surface of the laminate and to increase bond strength. Insufficient time under the shoe at higher velocities results in no void compression under the cooling shoe. At the optimal cooling shoe temperature, (a) the center

of the laminate is cooled to temperatures below T_g, and (b) the surface is exposed to temperatures exceeding T_g such that successful void compression is achieved. At higher velocities, the cooling shoe is maintained at room temperature as the residence time under the cooling shoe is greatly reduced thus limiting the processing window to the best-case result of reducing the center of the laminate below T_g and limiting void growth. Optimal values will be determined though experimental validation. It is noted however that the bond strength increase and void compression though cooling shoe temperature control did not improve significantly, and that the improvement in material properties were only achieved at the surface ply.

13.9 Experimental Laminator

Based on the simulation models and hardware design, an experimental "proof-of-concept" laminator has been designed and fabricated (Figure 155). The experimental laminator was then rigorously tested to meet the desired requirements. Modifications were made to the stages as required; however, the overall design concept has remained the same.

The laminator comprises five stages: preheat, induction, consolidation, cooling, and infeed/outfeed. The preheat stage establishes intimate contact between plies by heating the outer plies, which aids in heat generation in the induction stage. This is necessary, as intimate contact (surface quality of prepreg) drives the heat-generation capability in the induction stage, and prepreg quality can vary widely. The induction stage generates volumetric heating at high rates (~100 °C/s) and raises the temperature of the material to within the desired process window. An IR-sensor-based feedback control loop is used to maintain temperature to within ± 10 °C of the setpoint. The consolidation stage consists of chilled rolls that apply pressure to obtain the desired degree of bonding and void content. The cooling stage reduces the temperature of the laminate to below the glass transition temperature of the polymer. The infeed/outfeed stage is the drive system for the machine and pulls the material through, as well as controls the machine throughput. The laminator is fully automated; once the material feed is accomplished, the stages are automatically lowered and raised as the material goes through at the desired process velocity. A typical thermal profile in the heating zone is shown in Figure 156.

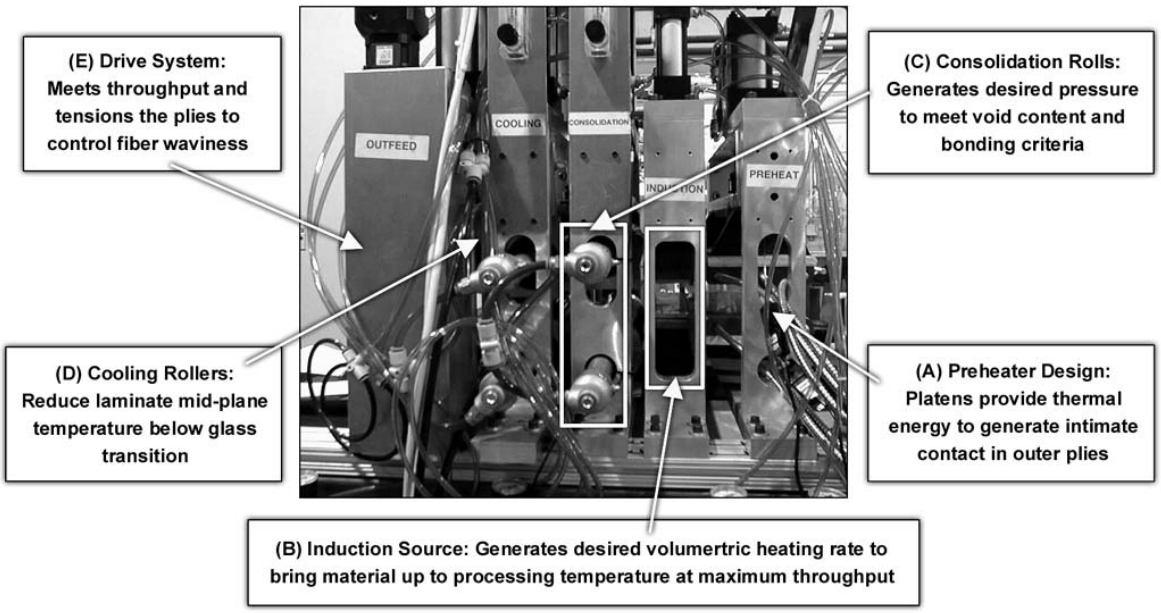

Figure 155. Induction-Based Lab-Scale Experimental Laminator.

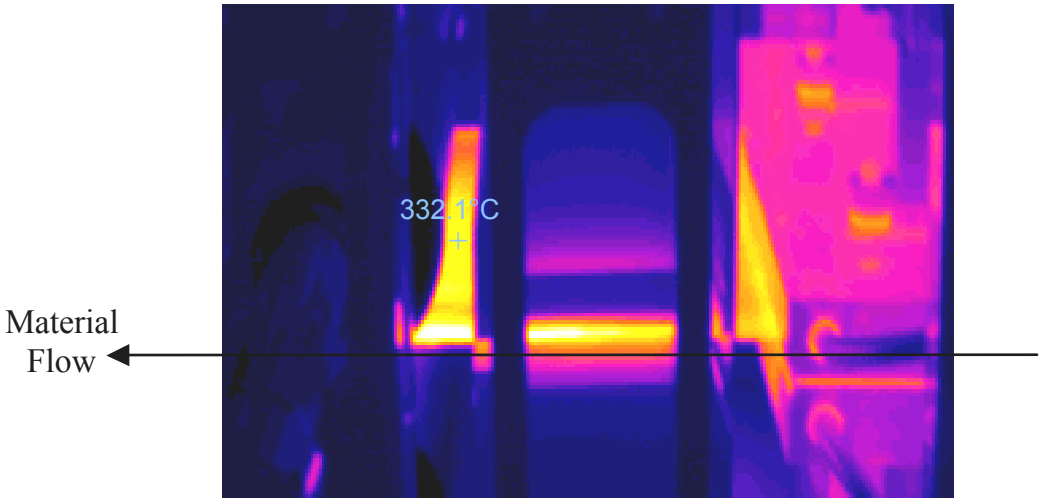

Figure 156. Infrared Temperature Profile of Heating Zones.

13.10 Performance and Quality

Laminator performance was quantified by measurements of void content and tensile properties of the laminate and compared to the vacuum debulk baseline, as shown in Figure 157. Void content measurements for induction-processed laminates showed that voids were primarily in the outer two layers, with almost zero voids in the inner layers (also predicted by process model). This is due to the chilled consolidation roller that "freezes" the outer two

layers and locks in the voids. The inner layers are still at high temperatures and the roller pressure acts to reduce void content. Average void contents were less than 1 %.

Table 62 shows the measured material properties (ASTM tests) for various laminates comparing the effect of different processing techniques and cycle times. The induction-processed laminates show identical properties to the vacuum debulk baseline with an order of magnitude decrease in cycle time.

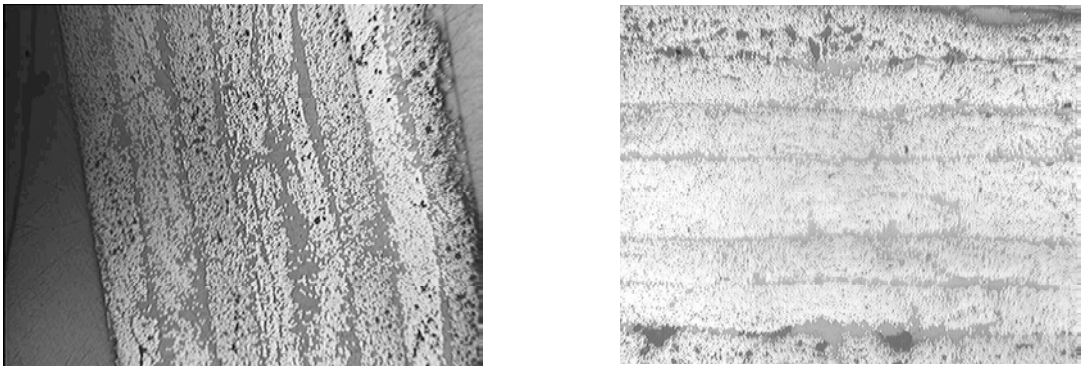

Figure 157. Void Content Comparison Between Vacuum Debulk Baseline (l) and Induction-Processed Laminate (r).

Table 62. Mechanical Performance of Induction-Processed Laminates

Process	Longitudinal Tensile Strength (ksi)	Longitudinal Tensile Modulus (Msi)	Transverse Tensile Strength (ksi)	Transverse Tensile Modulus (Msi)	Cycle Time (sec)
Vacuum Debulk	191.7 ± 7.1	13.3 ± 0.5	16.3 ± 1.1	1.45 ± 0.04	300
Laminator at 5 ft/min	182.4 ± 2.8	13.6 ± 0.3	16.5 ± 0.3	1.50 ± 0.03	36

Technology developed and proven in the lab-scale laminator was transitioned to a production line at Alliant TechSystems. Lessons learned during the laminator design, fabrication, and prove-out have been implemented as part of the design criteria for the factory floor laminator.

13.11 Conclusions to Induction-Based Thermoplastic Composite Lamination

The ability of induction heating to rapidly process carbon-fiber-based thermoplastic composites is a significant environmental asset. Assuming that the thermoplastic composite meets the performance and quality requirements of its thermoset counterpart, the limited-

shelf-life thermoset can be replaced with the unlimited shelf-life thermoplastic. This completely eliminates the problem of hazardous waste due to shelf-life expiration.

Work to date has established that induction heating is a key technology component for the use of carbon/thermoplastics in Army composite structures. The ability to fabricate laminates from thermoplastic polymers while meeting performance and throughput requirements will allow future designs to replace environmentally hazardous thermoset processing techniques with low-impact alternatives and potentially eliminate a substantial volume of hazardous waste production for the Army and Army contractors.

14 Induction Electromagnetic Effects

When considering induction as a process for repair and remanufacturing of composite parts, the electromagnetic effects on other performance characteristics of the parts must be considered.

14.1 Induction Processing

An induction field is a high frequency electromagnetic field, typically operating at frequencies between 1 kHz and 100 MHz. Some materials will heat in the presence of an inductive field. These materials are called susceptor materials. Susceptor materials include electrically conductive materials, such as metals and carbon fiber composites, and magnetic materials, such as magnetic metals and magnetic ceramics. Non-susceptor materials include polymers, glass– and Kevlar-fiber composites, and non-magnetic ceramics.

Induction heating of susceptor materials can be utilized to bond and repair damaged structures. One of the most likely applications is rapid bonding using elevated temperature–curing adhesives. By embedding metal screens or magnetic particles in the adhesive bond line, application of an induction field causes the bond line to heat and cure. Because the induction energy is localized to the bond line, heating is rapid and efficient and allows heating of deeply embedded bond lines.

Induction fields are typically generated by an induction coil attached to a high frequency power supply. Induction coils can be shaped to customize the dispersion of the induction field, although the field strength always drops rapidly with distance from the coil. Tuning considerations limit coil sizes, and areas of continuous induction field application, to a footprint between 5 and 50 cm per side. In a typical repair scenario, the induction coil would be held over the repair area until the adhesive was completely cured, which could take anywhere from a few seconds to a few hours.

14.2 Possible Deleterious Effects of Induction Fields on Aircraft Systems

Induction repair is under consideration for application to DoD aircraft and ground vehicles. A potential limitation of this application, however, is the secondary effects of induction fields on surrounding structural and electronic components. These secondary effects can be broadly categorized into two categories: heating effects and electromagnetic interference effects.

Heating effects include any unintentional heating of components in or near the repair area. High temperatures can permanently damage both structural and electronic components. Carbon fiber composites are especially sensitive to unintentional heating, since they both heat efficiently in induction fields and undergo thermal degradation at relatively low temperatures. Metal structures are more tolerant of high temperatures, but because they are often in proximity to lower temperature materials such as composites, plastics, and adhesives, their unintentional heating can still cause considerable damage. Electronic devices typically contain significant amounts of metal near or within extremely sensitive components and are therefore susceptible to thermal damage.

Electromagnetic interference effects include any decrease in performance in an electronic component due to the presence of the induction field itself. The induction field can either directly interfere with electromagnetic sensing devices, such as radar or communications sensors, or simply induce stray currents and electric fields within more general electronic devices.

The objective of this document is to briefly assess the potentially damaging effects of induction processing on overall performance of DoD aircraft and ground vehicles. Based on this assessment, recommendations are made for mitigating the risks introduced by performing structural repairs using induction fields.

14.3 Heating Effects

Induction fields can be quantified in terms of their frequency, amplitude, and distribution. In general, the heating power generated by susceptor materials will increase with induction field frequency and amplitude. Metals heat most efficiently, and can be induction heated even at relatively low frequencies. Carbon fiber composites require moderate frequencies in order to achieve efficient heating. Magnetic materials heat least efficiently, generally requiring MHz frequencies in order to induce sufficient heating for repair applications.

Due to the limitations of field portable induction processing equipment, it is unlikely that significant secondary heating will ever occur on parts located more than 0.5 m away from the repair area. The induction field strength drops off very rapidly with distance from the coil, and significant field strengths are necessary to induce significant heating effects. Therefore any parts more than 0.5 m from the repair area can be considered safe from secondary heating.

Components closer to the bond line need to be considered on a case-by-case basis, with parts nearer to the coil having the highest likelihood of heating. Metals and carbon fiber composites will, in general, heat faster than adhesives filled with magnetic susceptor particles. For this reason, it is unlikely that metal and carbon fiber composite parts can be induction repaired using magnetic susceptor adhesives. The substrate heating could be used directly to thermally cure the adhesive, but then temperature sensors and power regulation would be required to ensure that bond line heating was properly controlled. Such a scenario is possible but probably very complicated.

Bonding of non-susceptors with induction adhesives is straightforward. However, if secondary susceptor materials, such as metal fasteners or heavy gauge wiring, are nearby

secondary heating could be significant. These situations need to be considered on a case-by-case basis.

Some special properties of induction heating can be used to widen the applicability of induction for repair near secondary susceptor materials. For example, at very high frequencies metals begin to reflect induction fields, limiting their volumetric heating. Therefore induction processing in the presence of very thick metal components may be possible by using very high frequencies. Also, the heating behavior of carbon fiber composites is very sensitive to the laminate fiber architecture, as well as to the orientation of the induction field lines relative to the fiber directions. In some cases, it may be possible to utilize these effects to decrease the heating efficiency of secondary carbon fiber components, and instead selectively heat only the bond line. The orientation of field lines can be addressed by design of the inductive coil used in the repair schema.

14.4 Interference Effects

DoD Interface Standard MIL-STD-461E (1999) provides recommended standards for preventing interference effects in electronic devices [103]. These standards include both susceptibility requirements, which govern the minimum external fields under which devices are expected to function properly, as well as emission restrictions, which limit the maximum field strengths which may be safely emitted by devices.

The emission requirements provide a conservative bound on the likelihood of interference caused by induction fields. That is, if the induction fields meet these standards, then they are very unlikely to in any way interfere with other electronic devices. If instead the electromagnetic fields produced during induction far exceed these standards, then it is highly possible that induction processing would interfere with the operation of vehicle electronics.

It is important to consider, however, that repair would most likely be performed on a completely unpowered vehicle. In this case, interference with electronics on the vehicle may not be relevant (e.g., the vehicle will not be performing radar scans or communicating with central command while it is unpowered and being repaired). It is possible that electronics could still be permanently damaged by secondary electromagnetic fields through non-heating mechanisms, such as accumulation of residual electric charge or damage to magnetic memory devices. Unfortunately, the MIL standard does not separately consider such effects, and we are unaware of other, more applicable, standards. Therefore we will examine induction heating in light of the full MIL-STD-461E requirements, with the understanding that a far less stringent standard is probably more appropriate for evaluating induction processing on unpowered vehicles.

MIL-STD-461E has separate restrictions for emission of magnetic fields and electric fields. Although magnetic fields are the source of power generation during induction heating, they are accompanied by electric fields. We will consider both requirements separately.

14.5 Magnetic Field Emissions

Induction processing for repair typically requires magnetic field strengths (also called amplitudes) of 0.5 - 50 mT, at frequencies from 10 kHz to 10 MHz. Due to equipment design limitations, higher frequency devices typically produce lower field strengths. Also,

heating is typically more efficient at higher frequencies, so less amplitude is required to transmit high powers.

Table 63 shows the MIL-STD-461E limits for emitted magnetic field strength, requirement RE101. Separate limits are given for Army applications and Navy applications. The standards imply that these limits include all Army and Navy vehicles, including ground vehicles, rotorcraft, fixed-wing aircraft, and surface ships. Explicit limits are given only up to 100 kHz. Based on the trends in the standards, we have extrapolated the limits to 10 MHz. For the Army standard, we assume that the limits continue exponentially downward. For the Navy standard, since the maximum field strength limit is constant at 0.04 mT from 30 kHz – 100 kHz, we assume that this trend continues through higher frequencies.

Table 63. MIL-STD-461E RE101 limits on emitted magnetic field strength (B). Values in parentheses are extrapolated values.

Frequency (MHz)	Maximum B (mT) Army	Navy
0.01	1×10^4	0.4
0.1	100	0.04
1	(1)	(0.04)
10	(0.01)	(0.04)

The maximum field strength values in RE101 are to be measured a distance of 7 cm from the field source. For a typical coil (5-turn pancake coil, outer diameter 10 cm), the field strength will be reduced to about 25% of the source value at a distance of 7 cm.

According to the standard, the maximum allowable magnetic field strengths for Army applications are 100, 1, and 0.01 mT at frequencies of 100 kHz, 1 MHz, and 10 MHz, respectively. For Navy applications, the limits are 0.04 mT from 100 kHz through 10 MHz. By scaling our expected induction magnetic field strengths to 25% (based on the 7 cm standoff distance), we expect field strengths of 0.125 – 12.5 mT. Therefore, the expected induction magnetic field strengths will exceed the Navy standards for all cases, except for very low amplitude fields at very low frequencies. The Army standards will almost always be exceeded at high frequencies, while at low frequencies some induction fields would be acceptable.

14.5.1 Electric Field Emissions

We can estimate the electric field strength associated with an induction coil by using the relation

$$E = (\pi / 2) f R B_o$$

which expresses the electric field strength E for a uniform field B_o at frequency f acting over an area with radius R [104]. For a 10 cm diameter circular area, Table 64 shows electric field strength as a function of frequency and amplitude. The smallest electric field strength value is 3.9 V/m, while the largest value is 3.9×10^6 V/m (which is actually slightly higher than the dielectric strength of air!).

Table 64. Electric field strength E as a function of frequency for magnetic fields of amplitudes 0.5 and 50 T acting over a 10 cm diameter area.

Frequency (MHz)	Maximum E (V/m) B=0.5 T	B=50 T
0.01	3.9	3.9×10^3
0.1	3.9×10^2	3.9×10^4
1	3.9×10^3	3.9×10^5
10	3.9×10^4	3.9×10^6

Table 65 shows the limits for emitted electric field strength according to MIL-STD-461E requirement RE102. The standard does not mention standoff distance, so we will assume that the limits apply directly at the source location. Clearly, the expected induction electric fields will exceed the standards in nearly every case, in fact in most cases the standard is exceeded by several orders of magnitude.

Table 65. MIL-STD-461E RE102 limits on emitted electric field strength (E). Values in parentheses are extrapolated values.

Frequency (MHz)	Maximum E (V/m) Surface Ship	Aircraft	Army Ground Vehicle
0.01	10	1.0	(2.5×10^{-4})
0.1	1.58	0.025	2.5×10^{-4}
1	0.25	6.3×10^{-4}	2.5×10^{-4}
10	0.025	2.5×10^{-4}	2.5×10^{-4}

14.5.2 Emission Standards for Antennas

Communication antennas are expected to exceed the magnetic field and electric field limits of RE101 and RE102 by several orders of magnitude. The only emissions requirement for antennas in MIL-STD-461 is RE103, which limits the strength of emitted harmonics. Since fieldable induction equipment would likely be fixed frequency, it is possible that the induction equipment could be treated as an antenna. It is not clear how electronic devices are tested for, or protected against, interference due to antenna emissions.

14.6 Summary of Recommendations

The assessment of heating effects shows that secondary heating can only cause damaging effects to components located within 0.5 m of the induction repair area. Secondary heating in the repair area is extremely unlikely when the majority of components are non-susceptor materials, such as polymers, glass-fiber composites, and non-magnetic ceramics. However, there is a chance of significant secondary heating for metal or carbon fiber composite parts in the repair zone, including metal fasteners and heavy-gauge wiring. In some cases secondary heating of such parts can be minimized, but only through careful engineering on a case-by-case basis.

In general, due to the sensitivity of electronics to thermal damage induced by induction fields, sensitive electronics should not be located within 0.5 m of the repair area. In some cases shielding built into the device may protect it from stray induction fields, but such protection must be tested on a case-by-case basis.

The electromagnetic fields produced by induction equipment are very likely to interfere with the operation of electronic devices on the vehicle. Therefore induction repair should never be attempted on powered vehicles, unless the effects have been thoroughly tested. On an unpowered vehicle, it seems unlikely that induction fields would cause any permanent damage unless the electronics are very near to the repair zone. This damage could include both heating effects and more circuit-level effects, such as erasing of magnetic memory devices. Unfortunately, it is difficult to assess which devices are particularly susceptible to such circuit-level effects, and what electromagnetic field strengths are necessary to cause such damage. Again, shielding layers built into existing devices may provide some level of protection, but such protection would need to be tested on a case-by-case basis.

15 Co-Injection Resin Transfer Molding for Repair and Remanufacturing

The objectives of the Co-Injection Resin Transfer Molding (CIRTM) efforts under this program were to develop methods to reduce hazardous waste contamination, which resulted from multi-step processing. By integrating infusion of multiple resins into a structure under a single infusion step, bagging and infusion setup materials are decreased by nearly 50%. Additionally, the composite is cured in a single step, which minimizes emission potentials resulting from oven or autoclave thermal processing. Key issues that currently limit the use of this new technology for environmentally friendly repair and remanufacturing need to be addressed. While the potential for significant environmental-cost savings was demonstrated under this program, the technology was transferred to the Navy and Navy contract manufacturers for industrial level development during the early phases of the program.

VARTM processes have been proven to be cost-effective manufacturing techniques for large composite structures. However, their use has been limited to single-resin systems. A large variety of composite structures require multiple resins to serve different purposes while being integrated into a single structure. CIRTM enables the user to manufacture multi-layer hybrid composite parts in a single processing step. The CIRTM process was investigated to manufacture a dual layered structure consisting of a vinyl-ester layer for structural integrity and a phenolic layer for flammability, smoke, and toxicity (FST) protection. The two resins are simultaneously injected into a mold filled with a stationary fiber bed and co-cured. Resin separation is maintained by a 1-mil-thick polysulfone film sandwiched between two layers of 6.5-mil-thick adhesive. Differential Scanning Calorimetry (DSC) is used to select the optimum cure cycle for all of the materials. Mechanical testing is used to evaluate the performance of the interphase formed between dissimilar materials. Short Beam Shear (SBS) is used to evaluate the overall quality of the part produced.

Mechanical characterization of the CIRTM parts suggests that the choice of materials is critical to the CIRTM process. A number of alternatives were evaluated. Chemical compatibility of the base composite resins with the film adhesive is critical for interphase

quality. Results showed that with proper selection of constituent materials and cure cycles, the interlaminar shear strength provided by CIRTM is enhanced relative to the weakest resin in the specimen. In all CIRTM specimens, shear failure occurred within the phenolic. For the Mode I fracture toughness testing, failure of the co-injected samples was observed to be cohesive, while failure of the secondary bonded samples was adhesive failure between the epoxy adhesive and the phenolic composite. During Mode I crack propagation, multiple delamination planes formed in the phenolic laminate, which is a reflection of the higher toughness offered by the CIRTM interphase. Results of both interlaminar shear and Mode I fracture toughness for the CIRTM were comparable to or exceeded the phenolic baseline. The fire performance characteristics of the CIRTM laminates offered superior protection in terms of peak rate of heat release and time to ignition. Further improvements to the FST performance are possible through optimization of the relative thicknesses of each resin layer.

Table 66 shows the various resins system and fiber preforms that have been successfully co-injected.

Table 66. Co-injected Fiber Preforms and Resin Combinations

Fiber Preforms	Resin Combinations
Carbon Glass	Epoxy/urethane Epoxy/vinyl ester Epoxy/phenolic Vinyl ester/phenolic Vinyl ester/urethane Phenolic/urethane

Various end item articles and configurations, such as flat plates, angle bends, and integral armor components, have also been fabricated. Examples of these articles are shown in Figure 158--Figure 161.

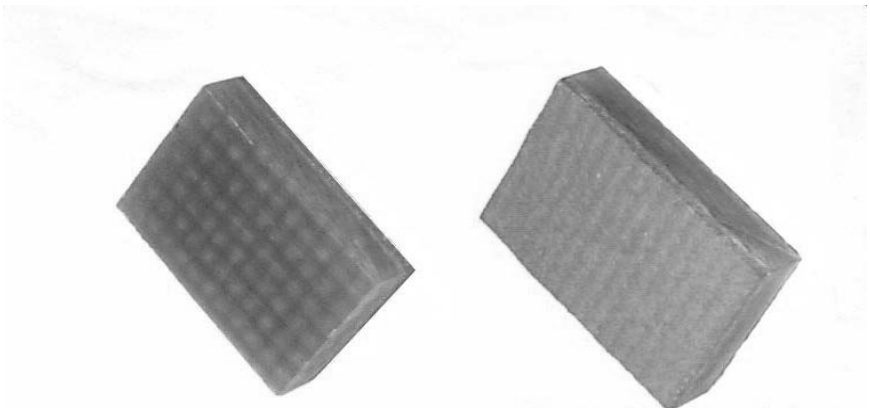

Figure 158. Example of a co-injected dual-resin component with a structural vinyl-ester resin on one side and a fire-protective phenolic resin on the other.

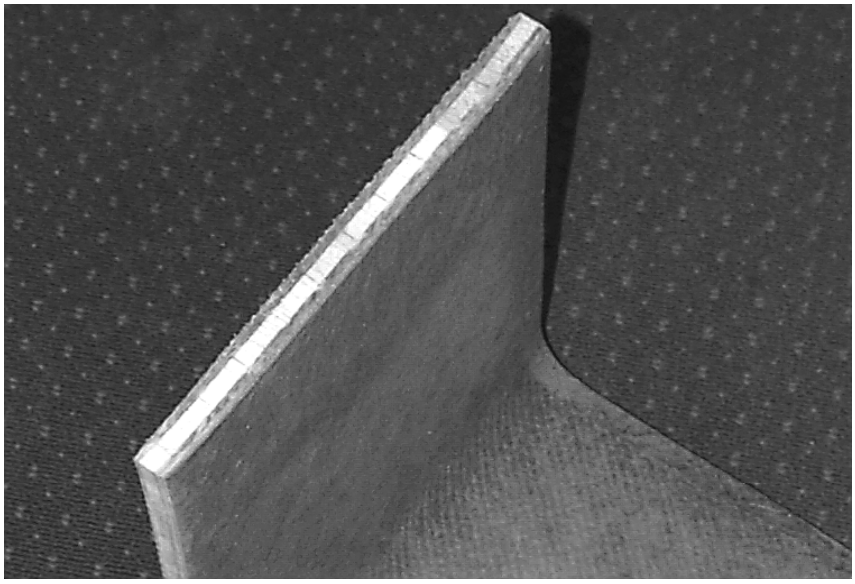

Figure 159. Example of a co-injected angle section with balsa core demonstrating scaleup of the process to large, angular components.

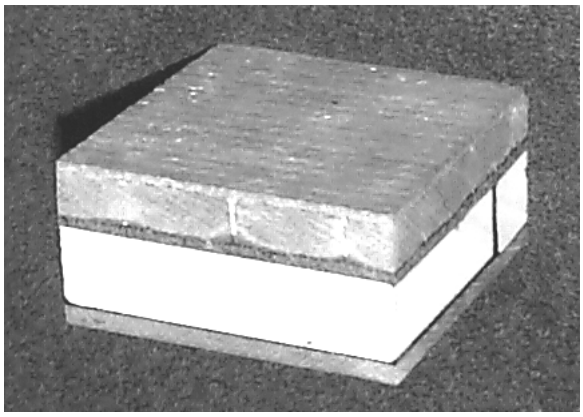

Figure 160. Co-injected integral armor section using three different resins (structural, fire-protective, and energy-dissipative), and through-thickness reinforcement enabled by the CIRTM process.

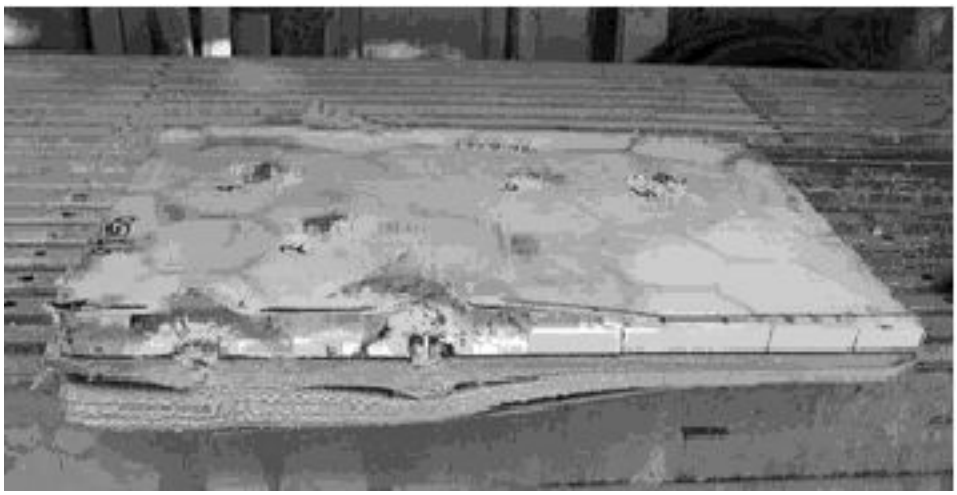

Figure 161. An example of the improved ballistic protection offered by a co-injected, stitched integral armor panel.

The benefits of low-cost VARTM processing are being explored for composite repair procedures. VARTM processing offers the advantage of room-temperature storage of materials, long to infinite storage life, and room/low-temperature-cure resin systems. The CIRTM process is now being evaluated for repair of multifunctional composites and cored composite structures. CIRTM offers the ability to repair these multifunctional hybrid composites in a single step, restoring the structure to its original state. An example of a VARTM repair to a honeycomb structure is shown in Figure 162.

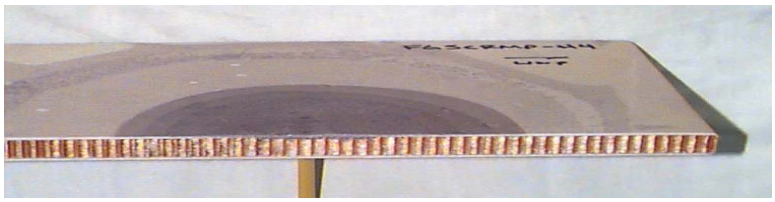

Figure 162. Example of a VARTM repair of a honeycomb core structure.

15.1 Scale-up of Resin Down-Selection and Testing of CIRTM Components for Navy Mast Enclosure

The application of CIRTM to Navy structures such as the Advanced Enclosed Mast/ Sensor (AEM/S) System, currently on the USS Radford and slated for production, is dependent on the identification of compatible resin systems that meet the needs of the Navy. The following sections outline processing and testing results for vinyl-ester/phenolic and urethane/epoxy composites.

15.2 Processing & Properties of Co-Injected Resin Transfer Molded vinyl-ester/phenolic composites

Composite materials have a number of advantages over traditional materials. Some of these advantages are lightweight, high stiffness-to-weight ratio, improved signature management, and resistance to corrosion. In most cases, one material cannot serve all of these functions, but various materials can be easily layered to serve multiple tasks while being integrated in a single structure. For example, vinyl esters are low-cost resins that offer good mechanical properties, room-temperature cure, and reliable processing. However, they are extremely flammable and produce toxic smoke upon combustion, limiting their use in applications where material flammability is a concern. Phenolic resins are low cost resins, but provide poor mechanical properties due to the evolution of water during cure. However, they offer outstanding FST protection [105]. Using CIRTM, a single structure can be manufactured with a thick layer of vinyl ester, to take advantage of its mechanical properties, and a thin layer of phenolic to act as an FST barrier.

Pike et al. [106] have shown that VARTM processes are cost-effective methods to the manufacture large structures. CIRTM takes advantage of these methods and improves them by enabling manufacture of multi-layer structures in a single processing step. Prior to CIRTM, the layers would typically be manufactured individually and then bonded together. This approach requires multiple steps, including surface pretreatments and adhesive bonding, which can introduce additional defects into the part. CIRTM eliminates all of these additional steps, lowers costs, and can improve quality and performance of the part due to the co-cure feature of the process. The fundamentals of CIRTM were reported in detail by Gillio and coauthors [107-108]. In this study, the CIRTM process is described and used to fabricate glass-reinforced vinyl-ester/phenolic hybrid composites. Parts are subjected to a variety of tests to characterize mechanical properties and durability of the interphase formed during co-injection and co-cure.

15.2.1 MANUFACTURING PROCEDURE

In the vast majority of structural applications, the vinyl-ester layer would be considerably thicker than the phenolic layer. However, in this research the co-injected preforms were of equal thickness. This was done because the mechanical tests performed to evaluate the interphase properties require that the interface between the dissimilar materials be located at the geometric mid-plane. Additionally, the Mode I interlaminar fracture specimens (DCB) and the wedge test require that the pre-crack be placed at the mid-thickness between two cantilever beams of comparable stiffness. Therefore, under the assumption that the modulus is a fiber-dominated property, the panels were manufactured with the same fiber reinforcement throughout the thickness. Sub laminates infiltrated with each type of resin were assumed to have the same modulus.

Figure 163 shows the experimental setup used to manufacture the co-injected specimens. Seven layers of S2-glass, twill weave, 18-oz./yd^2 fabrics were used for the phenolic and the vinyl-ester preforms. The vinyl ester used in this study was Dow Derakane 411-350, which is a room-temperature vinyl ester with a gel time of approximately 30 minutes. The phenolic used was J2027/L, which is manufactured by British Petroleum and cures at approximately 140°F. An impermeable separation layer was used between them to demonstrate the

feasibility of this method for large composite structures. The need for an impermeable separation layer was investigated by Gillio [109]. The setup used in this study is typical of the Seemann Composites Resin Infusion Molding Process (SCRIMP) [110]. The distribution medium placed on each side of the preforms is a high-permeability material that helps to carry the flow along the length and width of the part while the resin flows through the thickness of the preform. The distribution medium drastically reduces fill times and enables thick-section parts to be impregnated under vacuum only. The resins were simultaneously injected from the two injection locations shown in the figure. Once the part was infused and the resin had cured, the distribution medium was removed.

The impermeable separation layer was formed of a polysulfone film sandwiched between two layers of epoxy-based adhesive. This solution exploits the Diffusion Enhanced Adhesion (DEA) [111-113] mechanisms, whereby epoxy and the amine curing agent diffuse and react in the polysulfone barrier layer. A 1-mil-thick polysulfone film was selected to go into solution quickly with the epoxy and to toughen the interphase during cure. Additionally, the phenolic is co-cured with the compatible epoxy. The approach provides a toughened co-cured interphase between materials that would not otherwise be compatible.

The manufacturing took place in the following steps. First, the mold surface, a flat steel plate, was cleaned and mold release was applied to it. Then the distribution medium was placed on the plate. Placed on top of it was an impermeable layer, into which a window approximately one inch smaller than the preform had been cut on each side. The purpose of this window was only to avoid edge effects, and it was removed, together with the distribution medium, after the process was complete. A layer of release film was placed on top of these two layers so that they could be removed. The first seven layers of S2-glass were then placed on top of the release film so that the distribution medium would extend out from underneath the preform on one side. Then the separation layer was placed on top of the fiber preform. Generally, the polysulfone film was sandwiched between the epoxy adhesive before the part was laid up. Once the separation layer was in place, seven layers of S2-glass were placed on top of the preform followed by another layer of release ply and a layer of distribution medium. At this point, the lay-up was complete. Two inlet tubes were used. One was placed on top of the preform, and the second one on the part of the bottom distribution medium that extended out from underneath the preform. The vacuum tube was placed at the opposite end of the preforms. This whole assembly was then placed under a vacuum bag, sealed, and vacuum applied. The vacuum serves three purposes: (1) it compacts the fabric, (2) it removes the air, thus reducing the number of voids in the composite, and (3) it creates a pressure difference that drives the impregnation of the resin into the spaces between the fibers.

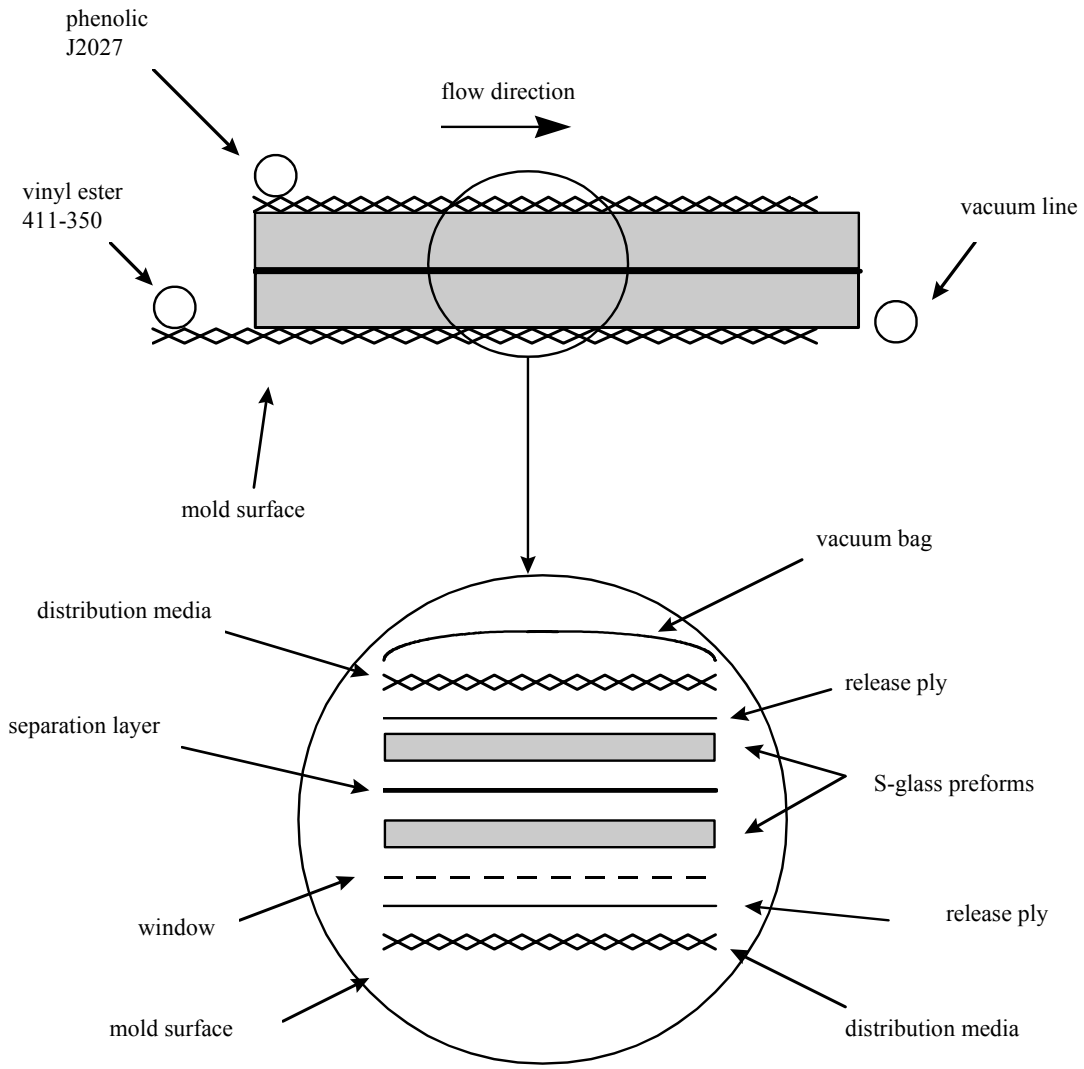

Figure 163. Experimental setup used to manufacture the co-injected specimens.

A number of baseline panels were manufactured and tested, and the results from all specimens were compared. Two single-resin baseline panels were manufactured: one with a vinyl-ester matrix and the other with a phenolic matrix. The main purpose of these baselines was to assess the performance of the co-injected parts. The co-injected specimens would not be expected to perform better than the weaker of the two constituent materials. Finally, a panel was manufactured in a three-step process to simulate the current multi-step procedure used to manufacture multi-layer structures. Two panels were manufactured, one using phenolic resin and the other using vinyl-ester resin. Then they were bonded together using the same adhesive film used in co-injection. To limit the number of variables, the polysulfone film was used together with the adhesive in an effort to compare manufacturing techniques.

15.2.2 MATERIALS

One of the primary challenges presented by co-injection is the selection of a cure cycle. During co-injection, two or more polymers co-cure together; therefore, a cure cycle must be selected that allows the successful cure of all polymers. Since this application of CIRTM is designed for large structures, the goal in selecting the materials was to maintain the cure cycle below 200°F (95°C). The vinyl ester used was Dow Derakane 411-350, which cures at room temperature using 0.2% by weight of cobalt napthenate as the accelerator and 2% by weight of Trigonox 239A (organic peroxide) as the initiator. The phenolic was BP's J2027/L, a low-viscosity resole phenolic, which was catalyzed using 5% by weight Phencat 381. This phenolic must be cured at approximately 140°F in order to limit void formation due to the water present in the phenolic resin. Two adhesive films were selected for this study. The first was 3M's AF-163-2OST, which is an amine-cured, epoxy-based adhesive. This adhesive is designed to cure at 225°F or higher. However, we have shown that it is possible to cure it at temperatures as low as 200°F if the time periods are extended significantly. Another adhesive, a phenolic-epoxy (PH/EP), was selected due to better compatibility between the adhesive and the bulk phenolic. This resin is manufactured by Cytec-Fiberite as a film adhesive, HT 424. The compatibility is improved with this adhesive because PH/EP has a similar curing reaction to the bulk phenolic resin, whereas the epoxy adhesive has a much different curing reaction. As in the previous case, the PH/EP is designed to cure at elevated temperatures, 350°F, but again it is possible to lower the cure temperature by increasing the cure time.

The infusion of the part takes place at room temperature to facilitate the manufacturing process, particularly when this technology is used to manufacture large composite structures. After the infusion, the part is cured at 140°F (60°C) for 4 hours to cure the phenolic. It is necessary to go through this slow cure cycle to limit the formation of voids in the phenolic layer.

After the 4-hour cure of the phenolic, several variations of adhesive cure times were investigated. Two separate cases were investigated for the materials with 3M epoxy adhesive. The first was 4 hours at 200°F, which provided adequate cure when tested in the DSC. In addition, another set was cured at 200°F for an additional 24 hours. This time length was chosen as a maximum limiting time for the epoxy to co-cure with phenolic at 200°F. This cure cycle was investigated because there is a reaction between the acidic curing of the resole phenolic resin and the basic amine-curing agent in the epoxy film adhesive. It was anticipated that this reaction could retard the cure of both resins in the interphase region. Therefore, an extended cure cycle was investigated to determine whether this retardation of the reaction could be compensated for by increased cure time. The goal of this new cycle schedule was to fully cure the adhesive while minimizing cure temperature for the manufacture of large structures.

The materials with the phenolic-epoxy film adhesive used the same 4-hour, 140°F cure cycle to cure the phenolic and then were cured for 4 hours at 200° F to cure the adhesive.

15.2.3 SHORT BEAM SHEAR TESTING

Short beam shear [66] is an extremely popular test due to its simplicity. This makes it a good tool to compare the shear strength and the overall quality of different composite specimens. Specimens were cut using a diamond-coated saw blade based on the dimensions dictated by the ASTM standard. Crosshead speed was set at 0.05 in/min (1.27 mm/min), and at least 10 specimens were tested for each type of specimen. The apparent shear strength was obtained using the following formula:

$$S_H = 0.75\frac{P_B}{bd} \tag{5}$$

where S_H is the apparent shear strength, P_B is the failure load, b is the width of the specimen, and d is the thickness. The majority of failures occurred at the interphase between dissimilar materials. Table 67 summarizes the results obtained. Results discussed in the text incorporate statistical variation (mean – 3 standard deviations (3σ)).

Table 67. Short Beam Shear Results.

Material	Apparent Shear Strength (psi)	Apparent Shear Strength Mean-3σ (psi)	Failure Type and Location
7Vinyl Ester 411-350	5360 ± 120	4990	brittle, mid-plane
Phenolic J2027/L	3280 ± 120	2930	brittle, mid-plane
Multi-step process	3420 ± 230	2720	adhesive
Co-injected w/ amine/epoxy adh. (8 hr. Cure)	2970 ± 70	2760	cohesive, phenolic side
Co-injected w/ amine/epoxy adh. (28 hr. Cure)	4470 ± 100	4170	cohesive, phenolic side
Co-injected w/ epoxy-phenolic adh. (8 hr. cure)	3450 ± 80	3210	1-in. ply phenolic

The vinyl ester performed considerably better than all of the materials with shear strength of 5.0 ksi. The phenolic sample exhibited significantly lower shear strength (2.9 ksi) than the vinyl- ester baseline. The multi-step and 8-hour cure co-injection panels using the amine/epoxy adhesive (2.7–2.8 ksi) were slightly lower than the phenolic baseline. Notable improvements in shear strength are achieved with co-injected panels using the extended cure amine/epoxy adhesive (28 hour–4.2 ksi), as well as the epoxy-phenolic adhesive (8 hour–3.2 ksi). Short beam shear tests show the potential for co-injected parts to provide equivalent or improved properties when cure cycles are optimized. Further research is required to fully optimize the process and performance.

15.2.4 DOUBLE CANTILEVER BEAM TESTING

The double cantilever beam (DCB) test measures Mode I fracture toughness, which is a measure of the resistance of the material to delamination within the interphase. The DCB

test [114] directly loads the interphase formed during processing. The DCB test is expected to be more sensitive to the performance of the various interphases created than the SBS test.

In the DCB specimen, an artificial flaw of known dimension was manufactured into the composite in the form of a precrack. The specimens were then cut from the composite panel. In this research the specimens were approximately 24 mm wide and 300 mm long. Two blocks were then bonded to the end of the specimen where the precrack was located to allow loading of the specimen. One of the sides of the specimen was carefully painted, and evenly spaced marks were placed 5 mm apart. The crosshead speed was set at 0.5 mm/min. The specimens were placed in the fixture and the load was applied. As the load was applied, the crack tip propagated along the specimen. During the test, the critical load, P_{cr}, and the crosshead displacement, v_{cr}, were recorded at every crack tip location.

This data was then used to obtain the fracture toughness of the material using the experimental compliance method, also known as Berry's method [115]. The benefit of this method is that it enables G_k vs. a to be determined and consequently the R-curve effects to be quantified through the following relationship:

$$G_{Ic} = \frac{nP_{cr}v_{cr}}{2Wa} \tag{6}$$

where the critical load and the crosshead displacement are measured during the test, n is the power law index relating compliance to crack length and fit to the data based on the following:

$$C = Ka^n \tag{7}$$

The results of the DCB tests are summarized in Table 68. The VE demonstrates the highest fracture toughness (980 J/m^2) followed by the co-injection panel using the epoxy-phenolic adhesive (730 J/m^2). The other two co-injection panels exhibit fracture toughness similar to the phenolic panel (530-560 J/m^2). The multi-step process exhibited significant scatter in the results and yielded the lowest performance at 360 J/m^2. All of the co-injected specimens showed cohesive failure. Note that the samples that used a phenolic-epoxy adhesive had the highest fracture toughness of any multiple resin material tested. The high Mode I fracture toughness of this material is most likely due to the chemical compatibility between the film adhesive and the phenolic resin. Additionally, the precrack was placed both between the phenolic and the epoxy and between the epoxy and the vinyl ester, but this did not appear to affect the results. In most of the DCB samples, the failure was between the epoxy adhesive and the phenolic. It should also be noted that the specimens manufactured through a multi-step process exhibited undesirable adhesive failure.

Table 68. Summary of DCB Results.

Material	Fracture Toughness (J/m^2)	Fracture Toughness Mean - 3σ (J/m^2)	Comments
Vinyl Ester 411-350	1220 ± 80	980	mostly brittle fracture at surface
Phenolic J2027/L	730 ± 60	550	SEM shows high void content
Multi-step process	720 ± 120	360	failure at adhesive/phenolic interface
Co-inj. (amine - 8 hr. cure)	860 ± 100	560	failure in the adhesive, on the phenolic side; ductile behavior suggests material is not fully cured
Co-inj. (amine 28 hr. cure)	740 ± 70	530	cohesive failure in epoxy, on phenolic side, cracks also developed in 1st ply of phenolic
Co-inj. (epoxy-phenolic 8 hr. cure)	940 ± 70	730	cohesive failure epoxy-phenolic adhesive

The co-injected specimens that used an epoxy/amine adhesive and were cured for only 8 hours exhibit a unique behavior: the fracture toughness decreases with increasing crack length. Additionally, during the tests it was noted that the failure that occurred in the epoxy adhesive was always extremely ductile, displaying a behavior indicating that the epoxy had not fully cured. This stimulated the development of the 24-hour cure cycle. Partially cured thermoset resins would be expected to exhibit this behavior. It is difficult to characterize the local effects on cure and viscoelastic behavior that evolves during processing and interphase formation. Consequently, the DCB tests were conducted at higher rates to substantiate the mechanism.

Smiley and Pipes [116], as well as Gillespie et al. [117], have studied the rate effects in the DCB test. These effects can be quantified by defining a crack opening displacement rate as the opening displacement rate at a small arbitrary distance, ε, from the crack tip. The crack opening displacement rate, $\acute{y}_{ct}$, is a function of both the crosshead speed, $\dot{v}$, and the crack length, α. The expression they derive is as follows:

$$\dot{y}_{ct} = \frac{3\dot{v}\varepsilon^2}{2a^2} \tag{8}$$

Taking this into account, specimens were retested at a rate 10 times the original crosshead speed (5 to 50 mm/min). Results are compared to the lower rate data and clearly show the rate effect on Mode I fracture toughness. The decreasing fracture toughness behavior is not present at the higher loading rate as shown in Figure 164.

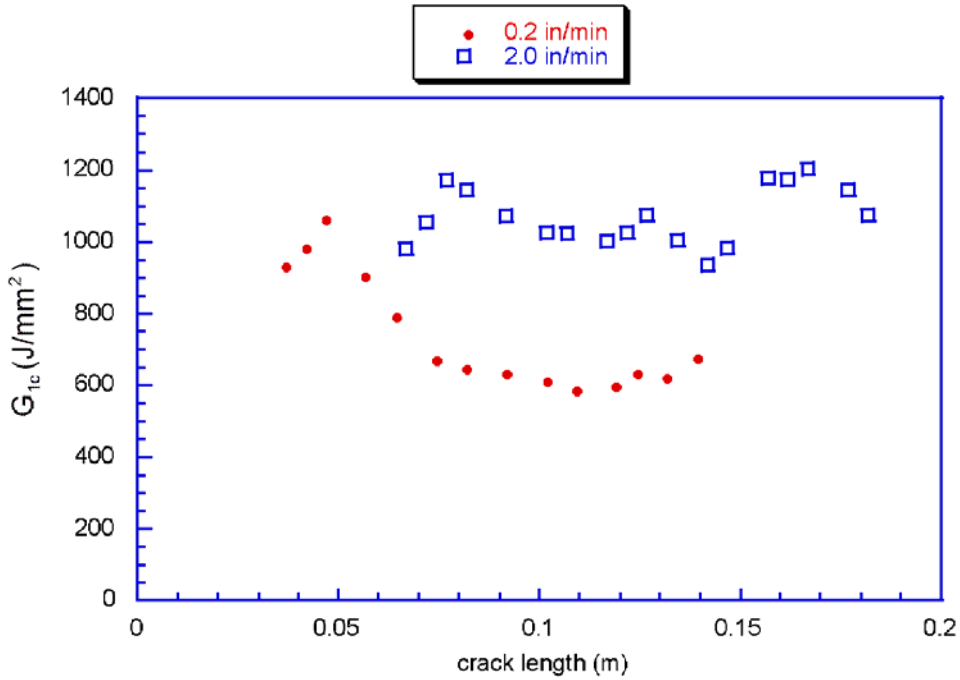

Figure 164. Fracture toughness vs. crack length for co-injected specimens tested at different crosshead speeds.

It is apparent from the behavior in these co-injected specimens that the epoxy adhesive did not fully cure. The joint exhibited rate-dependent behavior in both the DCB and in subsequent durability tests. This finding confirms that in co-injection it is not sufficient to define the cure cycle of the final part by simply combining the cure cycles of the individual materials.

An additional proof of the fact that the viscoelastic behavior is caused by a partially cured interphase is that the extended-cure-cycle (28 hours) specimens did not exhibit any kind of viscoelastic behavior. These specimens had a slight reduction of Mode I fracture toughness compared to the 8-hour-cure specimens. The fracture toughness remained constant or increased with increasing crack length, exhibiting a traditional R-curve behavior.

15.2.5 Durability Tests

The wedge test [11] was used to evaluate the performance of the interphase under adverse environmental conditions. The wedge test is performed on the same type of specimens used for the DCB. A wedge is inserted into the precrack to initiate a crack. The entire specimen is then inserted in water to simulate an adverse environment, and the crack propagation is recorded at regular time intervals. In this test, the highly stressed crack tip is continuously exposed to room-temperature water; therefore, its long-term durability can be evaluated. Figure 165 shows a graph of crack propagation vs. time for all phenolic/vinyl ester hybrid samples. Under initial wedge insertion, cracks propagated and arrested to the distance at time = 0 in Figure 165. The cracks are then measured at given time intervals over a testing period of 2 weeks. The crack in the co-injected specimen that uses the epoxy/amine adhesive

and the short cure cycle, on the other hand, keeps propagating for longer times, exhibiting reduced durability. This is consistent with the viscoelastic behavior observed in the DCB tests. All other materials demonstrate superior durability in this environment.

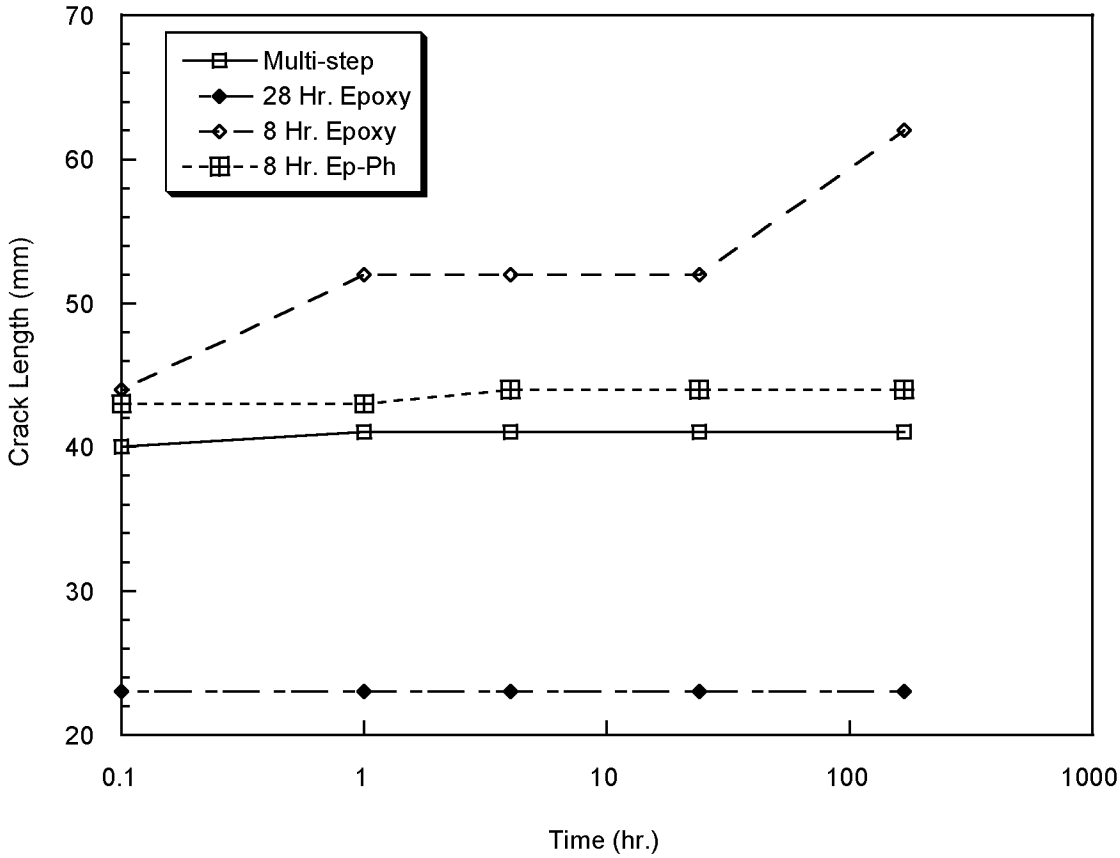

Figure 165. Crack length vs. time for all materials tested. Two cracks developed in the 28-hour specimens; only the interface crack length was reported.

15.3 Flammability Testing of Phenolic/Vinyl-Ester Co-Injected Components

Phenolic-matrix composites have two advantages over other forms of fire protection: (1) the material does contribute to stiffness and strength of the composite material and may be incorporated into the design of the structure; and (2) the cost of the phenolic resin is essentially equal to that of vinyl ester. This makes phenolic GRP an attractive material from a cost standpoint versus other costly fire protection such as intumescent paints and mats as well as ablative materials.

The cone calorimeter is widely used to assess the flammability properties of materials on a small scale [118,119]. It is a powerful tool for combustion analysis because it can monitor transient heat release rate, smoke production, and combustion gas evolution (CO_2, CO).

Organic-matrix composites have been studied previously using the cone calorimeter with and without incorporated fire barriers [120-123]. These studies demonstrate that the effective combustion properties of composite materials are dependent not only on the matrix material,

but also on the fiber type, volume fraction, and architecture. In addition, it has been shown that a fire-barrier material can provide vastly improved FST properties to composite materials with varying amounts of damage to the structural performance of the composite after exposure [124]. In this study, the cone calorimeter is used to ascertain HRR, smoke production, and TTI properties of a variety of co-injected multi-layer materials made of a vinyl-ester matrix composite structural layer and a phenolic-matrix fire-barrier layer. The results may be used to predict some of the full-scale FST trends for specific materials.

15.3.1 PROCESSING

The lay-up for this study is shown in Figure 166. The materials selected were chosen for end-use properties as well as processing performance. The vinyl ester chosen was the Dow Derakane 411-350 cured with an organic peroxide catalyst and cobalt napthenate accelerator. The fire-retardant vinyl ester selected was the Dow Derakane 510A also cured with organic peroxide and cobalt napthenate. The phenolic resin was the BP J2027 resole phenolic resin. The curing agent for this resin is BP Phencat 381 acid-based delayed action catalyst. Two different thickness materials were studied in this work. The first was a 19-mm thick-section material and the second was a 6.5-mm thin laminate typical of GRP sandwich structures.

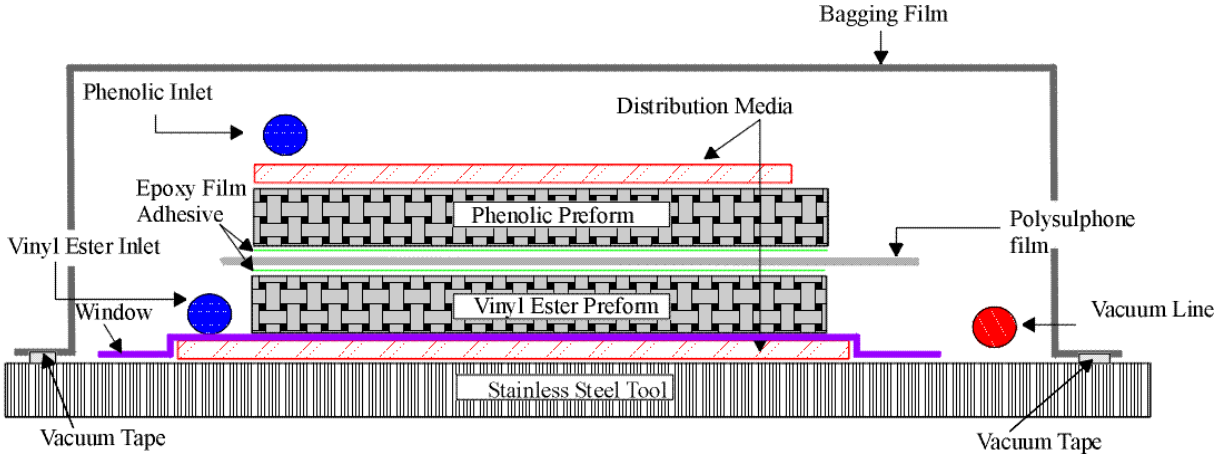

Figure 166. The CIRTM process for vinyl-ester/phenolic hybrid composites.

Three reinforcements were studied in the phenolic layer. First, an E-glass continuous strand mat (CSM) was used that produced a relatively low fiber volume fraction of 0.25. Second, a 2 x 2 weave S-glass woven roving (0.64 kg/m2) was used that gives a fiber volume fraction of 0.50-0.55. This was used instead of the E-glass WR used in the vinyl-ester layer, because the multi-purpose sizing of the E-glass WR was not compatible with the phenolic resin, whereas the S-glass had a more compatible urethane sizing. The last reinforcement was the same S-glass woven roving stitched through the thickness with Kevlar thread on a 1-in. square grid and a stitch density of 2 stitches/cm. The intent of the stitching was to determine whether through-thickness reinforcement could lessen the delaminations in the WR laminates. The thickness of each of the phenolic layers was 6 mm. This gave a total thickness of 19 mm for the thick-section hybrid composites. The thin-section materials were all composed of 10 plies of S-2 glass woven roving. The CIRTM materials were composed of 5 plies each for the vinyl-ester and phenolic sections.

The interface layer used for all CIRTM materials in this study was composed of a 0.0254 mm thick polysulfone (PSU) film sandwiched by 0.127 mm thick epoxy film adhesive. This, layer is designed to provide superior adhesion of the two layers through the use of diffusion enhanced adhesion [111].

The cure cycle used for these specimens consisted of two stages. After injection, the vinyl ester was allowed to gel at room temperature for 30 minutes. The part was then heated for 4 hours at 60° C to cure the phenolic layer. Next, the part was vacuum bagged again over the existing bag to provide compaction pressure during the cure of the adhesive. The temperature was then raised to 120° C for 4 additional hours to cure the film adhesive and post bake the phenolic and vinyl ester resins. The panels were then cooled, debagged, and cut into specimens for cone calorimeter testing.

15.3.2 CIRTM PANEL TESTING

All flammability testing was performed with the cone calorimeter using procedures outlined in ASTM D-1354. All materials were tested at an incident heat flux of 50 kW/m^2 in duplicate. An initial round of testing determined that the multi-layer specimens could not be tested reliably using the standard specimen size and edge frame. The reason for this decision is that the edges and back side of the vinyl-ester section would ignite and combust and dominate the test results. This edge behavior is not representative of the large-scale material response and thus could not be used to predict the response of an actual structure. A modified specimen setup was devised using a larger specimen with an equal size exposure area.

The actual specimen is 150 x 150 mm in size and is inset into a fiberglass fireboard about 5 mm. The fireboard measures 200 mm square total and has a 100-mm-square cutout placed in the center to define the exposure area of the specimen. The edges of the specimen are sealed to the fireboard with high-temperature silicone sealant to attempt to draw vinyl ester offgasses around the fireboard and away from the actual exposure area. This setup was successful and minimized edge behavior from affecting the results of the testing.

The test matrix is given as Table 69. The thick-section 19-mm CIRTM materials were tested only with 411-350 vinyl ester as the structural material. In the thin (6.5 mm) laminates, both the 411-350 and 510A vinyl esters were tested. In the thick-section laminates, the phenolic reinforcement was varied to study its effects, while in the thin laminates only woven roving reinforcements was used. The baseline materials were tested in the traditional specimen size and configuration. The phenolic materials were tested using a metal edge frame and retaining grid due to the explosive delamination tendencies demonstrated by this material. The CIRTM processed hybrid materials were tested using the modified specimen setup described above and were tested for a period of 30 minutes. After this time, the edge effects would begin to influence the test. This also allowed a visual comparison of damage in the panels after testing by means of sectioning the panels. All tests recorded time to ignition (TTI), rate of heat release (RHR), specific extinction area (SEA), as well as CO_2 and CO levels.

Table 69. Test Matrix for Cone Calorimeter Testing.

Material No.	Vinyl Ester Structural Layer	Phenolic Fire Barrier Layer	Processing	Thickness (mm)
(1)	Dow 411-350/WR	None	VARTM	19
(2)	Dow 510A/WR	None	VARTM	19
(3)	—	BP J2027/WR	VARTM	19
(4)	Dow 411-350/WR	BP J2027/CSM	CIRTM	19
(5)	Dow 411-350/WR	BP J2027/WR – stitched	CIRTM	19
(6)	Dow 411-350/WR	BP J2027/WR	CIRTM	19
(7)	Dow 411-350/WR	None	VARTM	6.5
(8)	Dow 510A/WR	None	VARTM	6.5
(9)	—	BP J2027/WR	VARTM	6.5
(10)	Dow 411-350/WR	BP J2027/WR	CIRTM	6.5
(11)	Dow 510A/WR	BP J2027/WR	CIRTM	6.5

15.3.3 CIRTM RESULTS

Average combustion parameters for the baseline and multi-layer materials are listed in Table 70. The values listed are averages of the two tests performed for each material. The time to ignition (TTI) of the hybrid materials shows a large increase over the 411-350 vinyl ester and the 510A brominated vinyl ester. The brominated vinyl ester actually ignited more quickly than the standard vinyl ester, most likely due to the tendency of the fire-retardant vinyl ester to char quickly and then become less combustive. The 19-mm-thick J2027 phenolic/WR materials did not ignite within 30 minutes at this heat flux. The specimens did delaminate explosively in a regular pattern, however. The highest TTI of the hybrid materials was the J2027/WR fire barrier, followed by the J2027/WR-ST. The TTI in the hybrid specimens appeared to be controlled by the permeability of the charred phenolic preform to the gasses given off by the vinyl ester during heating. This was a reason for the lower TTI in the stitched WR material. Although the fiber density is actually higher, the hole in the preform from the stitching provided a pathway for the vinyl-ester offgas, and flames could be seen to emerge from along the lines of stitching. This permeability effect also accounted for the lower TTI times in the thin-section materials.

Table 70. Summary of Cone Calorimetry Data at 50 kW/m^2

Material No.	Structural Mat.	Thickness (mm)	Barrier Material	Tig (s)	300 sec. after ignition			Total Heat Released (kW/m^2)	Ave Heat Released (kW/m^2)	Mass Loss (%)	Ave SEA (m^2/kg)
					Peak HRR (kW/m^2)	Time (s)	Av. HRR (kW/m^2)				
(1)	411-350	19	None	79	221	22	135	209	86	18	1012
(2)	510A	19	None	62	130	24	100	217	76.0	29	483
(3)	J2027	19	None	DNI (30min)	—	—	—	—	—	—	—
(4)	411-350	19	CSM	326.5	100	29.5	66.8	368	86	18	226
(5)	411-350	19	WRST	416.5	62	277	48	28	81	6	460
(6)	411-350	19	WR	571	26	127	22	138	46	12	283
(7)	411-350	6.5	None	72	272	21	221	75	176	18	472
(8)	510A	6.5	None	67	126	15	90	38	86	30	380
(9)	J2027	6.5	None	762	31.1	139	27.7	18	24.5	18.8	122
(10)	411-350	6.5	WR	310	198	233	125	86.7	124	18	472
(11)	510A	6.5	WR	404	61	300	37	45	34.6	22	228

The HRR is an extremely important parameter in determining the potential threat of a material involved in a fire situation. The brominated vinyl ester, 510A, provides a much lower heat release rate 411-350 vinyl ester in both thick and thin sections. The thick-section CIRTM materials all demonstrate much lower HRR peak and averages during the critical first five minutes as well as over the entire test as compared to the 510A material. The best CIRTM material was with the J2027/WR fire barrier. This material had peak and average values of 26 and 22 kW/m^2, respectively, at 300 seconds after ignition. This material did demonstrate explosive delamination in the phenolic layer during testing. The J2027/WR-stitched material did not delaminate during testing, probably due to the relief of water vapor pressure through the stitching holes in the preform. The HRR rate, however, was much higher than WR material alone, again due to the decrease in permeability due to the stitching. Finally, the J2027/CSM material showed the poorest performance among the hybrid materials due to the high permeability of the phenolic preform after the phenolic had burned and charred away.

In the thin-section materials, the 510A/J2027 material demonstrated performance approaching the phenolic baseline in both peak and average 300 second HRR. The 411-350/J2027 material substantially outperformed the 411-350 baseline but did not best the 510A material. This may be due to the decreased thickness of the phenolic layer. Thickness

effects in composite materials have been shown to cause a dramatic change in the heat release properties due to the presence of the fiber after the resin has burned away [46]. In this thickness material the use of fire-retardant vinyl esters is recommended for superior flammability performance.

The smoke production properties of the CIRTM processed hybrid composites as judged by the specific extinction area (SEA) are also improved over the fire-retardant vinyl ester. These values follow the HRR rate in general and are the lowest in the J2027/WR phenolic layer material.

15.3.4 CONCLUSIONS

The results of this testing have proven that CIRTM manufactured hybrid materials can provide greatly improved properties over those of fire-retardant vinyl-ester matrix materials. In addition, results here have demonstrated that a non-fire-retardant vinyl ester may be used in thick-section laminates in conjunction with a woven roving/phenolic fire barrier and still yield outstanding flammability performance. This material would provide some cost saving over using a fire-retardant vinyl ester. In thin-section multi-layer laminates, the fire-retardant vinyl ester provides far superior performance as compared to the non-fire-retardant vinyl ester. Here, the additional cost of a fire-retardant vinyl ester is justified.

15.4 Processing and Impact Testing of Multi-Layer Polyurethane/Epoxy Composites

Low-velocity impact of composite materials has been studied extensively due to the high loss in structural properties after an impact with little or no visual damage. Many techniques have been investigated to improve the impact toughness of advanced composite materials including matrix, fiber, and interface modifications [125]. This section focuses on the effects of matrix materials and these will be discussed in detail here. Many alterations to matrix materials have been made to improve the impact resistance of composite materials including toughened thermoset resin systems and thermoplastic matrices [126,127] and the combined use of both of these in a hybrid matrix composite [128]. These techniques have demonstrated some success in decreasing the size of damage area and increasing the residual compressive strength of the materials at the expense of reduced structural properties in the undamaged state. Masters and Evans have conducted a study that shows there is a high correlation between Mode II (forward shear) fracture toughness and compression after impact (CAI) properties. At low-impact velocities in brittle matrix composites, the dominant visual damage mechanism is generally interlaminar failure (delamination), which initiates and propagates due to stress wave propagation and flexural vibrations. Polyurethanes offer the potential to attenuate stress wave amplitude during impact loading as well as absorb significant amounts of energy due to their high fracture toughness.

This section addresses the manufacture and performance of a multi-functional hybrid composite material produced with CIRTM processing composed of CFRP epoxy structural layer and CFRP polyurethane protective layer. Polyurethane-matrix composites possess outstanding vibration damping and wear resistance properties. Very little information has been published concerning the effects of multiple matrix materials on low velocity impact properties. One study performed has investigated the use of hybrid matrix composites[5].

Here, the impact and energy absorption performance of materials with alternating thermoplastic and thermoset layers was studied. The authors concluded that the semi-crystalline thermoplastic matrix materials had fundamentally higher energy absorption attributes than the brittle epoxy layers due largely to the lower fiber-matrix bonding strength. However, these properties were not evidenced in the hybrid composites because of the poor interface toughness between the thermoplastic and thermoset layers. Delaminations between these two layers accounted for much of the energy absorbed in these systems, which led to low residual flexural strength.

15.4.1 CIRTM DEMO PROCESSING

Figure 167 shows the lay-up used for this study. The epoxy resin used was an anhydride cured standard bis-phenol A type epoxy system produced by Ciba-Geigy (GY 6010-HY 917). The polyurethane resin used was thermoset polyurethane manufactured by Uniroyal (Adiprene L100) cured with a temperature-blocked amine-curing agent (Caytur 21), also from Uniroyal. To isolate the effects of the urethane matrix material, only one reinforcement type was used for both layers of the composite. This was a woven roving fabric, 8k tow, AS4 carbon fiber, in a 5-harness satin weave. The resin flow separation was maintained through the use of a 0.127-mm-thick polysulfone (PSU) film. Epoxy film adhesive was placed on each side of the polysulfone film to provide good adhesion between the film and structural layers. This adhesive was an amine cured type and was designed to exploit the diffusion enhanced adhesion (DEA) mechanism where epoxy and amine diffuse into the thermoplastic layer and react to form a strong interpenetrating network between the thermoplastic and thermoset materials.

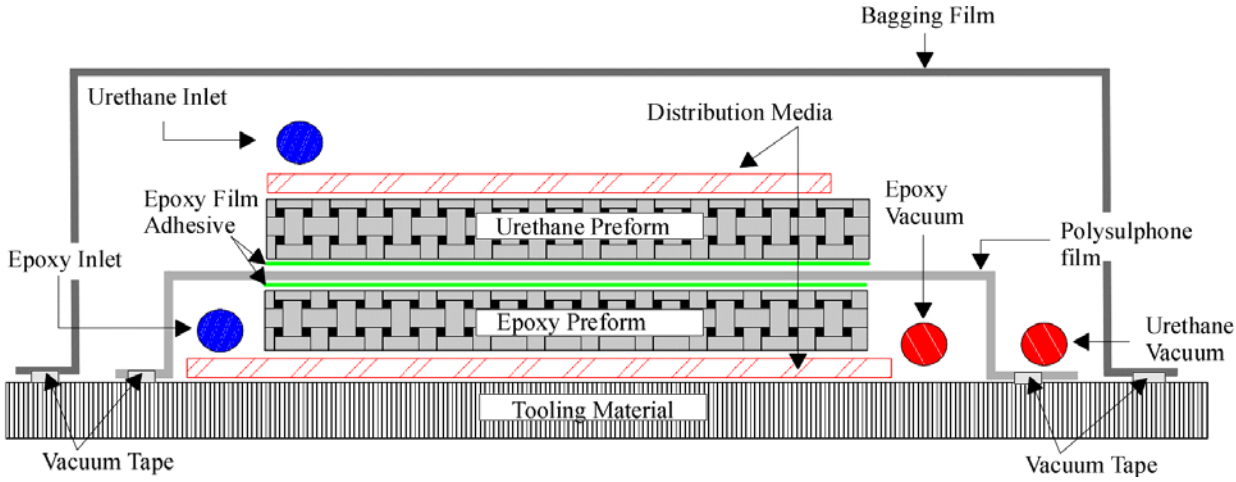

Figure 167. VARTM setup used for co-infusing epoxy and urethane resins simultaneously.

Much of the challenge in processing epoxy and urethane hybrid composites is the necessity of elevated-temperature injection and cure of the resins. The cure and viscosity information for the epoxy and urethane resins is summarized in Table 71. At elevated temperatures, the viscosity difference between the urethane and epoxy resins becomes extreme. The urethane has a tremendously high viscosity (>2000 cps) and that of the epoxy resin is very low (≈50 cps). Due to this dissimilarity, it was necessary to isolate each of the individual resins.

Table 71. Individual Processing Details for the Epoxy and Polyurethane Resins.

Resin	Curing Agent	Injection Temp. (C)	Gel Temp. (C)	Post Bake Temp (C)
Ciba-Geigy 6010 epoxy	Ciba-Geigy HY 917 anhydride	30	80	120
Uniroyal L100 polyurethane	Caytur 21, blocked amine catalyst	60	120	120

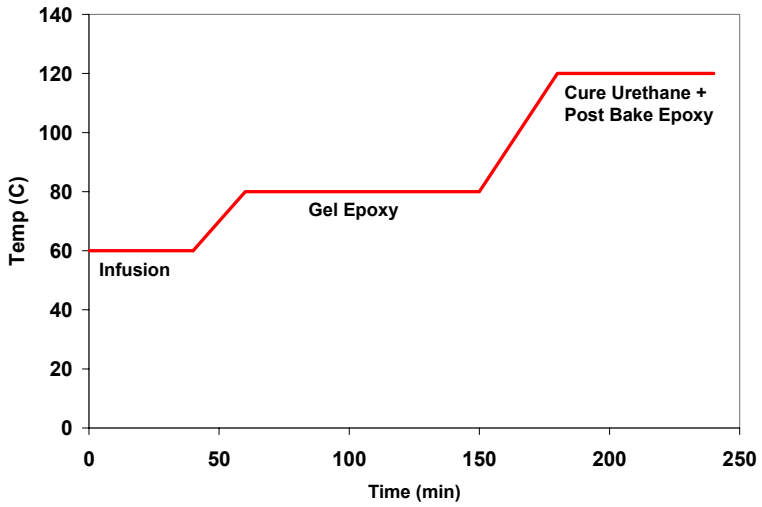

Figure 168. Processing temperatures for CIRTM processing of epoxy and urethane.

The temperature profile for the processing of urethane and epoxy simultaneously is shown in Figure 168. The schedule is a compromise between the optimum cure schedules for each of the two resins. Due to the high room-temperature viscosity of the urethane resin, the infusion must be performed at 60°C. This temperature was chosen as an optimal combination of the resin pot life and viscosity. Each of the resin components was preheated prior to infusion. Just before infusion, the resins were mixed and degassed, and then placed into the oven and connected to the injection lines. The infusion times of a typical 50 x 60 cm panel made were 30–60 minutes and were dependent on the thickness of the urethane layer. The urethane resin infusion through the thickness was determined with an ARL/CCM flow and cure sensor monitoring system [129,130]. The epoxy infused in 4-5 minutes. After the urethane was completely infused, the temperature was raised to the recommended epoxy gel temperature of 80°C. At this temperature, the viscosity of the epoxy resin becomes extremely low, and the vacuum pressure starts to pull large amounts of resin through the part. Once the resin gels in the supply tube, this effect will start to remove resin from the preform, resulting in a large void content within the part. To counter this effect, the vacuum pressure on the epoxy side only was decreased to 4-5 mm Hg, where very little epoxy was drawn from the part but still was not allowed to drain into the part.

The control specimens, made entirely of epoxy or urethane, were manufactured using similar VARTM processing. Here, the manufacturer's recommended processing temperatures were observed.

Impact specimens were machined from panels manufactured using the above outlined techniques of approximate dimensions 50 x 60 cm. Each of the specimens was cut from these panels to dimensions of 100 x 150 mm. Exact construction details of the specimens are provided in Table 72. The panels were fabricated to have an approximate thickness of 6.5 mm, which required the use of a total of 14 plies of fabric in each preform.

Table 72. Specimen Identification and Construction Details.

Material Name	No. of Epoxy Plies	No. of Urethane Plies	Epoxy %	Urethane %
14 E/0 U	14	0	100	0
12 E/2 U	12	2	86	14
10 E/4 U	10	4	71	29
7 E/7 U	7	7	50	50
0 E/14 U	0	14	0	100

15.4.2 Impact Testing

The impact testing was done using a standard instrumented drop tower apparatus and a hemispherical impact top15.9 mm in diameter. The specimens were each impacted with 6.67 J/mm (1500 in-lbs/in) energy with a constant mass including the impactor of 10.98 kg. The initial impact velocity of the tup for all specimens was 2.8 m/s. The specimen is supported over an impact area of dimensions 75 x 125 mm and is held in place by four point-type spring clamps. The impactor was caught after the initial impact to prevent multiple impacts. Data from the load cell was collected from a microcomputer-based data acquisition system at a rate of 400 kHz. The data was used to calculate the top energy, velocity, deflection, and acceleration from kinematics relationships.

15.4.3 Results and Discussion

Data collected from the impact event for each of the five materials studied indicate that the highest load values are in the 100% epoxy specimens and the lowest in the 100% urethane specimens. Each of the other three fractional panels falls in between these extremes. It was also noted that the total time of the impact event becomes increasingly longer for higher percentages of urethane in the specimen. The energy curves also indicated that the peak energy is constant as would be expected but the final energy increases for larger fractions of urethane in the specimen. This effect was calculated for all impacted specimens and is presented in Figure 169 as the normalized energy absorbed for each specimen. There is a noticeable trend for higher energy absorption as the urethane content of the material is increased. Examining the deflection curves, one can see that the deflection of the 100% urethane specimen is more than twice that of the epoxy baseline. The fractional samples have deflections somewhere in between, although it is interesting to note that there is a large jump between the 7-ply epoxy /7-ply urethane and the 10-ply epoxy /4-ply urethane.

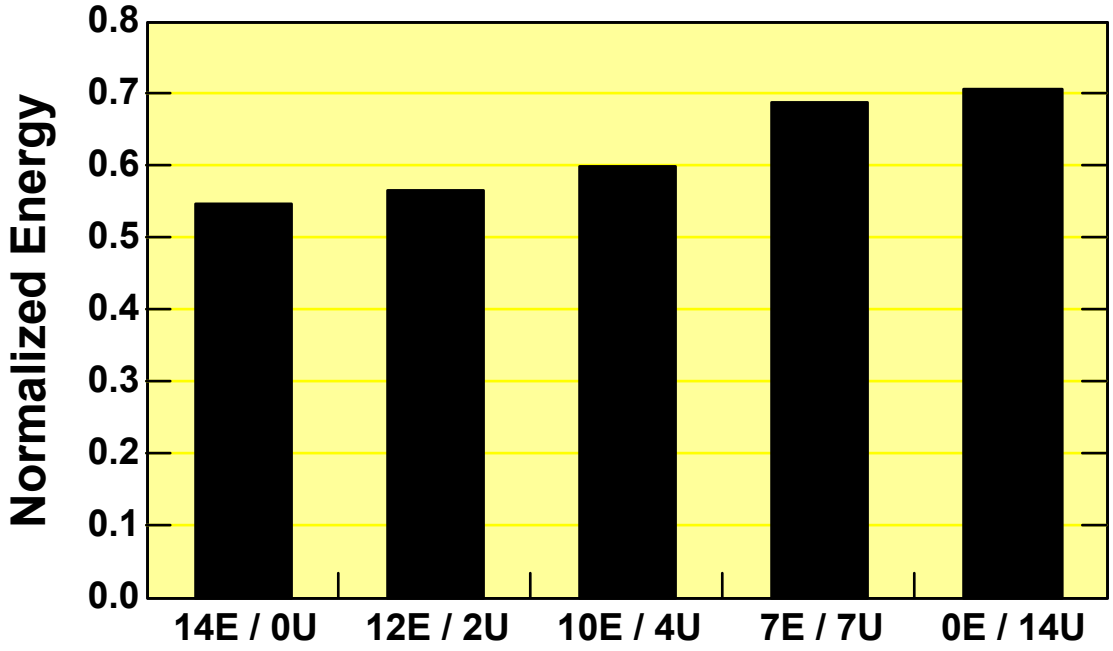

Figure 169. Normalized energy absorbed.

16 Armor Repair

16.1 Mechanical Performance of Undamaged and Repaired Armors

The need for lighter, faster, and stronger combat vehicles has recently led to the development of Composite Integral Armors (CIA). A CIA structure consists of different material layers stacked together to provide unique structural and ballistic properties, as well as satisfying fire, smoke, and toxicity resistance and electromagnetic electrical requirements.

The protection from ballistic threats is the most critical issue in the design of CIA structures. Previous studies (e.g., [131]) have shown that a ballistic impact may lead to the complete penetration of the cover layer, the destruction of ceramic tiles and to the development of damage in the backing plate. The damage may hence be thought to have greatly reduced the structural and ballistic performance of the structure. Innovative repair techniques are therefore required to increase the in-the-field availability and survivability of CIA structures (e.g. composite armored vehicles).

However, until recently most of the work on composite repairs has been done in the aerospace industry, where relatively thin carbon/epoxy structural elements are repaired. As a consequence, very little work has been done in developing repair methodology adapted to thick-section multi-functional structures, such as those found in armored vehicles.

Following, a previous program that set potential repair methodology for CIA repairs [131], the behavior of undamaged and repaired CIA structures is being investigated in the present work. The aim of this program is the understanding the behavior of repaired CIA panels under static and ballistic loadings.

The main aim was to investigate the mechanical performance of undamaged and repaired CIA panels. Special efforts were directed toward the development and characterization of efficient manufacturing processes and repair methods.

The work is divided into three parts outlined in Table 73.

Table 73. Aims of Mechanical Performance Evaluations for Repaired CIA.

Part 1	Undamaged and repaired, 35 in long x 4 in wide x 1¼ in, thick CIA panels were tested in static four-point bending. The mechanics of CIA panels in static bending was studied. In particular, the effect of different manufacturing techniques on the fracture behavior of the undamaged panels was looked at.
Part 2	Innovative bonding methods were then investigated by assessing the static mechanical performance of oven-cured and induction-cured bonded joints. Induction curing of adhesives was shown to lead to strong efficient joints and the method was applied to the repair of CIA.
Part 3	Building on the wealth of experience acquired in the development of Part I and Part II, the performance of repaired CIA beams subjected to static and fatigue loading is investigated in this last part. Also, the mechanics of CIA is being investigated using two commercially available finite element codes (ANSYS – static and LS-Dyna - dynamic). The work is still under progress under the CMT program.

16.2 Manufacturing Process Impact

A multi-functional CIA composite structure was initially developed by United Defense L.P (USA), as part of the Composite Armored Vehicle Advanced Technology Demonstrator. A typical CIA structures consist of different material layers stacked together to provide unique structural and ballistic properties, as well as satisfying fire, smoke, and toxicity resistance and electromagnetic requirements. The CIA structure considered in the present work as one baseline consists of four layers shown schematically in Figure 170:

- A 13.2mm thick polymer composite backing plate.
- A 1.5mm thick EPDM rubber layer
- A 14.1mm thick Alumina ceramic tile
- A 1.8mm thick composite cover layer

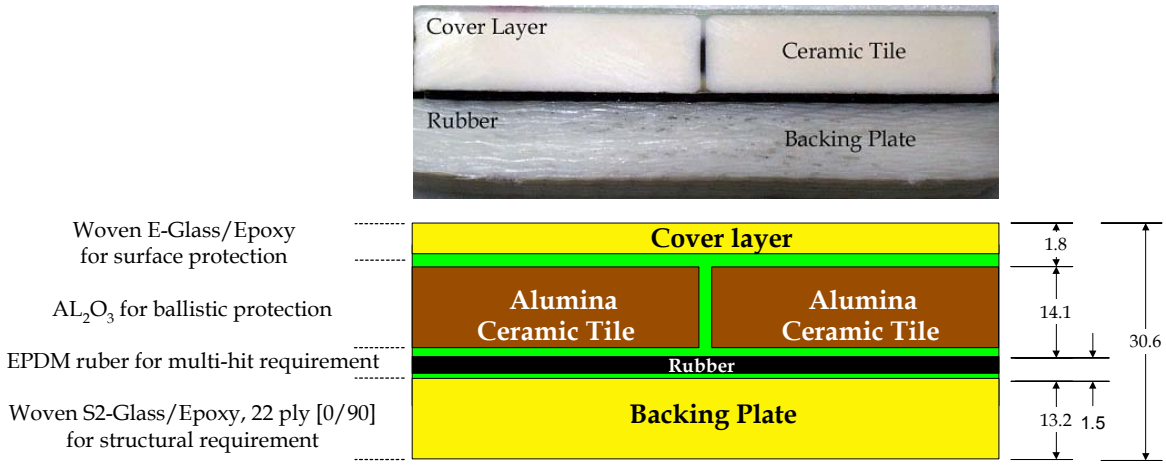

Figure 170. Example of Composite Integral Armor (CIA).

In this work, the effect of the manufacturing process on the static mechanical performance of CIA beams is investigated. The structural response of CIA beams, fabricated by the single-step and the multi-step techniques is compared in a four-point bending test. Loads, deflections, and surface strains of specimens are measured. The structural performance of single-step manufactured CIA is first described. The structural performance of multi-step CIA is then compared with that of the single-step CIA. Finally, we will discuss the effect of the surface mechanical preparation (i.e. mechanical roughening) of the rubber layer to the structural performance of the CIA.

16.3 Test Coupons

16.3.1 Manufacturing Considerations

To allow for an evaluation of the mechanical performance of the CIA structures, the size of the test pieces is reduced to the size of a beam, 889 mm long by 101.6 mm wide. The geometric arrangement of the ceramic tiles on the CIA beams is shown in Figure 171.

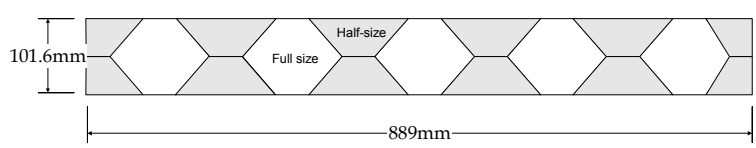

Figure 171. The arrangement of ceramic tiles.

The fabrication of the CIA beams is done by following a sequence of process steps:

16.3.1.1 Backing Plate

The backing plate consisted of 22 layers of Vetrotex plain weave S2-Glass fabric, with a [0/90] orientation. The fabric is typically impregnated with a tough epoxy resin system from

Applied Poleramic, as discussed below. The total thickness of the backing plate was about 13.2mm with a volume fraction of about 50%.

16.3.1.2 Rubber Layer

The rubber was a 1.5mm thick EPDM rubber. After being cut to the desired size, holes 6mm in diameter, spaced by two inches, starting one inch from the edge of the layer, are produced. The system of holes provided channels of resin and hence ensures a good bonding with the surrounding layers. The rubber surface may then be abraded, on both sides, using a rotary surface grinder with an Alumina disc. The rubber is subsequently washed with soap and water to remove grease and dirt. After drying, the rubber is further cleaned with acetone. Immediately prior the bonding/infusion operation a Chemlok® 7701 primer (Lord Corporation) is applied on both surfaces, using a paintbrush.

16.3.1.3 Ceramic Strike Face

Alumina hexagonal ceramic tiles (AD-99), 14.1mm thick, are degreased with acetone prior manufacturing. A soft rubber pad, 0.5mm in thickness is used to ensure a constant spacing between the tiles during and after the manufacturing operations.

16.3.1.4 Cover Layer

The cover layer consisted of 5 layers of Vetrotex twill weave 7781 E-glass fabric impregnated with an Applied Poleramic resin.

16.3.1.5 Impregnation Resin

As mentioned above the stack is impregnated and consolidated with an Applied Poleramic resin system. Typically, the SC15 toughened epoxy resin system is used. The SC15 system gels at room temperature, overnight, and under vacuum. Additionally, a four-hour post-cure at 149°C is done. However, a more compliant SC11 epoxy resin system was also used, depending on the application. On the other hand, the SC11 system cures at 121°C for 2 hours and at 149°C for another two hours, under vacuum. The manufacturing processes are discussed next.

16.3.2 MANUFACTURING PROCESSES

Two manufacturing processes were evaluated in the present work; a single-step and a multi-step process. Furthermore, the effect of rubber surface preparation is also investigated. The structures were manufactured at UD-CCM as presented below.

16.3.3 SINGLE-STEP VACUUM ASSISTED RESIN TRANSFER MOLDING

In the single-step manufacturing process, the entire CIA is made in one single operation. In the VARTM process, resin is injected in the part to be made with the assistance of vacuum. A flat face (steel plate), cleaned and coated with release agent (Freekote), is used as a mould. First, the five layers of the E-glass, that constitutes the cover layer, are stacked down inside a wood frame. The ceramic tiles are then laid down and arranged as shown in Figure 171. The arrangement is such that there is a full-size tile at the center of the beams, followed by an

arrangement of half-size and full-size tiles. A scrim cloth (one layer of Vetrotex 1659 E-glass mesh) is next placed in the mold, followed by the rubber layer. The scrim cloth provided a controlled bond line thickness between the ceramic tile and the rubber, as well as a path for the resin during infusion. Additionally, the holes produced in the rubber layer created an interconnected channel of resin between the two layers. The 22 layers of S2-Glass are finally stacked in the mould.

The assembly is then covered with peel ply and a resin distribution media. The resin inlet (a plastic omega channel) is placed in the middle of the stack and two vacuum lines are placed in breather cloth, outside the frame. A vacuum bag is next applied and the edges are sealed with a tacky tape. Vacuum is applied to the bag through a vacuum gage mounted resin trap. The resin is then infused in the part through the resin inlet. It is noted, that in order to minimize resin circulation and waste, a double vacuum bag technique, which has been developed at UD-CCM, was used. After the part is completely infiltrated with resin, the resin inflow is stopped and the part placed in a conventional oven for cure.

16.3.4 Multi-Step Process

In the multi-step manufacturing process the various layers are prepared individually and then consolidated in a vacuum bag. The backing plate is fabricated first and cured with SC15 resin by the VARTM process, as described above. After injection and cure, the plate is cut to dimensions, and its surface sandblasted and cleaned. The CIA is then assembled in a second operation. The cured backing plate, the rubber, the arrangement of ceramic tiles and the cover layer, are place in a mold and impregnated by the wet lay-up technique with either SC15 or SC11 resin systems.

Wet lay-up is a highly labor intensive method, in which the parts are combined while making the structure. In a wooden frame, and over a prepared mould face, the five plies, that constitute the cover layer, are laid down one at a time and are hand-impregnated by resin, which is spread out with a spatula. The ceramic tiles are then arranged, accordingly to the right part of Figure 171, followed by the rubber layer. It is important to impregnate the plies between each operation. Finally, the cured backing plate is finally stacked down in the mould. When the procedure is completed the part is placed under vacuum in order to gain compaction of the layers, and remove excess resin and air. The part is then cured in a conventional oven.

16.4 Experimental

16.4.1 Four-Point Bending

The beams were tested statically in four-point bending (4PB), as shown schematically in Figure 172. The 4PB test was selected because it is simple to perform and bending is a relevant deformation mode. The tests were conducted so that the cover layer is subjected to compression forces and the backing plate is subjected to tensile forces. The CIA beams were tested in an Instron 8562 machine. The sequence of failure events was noted as the applied displacement was increased at a constant displacement rate of 2.5mm/min, and as the load-displacement curve was recorded on a data acquisition system.

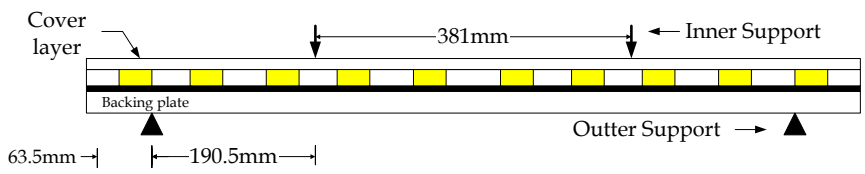

Figure 172. A CIA panel in four-point bending

16.4.2 TEST MATRIX

Several design configurations were investigated:

- Single-step VARTM manufacturing process with Applied Poleramic SC15 resin.
- Multi-step SC15 (backing plate and final consolidation are made with SC15 resin).
- Multi-step SC11 (backing plate is fabricated with SC15 first, the final consolidation is then made with Applied Poleramic SC11 resin).

In addition, the basic configurations described above are tested with and without a mechanical surface preparation on the rubber layer.

The test matrix is shown in Table 74. Four single-step CIA beams were prepared to allow for an analysis of the reproducibly of results. The reproducibility in the results was found to be very good (as will be shown later). Subsequent configurations required only two replicates.

Table 74: Test Matrix for the four-point bending testing of CIA beams

	Designation	Rubber with mechanical preparation	Rubber without mechanical preparation
Single-step SC15	SS-SC15	4	2
Multi-step SC15	MS-SC15	2	2
Multi-step SC11	MS-SC11	2	2

16.5 Fabrication Overview

The test results for the single-step and multi-step manufactured beams are shown in Table 75 and in Table 76, for the specimens with and without a mechanical surface preparation of the rubber layer, respectively.

As shown in the next section, the specimens did not fail catastrophically. Failure was seen to result from the progression of discrete and independent damage events. Consequently, in Table 75 and in Table 76, values of the first and maximum visible failure events (loads and displacements) are given. The load values are normalized by the width of the specimens (101.6mm). The first failure event (load and displacement) corresponded to the first visual drop in the load-deflection curve that was observed during the test. The values of maximum load and displacement are the values of the maximum load recorded during the test, and its corresponding displacement (not the maximum displacement recorded during the tests). The mechanical response of the specimens is described next.

Table 75: Partial test results for the CIA beams tested in four-point bending.

Specimens		Failure load / Unit width 1st Event (N/mm)	Displacement 1st Event (mm)	Maximum load / Unit Width (N/mm)	Corresponding displacement (mm)
Single-step SC15	**1**	150	23.3	204	59.1
	2	132	21.9	150	50.7
	3	145	22.9	197	62.4
	4	162	26.5	-	-
Average (SD) [COV]		147 (12.1) [8.2%]	23.7 (1.9) [8%]	184 (29) [15.7%]	57.4 (6) [10.4%]
Multi-step SC15	**1**	116	22.2	-	-
	2	30	4.8	-	-
Multi-step SC11	**1**	146	26.5	-	-
	2	126	25.6	-	-

16.5.1 SINGLE-STEP (VARTM) MANUFACTURED CIA BEAMS

The test results for the single-step manufactured CIA beams, for which the rubber layer was mechanically prepared, are shown in Table 75. In Figure 173, the load-deflection curves of the four single-step SC15 CIA beams (SS-SC15) are also shown. The reproducibility in results is very good. From Table 75, the coefficient of variations for the first visible failure load and displacement are only about 8%, respectively.

The load-displacement response of the CIA beams is non-linear. In Figure 173, the maximum displacement recorded were about 70mm and they were therefore several time the thickness of the beams (It is noted that this value is different from the value of displacement associated with the maximum load given in Table 75.). Therefore, large deformation and material non-linearity effects are thought to dominate the response of the beams.

In Figure 173, the load-displacement curves may be seen to be linear for all the specimens and for applied displacement below 5mm. A 'kink' in the load-displacement curves may then be clearly observed at an applied displacement of approximately 7mm. This 'kink' corresponds to a drastic change in the stiffness of the beams and may be thought to correspond to the onset of the plastic deformation of the resin at the interface between the tiles. The load may then be seen to increase steadily with the applied displacement until a first sudden drop in load is recorded. This drop in the load corresponds to the initiation of the separation of the cover layer from the ceramic tiles. The onset of this separation may be seen to consistently occur at an average applied displacement of 23.7mm (see Table 75). Above 24mm applied displacement, the CIA beams may still be seen to be able to carry a high load. The cover layer then progressively separate from the ceramic tiles.

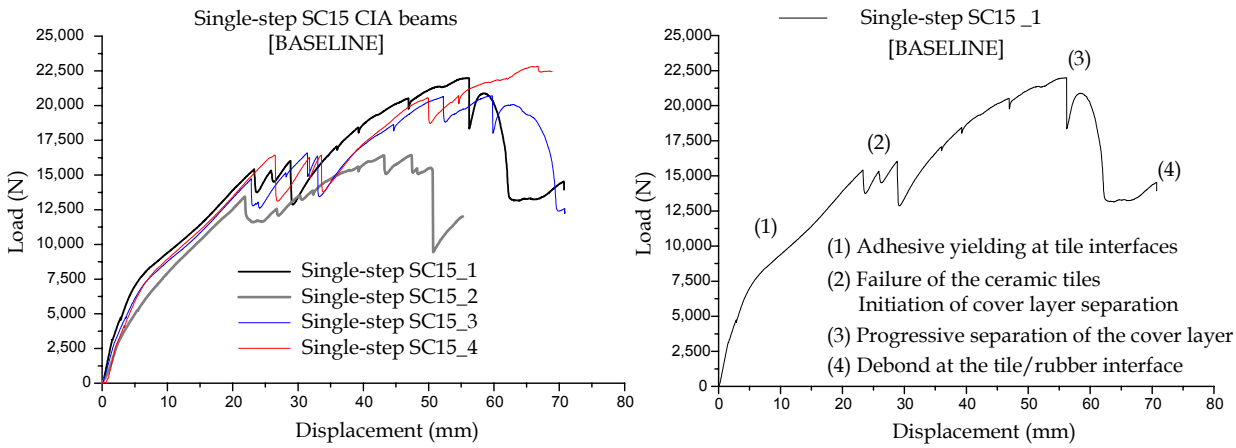

Figure 173. Load-deflection responses of single-step SC15 (VARTM) CIA beams

16.5.2 MULTI-STEP MANUFACTURED SPECIMENS

The test results for the beams manufactured by the multi-step manufacturing process with the Applied Poleramic SC15 and SC11 (MS-SC11) resin systems are shown in Table 75.

16.5.3 SC15 MULTI-STEP CIA BEAM

In Table 75, the scatter in results may be seen to be large for the MS-SC15 beams. The load-deflection curves of the two MS-SC15 beams tested are further compared with that of a single-step SC15 beam in Figure 174. As it may be seen in Figure 174, the MS-SC15_2 beam was found to be very weak and failed prematurely at a low load, by the separation of the cover layer from the ceramic tiles and by the separation of the ceramic tiles from the rubber layer. The premature failure of the MS-SC15_2 beam may be seen to be as a result of damages, introduced during the manufacturing of the beams, which were not identified in the present work.

The MS-SC15_1 beam was however found to be much stronger, but not as strong as the SS-SC15 specimens. Although failure initiation of the MS-SC15_1 specimens was by the separation of the cover layer from the ceramic tile (as for the SS-SC15 beams), the specimen was seen to fail by the premature separation of the ceramic tiles from the rubber layer shortly after. Consequently, the structural performance of the MS-SC15 specimens may be seen to be poorer than that of the SS-SC15 specimens. Furthermore, the initial stiffness of the beam (for applied displacement lower than 20mm) may be seen to be lower than that of the single-step manufactured beam. This was identified as being as a result of the poor consolidation of the tiles during the multi-step fabrication process.

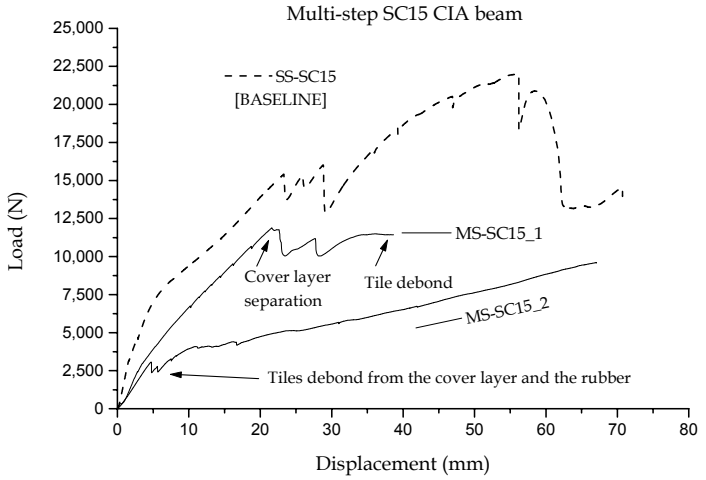

Figure 174. Load-deflection response of a multi-step SC15 CIA beam

16.5.4 SC11 MULTI-STEP CIA BEAM

The test results for the beams manufactured by the multi-step manufacturing process with the Applied Poleramic SC11 (MS-SC11) resin system are also shown in Table 75. The scatter in results may be seen to be small for these beams. The load-deflection curves of the two MS-SC11 CIA beams tested are compared with that of a single-step SC15 beam in Figure 175 below. As it may be seen in Figure 175, the structural performance of the MS-SC11 beams compares well with that of a SS-SC15 beam, although their initial stiffness may also be seen to be lower.

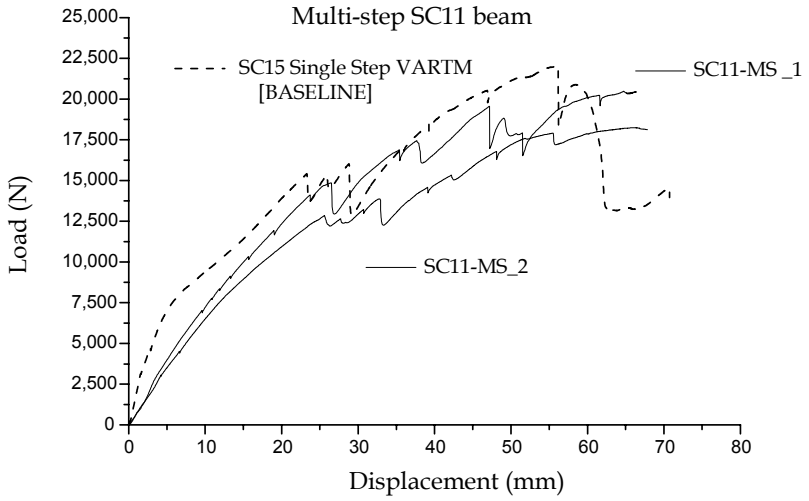

Figure 175. Load-deflection response of a multi-step SC11 CIA beam

The evolution of the failure events was seen to be identical for both MS-SC11 beams, and is presented for the MS-SC11_2 beam in Figure 176 below. The sequence of failure events was furthermore seen to be identical to that of the single-step SC15 beams (e.g., see Figure 173). The progressive degradation of the beams was observed to have resulted from a combination of adhesive and cover layer failure at the interfaces between two tiles, separation of the cover layer from the ceramic tiles and compression failure of the ceramic tiles. The damage to the adhesive between two tiles was however clearly observable in this case, as a whitening of the cover layer could be observed during the tests as the applied displacement was increased. Again, the separation of the cover layer was observed to initiate at the edge of the beams. The load and displacement at failure initiation may be seen to be close to that of the baseline beams. Overall, the MS-SC11 beams behaved in much the same way as the single-step SC15 beams did.

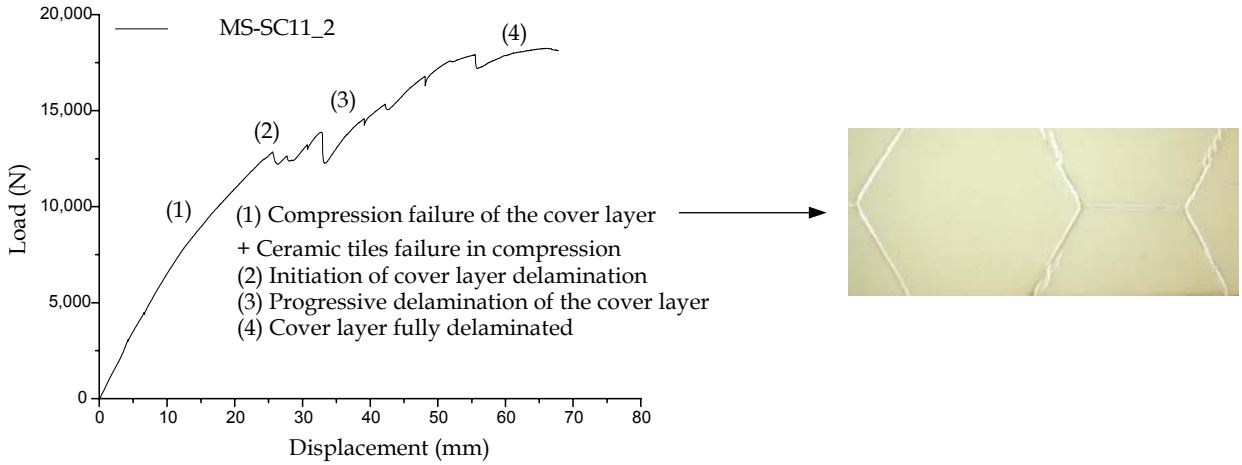

Figure 176. Evolution of the failure event on multi-step SC11 CIA beams

16.5.5 EFFECT OF THE SURFACE MECHANICAL PREPARATION ON THE RUBBER LAYER

The effect of the surface mechanical preparation of the rubber layer on the mechanical performance of SC15 and SC11 single and multi-step beams is shown in Table 76. The failure load and displacement may be seen to be much smaller that than observed on the specimens for which the rubber layer was prepared (compare Table 75 and Table 76).

Furthermore, the mechanical response of single- and multi-step manufactured beams is compared with that of their respective beams for which the rubber layer was mechanically prepared. The mechanical response of single- and multi-step SC15 manufactured beams is shown on the left-hand side of Figure 177. Conversely, the mechanical response of multi-step SC11 beams is compared in the right-hand side of Figure 177.

Table 76: Failure load and displacement results for the CIA beams tested in four-point bending.

Specimens		Failure load (N)	Displacement at failure (mm)
Single-step	**-1**	4522	5.27
SC15*	**-2**	3826	5.51
Multi-step	**-1**	753	3.04
SC15*	**-2**	1707	6.81
Multi-step	**-1**	10,466	25.4
SC11*	**-2**	14,234	30.7

In the left-hand side of Figure 177, it may be seen that the single- and multi-step SC15 beams for which the rubber layer was not mechanically prepared did not perform very well, when compared with a single-step SC15 beam for which the rubber layer was mechanically prepared. The specimens were observed to fail, prematurely, by the separation of the rubber layer from the backing plate. The separation initiated at the outer ends of the beams and propagated toward the center of the beams. The failure may be seen to be as a result of the poor adhesion between the rubber and the backing plate.

In the right-hand side of Figure 177, the mechanical performance of multi-step SC11 beams for which the rubber layer was and was not mechanically prepared are compared. Again, it may be seen that the mechanical performance is poorer for the specimen for which the rubber layer was not mechanically prepared. However, the response may seen to be better than that of the SC15 specimens for which the rubber layer was also not mechanically prepared.

Nonetheless, in both cases, the beams for which the surface of the rubber layer was not mechanically were seen to fail, prematurely, by the separation of the rubber from the backing plate. This may be seen as a result of a poorer level of adhesion between the two constituents. Consequently, it may be seen that the surface mechanical preparation of the rubber layer appears necessary to achieve optimum mechanical performance of the beams.

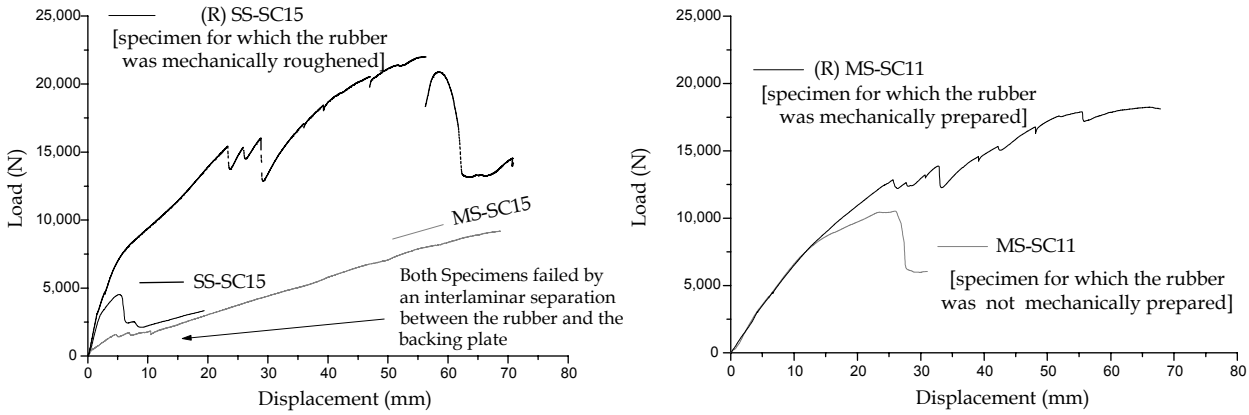

Figure 177. Load-deflection responses of single- and multi-step SC15 and SC11 CIA beams: Effect of the mechanical roughening of the rubber.

Assuming that the rubber layer is properly prepared, the structural performance of single-step SC15 beams (SS-SC15) may be seen to be better than any of the beams tested in the present work. The progressive degradation of the structural performance of the single-step beams was shown to have resulted from a combination of adhesive and cover layer failure at the interface between two consecutive tiles. This failure mode was then followed by the progressive separation of the cover layer from the ceramic tiles. Compression failure of the ceramic tiles was also observed to have occurred, but the exact sequence of failure event could not be determined. The cover layer then progressively delaminated with the increased in applied displacement.

The structural performance of the multi-step SC15 (MS-SC15) beams was seen to be the poorest of all beams. The sequence of failure of the MS-SC15 beams was seen to be initially identical to that of the SS-SC15 beams, but the beams were shown to fail by the separation of the cover layer from the ceramic tiles on one hand, and by the premature separation of the ceramic tiles from the rubber on the other.

The structural performance of the multi-step SC11 beam may be seen to be comparable although slightly inferior, to that of the single-step manufactured beams. The sequence of failure of the multi-step SC11 beams was furthermore seen to be identical to that of the single-step SC15 beams. Consequently, it may be said that the multi-step SC11 beams performed as well as the single-step SC15 beams.

16.5.6 Effect of the Surface Mechanical Preparation of the Rubber Layer

The specimens for which the rubber was not mechanically abraded failed, prematurely, by an interlaminar failure between the rubber and the backing plate. The failure was observed to initiate at the outer ends of the beams where the relative motion between the backing plate and the ceramic tiles-cover layer is the greatest, as shown schematically in Figure 178.

The mechanical preparation of the rubber layer prevented this mechanism to occur, and the failure mode was therefore seen as being more complex and included the debond of the cover

layer and compressive failure of the ceramic tiles. The surface preparation of the rubber layer may be seen essential to obtain an optimum structural performance of the CIA beams.

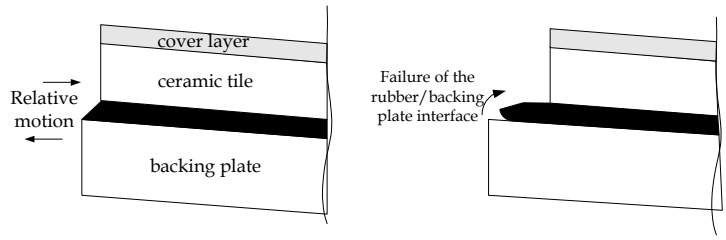

Figure 178. Failure at the interface of the backing and the rubber

It is noted that Double Cantilever Beam (DCB), Mode I, fracture mechanics specimens have successfully been developed to quantify the influence of the surface treatment of the rubber on the mechanical performance of the CIA beams. The DCB specimens were representative of the backing plate/rubber interface of corresponding CIA beams. The tests showed that with no mechanical preparation of the rubber, the interface between GFRP and rubber is very weak, with a critical fracture energy of 390J/m^2. The mechanical preparation of the rubber layer resulted in an improvement in the adhesion between the GFRP and the rubber, with values of critical fracture energies of 1500 J/m^2 and 6700 J/m^2 for single-step and multi-step manufactured specimens, respectively.

16.6 Fabrication Summary

Beams, representative of composite integral armors were tested in four-point bending and have been shown to be able to support loads far exceeding the load associated with the initial failure events. The structural performance of the beams has been shown to degrade progressively with the increasing applied displacement.

The structural performance of a CIA beam has also been related to its fabrication process. CIA beams fabricated from a single-step VARTM manufacturing process were seen to outperform 'equivalent' beams manufactured by a more conventional multi-step process. It is encouraging since single-step manufacturing methods are more efficient and are less time-consuming.

The structural performance of the beams was furthermore seen to be dependent on the performance of the interfaces that compose the beams. Firstly, the surface preparation of the rubber layer was seen to be essential for the structural performance of the CIA beams. Secondly, the adhesion between the rubber and the backing plate on one hand, and the ceramic tiles on the other, was also seen to be critical. Consequently, an increase in the mechanical performance of the CIA beams may be achieved by the tailoring of the strength of its interfaces.

16.7 STATIC AND BALLISTIC PERFORMANCE

Building on the wealth of experience acquired in the development of Part I and Part II, the performance of repaired CIA beams subjected to static and ballistic loading is investigated.

Considering the great amount of work necessary to complete this part, the project is still under progress under the CMT program. The proposed repair designs and some initial results are presented in this section.

16.7.1 REPAIR DESIGNS

The following repair criteria are envisaged:

- One-step process for multiple interfaces.
- Heated from outer surface (one-side access).
- Vacuum consolidation.
- Renew the structural and ballistic performance.
- Pre-cured VARTM repair patches.
- Room temperature cured and Induction-assisted cured adhesive systems.

Three potential repair designs may be thought to repair the backing plates (Figure 179):

- *Repair Design 1* is a flush scarf repair.
- The scarf angle may be varied from 1/1 (45°) to 1/5 (11.3°).
- *Repair Design 2* is a flush scarf repair that incorporates an overlapping ply.
- The scarf angle may be varied from 1/1 (45°) to 1/4 (14°).
- *Repair Design 3* is a step-lap repair.

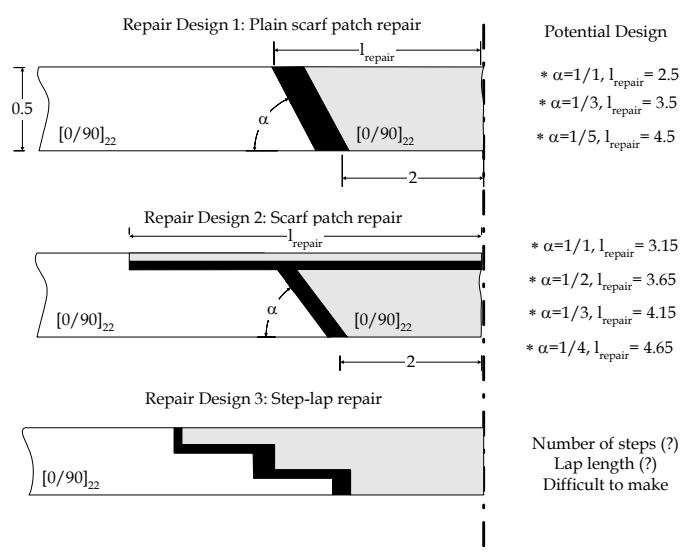

Figure 179. Three potential repair designs (focus on the backing plate)

The mechanical performance of the repaired CIA panels (1/1 (45°), 1/3 (18.4°) and 1/5 (11.3°) scarf patch repairs, as shown in Figure 180,) will initially be assessed in static four-point bending. Figure 181 shows a CIA beams ready to be repaired with a 1/1-scarf patch.

The repair will initially be induction-cured, although the possibility of using a tough room-temperature methacrylate adhesive system is being investigated.

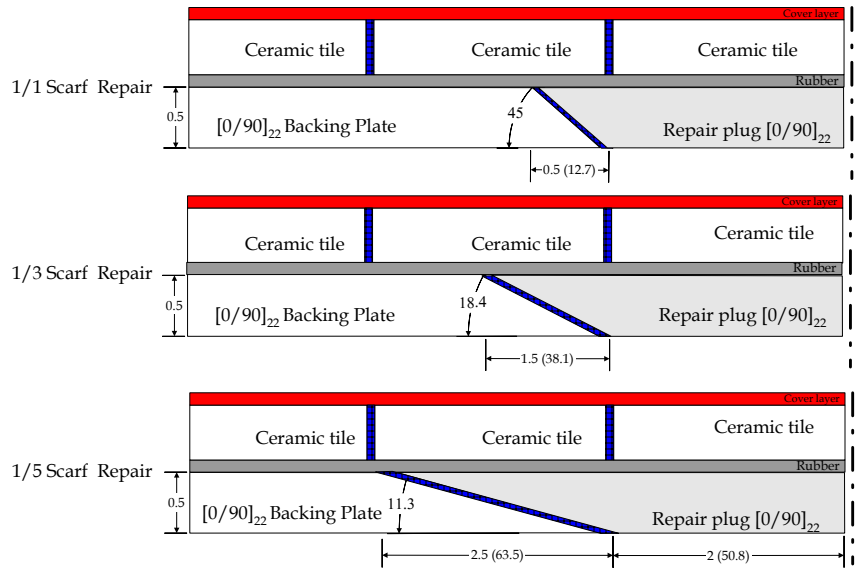

Figure 180. CIA panels repaired with a scarf patch repair

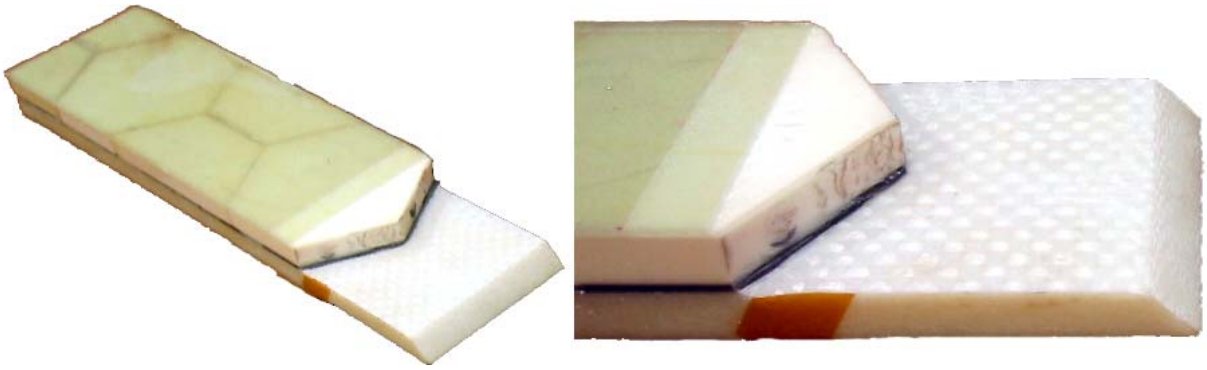

Figure 181. CIA beam ready to be repaired with a 1/1-scarf patch

16.7.2 Initial Results

Backing plates, representative of the CIA panels, were fabricated by the VARTM process and repaired with induction-cured Hysol adhesives (EA9359.3 and EA9394). The efficiency of three scarf angles was assessed. The repaired beams were tested in four-point bending, providing the results summarized in Figure 182. The strength of the repaired beam may be seen to increase up 60% of the original strength for the 1/5 scarf beam repaired with Hysol EA9359.3 adhesive. The 2D scarf repaired backing plates are shown to be able to restore a high proportion of the undamaged strength.

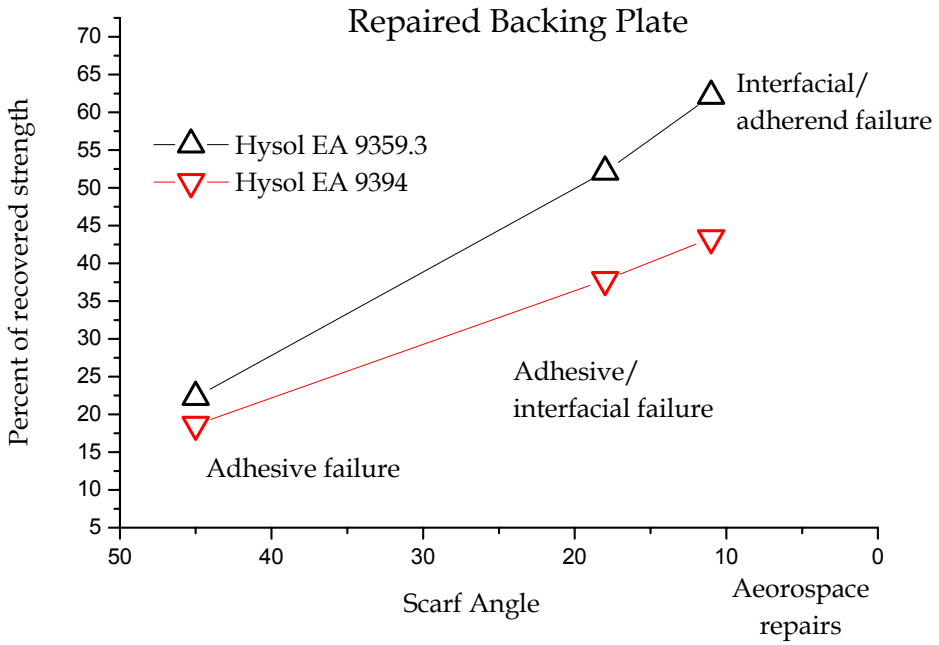

Figure 182. Efficiency of induction-cured scarf repaired backing plates

16.7.3 On-Going Research

The remaining studies are being continued under funding provided through congressional support to the University of Delaware's Center for Composite Materials (UD-CCM) as part of the "Composite Materials Technology" program.

- Static testing of scarf repaired CIA beams.
- Ballistic testing of undamaged and scarf repaired CIA beams.
- The mechanics of CIA is being investigated using two commercially available finite element codes (ANSYS – static for static analyses and LS-Dyna – for dynamic analysis). The aim is to predict the stiffness and the strength of the undamaged and repaired CIA beams.

17 Cost Estimates from Current Practice

Recent (1996) figures for annual defense usage of polymer-matrix composite materials (PMC) are 23.7 M-lb [132]. Total composite shipments by the US in 1997 were 3.42 billion pounds [133], with transportation use of composites exceeding one billion pounds for the first time [134]. PMC materials are currently used in DoD-fielded applications, including the Army's Apache and Blackhawk helicopter rotorblades, Navy surface ship superstructure components, and Air Force and Navy high-performance aircraft. Common materials used in aircraft applications are carbon-fiber-reinforced epoxies and polyimides. The most prevalent fabrication method is prepreg lay-up with autoclave cure. For expanding marine and ground

vehicle applications, increased use of glass-fiber-reinforced epoxies, vinyl esters, and phenolics is anticipated.

Use of adhesives for aircraft and aerospace has been reported as 21 M-lb in 1996, with a predicted increase in usage of 7.4% a year to 30.0 M-lb in 2001 [135]. Overall usage of structural adhesives by DoD is estimated as 45 M-lb, 5% of total industrial usage of 900 M-lb. Total amount of common adhesives sold by type is shown in Figure 183. While a breakdown in DoD usage was not available for this report, use of epoxy adhesives is common for DoD repair applications.

In addition, use of PMC materials and structural adhesives is on the verge of an unprecedented increase as a result of such developmental and future programs as the Army's Comanche helicopter, Composite Armored Vehicle (CAV), and Crusader Howitzer as well as the Navy's Advanced Enclosed Mast Sensor (AEM/S) System and other surface ship superstructures. These applications could all be in production within the next five to fifteen years, consuming millions of pounds per year of raw materials. An important part of these current and future programs is the development and implementation of applicable field and depot repair procedures. It is recognized that repair techniques and materials used for the current applications have deleterious environmental effects and that technological improvements can be made to significantly reduce hazardous waste and emissions and reduce costs. In addition, remanufacturing of previously developed PMC components must be considered from two perspectives. First, the same technological improvements may be useful in reducing environmental impact and cost for the manufacture of these PMC components. Second, some of the PMC components in these programs were designed, or are currently being designed, with no provision for practical, environmentally friendly, and affordable repair. The redesign of components to incorporate these processing changes and enable repair is called *remanufacturing*.

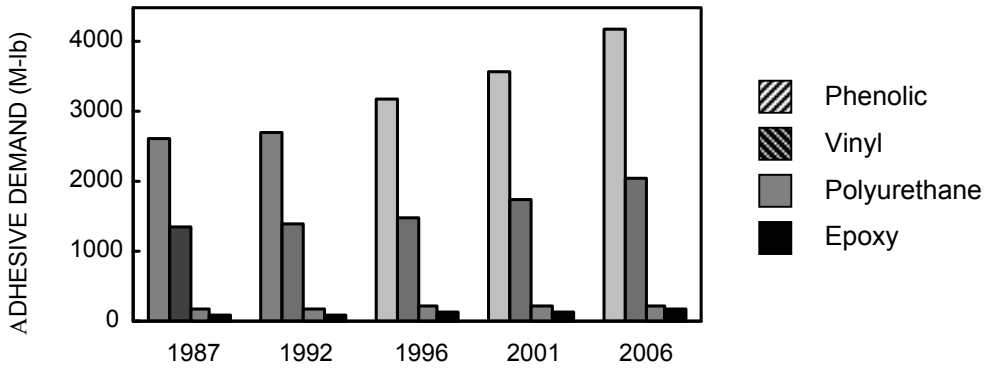

Figure 183: Steady growth of adhesive demand is predicted [135].

There are unique requirements for DoD environmental issues and use of composites. The DoD must be prepared to repair fielded composite applications in the theater of operations where required raw materials are not generally available. Consequently, raw materials are stockpiled in anticipation of use. Often raw materials with limited shelf life are shipped to the repair location, the shelf life expires, and the resulting hazardous waste must be shipped back

to CONUS for disposal. These resins often expire before delivery to the remote repair facility and must immediately be disposed of as hazardous waste [136]. Composite repair processing sites must meet emissions and hazardous waste standards that vary from nation to nation as well as from state to state within the US. While the amount of PMCs and adhesives used for DoD applications is small relative to the overall use of these materials, specific materials and processes are used predominantly for DoD applications. Structural adhesives are an example of a material class that has relatively high DoD usage. Consequently, the organization with the predominant interest in addressing environmental issues specific to these materials, processes, and repair scenarios must be DoD.

PMC manufacturing and repair processes result not only in a repaired or manufactured part but also in hazardous waste, hazardous emissions, and solid waste. The increased use of composite materials will lead to increased waste stream (trim, consumables, VOC emissions) for repair, increased hazardous waste stream due to shelf life expiration, and increased dependence on autoclave (NO_x, refrigeration). Eliminating or at least minimizing the contribution of composite repair and remanufacture to the waste stream will grow in importance as the use of composite materials expands.

Consequently, DoD requires (1) a reassessment of current repair procedures; (2) the maturation of new technologies that reduce hazardous emissions and waste due to repair; and (3) the redesign and remanufacture of components incorporating new technologies that maximize the opportunity for practical, affordable, and reliable repairs. Any new technologies are expected to reduce environmental impact and its associated costs. An analysis of environmental impact and cost is appropriate to evaluate the anticipated benefits of new technologies at the beginning of new technology maturation programs to ascertain whether such improvements are cost beneficial. This environmental and cost analysis is presented in terms of current and future material usage and resulting environmental impact and costs.

17.1 Environmental Baseline

An environmental analysis of current and potential replacement technologies has been performed to demonstrate how potential replacement technologies would significantly reduce hazardous emissions and hazardous waste. This analysis establishes methods and best-practice numbers.

During repair and manufacturing with structural adhesives and composite materials, hazardous emissions, hazardous waste, and solid waste are generated. Hazardous emissions, primarily volatile organic compounds (VOCs) and nitrogen oxides (NO_x) are given off during repair and manufacturing processes. Hazardous and solid wastes result from the raw materials and from subsequent processing. Hazardous wastes include hazardous raw materials whose effective usage has expired and process-dependent materials that are scrapped or contaminated as part of the production process. Non-hazardous solid wastes are not considered a high-cost factor, however, in environmentally sensitive areas or in Europe or Canada, the additional costs of rubbish should be considered.

Volatile Organic Compounds (VOCs). Volatile organic compounds (VOCs) are released from adhesives and from the resin component of composite materials during processing.

Typical VOC content ranges from 2% by weight for epoxy to 15% for polyimides. The more conservative 2% value has been used in estimates for this analysis. Advantages and disadvantages of closed and open processes are shown in Figure 184. At least equally important are accelerated curing processes in which the raw materials polymerize before they can escape as emissions.

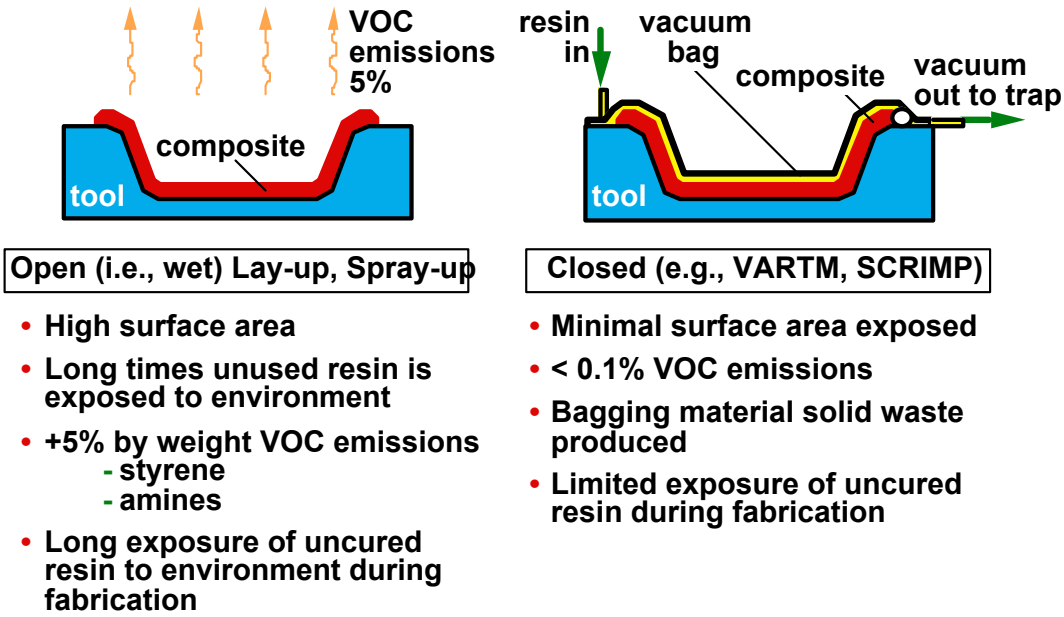

Figure 184: Containing VOCs reduces emissions and enables recycling.

Nitrogen Oxides (NO_x). Nitrogen or nitrous oxides (NO_x) are considered the sum of nitric oxide (NO), nitrogen dioxides (NO_2), and nitrogen tetroxide (N_20_4) emitted from combustion sources. The gases affect ozone and are regulated as hazardous emissions. Amounts of NO_x generated are related to the volume pressurized with nitrogen gas during processing. The greatest source for NO_x in composites manufacturing and repair is autoclaves. NO_x generated in two different autoclaves was monitored by Northrop-Grumman for a one-month period. Data was obtained for an 8,500-BTU autoclave for March 1998. During this period, aircraft control surfaces and composite patches and skins for space vehicles were processed in the autoclave. A total of 85.1 lb of NO_x was generated in 48 runs (averaging 1.77 lb NO_x per run) and 270 hours (averaging 0.31 lb NO_x per hour). For the second data set, information was gathered for a 12,000-BTU autoclave for the month of April 1998. Parts processed were aircraft control surfaces and skins for space vehicles. A total of 21.3 lb of NO_x was generated for 110 parts (average 0.2 lb NO_x per part), 39 runs (average 0.55 lb NO_x per run), and 340 hours (average 0.5 lb NO_x per hour). Based on these numbers and typical part sizes, an estimate of 0.02 lb NO_x per lb composite was used to evaluate environmental savings. For adhesives, this number was increased to 0.2 lb NO_x per lb adhesive because the pressure is applied to the entire part that is processed. This estimate provides some allowance for the influence of part size but is probably extremely conservative, since the ratio of part size to adhesive is generally higher than 9:1.

Hazardous Waste Caused by Shelf Life Expiration. Most adhesive and composite material resin systems cure slowly during storage prior to use. For these systems, processing

and performance requirements can be met only within the designated storage period or shelf life. Shelf-life limitations for commonly used composite material systems and adhesives are shown in Table 77 and Table 78, respectively. No commercially available structural adhesives approved for use in DoD applications having a shelf life longer than 12 months have been identified. Shelf life is generally documented under a required level of reduced-temperature storage. Once the partially cured material is removed from cold storage, the limit on useful life is called "out-time." Materials that have exceeded shelf life or out-time are partially cured beyond acceptable limits, can no longer be used, and are considered hazardous waste. Epoxy and other commonly used resins have finite shelf lives and must be disposed of after expiration, creating unnecessary and expensive ($25–50 per lb) waste. Each year, millions of pounds of expired material and associated packaging are processed for disposal by DoD.

Table 77. Shelf-Life Limitations of Commonly Used Composite Materials [137]

Resin/Fiber System	Processing Temperature (°F)	Service Temperature (°F, Dry)	Shelf Life at 0°F (Months)	Out-Time at RT (Days)
Epoxy/Carbon Fiber	250-350	180-450	6-12	10-30
Epoxy/Aramid Fiber	250-285	250	6	10-30
Epoxy/S-2 Glass Fiber	250-350	250-350	6	12
Bismaleimide/Carbon Fiber	350-475	450-600	6	28
Cyanate Ester/Carbon Fiber	250-450	450-480	12	30
Cyanate Ester/Quartz Fiber	250-350	200-350	6	21
Polyimide/Quartz Fiber	550-650	600	6	10

Table 78. Shelf-Life Limitations of Commonly Used Adhesives

Adhesive System	Processing Temperature (°F)	Service Temperature (°F, Dry)	Shelf Life at <40°F (Months)	Shelf Life at <77°F (Months)	Out-Time at RT
Hysol EA 9390 2-part epoxy paste [138]	200	350	12	6	2 hours
Hysol EA 9394 2-part epoxy paste [139]	RT	350	12	12	1.5 hours
Hysol EA 9396/C-2 2-part epoxy paste [140]	200	400	12	12	8 hours
Hysol EA 9695 epoxy film [141]	250-350	300	6 at 0°F	3	90 days

Table 79. Hazardous Materials in Uncured and Partially Cured Composites & Adhesives

	Chemical Name	Carcinogen	Mutagen
Epoxy	Boron Trifluoride, BF3	IARC Group 3 unclassified carcinogen to humans	No data available
	Bisphenol A	No data available	Potential mutagen
	Diglycidyl Ether of Bisphenol A, $C_{21}H_{24}O_4$	IARC Group 3 unclassified carcinogen to humans	Ames test both positive and negative results
	Epichlorohydrin, C_3H_5ClO	IARC Group 2A probable carcinogen to humans	Mutagenic activity in bacteria, animal tests positive
	Tetraglycidylbis (P-aminophynyl) methane	IARC Group 3 unclassified carcinogen to humans	Ames test positive
Epoxy Curing Agents	4,4' Methylene bis (2-Choloraniline) (MOCA), $C_{13}H_{10}Cl_2O_2$	IARC Group 2A probable carcinogen to humans	Ames test positive
	4,4' Methylenedianiline (MDA), $C_{13}H_{14}N_2$	IARC Group 2B possible carcinogen to humans	No data available
	Diethylenetriamine (DETA) $C_4H_{13}N_3$	No data available	Positive results in cultured mammalian cells
	Triethylenetetramine (TETA), $C_6H_{18}N_4$	Not classified	Ames test positive, found to be a direct acting mutagen
	Dicydiamide (DICY), $C_2H_4N_4$	Has not been investigated	Has not been investigated
	4,4' Sulfodianiline (DDS), $C_{12}H_{12}N_2O_2S$	Similar to MDA	Similar to MDA
Vinyl Ester	Styrene, C_8H_8	IARC Group 2B possible carcinogen to humans	Positive in vivo tests of animals
	Divinylbenzene, $C_{10}H_{10}$	no data available	No data available
Vinyl Ester Curing Agents	Benzoyl peroxide, $C_{14}H_{10}O_4$	IARC Group 3 unclassified carcinogen to humans	No data available
	Methyl ethyl ketone peroxide, $C_8H_{16}O_4$	No data available	No data available
	2,5-Dimethyl-2,5-di(2-ethylhexanoyl peroxy) Hexane, $C_{24}H_{46}O_6$	No data available	No data available
	Cumene hydroperoxide, $C_9H_{12}O_2$	No data available	Ames test positive
Phenolic	Phenol, C_6H_6O	IARC Group 3 unclassified carcinogen to humans	no data available
	Formaldehyde, CH_2O	IARC Group 2A probable carcinogen to humans	Positive in bacterial tests and in isolated human and animal tests
Phenolic Curing Agents	p-Phenolsulfonic acid, sodium salt, $C_6H_5SO_4Na$	Byproduct sulfuric acid mist is a Group 1 carcinogen	No data available
	p-Toluenesulfonic acid, $C_7H_8O_3S{\cdot}H_2O$	Byproduct sulfuric acid mist is a Group 1 carcinogen	No data available
Urethane	Methylenedi-p-Phenyl Diisocyanate (MDI), $C_{15}H_{10}N_2O_2$	IARC Group 3 unclassified carcinogen to humans	No data available
	Toluene-2,6-diisocyanate, (TDI) $C_9H_6N_2O_2$	IARC Group 2B possible carcinogen to humans	Positive in a number of vitro tests
Urethane Curing Agents	4,4' Methylene bis (2-Choloraniline) (MOCA), $C_{13}H_{10}Cl_2O_2$	IARC Group 2A probable carcinogen to humans	Ames test positive

Hazardous Waste—Production Debris. Production debris comprises scrap raw materials as well as vacuum bag material, sealants, and liquid shim. While the bagging, sealants, and shim may not be hazardous, they can become contaminated with partially cured resins and adhesives during the production process. In this case, they must be treated as hazardous waste. Figures for production debris were identified for one site producing B-2 bomber and F-18 fighter composite parts. For 112 tons of raw material, 38 tons (34%) of production debris was generated [142].

Information on solid waste for composite materials for military vehicles was reported in 1995 [143]. The most common composite material system was carbon/epoxy (Figure 185). The largest component of solid waste was prepreg (Figure 186). For this study, at least two-thirds of the waste material requires treatment as hazardous waste. Conservative estimates of production debris for this evaluation are 30% for composites and 10% for adhesives.

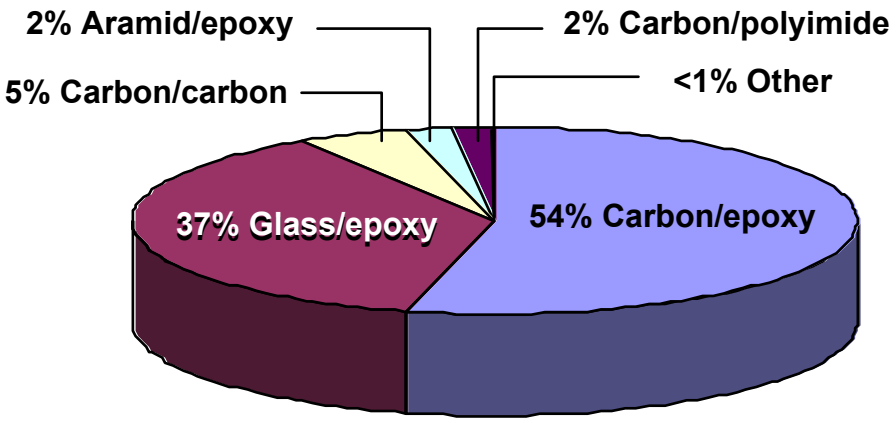

Figure 185. Waste in manufacturing composite materials for military vehicles is composed primarily of carbon/epoxy and glass/epoxy materials.

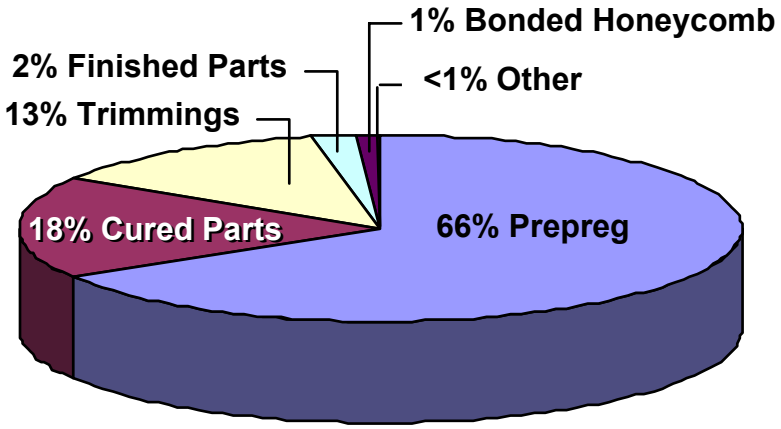

Figure 186. Prepreg hazardous waste is by far the largest component of waste in manufacturing military vehicles.

17.2 Potential Environmental Savings

No single solution can reduce the environmental impact of the entire range of materials, applications, and processing scenarios for composite repair and remanufacture throughout DoD. However, there are a number of approaches to mitigating environmental impact. Localized heating, reduction in shelf-life limitations, reduction in processing steps, and containment and recycling of VOCs can achieve reducing the production of hazardous emissions and wastes.

Global heating in an autoclave requires the application of pressure on the entire part. Nitrogen is used to provide the pressure and leads to the large amount of NO_x generated in an autoclave. Curing processes with localized heating do not require the application of pressure on the entire part and are expected to reduce NO_x emissions. A secondary effect of localized heating is greater control of the cure process. A reduction in the number of parts that need to be reprocessed helps reduce production debris hazardous waste. The change to localized heating is the primary enabler for "moving-out-of-the-autoclave."

Using alternative processing where appropriate can eliminate hazardous waste generated as a result of shelf-life expiration. Furthermore, the number of processing steps can be reduced by combining processing steps with co-injection and, to a lesser extent, with localized heating. Primarily rapid curing reduces VOC emissions, which ensures that low-molecular-weight materials polymerize before evaporating, thus providing large reductions in the production of volatile species. Remanufacturing thermoset-based composite components with thermoplastic-based designs and processes can also eliminate shelf-life expiration. The use of thermoset-based composites also eliminates VOC emissions.

Each replacement technology may produce different environmental savings. Depending on the selection and identification of criteria for the most appropriate replacement method for any given scenario, the savings will be different. For each type of savings, the amount expected for each procedure is provided below. Global savings are estimated, but the immediate target savings must be considered on a per-pound or per-part basis.

17.2.1 Reduction in VOCs

A 50% reduction in VOC emissions is anticipated for thermoset-based composite processes that do not require an autoclave. For every pound of adhesive or resin in a composite, current VOC emission is conservatively estimated at 0.02 lb. The greatest reduction in VOC emissions among the replacement thermoset curing techniques is expected from E-beam curing. VOC emission for E-beam curing is expected to be 0.01 pound per pound of adhesive or resin. Reduction in VOC emissions for induction curing is not as substantial. It can be generalized that half of all current composites processing is in the autoclave, producing an average resin content of 50% by weight. With overall DoD composites usage of 23.7 M-lb, the estimate of VOC emission from autoclave processing is 118,000 lb. If E-beam curing replaces autoclave cure, VOCs emitted will be reduced to 58,000 lb (Figure 187).

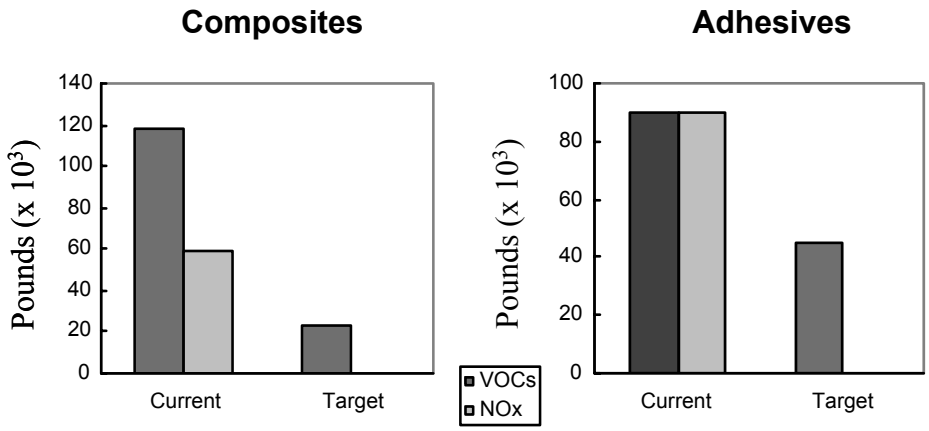

Figure 187. Replacing autoclave cure (current) with E-beam cure (target) enables reduction of hazardous emissions.

For adhesives, much less material is processed in the autoclave. For the examples given in the appendix, that amount has been estimated as 10% of all adhesives processed for DoD applications. Consequently, current VOC emissions generated in the autoclave are estimated at 90,000 lb/yr. Assuming that processing improvements permit elimination of autoclave processing, the VOCs generated will be reduced to 45,000 lb/yr.

17.2.2 REDUCTION IN NO_X.

Based on the numbers above, current NO_x generated in autoclave processing is estimated as 0.02 lb per lb composite. Thus, an estimate for current NO_x production is 23,700 lb. Eliminating the autoclave reduces this number to zero. Both E-beam and induction curing meet these requirements. Estimates for adhesive processing in the autoclave are based on a factor-of-ten increase in the amount of NO_x per pound of adhesive, since the adhesive is processed with the adherends it joins. The factor-of-ten increase is based on the assumption that the part is nine times larger than the amount of adhesive.

17.2.3 REDUCTION IN WASTE DUE TO SHELF-LIFE EXPIRATION.

Extending or eliminating shelf-life restrictions is expected to reduce hazardous waste of expired material. Costs of rotating expired materials and replacing them with fresh materials would also be eliminated. Based on the proposed technologies, resins and adhesives that have limited shelf life can be replaced by materials with infinite shelf life. This replacement eliminates all hazardous waste from shelf life and out-time expiration. Such hazardous waste generated currently is estimated as 20% of composites, or 4.7 M-lb, and 40% of adhesives, or 22 M-lb (Figure 188).

17.2.4 REDUCTION IN PRODUCTION DEBRIS HAZARDOUS WASTE.

Decreasing the number of processing steps can reduce production debris. Incorporating co-injection resin transfer molding technology, predictions for reduction in production debris

hazardous waste are 33% for composite materials and 50% for adhesives. In addition, greater control associated with localized heating reduces requirements for reprocessing and thus reduces production debris. Estimates indicate that current production debris of 30% or 7.1 M-lb for composites can be reduced to 4.7 M-lb (Figure 188). Combined savings in hazardous waste (and, consequently, raw materials) is 7.1 M-lb/yr, or 78%, for composite materials and 20.3 M-lb/yr, or 95%, for adhesives. This represents a total potential reduction in hazardous waste produced by DoD of nearly 24 M-lb/yr.

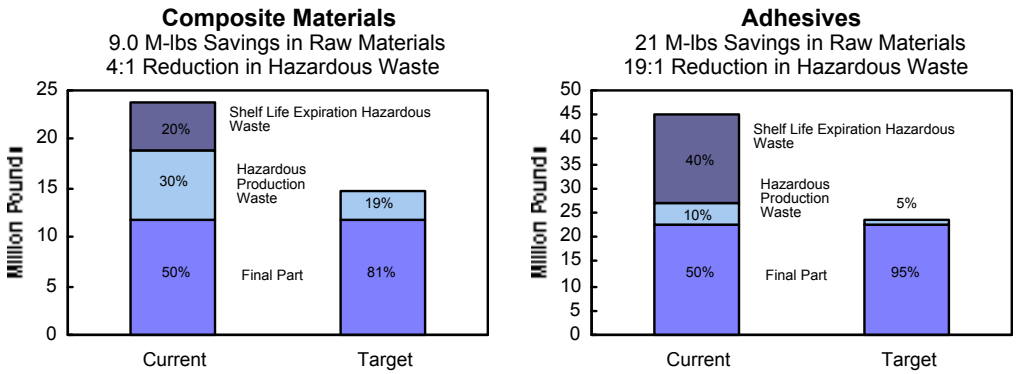

Figure 188. E-beam cure combined with reduced-step manufacturing processes enables reduction of hazardous waste for composites and adhesives.

17.3 Cost Savings.

Assuming that all composites used at current annual DoD rates could be processed with the proposed methods, estimates of cost savings in raw materials exceed $270 million for composites ($30/lb) and $210 million for adhesives ($10/lb). A conservative estimate for handling hazardous waste for both composites and adhesives is $5/lb, with anticipated savings of $152 million. Thus, a conservative order-of-magnitude estimate for potential cost savings is $630 million. Furthermore, 10% is a reasonable estimate for repair usage and 25% for appropriate remanufacturing applications. Thus, 35%, or approximately $220 million, is an ultra-conservative estimate for combined raw material and hazardous waste savings.

An example cost analysis was presented previously in this report, where EB curing is compared to the lowest cost processing methods with low cost resins to demonstrate current technical barriers and potential insertion areas for EB processing in current commercial practices.

The best-case events would involve replacement of many of these technologies with alternative curing approaches that may increase initial materials costs, but could reduce net production costs by reducing wastes and eliminating hazardous materials disposal fees. A number of example platforms where sufficient technical performance is available using alternative technologies are presented in the appendix to this report. The costs basis is determined to demonstrate potential buy-back or return on investment associated with some of these changes. However, due to the great variability in technologies, the previous discussion using activity based modeling could be applied across additional platforms to

demonstrate quantitative changes. Regardless, the trend and savings potential of environmentally friendly alternative approaches is evident from the examples provided.

17.4 Expanding Composites Usage in Military Environments

Predictions for future DoD usage of composite materials begin with consideration of a number of recent and current advanced development programs:

- Unmanned aerial vehicles Predator and Dark Star (Air Force) [144, 145]
- Comanche helicopter (Army)
- Composite Armored Vehicle (Army)
- Crusader self-propelled howitzer (SPH) and resupply vehicle (RSV) (Army)
- Composite Army Bridge (Army/DARPA)
- Future Scout and Cavalry System (Army/UK)
- Composite/metal matrix technologies for artillery (Army)
- Objective Individual Combat Weapons (Marines) [146]
- Advanced Enclosed Mast/Sensor System (Navy)
- Low Observable Multi-function Stack (Navy) [147]
- Multi-function Electromagnetic Radiating System (Navy) [147]
- Composite bumpers (Navy)
- Composite helicopter hangars and hangar doors (Navy) [147]
- Joint Strike Fighter (multi-service)

Other applications for composite materials under development include Navy corvette, mine hunter, and small combatant hulls, topside armor, internal decks, diesel power system components, and waterfront upgrades of reinforced concrete structures. Three of the advanced technology programs are considered as examples for the expanded use of composites.

17.4.1 JOINT STRIKE FIGHTER.

The Joint Strike Fighter (JSF) program is currently at the stage of competing concept demonstrations by two design teams [148, 149]. Scheduled to go into production in 2008, over 3000 aircraft are planned for the combined needs of the U.S. Air Force, Navy, and Marines and the U.K. Royal Navy. Expected composite usage on the JSF is 45% by weight. The Air Force plan is for 2036 JSFs to replace F-16s and A-10s. Use of composites on an F-16 is less than 5%, so replacement with a JSF increases use greater than eight-fold. The US Navy (300) and US Marine Corps (642) will replace F-18s (9%) and AV-8Bs (~22%), for smaller relative increases. Repair of the JSFs is estimated as approximately 3000 planes x 45% composite x 5800 lb/plane x 1% repair = 78,000 lb/yr. Manufacture of the JSF is conservatively estimated at 200 planes per year, or 522,000 lb/yr.

17.4.2 ADVANCED ENCLOSED MAST SENSOR SYSTEM.

With a prototype currently in use on the USS Radford, the Advanced Enclosed Mast Sensor (AEM/S) System is planned for the next twelve amphibious transport dock ships, LPD 17 onward, as well as the replacement carrier CV(X), the Mid-term Sealift, LH(X), and the 21st Century Surface Combatant family, including 32 destroyers and additional cruisers [147,150,151]. Thus, equivalents of the mast/sensor system and more extensive use of composite structures are expected on more than 50 ships. If the same amount of composite material as on the initial AEM/S System is used on 45 ships, the manufacture of composites would average 6 ships/yr x 30 tons/ship = 360,000 lb/yr. Repair for 50 ships is estimated at 50 ships x 30 tons/ship x 1% repair/yr = 30,000 lb/yr. The amount of composites used per ship is expected to increase. The 21st Century Surface Combatant family includes advanced technology programs for composite helicopter hangar and hangar doors [148]. The hangar is viewed as a test case for meeting more stringent fire and structural requirements than the AEM/S System. In addition, the possibility of using composites for the entire topside of the replacement carrier has been suggested.

17.4.3 FUTURE SCOUT AND CAVALRY SYSTEM.

The Future Scout and Cavalry System (FSCS) is a ground-vehicle application of composite materials, with the first production vehicle scheduled for 2007 as part of Army XXI transitioning into the Army After Next (AAN) [152]. Each vehicle is estimated at 30% composite by weight. Anticipated manufacturing can be estimated at 80 per year for composites usage of 61 vehicles/yr x 20 tons x 30% composite = 730,000 lb/yr. Repair for 1042 vehicles is predicted at 125,000 lb/yr. This represents an immense increase in composite usage by the Army, as very little composite material is used at the present time. A number of similar vehicle structures are in the development and scale-up stages for Future Combat Systems (FCS).

Based on these example programs, a gross estimate of future (2028 timeframe) use of composite materials by DoD can be made. Current use of composites is primarily for fixed (Air Force and Navy) and rotary wing aircraft (Army and Navy) with some shipboard applications (Navy). A gross estimate of the increase of composites usage by the Air Force is one order of magnitude. Increased use by the Navy is significantly higher, with composites just beginning to be used for shipboard superstructure. The increase in use of composites by the Army is more difficult to address in terms of a percentage increase, since current usage is limited to rotorcraft applications, while composites are being considered for use in ground vehicles, bridging, and other applications that require relatively large amounts of material. The use of composite materials in military aircraft has expanded at an increasing rate over the past thirty years (Figure 189). If the use of composites in ground vehicles, marine structures, infrastructure, etc., increases at the same rate, a tremendous overall increase in the use of composites by DoD can be expected. In addition, these new applications can build on the experience garnered from aircraft, and the use of composite materials may increase at even higher rates. Consequently, an overall estimate of an increase of composite materials in DoD use by 2028 might reasonably be two orders of magnitude.

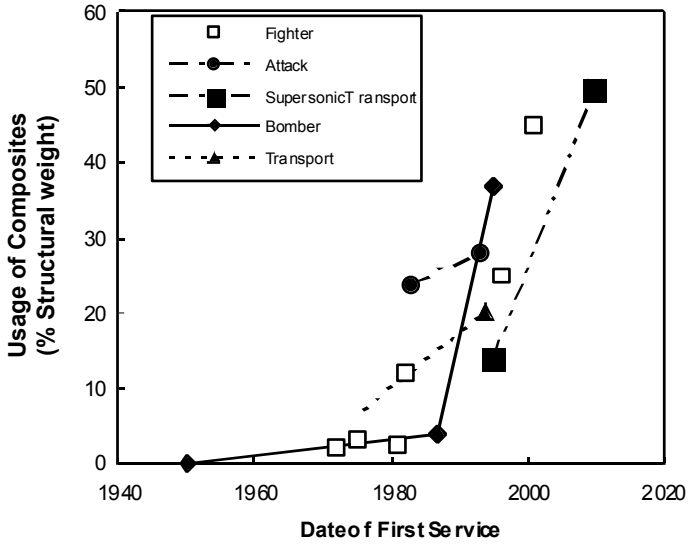

Figure 189. The use of composites in aircraft manufacture has shown a rapid increase in the past decade.

Environmental savings can be scaled by a corresponding two orders of magnitude. Cost savings are not expected to expand at exactly the same rate, as current composites usage has not yet reached the point of greatest economies of scale. However, cost savings on overall implementation of the proposed techniques are estimated to increase by a factor of 70. Using the same 10% repair and 25% remanufacturing estimates noted above, annual savings of $15 billion (1998) are predicted for 2028.

The use of adhesives is somewhat more difficult to predict. Based on 1996 figures and usage, aircraft and aerospace use of adhesives was predicted to expand at a rate of 7.4% per year [135]. As composites usage increases, the use of adhesives is likely to increase, but relative rates depend on particular processing methods. It should also be noted that repair of metallic military aircraft structures is reported to be transitioning from bolted repair to bonded repair [136] and, in some cases, composite patches are being adhesively bonded to metal substrates. A significant increase in the use of adhesives is expected to result from this transition. An overall estimate of the increase in DoD adhesives is a factor of 20 by 2028.

17.5 Summary of Composite Use and Cost Evaluation

Reductions in the environmental impact of repair and remanufacture of composite materials implemented now provide improvements in the short-term DoD usage of composite materials. Based on the expected increase in composites usage, reductions in environmental impact will have a much greater effect in the future. For adhesives, reductions in environmental impact implemented now provide improvements in the short term. Anticipated increases in DoD usage of structural adhesives support a prediction of significant increases in environmental improvement based on future usage.

Using an analysis of baseline and predicted environmental improvements, significant savings have been demonstrated for proposed technologies for repair and remanufacturing of DoD polymer-matrix composite applications. The baseline and current practice is described in terms of commonly used hazardous materials and current and future usage of composite materials. Anticipated environmental cost savings are estimated for the improved technologies as a result of reducing or eliminating shelf-life limitations, moving curing out of the autoclave, and reducing the number of processing steps. The proposed technologies include radiation and electromagnetic curing and improved resin transfer molding processing. Evaluation of environmental cost savings and descriptions of the improved technologies have focused on electron beam curing, induction curing, and co-injection resin transfer molding.

Technical barriers that were addressed in this program are as follows:

- Formulated toughened resins and adhesives;
- Optimized process parameters and kinetics models;
- Demonstrated acceptable performance and potential applications;
- Developed and documented repair sequencing and procedures; and
- Optimized repair schemes for specific applications.

The particular steps needed for process optimization and repair procedure development depend on the method as discussed above. Optimizing repair schemes for various applications depends both on the application and on the selected method. The proposed technologies constitute a family of solutions. Each technology is not universally applicable, but environmental improvements over the existing practice are possible by proper selection from among these technologies.

Appendix A: Strain Gauge Data Aircraft Skin Repair

Appendix A: Strain Gage Results for Aircraft Repair

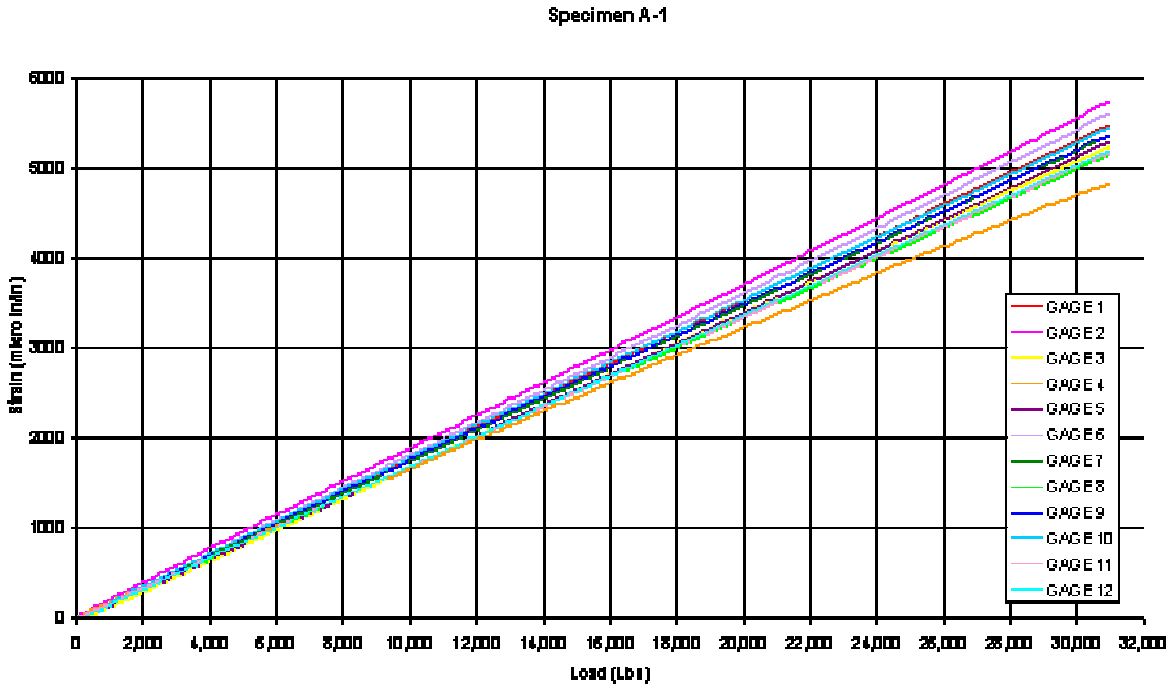

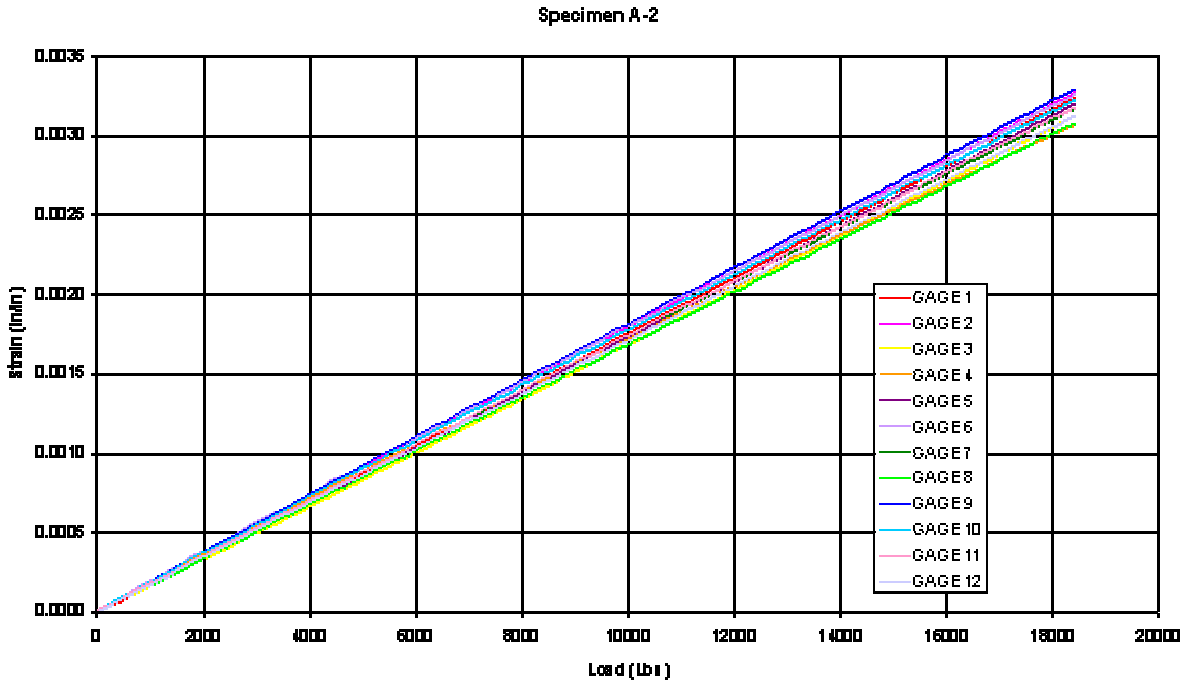

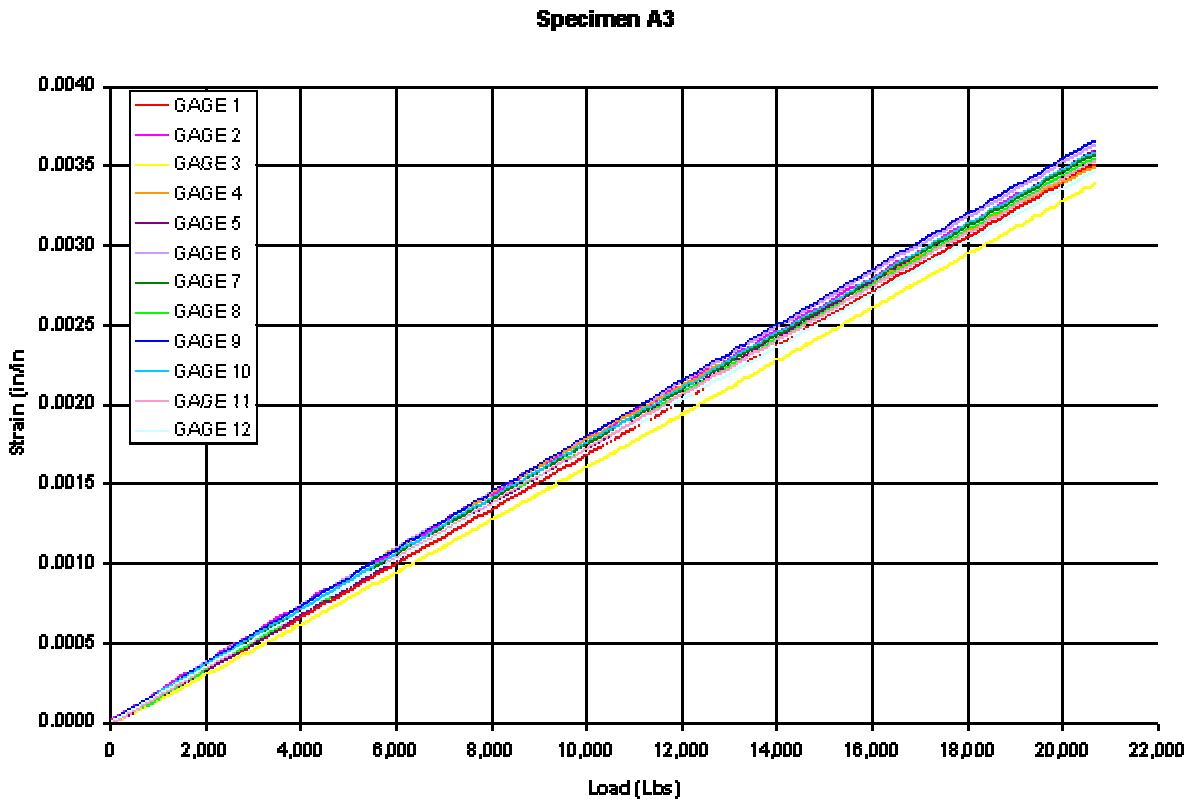
Specimen A3
GAGE 1
GAGE 2
GAGE 3
GAGE 4
GAGE 5
GAGE 6
GAGE 7
GAGE 8
GAGE 9
GAGE 10
GAGE 11
GAGE 12
Strain (in/in
0.0040
0.0035
0.0030
0.0025
0.0020
0.0015
0.0010
0.0005
0.0000
0
2,000
4,000
6,000
8,000
10,000
12,000
14,000
16,000
18,000
20,000
22,000
Load (Lbs)

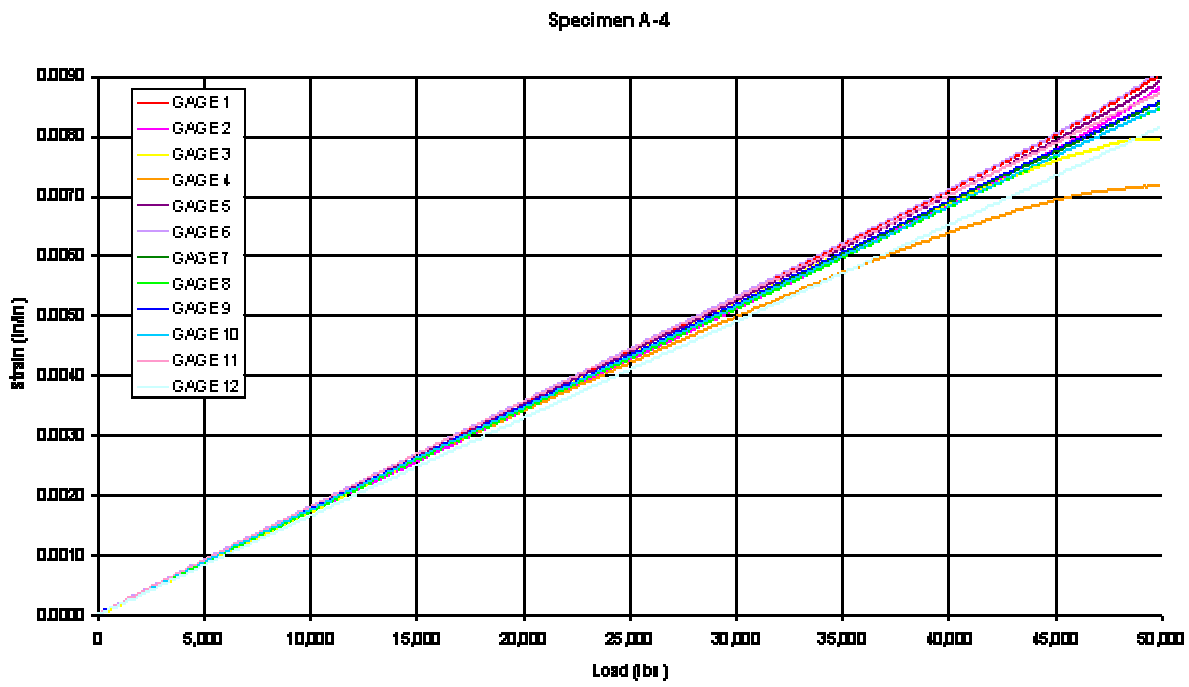
Specimen A-4
GAGE 1
GAGE 2
GAGE 3
GAGE 4
GAGE 5
GAGE 6
GAGE 7
GAGE 8
GAGE 9
GAGE 10
GAGE 11
GAGE 12
strain (in/in)
0.0090
0.0080
0.0070
0.0060
0.0050
0.0040
0.0030
0.0020
0.0010
0.0000
0
5,000
10,000
15,000
20,000
25,000
30,000
35,000
40,000
45,000
50,000
Load (lbs)

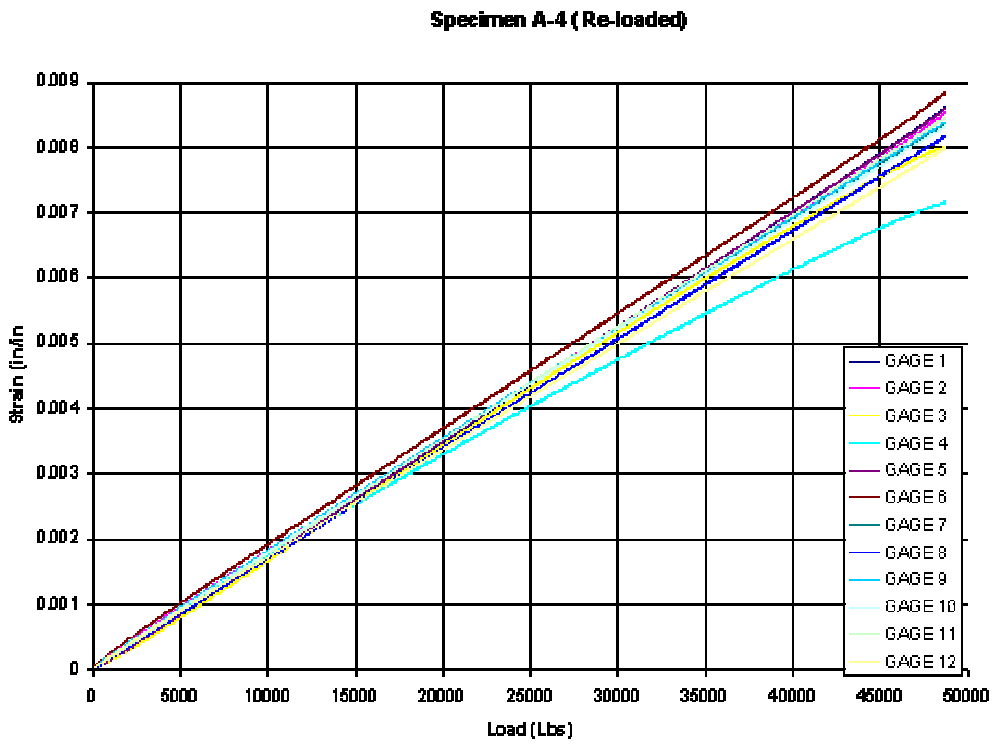
Specimen A-4 (Re-loaded)
Strain (in/in
Load (Lbs)
0.009
0.008
0.007
0.006
0.005
0.004
0.003
0.002
0.001
0
0
5000
10000
15000
20000
25000
30000
35000
40000
45000
50000
GAGE 1
GAGE 2
GAGE 3
GAGE 4
GAGE 5
GAGE 6
GAGE 7
GAGE 8
GAGE 9
GAGE 10
GAGE 11
GAGE 12

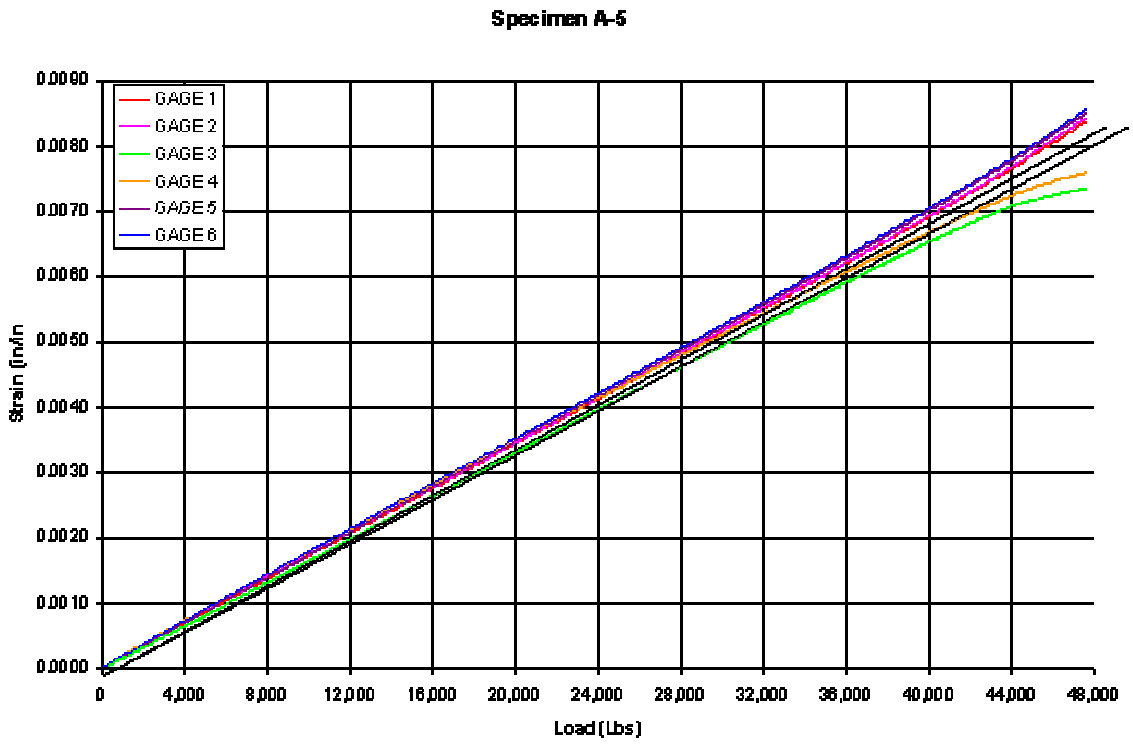
Specimen A-5
Strain (in/in
Load (Lbs)
0.0090
0.0080
0.0070
0.0060
0.0050
0.0040
0.0030
0.0020
0.0010
0.0000
0
4,000
8,000
12,000
16,000
20,000
24,000
28,000
32,000
36,000
40,000
44,000
48,000
GAGE 1
GAGE 2
GAGE 3
GAGE 4
GAGE 5
GAGE 6

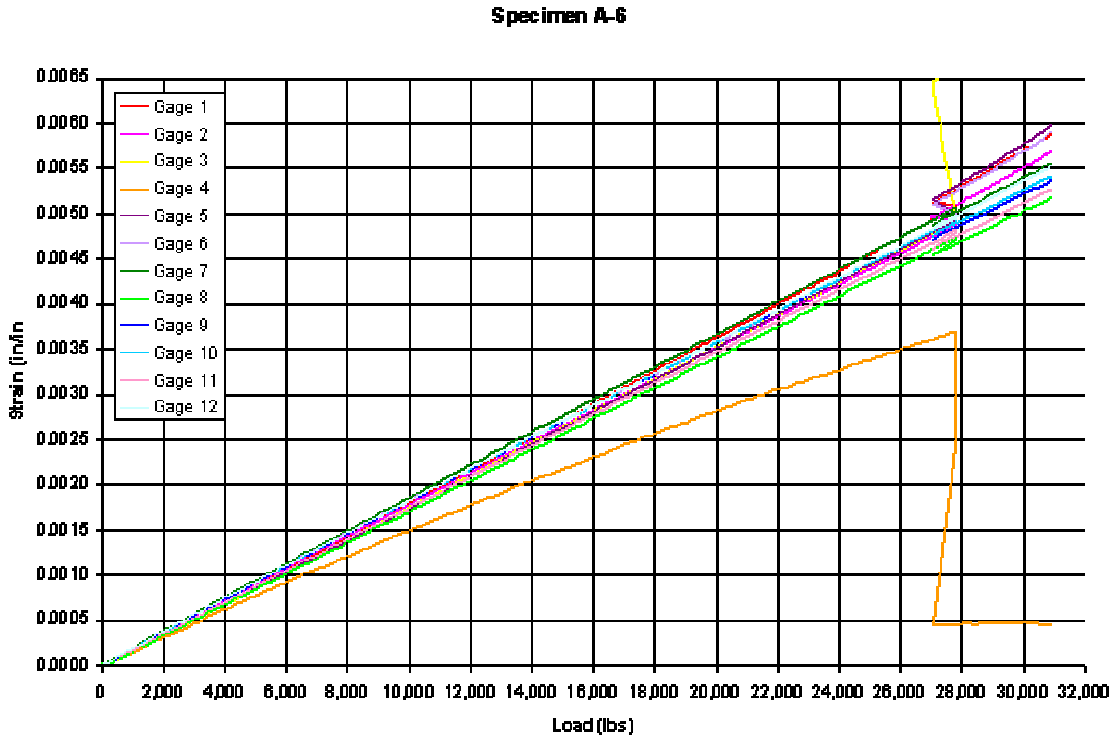
Specimen A-6
Strain (in/in
Load (lbs)
Gage 1
Gage 2
Gage 3
Gage 4
Gage 5
Gage 6
Gage 7
Gage 8
Gage 9
Gage 10
Gage 11
Gage 12
0.0065
0.0060
0.0055
0.0050
0.0045
0.0040
0.0035
0.0030
0.0025
0.0020
0.0015
0.0010
0.0005
0.0000
0
2,000
4,000
6,000
8,000
10,000
12,000
14,000
16,000
18,000
20,000
22,000
24,000
26,000
28,000
30,000
32,000

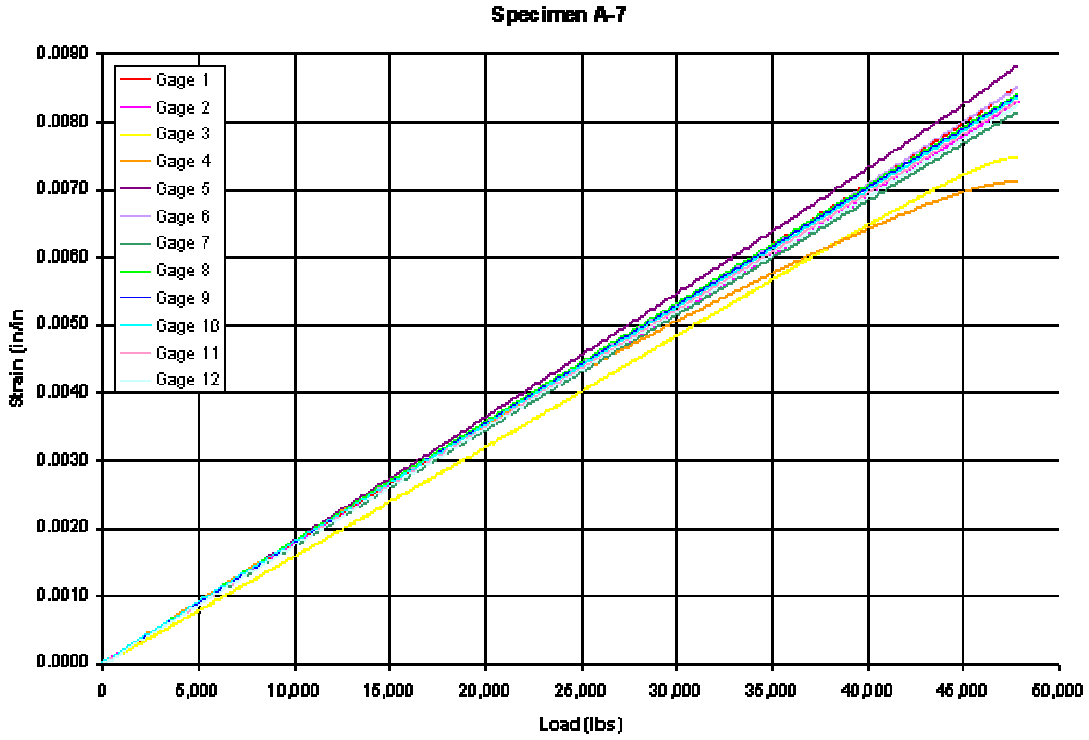
Specimen A-7
Strain (in/in
Load (lbs)
Gage 1
Gage 2
Gage 3
Gage 4
Gage 5
Gage 6
Gage 7
Gage 8
Gage 9
Gage 10
Gage 11
Gage 12
0.0090
0.0080
0.0070
0.0060
0.0050
0.0040
0.0030
0.0020
0.0010
0.0000
0
5,000
10,000
15,000
20,000
25,000
30,000
35,000
40,000
45,000
50,000

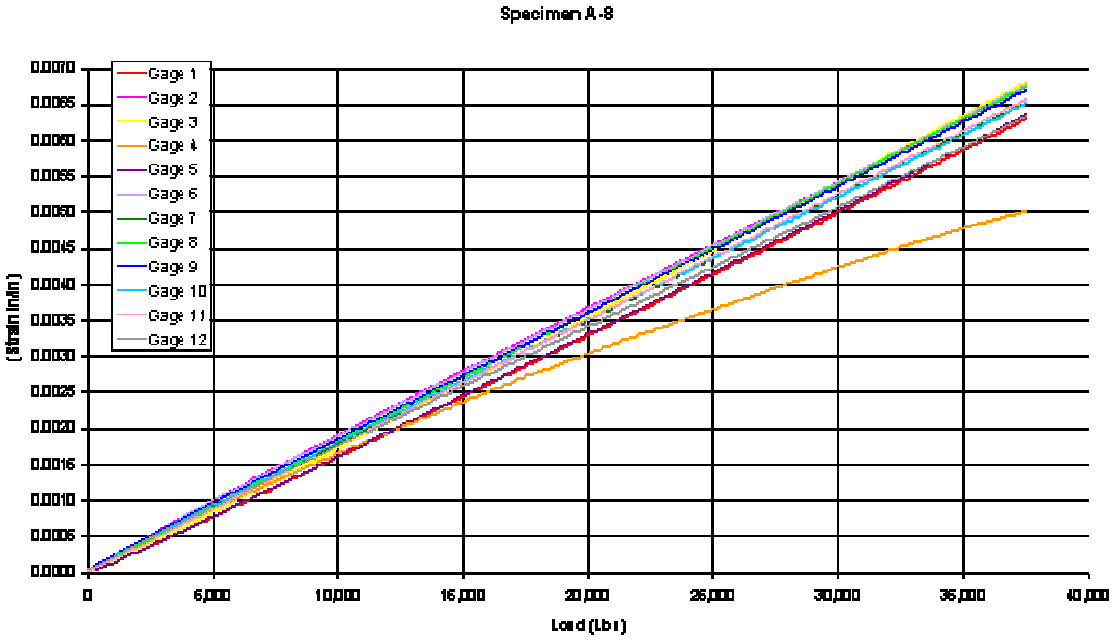
Specimen A-8
Gage 1
Gage 2
Gage 3
Gage 4
Gage 5
Gage 6
Gage 7
Gage 8
Gage 9
Gage 10
Gage 11
Gage 12
(Strain in/in)
Load (Lbs)

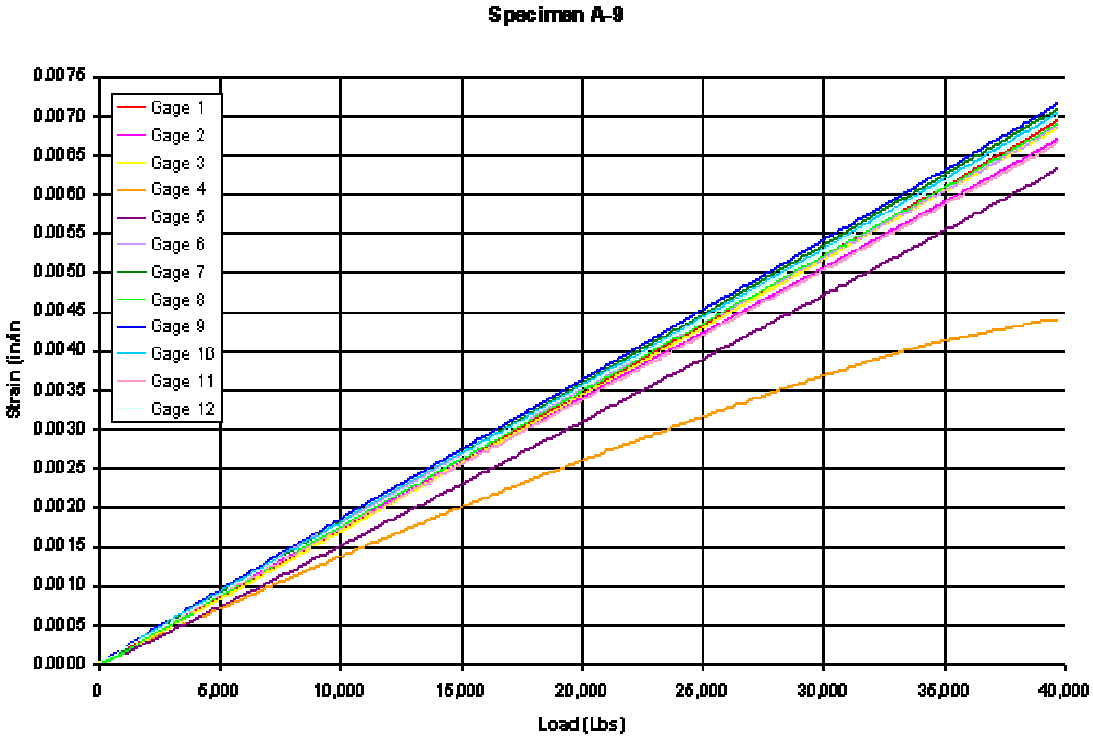
Specimen A-9
Gage 1
Gage 2
Gage 3
Gage 4
Gage 5
Gage 6
Gage 7
Gage 8
Gage 9
Gage 10
Gage 11
Gage 12
Strain (in/in
Load (Lbs)

Appendix B: Cost Analyses for Example Cases

Appendix B: Cost Analyses for Example Cases

Example Application 1: Repair of Aircraft Skin

BASELINE PRACTICE

Heat blanket —film adhesive and prepreg repair of aircraft skin

REPLACEMENT TECHNOLOGY ALTERNATIVE

E-beam—film adhesive and prepreg repair of aircraft skin

LOCATION

Depot

ADVANTAGES

- Reduction by half of VOC emissions
- Reduction in shelf life expiration and production debris hazardous waste
- Faster cure

DISADVANTAGES

- Training in new technology

Note that costs presented in this example may vary greatly depending on labor costs, number of repairs, volume, material disposed, unit costs, and uncertainties in available data.

CAPITAL COSTS	
BEFORE alternative	**AFTER alternative**
Not applicable.	$C_C = C_{C(E)}$ Where: C_C = Total capital costs $C_{C(E)}$ = Capital costs of equipment
CAPITAL COSTS include the cost of a portable E-beam unit. **DATA RANGES FOR CAPITAL COSTS** (based on available information): portable E-beam unit ($400,000)	

ANNUAL OPERATING COSTS	
Supply Costs	
BEFORE alternative	**AFTER alternative**
$C_{S(tot)} = N_{repairs}[(C_{RM} + C_L) + Q_{W(HW)} (C_{RM})]$ Where: $C_{S(tot)}$ = Total supply cost per year $N_{repairs}$ = Number of repairs C_{RM} = Raw materials cost per repair C_L = Labor cost per repair $Q_{W(HW)}$ = Waste disposal quantity of hazardous waste	$C_{S(tot)} = N_{repairs}[(C_{RM} + C_L) + Q_{W(HW)} (C_{RM})]$ Where: $C_{S(tot)}$ = Total supply cost per year $N_{repairs}$ = Number of repairs C_{RM} = Raw materials cost per repair C_L = Labor cost per repair $Q_{W(HW)}$ = Waste disposal quantity of hazardous waste
SUPPLY COSTS are equal to the cost per repair times the number of repairs plus stockpiling costs. **DATA RANGES FOR SUPPLY COSTS** (based on available information): cost of raw materials (1 lb composite @ $30/lb; 1/4 lb adhesive @ $10/lb per repair); labor cost per repair (heat blanket) is $1600, labor cost per repair (E-beam - reduced cure monitoring time) is $1400*; percentages of shelf life expiration and production debris hazardous waste from Figure 8. For cost estimate only, assume 400 repairs per year. Production materials assumed equivalent	
Waste Disposal Costs	
BEFORE alternative	**AFTER alternative**
$C_{W(tot)} = N_{repairs}[(C_{W(HE)})(Q_{W(HE)}) + Q_{W(HW)} (C_{HW})]$ Where: $C_{W(tot)}$ = Total waste disposal cost per year $N_{repairs}$= Number of repairs $C_{W(HE)}$ = Waste disposal cost of VOC $Q_{W(HE)}$= Waste disposal quantity of VOC $Q_{W(HW)}$ = Waste disposal quantity of hazardous waste C_{HW} = Cost of disposing expired shelf life and production debris material as hazardous waste.	$C_{W(tot)} = N_{repairs}[(C_{W(HE)})(Q_{W(HE)}) + Q_{W(HW)} (C_{HW})]$ Where: $C_{W(tot)}$ = Total waste disposal cost per year $N_{repairs}$= Number of repairs $C_{W(HE)}$ = Waste disposal cost of VOC $Q_{W(HE)}$= Waste disposal quantity of VOC $Q_{W(HW)}$ = Waste disposal quantity of hazardous waste C_{HW} = Cost of disposing expired shelf life and production debris material as hazardous waste.

WASTE DISPOSAL COSTS. Before the alternative, waste disposal costs are equal to the amount of VOC times the cost of hazardous emission treatment plus the cost of the disposal of materials treated as hazardous waste for materials with expired shelf life or out time. After the alternative, waste disposal costs are equal to the amount of VOC times the cost of hazardous emission treatment.

DATA RANGES FOR WASTE DISPOSAL COSTS: Data above; percentages from Figures 7 and 8; hazardous emission disposal cost is $100/lb**; hazardous waste disposal cost is $40/lb.

Total Operating Costs	
BEFORE alternative	**AFTER alternative**
$C_{OB(tot)} = C_{S(tot)} + C_{W(tot)}$ Where $C_{OB(tot)}$ =Total operating costs before alternative	$C_{OA(tot)} = C_{S(tot)} + C_{W(tot)}$ Where $C_{OA(tot)}$ =Total operating costs after alternative

* Note greatest cost savings will result from automated scarfing equipment.
** While VOC emissions are currently released, restrictions on this practice are anticipated.

INCREASE OR DECREASE IN ANNUAL OPERATING COSTS	
BEFORE alternative	**AFTER alternative**
$C_O = C_{OB(tot)} - C_{OA(tot)}$ Where: C_O = Increase or decrease in annual operating costs	

PAYBACK PERIOD
$T_{PAY} = (C_C)/(-C_O)$ (in years) Where: T_{PAY} = Time required for implementation of alternative to payback any capital costs

Cost Example

CAPITAL COSTS	
BEFORE alternative	**AFTER alternative**
Not applicable.	$C_C = C_{C(E)}$ $C_C = \$400,000$

ANNUAL OPERATING COSTS	
Supply Costs	
BEFORE alternative	**AFTER alternative**
$C_{S(tot)} = N_{repairs}[(C_{RM} + C_L) + Q_{W(HW)} (C_{RM})]$ $C_{S(tot)}$ = 800 repairs [(1 lb composite)($30/lb) + (0.25 lb adhesive)($10/lb) + $1600 + (30%+20%)/50%· (1 lb composite)($30/lb) + (40%+10%)/50%·(0.25 lb adhesive)($10/lb)] $C_{S(tot)}$ = 800($32.50 + $1600 + $32.50) $C_{S(tot)} = \$1,332,000$	$C_{S(tot)} = N_{repairs}[(C_{RM} + C_L) + Q_{W(HW)} (C_{RM})]$ $C_{S(tot)}$ = 800 repairs [(1 lb composite)($30/lb) + (0.25 lb adhesive)($10/lb) + $1400 + (19%/81%)· ($30/lb) + (5%/95%)·(0.25 lb adhesive)($10/lb)] $C_{S(tot)}$ = 800($32.50 + $1400 + $8.15) $C_{S(tot)} = \$1,152,500$
Waste Disposal Costs	
BEFORE alternative	**AFTER alternative**
$C_{W(tot)} = N_{repairs}[(C_{W(HE)})(Q_{W(HE)}) + Q_{W(HW)} (C_{HW})]$ $C_{W(tot)}$ = 800 repairs {[(2.5%)(1 lb)+(5%)(0.25lb)] · $100/lb + [(30%+20%)/50%·(1 lb composite) + (40%+10%)/50%·(0.25 lb adhesive)]($40/lb)]} $C_{W(tot)}$ = 800 ($3.75 + $50) $C_{W(tot)} = \$43,000$	$C_{W(tot)} = N_{repairs}[(C_{W(HE)})(Q_{W(HE)}) + Q_{W(HW)} (C_{HW})]$ $C_{W(tot)}$ = 800 repairs {[0.5(2.5%)(1 lb) + 0.5(5%)(0.25 lb)]$100/lb + [(19%)/81%·(1 lb composite) + (5%)/95%·(0.25 lb adhesive)]($40/lb)]} $C_{W(tot)}$ = 800 ($1.88 + $9.70) $C_{W(tot)} = \$9,300$
Total Operating Costs	
BEFORE alternative	**AFTER alternative**
$C_{OB(tot)} = C_{S(tot)} + C_{W(tot)}$ $C_{OB(tot)} = \$1,332,000 + \$43,000$ $C_{OB(tot)} = \$1,375,000$	$C_{OA(tot)} = C_{S(tot)} + C_{W(tot)}$ $C_{OA(tot)} = \$1,152,500 + \$9,300$ $C_{OA(tot)} = \$1,161,800$

INCREASE OR DECREASE IN ANNUAL OPERATING COSTS	
BEFORE alternative	**AFTER alternative**
$C_O = C_{OB(tot)} - C_{OA(tot)}$ $C_O = \$1,375,000 - \$1,161,800$ $C_O = \$ 213,200$	

PAYBACK PERIOD
$T_{PAY} = (C_C)/(C_O)$ (in years) $T_{PAY} = \$400,000/\$213,200$ $T_{PAY} = 1.88$ years

Example Application 2: Remanufacture of Airframe Component

BASELINE PRACTICE
Autoclave cure—manufacture of panel with stiffeners

REPLACEMENT TECHNOLOGY ALTERNATIVE
E-beam/VARTM—remanufacture of panel with stiffeners

LOCATION
Manufacturer

ADVANTAGES

- Elimination of NO_x
- Reduction by half of VOC emissions
- Reduction in shelf life expiration and production debris hazardous waste
- Faster cure

DISADVANTAGES

- Training in new technology

Note that costs presented in this example may vary greatly depending on labor costs, number of parts, volume, material disposed, unit costs, and uncertainties in available data.

CAPITAL COSTS	
BEFORE alternative	**AFTER alternative**
Not applicable.	$C_C = C_{C(E)}$ Where: C_C = Total capital costs $C_{C(E)}$ = Capital costs of equipment
CAPITAL COSTS include the cost of an E-beam unit. **DATA RANGES FOR CAPITAL COSTS** (based on available information): E-beam unit ($400,000)	

ANNUAL OPERATING COSTS	
Supply Costs	
BEFORE alternative	**AFTER alternative**
$C_{S(tot)} = N_{parts}[(C_{RM} + C_L) + Q_{W(HW)} (C_{RM})]$ Where: $C_{S(tot)}$ = Total supply cost per year N_{parts} = Number of parts C_{RM} = Raw materials cost per part C_L = Labor cost per part $Q_{W(HW)}$ = Waste disposal quantity of hazardous waste	$C_{S(tot)} = N_{parts}[(C_{RM} + C_L) + Q_{W(HW)} (C_{RM})]$ Where: $C_{S(tot)}$ = Total supply cost per year N_{parts} = Number of parts C_{RM} = Raw materials cost per repair C_L = Labor cost per repair $Q_{W(HW)}$ = Waste disposal quantity of hazardous waste
SUPPLY COSTS are equal to the cost per repair times the number of parts plus stockpiling costs. **DATA RANGES FOR SUPPLY COSTS** (based on available information): cost of raw materials (26.1 lb composite @ $30/lb; 1 lb adhesive @ $10/lb per repair); labor cost per part (before) is $1600, labor cost per repair (E-beam - reduced cure monitoring time) is $1400; percentages of shelf life expiration and production debris hazardous waste from manufacturer's data and Figure 8 For cost estimate only, assume 2,000 parts per year. Production materials assumed equivalent	
Waste Disposal Costs	
BEFORE alternative	**AFTER alternative**
$C_{W(tot)} = N_{parts}[(C_{W(HE)})(Q_{W(HE)}) + Q_{W(HW)} (C_{HW})]$ Where: $C_{W(tot)}$ = Total waste disposal cost per year N_{parts}= Number of parts $C_{W(HE)}$ = Waste disposal cost of NOx and VOC $Q_{W(HE)}$= Waste disposal quantity of NOx and VOC $Q_{W(HW)}$ = Waste disposal quantity of hazardous waste C_{HW} = Cost of disposing expired shelf life and production debris material as hazardous waste.	$C_{W(tot)} = N_{parts}[(C_{W(HE)})(Q_{W(HE)}) + Q_{W(HW)} (C_{HW})]$ Where: $C_{W(tot)}$ = Total waste disposal cost per year N_{parts}= Number of parts $C_{W(HE)}$ = Waste disposal cost of NOx and VOC $Q_{W(HE)}$= Waste disposal quantity of NOx and VOC $Q_{W(HW)}$ = Waste disposal quantity of hazardous waste C_{HW} = Cost of disposing expired shelf life and production debris material as hazardous waste.

WASTE DISPOSAL COSTS. Before the alternative, waste disposal costs are equal to the amount of NOx and VOC times the cost of hazardous emission treatment plus the cost of the disposal of materials treated as hazardous waste for materials with expired shelf life or out time. After the alternative, waste disposal costs are equal to the amount of VOC times the cost of hazardous emission treatment.

DATA RANGES FOR WASTE DISPOSAL COSTS: Data above; percentages from Figures 7 and 8; hazardous emission disposal cost is $100/lb*; hazardous waste disposal cost is $40/lb.

Total Operating Costs	
BEFORE alternative	**AFTER alternative**
$C_{OB(tot)} = C_{S(tot)} + C_{W(tot)}$ Where $C_{OB(tot)}$ =Total operating costs before alternative	$C_{OA(tot)} = C_{S(tot)} + C_{W(tot)}$ Where $C_{OA(tot)}$ =Total operating costs after alternative

* While VOC emissions are currently released, restrictions on this practice are anticipated.

INCREASE OR DECREASE IN ANNUAL OPERATING COSTS	
BEFORE alternative	**AFTER alternative**
$C_O = C_{OB(tot)} - C_{OA(tot)}$ Where: C_O = Increase or decrease in annual operating costs	

PAYBACK PERIOD
$T_{PAY} = (C_C)/(-C_O)$ (in years) Where: T_{PAY} = Time required for implementation of alternative to payback any capital costs

Cost Example

CAPITAL COSTS	
BEFORE alternative	**AFTER alternative**
Not applicable.	$C_C = C_{C(E)}$ $C_C = \$400,000$

ANNUAL OPERATING COSTS	
Supply Costs	
BEFORE alternative	**AFTER alternative**
$C_{S(tot)} = N_{parts}[(C_{RM} + C_L) + Q_{W(HW)} (C_{RM})]$ $C_{S(tot)}$ = 2000 parts {(26.1 lb composite)($30/lb) + (1.0 lb adhesive)($10/lb) + $1600 + [(34%)(66%)+15%] (26.1 lb composite)($30/lb) +·[(34%)(66%) +40%](1.0 lb adhesive)($10/lb)]}$C_{S(tot)}$ = 2000($793 + $1600 + $299)$C_{S(tot)}$ = $5,384,000	$C_{S(tot)} = N_{parts}[(C_{RM} + C_L) + Q_{W(HW)} (C_{RM})]$$C_{S(tot)}$ = 2000 parts {(26.1 lb composite)($30/lb) + (1.0 lb adhesive)($10/lb) + $1400 + [(34%)(66%)/4] (26.1 lb composite)($30/lb) +·[(34%)(66%)/4](1.0 lb adhesive)($10/lb)]}$C_{S(tot)}$ = 2000($793 + $1400 + $44)$C_{S(tot)}$ = $4,474,000
Waste Disposal Costs	
BEFORE alternative	**AFTER alternative**
$C_{W(tot)} = N_{parts}[(C_{W(HE)})(Q_{W(HE)}) + Q_{W(HW)} (C_{HW})]$ $C_{W(tot)}$ = 2000 parts {[(2.5%)(26.1 lb)+(5%)(1.0 lb) + 1.0 lb] · $100/lb + [(34%)(66%)+15%] (26.1 lb composite)($40/lb) +·[(34%)(66%) +40%](1.0 lb adhesive)($40/lb)]}} $C_{W(tot)}$ = 2000 ($170 + $416) $C_{W(tot)}$ = $1,172,000	$C_{W(tot)} = N_{parts}[(C_{W(HE)})(Q_{W(HE)}) + Q_{W(HW)} (C_{HW})]$ $C_{W(tot)}$ = 2000 parts {[0.5(2.5%)(26.1 lb) + 0.5(5%)(1.0 lb)] $100/lb + [(34%)(66%)/4] (26.1 lb composite)($40/lb) +·[(34%)(66%)/4](1.0 lb adhesive)($40/lb)]}} $C_{W(tot)}$ = 2000 ($35 + $61) $C_{W(tot)}$ = $192,000
Total Operating Costs	
BEFORE alternative	**AFTER alternative**
$C_{OB(tot)} = C_{S(tot)} + C_{W(tot)}$ $C_{OB(tot)}$ = $5,384,000 + $1,172,000 $C_{OB(tot)}$ = $6,556,000	$C_{OA(tot)} = C_{S(tot)} + C_{W(tot)}$ $C_{OA(tot)}$ = $4,474,000 + $192,000 $C_{OA(tot)}$ = $4,666,000

INCREASE OR DECREASE IN ANNUAL OPERATING COSTS	
BEFORE alternative	**AFTER alternative**
$C_O = C_{OB(tot)} - C_{OA(tot)}$ C_O = $6,556,000 - $4,666,000 C_O = $ 1,890,000	

PAYBACK PERIOD
$T_{PAY} = (C_C)/(C_O)$ (in years) T_{PAY} = $400,000/$1,189,000 T_{PAY} = 0.34 years

Example Application 3: Repair of Rotorblade

BASELINE PRACTICE
Heat blanket(pressure application by autoclave)—film adhesive and prepreg repair of rotorblade

REPLACEMENT TECHNOLOGY ALTERNATIVE
Induction—film adhesive and prepreg repair of rotorblade

LOCATION
Depot

ADVANTAGES

- Faster cure

DISADVANTAGES

- Training in new technology
- Stringent recertification requirements

Note that costs presented in this example may vary greatly depending on labor costs, number of repairs, volume, material disposed, unit costs, and uncertainties in available data.

CAPITAL COSTS	
BEFORE alternative	**AFTER alternative**
Not applicable.	$C_C = C_{C(E)} + C_{C(C)}$ Where: C_C = Total capital costs $C_{C(E)}$ = Capital costs of equipment $C_{C(E)}$ = Costs of certification
CAPITAL COSTS include the cost of an induction unit and the cost of certifying processing change. **DATA RANGES FOR CAPITAL COSTS** (based on available information): induction unit ($50,000); certification of processing change ($500,000)	

ANNUAL OPERATING COSTS	
Supply Costs	
BEFORE alternative	**AFTER alternative**
$C_{S(tot)} = N_{repairs}[(C_{RM} + C_L) + Q_{W(HW)} (C_{RM})]$ Where: $C_{S(tot)}$ = Total supply cost per year $N_{repairs}$ = Number of repairs C_{RM} = Raw materials cost per repair C_L = Labor cost per repair $Q_{W(HW)}$ = Waste disposal quantity of hazardous waste	$C_{S(tot)} = N_{repairs}[(C_{RM} + C_L) + Q_{W(HW)} (C_{RM})]$ Where: $C_{S(tot)}$ = Total supply cost per year $N_{repairs}$ = Number of repairs C_{RM} = Raw materials cost per repair C_L = Labor cost per repair $Q_{W(HW)}$ = Waste disposal quantity of hazardous waste
SUPPLY COSTS are equal to the cost per repair times the number of repairs plus stockpiling costs. **DATA RANGES FOR SUPPLY COSTS** (based on available information): cost of raw materials ($100 per repair); labor cost per repair (heat blanket) is $2400, labor cost per repair (induction- reduced cure monitoring time) is $2370; percentages of shelf life expiration and production debris hazardous waste from CCAD. For cost estimate only, assume 1000 repairs per year. Production materials assumed equivalent	
Waste Disposal Costs	
BEFORE alternative	**AFTER alternative**
$C_{W(tot)} = N_{repairs}[(C_{W(HE)})(Q_{W(HE)}) + Q_{W(HW)} (C_{HW})]$ Where: $C_{W(tot)}$ = Total waste disposal cost per year $N_{repairs}$= Number of repairs $C_{W(HE)}$ = Waste disposal cost of VOC $Q_{W(HE)}$= Waste disposal quantity of VOC $Q_{W(HW)}$ = Waste disposal quantity of hazardous waste C_{HW} = Cost of disposing expired shelf life and production debris material as hazardous waste.	$C_{W(tot)} = N_{repairs}[(C_{W(HE)})(Q_{W(HE)}) + Q_{W(HW)} (C_{HW})]$ Where: $C_{W(tot)}$ = Total waste disposal cost per year $N_{repairs}$= Number of repairs $C_{W(HE)}$ = Waste disposal cost of VOC $Q_{W(HE)}$= Waste disposal quantity of VOC $Q_{W(HW)}$ = Waste disposal quantity of hazardous waste C_{HW} = Cost of disposing expired shelf life and production debris material as hazardous waste.

WASTE DISPOSAL COSTS. Before the alternative, waste disposal costs are equal to the amount of VOC times the cost of hazardous emission treatment plus the cost of the disposal of materials treated as hazardous waste for materials with expired shelf life or out time. After the alternative, waste disposal costs are equal to the amount of VOC times the cost of hazardous emission treatment.

DATA RANGES FOR WASTE DISPOSAL COSTS: Data above; percentages from CCAD; hazardous emission disposal cost is $100/lb*; hazardous waste disposal cost is $30/lb.

Total Operating Costs	
BEFORE alternative	**AFTER alternative**
$C_{OB(tot)} = C_{S(tot)} + C_{W(tot)}$ Where $C_{OB(tot)}$ =Total operating costs before alternative	$C_{OA(tot)} = C_{S(tot)} + C_{W(tot)}$ Where $C_{OA(tot)}$ =Total operating costs after alternative

* While VOC emissions are currently released, restrictions on this practice are anticipated.

INCREASE OR DECREASE IN ANNUAL OPERATING COSTS	
BEFORE alternative	**AFTER alternative**
$C_O = C_{OB(tot)} - C_{OA(tot)}$ Where: C_O = Increase or decrease in annual operating costs	

PAYBACK PERIOD
$T_{PAY} = (C_C)/(-C_O)$ (in years) Where: T_{PAY} = Time required for implementation of alternative to payback any capital costs

Cost Example

CAPITAL COSTS	
BEFORE alternative	**AFTER alternative**
Not applicable.	$C_C = C_{C(E)} + C_{C(C)}$ $C_C = \$550,000$

ANNUAL OPERATING COSTS	
Supply Costs	
BEFORE alternative	**AFTER alternative**
$C_{S(tot)} = N_{repairs}[(C_{RM} + C_L) + Q_{W(HW)}(C_{RM})]$ $C_{S(tot)}$ = 1000 repairs [($100/repair) + $2400 + 5%·($100/repair)] $C_{S(tot)}$ = 1000($100 + $2400 + $5) $C_{S(tot)} = \$2,505,000$	$C_{S(tot)} = N_{repairs}[(C_{RM} + C_L) + Q_{W(HW)}(C_{RM})]$ $C_{S(tot)}$ = 1000 repairs [($100/repair) + $1400 + (4.5%)·($100/repair)] $C_{S(tot)}$ = 1000($100 + $2370 + $4.50) $C_{S(tot)} = \$2,474,500$
Waste Disposal Costs	
BEFORE alternative	**AFTER alternative**
$C_{W(tot)} = N_{repairs}[(C_{W(HE)})(Q_{W(HE)}) + Q_{W(HW)}(C_{HW})]$ $C_{W(tot)}$ = 1000 repairs {[(0.02 lb) $100/repair] + [5%·($30/repair)]} $C_{W(tot)}$ = 1000 ($2.00 + $1.50) $C_{W(tot)} = \$3,500$	$C_{W(tot)} = N_{repairs}[(C_{W(HE)})(Q_{W(HE)}) + Q_{W(HW)}(C_{HW})]$ $C_{W(tot)}$ = 1000 repairs {[50%(0.02 lb) $100/repair] + [4.5%·($30/repair)]} $C_{W(tot)}$ = 1000 ($1.00 + $1.35) $C_{W(tot)} = \$2,350$
Total Operating Costs	
BEFORE alternative	**AFTER alternative**
$C_{OB(tot)} = C_{S(tot)} + C_{W(tot)}$ $C_{OB(tot)} = \$2,505,000 + \$3,500$ $C_{OB(tot)} = \$2,508,500$	$C_{OA(tot)} = C_{S(tot)} + C_{W(tot)}$ $C_{OA(tot)} = \$2,474,500 + \$2,350$ $C_{OA(tot)} = \$2,476,900$

INCREASE OR DECREASE IN ANNUAL OPERATING COSTS	
BEFORE alternative	**AFTER alternative**
$C_O = C_{OB(tot)} - C_{OA(tot)}$ $C_O = \$2,508,500 - \$2,476,900$ $C_O = \$\ 31,600$	

PAYBACK PERIOD
$T_{PAY} = (C_C)/(C_O)$ (in years) $T_{PAY} = \$550,000/\$31,600$ $T_{PAY} = 17.4$ years

Example Application 4: Repair of AEM/S System

BASELINE PRACTICE
Heat blanket —film adhesive and prepreg repair of mast

REPLACEMENT TECHNOLOGY ALTERNATIVE
Room-temperature cure CIRTM—integrally cured resin/reinforcement repair of mast

LOCATION
Shipboard

ADVANTAGES

- Elimination of VOC emissions
- Reduction in shelf life expiration and production debris hazardous waste
- Faster cure/improved readiness

DISADVANTAGES

- Training in new technology
- Challenge to use CIRTM with two-sided, not through, access

Note that costs presented in this example may vary greatly depending on labor costs, number of repairs, volume, material disposed, unit costs, and uncertainties in available data.

CAPITAL COSTS	
BEFORE alternative	**AFTER alternative**
$C_C = C_{C(E)}$ Where: C_C = Total capital costs $C_{C(E)}$ = Capital costs of equipment	$C_C = C_{C(E)}$ Where: C_C = Total capital costs $C_{C(E)}$ = Capital costs of equipment
CAPITAL COSTS include the cost of heat blanket thermal-cure equipment (BEFORE) and cost of CIRTM equipment (AFTER). BEFORE costs are included as neither alternative is currently implemented. Analysis is on a per ship basis. **DATA RANGES FOR CAPITAL COSTS** (based on available information): Heat blanket thermal-cure equipment ($10,000); CIRTM equipment ($15,000)	

ANNUAL OPERATING COSTS	
Supply Costs	
BEFORE alternative	**AFTER alternative**
$C_{S(tot)} = Q_{repairs}[(C_{RM} + C_L) + Q_{W(HW)}(C_{RM})]$ Where: $C_{S(tot)}$ = Total supply cost per year $Q_{repairs}$ = Quantity of repaired material C_{RM} = Raw materials cost C_L = Labor cost $Q_{W(HW)}$ = Waste disposal quantity of hazardous waste	$C_{S(tot)} = Q_{repairs}[(C_{RM} + C_L) + Q_{W(HW)}(C_{RM})]$ Where: $C_{S(tot)}$ = Total supply cost per year $Q_{repairs}$ = Quantity of repaired material C_{RM} = Raw materials cost C_L = Labor cost $Q_{W(HW)}$ = Waste disposal quantity of hazardous waste
SUPPLY COSTS are equal to the cost per repair times the number of repairs plus stockpiling costs. **DATA RANGES FOR SUPPLY COSTS** (based on available information): cost of raw materials ($15/lb); quantity of repaired material (1% of 30 tons); labor cost per pound (heat blanket) ($200), labor cost per pound (CIRTM) ($200); production debris hazardous waste same ratio as manufacturing (1.5 tons/30 tons per step); steps (BEFORE) (3), steps (AFTER) (1), shelf life expiration (BEFORE) (Figure 8), (AFTER) (reduced by half).	
Waste Disposal Costs	
BEFORE alternative	**AFTER alternative**
$C_{W(tot)} = Q_{repairs}(Q_{W(HW)})(C_{HW})$ Where: $C_{W(tot)}$ = Total waste disposal cost per year $Q_{repairs}$ = Quantity of repaired material $Q_{W(HW)}$ = Waste disposal quantity of hazardous waste C_{HW} = Cost of disposing expired shelf life and production debris material as hazardous waste.	$C_{W(tot)} = Q_{repairs}(Q_{W(HW)})(C_{HW})$ Where: $C_{W(tot)}$ = Total waste disposal cost per year $Q_{repairs}$ = Quantity of repaired material $Q_{W(HW)}$ = Waste disposal quantity of hazardous waste C_{HW} = Cost of disposing expired shelf life and production debris material as hazardous waste.
WASTE DISPOSAL COSTS. Waste disposal costs are equal to the cost of the disposal of materials treated as hazardous waste for production debris and materials with expired shelf life or out time. **DATA RANGES FOR WASTE DISPOSAL COSTS**: Data above; hazardous waste disposal cost is $50/lb.	

Total Operating Costs	
BEFORE alternative	**AFTER alternative**
$C_{OB(tot)} = C_{S(tot)} + C_{W(tot)}$ Where $C_{OB(tot)}$ =Total operating costs before alternative	$C_{OA(tot)} = C_{S(tot)} + C_{W(tot)}$ Where $C_{OA(tot)}$ =Total operating costs after alternative

INCREASE OR DECREASE IN ANNUAL OPERATING COSTS	
BEFORE alternative	**AFTER alternative**
$C_O = C_{OB(tot)} - C_{OA(tot)}$ Where: C_O = Increase or decrease in annual operating costs	

PAYBACK PERIOD
$T_{PAY} = (C_C)/(-C_O)$ (in years) Where: T_{PAY} = Time required for implementation of alternative to payback any capital costs

Cost Example

CAPITAL COSTS	
BEFORE alternative	**AFTER alternative**
$C_C = C_{C(E)}$ $C_C = \$15{,}000$	$C_C = C_{C(E)}$ $C_C = \$15{,}000$

ANNUAL OPERATING COSTS	
Supply Costs	
BEFORE alternative	**AFTER alternative**
$C_{S(tot)} = Q_{repairs}[(C_{RM} + C_L) + Q_{W(HW)}(C_{RM})]$ $C_{S(tot)}$ = 1%(30 tons) {\$15/lb + \$200/lb + [(3)(1.5/30) + 15%/50%](\$15/lb)} $C_{S(tot)}$ = 600 lb. {\$15/lb + \$200/lb + 0.45(\$15/lb)} $C_{S(tot)} = \$133{,}050$	$C_{S(tot)} = Q_{repairs}[(C_{RM} + C_L) + Q_{W(HW)}(C_{RM})]$ $C_{S(tot)}$ = 1%(30 tons) {\$15/lb + \$200/lb + [(1)(1.5/30) + (15%/50%)/2](\$15/lb)} $C_{S(tot)}$ = 600 lb. {\$15/lb + \$200/lb + 0.20(\$15/lb)} $C_{S(tot)} = \$130{,}800$
Waste Disposal Costs	
BEFORE alternative	**AFTER alternative**
$C_{W(tot)} = Q_{repairs}(Q_{W(HW)})(C_{HW})$ $C_{W(tot)}$ = 1%(30 tons) [(3)(1.5/30) + 15%/50%](\$50/lb) $C_{W(tot)}$ = 600 lb. (0.45)(\$50/lb) $C_{W(tot)} = \$13{,}500$	$C_{W(tot)} = Q_{repairs}(Q_{W(HW)})(C_{HW})$ $C_{W(tot)}$ = 1%(30 tons) [(1)(1.5/30) + (15%/50%)/2](\$50/lb) $C_{W(tot)}$ = 600 lb. (0.20)(\$50/lb) $C_{W(tot)} = \$6{,}000$
Total Operating Costs	
BEFORE alternative	**AFTER alternative**
$C_{OB(tot)} = C_{S(tot)} + C_{W(tot)}$ $C_{OB(tot)} = \$133{,}050 + \$13{,}500$ $C_{OB(tot)} = \$146{,}550$	$C_{OA(tot)} = C_{S(tot)} + C_{W(tot)}$ $C_{OA(tot)} = \$130{,}800 + \$6{,}000$ $C_{OA(tot)} = \$136{,}800$

INCREASE OR DECREASE IN ANNUAL OPERATING COSTS	
BEFORE alternative	**AFTER alternative**
$C_O = C_{OB(tot)} - C_{OA(tot)}$ $C_O = \$146{,}550 - \$136{,}800$ $C_O = \$9{,}750$	

PAYBACK PERIOD
$T_{PAY} = (C_{CA} - C_{CB})/(C_O)$ (in years) T_{PAY} = (\$15,000 - \$10,000/\$9,750 T_{PAY} = 0.51 years

Example Application 5: Remanufacture of AEM/S System

BASELINE PRACTICE
Room-temperature cure VARTM—resin/reinforcement manufacture of mast

REPLACEMENT TECHNOLOGY ALTERNATIVE
Room-temperature cure CIRTM—resin/reinforcement manufacture of mast

LOCATION
Manufacturer

ADVANTAGES

- Reduction in production debris hazardous waste
- Faster processing

DISADVANTAGES

- Training in new technology

ASSUMPTION

- Assumes inclusion of phenolic liner

Note that costs presented in this example may vary greatly depending on labor costs, number of repairs, volume, material disposed, unit costs, and uncertainties in available data.

CAPITAL COSTS	
BEFORE alternative	**AFTER alternative**
Not applicable	$C_C = C_{C(E)}$ Where: C_C = Total capital costs $C_{C(E)}$ = Capital costs of equipment
CAPITAL COSTS include the cost of CIRTM equipment. **DATA RANGES FOR CAPITAL COSTS** (based on available information): CIRTM equipment ($150,000)	

ANNUAL OPERATING COSTS	
Supply Costs	
BEFORE alternative	**AFTER alternative**
$C_{S(tot)} = N_{ships}\, Q_{material}\, [(C_{RM} + C_L) + Q_{W(HW)}\, (C_{RM})]$ Where: $C_{S(tot)}$ = Total supply cost per year N_{ships} = Number of ships $Q_{material}$ = Quantity of material per ship C_{RM} = Raw materials cost C_L = Labor cost $Q_{W(HW)}$ = Waste disposal quantity of hazardous waste	$C_{S(tot)} = N_{ships}\, Q_{material}\, [(C_{RM} + C_L) + Q_{W(HW)}\, (C_{RM})]$ Where: $C_{S(tot)}$ = Total supply cost per year N_{ships} = Number of ships $Q_{material}$ = Quantity of material per ship C_{RM} = Raw materials cost C_L = Labor cost $Q_{W(HW)}$ = Waste disposal quantity of hazardous waste
SUPPLY COSTS are equal to the cost per repair times the number of repairs plus stockpiling costs. **DATA RANGES FOR SUPPLY COSTS** (based on available information): cost of raw materials ($8/lb); number of ships per year (6); quantity of material per ship (30 tons); labor cost per pound (VARTM) ($40), labor cost per pound (CIRTM) ($30); production debris hazardous waste same ratio as manufacturing (1.5 tons/30 tons per step); steps (BEFORE) (3), steps (AFTER) (1).	
Waste Disposal Costs	
BEFORE alternative	**AFTER alternative**
$C_{W(tot)} = N_{ships}\, Q_{material}\, (Q_{W(HW)})(C_{HW})$ Where: $C_{W(tot)}$ = Total waste disposal cost per year N_{ships} = Number of ships $Q_{material}$ = Quantity of material per ship $Q_{W(HW)}$ = Waste disposal quantity of hazardous waste C_{HW} = Cost of disposing expired shelf life and production debris material as hazardous waste.	$C_{W(tot)} = N_{ships}\, Q_{material}\, (Q_{W(HW)})(C_{HW})$ Where: $C_{W(tot)}$ = Total waste disposal cost per year N_{ships} = Number of ships $Q_{material}$ = Quantity of material per ship $Q_{W(HW)}$ = Waste disposal quantity of hazardous waste C_{HW} = Cost of disposing expired shelf life and production debris material as hazardous waste.
WASTE DISPOSAL COSTS. Waste disposal costs are equal to the cost of the disposal of materials treated as hazardous waste for production debris and materials with expired shelf life or out time. **DATA RANGES FOR WASTE DISPOSAL COSTS**: Data above; hazardous waste disposal cost is $30/lb.	

Total Operating Costs	
BEFORE alternative	**AFTER alternative**
$C_{OB(tot)} = C_{S(tot)} + C_{W(tot)}$ Where $C_{OB(tot)}$ =Total operating costs before alternative	$C_{OA(tot)} = C_{S(tot)} + C_{W(tot)}$ Where $C_{OA(tot)}$ =Total operating costs after alternative

INCREASE OR DECREASE IN ANNUAL OPERATING COSTS	
BEFORE alternative	**AFTER alternative**
$C_O = C_{OB(tot)} - C_{OA(tot)}$ Where: C_O = Increase or decrease in annual operating costs	

PAYBACK PERIOD
$T_{PAY} = (C_C)/(-C_O)$ (in years) Where: T_{PAY} = Time required for implementation of alternative to payback any capital costs

Cost Example

CAPITAL COSTS	
BEFORE alternative	**AFTER alternative**
Not applicable	$C_C = C_{C(E)}$ $C_C = \$150,000$

ANNUAL OPERATING COSTS	
Supply Costs	
BEFORE alternative	**AFTER alternative**
$C_{S(tot)} = N_{ships}\ Q_{material}\ [(C_{RM} + C_L) + Q_{W(HW)}\ (C_{RM})]$ $C_{S(tot)} = 6(30\text{ tons})\ \{\$8/\text{lb} + \$40/\text{lb} + (3)(1.5/30)\ (\$8/\text{lb})\}$ $C_{S(tot)} = 360,000\text{ lb.}\ \{\$8/\text{lb} + \$40/\text{lb} + 0.15(\$8/\text{lb})\}$ $C_{S(tot)} = \$17,712,000$	$C_{S(tot)} = N_{ships}\ Q_{material}\ [(C_{RM} + C_L) + Q_{W(HW)}\ (C_{RM})]$ $C_{S(tot)} = 6(30\text{ tons})\ \{\$8/\text{lb} + \$30/\text{lb} + (1)(1.5/30)\ (\$8/\text{lb})\}$ $C_{S(tot)} = 360,000\text{ lb.}\ \{\$8/\text{lb} + \$40/\text{lb} + 0.05(\$8/\text{lb})\}$ $C_{S(tot)} = \$13,824,000$
Waste Disposal Costs	
BEFORE alternative	**AFTER alternative**
$C_{W(tot)} = N_{ships}\ Q_{material}\ (Q_{W(HW)})(C_{HW})$ $C_{W(tot)} = 6(30\text{ tons})\ (3)(1.5/30)\ (\$30/\text{lb})$ $C_{W(tot)} = 360,000\text{ lb.}\ (0.15)(\$30/\text{lb})$ $C_{W(tot)} = \$1,620,000$	$C_{W(tot)} = N_{ships}\ Q_{material}\ (Q_{W(HW)})(C_{HW})$ $C_{W(tot)} = 6(30\text{ tons})\ (1)(1.5/30)\ (\$30/\text{lb})$ $C_{W(tot)} = 360,000\text{ lb.}\ (0.05)(\$30/\text{lb})$ $C_{W(tot)} = \$540,000$
Total Operating Costs	
BEFORE alternative	**AFTER alternative**
$C_{OB(tot)} = C_{S(tot)} + C_{W(tot)}$ $C_{OB(tot)} = \$17,712,000 + \$1,620,000$ $C_{OB(tot)} = \$19,332,000$	$C_{OA(tot)} = C_{S(tot)} + C_{W(tot)}$ $C_{OA(tot)} = \$13,824,000 + \$540,000$ $C_{OA(tot)} = \$14,364,000$

INCREASE OR DECREASE IN ANNUAL OPERATING COSTS	
BEFORE alternative	**AFTER alternative**
$C_O = C_{OB(tot)} - C_{OA(tot)}$ $C_O = \$19,332,000 - \$14,364,000$ $C_O = \$4,968,000$	

PAYBACK PERIOD
$T_{PAY} = (C_C)/(C_O)$ (in years) $T_{PAY} = \$150,000/\$4,968,000$ $T_{PAY} = 0.03$ years

Example Application 6: Repair of Integral Armor

BASELINE PRACTICE
Heat blanket —film adhesive and prepreg multi-step repair of integral armor

REPLACEMENT TECHNOLOGY ALTERNATIVE
Induction—film adhesive and prepreg single-step repair of integral armor

LOCATION
Theater depot

ADVANTAGES

- One-step process – significant increase in readiness
- Reduction in shelf life expiration and production debris hazardous waste
- Faster cure
- Relatively large cost reduction by eliminating shipping extra raw material to and hazardous waste from theater of operations

DISADVANTAGES

- Training in new technology

Note that costs presented in this example may vary greatly depending on labor costs, number of repairs, volume, material disposed, unit costs, and uncertainties in available data.

CAPITAL COSTS	
BEFORE alternative	**AFTER alternative**
Not applicable.	$C_C = C_{C(E)}$ Where: C_C = Total capital costs $C_{C(E)}$ = Capital costs of equipment
CAPITAL COSTS include the cost of an induction unit. **DATA RANGES FOR CAPITAL COSTS** (based on available information): induction unit ($15,000)	

ANNUAL OPERATING COSTS	
Supply Costs	
BEFORE alternative	**AFTER alternative**
$C_{S(tot)} = N_{repairs}[(C_{RM} + C_L) + Q_{W(HW)} (C_{RM})]$ Where: $C_{S(tot)}$ = Total supply cost per year $N_{repairs}$ = Number of repairs C_{RM} = Raw materials cost per repair C_L = Labor cost per repair $Q_{W(HW)}$ = Waste disposal quantity of hazardous waste	$C_{S(tot)} = N_{repairs}[(C_{RM} + C_L) + Q_{W(HW)} (C_{RM})]$ Where: $C_{S(tot)}$ = Total supply cost per year $N_{repairs}$ = Number of repairs C_{RM} = Raw materials cost per repair C_L = Labor cost per repair $Q_{W(HW)}$ = Waste disposal quantity of hazardous waste
SUPPLY COSTS are equal to the cost per repair times the number of repairs plus stockpiling costs. **DATA RANGES FOR SUPPLY COSTS** (based on available information): cost of raw materials (5 lb composite @ $30/lb; 1 lb adhesive @ $10/lb per repair) plus shipping ($50/lb); labor cost per repair (heat blanket) is $800, labor cost per repair (induction - reduced steps) is $400; percentages of shelf life expiration and production debris hazardous waste (BEFORE) (Figure 8), (AFTER) shelf life expiration hazardous waste reduced by 20%, production debris reduced by 75%. For cost estimate only, assume 200 repairs per year. Cost of other components is constant and neglected	
Waste Disposal Costs	
BEFORE alternative	**AFTER alternative**
$C_{W(tot)} = N_{repairs}(Q_{W(HW)} (C_{HW}))$ Where: $C_{W(tot)}$ = Total waste disposal cost per year $N_{repairs}$= Number of repairs $Q_{W(HW)}$ = Waste disposal quantity of hazardous waste C_{HW} = Cost of disposing expired shelf life and production debris material as hazardous waste.	$C_{W(tot)} = N_{repairs}(Q_{W(HW)} (C_{HW}))$ Where: $C_{W(tot)}$ = Total waste disposal cost per year $N_{repairs}$= Number of repairs $Q_{W(HW)}$ = Waste disposal quantity of hazardous waste C_{HW} = Cost of disposing expired shelf life and production debris material as hazardous waste.
WASTE DISPOSAL COSTS. Waste disposal costs are equal to the cost of the disposal of materials treated as hazardous waste for production debris and materials with expired shelf life or out time. **DATA RANGES FOR WASTE DISPOSAL COSTS**: Data above; hazardous waste disposal cost is $40/lb plus shipping ($50/lb).	

Total Operating Costs	
BEFORE alternative	**AFTER alternative**
$C_{OB(tot)} = C_{S(tot)} + C_{W(tot)}$ Where $C_{OB(tot)}$ =Total operating costs before alternative	$C_{OA(tot)} = C_{S(tot)} + C_{W(tot)}$ Where $C_{OA(tot)}$ =Total operating costs after alternative

INCREASE OR DECREASE IN ANNUAL OPERATING COSTS	
BEFORE alternative	**AFTER alternative**
$C_O = C_{OB(tot)} - C_{OA(tot)}$ Where: C_O = Increase or decrease in annual operating costs	

PAYBACK PERIOD
$T_{PAY} = (C_C)/(-C_O)$ (in years) Where: T_{PAY} = Time required for implementation of alternative to payback any capital costs

Cost Example

CAPITAL COSTS	
BEFORE alternative	**AFTER alternative**
Not applicable.	$C_C = C_{C(E)}$ $C_C = \$15{,}000$

ANNUAL OPERATING COSTS	
Supply Costs	
BEFORE alternative	**AFTER alternative**
$C_{S(tot)} = N_{repairs}[(C_{RM} + C_L) + Q_{W(HW)}(C_{RM})]$ $C_{S(tot)}$ = 200 repairs [(5 lb composite) ($30/lb+$50/lb) + (1 lb adhesive)($10/lb+$50/lb) + $800 + (30%+20%)/50%· (5 lb composite) ($30/lb+$50/lb) + (40%+10%)/50%·(1 lb adhesive)($10/lb+$50/lb)] $C_{S(tot)}$ = 200($400 + $60 + $800 + $400 + $60) $C_{S(tot)} = \$344{,}000$	$C_{S(tot)} = N_{repairs}[(C_{RM} + C_L) + Q_{W(HW)}(C_{RM})]$ $C_{S(tot)}$ = 200 repairs {(5 lb composite) ($30/lb+$50/lb) + (1 lb adhesive)($10/lb+$50/lb) + $400 + [(30%)(80%)+(20%)/4]/50%· (5 lb composite) ($30/lb+$50/lb) + [(40%)(80%)+(10%)/4]/50%·(1 lb adhesive)($10/lb+$50/lb)} $C_{S(tot)}$ = 200($400 + $60 + $400 + $232 + $41.40) $C_{S(tot)} = \$226{,}680$
Waste Disposal Costs	
BEFORE alternative	**AFTER alternative**
$C_{W(tot)} = N_{repairs}(Q_{W(HW)}(C_{HW})$ $C_{W(tot)}$ = 200 repairs {(30%+20%)/50%· (5 lb composite) ($40/lb+$50/lb) + (40%+10%)/50%·(1 lb adhesive)($40/lb+$50/lb)} $C_{W(tot)}$ = 200 ($540) $C_{W(tot)} = \$108{,}000$	$C_{W(tot)} = N_{repairs}(Q_{W(HW)}(C_{HW})$ $C_{W(tot)}$ = 200 repairs {[(30%)(80%)+(20%)/4]/50%· (5 lb composite) ($40/lb+$50/lb) + [(40%)(80%)+(10%)/4]/50%·(1 lb adhesive)($40/lb+$50/lb)] $C_{W(tot)}$ = 200 ($261 + $62.10) $C_{W(tot)} = \$64{,}620$
Total Operating Costs	
BEFORE alternative	**AFTER alternative**
$C_{OB(tot)} = C_{S(tot)} + C_{W(tot)}$ $C_{OB(tot)} = \$344{,}000 + \$108{,}000$ $C_{OB(tot)} = \$452{,}000$	$C_{OA(tot)} = C_{S(tot)} + C_{W(tot)}$ $C_{OA(tot)} = \$226{,}680 + \$64{,}620$ $C_{OA(tot)} = \$291{,}300$

INCREASE OR DECREASE IN ANNUAL OPERATING COSTS	
BEFORE alternative	**AFTER alternative**
$C_O = C_{OB(tot)} - C_{OA(tot)}$ $C_O = \$452{,}000 - \$291{,}300$ $C_O = \$\ 160{,}700$	

PAYBACK PERIOD

$$T_{PAY} = (C_C)/(C_O) \text{ (in years)}$$
$$T_{PAY} = \$15{,}000/\$160{,}700$$
$$T_{PAY} = 0.10 \text{ years}$$

Example Application 7: Remanufacturing of Sabots

BASELINE PRACTICE
Hot press — thermoset prepreg multi-step manufacture of sabots

REPLACEMENT TECHNOLOGY ALTERNATIVE
Induction — thermoplastic prepreg single-step manufacture of sabots

LOCATION
Manufacturer

ADVANTAGES

- One-step process
- Elimination of shelf life expiration and production debris hazardous waste
- Faster cure
- Reduction in VOC emissions

DISADVANTAGES

- Training in new technology

Note that costs presented in this example are for one particular round. Total emission and hazardous wastes figures are presented without providing specific numbers of parts based on information available for unlimited distribution.

CAPITAL COSTS	
BEFORE alternative	**AFTER alternative**
Not applicable.	$C_C = C_{C(E)}$ Where: C_C = Total capital costs $C_{C(E)}$ = Capital costs of equipment
CAPITAL COSTS include the cost of an induction unit. **DATA RANGES FOR CAPITAL COSTS** (based on available information): induction unit ($100,000)	

ANNUAL OPERATING COSTS	
Supply Costs	
BEFORE alternative	**AFTER alternative**
$C_{SE(tot)} = Q_{W(HW)} (C_{RM})$ Where: $C_{SE(tot)}$ = Total supply cost per year from environmental factors C_{RM} = Raw materials cost per part $Q_{W(HW)}$ = Waste disposal quantity of hazardous waste	$C_{SE(tot)} = Q_{W(HW)} (C_{RM})$ Where: $C_{SE(tot)}$ = Total supply cost per year from environmental factors C_{RM} = Raw materials cost per part $Q_{W(HW)}$ = Waste disposal quantity of hazardous waste
SUPPLY COSTS are equal to the cost per part times the number of parts plus stockpiling costs. **DATA RANGES FOR SUPPLY COSTS** (based on available information): cost of raw materials (composite @ $30/lb); shelf life expiration and production debris hazardous waste (BEFORE) 30,000 lbs, (AFTER) shelf life expiration hazardous waste and production debris is eliminated For cost estimate only, assume 200 parts per year. Cost of other components is constant and neglected	
Waste Disposal Costs	
BEFORE alternative	**AFTER alternative**
$C_{W(tot)} = Q_{W(HE)} (C_{HE}) + Q_{W(HW)} (C_{HW})$ Where: $C_{W(tot)}$ = Total waste disposal cost per year $C_{W(HE)}$ = Waste disposal cost of VOC $Q_{W(HE)}$= Waste disposal quantity of VOC $Q_{W(HW)}$ = Waste disposal quantity of hazardous waste C_{HW} = Cost of disposing expired shelf life and production debris material as hazardous waste	$C_{W(tot)} = Q_{W(HE)} (C_{HE}) + Q_{W(HW)} (C_{HW})$ Where: $C_{W(tot)}$ = Total waste disposal cost per year $C_{W(HE)}$ = Waste disposal cost of VOC $Q_{W(HE)}$= Waste disposal quantity of VOC $Q_{W(HW)}$ = Waste disposal quantity of hazardous waste C_{HW} = Cost of disposing expired shelf life and production debris material as hazardous waste
WASTE DISPOSAL COSTS. Waste disposal costs are equal to the cost of the disposal of materials treated as hazardous waste for production debris and materials with expired shelf life or out time plust cost of treating VOCs to meet relevant standards **DATA RANGES FOR WASTE DISPOSAL COSTS**: Data above; hazardous waste disposal cost is $20/lb., amount of hazardous emissions 1,200 lbs., reduction in hazardous emissions 60%, cost of treating VOCs $100/lb.	

Total Environmental Operating Costs	
BEFORE alternative	**AFTER alternative**
$C_{OB(tot)} = C_{SE(tot)} + C_{W(tot)}$ Where $C_{OB(tot)}$ =Total operating costs before alternative	$C_{OA(tot)} = CE_{S(tot)} + C_{W(tot)}$ Where $C_{OA(tot)}$ =Total operating costs after alternative

INCREASE OR DECREASE IN ANNUAL OPERATING COSTS	
BEFORE alternative	**AFTER alternative**
$C_O = C_{OB(tot)} - C_{OA(tot)}$ Where: C_O = Increase or decrease in annual operating costs	

PAYBACK PERIOD
$T_{PAY} = (C_C)/(-C_O)$ (in years) Where: T_{PAY} = Time required for implementation of alternative to payback any capital costs

Cost Example

CAPITAL COSTS	
BEFORE alternative	**AFTER alternative**
Not applicable.	$C_C = C_{C(E)}$ $C_C = \$100,000$

ANNUAL OPERATING COSTS	
Supply Costs	
BEFORE alternative	**AFTER alternative**
$C_{SE(tot)} = Q_{W(HW)} (C_{RM})$ $C_{SE(tot)} = 30,000$ lb($30/lb) $C_{S(tot)} = \$90,000$	$C_{SE(tot)} = Q_{W(HW)} (C_{RM})$ $C_{SE(tot)} = 10\%30,000$ lb($30/lb) $C_{S(tot)} = \$9,000$
Waste Disposal Costs	
BEFORE alternative	**AFTER alternative**
$C_{W(tot)} = Q_{W(HE)} (C_{HE}) + Q_{W(HW)} (C_{HW})$ $C_{W(tot)} = (1,200$ lb) ($100/lb) + (30,000 lb) ($20/lb) $C_{W(tot)} = \$120,000 + \$600,000$ $C_{W(tot)} = \$720,000$	$C_{W(tot)} = Q_{W(HE)} (C_{HE}) + Q_{W(HW)} (C_{HW})$ $C_{W(tot)} = 40\%(1,200$ lb) ($100/lb) + 0%(30,000 lb) ($20/lb) $C_{W(tot)} = \$48,000 + \$0$ $C_{W(tot)} = \$48,000$
Total Environmental Operating Costs	
BEFORE alternative	**AFTER alternative**
$C_{OB(tot)} = C_{SE(tot)} + C_{W(tot)}$ $C_{OB(tot)} = \$90,000 + \$720,000$ $C_{OB(tot)} = \$810,000$	$C_{OA(tot)} = C_{SE(tot)} + C_{W(tot)}$ $C_{OA(tot)} = \$9,000 + \$48,000$ $C_{OA(tot)} = \$57,000$

INCREASE OR DECREASE IN ANNUAL OPERATING COSTS	
BEFORE alternative	**AFTER alternative**
$C_O = C_{OB(tot)} - C_{OA(tot)}$ $C_O = \$810,000 - \$57,000$ $C_O = \$ 753,000$	

PAYBACK PERIOD
$T_{PAY} = (C_C)/(C_O)$ (in years) $T_{PAY} = \$100,000/\$753,000$ $T_{PAY} = 0.13$ years

Appendix C: Publications from Program

Appendix C: Publications from SERDP PP-1109 Funding

Peer Reviewed Journal Papers

- Tay, T.E., S. Yarlagadda, J.W. Gillespie Jr., B.K. Fink, and S.H. McKnight, "Accelerated Curing of Adhesives in Bonded Joints by Induction Heating," *Journal of Composite Materials*, 33 no.17, pp. 1643-1664, 1999.
- Sands, J.M., B.K. Fink, S.H. McKnight, C.H. Newton, J.W. Gillespie, Jr., and G.R. Palmese, "Environmental Issues for Polymer Matrix Composites and Structural Adhesives," *Clean Products and Processes*, 2 (2001), 228-235.
- Sands, J.M., R.E. Jensen, B.K. Fink, and S.H. McKnight, "Synthesis and Properties of Elastomer-Modified Epoxy-Methacrylate Sequential Interpenetrating Networks" *Journal of Applied Polymer Science*, 81, pp. 531-545, 2001.
- Kim, H.J., S. Yarlagadda, J.W. Gillespie Jr., N.B. Shevchenko, and B.K. Fink, "A Study on the Induction Heating of Carbon Fiber Reinforced Thermoplastic Composites," *Advanced Composite Materials*, Volume 11, No. 1, pp. 71-80, 2002.
- Yarlagadda, S., H.J. Kim, J.W. Gillespie Jr., N. Shevchenko, and B.K. Fink, "A Study on the Induction Process of Conductive Fiber Reinforced Composites," *Journal of Composites*, 36, 4, 401-421, 2002.
- Palmese, G.R. and U.P. Dalal, "Synthesis and Characterization of Partially Methacrylated Monomers," *Journal of Polymer Science: Polymer Chemistry*, (Accepted, May 2001.)
- Palmese, G.R. and U. Dalal, "Formation of In Situ Sequential Interpenetrating Polymer Networks by Radiation Induced Polymerization," *Journal of Polymer Science: Polymer Physics*, (Submitted May 2000.)
- Kim, H.J., S. Yarlagadda, J.W. Gillespie Jr., N.B. Shevchenko, B.K. Fink, "A Numerical Study On In-plane Heat Generation for Induction Process of AS4/PEI Prepreg Stacks," *Journal of Composite Materials*, (submitted May 2002).
- Mahdi, S., H.J. Kim, B.A. Gama, S. Yarlagadda, J.W. Gillespie Jr., "A Comparison of Oven-Cured and Induction-Cured Adhesively Bonded Composite Joints," *Journal of Composite Materials*, (submitted July 2002).
- Mascioni, M., J.M. Sands, G.R. Palmese, "Real Time In-Situ Spectroscopic Characterization of Radiation Induced Cationic Polymerization of Glycidyl Ethers," *Nucl. Instrum. And Meth. B.*, (accepted November 2002).

Chapters in Books

- Palmese, G.R. and D.L. Goodman, Handbook of Polymer Blends and Composites, Vol 1. Eds. A.K. Kulshreshtha, C. Vasile. Rapra Technology Limited: Shawbury,

UK. 2002. Chap.11 "Curing and Bonding of Composites Using Electron Beam Processing," pp. 459-499.

Technical Reports

- Fink, B.K., R.L. McCullough, and J.W. Gillespie, Jr., "Induction Heating of Carbon-Fiber Composites: Electrical Potential Distribution Model," *Army Research Laboratory Technical Report*, ARL-TR-2130, November 1999.
- Fink, B.K., S.H. McKnight, S. Yarlagadda, and J.W. Gillespie, Jr., "Non-Polluting Composites Repair and Remanufacturing for Military Applications: Induction-Based Repair of Integral Armor," *Army Research Laboratory Technical Report*, ARL-TR-2121, November 1999.
- Fink, B.K. and J.W. Gillespie, Jr., "Non-Polluting Composites Repair and Remanufacturing for Military Applications: Co-Injection Resin Transfer Molding," *Army Research Laboratory Technical Report*, ARL-TR-2125, November 1999.
- Fink, B.K., S.H. McKnight, C. Newton, J.W. Gillespie Jr., and G.R. Palmese, "Nonpolluting Composites Repair and Remanufacturing for Military Applications: An Environmental and Cost-Savings Analysis," *Army Research Laboratory Technical Report*, ARL-TR-2139. December 1999.
- Mcknight, S.H., B.K. Fink, S. Wells, S. Yarlagadda, J.W. Gillespie Jr., "Accelerated Adhesive Curing for Induction-Based Repair of Composites" *Army Research Laboratory Technical Report*, ARL-TR-2103, October 1999.
- Fink, B.K., "Co-Injection Resin Transfer Molding of Vinyl-Ester and Phenolic Resins," *Army Research Laboratory Technical Report*, ARL-TR-2150, December 1999.
- Fink, B.K., J.W. Gillespie, Jr., "Nonpolluting Composites Repair and Remanufacturing for Military Applications: Co-Injection Resin Transfer Molding," Army Research Laboratory Technical Report ARL-TR-2125, December 1999.
- Fink, B.K., Gillio, S. Advani, and J.W. Gillespie Jr., "The Role of Transverse Flow in Co-Injection Resin Transfer Molding," *Army Research Laboratory Technical Report*, ARL-TR-2135, December 1999.
- Fink, B.K., S. Yarlagadda, and J.W. Gillespie Jr., "Design of a Resistive Susceptor for Uniform Heating During Induction Bonding of Composites," *Army Research Laboratory Technical Report*, ARL-TR-2148, December 1999.
- Fink, B.K., "Induction Heating of Carbon-Fiber Composites: Experimental Verification of Models," *Army Research Laboratory Technical Report*, ARL-TR-2247. June 2000.
- Fink, B.K., S.H. McKnight, J.M. Sands, G.R. Palmese, U. Dalal, N. Sisofo, and A. Yen, "Non-Polluting Composites Repair and Remanufacturing for Military Applications: Formulation of Electron Beam Curable Resins With Enhanced

Toughening," *Army Research Laboratory Technical Report*, ARL-TR-2266, July 2000.

- Sands, J.M., S.H. McKnight, and B.K. Fink, "Interpenetrating Polymer Network (IPN) Adhesive for Electron Beam Cure," *Army Research Laboratory Technical Report*, ARL-TR-2321, September 2000.
- Sands, J.M., S.H. McKnight, and B.K. Fink, "Formulation of Toughened Paste Adhesives for Reduced-Pollutant Electron Beam Repair and Assembly of Composite Structures," *Army Research Laboratory Technical Report*, ARL-TR-2270, September 2000.
- Fink, B.K., R.L. McCullough, and J.W. Gillespie Jr., "Induction Heating of Carbon-Fiber Composites: Thermal Generation Model," *Army Research Laboratory Technical Report* ARL-TR-2261. September 2000.
- Fink, B.K., J.W. Gillespie Jr., S. Yarlagadda, Xiao, and Laverty, "Functional Nanostructures for Induction Heating: A Review of Literature and Recommendations for Research," *Army Research Laboratory Technical Report* ARL-TR-2365. November 2000.
- Wetzel, E.D., B.K. Fink, "Feasibility of Magnetic Particle Films for Curie Temperature-Controlled Processing of Composite Materials," *ARL Technical Report*, ARL-TR-2431, March 2001.
- Fink, B.K., N. Shevchenko, J.M. Sands, S. Yarlagadda, and J.W. Gillespie Jr., "Non-Polluting Composites Repair and Remanufacturing for Military Applications: Induction-Based Processing," *ARL Technical Report*, ARL-TR-2457, April 2001.
- Wetzel, E.D., and B.K. Fink, "Adherend Thermal Effects During Bonding with Inductively Heated Films," *Army Research Laboratory Technical Report*, ARL-TR-2461. April 2001.
- Sands, J.M., B.K. Fink, S.H. McKnight, C.H. Newton, J.W. Gillespie Jr., G.R. Palmese, "Environmental Issues for Polymer Matrix Composites and Structural Adhesives," *ARL Technical Report Reprint* ARL-RP-27, June 2001.
- Sands, J.M., R.E. Jensen, B.K. Fink, and S.H. McKnight, "Synthesis and Properties of Elastomer-Modified Epoxy-Methacrylate Sequential Interpenetrating Networks," *ARL Technical Report Reprint* ARL-RP-44 November 2001.
- Sands, J.M., S.H. McKnight, B.K. Fink, G.R. Palmese, and A. Yen, "Electron Beam Processing as a Means of Achieving High Performance Composite Structures," *ARL Technical Report*, ARL-TR-2613, December 2001.
- Kit, K.M., J.M. Sands, S.H. McKnight, "Design and Control of Network Architecture in Radiation Curable Toughened Semi-Interpenetrating Network Resin Systems," *ARL Technical Report*, ARL-TR-2693, March 2002.
- Dabestani, R., I.N. Ivanov, and J.M. Sands, "Cationic Polymerization (Cure Kinetics) of Model Epoxide Systems," *Army Research Laboratory Technical Report*, ARL-TR-2714, April 2002.

Conference/Symposium Proceedings

- Bernetich, K.R., G.P. McKnight, R.M. Crane, and B.K. Fink, and J.W. Gillespie Jr., "Co-injection Resin Transfer Molding of Vinyl Ester and Phenolic Composites," *Proceedings of the 43rd International SAMPE Symposium/Exhibition: Materials and Process Affordability—Keys to the Future*, Covina, CA, May 1998.
- Fink, B.K., S.H. McKnight, and J.W. Gillespie Jr., "Co-Injection Resin Transfer Molding for Optimization of Integral Armor," *Proceedings of the 21st Army Science Conference: Science and Technology for Army After Next*, Norfolk, VA, June 15–17, 1998, winner of Paul A. Siple Memorial Award.
- Fink, B.K., S.H. McKnight, J.W. Gillespie Jr., and S. Yarlagadda, "Nano-Particulate and Conductive Mesh Susceptors for Induction-Based Repair of Composites," *Proceedings of the 21st Army Science Conference: Science and Technology for Army After Next*, Norfolk, VA, June 15–17, 1998.
- Tay, T.E., S. Yarlagadda, B.K. Fink, S.H. McKnight, S. Wells, and J.W. Gillespie Jr., "Application of Induction Heating to Accelerate Curing of Adhesives in Bonded Joints," *Proceedings of the American Society for Composites Thirteenth Technical Conference*, Baltimore, MD, September 21-23, 1998.
- Firko, J., S. Yarlagadda, B.K. Fink, and J.W. Gillespie, Jr., "Optimization of Heat Generation in Induction Bonding Using Metal Mesh Susceptors," *Proceedings of the American Society for Composites Thirteenth Technical Conference*, Baltimore, MD, September 21-23, 1998.
- McKnight, G.P., K.R. Bernetich, J.W. Gillespie Jr., and R.M. Crane, "Flammability Performance of Multi-layer Phenolic/Vinyl Ester Composites Manufactured Using Co-Injection Resin Transfer Molding (CIRTM)," *Proceedings of the American Society for Composites Thirteenth Technical Conference*, Baltimore, MD, September 21-23, 1998.
- McKnight, G.P., K.R. Bernetich, J.W. Gillespie Jr., and R.M. Crane, "Manufacture and Testing of Multi-Layer Polyurethane and Epoxy Composites," *Proceedings of the American Society for Composites Thirteenth Technical Conference*, Baltimore, MD, September 21-23, 1998.
- McKnight, S.H., B.K. Fink, S. Wells, S. Yarlagadda, and J.W. Gillespie Jr., "Accelerated Curing of Epoxy Paste Adhesives for Repair of Composites Using Induction Heating," *Proceedings of ANTEC 98*, Society of Plastics Engineers, Brookfield, CT, April 1998.
- Sands, J.M., S.H. McKnight, and B.K. Fink, "Novel SIN and Seq-IPN Adhesives For Electron Beam Cure," *Proceedings of 45th International SAMPE Symposium and Exhibition – Society of Advanced Materials and Process Engineering Series*, Vol 45. Long Beach, CA. May 21-25, 2000, 2211-2222.
- Byrne, C.A., D.L. Goodman, G.R. Palmese, J.M. Sands, and S.H. McKnight, "Electron Beam Curable Adhesives for Out-of-Autoclave Bonding," *Proceedings of 45th International SAMPE Symposium and Exhibition – Society of Advanced*

Materials and Process Engineering Series, Vol 45. Long Beach, CA. May 21-25, 2000, 2187-2199.

- Yarlagadda, S., D. Heider, J.J. Tierney, J.W. Gillespie Jr., N. Shevchenko, and B.K. Fink, "Rapid Automated Induction Lamination (RAIL) for High-Volume Production of Carbon/Thermoplastic Laminates," *Midwest Advanced Materials and Processing Conference/SAMPE-DOE-SPE Advanced Composites Conference & Exposition,* Dearborn, MI, September 12-14, 2000.
- Yarlagadda, S., H.J. Kim, J.W. Gillespie Jr., N. Shevchencko, and B.K. Fink, "Heating Mechanisms in Induction Processing of Carbon Fiber Reinforced Thermoplastic Prepreg," *Proceedings of 45th International SAMPE Symposium and Exhibition – Society of Advanced Materials and Process Engineering Series*, Vol. 45. Long Beach, CA. May 21-25, 2000. 79-89.
- Gama, B.A., T.A. Bogetti, B.K. Fink, and J.W. Gillespie Jr., "Processing, Ballistic Testing and Repair of Composite Integral Armor," *Proceedings of the 32nd International SAMPE Technical Conference*, Boston, Massachusetts, November 5–9, 2000.
- Sands, J.M., "Toughened Interpenetrating Polymer Networks (IPNs) for Electron-Beam Cure of Composites and Adhesives," *Proceedings of the 22nd Army Science Conference*, (VIP presentation to L. Caldera) Baltimore, MD. 12 December 2000.
- Sands, J.M., R.M. Jensen, B.K. Fink, and S.H. McKnight, "Synthesis and Properties of Elastomer-modified Epoxy-methacrylate Sequential Interpenetrating Networks," *Proceedings of the 21st Adhesion Society,* Williamsburg, VA. February 2001.
- Dabestani, R., I. Ilanovic, and J.M. Sands, "Cure Kinetics of Cationic Polymerization of Phenyl Glycidyl Ether (PGE) and Tactix 123 using CD-1012 as Photoinitiator," *Proceedings of 46th International SAMPE Symposium and Exhibition – Society of Advanced Materials and Process Engineering Series*, Vol 46. Long Beach, CA. 6–10 May 2001.
- Gama, B. A., S. Yarlagadda, T.A. Bogetti, B.K. Fink, and J.W. Gillespie Jr., "Repair of Composite Integral Armor," *Proceedings of the 46th International SAMPE Symposium and Exhibition – Society of Advanced Materials and Process Engineering Series,* Long Beach Convention Center, Long Beach, CA, 6–10 May 2001. Vol. 46, pp. 1174–1184.
- Yarlagadda, S., D. Heider, J. Tierney, J.W. Gillespie Jr, N. Shevchenko, B.K. Fink, J. Gerhard, E. Lynam, K. Beck, and H. Laudern, "Rapid Automated Induction Lamination (RAIL) of Carbon/Thermoplastics: Factory Implementation and Prove-Out," *Proceedings of the 46th International SAMPE Symposium and Exhibition – Society of Advanced Materials and Process Engineering Series,* Vol. 46. Long Beach, CA, 6–9 May 2001. pp 886–897.
- R. E. Jensen, S. H. McKnight, G. R. Palmese "Viscoelastic Characterization of E-Beam Curable Epoxy-Methacrylate Interpenetrating Networks", The Society of the Plastic Industry, Inc. *Epoxy Resin Formulators Division Meeting*, Baltimore MD, September 2001. Invited presentation.

- Sands, J.M., E.D. Wetzel, C. Yungwirth, "Induction Processed Adhesives for Military Applications," *Proceedings of the 33rd SAMPE Technical Conference – Society of Advanced Materials and Process Engineering Series*, Vol. 33. Seattle, WA. 4–10 November 2001, 383-392.
- Yen, A., R. Moulton, J.M. Sands, "Effect of Electron Beam (EB) Curing on Composite Properties," *Proceedings of 47th International SAMPE Symposium and Exhibition – Society of Advanced Materials and Process Engineering Series*, Vol. 47. Long Beach, CA. 13-16 May 2002, 862-873.
- Mascioni, M., G.R. Palmese, J.M. Sands, "Real Time In-Situ Characterization of Epoxy Cure Kinetics Induced by Ultraviolet (UV) and Electron Beam (EB) Irradiation," *Proceedings of 47th International SAMPE Symposium and Exhibition – Society of Advanced Materials and Process Engineering Series*, Vol. 47. Long Beach, CA. 13-16 May 2002, 93-108.
- Sands, J.M., G.R. Palmese, A. Paesano, "Stage-able Resins for Electron Beam Cured Composites Manufacture," *Proceedings of 47th International SAMPE Symposium and Exhibition – Society of Advanced Materials and Process Engineering Series*, Vol. 47. Long Beach, CA. 13-16 May 2002, 889-901.
- Dabestani, R., I. N. Ivanov, J.M. Sands, "Application of Time-Resolved Pulse Radiolysis Technique in the Investigation of the Mechanism of Epoxy Resin Cationic Polymerization," *Proceedings of 47th International SAMPE Symposium and Exhibition – Society of Advanced Materials and Process Engineering Series*, Vol. 47. Long Beach, CA. 13-16 May 2002, 56-64.
- Kim, H.J., S. Yarlagadda, J.W. Gillespie Jr., N. Shevchenko, B.K. Fink, "A Numerical Study on the In-plane Heating Patterns of Carbon-Fiber Reinforced Composites," *9th US-Japan Conference on Composite Materials*, Mishma, Japan, July 2002, pp. 117-124.
- Kim, H.J., S. Yarlagadda, B.K. Fink, and J.W. Gillespie Jr., "Through-thickness Heating Behavior of Carbon Fiber Reinforced Prepeg Stacks in Induction Heating Process," *34th International SAMPE Technical Conference*, Baltimore, MD November 4-7, 2002 (submitted July 2002).

Published Technical Abstracts

- McKnight, S.H., J.M. Sands, and B.K. Fink, "Structural Adhesives Cured by Electron Beam Radiation," *Annual Meeting of the American Institute of Chemical Engineers,* Miami, FL, 20–25 November 1998.
- Palmese, G.R. and U.P. Dalal, "Synthesis and Characterization of Partially Methacrylated Polyfunctional Epoxy Monomers for E-Beam-Curable Resins," *Annual Meeting of the American Institute of Chemical Engineers,* Miami, FL, 20–25 November 1998.

- Sands, J.M., B.K. Fink, and S.H. McKnight, "Preparation and Characterization of Novel E-beam Adhesives," *American Physical Society Centennial Meeting*, Atlanta, GA, 22 March 1999.
- Sands, J.M., S.H. McKnight, and B.K. Fink, "Electron Beam Curable Adhesives for Structural Bonding and Repair," *Annual Meeting of American Institute of Chemical Engineers*, Dallas, TX, 5 November 1999.
- Sands, J.M. and B.K. Fink, "Green Composites for Military Applications," *National Defense Industrial Association Environmental Symposium*, Morristown, NJ. 18 November 1999.
- Sands, J.M., S.H. McKnight, and B.K. Fink, "Electron Beam Cure for Manufacture and Repair of Army Composite Structures," *Defense Manufacturing Conference 1999*, Miami Beach, FL. 1 December 1999.
- Fink, B.K., J.M. Sands, S.H. McKnight, J.W. Gillespie Jr., and G.R. Palmese, "Non-polluting Composites Repair and Remanufacture for Military Applications," *SERDP Partners in Environmental Technology*, Arlington, VA. 30 November–2 December 1999.
- Sands, J.M., S.H. McKnight, and B.K. Fink, "Electron Beam Processed SIN and Seq-IPN Adhesives," *Annual Meeting of the American Physical Society*, Minneapolis, MN. 22 March 2000.
- Kim H. J., S. Yarlagadda, J. W. Gillespie, Jr., N. B. Shevchenko, B. K. Fink, "Induction-Based Processing of Thermoplastic Carbon Fiber Laminates – A Numerical Study of Heat Generation of AS4/PEI Prepreg Stacks," *International Conference for Manufacturing of Advanced Composites,* Belfast, Northern Ireland, 27–28 September 2001.
- Mascioni, M. and G.R. Palmese, "Cationic Polymerization of Epoxy Resins by UV and E-Beam Irradiation," *Annual Meeting of the American Institute of Chemical Engineers*, Reno, NV. 8 November 2001.
- Mascioni, M. and G.R. Palmese, "In-situ Investigation of Cure Kinetics of Photo-Initiated Cationic Polymerization of Epoxy Resins" *Annual Meeting of the American Institute of Chemical Engineers*, Reno, NV. 8 November 2001.
- Sands, J.M., "Green Composites for Military Applications," *Defense Manufacturing Conference 2001*, Las Vegas, NV. 26 November 2001.
- Sands, J.M., G.R. Palmese, and S.H. McKnight "Non-Polluting Composites Repair and Remanufacturing for Military Applications," *Partners in Environmental Technology Technical Symposium and Workshop*, Washington, DC. 27–29 November 2001.
- Sands, J.M., "Composite Repair for Military Applications," *Partners in Environmental Technology Technical Symposium and Workshop*, Washington, DC. 27–29 November 2001.

- Sands, J.M., "Low-Cost Environmental Solutions For Military Composites," *Army Industrial Ecology Information Exchange*, Lake Harmony, PA, 26 June 2002.

Other Presentations

- Fink, B.K. "Environmental Issues in Composites Manufacturing." *Eighth Annual Environmental Symposium, NDPA*, Morristown, NJ, November 18–20 1997. Invited presentation.
- Fink, B.K., "Advanced Materials for Tactical Deployment," *PM Tactical Missiles Briefing*, Huntsville, AL, 16 March 1998.
- Fink, B.K., "Thermoplastic Composites Process Modeling," *ARDEC Visit*, Aberdeen Proving Ground, MD, 15 April 1998.
- Sands, J.M., "Toughened Resins for Electron Beam Repair of Composites," presented at the U.S. Army Research Laboratory, Aberdeen Proving Ground, MD, 2 February 1999.
- McKnight, S.H., J.M. Sands, and B.K. Fink, "Opportunities For Electron-Beam Composites Processing Applied To Future Army Applications," *Third Annual Electron Beam Workshop*, Oak Ridge National Laboratory, Oak Ridge, TN, 21 April 1999. Invited presentation.
- Sands, J.M. and B.K. Fink, "Non-Polluting Composites Remanufacturing and Repair for Military Applications," presented at the *Army Pollution Prevention Technology Integration Review*, Mt. Pocono, PA, 14 July 1999. Invited presentation.
- McKnight, S.H., J.M. Sands, and B.K. Fink, "Non-autoclave processing of Composites," presented at *NASA Intergovernmental Workshop on Nonautoclave Processing*, Langley, VA, 9 August 1999. Invited presentation.
- Sands, J.M. and B.K. Fink, "Non-Polluting Composite Remanufacturing and Repair for Military Applications," Meeting of the *Strategic Advisory Board of the Strategic Environmental Research and Development Program*, Rosslyn, VA, 14 March 2000.
- Sands, J.M. and B.K. Fink, "Materials and Methods for Repair of Polymer Matrix Composite Structures," *North Dakota State University, Department of Mechanical Engineering*, Fargo, ND, 20 March 2000. Invited presentation.
- Sands, J.M., "Induction and Electron Beam Processed Adhesives for Military Composite Applications," *Minnesota Mining and Manufacturing: Adhesives Technology Center*, St. Paul, MN, 23 March 2000. Invited presentation.
- Sands, J.M.and B.K. Fink, "Non-Polluting Composite Remanufacturing and Repair for Military Applications," *Internal Program Review of the Strategic Environmental Research and Development Program*, Arlington, VA, 6 April 2000.
- Sands, J.M., S.H. McKnight, and G.R. Palmese, "Free Radical Induced Polymerizations by Electron Beam for Composites Applications," *Electron Beam Cure Kinetics Workshop*, Newark, DE, 17 April 2000. Invited presentation.

- Sands, J.M., S.H. McKnight, and B.K. Fink, "Processing and Property Relationships in E-Beam Adhesives and Prepregs," *4th Annual Electron Beam Curing of Composites Workshop*, Oak Ridge, TN, 14 June 2000. Invited presentation.
- Sands, J.M., S.H. McKnight, and B.K. Fink, "Development of Green Composites for Military Applications," *Army Environmental Quality Information Exchange*, Williamsburg, VA, 20 July 2000.
- Sands, J.M., E.D. Wetzel, and B.K. Fink, "Application of Electron Beam and Induction Repair Techniques to United States Navy Composite Structures," *NAVAIR Composites Workgroup*, Patuxent River, MD. 8 August 2000. Invited presentation.
- Palmese, G.R., N. Ghosh, J.M. Sands, S.H. McKnight, "A Fundamental Investigation of Epoxy Cure by E-beam Irradiation," *Composites Materials Research (CMR) Collaborative Program*, Newark, DE. 10 October 2000.
- Yen, A., J.M. Sands, "Processing of E-Beam Cured Composites," *Defense Manufacturing Conference 2000 (DMC 2000)*, Tampa, FL. 27 November 2000.
- Sands, J.M., T.A. Bogetti, B.K. Fink, S. Yarlagadda, B. Gama, and J.W. Gillespie, Jr., "Induction-Assisted Repair of Multi-Functional Composite Armor," *5th DoD Composites Repair Workshop*, Coeur d'Alene, ID. (Invited) 13–16 November 2000.
- Wetzel, E.D., and J.M. Sands, "Self-regulating Induction-Cured Elevated Temperature Adhesives," *5th DoD Composites Repair Workshop*, Coeur d'Alene, ID. 13–16 November 2000.
- Sands, J.M., T.A. Bogetti, B.K. Fink, B. Gama, and J.W. Gillespie, Jr., "Repair of Ballistic-Damaged Composite Integral Armor," *5th DoD Composites Repair Workshop*, Coeur d'Alene, ID. (Invited) 13–16 November 2000.
- Sands, J.M., R. Dabestani, I. Ivanon, "Electron Beam Cure Mechanisms for Cationic Initiated Epoxides," *Cooperative Research and Development Agreement (CRADA) Kinetics Integrated Process Team (IPT) Meeting*, Long Beach, CA. 7 May 2001.
- Sands, J.M., "Electron Beam Cure of Composites," *ARL Technical Advisory Board (TAB), Panel on Armor and Armaments*, Aberdeen Proving Ground, MD. 16 July 2001. (Official Commendation presented)
- Sands, J.M., "Green Composites Repair for Military Applications," *U.S. Army Environment and Ecology Information Exchange*, Mt. Pocono, PA. 17 July 2001.
- Yen, A., J.M. Sands, "E-Beam Curing of VARTM Processed Composites," *2001 Aerospace Congress and Exhibition by Aerospace North America and Society of Aerospace Engineering*, Seattle, WA. 10 September 2001.
- Sands, J. M., "Non-Polluting Composites Remanufacturing and Repair for Military Applications: Final Program Review," *SERDP Program Monitors and Technology Experts Team*, Newark, DE, 25 March 2002.
- Sands, J. M., G. R. Palmese, "Electron Beam Processing for Composite and Adhesive Applications," *SERDP Program Monitors and Technology Experts Team*, Newark, DE, 25 March 2002.

- Dabestani, R., "Application of Time-Resolved Pulse Radiolysis Technique in the Investigation of the Mechanism of Epoxy Resins Cationic Polymerization," *SERDP Program Monitors and Technology Experts Team*, Newark, DE, 25 March 2002.
- Palmese, G.R., M. Mascioni, J.M. Sands, "Cationic Polymerization of Epoxy Resins by UV and EB Irradiation"*SERDP Program Monitors and Technology Experts Team*, Newark, DE, 25 March 2002.
- Yen, A. "Effect of Electron Beam Dose and Processing Changes on Composite Properties," *SERDP Program Monitors and Technology Experts Team*, Newark, DE, 25 March 2002.
- Yarlagadda, S., "Induction-Based Repair and Remanufacturing of Composites," *SERDP Program Monitors and Technology Experts Team*, Newark, DE, 25 March 2002.
- Shevchenko, N., "Remanufacture of the M829E3 Sabot," *SERDP Program Monitors and Technology Experts Team*, Newark, DE, 25 March 2002.
- Wetzel, E.D., "Curie Temperature Controlled Induction Curing of Adhesives Using Magnetic Particle Susceptors," *SERDP Program Monitors and Technology Experts Team*, Newark, DE, 25 March 2002.
- Gama, B, "Processing, Ballistic Testing and Repair of Composite Integral Armor," *SERDP Program Monitors and Technology Experts Team*, Newark, DE, 25 March 2002.
- Mahdi, S., "Mechanics and Repair of Multi-Functional Hybrid Composite Structures," *SERDP Program Monitors and Technology Experts Team*, Newark, DE, 25 March 2002.
- Wetzel, E.D., J.M. Sands, "Curie-Temperature Controlled Induction Curing of Adhesives Using Magnetic Particle Susceptors," *Cytec Engineered Materials Cooperative Invitational Meeting*, Havre de Grace, MD, 16 April 2002.
- Sands, J. M., "Induction Processed Adhesives: Materials Considerations and Experimental Test Case," *Cytec Engineered Materials Cooperative Invitational Meeting*, Havre de Grace, MD, 16 April 2002.
- Sands, J.M., E.D. Wetzel, "Curie-Temperature Controlled Induction Curing of Adhesives Using Magnetic Particle Susceptors." *ARL/Cytec Engineered Materials Cooperative Agreement Discussions Kickoff*, Aberdeen Proving Ground, MD, 6 May 2002.
- Sands, J. M., "Induction Processed Adhesives: Materials Considerations" *ARL/Cytec Engineered Materials Cooperative Agreement Discussions Kickoff*, Aberdeen Proving Ground, MD, 6 May 2002.
- Sands, J. M., "Environmental Solutions for Military Composites," *Northrop Grumman Corporation, Joint Strike Fighter Environmental Strategies Managers Meeting*, El Segundo, CA. 10 May 2002.

- Sands, J. M., "Kinetics of Cure in Cationic Initiated Epoxide Matricies," *KIPT leadership update for ORNL led Interfacial Properties CRADA*, Long Beach, CA. 13 May 2002.
- Sands, J. M., "Electron Beam Curing and the Army Vision," *Society for the Advancement of Materials and Process Engineering – Panel Discussion EB 2002*, Long Beach, CA. 16 May 2002.
- Sands, J.M., E.D. Wetzel, "Novel (Curie Temperature–Controlled Induction) Curing of Adhesives For Composite Repair Applications," *DoD Advanced Composite Users Meeting*, Ogden, UT, 10 July 2002.

Appendix D: References

Appendix D: References

1 American Society for Testing and Materials ASTM D790-96a, "Standard Test Method for Flexural Properties of Unreinforced and Reinforced Plastics and Electrical Insulating Materials," ASTM Electronic Media (1998).

2 American Society for Testing and Materials ASTM 2344-84, "Standard Test Method for Apparent Interlaminar Shear Strength of Parallel Fiber Composites by Short-Beam Method," ASTM Electronic Media (1998).

3 Huang, Y.; Hunston, D.L.; Kinloch, A.J.; Riew, C.K. In Toughened Plastics I; Riew, C.K; Kinloch, A.J., Eds.; American Chemical Society: Washington DC, 1993.

4 Zhou, J. and J.P. Lucas, "Hygrothermal Effects of Epoxy Resin: Part II: Variations of Glass Transition Temperature," Polymer 40 (1999) 5513.

5 American Society for Testing and Materials ASTM D 5045-93, "Standard Test Methods for Plane-Strain Fracture Toughness and Strain Energy Release Rate of Plastic Materials," ASTM Electronic Media.

6 American Society for Testing and Materials ASTM D 3039/ D 3039M–95a, "Standard Test Method for Tensile Properties of Polymer Matrix Composite Materials," ASTM Electronic Media.

7 American Society for Testing and Materials ASTM D 3410/ D 3410M-95, "Standard Test Method for Compressive Properties of Polymer Matrix Composite Materials with Unsupported Gage Sections by Shear Loading," ASTM Electronic Media.

8 American Society for Testing and Materials ASTM D 5379/ D 5379M-98, "Standard Test Method for Shear Properties of Composite Materials by the V-Notched Beam Method," ASTM Electronic Media.

9 American Society for Testing and Materials ASTM D 1781-93, "Standard Test Method for Climbing Drum Peel for Adhesives," ASTM Electronic Media.

10 American Society for Testing and Materials (ASTM) D 1002-94. "Standard Test Method for Apparent Shear Strength of Simgle-Lap-Joint Adhesively Bonded Metal Specimens by Tension Loading (Metal-to-Metal)," ASTM Electronic Media.

11 American Society for Testing and Materials ASTM D 3762-79, "Standard Test Method for Adhesive-Bonded Surface Durability of Aluminum (Wedge Test)," ASTM Electronic Media.

12 Martuscell, E., P. Musto, and G. Ragosta, *Advanced Routes for Polymer Toughening*, Amsterdam, Elsevier, p. 13, 1996.

13 Janke, C. J, D. Howell, R. E. Norris, J. Gray, S. Havens, J. Nelson, V. J. Lopata, and M. Schultz, "Electron Beam Curing of Polymer Matrix Composites," Oak Ridge National Laboratory Report M6115, Final Report for CRADA Number Y-1293-0233, May 1997.

14 Janke, C. J., SAMPE International Technical Conference, Vol. 28, No. 277, 1996.

15 *Toughened Plastics 1*. Ed. A. J. Kinloch and C. K. Riew, ACS Publishing, Washington D.C., ACS Advances in Chemistry Series No. 233, 1993.

16 Pearson, R. A., "Toughening Epoxies Using Rigid Thermoplastic Particles," in *Toughened Plastics I*, ed. C. K. Riew and A. J. Kinloch, ACS Advances in Chemistry Series, No. 233, ACS Publishing, Washington D.C., pp.405-425, 1993.

17 Lu, F, W. J. Cantwell, and H. H. Kausch, "The Role of Cavitation and Debonding in the Toughening of Core-Shell Rubber Modified Epoxy Systems," *Journal of Materials Science*, Vol. 32 No. 11, p. 3055, 1997.

18 Kinloch, A. J., *Adhesion and Adhesives: Science and Technology*, Chapman and Hall, London, Ch.8 and 15, 1987.

19 Bradley, W. L., et. al., "The Synergistic Effect of Crosslink Density and Rubber Additions on the Fracture Toughness of Polymers," in *Toughened Plastics I*, ed. C. K. Riew and A .J. Kinloch, ACS Advances in Chemistry Series, No. 233 p. 317, 1993.
20 Kinloch, A. J., "Relationships Between the Microstructure and Fracture Behavior of Rubber-Toughened Thermosetting Polymers," in *Rubber Toughened Plastics*, Ed. C.K. Riew, ACS Publishing, Washington D.C., ACS Advances in Chemistry Series, No. 222, p. 67, 1989.
21 Wegman, R.F. "Surface preparation techniques for adhesive bonding," Park Ridge, N.J., U.S.A. Noyes Publications 1989.
22 Sands, J. M., S.H. McKnight, R. Jensen, and K. Kit, "Experimental Preparation of Novel Sequential Interpenetrating Polymer Network Resins for Cure by Electron Beam Dose," *Journal of Applied Polymer Science*, accepted, May 2000.
23 Horalek, J., S. Svestka, E. Krejcar, and J. Novak, "Reactions of Primary Aliphatic and Cycloaliphatic Amines with 1-butyl acrylate," *Coll. Czech. Chem. Comm.*, 53 pp. 3149-3153, 1988.
24 D. Benziers and B. Capdepuy, *SAMPE International symposium*, 35 1220 (1990).
25 C.B. Saunders, V.J. Lopata, W. Kremers, T.E. McDougall, M. Tateishi and A. Singh, *SAMPE International Symposium*, 38, 1682 (1993).
26 C.B. Saunders, V.J. Lopata, W. Kremers, M. Chung and J.W. Barnard, *SAMPE International Symposium*, 40, 112 (1995).
27 C.J. Janke, S.J. Havens, G.F. Dorsay and V.J. Lopata, *SAMPE International Technical conference*, 41, 196 (1996).
28 C.J. Janke, S.J. Havens, G.F. Dorsay and V.J. Lopata, *SAMPE International Technical Conference*, 28, 901 (1996).
29 C.J. Janke, S.J. Havens, V.J. Lopata and M. Chung, *SAMPE International Technical Conference*, 28, 911 (1996).
30 D.L. Goodman, D.L. Birx, G.R. Palmese and A. Chen*, SAMPE International Symposium,* 41, 207 (1996).
31 C.J. Janke, R.E. Norris, K. Yarborough, S.J. Havens, and V.J. Lopata, *SAMPE International Symposium,* 42*,* 477 (1997).
32 R.Dabestani, I.Ivanov, *SAMPE International Symposium* 46, 2075 (2001).
33 D.F. Rohr and M.T. Klein - "Modeling Diffusion and Reaction in Epoxy-Amine Polymerization Kinetics", *Center for Composite Materials, University of Delaware Report* 87-44, (1987).
34 Bueche,F. "Physical Properties of Polymers",1962.
35 A. DiBenedetto, *Journal of Polymer Science B*, 25, 1949 (1987).
36 G.Palmese,N.N.Ghosh,S.McKnight, *SAMPE International Technical Conference,* 45, 1874 (2000).
37 M.V. Hosur, U.K. Vaidya, S. Jones, R. Eduljee, J.W. Gillespie Jr., S. Jeelani, "Activity Based Cost Modeling of Liquid Molding Process Technique for Thick Section Composites," American Society of Composites, 1999.
38 "Guidance on Clean Air Act Title III Regulations: National Emissions Standards for Hazardous Air Pollutants (NESHAPS)," Code of Federal Register, 40 CFR 63:463, August 2001.
39 Wilenski, M., "Non-Autoclave Materials for Large Composite Structures," Progress Report to Air Force for contract No. F33615-99-C-5019, 16 November 2000.
40 Carstensen, T., C. Rogg, M. Wilenski, R. Aiken, "Electron Beam Curing of Secondary Structural Aircraft Components," SAMPE 2002, Long Beach, CA. 12-15 May 2002. Closed paper.

41 Wilenski, M., C. Baker, "Process Development of E-Beam Curing for Large Structures," SAMPE 2002. Long Beach, CA, 12-15 May 2002.
42 Blue M Company, Williamsport, PA. Private communication with Bernard Hart, April 2002.
43 CF Motor Freight, Baltimore, Maryland. Private communication with Bernard Hart, May 2002.
44 IBA, Swedensborough, NJ. Private communication between Song Cheng and David Kerluke (IBA) and James Sands (ARL) at SAMPE 2002, Long Beach, CA. 14 May 2002.
45 Schweitzer, J., "The Cost of Control", *Composites Fabrication*, June 2001, pp 10-43.
46 "Polyester Resin Operations," SCAQMD Rule 1162, Amended 5/13/1994.
47 R. Plonsey and R.E. Collin, Principles and Applications of Electromagnetic Fields, McGraw-Hill: New York. 1961
48 B.K. Fink, R.L. McCullough and J.W. Gillespie Jr., "Experimental Verification of Models for Induction Heating of Continuous-Carbon-Fiber Composites," Polymer Composites, Vol. 17, No. 2, pp. 198-209 , 1996.
49 B. K. Fink, J. W. Gillespie Jr., and R. L. McCullough, "Induction Heating of Cross-Ply Carbon Fiber Thermoplastic Composites," Proceedings of ANTEC 92, Society of Plastics Engineers, Brookfield, CT, 1992.
50 W. Lin, A. K. Miller, and O. Buneman, "Predictive Capabilities of an Induction Heating Model for Complex-Shape Graphite Fiber/Polymer Matrix Composites," 24th International SAMPE Technical Conference, October 20-22, 1992.
51 A. K. Miller, C. Chang, A. Payne, M. Gur, E. Menzel, and A. Peled, "The Nature ofInduction Heating in Graphite-Fiber Polymer-Matrix Composite Materials," SAMPE Journal, Vol 26(4). August 1990. pg. 37.
52 B.K. Fink, S. Yarlagadda, and J.W. Gillespie, Jr., "Design of a Resistive Susceptor for Uniform Heating During Induction Bonding of Composites," ARL Technical Report ARL-TR-2148. January 2000.
53 Consenza, F. "Mechanical Fasteners for Composites." *Materials Engineering*, vol.104, no. 8, pp.33-37, 1987.
54 Marinelli, J.M., and C.L.T. Lambing. "Study of Surface Treatments for Adhesive Bonding of Composite Materials." Advanced Materials: Performance Through Technology Insertion International SAMPE Symposium and Exhibition (Proceedings), Covina, CA, vol. 38, pp. 1196-1210, 1993.
55 B. K. Fink, S.H. McKnight, J. W. Gillespie Jr., and S. Yarlagadda. "Nano-Particulate and Conductive Mesh Susceptors for Induction-Based Repair of Composite Materials." Proceedings of the 21st Army Science Conference. Norfolk, VA. June 15-17, 1998.
56 Wetzel, E.D., and B.K. Fink. "Feasibility of Magnetic Particle Films for Curie Temperature-Controlled Processing of Composite Materials." ARL-TR-2431, U.S. Army Research Laboratory, Aberdeen Proving Grounds, MD.
57 E. D. Wetzel and B. K. Fink. "Feasibility of Magnetic Particle films for Curie Temperature Controlled Processing of Composite Materials." Army Research Laboratory Technical Report ARL-TR-2431. March 2001.
58 E. D. Wetzel, B. K. Fink, Y. F. Li, and J. Q. Xiao. "Advanced Magnetic Materials For Curie Temperature Controlled Bonding." Proceedings of the 22nd Army Science Conference. Baltimore, MD. Dec. 11-13, 2000.
59 S. H. McKnight, B. K. Fink, S. Wells, S. Yarlagadda, and J. W. Gillespie, Jr. "Accelerated Curing of Epoxy Paste Adhesives for Repair of Composites Using Induction Heating." Proceedings of SPE ANTEC 1998. Atlanta, GA. April 26-30, 1998.

60 G. Eagle. "Induction Heat Curing of Adhesives." Proceedings of the SPE ANTEC 1987. Detroit, MI. 1987.
61 E. J. Stefanides. "Epoxy Cured By Induction Heating Gives Strong Sheet Metal Joint." Design News (Boston). V.43 n12. June 22, 1987. pp.102-103.
62 J. M. Sands, E. D. Wetzel, and C. J. Yungwirth. "Induction Processed Adhesives for Military Applications." 33rd International SAMPE Technical Conference. Seattle, WA. November 5-8, 2001. pp 383-392.
63 W.J. Sarjeant, "A Cursory Examination of the Nature, Effects and Control of Electromagnetic Fields," ARL Technical Report, ARL-TR-2232, May 2000.
64 B.K. Fink, R.L. McCullough, and J.W. Gillespie, Jr., "Induction Heating of Carbon-Fiber Composites: Electrical Potential Distribution Model," ARL Technical Report, ARL-TR-2130, November 1999
65 B.K. Fink, R.L. McCullough, and J.W. Gillespie, Jr., "On the Influence of Moisture on Dielectric Properties of Polyetheretherketone (PEEK) Carbon-Fiber Composites," ARL Technical Report, ARL-TR-2236, June 2000
66 American Society for Testing and Materials ASTM 2344-84, "StandardTest Method for Apparent Interlaminar Shear Strength of Parallel Fiber Composites by Short-Beam Method," ASTM Electronic Media
67 American Society for Testing and Materials ASTM 695-96, "Standard Test Method for Compressive Properties of Rigid Plastics," ASTM Electronic Media
68 American Society for Testing and Materials, ASTM D1002-01 Standard Test Method for Apparent Shear Strength of Single-Lap-Joint Adhesively Bonded Metal Specimens by Tension Loading (Metal-to-Metal)," ASTM Electronic Media (2001).
69 S. M. Weider, H. J. Lause and R. Fountain. "Structural Repair Systems for Thermoplastic Composites." *Composite Repairs: SAMPE Monograph No. 1*, edited by Brown, SAMPE, Covina, CA, 1985.
70 A. Benatar and T. G. Gutowski. "Methods for Fusion Bonding Thermoplastic Composites." *SAMPE Quarterly*, October 1986.
71 J. Border and R. Salas. "Induction Heated Joining of Thermoplastic Composites Without Metal Susceptors." *34th SAMPE Symposium*, 1989.
72 T. Nagumo, H. Makamura, Y. Yoshida, and K. Hiraoka. "Evaluation of PEEK Matrix Composites," *Proceedings of the 32nd International SAMPE Symposium*, SAMPE, 1987.
73 J. D. Buckley, R. L. Fox, and J. R. Tyeryar. "Seam Bonding of Graphite Reinforced Composite Panels." *NASA Advanced Composites Conference*, 1986.
74 C. F. Lewis, "Materials Keep a Low Profile." *Materials Engineering*, Vol. 105, 1988.
75 J. D. Buckley and R. L. Fox. "Rapid Electromagnetic Induction Bonding of Composites, Plastics and Metals." *Materials Research Society Symposium*, Vol. 124, 1988.
76 G. W. Lawless and T. J. Reinhart. "Study of the Induction Heating of Organic Composites." *Proceedings of the 37th International SAMPE Symposium,* Toronto, Canada, October 1992.
77 A. R. Wedgewood and P. E. Hardy. "Induction Welding of Thermoset Composite Adherends using Thermoplastic Interlayers and Susceptors." *Proceedings of the 41st International SAMPE Symposium*, Vol. 28, Seattle, WA, November 1996.
78 J. M. Sands, Steven H. McKnight, and Bruce. K. Fink. "Formulation of Toughened Paste Adhesives for Reduced-Pollutant Electron Beam Repair and Assembly of Composite Structures." ARL-TR-2270, U.S. Army Research Laboratory, Aberdeen Proving Grounds, MD.
79 A.J. Kinloch "Relationships Between the Microstructure and Fracture Behavior of Rubber-Toughened Thermosetting Polymers," in *Rubber Toughened Plastics*, Ed. C.K. Riew, ACS: Washington DC, No. 222 (1989).

80 "Design and Control of Network Architecture in Radiation Curable Toughened Semi-Interpenetrating Network Resin Systems," K. Kit, J.M. Sands, S.H. McKnight, *ARL Technical Report*, ARL-TR-2693. March 2002.
81 López Vega, J. "Induction-Assisted Repair of Integral Armor," Internal Report, University of Delaware Center for Composite Materials, August 2000.
82 Motuku, M., U.K. Vaidya, and G.M. Janowski, *Smart Materials and Structures*, 8(5), 623, 1999.
83 A. J. Russel, C. P. Bowers and A. J. Moss, *International Conference on Composite Structures*, Elsevier Science Publ Ltd., p. 145, 1991.
84 J. Paul and R. Jones, *Engineering Fracture Mechanics*, 41(1) 127, 1992.
85 W. I. Cantwell, P. Davies, and H. H. Kausch, *SAMPE J.*, 27(6) 30, 1991.
86 C-L. Ong, M-F. Sheu, and Y-Y. Liou, *Proceedings of the 34th International SAMPE Symposium*, 34(1) 458, 1989.
87 *General Composite Repair – Organizational and Intermediate Maintenance: Technical Manual*, Naval Air Systems Command Report No. NAVAIR 01-1A-21, Final Draft, December 1993.
88 A. M. Monib, J. W. Gillespie Jr. and D. J. Wilkins, "Assessment of the Effectiveness of Resin Infusion Repair Techniques on Thick-Section Composites," CCM Report No. 96-27, University of Delaware, 1996.
89 S. P. Wanthal, "Delamination Methodology for Composite Structures," NAWCADWAR-94137-60, Vol. I & II, McDonnell Douglas Co., 1994.
90 Gama, B. A., T. A. Bogetti, B. K. Fink, and J. W. Gillespie Jr., "Processing, Ballistic Testing, and Repair of Composite Integral Armor," *Proceedings of the 32nd International SAMPE Technical Conference*, SAMPE, Boston, MA, November 5–9, 2000.
91 Fink, B.K., S.H. McKnight, C. Newton, J.W. Gillespie Jr., and G.R. Palmese, "Nonpolluting Composites Repair and Remanufacturing for Military Applications: An Environmental and Cost-Savings Analysis," *Army Research Laboratory Technical Report*, ARL-TR-2139. December 1999.
92 Ranganathan, S., S. G. Advani, and M. A. Lamontia, "A Model for Consolidation and Void Reduction during Thermoplastic Tow Placement," *Proceedings of the 25th International SAMPE Technical Conference*, pp. 620-631, October 1993.
93 Pitchumani, R., R. C. Don, J. W. Gillespie Jr., and S. Ranganathan, "Analysis of On-Line Consolidation During the Thermoplastic Tow-Placement Process," in *Heat and Mass Transfer in Composites Processing*, M. K. Alam and R. Pitchumani eds. ASME Press, 1994.
94 Mantell, S. C., and G. S. Springer, "Manufacturing Process Models for Thermoplastic Composites," *Journal of Composite Materials,* Vol.26 (16), pp. 2348-2377, 1992
95 Bastien, L. J. and J. W. Gillespie Jr. "A Nonisothermal Healing Model for Strength and Toughness of Fusion Bonded Joints for Amorphous Thermoplastics," *Polymer Engineering and Science*, Vol. 31 (24), pp. 1720-1730, 1991.
96 Agarwal, V., "The Role of Molecular Mobility in the Consolidation and Bonding of Thermoplastic Composite Materials," Center for Composite Materials Technical Report 91-39, University of Delaware, 1991.
97 Chao, M. and J. W. Gillespie Jr., "The Influence of Healing and Bond line Thickness on Mechanical Performance of Fusion-Bonded Thermoplastic Composite Joints." CCM Technical Report 93-43, Center for Composite Materials, University of Delaware, 1993.
98 Bastien, L. J., J. W. Gillespie Jr., and C. L. T. Lambing, "Strength Prediction of Semicrystalline Thermoplastic Composite Joints Using Dual Film Technology," *Proceedings of the American Society for Composites Fifth Technical Conference*, Technomic Publishing Co., Inc., Lancaster, PA, pp. 59–70, 1990.

99 Wool, R. P., B. L. Yuan, and O. J. McGrarel, "Welding of Polymer Interfaces." *Polymer Engineering and Science*, 1989, Vol. 29, No. 19, pp. 1340–1366.
100 Kline, D. B. and R. P. Wool. "Polymer Welding Relations Investigated by a Lap Shear Joint Method." *Polymer Engineering and Science*, 1988, Vol. 28, No. 1, p. 52.
101 Ersoy, N. B. O. Vardar, B. K. Fink, Gillespie, J. W. Jr. "Effect of Processing Variables on Consolidation and Bonding in Thermoplastic Fiber Placement Process." Center for Composite Materials Technical Report 95-35, 1995.
102 Butler. C. A., R. Pitchumani, J. W. Gillespie, Jr., and A. G. Wedgewood, "Coupled Effects of Healing and Intimate Contact on the Strength of Fusion-Bonded Thermoplastics," in *Proceedings of the 10th Annual ASM/ESD Advanced Composites Conference,* Dearborn, MI. pp. 595-604, 1994.
103 DoD Interface Standard MIL-STD-461E (1999).
104 D. J. Griffiths. Introduction to Electrodynamics. Englewood Cliffs, NJ: Prentice Hall. (1989)
105 Sorathia, U. and D. Beck, "Fire Protection of Glass/Vinyl Ester Composites for Structural Composites," Proceedings of the 41st International SAMPE Symposium and Exhibition, Anaheim, CA, March 1996.
106 Pike, T., M. McArthur, and D. Schade, "Vacuum Assisted Resin Transfer Molding of a Layered Structural Laminate for Application on Ground Combat Vehicles," Proceedings of the 28th International SAMPE Technical Conference, Seattle, WA, pp. 374-380, November 1996.
107 Gillio, E. F., "Co-Injection Resin Transfer Molding of Hybrid Composites," MS Thesis, Department of Mechanical Engineering, University of Delaware, 1998.
108 Gillio, E. F., J. W. Gillespie Jr., R. F. Eduljee, S. G. Advani, K. R. Bernetich and B. K. Fink, "Manufacturing of Composites with the Co-injection process," Proceedings of the 38th AIAA Structures, Structural Dynamics and Materials Conference, Kissimmee, FL, April 1997.
109 Gillio, E. F., S. G. Advani, J. W. Gillespie Jr., and B. K. Fink, "Investigation of the Role of Transverse Flow in Co-Injection Resin Transfer Molding," accepted for publication, Polymer Composites, August 1998.
110 Seemann III, W. H., "Plastic Transfer Molding Techniques for the Production of Fiber Reinforced Plastic Structures," U.S. Patent # 4,902,215, Feb. 1990.
111 Don, R. C., S. H. McKnight, E. D. Wetzel, and J. W. Gillespie Jr., "Application of Thermoplastic Resistance Welding Techniques to Thermoset Composites," Proceedings of the Society of Plastic Engineers, San Francisco, CA, pp. 1295-1299, 1994.
112 Immordino, K. M., "Characterization of the Polysulfone/Epoxy Interphase for Bonding Thermoplastic Composites," MS Thesis, Materials Science Program, University of Delaware, also published as CCM Technical Report No. 96-29, 1996.
113 Don, R. C., J. W. Gillespie, Jr. and S. H. McKnight, "Bonding Techniques for High-Performance Thermoplastic Compositions," U.S. Patent # 5,643,390, July 1, 1997.
114 American Society for Testing and Materials ASTM D-5588, "StandardTest Method Dual Cantilever Beam," ASTM Electronic Media
115 Berry, J. P., *Journal of Applied Physics*, Vol. 34, p. 62, 1963.
116 Smiley, A. J. and R. B. Pipes, Journal of Composite Materials, Vol. 21, pp. 670-687, July 1987.
117 Gillespie, J. W. Jr., L. A. Carlsson, and A. J. Smiley, Composites Science and Technology, Vol. 28, No. 1, pp. 1-15, 1987.
118 Scudamore, M., P. Briggs, and F. Prager, "Cone Calorimetery—A Review of Tests carried out on plastics for the Association of Plastics Manufacturers in Europe," Fire and Materials, Vol. 15, No. 2, pp. 65-84, 1991.

119 Babruaskus, V., "Development of the Cone Calorimeter-A Bench Scale Heat Release Apparatus Based on Oxygen Consumption," Fire and Materials, Vol. 8, No. 2, pp. 81-95, 1984.
120 Brown, R. and Z. Mathys, "Reinforcement and Matrix Effects on the Combustion Properties of Glass-Reinforced Polymer Composites," Composites Part A, Vol. 28A, pp. 675-681, 1997.
121 Scudamore, M J., "Fire Performance Studies on Glass-reinforced Plastic Laminates," Fire and Materials, Vol. 18, No. 5, pp. 313-325, 1994.
122 Sorathia, U., C. Rollhauser, and W. Hughes, "Improved Fire Safety of Composites for Naval Applications," Fire and Materials, Vol. 16, pp. 119-125, 1992.
123 Sorathia, U., H. Teledegas, and M. Bergen, "Mechanical and Flammabilty Characteristics of Phenolic Composites for Naval Applications," 39th International SAMPE Symposium and Exhibition, pp. 2991-3002, April 1994.
124 Sorathia, U. and C. Beck, "Fire Protection of Glass/Vinyl Ester Composites for Structural Applications," 41st International SAMPE Symposium and Exhibition, March 24-28, pp. 687-698, 1994.
125 Cantwell, W. J., and J. Morton, "The Impact Resistance of Composites—A Review," Composites, Vol. 22, No. 5, pp. 347-362, September 1991.
126 Gottesman, T., E. Girshovich, N. Sela, and J. Loy," Residual Strength of Impacted Composites: Analysis and Tests," Journal of Composites Technology and Research, JCTRER, Vol. 16, No. 3, pp. 244-255.
127 Evans, R. E. and J. E. Masters, "A New Generation of Epoxy Composites for Primary Structural Applications: Materials and Mechanics," ASTM STP 937 ed. N. Johnson (American Society for Testing and Materials) pp. 413-436, 1987.
128 Wang, C.J., B. Z. Jang, J. Panus, and B. T. Valaire, "Impact Behavior of Hybrid-Fiber and Hybrid-Matrix Composites," Journal of Reinforced Plastics and Composites, Vol. 10, pp. 356-378, July 1991.
129 Fink, B. K., S. M. Walsh, D. C. DeSchepper, J. W. Gillespie Jr., R. L. McCullough, R. C. Don, and B. J. Waibel. "Advances in Resin Transfer Molding Flow Monitoring Using SMARTweave Sensors." ASME International Mechanical Engineering Congress and Exposition, San Francisco, CA, edited by J. Coulter et al., ASME, pp. 999-1015, November 12-17, 1995.
130 England, K. M., J. W. Gillespie Jr., B. K. Fink, "In-Situ Sensing of Viscosity by Direct Current Measurements," Proceedings of the 1996 ASME International Mechanical Engineering Congress & Exhibition, Atlanta, GA, November 17-22, 1996.
131 B A Gama, T A Bogetti, B K Fink, CJ Yu, T D Claar, H H Eifert, J W Gillespie, Composite Structures, 52, pp. 381-395, 2001.
132 *The Composites & Adhesives Newsletter*, SPI, Vol. 13, No. 3, pp. 14-15, April–June 1997.
133 *Modern Plastics*, March 1998.
134 *Adhesives to 2001*, Freedonia Group Report 897, The Freedonia Group, Inc., May 1997.
135 Report on Audit of Repair of Weapon Systems Containing Advanced Composite Materials, Report No. 92139, Inspector General, Department of Defense.
136 *High Performance Composites*, 1997 Sourcebook, 1997, p. 27.
137 Paul Mehrkam, "Support of Composite Structures on Naval Aircraft," presented at the Second Joint NASA/FAA/DoD Conference on Aging Aircraft, Williamsburg, VA, 31 August–3 September 1998.
138 "Hysol EA 9390," Technical Data Sheet, Dexter Aerospace Materials Division, Pittsburg, CA, November 1996.
139 "Hysol EA 9394," Technical Data Sheet, Dexter Aerospace Materials Division, Pittsburg, CA, April 1994.

140 "Hysol EA 9396/C-2," Technical Data Sheet, Dexter Aerospace Materials Division, Pittsburg, CA, November 1996.
141 "Hysol EA 9695," Technical Data Sheet, Dexter Aerospace Materials Division, Pittsburg, CA, October 1997.
142 J. F. Unser, "Advanced Composites Recycling/Reuse Program," Final Report, WL-TR-95-7014, Wright Laboratory, Armament Directory, Eglin AFB, FL, April 1995.
143 "RQ-1A Predator Unmanned Aerial Vehicle (UAV)," Director, Operational Test & Evaluation, FY 1997 Annual Report, submitted to Congress, February 1998.
144 "High Altitude Endurance (HAE) Unmanned Aerial Vehicle (UAV) Systems: RQ-4A Global Hawk and RQ-3A Dark Star," Director, Operational Test & Evaluation, FY 97 Annual Report, submitted to Congress, February 1998.
145 "Objective Individual Combat Weapons (OICW)," US Marine Corps Science Program Plan for Fiscal Year 1998, Program Element 63640M.
146 B. Cole, "AEGIS PEO SC/AP ATD Proposals," presented at Industry Day, The Johns Hopkins University, Applied Physics Laboratory, 31 July 1997.
147 Major General L. Kenne, "The Affordable Solution – JSF," Joint Strike Fighter Program Office Briefing, April 30, 1998.
148 "JSF-Program: Boeing und Lockheed in Zweikampf um der nästen US-Fighter," *Flug Revue*, January 1997, p.15.
149 "Novel Composite Mast Leads the Fleet into the 21st Century," *Wavelengths*, Carderock Division, Naval Surface Warfare Center, July 1997.
150 Capt. T. Bush, "PEO /SC VISION," presented at The Johns Hopkins University, Applied Physics Laboratory, 31 July 1997.
151 Col. J. F. Kalb, "Opportunities in Partnering 1998," 28 October 1997, Dearborn, MI.
152 D. L. Goodman, C.A. Byrne, and G. R. Palmese, "Advanced Electron Beam Curing and Bonding of Ground Vehicles," *Proceedings of the 43rd International SAMPE Symposium*, Anaheim, CA, May 31–June 4, 1997.